EFFECTS OF VOID REDISTRIBUTION ON LIQUEFACTION-INDUCED GROUND DEFORMATIONS IN EARTHQUAKES: A NUMERICAL INVESTIGATION

by

MAHMOOD SEID-KARBASI

M. Sc., Iran University of Science & Technology, Tehran
B. Sc., Iran University of Science & Technology, Tehran

A THESIS SUBMITTED IN PARTIAL FULFILLMENT OF
THE REQUIREMENTS FOR THE DEGREE OF

DOCTOR OF PHILOSOPHY

in

THE FACULTY OF GRADUATE STUDIES

(Civil Engineering)

THE UNIVERSITY OF BRITISH COLUMBIA
(Vancouver)
March 2009

ABSTRACT

Liquefaction-induced ground failure continues to be a major component of earthquake-related damages in many parts of the world. Experience from past earthquakes indicates lateral spreads and flow slides have been widespread in saturated granular soils in coastal and river areas. Movements may exceed several meters even in very gentle slopes. More interestingly, failures have occurred not only during, but also after earthquake shaking.

The mechanism involved in large lateral displacements is still poorly understood. Sand deposits often comprise of low permeability sub-layers e.g., silt seams. Such layers form a hydraulic barrier to upward flow of water associated with earthquake-induced pore pressures. This impedance of flow path results in an increase of soil skeleton volume (or void ratio) beneath the barrier. The void redistribution mechanism as the focus of this study explains why residual strengths from failed case histories are generally much lower than that of laboratory data based on undrained condition.

A numerical stress-flow coupled procedure based on an effective stress approach has been utilized to investigate void redistribution effects on the seismic behavior of gentle sandy slopes. This study showed that an expansion zone develops at the base of barrier layers in stratified deposits subjected to cyclic loading that can greatly reduce shear strength and results in large deformations. This mechanism can lead to a steady state condition within a thin zone beneath the barrier causing flow slide when a threshold expansion occurs in that zone. It was found that contraction and expansion, respectively at lower parts and upper parts of a liquefiable slope with a barrier layer is a characteristic feature of seismic behavior of such deposits. A key factor is the pattern of deformations localized at the barrier base, and magnitude that takes place with some delay. In this thesis, a framework for understanding the mechanism of large deformations, and a practical approach for numerical modeling of flow slides are presented.

The study was extended to investigate factors affecting the seismic response of slopes, including: layer thickness, barrier depth and thickness, ground inclination, permeability contrast, base motion characteristics and soil consistency.

Another finding of this study was that a partial saturation condition results in delay in excess pore pressure rise, and this factor may be responsible for the controversial behavior of the Wildlife Liquefaction Array, California (USA) during the 1987 Superstition earthquake.

It was demonstrated that seismic drains are a promising measure to mitigate the possible devastating effects of barrier layers.

TABLE OF CONTENTS

LIST OF TABLES

LIST OF FIGURES

LIST OF SYMBOLS

B: Skempton's coefficient for pore pressure ($\Delta u/\Delta\sigma_m$)

CRR: cyclic resistance ratio

CSR: cyclic stress ratio

D_r: relative density

D_B: Depth of barrier layer

D_{50}: mean size of soil grains (50% passing)

e: void ratio

e_{max}: maximum void ratio

e_{min}: minimum void ratio

e_i: initial void ratio

e_c: intergranular void ratio

e_f: interfine void ratio

F.C: fines content

i: hydraulic gradient

I_{RD}: dilatancy index (Bolton, 1986)

LL: liquid limit

LI: liquidity index

μ: fluid dynamic viscosity (e.g., units of N-sec/m^2)

k: soil permeability

$k_{Barrier}$: barrier layer permeability

k_{Sand}: sand layer permeability

k_{FLAC}: mobility coefficient used by *FLAC* for porous medium permeability

v: volume

v_v: volume of voids

V: specific discharge (in *Darcy's* law)

V_p: compression wave velocity

V_s: shear wave velocity

g: the gravitational acceleration

ρ_w: the fluid mass density

K_o: at-rest soil pressure coefficient

K_c: consolidation stress ratio

K_σ: correction factor for overburden

K: bulk modulus

K_w: bulk modulus of fluid (water)

K_{mix}: bulk modulus of air-fluid mixture

M: constrained bulk modulus

K_m: earthquake magnitude correction factor

N: Standard Penetration Test, SPT blow count, *N-value*

N_1: SPT blow count normalized for a reference overburden pressure (i.e.100 kPa)

N_{60}: SPT blow count normalized for theoretical 60% energy

$(N_1)_{60}$: SPT blow count normalized for energy and overburden

$(N_1)_{60\text{-}cs}$: SPT blow count normalized for clean sand

$(N_1)_{60\text{-}UBCSAND}$: *UBCSAND* model *N-value* correlated to basic soil parameters

OCR: overcondoilidation ratio

PI: soil plastic index

Q: empirical constant in *Bolton's* dilatancy Eq.

q: deviatoric stress

R_c: contraction ratio (Verdugo & Ishihara, 1996)

R_f: failure ratio

G: shear modulus

G^e: elastic shear modulus

G^P: plastic shear modulus

G_{liq}: shear modulus of liquefied soil

U: pore pressure

U_e: excess pore pressure

n: porosity

P_a: atmospheric pressure

P'_m: mean effective stress

S_r: saturation

S_r: residual undrained strength

S_{ss}: steady state strength

SPT: Standard Penetration Test

T_B: thickness of barrier layer

T_L: thickness of liquefied soil layer beneath barrier layer

PGA: peak ground acceleration

Y-Flow: vertical specific discharge, vertical flow rate

q_i: element inflow rate

q_o: element outflow rate

t: time

α: ground inclination, sand placement direction

σ: stress

σ_m: mean stress

σ'_{vo}: effective initial verical stress

σ_v: verical stress

σ': effective stress

τ_d: dynamic shear stress

ε: strain

ε_1: axial strain

ε_a: axial strain

ε_v: volumetric strain

$(\varepsilon_v)^*$: Equivalent volumetric strain for an element corrected for mesh size

$(\varepsilon_v)_{max}$: potential maximum volumetric strain

ε^e: elastic strain

ε^p: plastic strain

φ: soil friction angle

φ_{pt}: friction angle at phase transformation condition

φ_{cv}: friction angle at constant volume condition

φ_p: peak friction angle

$\varphi_{cs/ss}$: quasi/*steady-state* friction angle

γ: shear strain

γ^e: elastic shear strain

γ^p: plastic shear strain

γ_w: water unit weight

η: stress ratio, $\tau/\ \sigma'$

μ: *Poisson's* ratio

μ: fluid dynamic viscosity (e.g., units of N-sec/m^2)

ρ: unit density

τ: shear stress

ξ_R: relative state parameter (Boulanger, 2003a)

ψ: dilation angle and *s*tate parameter in e-p' space (Been & Jefferies, 1985)

2D: two-dimensional

ACKNOWLEDGEMENTS

I learned from several years engagement in engineering practice that the best way to grasp cutting-edge technical knowledge is to return to student-status. However, this change in life style was a challenge and indulgent. This could happen with support from many people.

It was my fortune and privilege of working under the supervision and advice of Professor Peter M. Byrne who made it possible for me to do that. I express my sincere appreciation for his continuous support and passion throughout my time at UBC to pursue a fundamental understanding of soil behavior and geomechanics. I would also like to thank Dr. John Howie my co-advisor for his guidance and in-depth comments. Grateful appreciation is extended to Professor D. Anderson, Dr. D. Wijewickreme, Professor O. Hungr, Professor J. Fannin, and Dr. L. Yan who served on my final/qualifying exam committee. Special thanks go to Professor Y. Vaid for his generosity and helpful discussion I had in the early stage of my research. I should also thank Professor L. Finn for his encouragement I received from him.

Financial supports provided by BC-Hydro and National Science and Engineering Research Council of Canada (NSERC) are gratefully acknowledged. I had also the opportunity to work at BC-Hydro office during my studies; I had valuable discussions with Dr. M. Lee, I wish to thank him. I also extend my thanks to Mr. Al Imrie, Mr. K. Lum and his colleagues at the Geotechnical group of BC-Hydro.

Over the last three years, I have returned to my profession at Golder Associates Ltd., where I had constructive discussions with Drs. U. Atukorala, H. Puebla, J. Ji, G. Wu and other colleagues which are acknowledged. In particular, supports and invaluable comments from Dr. Upul Atukorala on the manuscript are deeply appreciated.

I also would like to express my appreciation to Professors H. Poorooshasb, A. Afshar, A. Kaveh and Dr. P. Brenner for their encouragement in perusing my studies.

During the course of this research at UBC, I had helpful discussions with my fellow graduate students Ken, A. Amini, S. Sriskandakumar, S. Park and M. Sanin, I thank them. Particularly, I thank E. Naesgaard for his constant willingness to discuss on mutual interests in variety of technical issues.

In preparation of this thesis, I have used a number of figures from other sources which I hereby acknowledge the permissions granted me by publishers and individuals, namely:

- American Society of Civil Engineers
- American Association for the Advancement of Science
- Professor John Berrill
- BiTech Publisher Ltd.
- University of California at Davis, Center for Geotechnical Modeling
- Earthquake Engineering Research Center
- Elsevier Ltd.
- John Wiley & Sons Inc.
- National Research Council Canada
- Oxford University Press
- Sung-Sik Park
- Professor Shamsher Prakash
- Dr. Alan Rauch
- Somasundaram Sriskandakumar
- Taylor & Francis Group, LLC
- Thomas Telford Ltd.
- Dr. Jun Yang
- Professor Mitsutoshi Yoshimine
- Professor Leslie Youd

The last but by no means the least, I would like to extend my deepest gratitude to my parents and sisters and other family members for their support and patience. Finally, the contribution and understanding of my wife, Naghmeh and my son, Puya and my lovely little daughter, Noura that would not be possible to describe with words are fully appreciated.

Nothing would become true without God willing who gives us every thing. Thanks to God.

DEDICATION:

To my Parents

CHAPTER 1

INTRODUCTION

1 Background

The effects of liquefaction on foundations of buildings, bridges, port facilities, and lifelines continue to cause large economic and human losses after earthquakes. Following the devastating 1964 Niigata earthquake in Japan, and the 1964 Good Friday earthquake in Alaska, USA, many geotechnical earthquake engineering research programs on liquefaction were initiated in Japan and North America. These have provided researchers with better insight into the liquefaction phenomenon and associated failures. Nevertheless, recent earthquakes, e.g. 1994 Loma Prieta (USA), 1995 Northridge (USA), 1999 Kocaeli (Turkey), and 1999 Chi-Chi (Taiwan) indicate the need for further research into the complex behavior of liquefying soils.

Over the past four decades, significant progress has been made in understanding the factors that cause soil liquefaction and the consequences of liquefaction. Initially, progress was largely confined to improving the ability to assess the likelihood of initiation (or "triggering") of liquefaction in clean, sandy soils. As the years passed, researchers became increasingly aware of the liquefaction susceptibility of both silty and gravelly soils, stratification, post-liquefaction shear strength, and the deformation behavior of liquefied soils.

Currently, the area of "soil liquefaction engineering" is emerging as a semi-mature field of practice in its own right (Seed et al., 2003). This area now involves a number of discernable sub-issues, or subtopics, as illustrated schematically in Fig. 1-1. As the figure shows, the first step in most engineering treatments of soil liquefaction is the assessment of "liquefaction potential" or the risk of "liquefaction triggering". Some recent advances in this area have been described by various authors (Youd et al., 2001; Seed et al., 2003; Byrne et al. 2006 and Idriss & Boulanger, 2006).

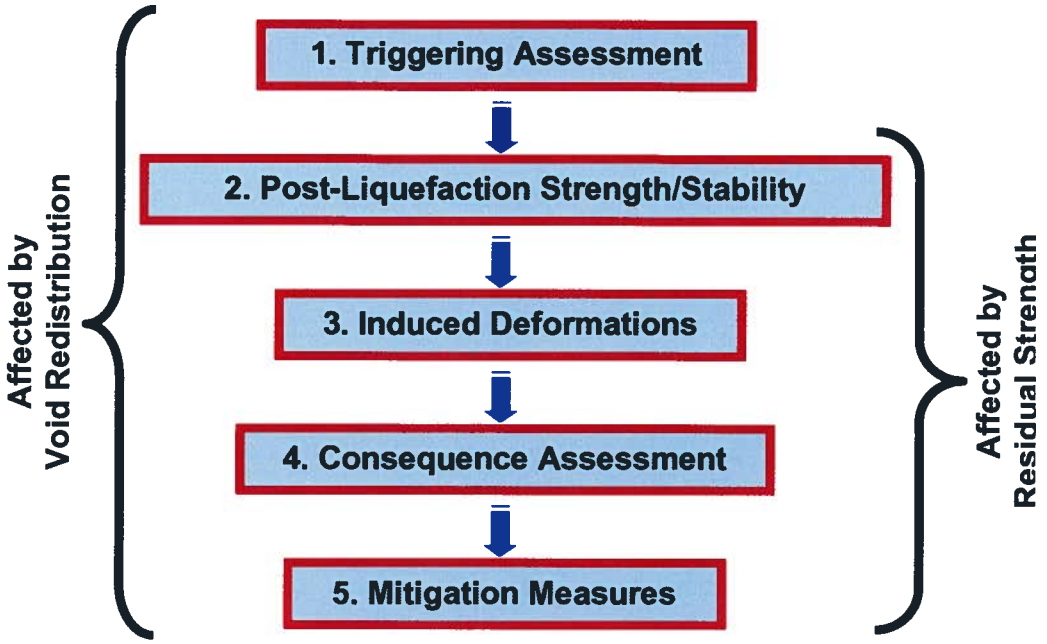

Fi.g. 1-1: Key elements of soil liquefaction engineering

Once liquefaction is determined to be a potentially serious hazard, the next step is to assess the potential consequences of liquefaction. This would likely involve an assessment of the available post-liquefaction strength/stiffness, and the resulting post-liquefaction overall stability (flow-slide). The post-liquefaction strength (residual strength) is a key factor in this process and controls the scope of further actions (see Fig. 1-1). The soil strength is affected by void redistribution, which is involved in all stages of the process (Fig. 1-1) and this is the prime focus of the present study. If post-liquefaction stability is found to be low, then the deformation/displacement potential is large, and engineered remediation measures would be warranted. When the post-liquefaction overall stability is acceptable (no occurrence of flow slide), an assessment of the anticipated displacements is required. This area of research is still immature, and much needs to be done with regards to the development and calibration/verification of the engineering tools and methods. The tools range from empirical and simplified methods (e.g., Youd et al., 2002 and Newmark, 1965) to sophisticated numerical procedures using total stress and effective stress approaches (e.g., Beaty & Byrne, 1999; and Byrne et al., 2004). Similarly, a few engineering tools and guidelines are available for assessing the effects of liquefaction-induced deformations and displacements on the performance of structures and other engineered

facilities. Establishing criteria for "acceptable" performance are more frequently considered in various design standards, though they are not fully developed or well-established.

Finally, in cases where the engineer(s) conclude that a satisfactory performance cannot be counted on, engineered mitigation of liquefaction risk is generally warranted. This is also a rapidly evolving area, and one which is rife with potential controversy. The ongoing evolution of new methods for mitigation of liquefaction hazard is providing an ever-increasing suite of engineering options, but the efficiency and reliability of some of these remain contentious. Accurate and reliable engineering analyses, to confirm the improved performance provided by many of these mitigation techniques, continue to be difficult.

Our understanding of soil behavior, and in particular, liquefaction, has been improved from:

- Observations of field case histories;
- Extensive laboratory testing of soil samples (or elements) under monotonic and cyclic loading conditions;
- Model testing of earth structures under simulated earthquake loading; and
- The development of numerical modeling procedures.

Numerical procedures have proven to be particularly useful tools for studying soil liquefaction and associated displacements caused by earthquakes.

Two key aspects that control the response of an earth structure to earthquakes are:

1. Mechanical conditions.
2. Flow of water within and between soil layers (flow/hydraulic conditions).

Mechanical conditions that encompass soil properties (i.e., soil density, stiffness, strength, etc.) and the characteristics of applied loads (i.e., static and cyclic stresses) are primarily responsible for generating excess pore water pressures during earthquake shaking.

Flow (hydraulic) conditions; i.e., drainage path, soil hydraulic conductivity/permeability and its spatial variation (permeability contrast) within the soil layers control excess pore pressure redistribution during and after earthquakes.

Most, if not all, of the previous liquefaction studies have been based on the assumption that undrained conditions exist within the soil layers (i.e., no flow occurs during or after

earthquake loading) and were therefore focused on the mechanical behavior of soils without accounting for the flow conditions.

Liquefaction was defined in the proceedings of the NCEER (1997) workshop, adapted from Marcuson (1978), as: the transformation of a saturated granular material from a solid to a liquefied state as a consequence of increased pore-water pressure and reduced effective stress. In this thesis, seismic liquefaction refers to a sudden loss in stiffness and strength of soil due to the effects of cyclic loading from an earthquake. The loss arises from a tendency for granular soil to contract under cyclic loading and, if such contraction is prevented or curtailed by the presence of water in the pores that cannot escape, it leads to a rise in pore water pressure and a resulting drop in effective stress. If the effective stress drops to zero (100% pore water pressure rise), the strength and stiffness also drop to zero and the soil behaves as a heavy liquid. However, unless the soil is very loose, it will dilate with the continued application of shear strains and regain some stiffness and strength. The change of state occurs most readily in loose to moderately dense granular soils with poor drainage. As liquefaction occurs, the soil stratum softens, allowing large cyclic deformations to occur. Liquefaction and the associated excess pore water pressures results in a pore pressure redistribution within the soil strata driven by the hydraulic gradient developed both during and after earthquake shaking.

The liquefaction manifestation and consequences are typically divided into two classes:

- Level ground conditions, and
- Sloping ground conditions.

In level ground conditions (without shear stress bias), liquefaction causes settlement from the reconsolidation and sedimentation (Florin & Ivanov, 1961; Scott, 1986; Ragheb, 1994; Butterfield & Bolton, 2003; and Miyamoto et al., 2004). Structures supported on, or in, such liquefied materials, may experience large displacements or (bearing) failure. In sloping ground conditions (with shear stress bias), liquefaction leads to lateral displacements/spreading and, if the available post-liquefaction strength is lower than the driving stresses, it leads to flow failure.

1.1 Post-Liquefaction Strength and Void Redistribution

The state-of-practice for assessing the post-liquefaction strength of soil relies on the pre-earthquake soil properties and an estimation of residual shear strength, S_r, based on values that are back-calculated from case histories (e.g., Seed & Harder, 1990; Mesri & Stark, 1992; and

Olson & Stark, 2002), which involved flow-slides. Fig. 1-2 shows the relationship between the residual strength and the normalized Standard Penetration Test, $(N_1)_{60\text{-}cs}$ for clean sands developed by Idriss (1998) from a reevaluation of Seed & Harder (1990) data. These values are generally much lower than the values derived from laboratory tests on (undisturbed) soil samples, based on the undrained *steady-state* strength approach (Poulos et al., 1985). This issue has been pointed out by a number of investigators (e.g., Seed, 1987; Byrne & Beaty, 1997; Seed, 1999; Kokusho, 2003; and Seid-Karbasi & Byrne, 2004a among others). Fig. 1-3, for example, shows the undrained residual strength of undisturbed samples (solid symbols) from the Lower San Fernando dam that failed after the 1971 earthquake. The test results suggest much larger strengths (at the initial void ratio) than those obtained from back analysis and shown in Fig. 1-2 (shown with an arrow in the figure). The void redistribution mechanism, occurring during, and after, an earthquake, can explain these differences in residual strengths.

The significance of the void redistribution mechanisms was conceptually outlined by Whitman (1985), though detailed experimental studies to investigate the mechanism have been performed only recently. If a liquefiable soil layer is overlain by a (practically) impermeable layer, earthquake-induced liquefaction can cause loosening of a zone of soil below the impermeable layer. The lower portion of the liquefied soil layer densifies as the earthquake-induced pore pressures dissipate by upward water flow, while, the upper portion of this layer loosens because of the impedance to the water flow, caused by the impermeable layer. These local volume changes (void redistribution) can take place without global volume changes, referred to as "Mechanism B" by the NRC (1985).

A soil that is initially dense (comparing to the critical state void ratio) can expand due to water migration (injection) and loosen by Mechanism B, so that its shear strength, S_r becomes smaller than the static shear stresses, and flow liquefaction develops (see Fig. 1-4a). High excess pore water pressures in liquefied zones can cause flow of water into other zones with initially low or negligible excess pore water pressures (see Fig. 1-4b). This can cause loosening of cohesionless soils and the cracking of cohesive soils. This process takes place with both local and global volume changes and was named "Mechanism C" by the NRC (1985). Mechanism C causes reductions in the available shear strength of different soil zones, and can also lead to flow liquefaction in soils that are initially dense (comparing to the critical state void ratio).

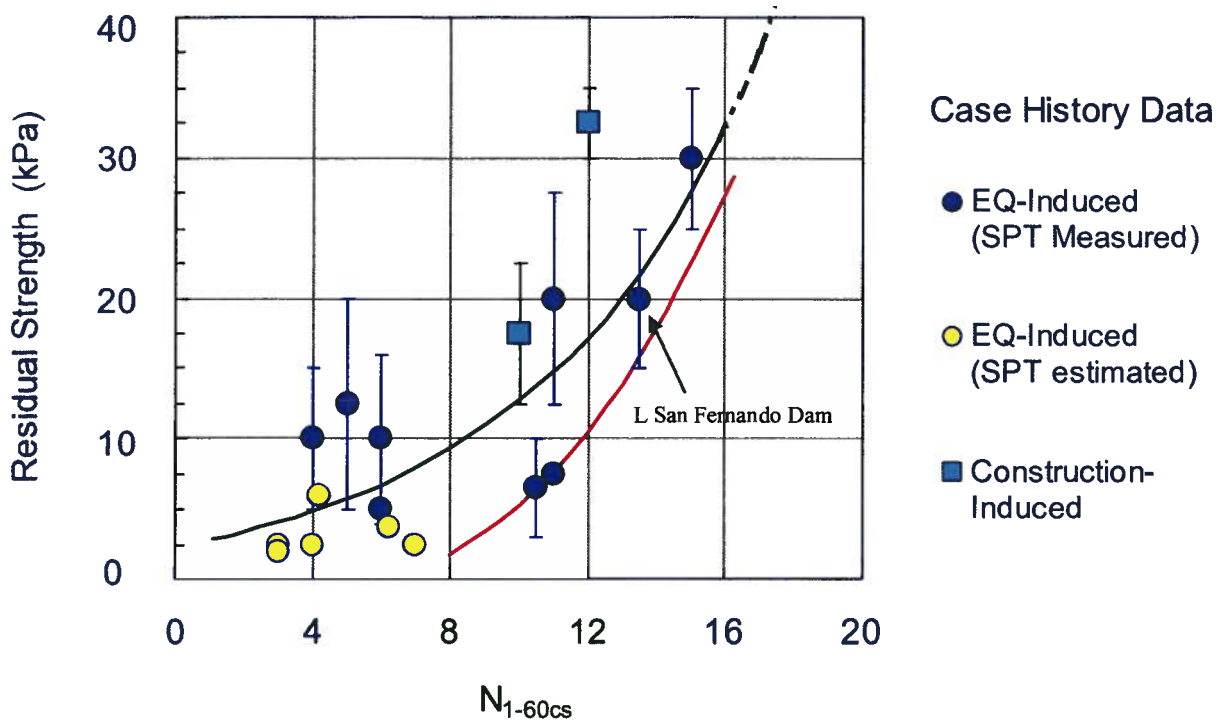

Fig. 1-2: Back calculated residual strength from failed case histories.

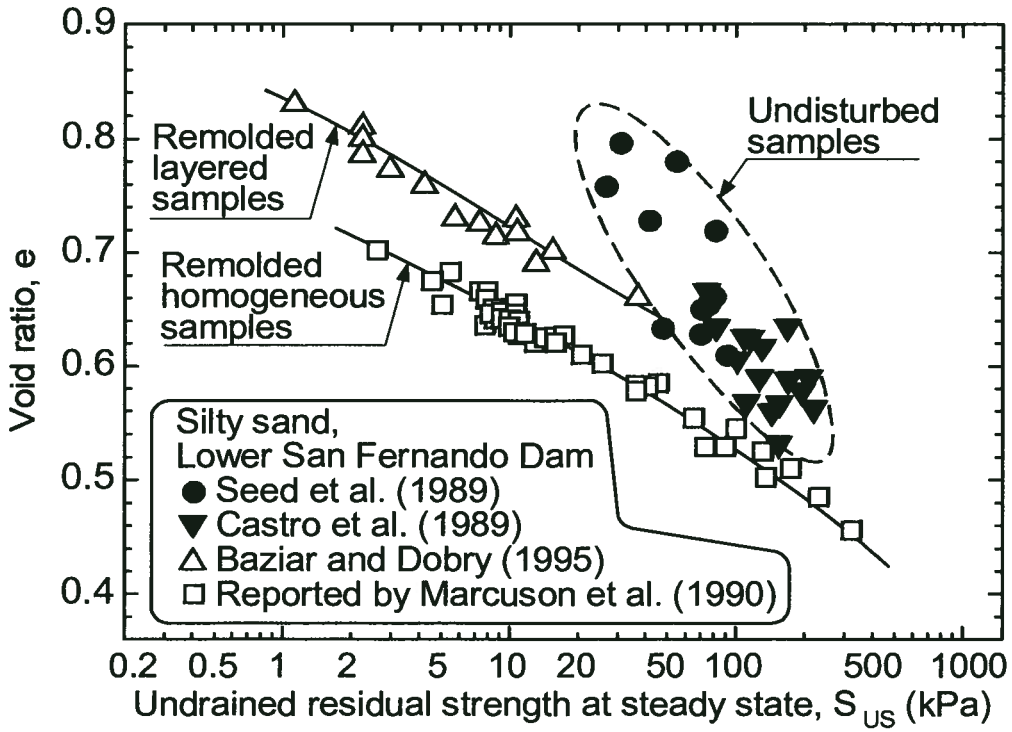

Fig. 1-3: Undrained residual strength of Lower San Fernando dam from laboratory tests (adapted from Yoshimine & Koike, 2005).

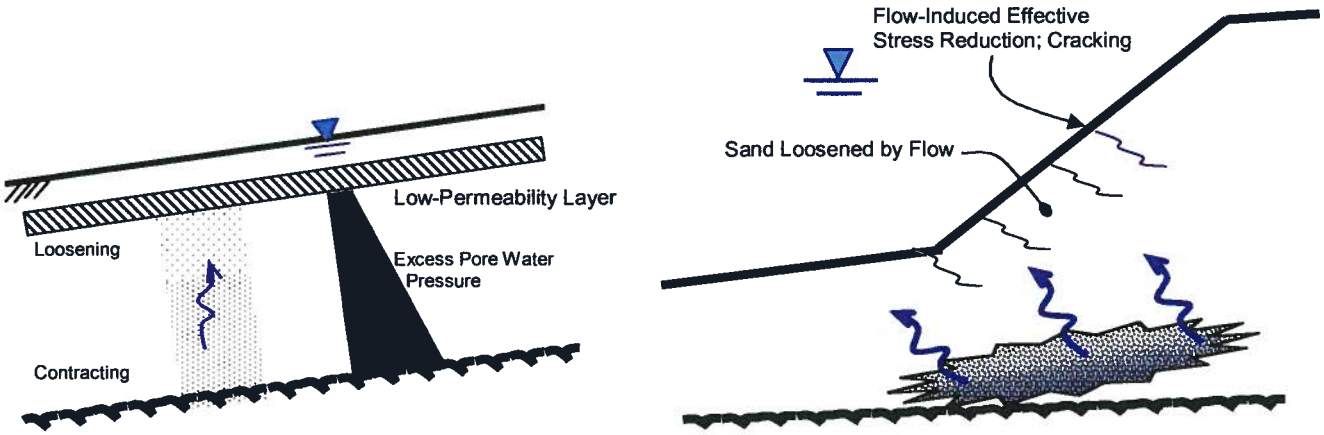

(a) Mechanism B **(b)** Mechanism C

Fig. 1-4: (a) Mechanism B - globally undrained but with local volume changes; (b) Mechanism C - global and local volume changes.

Any of the above mechanisms on their own, or in combination, can cause flow liquefaction. For example, different parts of a given slope may become unstable due to different mechanisms, and together, can cause an overall flow failure.

Experience from past earthquakes indicates that lateral displacements (or spreads) and flow failures have occurred in liquefied soils in coastal regions, river deltas, and near river banks, in many regions of the world, including: Alaska (US), Niigata (Japan), and Turkey. Movements may exceed several meters, even in gentle slopes of less than a few percent (Kokusho, 2003). Submarine slides have been seismically triggered in many regions, as reported by Scott & Zukerman (1972) and by Hamada (1992). More interestingly, lateral spreads or flow slides have occurred not only during, but also after, earthquake shaking has stopped. These large movements are mainly driven by gravity, though the initial triggering of liquefaction is caused by seismic stresses. The slopes in these slides were gentle, normally less than 5° and sometimes less than 1° (Hampton & Lee, 1996).

Although lateral flow failures have been reported in past earthquakes, causing damage to structures, the mechanism leading to large lateral displacements is poorly understood. Sand and silt deposits often comprise many sub-layers as a result of the sedimentation process. A number of researchers have examined the effect of layering on post-liquefaction sliding, including: Scott

& Zukerman (1972); Huishan & Taiping (1984); Liu & Qiao (1984); Elgamal et al. (1989); Adalier & Elgamal (1992); Fiegel & Kutter (1992); Kokusho (1999, 2000); Kulasingam et al. (2001); Malvick et al. (2002, 2005, & 2006); Yang & Elgamal (2002); Kulasingam (2003); Seid-Karbasi & Byrne (2004a, 2007); Sento et al. (2004); Kulasingam et al. (2004); and Yoshimine et al. (2006). Based on physical model tests and site investigations, Kokusho (1999) and Kokusho & Kojima (2002) concluded that liquefaction failure can be caused by the formation of a water-rich zone at the base of a sub-layer leading to a zone of essentially zero strength. Such failures can only be explained by the void redistribution mechanism. This mechanism influences all processes involved in engineering of earth structures for seismic safety (see Fig. 1-1). The use of residual strength from undrained laboratory tests on undisturbed samples (if possible) taken before earthquake shaking does not represent the conditions that develop during and following void redistribution.

The mechanism of void ratio change due to pore pressure redistribution has been addressed in a general sense by pioneering researchers as a possible cause of embankment failure. Terzaghi & Peck (1967) suggested a possible mechanism for pore pressure redistribution in a clay foundation with sand seams under a fill embankment (see Fig. 1-5). The high pore pressures, induced in the middle of the embankment foundation from the construction of the fill, can be transferred by a preferred drainage path provided with higher permeability sand seams, to the critical toe region of the slope, to create instability.

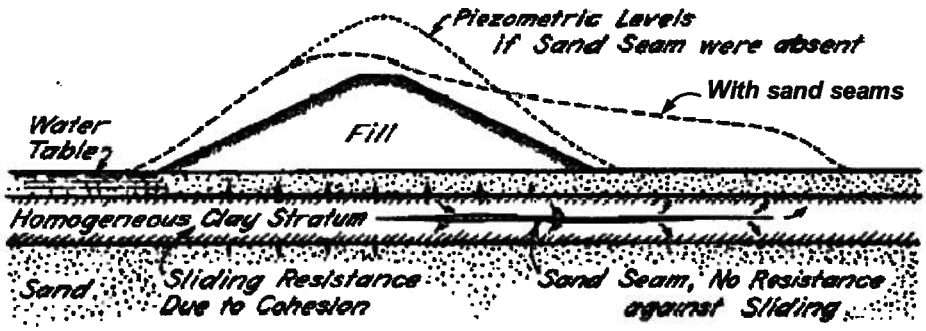

Fig. 1-5: Effect of sand seems on slope stability by transferring consolidation pore pressures (Terzaghi, et al. 1996).

The mechanism of void redistribution needs to be thoroughly understood to be able to account for its effect on the shear strength and deformations. Natural and man-made soil deposits

are heterogeneous in nature. Heterogeneities can be present at both macro and micro scales. Pore pressure increases, due to an earthquake, cause hydraulic gradients and associated pore fluid flow during, and after, earthquake shaking. Stratifications affect the pore fluid flow due to the permeability contrasts. These features can therefore result in void redistribution, with certain zones becoming loosened and others becoming densified. The result is that the state of soil properties changes during, and after, shaking. The change in properties implies that the current practice of estimating a design (residual) shear strength, based on pre-earthquake soil properties, has a high degree of uncertainty. This can lead to highly unreliable or unsafe designs that are not supportable from a fundamental soil mechanics point of view.

A major difficulty associated with either field or physical model data (e.g., centrifuge tests), is the lack of direct measurements of void redistribution. Recent experimental investigations, such as those by Sento et al. (2004) and Yoshimine et al. (2006) using laboratory testing and Malvick et al. (2005) employing physical models have improved the understanding of void redistribution, though they still lack the exploration of all factors and conditions needed for flow failure, especially in regards to the context of volume change driven by flow conditions. Numerical modeling, using the effective stress approach, and based on the fundamentals of soil mechanics, could be a unique alternative that provides good insight into such problems. This approach is used in this thesis to develop a sound explanation for the mechanism.

1.2 Objectives and Scope of Work

The prime objective of this research is to gain a concrete understanding of the void redistribution mechanism involved in the seismic behavior of earth structures and to understand how this mechanism controls the low residual strength and large deformations and/or failures in gentle slopes of sandy soils. To achieve this purpose, a coupled stress-flow analysis procedure based on an effective-stress approach is used to numerically investigate the phenomenon, and the results are supported by observations from field, physical models, and laboratory test data. The insight gained from this study provides a rational basis for designing remedial measures for liquefiable earth structures and foundations.

Several researchers, using physical test models (e.g., Elgamal et al., 1989; Dobry & Liu 1992; Kokusho 2003; Kulasingam 2003; and Malvick 2005) and numerical modeling (Yang & Elgamal 2002) have also noted the occurrence of void redistribution in the presence of inclusions,

but their conclusions were not justified by a framework based on the characteristic behavior of sands in the context of volume changes arising from the flow/hydraulic conditions, as observed in laboratory element testing. Furthermore, these authors did not investigate the required conditions for a flow-slide. Therefore, the mechanism is still poorly understood or unknown.

This thesis presents the results and findings of a numerical study of seismic behavior for layered, infinite, and gentle slopes using the *UBCSAND* constitutive model. The findings are not limited to these situations only. The employed constitutive model can capture the element sand behavior under various boundary conditions (i.e. drained, undrained, or partially drained), subjected to different loading types (i.e. monotonic or cyclic).

The main purposes of this study are:

- To investigate the conditions that lead to development of localized shear strains in slopes of liquefiable soils.
- To explore the characteristic behavior of gentle liquefiable slopes (with a low permeability sub-layer) in earthquakes to obtain a coherent explanation for observations from field data (e.g. low residual strengths).
- To investigate the effects and significance of flow (hydraulic) conditions on the seismic behavior of liquefiable grounds.
- To study the requirements for liquefaction-induced flow-slide.

1.3 Organization of the Thesis

The thesis is organized into nine chapters and six appendices, as follows:

Chapter 1: Background and scope of the research and general organization of the thesis.

Chapter 2: Characteristic behavior of sands in monotonic and cyclic loading, using element test data.

Chapter 3: Review of previous studies on void redistribution and description of a typical case history from past earthquakes as evidence in support of the occurrence of void ratio redistribution.

Chapter 4: Principles of the applied numerical procedure, demonstrating its ability to capture the void ratio redistribution mechanism and associated localization; highlighting of the significance of liquefiable soil permeability and flow conditions in the seismic ground response.

Chapter 5: Exploration of the seismic characteristic behavior of a liquefiable sandy slope comprised of a low permeability sub-layer. Also, the effects of mesh size involved in the numerical analysis are addressed and an approach is proposed for

overcoming the problem. A framework is presented for ascertaining the likelihood of lateral spreading and/or flow slide.

Chapter 6: Investigation of the effects of various factors affecting void ratio redistribution; i.e., barrier depth, liquefiable layer thickness, permeability contrast, barrier thickness, ground inclination, soil consistency, and base motion characteristics.

Chapter 7: Presents the results of a study on the effects of partial saturation conditions on the seismic liquefiable ground response. Presents findings and an explanation for the behavior of the Wildlife Liquefaction Array (WLA) experimental site (California, USA), that was observed during the 1987 Superstition Hill earthquake.

Chapter 8: Provides the results of implementing seismic drain as a remedial measure to mitigate the barrier effects and localization. The seismic drain is shown to be a promising treatment technique to alleviate associated large deformations caused by void redistribution.

Chapter 9: Summarizes the conclusions and makes recommendations for future research.

Appendix I: Current practice for liquefaction assessment and related issues; e.g., fines content.

Appendix II: List of previous studies on void redistribution using physical model testing.

Appendix III: Catalogue of case histories with void redistribution involvement.

Appendix IV: Detailed derivation of bulk modulus for pore fluid of air-water mixture.

Appendix V: Detailed derivation of *Skempton's B* value for partially saturated soils.

Appendix VI: Includes related geotechnical data used to characterize the WLA experimental site.

CHAPTER 2

CHARACTERISTIC BEHAVIOR OF SANDS AND LIQUEFACTION

2. Introduction

Any numerical approach in geo-mechanics is an attempt to simulate the actual behavior of geo-materials under applied loads. Such simulation should capture the behavior of an element of soil under different loading conditions. Therefore, having a clear picture of sand behavior and its complex stress-strain relationship will greatly facilitate the development of a suitable modeling technique.

The main features of sand behavior are stiffness and strength, both before and after liquefaction onset. Liquefaction in granular materials is associated with a large decrease in effective stress due to pore pressure rise during monotonic or cyclic loading. This leads to large reductions in the shear stiffness and strength of soils. In addition, the bulk stiffness of the soil skeleton is greatly reduced upon liquefaction and gives rise to post-liquefaction settlements, as pore water pressures dissipate.

Most studies on liquefaction have focused on its triggering using undrained loading as the relevant condition. However, the sand response is controlled by the skeleton and volumetric constraint of the water as noted by Martin et al. (1975). Since water is essentially incompressible, the constraint is related to whether or not water in the pores has time to flow and cause significant volume change during and after the period of strong shaking. This can greatly affect the soil shear response.

In this chapter, the characteristic behavior of clean sands is presented based on observations from laboratory element testing in monotonic and cyclic loading conditions (drained and undrained). This forms the framework for further discussions on the key factors that affect liquefaction behavior. The partially-drained condition is the most relevant condition to void

redistribution and is discussed in this chapter. Other experimental studies associated with void redistribution are treated in *Chapter 3*.

For earthquake loading a simple shear test can better mimic the induced loading condition (Peacock & Seed, 1968 and Silver & Seed, 1971). During earthquake excitation, the application of cyclic shear stress results in a gradual change of principal stress direction that can be reproduced better in a simple shear test. This test can also better represent the conditions of post-liquefaction flow slide. Nevertheless, most results in the literature are related to compression triaxial tests, traditionally used in many studies; therefore, the test data presented in this chapter are mainly taken from triaxial testing methods.

2.1. Characteristic Behavior of Sands

2.1.1. Monotonic Loading Condition

Sand is a granular material and its particles are packed in states ranging from very loose to very dense as illustrated in Fig. 2-1 in terms of void ratio vs. effective mean stress (this figure is discussed in more detail later in this section). The particles are generally not bonded and, under the action of loading, they tend to rearrange themselves to cope with the load. In contrast to metals, which only exhibit volumetric deformations when the mean stress is changed, sands change in volume if they are sheared.

Many researchers (e.g., Casagrande, 1936; Roscoe et al., 1963; Cole, 1967; Castro, 1969; among others) have extensively investigated the drained static behavior of saturated sands. These studies suggest that sands at very large shear strain, whether starting from an initial loose or dense state, will end up at a unique state (ultimate state) at which point the strength depends only on applied effective stress. Based on this finding, two terms, *"Critical-State"* and *"Steady-State"* were introduced by various investigators (e.g., Roscoe et al., 1968; and Poulos et al., 1981) to describe the ultimate sand strength. In fact, as noted by Poorooshasb (1989) and Verdugo (1992), the two terms are essentially the same and represent the state of a sand element at large shear strain.

Casagrande (1936) observed that sand experiences significant volumetric deformations during shearing. This phenomenon, known as shear-induced volumetric strain, is a key feature of sand behavior.

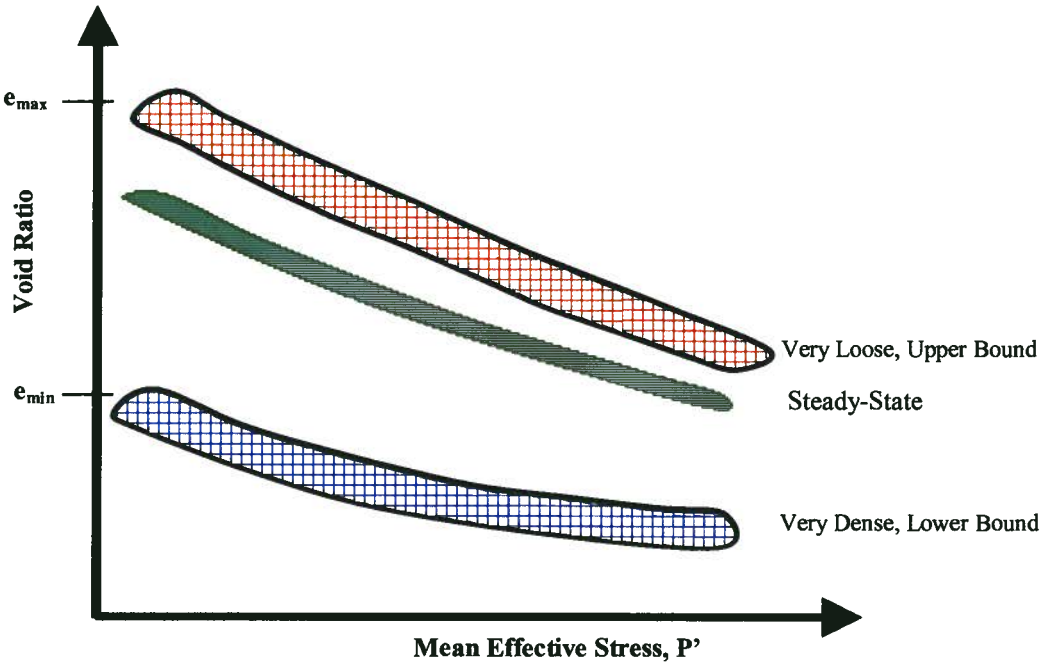

Fig. 2-1: Sand state in e-p' space.

The term, *dilatancy,* was first suggested by Reynolds (1885) to describe the shear-induced expansion. One of the earliest attempts to account for the increased shear strength due to *dilatancy* in dense sand, was made by Taylor (1948), who used the term, *"interlocking"* to describe the effects of *dilatancy*. Fig. 2-2 shows the response of a dense sand to shear loading, in experiments conducted by Taylor (1948), using a direct shear apparatus (Schofield & Wroth, 1968). In fact, the results represent the coupling between shear and volumetric strains, which leads to very different responses to drained and undrained loading. Casagrande (1936), from test results on loose and dense sands using a shear-box device, concluded that sand reaches a limit void ratio wherein deformation continues under constant volume (with corresponding friction angle, φ_{cv}) and load. He postulated the existence of a unique critical void ratio for a sand, that depends only on confining stress, to which loose sands would compress and dense sands would dilate (Fig. 2-3). He defined *"critical density"* or *"critical void ratio"* (the horizontal line, M, in Fig. 2-3b) as a state at which shear deformation occurs without volume change. Wroth (1958) used 1 mm diameter steel beads to justify Casagrande's *"critical void ratio"* concept (Fig. 2-3c).

The typical drained response of a dense sand, at different confining stresses, in terms of stress ratio and volumetric strain vs. axial strain, as observed in triaxial tests, is shown in Fig. 2-6 (Fukushima & Tatsuoka, 1984). The relatively dense sand is seen to initially exhibit a contractive behavior, which changes to dilation with further straining (as depicted in Fig 2-4).

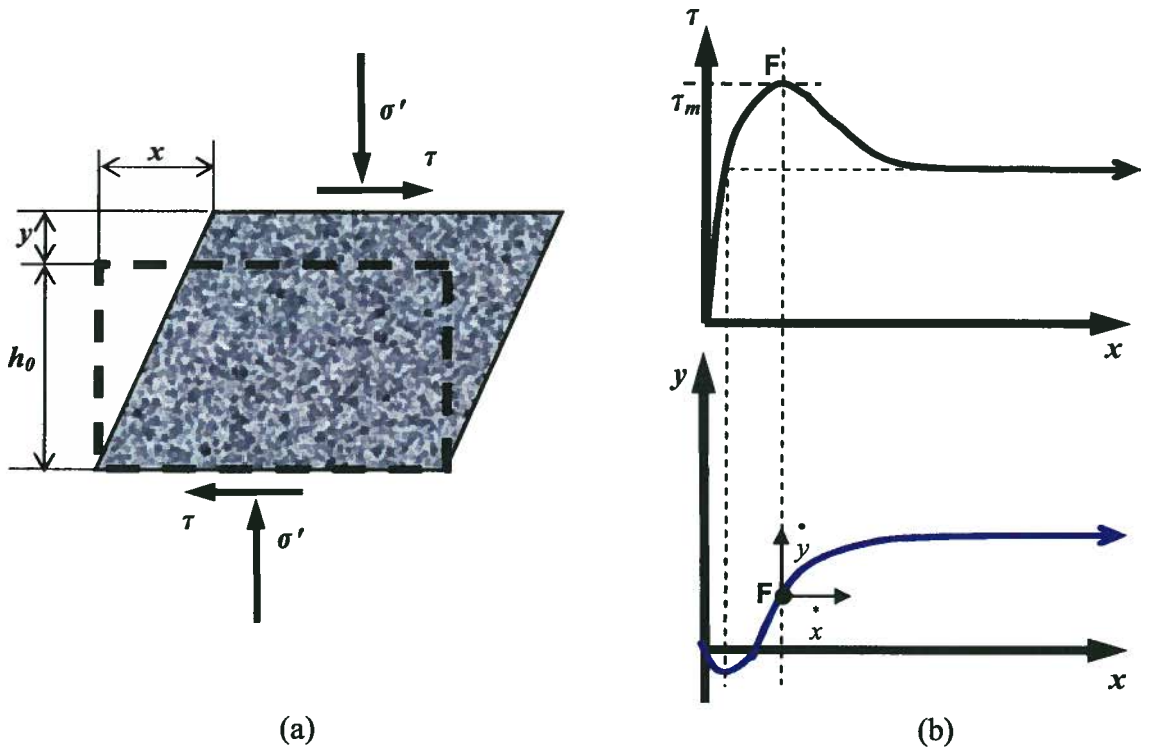

Fig. 2-2: Typical response of a dense sand to shear loading tested by Taylor (1948), (a) sample loading condition, (b) sand response, i.e., lateral and vertical displacements.

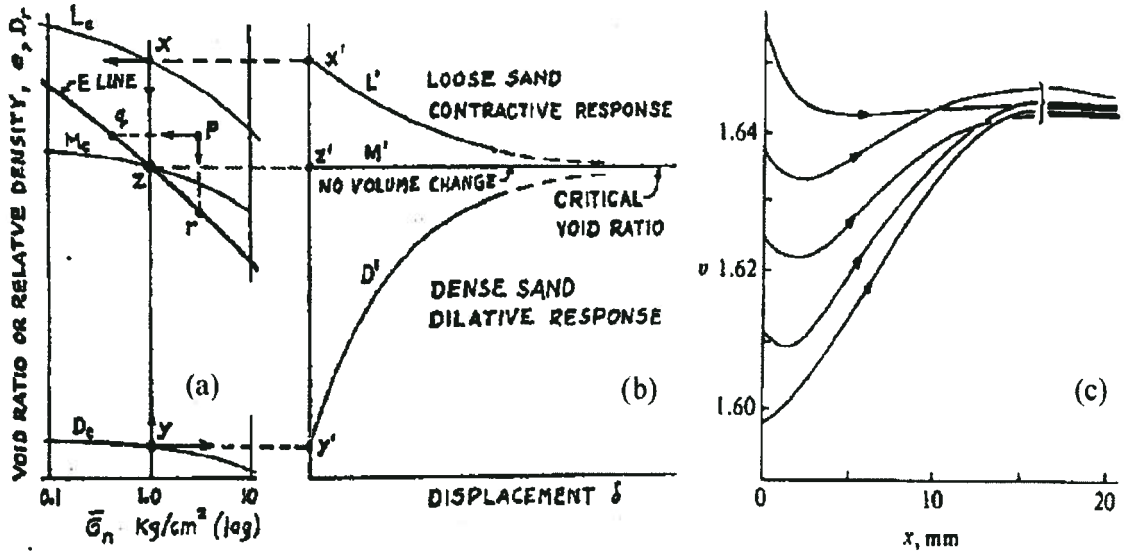

Fig. 2-3: Casagrande's critical void ratio concept: (a) & (b) hypothesis of critical void ratio derived from drained direct shear tests, and (c) Wroth's (1958) simple shear test results on 1 mm diameter steel beads, σ'_n = 138 kPa, in terms of specific volume, v (v = 1+ e) and shear displacement, x (adapted from Park, 2005).

A very loose sand would contract throughout its loading path from the initial loading stages. Lee & Seed (1967) reported similar behavior for sands from drained triaxial tests. The same pattern of sand response is observed in simple shear tests (Fig. 2-5) (Vaid et al., 1981). As may be seen (from Fig. 2-4 and Fig. 2-5) in triaxial tests the strength ratio drops after (axial) strain of about 5% whereas in simple shear tests, drop in strength ratio is noted only for the very dense sand. This difference in response may be due to localization that can occur in triaxial tests (Byrne, 2007).

Roscoe et al. (1958) extended Casagrande's work and defined the *critical-state* as *"the condition at which a soil shears at constant stress and constant void ratio"*. Based on this concept, and using plasticity theory, Roscoe and coworkers (e.g., Wroth, 1958; Schofield, 1959; and Poorooshasb, 1961) founded a school of thought called "Critical-State Soil Mechanics".

Casagrande and his students (e.g., Castro, 1969; Poulos, 1981; and Poulos, et al., 1985) at Harvard University, US, used undrained tests and introduced the *"steady-state"* concept. The steady-*state* strength represents the constant stress condition, while the material is straining at constant volume and constant strain rate, and such behavior is known as (*static*) *flow liquefaction failure* (Poulos, 1981). While the *critical-state* data is commonly related to the drained condition, its corresponding *steady-state* data are mainly derived from undrained tests (Poulos, 1981).

In general, sand behavior can be expressed in terms of void ratio, *e,* and mean effective stress, *p'*, regarding the two extreme limits, namely: a dense state corresponding to a lower bound void ratio, and loose state, corresponding to an upper bound void ratio (Fig. 2-1). In this figure, the band between these two bounds is seen to narrow with increases in *p'* and these limit lines and the steady-state line are not parallel. The two bounds correspond to pure compression (no shear stress), whereas, the *steady-state* (Poulos, 1981) represents a condition at which a soil sample is subjected to a critical stress ratio (deviator stress to effective mean stress, *q/p'*).

The granular material is observed to contract when subjected to shearing if the stress ratio ($\eta = \tau/\sigma$) is lower than a certain value and dilate when the stress ratio exceeds that value. The stress ratio value/line at which the change from contraction to dilation occurs is called *"Phase Transformation"* ratio/line (Ishihara et al., 1971 and Ishihara, 1993). This concept is illustrated in Fig. 2-6 showing that when the mobilized shear stress ratio, η, exceeds this particular state (sin φ_{pt}), the material dilates.

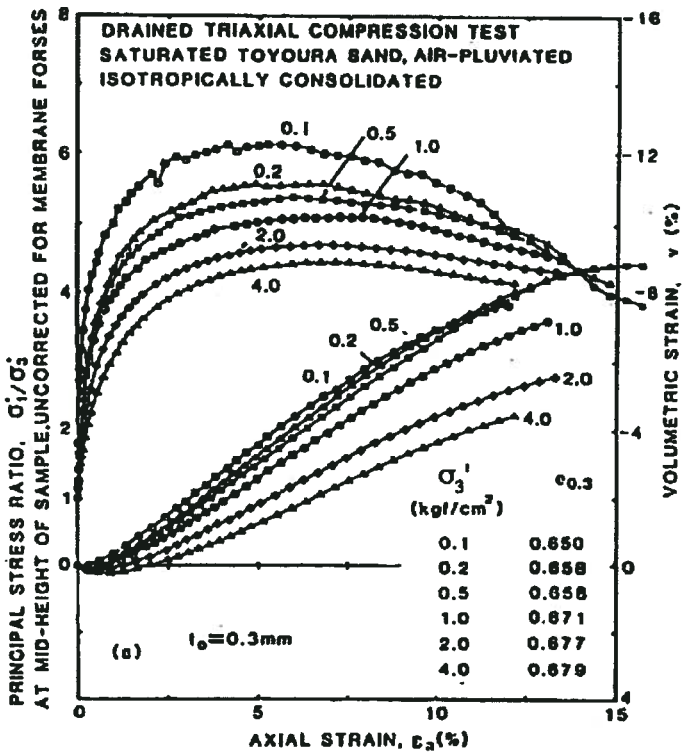

Fig. 2-4: Monotonic drained test results of Toyoura sand in terms of stress ratio and volumetric strain vs. axial strain (Fukushima & Tatsuoka, 1984).

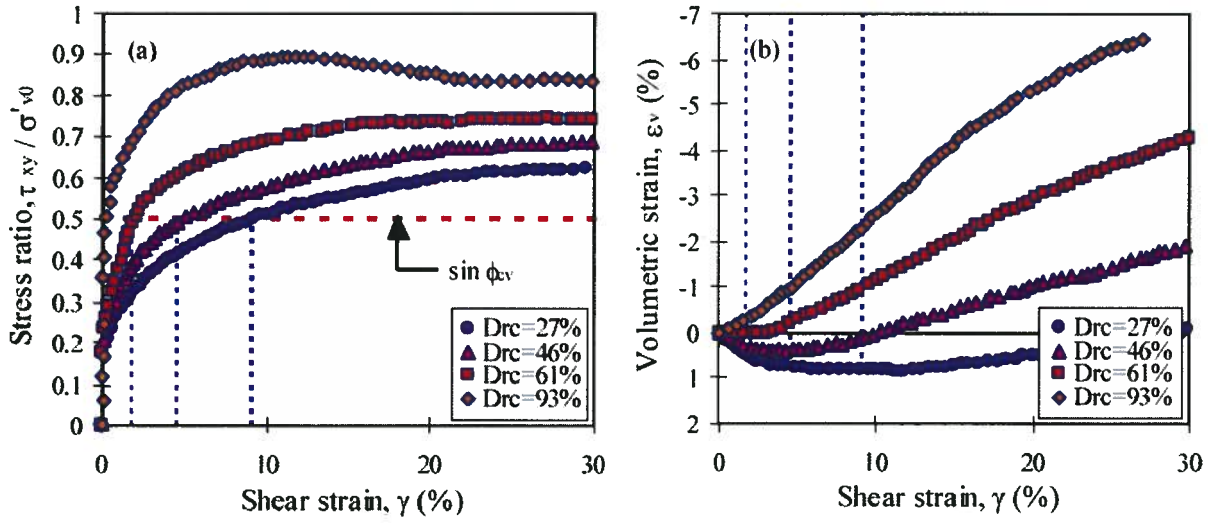

Fig. 2-5: Response of Ottawa sand in drained monotonic simple shear test, reported by Vaid, et al. (1981) in terms of: (a) stress-strain; and (b) volumetric strain vs. shear strain (adapted from Park, 2005).

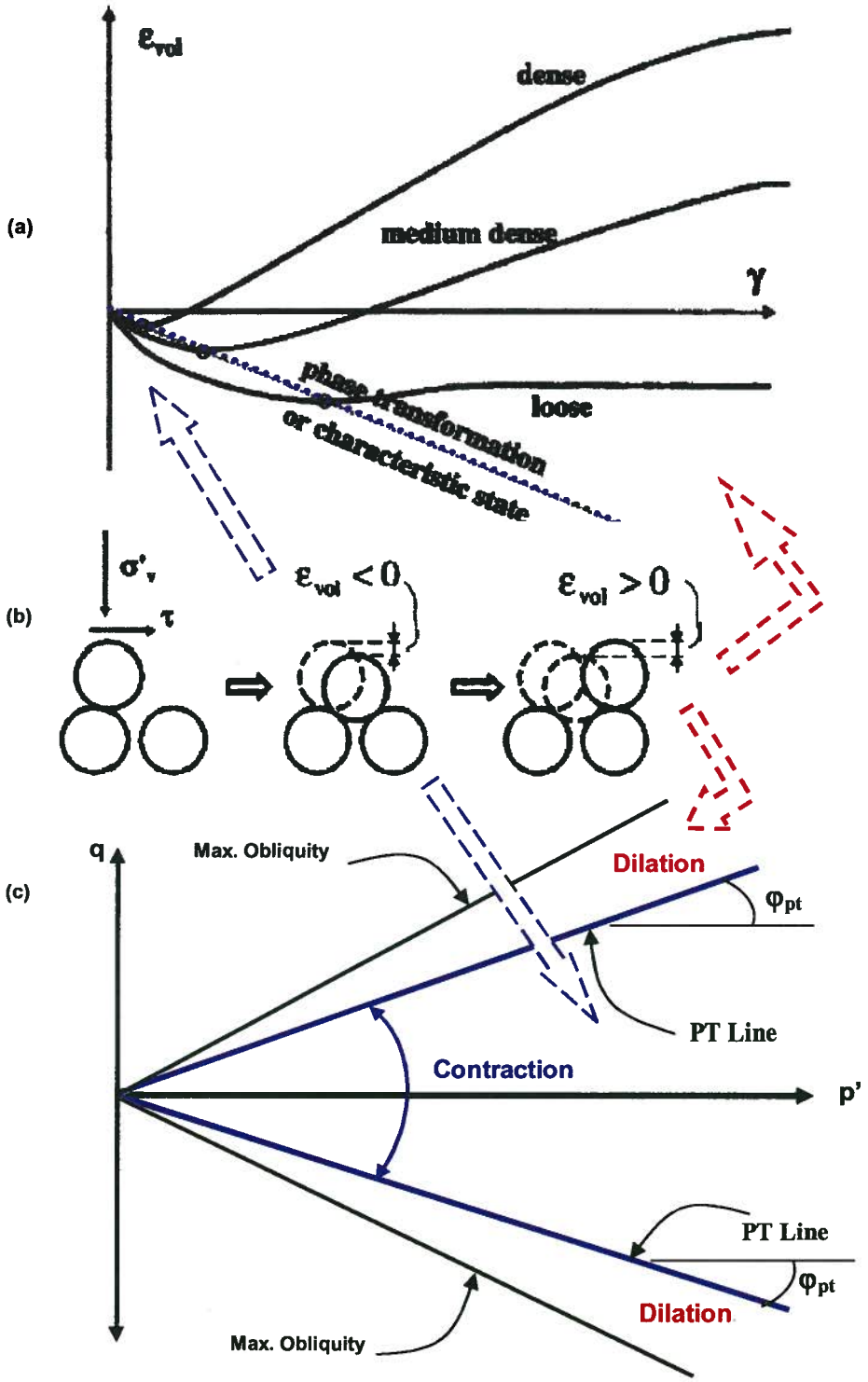

Fig. 2-6: Typical dilation and contraction regions for sands: (a) in strain space, ε_v vs. γ; (b) grains distortion; and (c) stress space, q vs. p'.

Fig. 2-7 shows the stress paths for a tailings sand tested in the undrained condition with different initial state variables, i.e., relative density, confining stress, and shear stress bias (K_c),

along with the *PT* line (Vaid & Sivathayalan, 2000). It indicates that before the commencement of *Phase Transformation* state, shear-induced excess pore pressure increases, whereas it decreases after *PT* state due to material dilation.

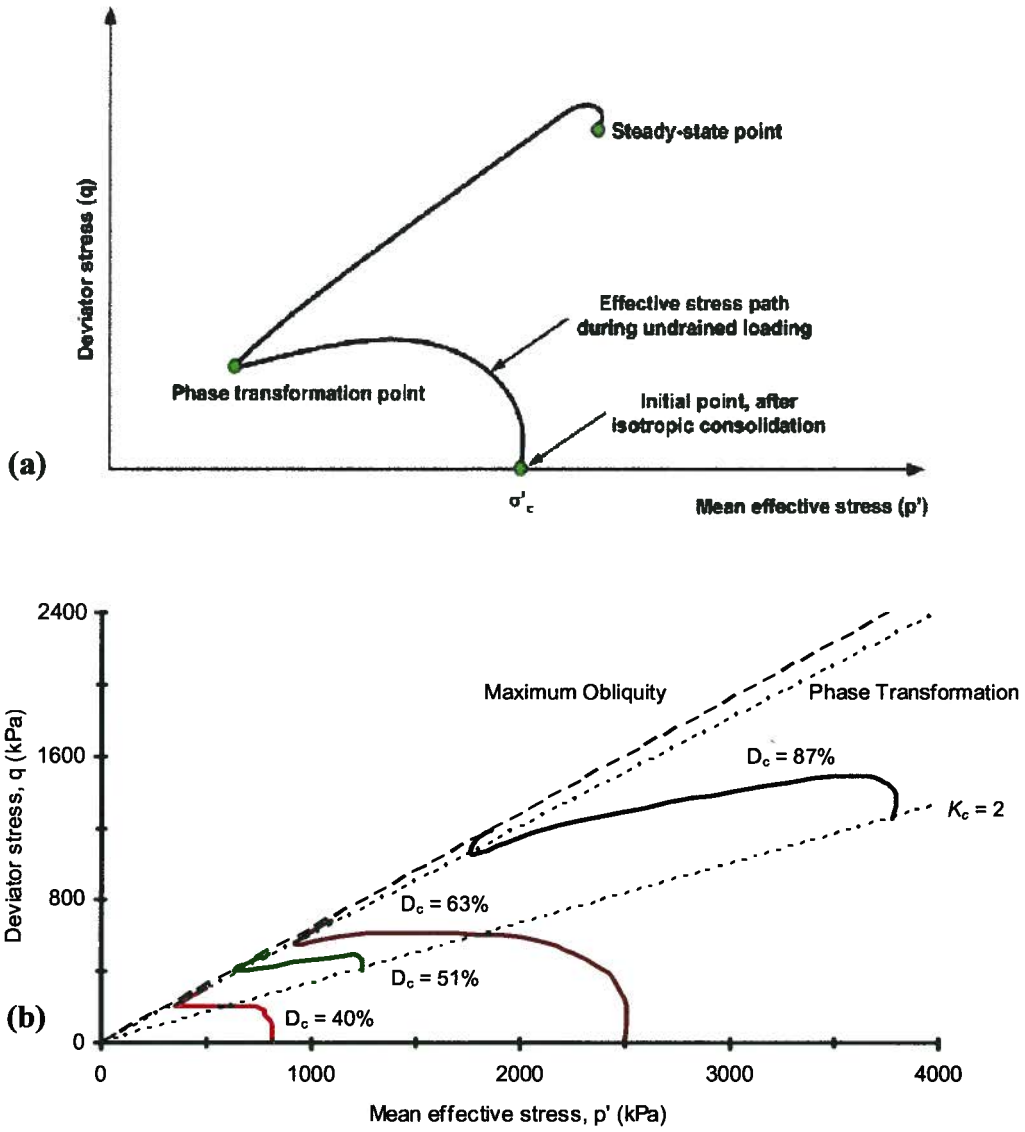

Fig. 2-7: Stress path and phase transformation line for a tailings sand, showing its independence from initial state variables, i.e., void ratio, confining stress, stress ratio, K_c: (a) key diagram, and (b) test results ($q = (\sigma_v - \sigma_h)/2$, $p' = (\sigma_v + \sigma_h)/2$ (data from Vaid & Sivathayalan, 2000).

The *Phase Transformation* state separating shear induced contraction and shear induced expansion states is well established in the literature (e.g., Bishop 1966; Castro, 1975; Hanzawa,

1980; Been et al., 1991; Konrad, 1990 and Vaid & Thomas, 1995). In addition, test data from triaxial and hollow cylinder tests suggests that the *Phase Transformation* state (*PT*) line is a characteristic property of a granular material and is essentially independent of initial variables, stress path, and the shearing mode (e.g., Vaid & Sivathayalan, 1996; and Uthayakumar, 1996). Negussey et al. (1988) and Vaid & Thomas (1995) demonstrated that friction angles, at the phase transformation state ϕ_{pt}, with constant volume condition, ϕ_{cv} and *steady-state*, ϕ_{ss} all are identical.

In fact, during undrained loading, the excess pore pressure reflects the contraction tendency of (loose) granular soils when subjected to shearing. This leads to effective stress reduction, and as soil stiffness is a stress-level dependent property, this reduction results in material softening. The strain softening behavior following initial peak shear strength is considered as liquefaction condition by NCR (1985). Fig. 2-8 shows a typical response of dense

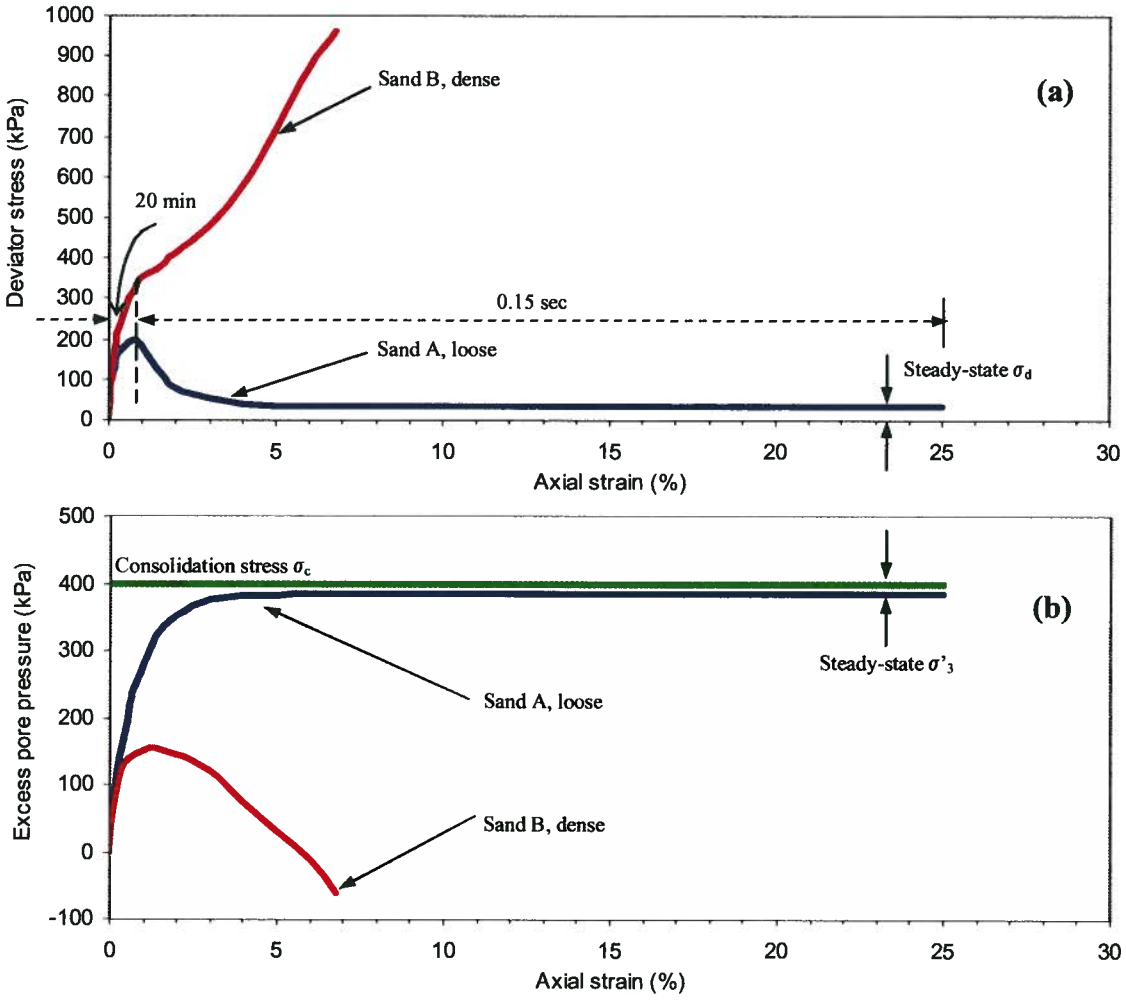

Fig. 2-8: Characteristic behavior of dense and loose sands in a monotonic undrained stress-controlled triaxial test: (a) deviator stress vs. axial strain; (b) excess pore pressure vs. axial strain

and loose sands to undrained monotonic loading as observed by Castro (1969). He conducted stress-controlled triaxial tests on two sands at different void ratios (called sand A and B) at the same confining stress. Sand A exhibited a continuous increase in excess pore pressure during shearing (Fig. 2-8b) with sudden strength loss after a peak. Sand B showed a strain-hardening response (after initial contraction), with decreasing excess pore pressure that became negative, and strength increased to values even higher than those obtained in the drained condition. Other investigators, e.g., Vaid & Sivathayalan (1996) performed simple shear tests (as shown in Fig. 2-9) and reported the same effect of density (void ratio) on the undrained behavior of sands.

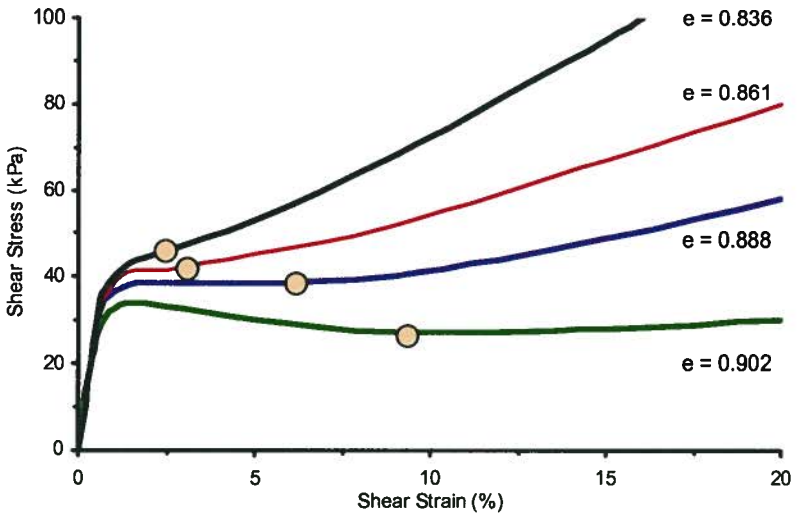

Fig. 2-9: Effect of density on undrained stress-strain behavior of water pluviated Fraser River sand in simple shear test with σ'_{vc} = 200 kPa; solid dots denote *PT* condition (data from Vaid & Sivathayalan, 1996).

2.1.2 Stress Path, Anisotropy, and Fabric

Stress-strain response and strength of sand at a given state (i.e., *Dr* and σ_c) also depends on loading path and direction of principal stresses, as addressed by many researchers (Arthur & Menzies, 1972; Bishop, 1971; Kuerbis & Vaid, 1989; Vaid & Thomas, 1995; Riemer & Seed, 1997). Different responses of sand can be due to the inherent material properties or the anisotropic consolidation loading (Wijewickreme & Vaid, 1993).

Vaid & Sivathayalan (2000) reported data from a hollow-cylindrical torsion, HCT test (Fig. 2-10) and demonstrating that a given sand exhibits a wide range of behavior (dilative to contractive) depending on the principal stress direction relative to sand placement direction

(angle of α.). In this figure where $b = (\sigma_2 - \sigma_3)/(\sigma_1 - \sigma_3)$ the condition of $b = 0$, $\alpha = 0°$ and $b = 1$, $\alpha = 90°$ represent triaxial compression and extension test conditions that give the upper and lower bounds of shear strength, respectively. At a given initial state, a gradual transformation of the sand response occurs from dilative to strain softening, reflecting the sole influence of α, as it increases from zero to 90° at constant $b = 0$ (Uthayakumar & Vaid, 1998).

Particle orientation and particle contacts within the sand matrix is referred to as the fabric (Oda, 1972; Oda et al., 1978). Various sample placement techniques, i.e., moist tamping (MT), air pluviation (AP), and water pluviation (WP) give rise to a considerable different behavior. The moist tamped sample shows the lowest strength and the water pluviated sample shows the highest strength (see Fig. 2-11). However, Mulilis et al. (1977) reported that cyclic undrained strength (in terms of *CRR*) from CT tests for MT samples are higher, compared to the resistance in AP samples.. Data from cyclic simple shear tests (Sriskandakumar, 2004) suggests that WP samples exhibit greater *CRR* than that of AP samples. Other investigators (e.g. Ishihara, 1996) have also noted the effects of sample placement method on sand liquefaction resistance.

As mentioned earlier, regardless of these contributing effects, the contractive and dilative response, before and after the *phase transformation* condition, respectively, is a characteristic behavior exhibited by sands in various conditions and fabrics.

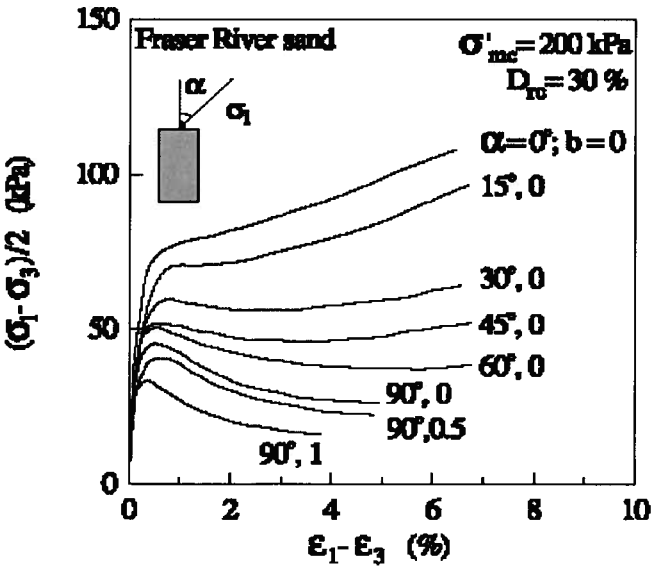

Fig. 2-10: Fraser River sand respose change due to major principal stress rotation in undrained HCT test: $b = (\sigma_2 - \sigma_3)/(\sigma_1 - \sigma_3)$ (Vaid & Sivathayalan, 2000).

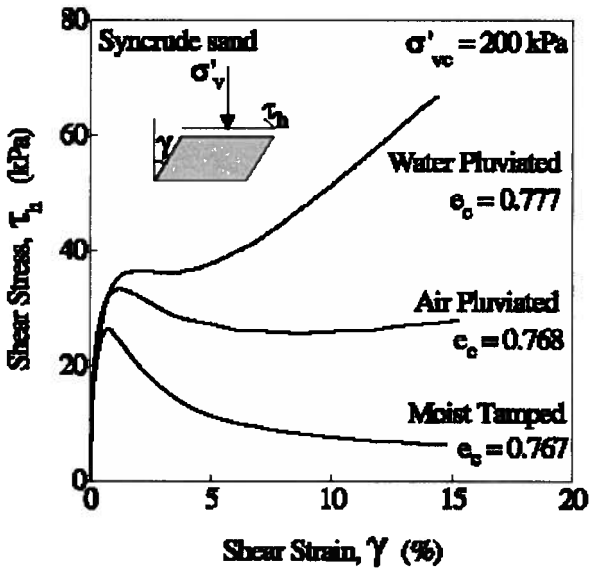

Fig. 2–11: Effect of fabric on undrained monotonic response of Fraser River sand with nominal D_r = 40%, in simple shear test (Vaid et al., 1995).

2.1.3. Cyclic Loading Condition

Liquefaction may also occur during dynamic (cyclic) loading due to the material contractive response. Laboratory strain-controlled drained cyclic simple shear tests on sand by Silver & Seed (1971), Seed & Silver (1972), Youd (1972), Martin et al. (1975), and Finn et al. (1982) have shown that a progressive decrease in volume occurs with the applied number of load cycles. When the test is conducted in the undrained condition, the tendency of the soil towards contraction results in the generation of excess pore pressure. Similar to the monotonic condition, the skeleton controls the sand response and the pore fluid contributes as a volumetric constraint.

Silver & Seed (1971) and Youd (1972) performed drained cyclic tests and concluded that the level of confining stress does not have a significant effect on volumetric compression and that the volumetric strains also increase linearly with increasing cyclic strain amplitude. Youd (1972) reported that the frequency of shear strain application has no effect on the shear-induced volumetric compression.

Fig. 2-12 presents the results of drained strain-controlled cyclic simple shear, *CSS,* tests performed on air-pluviated Fraser River sand from a study reported by Wijewickreme et al. (2005). The sand samples had Dr = 40% and were subjected to a cyclic shear strain amplitude,γ, of 2%. As may be seen from stress-strain curve (Fig. 2-12a), the material shows softer response in the first time loading; however, over the cycling, the larger shear strain amplitude causes more degradation. Fig. 2-12b and Fig. 2-12c indicate that shear-induced volumetric strain is accumulating (with decreasing rate) upon loading and unloading during cyclic shearing and reaches to more than 2.5% after 6 cycles.

The effects of Dr on sand behavior in the drained cyclic loading condition can be seen from Fig. 2-13, which compares the sand response to cyclic loading with 4% shear strain amplitude at loose (Dr = 40%) and dense (Dr = 80%) states. From Fig. 2-12b and Fig. 2-13b, it is inferred that an increase in shear strain amplitude results in larger volumetric strain. This is in agreement with findings by Martin et al. (1975) that the shear-induced volumetric strain is proportional to the applied cyclic shear strain amplitude. In contrast to the loose sample, the dense sample shows significant dilation (after *PT*) during loading cycles (see Fig. 2-13c) and relatively small cumulative volumetric strains. As can be seen in Fig. 2-13b, the dense sample also shows a progressive increase in cumulative volumetric strain with the number of shear cycles but to a lesser extent compared with loose sand (e.g. $\varepsilon_v < 0.5\%$ after 2 cycles comparing to

$\varepsilon_v > 2\%$ in the loose case). Although dense sands may dilate during a portion of a cycle of loading, the overall effect is a reduction in volume during any cycle of loading and a net contraction in volume with number of cycles as seen in Fig. 2-13b. This observation is also in accord with the undrained cyclic shear response of sands where the excess pore water pressure gradually increases with the number of cycles, despite the larger dilation spikes in the loading cycles for dense sands (see Fig. 2-14).

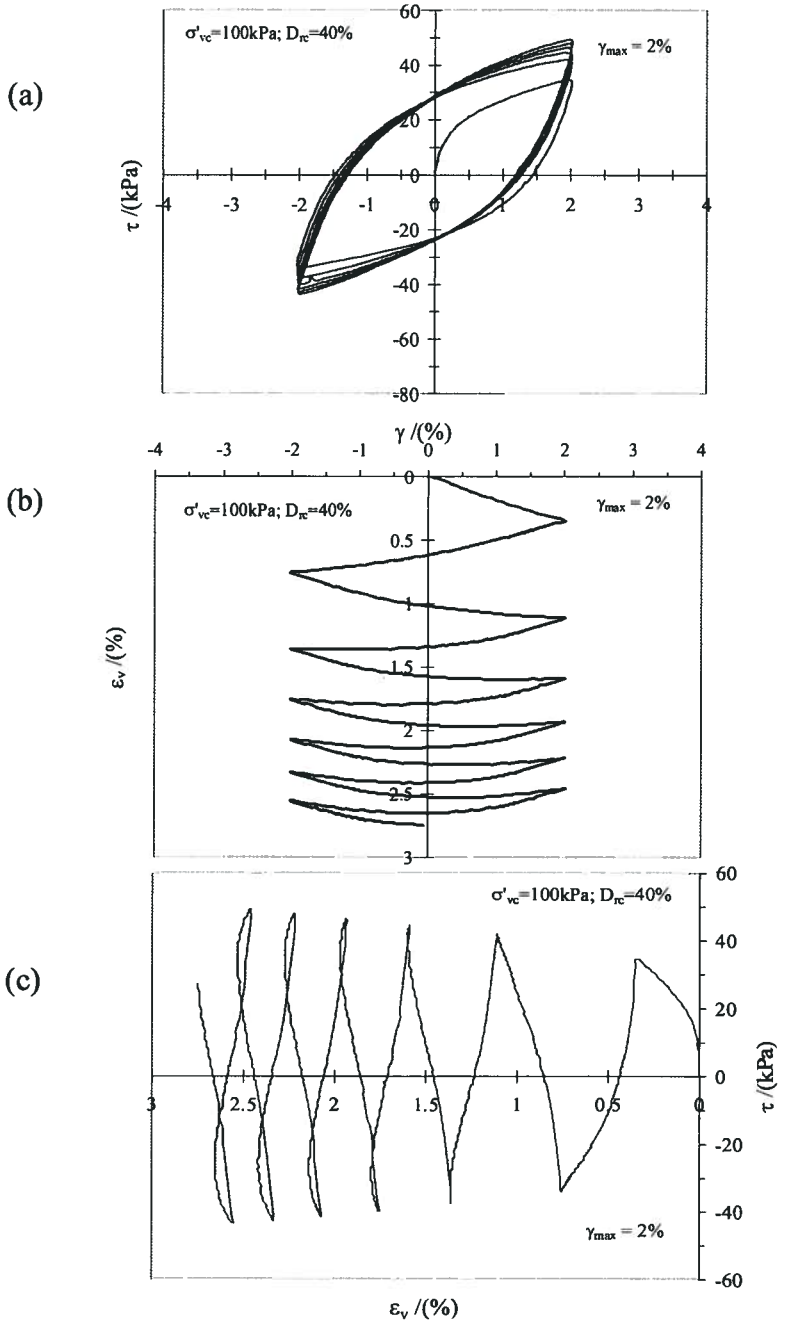

Fig. 2-12: Cyclic drained simple shear response of loose Fraser River sand D_r = 40% in terms of (a) stress-strain, (b) & (c) volumetric strain vs. shear strain and shear stress, respectively (Sriskandakumar, 2004).

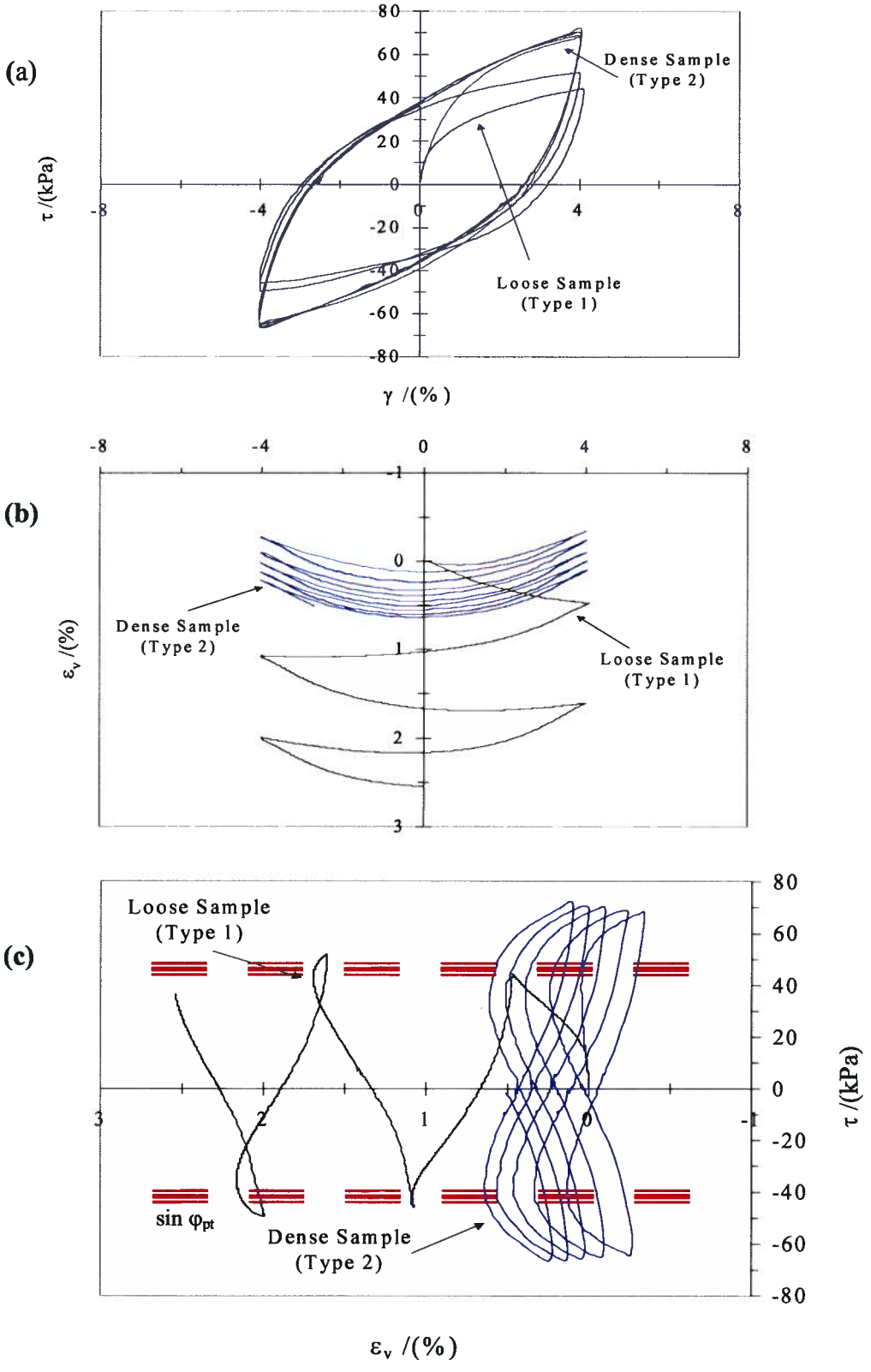

Fig. 2-13: Responses of dense and loose samples of air-pluviated Fraser River sand in cyclic drained simple shear test in terms of (a) stress-strain, (b) & (c) volumetric strain vs. shear strain and shear stress respectively (modified from Sriskandakumar, 2004).

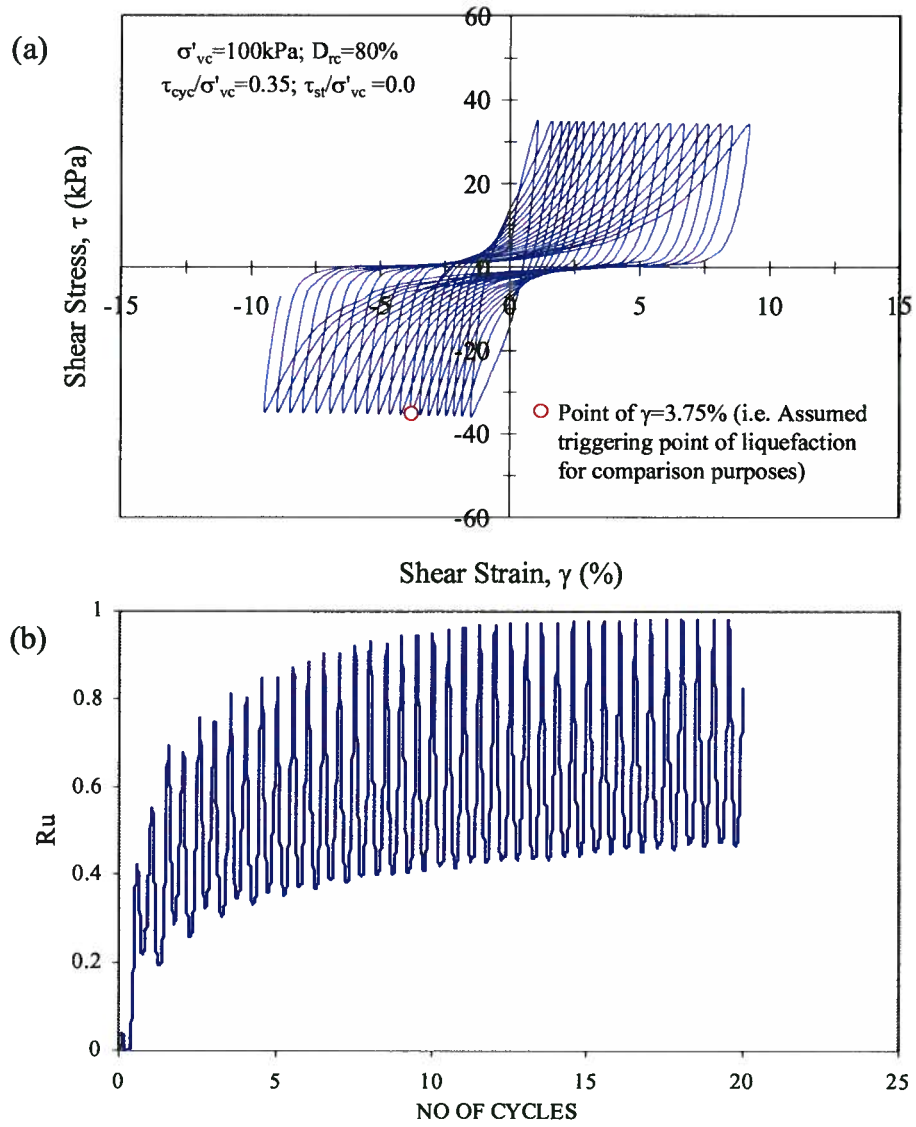

Fig. 2-14: Responses of dense air-pluviated Fraser River sand in cyclic undrained simple shear test in terms of (a) stress-strain, (b) R_u vs. No. of cycles.(Sriskandakumar, 2004).

Commonly, undrained cyclic tests, i.e., cyclic triaxial (CT) test, cyclic simple shear (CSS) test, and the cyclic hollow-cylindrical tortional (CHCT) test have been extensively utilized by many researchers to investigate soil liquefaction triggering (e.g., Seed & Lee, 1966; Finn & Vaid, 1971; Ishihara, 1972; and Vaid & Chern, 1985, among others). As mentioned earlier, with regards to the stress path that can be applied during testing, the CSS test and the CHCT test can better mimic the change of shear stress (and principal stress) direction that occurs during an earthquake excitation. In any case, most of the test data available in the literature is from CT tests.

Fig. 2-15 shows the results of an undrained cyclic simple shear test on air-pluviated Fraser River sand of D_r = 44% (Sriskandakumar, 2004). The stress path followed is shown in Fig. 15a where it may be seen that starting from an initial vertical effective stress of 200 kPa, the effective normal stress drops with each cycle until the *phase transformation* line (denoted by dashed line), or constant volume friction angle $\varphi_{cv} \approx 33°$ is reached after 4 cycles. Once this has occurred, loading and unloading takes place close to the φ_{cv} line, with loading involving an increase in effective stress and unloading involving a decrease in effective stress. It may be seen from Fig. 2-15b that the shear stress-strain response is stiff for a number of cycles in the pre-liquefaction stage, with shear strain less than 0.2%, followed by an abrupt change to a post liquefaction stage with very much softer response and strains greater than 15%.

This typical liquefaction response is illustrated in more detail in Figure 2-16 schematically where it is divided into five phases. During phase 1 prior to liquefaction, the stress path is below the *PT* line (before point A) and pore water pressure rises gradually causing the soil stiffness to decrease slowly upon cyclic loading. Once the *PT* line is reached (phase 2), further loading causes dilation as the stress point moves up just above the *PT* line (point B). Upon unloading (phase 3), the stress point drops slightly below the *PT* line and the soil contracts, driving the stress point back to the origin or zero effective stress (momentarily R_u =100%) and liquefied state (phase 4). Upon reloading (phase 5) the soil dilates, moving up just above the *PT* line gaining strength (de-liquefies). In subsequent unloading and reloading cycles, the pattern repeats itself. Note that although the soil liquefies during cyclic unloading, it recovers its *critical-state* strength at large strain as it is loaded. The post-liquefaction strength and stiffness depends very much on its density. Higher densities will have much higher post liquefaction stiffness and *critical-state* strengths. The cyclic strains are small while the stress point is below *PT* line and become large once the stress point reaches and exceeds *PT* line.

The same characteristics for undrained cyclic sand response was reported by Ishihara (1996) using cyclic hollow cylinder test with a lateral deformation constraint that reproduces the infinite level-ground condition (no axial and lateral strain). He showed that the increase of excess pore water pressure and liquefaction bring a sample (from an anisotropically consolidated stress condition, $K_o \neq 1$) to the isotropic stress condition (K_o = 1). Fig. 2-17 shows the test results of a sample of Toyoura sand with D_r = 55% anisotropically consolidated to a vertical stress of σ'_{vo} = 100 kPa and a lateral stress σ'_{ho} = 50 kPa (K_o = 0.5), and then subjected to 10 cycles of uniform

torsional stress with an amplitude of τ_d = 15 kPa. It may be seen from Fig. 2-17b that the shear strain, after 9 cycles increases rapidly associated with high excess pore water pressure ratio, R_u (Fig. 2-17d). Fig. 2-17c shows that the lateral stress ratio, K_o continues to increase during cyclic loading until the lateral stress becomes equal to the initial vertical stress (K_o = 1.0). This is accompanied by the concurrent build-up of pore pressure which also becomes equal to the initial vertical stress. Same finding was observed by Vaid & Chern (1985) from cyclic triaxial testing.

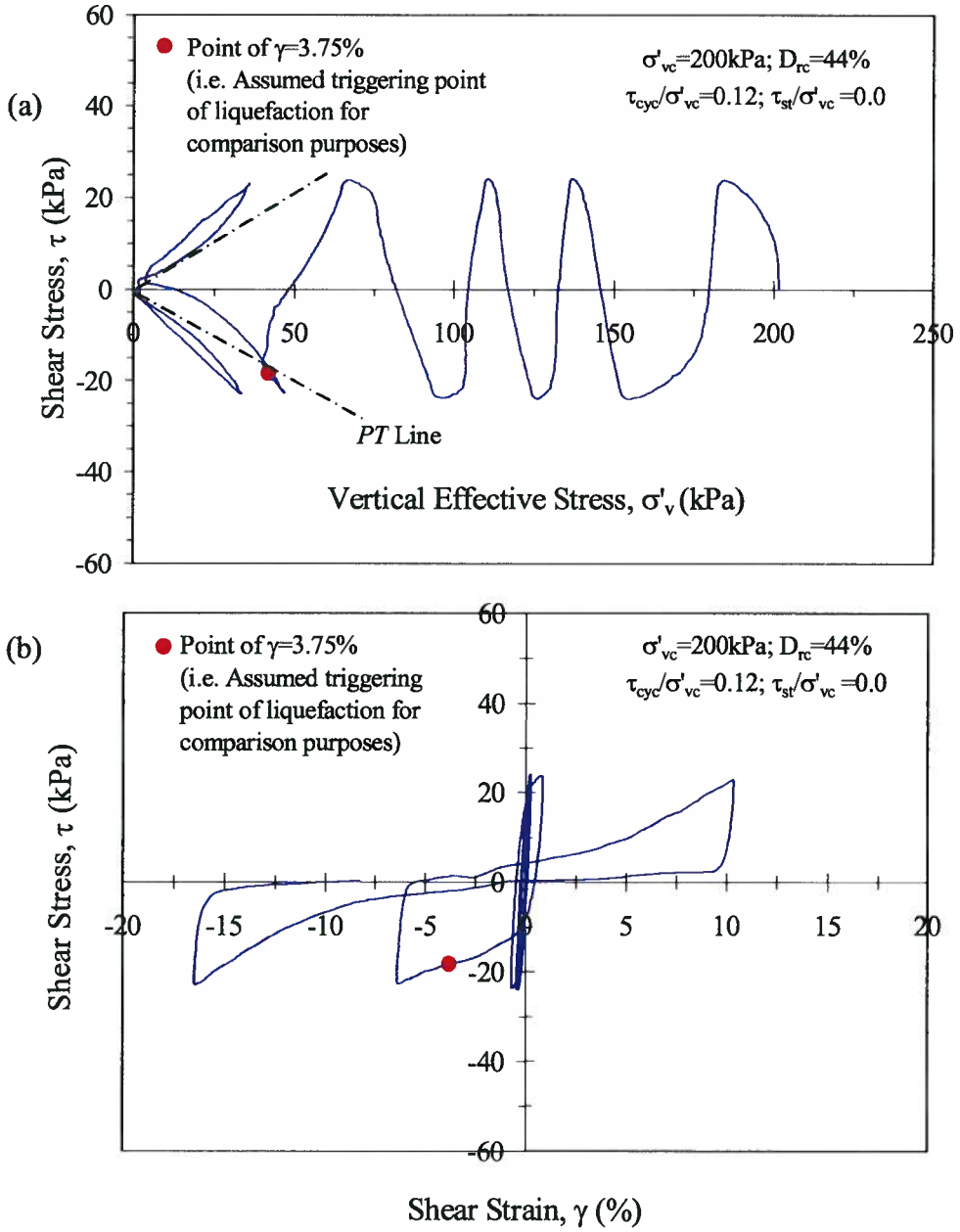

Fig. 2-15: Response of Fraser River sand to cyclic undrained loading in simple shear test in terms of: (a) stress path, and (b) stress-strain (modified from Sriskandakumar, 2004).

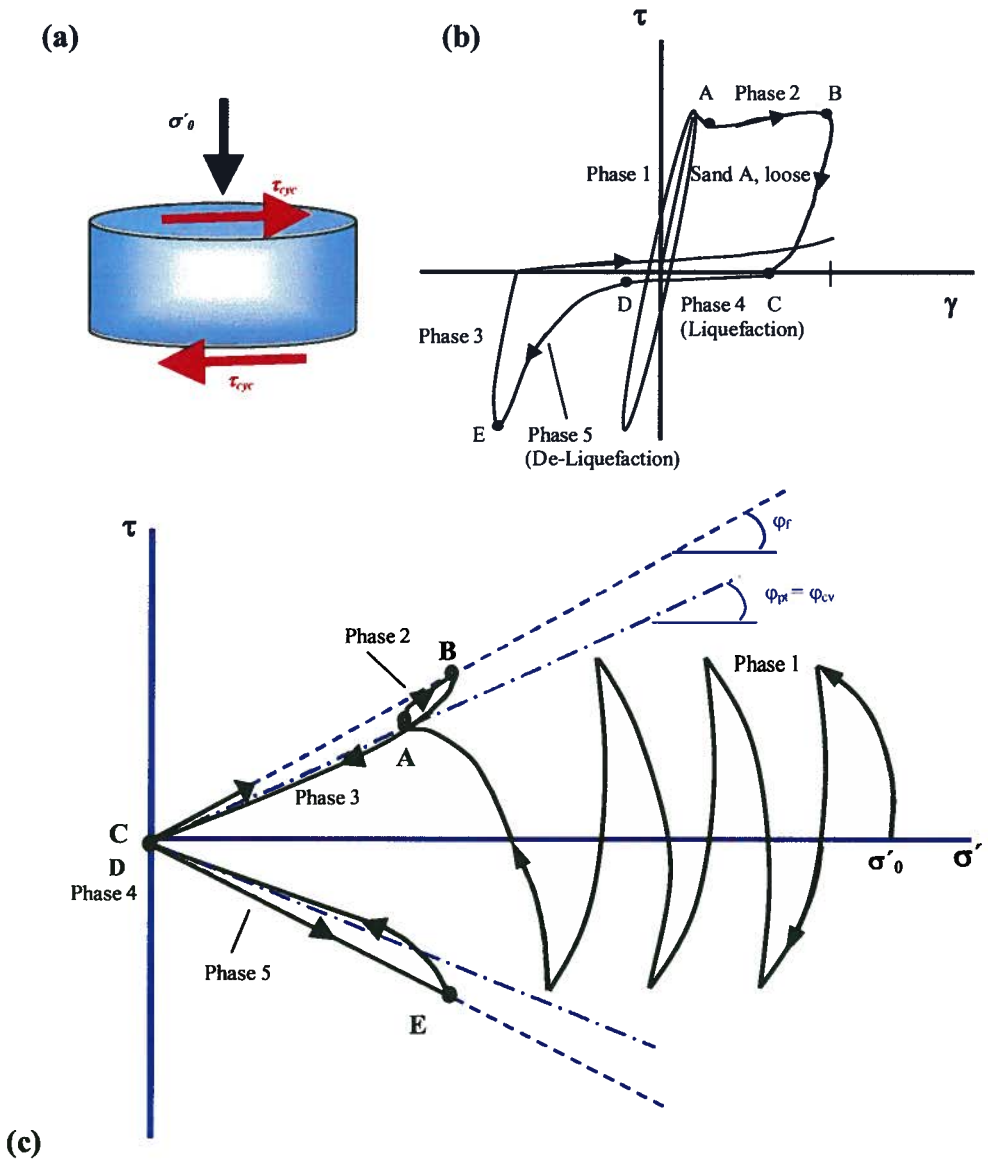

Fig. 2-16: Conceptual illustration of different stages in a typical response of a liquefied sand in undrained cyclic simple shear testing: (a) applied stresses in a simple shear test, (b) stress-strain curve, and (c) stress path (note dilaton is invoked after poit A when loading occurs).

The test results in terms of effective stress path and stress-strain curve is shown in Fig. 2-18, where $p' = (\sigma'_{vo} + 2\sigma'_{ho})/3$, and τ_d are the effective mean stress and the (dynamic) cyclic shear stress, respectively. This behavior is quite comparable to what was observed in the simple shear tests presented earlier.

Fig. 2-19 shows the results for an undrained cyclic simple shear test with a shear stress bias that represents sloping ground conditions. Again, the same characteristic behavior

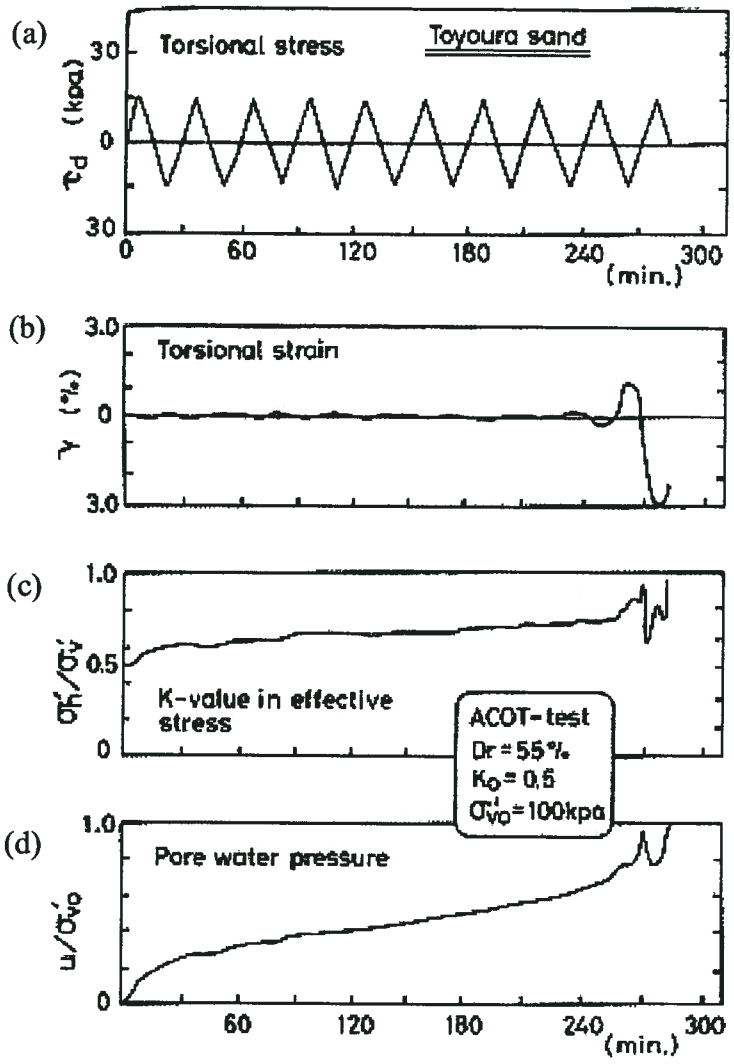

Fig. 2-17: Cyclic cylindrical torsional test results for Toyoura sand (D_r = 55%, K_o = 0.5, σ'_{vo} = 100 kPa), (a) cyclic shear, (b) shear strain, (c) effective stress ratio, and (d) excess pore pressure ratio (Ishihara, 1996).

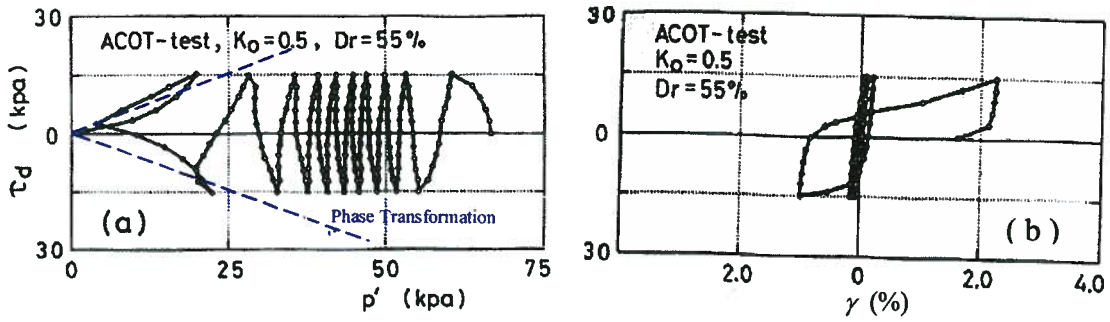

Fig. 2-18: Cyclic response of Toyoura sand in terms of: (a) stress path, (b) stress-strain (modified from Ishihara, 1996).

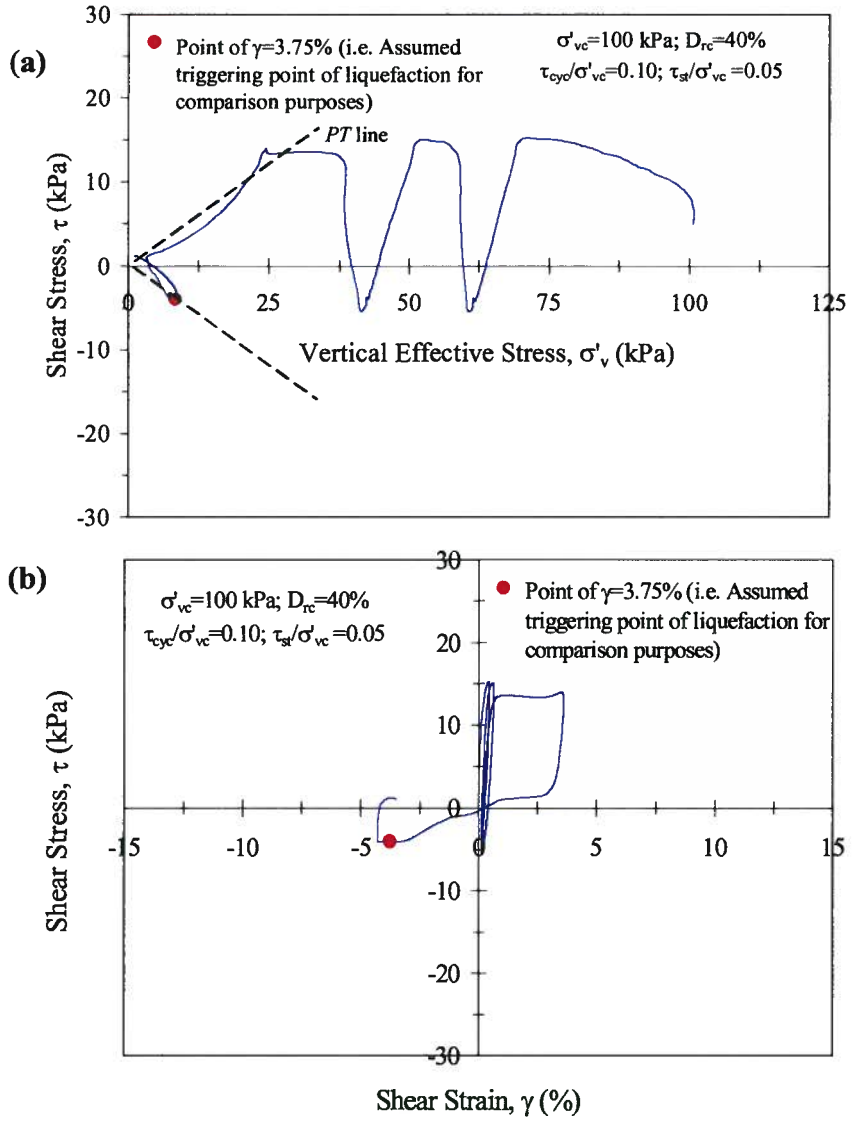

Figure 2.19: Cyclic (a) stress path and (b) stress-strain response of loose sand with initial static shear stress (modified from Sriskandakumar, 2004).

indicates a pore pressure rise in each cycle before *PT* line and subsequent liquefaction and de-liquefaction upon unloading and loading (after *PT*).

As noted earlier, sand contractiveness decreases with (relative) density and as a result, its resistance to liquefaction increases. This is seen in Fig. 2-20 that shows results for a cyclic triaxial test, in terms of the cyclic resistance ratio, *CRR* vs. D_r for Toyoura sand. This conforms with observations what was inferred from liquefied case histories where *CRR* increases with normalized penetration resistance (e.g., Seed & Idriss, 1971; and Youd et al., 2001).

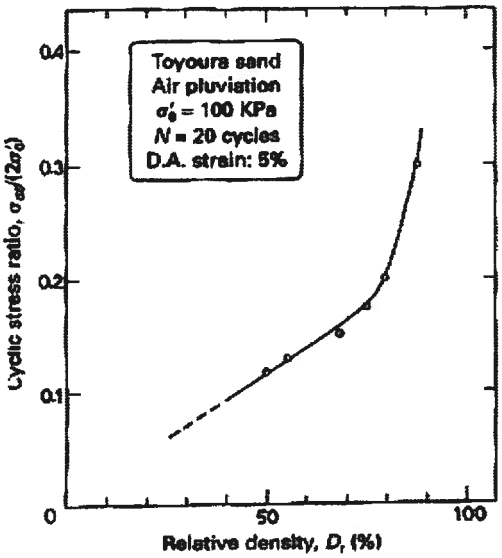

Fig. 2-20: *CSR* to cause liquefaction vs. relative density for Toyoura sand at 100 kPa confining stress (Ishihara, 1996).

2.2. Impact of Partially-Drained Condition on Sand Behavior

Under conditions in the field, excess pore water pressures generated by seismic loading will induce flow of water and change in volume leading to void expansion or contraction (void redistribution) during or after shaking and this should be considered. A saturated soil mass is a two-phase material, i.e., grains skeleton, and water. The presence of pore fluid only provides the volumetric constraint on the soil skeleton, and it is the behavior of the skeleton; in terms of effective stresses at near constant volume, that is the basis for our understanding. Based on this concept, undrained (simple shear) tests can be simulated using dry sands under constant volume conditions (Finn et al., 1978) and the effect of void redistribution can be simulated by controlling the volume. When using triaxial testing, the volumetric constraint (flow condition) during shearing can be controlled through drainage system as depicted in Fig. 2-21. This system can mimic the spectrum of volume change condition (drainage) that may apply to a sample in (triaxial) testing to account for different volumetric constraint conditions (flow conditions). This implies that the conventional testing procedures (i.e., fully drained and undrained) are just two particular cases of a wide range of possible conditions for volume change.

To understand the physics of liquefaction, a knowledge of the stress-strain behavior of the soil skeleton alone as well as that of the soil and pore fluid phases in combination is required, as follows:

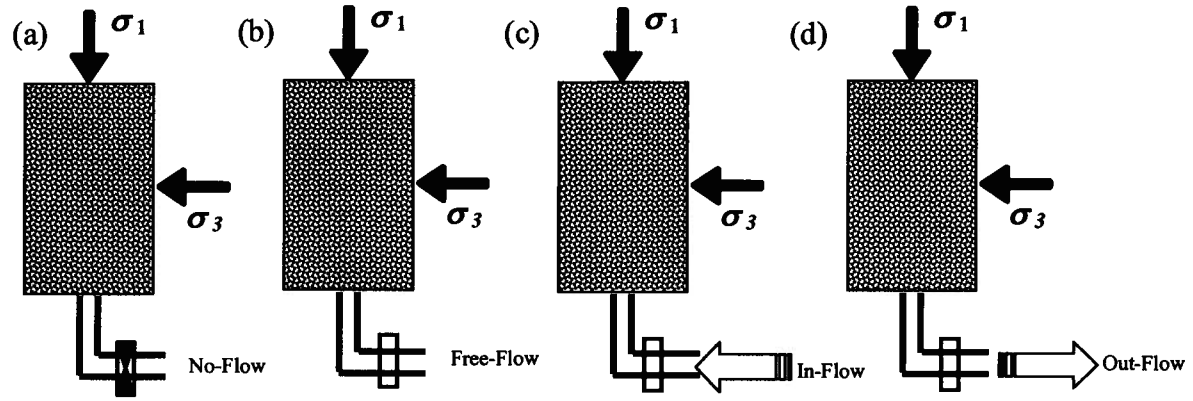

Fig. 2-21: Control of volumetric constraint in triaxial testing, (a) no-flow (undrained), (b) free-flow (drained), (c) in-flow (partially drained, expansion), and (d) out-flow (partially drained, contraction).

1. The behavior of soil skeleton, representing the drained condition;
2. The behavior of (fully) saturated undrained soil, assuming that the pore water is completely incompressible (no flow, constant volume), and
3. The behavior of partially-drained (saturated) soil, to account for various volumetric constraint conditions (driven by flow conditions).

The first two cases were discussed earlier; the third case (partially-drained) is treated in this section. This case is the most relevant loading condition to the void redistribution mechanism. Other investigation methods employed to study void redistribution (including physical model testing) are discussed in *Chapter 3*.

The majority of the previous liquefaction studies are based on the assumption that no flow (undrained condition) occurs during or after earthquake loading. However, this condition may not represent the real situation since, during and after shaking, water migrates from zones with higher excess pore pressure towards zones with lower excess pressure. Transient flow may temporarily increase or decrease the pore pressure in a zone. This *pore pressure redistribution* results in different flow conditions and, as a result, the volumetric constraint changes in soil deposits during a seismic event . Thus, shear strength and other measures of sand behavior may be enhanced or degraded. To investigate this effect, the imposed volumetric conditions must be controlled during the testing, in terms of shear and volumetric strain, simultaneously, which is not the usual practice in element laboratory testing. Recently, a few researchers have reported results of their work on sand behavior under *partially-drained conditions* (Chu, 1991; Lo & Chu,

1993; Vaid & Eliadorani, 1998; Eliadorani, 2000; Bobei & Lo, 2003; Lancelot et al., 2004; Sento et al., 2004; Yoshimine et al., 2006; and Sivathayalan & Logeswaran, 2007).

Fig. 2-22 illustrates the consequences of partially-drained loading (dashed line) as reported by Eliadorani (2001) from traixal tests that can be compared to the results from conventional undrained monotonic triaxial testing (solid lines). In partially-drained tests, the specimen is forced to expand proportionally to the axial strain ($\Delta\varepsilon_v/\Delta\varepsilon_a = 0.6$). The figure shows that a strain hardening and dilative material under undrained condition (no volume change) can be strain-softening because of the water injection (volume expansion) in the partially-drained condition.

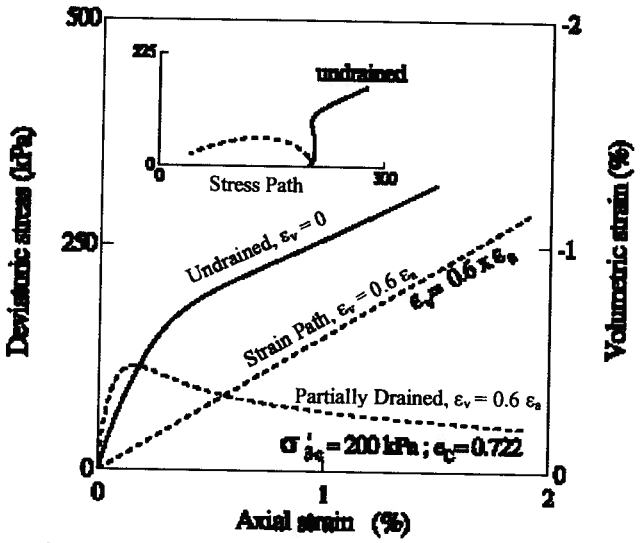

Fig. 2-22: Transformation of dilative response under constant volume condition into strain softening in volume expansion condition (modified from Eliadorani, 2001).

As mentioned earlier, the shear strength of sand, under a partially-drained condition can vary widely depending on volumetric constraint. Results of a series of partially-drained triaxial tests, with the strain paths depicted in Fig. 2-23 (expansion as negative) are shown in Fig. 2-24, in terms of the effective stress path, in comparison to that of the special cases, i.e., undrained and drained conditions (Eliadorani, 2001). The figure shows that the ratio of volumetric strain increment to that of the axial strain ($\Delta\varepsilon_v/\Delta\varepsilon_a$) has significant impact on sand reponse. It demonstrates that the partial drainage condition is not bounded between drained ($d\sigma'_r = 0$) and undrained conditions ($\Delta\varepsilon_v/\Delta\varepsilon_a = 0$), and can be more destructive to sand behavior. Vaid & Eliadorani (1998) also demonstrated that a (dense) sand with dilative behavior under undrained

conditions exhibits strain-softening behavior under (inflow/injection) partially drained condition when the injection rate exceeds the dilation rate. In field conditions the imposed volume change ($\Delta\varepsilon_v/\Delta\varepsilon_a$) can be variable, and produce different senarios. The in-flow condition in which the element expands can result in a very large reduction in soil resistance.

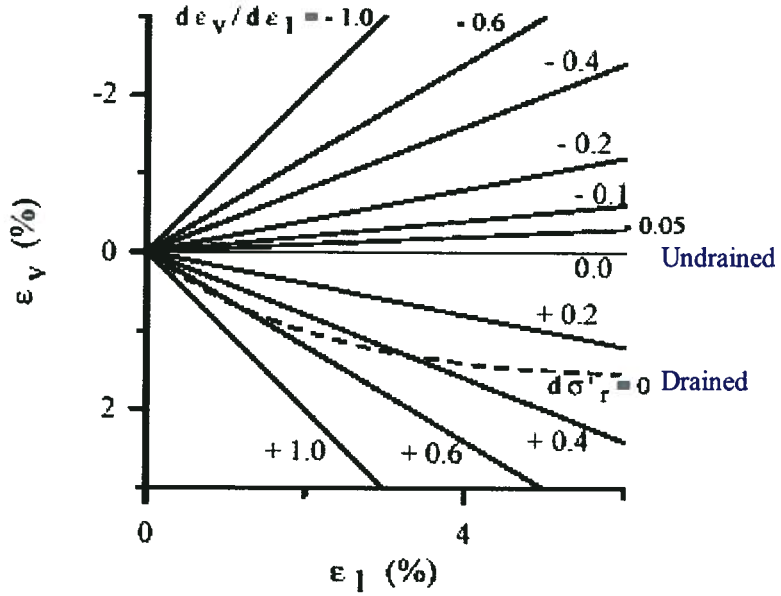

Fig. 2-23: Range of imposed volumetric strain change ratio comparing to that of undrained and fully drained conditions ($d\sigma'_r = 0$), (modified from Eliadorani, 2001).

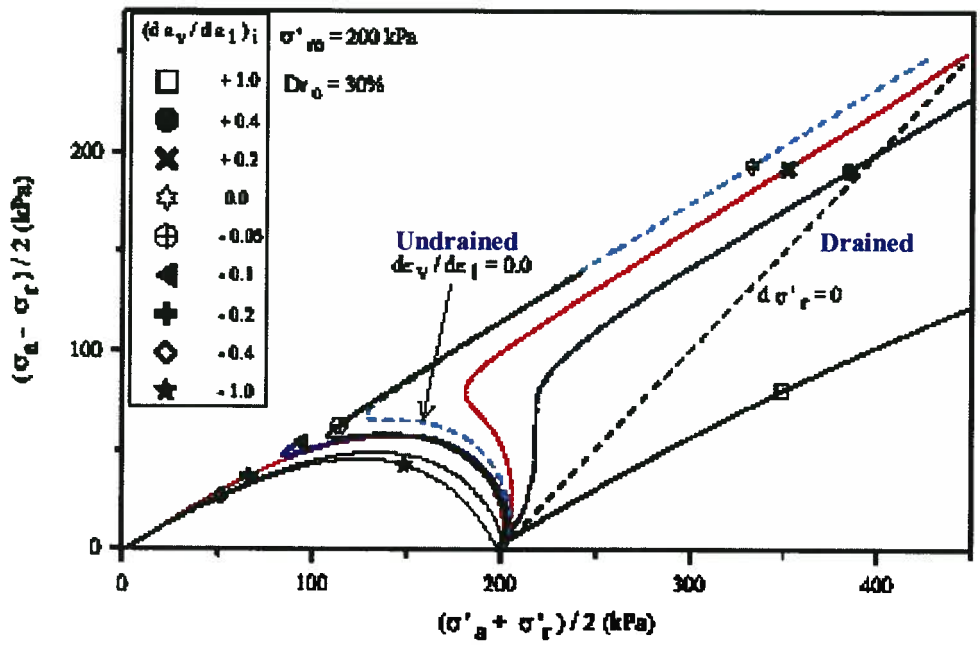

Fig. 2-24: Effective stress paths for various $\Delta\varepsilon_v / \Delta\varepsilon_a$ (modified from Eliadorani, 2001).

Recently, Sento et al. (2004) reported results of an experimental study on Toyoura sand under constant shear and partially drained condition using triaxial and torsional hollow cylinder apparatus. This test can represent a sloping ground subjected to inflow condition. Fig. 2-25 shows injection triaxial test results followed by drainage for various relative densities with the same initial (bias) shear stress. The samples reached the failure line (point C), at volumetric strain from about 0.5% to 1.0% and then large shear strains (limited to less than 8% due to apparatus

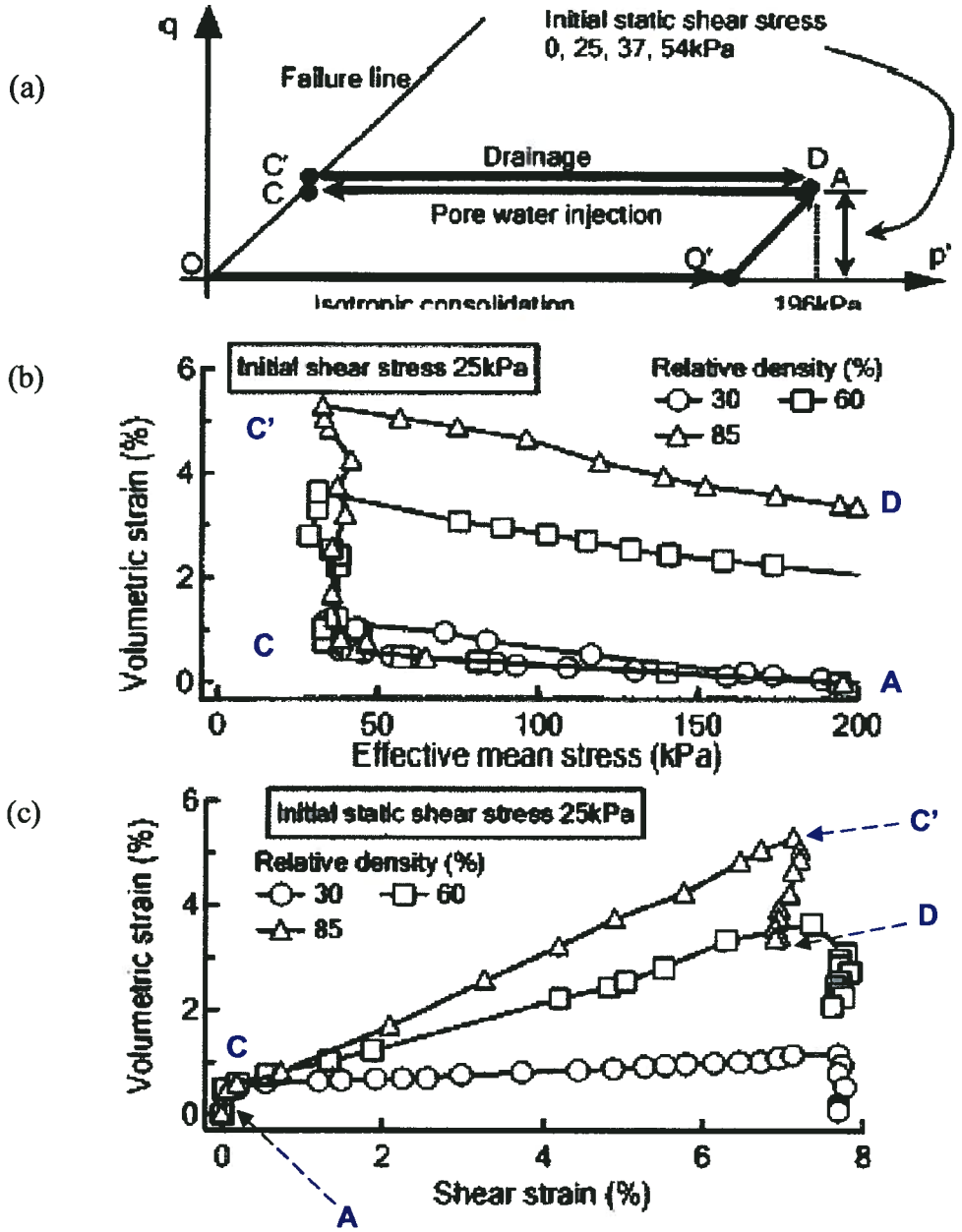

Fig. 2-25: Triaxial injection testing, (a) stress path, (b) & (c) effect of relative density on volumetric strain over the flow failure path due to pore water inflow in terms of mean effective stress and shear strain, respectively (modified from Sento et. al., 2004, with permission from ASCE).

constraints) developed with continuation of inflow at constant shear and effective stresses. As may be seen, looser sands develop larger shear strain when equivalent volumetric strain was applied (see Fig. 2-25c path C to C'). The results shown in Fig. 2-25b in terms of ε_v vs. P' suggest that the drainage volume (volume change from C' to D) during effective stress recovery (path C' to D) after flow-slide is independent of initial sand density. However, such failure is a runaway type, and hence the drained path (C' to D) cannot represent the real failure condition as noted by Chu (2006). In addition, Fig. 2-25c indicates that shear strain was essentially constant during drainage process (path C' to D).

Fig. 2-26 compares consolidated drained triaxial, *CD* test results for the same relative densities with that of injection tests (solid symbols) in terms of volumetric strain vs. shear strain. As may be seen the expansion rate ($d\varepsilon_v/d\varepsilon_l$) for both tests are almost the same. Yoshimine et al. (2006) reported similar results from triaxial injection tests. This suggests that development of shear strain during failure is governed by dilatancy characteristics. Consequently, to develop the same level of shear strain, denser sand requires much more inflow pore water. This means that a denser sand has more resistance to injection flow failure due to greater expansion potential.

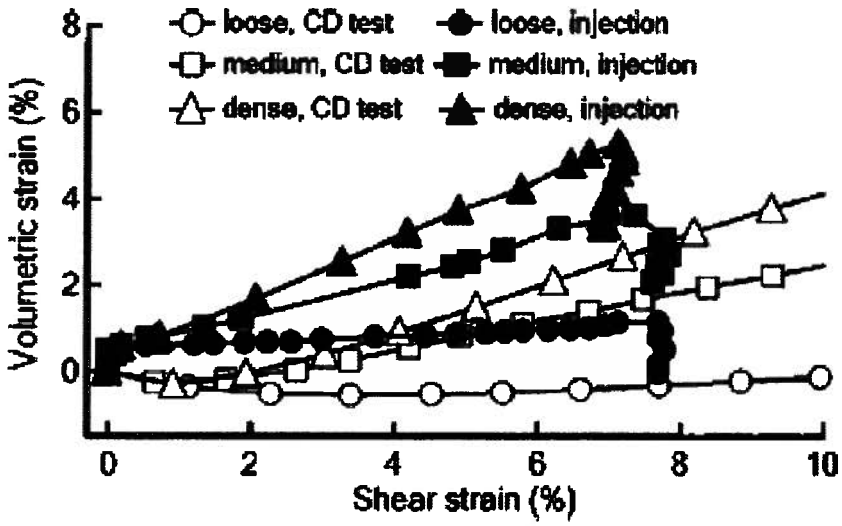

Fig. 2-26: Comparison of dilatancy characteristics in CD and injection tests (Sento et al., 2004, with permission from ASCE).

Regarding practical difficulties involved in triaxial testing to maintain a constant volumetric strain rate by increasing the back pressure, they performed torsional hollow cylinder (volumetric strain-controlled, constant shear stress, V-CSH) tests to study the dilation limits of

sand specimens subjected to pore water inflow. In these tests, the volumetric strain rates and initial static shear stress were constant (τ_c = 10 kPa, σ'_c = 100 kPa) and the pore water injection volume was continuously increased until shear strain of 80% developed. Fig. 2-27 shows the test results in terms of volumetric strain and corresponding void ratio vs. shear strain, γ (up to γ = 80%) for Toyoura sand of various relative densities. Fig. 2-27 implies that for a given shear stress there is a limiting void ratio, at which no further dilation is possible in the sample. This limit is related to the *critical-state* void ratio. The figure denotes that required volumetric strain for the *Dr* =36, 57, 79% samples, were 4.7, 6.4 and 10%, respectively for a shear strain of 80% at which shearing was stopped due to equipment limitation. As the void ratios did not reach the same value at 80% shear strain thus, the *steady-state* should correspond to larger strain levels.

Based on a similar study (using triaxial injection test under constant shear stress), Yoshimine et al. (2006) proposed Fig. 2-28 to estimate the volumetric strain required to reach different distortion levels including *steady-state* condition ($\varepsilon_l = \infty$) for Toyoura sand. This suggests that a volumetric strain of 6% brings a typical sloping ground of loose sand (e.g. *Dr* = 40%) to *steady-state* and *flow-slide*. They also reported that effective stress was essentially constant during distortion (path C to C' in Fig. 2-25b). The same finding was reported by Sivathayalan & Logeswaran (2007) from triaxial inflow test with constant injection rate ($\Delta\varepsilon_v/\Delta\varepsilon_a$). This suggests that an injected soil at *steady-state* can fail due to a minimal applied stress.

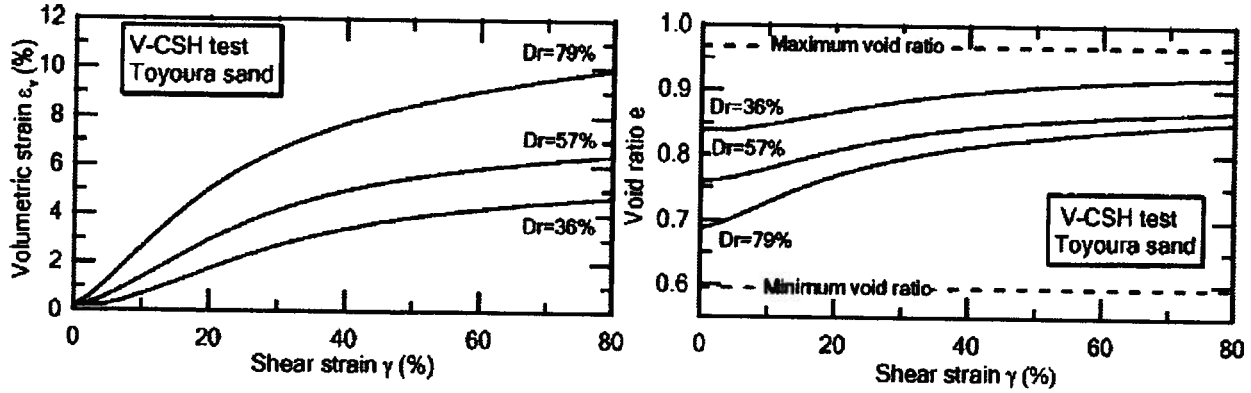

Fig. 2-27: V-CSH tests results for *Dr* =36, 57, and 79%, (a) volumetric strain and (b) void ratio vs. shear strain (Sento et al., 2004, with permission from ASCE).

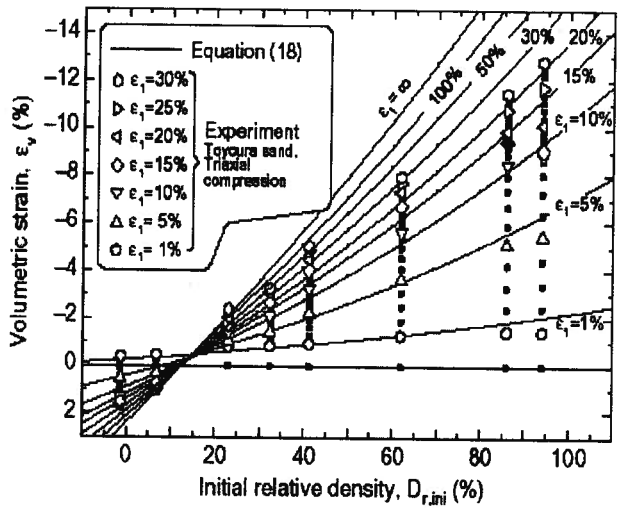

Fig. 2-28: Volumetric strain for various initial D_r required for reaching different levels of deformation (Yoshimine et al., 2006).

2.3. Post-Liquefaction Response and Flow Slide

The behavior of a softened material after liquefaction onset is called *post-liquefaction* response. The post liquefaction strength is crucial as the flow slide in liquefied grounds usually takes place after shaking due to applied static shear stresses.

Extensive attempts have been made to describe the post liquefaction strength of sands, based on the undrained *steady-state strength* concept. Fig. 2-29 shows the *steady-state* line (curve) for Toyoura sand along with the upper and lower bound of the compression line reported by Ishihara (1996). Laboratory data from a number of investigators (e.g., Baziar & Dobry, 1995) suggest that residual strength is normalized with respect to consolidation stress. Fig. 2-30 shows the undrained residual strength, S_u with depth, for Tia Juana silty sand (Ishihara, 1996). In accordance with this finding from element testing, a few researchers (e.g. Stark & Mesri, 2002 and Mesri, 2007) have also suggested normalized residual strength correlations, back-calculated from failed case histories.

During cyclic loading (earthquake shaking) in a typical loose sand element, the stress path may reach the zero effective stress/zero shear strength origin, and true liquefaction occurs (Phase 4 in Fig. 2-16). Upon continued monotonic shearing to large strains, however, the soil will dilate, and move up the failure envelope, gaining strength. If the undrained condition continues, the so-called (undrained) *residual strength* will not be reached until:

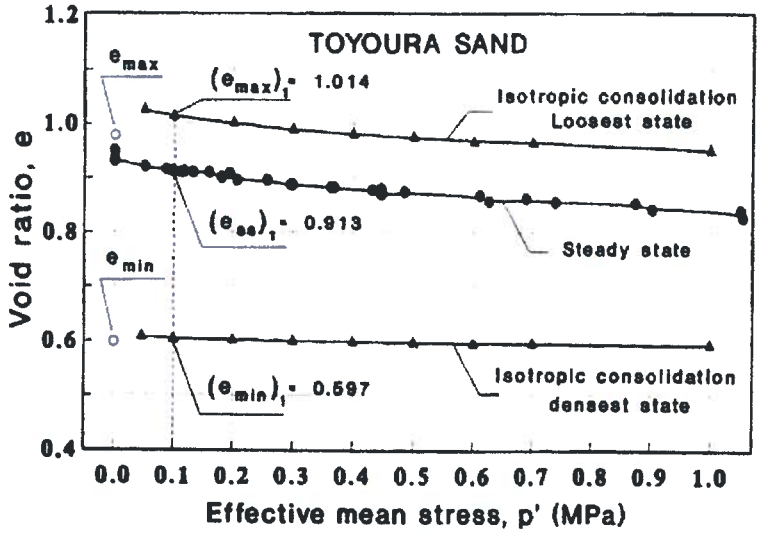

Fig. 2-29: *Steady-state* line of Touyora sand (Verdugo & Ishihara, 1996).

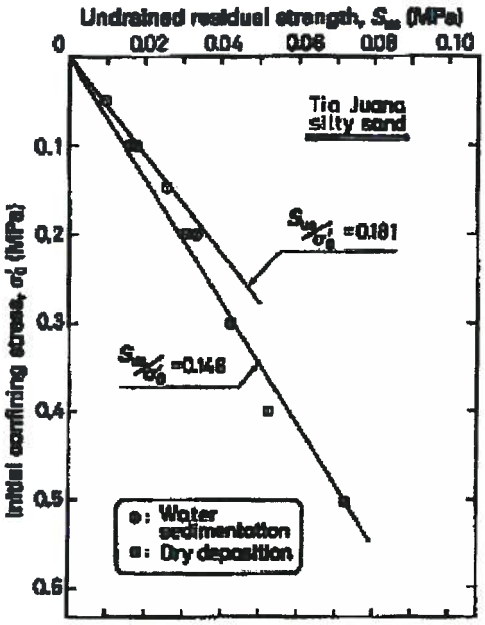

Fig. 2-30: *Steady-state* strength of Tia Juana silty sand vs. consolidation stress (Ishihara, 1996).

(i) The pore-water cavitates and thus allows the sample to increase in volume and reach the *steady-state*, or

(ii) The high mean effective stress generated by dilation suppresses the dilation and the soil reaches its *critical-state strength*, or

(iii) The sand grains crush and the soil reaches a *critical-state* of the crushed material.

The strength of the sand reached in (i), (ii) or (iii) is generally much higher than the commonly accepted *undrained* residual strengths, back-calculated from case histories, and is likely much higher than the drained strength (Naesgaard et al., 2006), hence, a flow slide would not occur. However, as shown earlier, if, in lieu of undrained loading, a small inflow of water occurs, it will reduce or eliminate the strength gain from dilation. When the inflow volume exceeds the shear-induced dilation, then the soil quickly reaches the state of zero effective stress and is truly liquefied.

More recently, a few investigators, recognizing the void redistribution (pore water migration) effects, have proposed correlations for residual strength to account for this mechanism (Kokusho & Kabasawa, 2003; Idriss, 2006 and Idriss, & Boulanger, 2007). These authors developed suggestions based on physical model tests (i.e., shaking table and centrifuge models) of slopes with a barrier layer. Fig. 2-31 shows the correlation suggested by Idriss and Boulanger

(2007) for conditions where a void redistribution mechanism is involved and for situations without void redistribution effects.

Field-based strengths may be reasonable postulated to reflect all factors involved in previous failures that could also be the case in future probable failures, and should be recommended for current engineering design, as noted by Byrne et al. (2006). The issue of post-liquefaction strength of deposits comprising barrier layers needs to be further explored. Current practice for estimating residual strength is found in *Appendix I.*

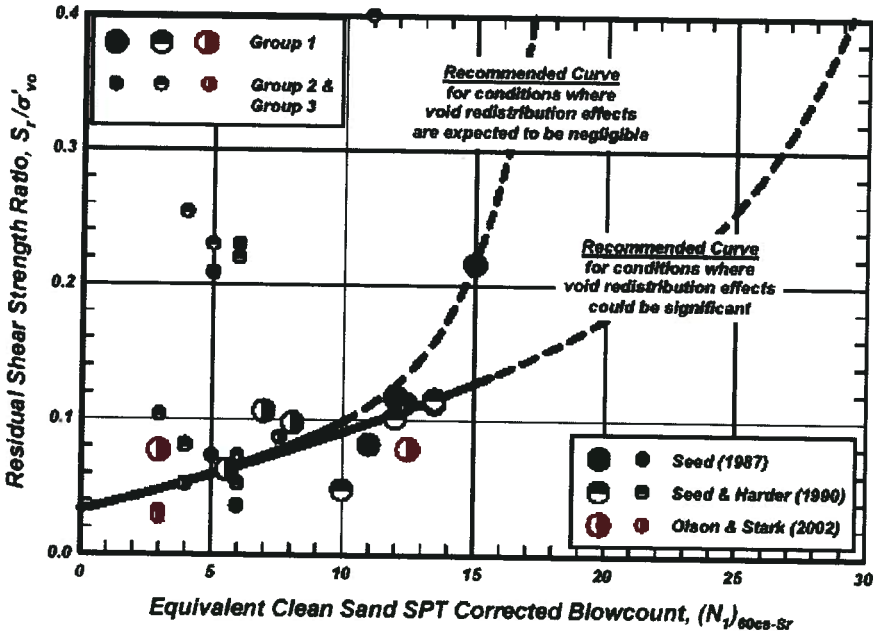

Fig. 2-31: Normalized residual strength with and without void redistribution involvement (Idriss & Boulanger, 2007).

2.4. Flow Properties

Pore water migration within an earth structure, leading to soil element expansion or contraction is controlled by its flow characteristics. Therefore, in addition to mechanical conditions the seismic response of an earth structure depends on flow conditions that include:

1. Soil permeability (hydraulic conductivity, k).
2. Permeability difference within the soil layers (permeability contrast).
3. Spatial distribution of different soils types (flow path).

The hydraulic conductivity, or coefficient of permeabilty, k (in *Darcy's law*) can vary in a wide range. Table 2-1 presents typical values of k, as suggested in textbooks for various materials (e.g., Lee et al., 1983; and Coduto, 1999). For sands, the recommended values range from 10^{-2} to 10^{-5} m/s, depending on gradation and fines content. This permeabilty is sufficient for excess pore pressure dissipation in a (relatively) short time, in many cases, when subjected to earthquake loading. The range can decrease by 100 times or more, for silty sand and silt materials. Hence, a liquefiable deposit with lower permeability will experience large excess pore pressures for a longer time in earthquakes. Thus, the response of a liquefiable deposit to a given earthquake will vary with its permeabilty. This cannot be investigated using conventional element testing procedures and will be explored by numerical modeling in more detail in *Chapter 4*.

Table 2-1: Range of k (m/s) for different soils, as suggested in textbooks.

Soil type	Reference	
	Lee, White, & Ingles, 1983[a]	**Coduto, 1999**
Gravel	10^{-2}	10^{-1} to10^{-4}
Sand	10^{-2} to10^{-5}	10^{-2} to 10^{-5}
Silty sand	2×10^{-5} to 10^{-6}	10^{-4} to 10^{-5}
Silt	5×10^{-6} to 10^{-7}	10^{-5} to 10^{-10}
Clay	$<10^{-8}$	10^{-5} to 10^{-12}

[a] Proposed values based on Harr, 1977; Terzaghi and Peck, 1967; and Lambe and Whitman, 1969.

2.5. Partial Saturation

The majority of investigations on liquefaction of granular soils have been centered on fully saturated soil. *In situ* test results, including compression wave velocity measurements, V_p, indicate that partial saturation conditions may exist below ground water level for a few meters due to the presence of air bubbles (Ishihara et al., 2001; and Nakazawa et al., 2004) or gas bubbles in marine sediments and oil sands, as noted by Mathiroban and Grozic (2004).

Some investigators (e.g., Kokusho, 2000; Yang & Sato, 2001; Pietruszczak et al., 2003; Atigh & Byrne, 2004; Mathiroban & Grozic, 2004; Seid-Karbasi & Byrne, 2006a; and Yegian et al., 2007) have recently addressed the effects of partial saturation conditions on the liquefiable ground response. The saturation condition of soil samples in the laboratory can be evaluated by measuring *Skempton's B* value and/or the compression wave velocity, V_p, as suggested by Ishihara et al. (2001). Laboratory test data have shown that the resistance of sands to liquefaction onset increases as saturation decreases (Ishihara et al., 2001 & 2004; Yang, 2002; and Yang et al. 2004). Fig. 2-32 shows the cyclic stress ratio, *CSR*, vs. number of cycles required for liquefaction

of Toyoura sand at different saturation states, S_r, that is evaluated in terms of *Skempton's B* value. The effects of partial saturation are discussed in more detail in *Chapter 7*.

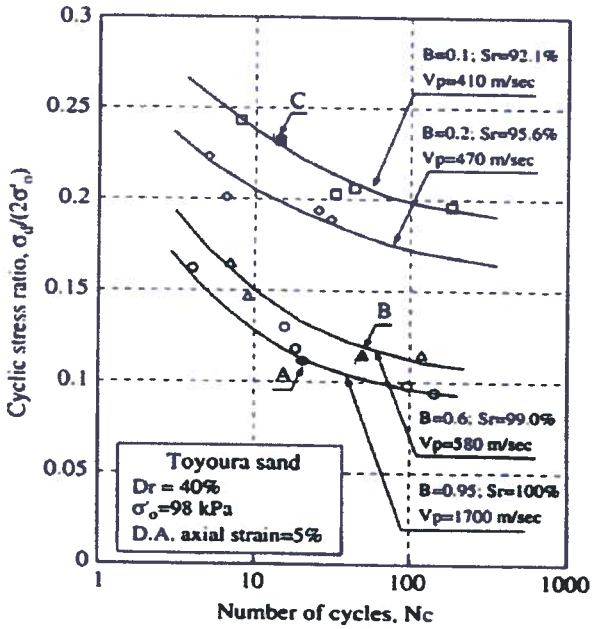

Fig. 2-32: Cyclic stress ratio vs. No. of cycles for Toyoura sand with different degrees of saturation (Ishihara et al., 2004, reproduced by permission of Taylor & Francis Group)

2.6. Summary and Concluding Remarks

This chapter presents a literature review of characteristics and behavior of sands in connection with the liquefaction problem based on data from laboratory element tests. The main factors related to the scope of this study were addressed. Other issues, including current practice in liquefactuion engineering e.g. liquefaction triggering assessment, residual strength, post-liquefation settlement, and fines content effects are treated in *Appendix I* for the sake of completeness. The main conclusions from this overview are as follows:

1. Key issues in sand behavior

- Volume change in granular materials is coupled with applied shear strain that results in dilation or contraction.
- The amount of dilation increases with sand relative density and reduces at higher normal stress values.
- The stress-strain behavior of sand is controlled by its skeleton and the volumetric constraint of the pore fluid. The volume change condition can vary in a broad range, and

the undrained (constant volume) and the fully drained (free) conditions are just two special cases within this wide range.

- A given sand, depending on the volumetric constraint conditions, exhibits significantly different responses to loading.

These fundamental features of sands behavior are reflected in both monotonic and cyclic laboratory element test data. To capture seismic response of an earth structure, numerical modelling should be able to predict a soil element behavior in different loading conditions.

2. Excess pore pressure build-up and redistribution

Characteristic undrained sand behavior and recent data from partially-drained laboratory tests were reviewed. From this review, the following points are inferred:

- Generation of excess pore pressure in saturated granular soils during undrained loading is a reflection of the tendency of sand to contract when loaded. The fluid in soil pores when saturated with water provides a near constant-volume condition when no flow takes place, and causes normal stress to be transferred from the skeleton to the water.

- Pore pressure rises in each cycle of undrained shearing and if the stress path reaches the zero-effective stress state, liquefaction occurs momentarily. Further shear loading will cause the stress path to follow up the failure envelope and dilate regaining stiffness and strength

- When undrained loading exceeds the *phase transformation state* while moving up the failure line, pore pressure reduces due to the dilation effects.

- Element tests suggest that a small amount of water injected into the soil sample results in large strength loss and eventually instability. This strength loss depends on the volume of injected water (final void ratio) and corresponding effective stress. This effect suppresses the strain hardening effect of dilation.

- When a sand element is brought to *steady-state* by inflow expansion (flow threshold) it deforms with minimal driving shear force and the subsequent deformations are not controlled by the initial soil state (i.e., D_{ri}, and σ_{ci}).

3. Post-liquefaction behavior and residual strength

Post-liquefaction stability of earth structures (*flow-slide*) and resulting deformations are significantly affected by residual strength. Two possible senarios arise in determining the post-earthquake deformations of earth structures i.e.:

a) Cases where the void redistribution effect (i.e., soil expansion) is not significant, e.g., practically homogenous deposits (with uniform permeability), such as clean sands that exhibit strain hardening behavior and gain strength while deforming after liquefaction. A

flow-slide is unlikely to take place in these situations, as the residual strength can be large or even greater than the drained strength.

b) Cases where the void redistribution effect (i.e., soil expansion) is significant, e.g., stratified deposits with permeability contrast. For these cases, the standard practice approach is to determine the residual strength based on data that is back-calculated from failed case histories.

4. *Partial saturation*

- Sands in the partially saturated condition exhibit greater resistance to liquefaction.

CHAPTER 3

LIQUEFACTION INDUCED-GROUND FAILURES

3.1 Introduction

Liquefaction induced-deformations are influenced by several mechanisms and factors. Flow failures, lateral spreads, and differential settlements are some forms of liquefaction deformations that can cause very severe damage. Understanding the underlying mechanisms that cause liquefaction deformations is essential for the successful prediction of performance and selection of suitable mitigation methods.

The consequences of liquefaction vary for level ground and slopes. Level ground sites undergo ground oscillations accompanied by opening and closing of fissures and settlements (NRC, 1985). Surface manifestations of level ground liquefaction include bearing failure, cracks, settlement and sand boils (see Fig.3-1). Sand boil formation seems to occur only in the presence of a low permeability soil layer above the liquefied sand layer (e.g. Scott & Zuckerman 1972; Fiegel & Kutter, 1994a). For sloping ground or embankments liquefaction can result in *"flow-slide"* or *"lateral spreading"*. *Flow-slides* (or *flow-failure*) with very large movements occur during or after shaking when the *post-liquefaction* strength drops below the *"static driving shear stresses"*. *Lateral spreads* occur intermittently (and progressively increase even more than 1m) essentially during earthquake shaking when the combined *"static and inertial driving forces"* exceed the soil strength. However the *post-liquefaction* strength is greater than the *"static driving shear stress"* and movements stop when shaking ceases (Byrne et al., 2006).

Fig. 3-2 to Fig. 3-4 illustrate examples of liquefaction-induced deformations corresponding to situations of vertical displacements and also limited and global instability or large lateral spreading (even more than 10m), respectively. Such large deformations can be very destructive and lead to catastrophic failure in structures or lifelines (Fig. 3-4 and Fig.3-5).

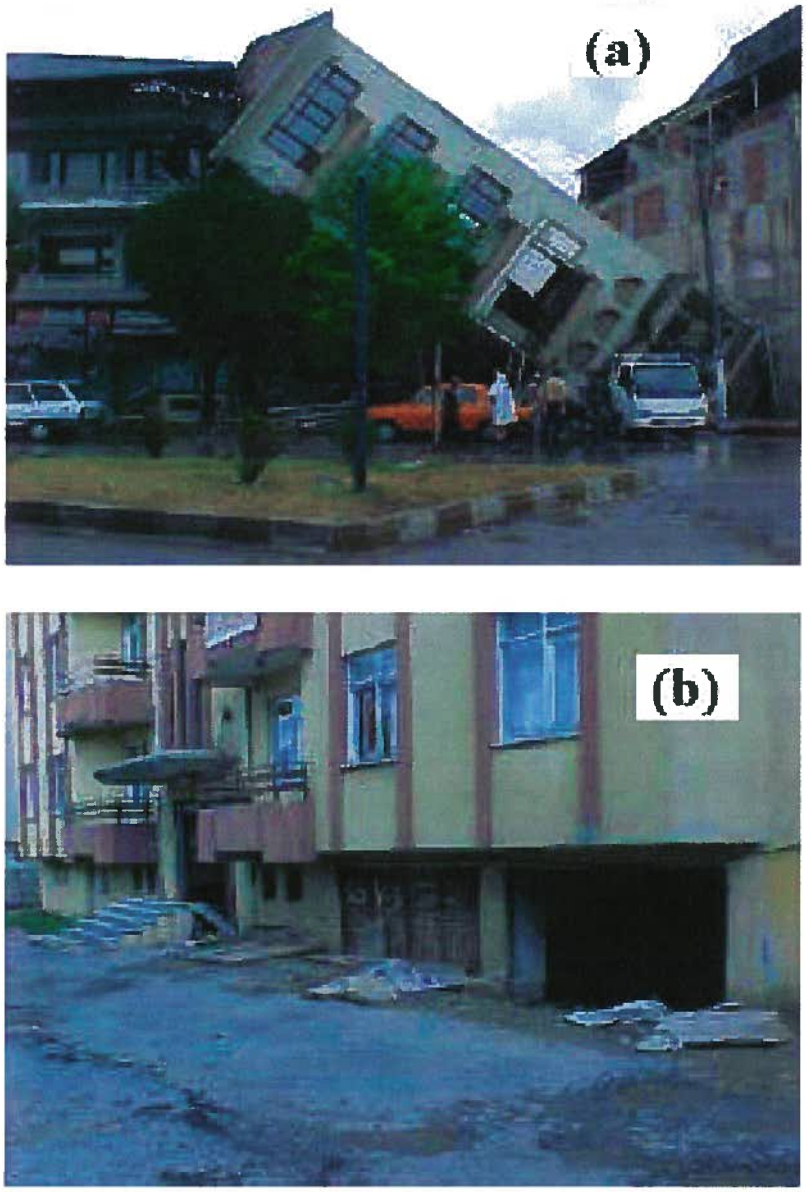

Fig. 3-1: Liquefaction foundation failure, (a) Overturning and (b) settlement of structures resulting from liquefaction of foundation soils in Adapazari, Turkey, 1999 (adapted from Kammerer, 2002).

Experiences from past earthquakes indicate that many of these large lateral displacements have taken place in sloping grounds with very gentle inclination during or after the main shock. Recent evidences have revealed that in all these cases, soil stratification and low-permeability sub-layer causing a void redistribution mechanism (as described in *Chapter I*) were involved.

In this chapter, physical model test studies (using shaking table and centrifuge dynamic testing) are first discussed followed by results of laboratory element tests. Afterwards, some

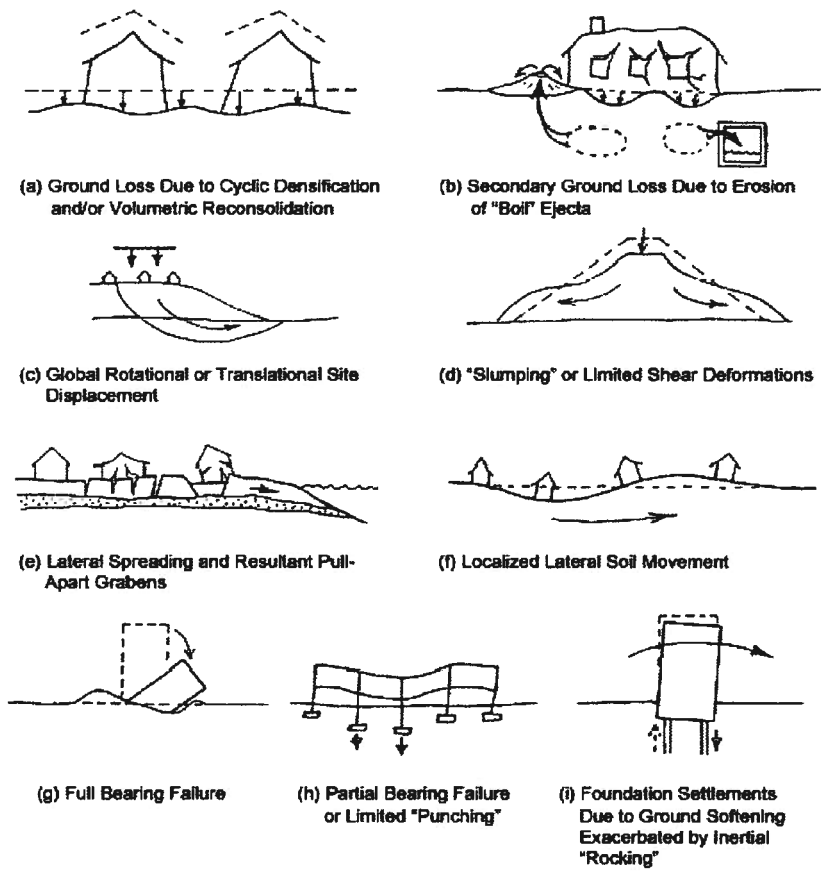

Fig. 3-2: Modes of liquefaction-induced vertical displacements (Seed et al., 2001).

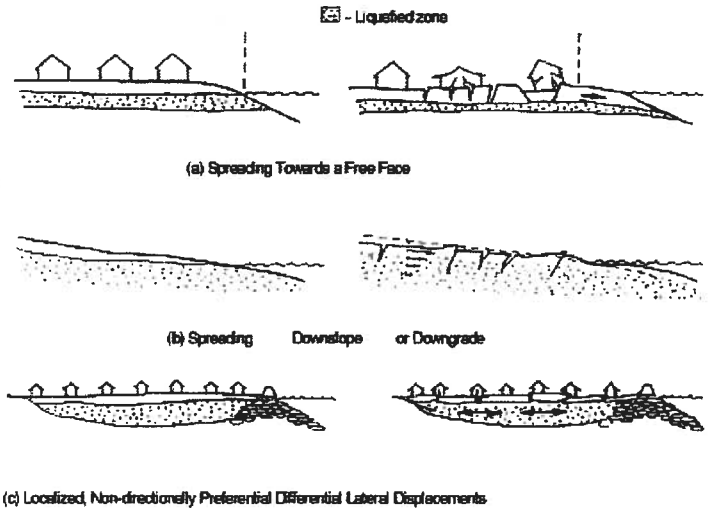

Fig. 3-3: Modes of "Limited" liquefaction-induced lateral translation (Seed et al., 2001).

case histories are reviewed and mechanism described. At the end of the chapter some related numerical investigations are discussed. A more complete list of physical model tests data and case histories are described in *Appendix II* and *Appendix III* respectively.

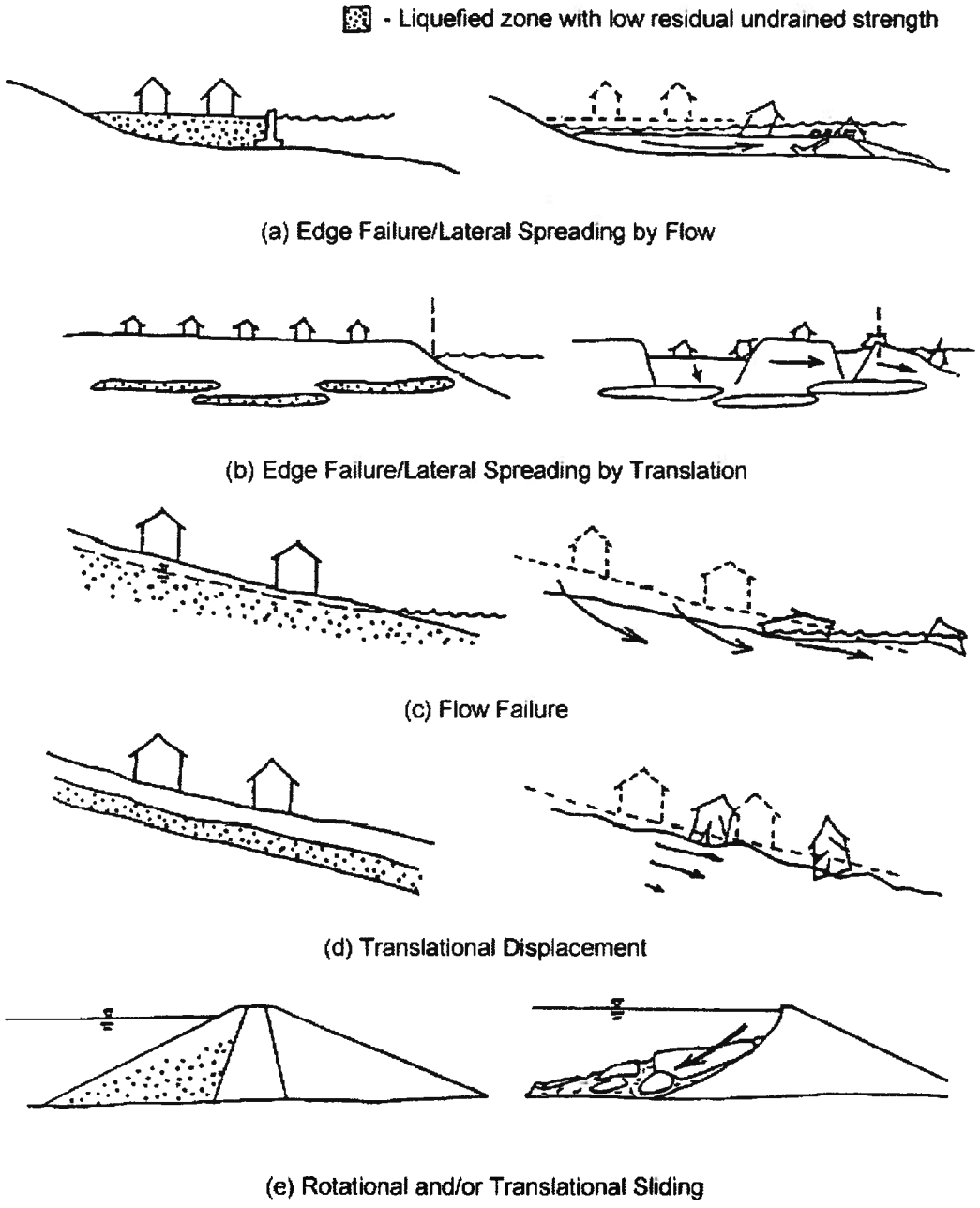

Fig. 3-4: Examples of liquefaction-induced global instability and/or "Large" lateral spreading (Seed et al., 2001).

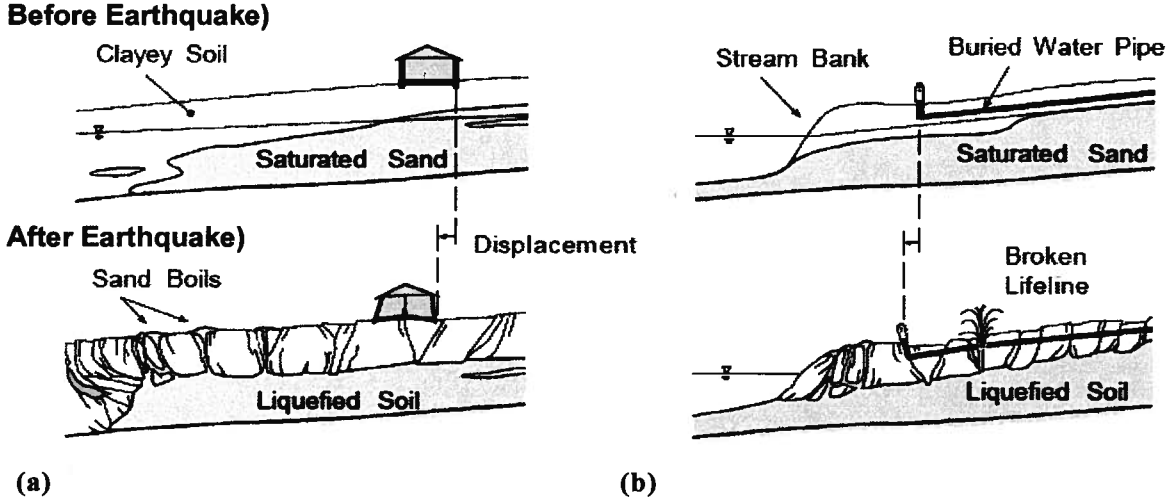

Fig. 3.5: Liquefaction induced lateral spreading, (a) gently sloping ground, (b) free face area (Rauch, 1997).

3.2 Physical Model Studies on Void-Redistribution

A number of researchers have investigated the void redistribution mechanism using model tests on layered soil profiles with permeability contrasts. These model tests included one-dimensional sand column, 1-g shake table, and centrifuge tests. Formation of water inter-layers were observed in some tests, whereas loosening due to void redistribution was inferred using photographs and instrument recordings in others. In some of the earliest studies, void redistribution observations were made on tests that were carried out to study some other problems. Later, researchers designed tests to study void redistribution specifically.

After the pioneering work of Kokusho (1999) that demonstrated significant impact of low permeability sub-layer on liquefiable ground *flow-slide*, recently this issue has drawn more attention. This led to more experimental studies on this phenomenon and in particular by Kokusho and his co-workers at Chuo University in Japan and at the University of California, Davis, U.S as well as a joint work by University of British Columbia and C-CORE, Canada.

Table *AII-1* of *Appendix II* summarizes the results of past model tests and some of them will be examined in more detail in this chapter (complete description for all of them are provided in *Appendix II*). The results of a recent joint research program between Chuo U. and Davis U. (Kulasingam, 2003 and Malvick, 2005) that focused on void-redistribution will be also discussed in this chapter.

Huishan & Taiping (1984) reported results of shaking table tests on homogeneous deposits and horizontally stratified deposits in the presence or absence of a model foundation. A rigid model container with Plexiglas sidewalls was used. The sand was water pluviated and brought to the desired density by vibration. The sand had a D_{10} of 0.053 mm and a D_{60} of 0.114 mm. The models were prepared by pluviating sand in about 2 cm layers and waiting for it to consolidate before pluviating the next layer in order to form a stratified deposit. This resulted in each of these layers having a coarser bottom layer and a finer top layer. The model of this stratified deposit was constructed and tested for two relative densities (i.e. 14% and 28%). A sinusoidal excitation of 3-5 Hz frequency was applied to the models and continued until evidence of liquefaction was observed. The sinusoidal motion applied to the stratified models had a 0.3 g acceleration. The observations from the test with 14% relative density are shown in Fig 3-6. Huishan and Taiping (1984) described the observations as follows, "When the pore pressure increases, the small horizontal fissures filled with water appear symmetrically or asymmetrically outside the foundation. If vibration continues, the fissures grow up rapidly to form water inter-layers or water lenses. With further build up of pore pressure water lenses located at the same elevation will be interconnected to form a long water interlayer. Meanwhile, the other fissures may appear somewhere. With increasing thickness of water interlayer the ground surface is uplifted. Once the first water interlayer reaches its maximum thickness, the water burst out with a noise through the overburden stratum and boiling occurs. After boiling the water interlayer soon disappears and the fissure is closed". The maximum thickness of the observed water inter-layers for the 14% and 28% relative density sands were 2.5 cm and 1.5 cm respectively".

Elgamal et al. (1989) performed a series of qualitative 1-g shake table tests to investigate the effect of stratification of soil deposits on liquefaction. Three different models, a uniform silty sand layer, a silty sand layer underlying a silty clay blanket and an inter-layered clay-loose sand stratum were tested (no specific materials density/relative density was noted). The models were prepared by water pluviation. Water inter-layers were observed to form below the less permeable layers in the second and third models. These water inter-layers continued to grow as the dynamic excitation progressed and reached a maximum thickness of about 5% of the underlying sand layer. Finally after about 100 seconds of continued dynamic excitation the water inter-layers gradually shrunk and a combination of sand and clay boils erupted to the surface. They addressed two points in this regard i.e. the relatively large thickness of the water inter-layers and the long time

duration during which this thickness is sustained following the end of dynamic excitation. Fig. 3-7 depicts their observation from the test.

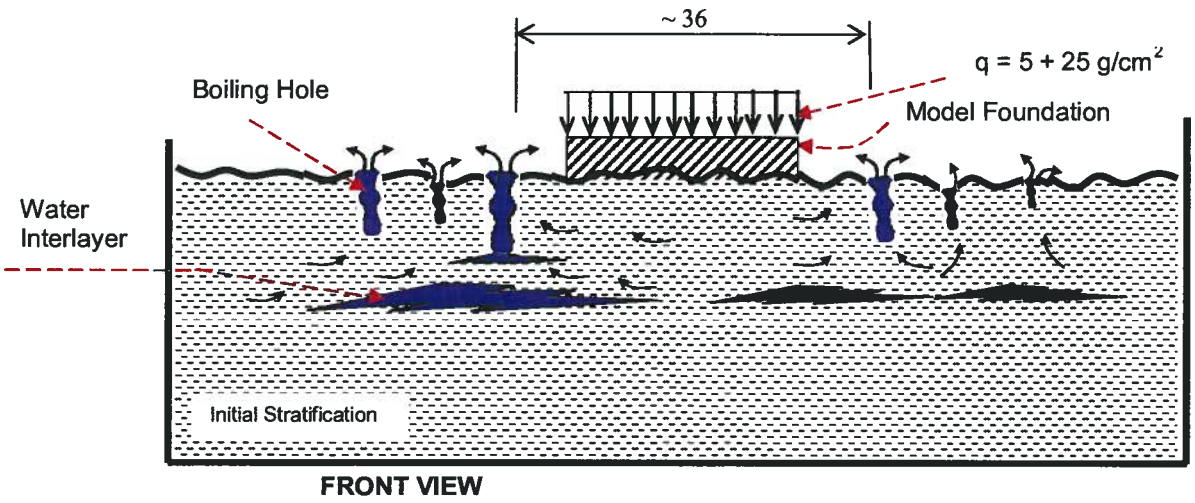

Fig. 3-6: Observation of water interlayer by Huishan & Taiping (1984) in shaking table test of stratified (alternating coarse sand and fine sand) deposit (test R-5, dimensions in cm).

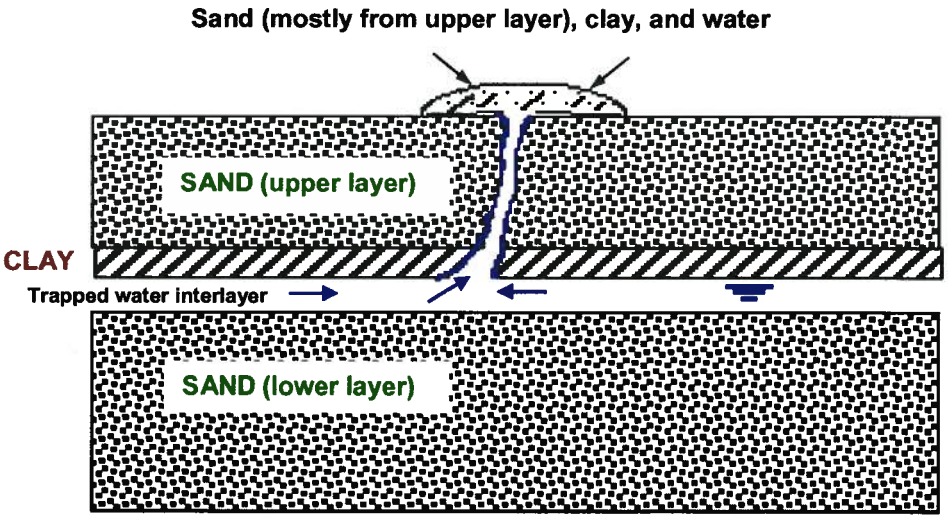

Fig. 3-7: Formation of trapped water interlayer, and delayed sand boil following a hydraulic fracture mechanism.

Fiegel & Kutter (1991 and 1994a) reported results of centrifuge model tests carried out to study the liquefaction mechanism for layered level-grounds. Four models were tested with the first model having homogeneous Nevada sand ($k = 5 \times 10^{-3}$ cm/s) air pluviated at 60% relative

density and the next three models with a non-plastic silt layer ($k = 3 \times 10^{-6}$ cm/s) on top of the Nevada sand. The silt was placed in a slurry form and consolidated in-flight. Water was used as the pore fluid. During the last three tests, the accelerations in the silt layer followed the base shaking (and the acceleration in the sand layer) only for a few cycles and then damped out, indicating that the silt layer became isolated from the base. Pore pressure records showed that pore pressure ratio remained at 100% at the sand-silt interface for a relatively long time. Surface settlement recordings indicated that the silt surface bulged first before finally settling. These observations were not obsereved for the homogeneous Nevada sand test. Based on these test results they concluded that an overlying, relatively impermeable soil tends to restrict the escape of pore water produced by the settlement of an underlying liquefiable sand layer. This can result in the formation of a water gap or a very loose zone of soil at the interface between the two soil layers.

Dobry & Liu (1992) presented two centrifuge tests results conducted on layered soil deposits representing level-ground condition. In the first test, sand was placed at a relative density of 40% with a silt layer on top. These soils were the same as used by Fiegel & Kutter (1991 and 1994a) for their tests. Based on the pore pressures and accelerations measured in these tests, they inferred four stages of behavior, which included the formation of a water interlayer. These are shown in Fig. 3-8a to Fig.3-8d. The first stage lasted 2 seconds where pore pressure generation took place with resulting upward water flow. The second stage lasted from 2 seconds to the end of shaking at 5 seconds, and extended a little bit beyond shaking (initial part of consolidation). Initial liquefaction had been reached at the upper part of the sand layer and a water film at the sand-silt interface grew during this stage, most of upper part of the sand layer experienced complete liquefaction, $R_u \approx 100\%$ (see Fig. 8-3b). The third stage lasted for about 4 minutes during which the only point of the sand layer that had a R_u of 100% was at the interface of the two layers (Fig. 3-8c). During this stage the water film was shrinking. After this the fourth (last) stage took place where there was no water film and coupled consolidation of the two layers took place (Fig. 3-8d). The second test had a model with a very similar two-layer horizontal soil deposit. The main difference was that a shallow foundation was placed on the soil surface. The relative density of the sand was 45%. Dobry & Liu (1992) reported that a water interlayer formed in this case also. The thickness of the water interlayer was thought to be larger in the free field than under the structure, since the weight of the structure was forcing the water out towards the free field. Water was used as pore fluid in the two tests described above.

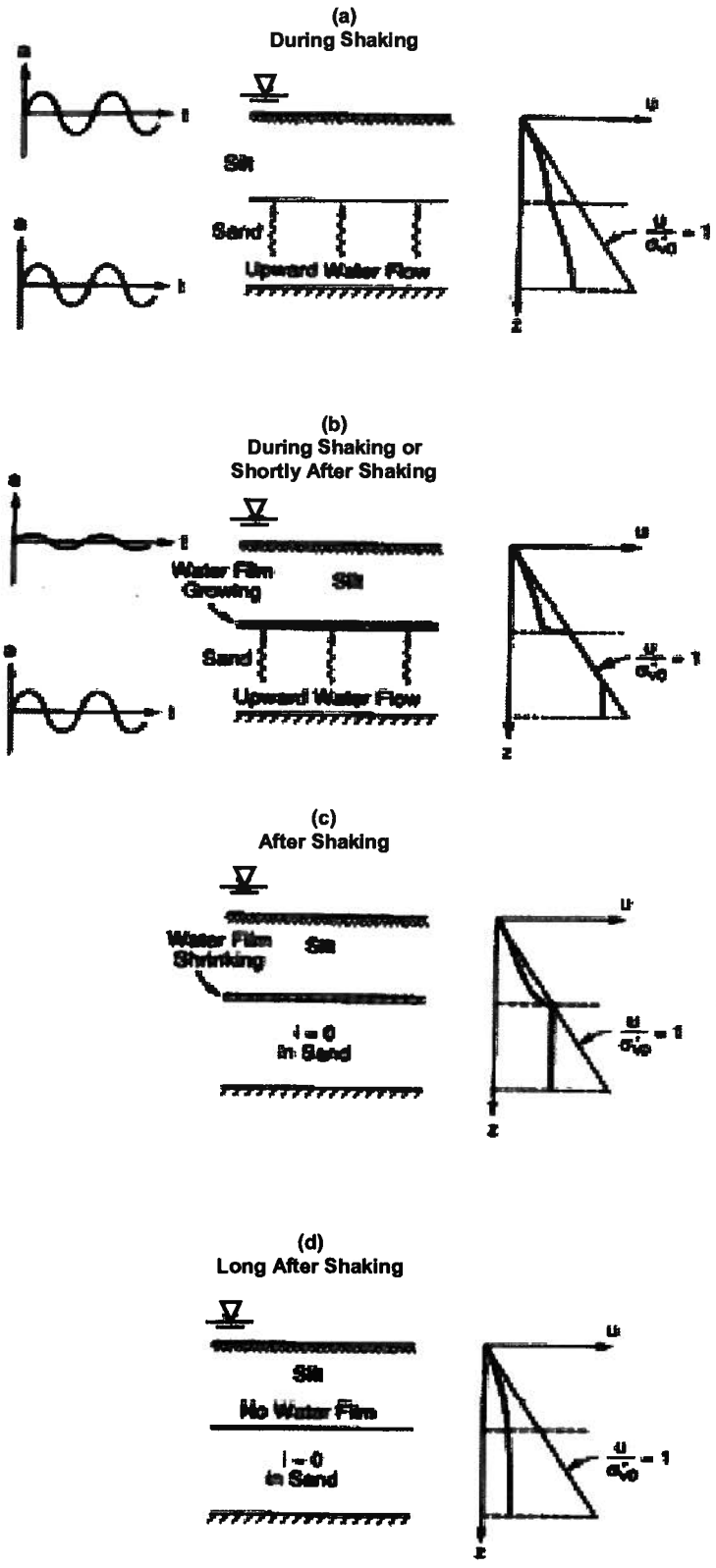

Fig. 3-8: Four stages (i.e. a, b, c and d) in centrifuge test model of two-layer deposit, (modified from Kulasingam, 2003).

Fiegel & Kutter (1994b) reported details of two centrifuge model tests carried out to study the liquefaction-induced lateral spreading of mildly sloping ground (slope angle 2.6 degrees). The first model consisted of homogenous Nevada sand and the second consisted of a layer of Nevada sand overlain by a layer of non-plastic silt.

The Nevada sand was air pluviated at a relative density of 60%. Silt was placed in a slurry form and consolidated in-flight. Water was used as the pore fluid. Both models were subjected to a base motion with a 30 s duration. The homogenous and layered models had maximum base accelerations of 0.9 g and 0.7 g respectively. Pore pressure records during the test indicate that they remained high for a longer duration for the layered model than for the homogeneous model. In both tests approximately 0.8 m of prototype lateral displacement was measured at the surface. As shown in Figure 3-9 in the homogeneous sand model this lateral displacement was distributed throughout much of the layer, whereas in the layered model displacement was concentrated along the interface between layers. Almost all the lateral displacements occurred during shaking for both the tests. Based on *Newmark* sliding block calculation and previous lab tests (Kutter et al., 1994) they pointed out that the undrained steady state strength of the sand far exceeds the strength required to prevent lateral displacement of a 2.6 degree slope, even with 0.7g of lateral acceleration. They attributed the reduced sliding resistance between the silt and the sand layers and the concentration of displacement to the redistribution of voids at the interface.

In an attempt to investigate the mechanism involved in the extensive lateral slides reported from the 1964 Alaska earthquake (e.g. Seed, 1968), Zeng & Arulanandan (1995) conducted a centrifuge model of silty slope with a seam of liquefiable sand. They demonstrated that liquefaction of the sand seam led to slope failure due to pore water redistribution.

3.2.1 Studies carried out in Chuo U. and Davis U.

An experimental research program was conducted by professor Kokusho at Chuo University in the late 90s to investigate the mechanism involved in liquefaction *flow-slide* and in particular in gently sloping grounds. Kokusho (1999) reported results of layered soil column liquefaction models tested to study the mechanism of water film formation in level-ground condition.

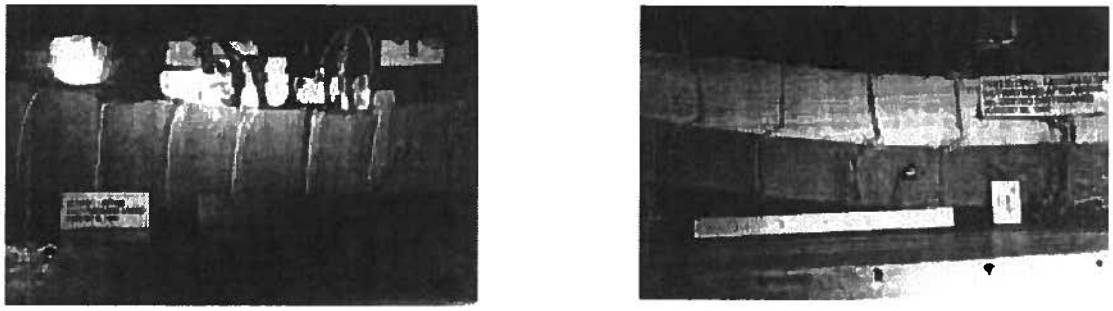

(a) (b)

Fig. 3-9: Lateral displacement patterns in centrifuge tests models of mildly sloping layered grounds, (a) homogenous sand, (b) layered soil (Fiegel & Kutter, 1994b, with permission from ASCE).

An instant shock was used to liquefy a tube of a water-sedimented sand. The test was conducted for a uniform soil with and without a thin non-plastic silt seam (of 4cm thick at z = 96cm) sandwiched between sand layers (see Fig. 3-10). A water film started developing below the silt seam, reached a maximum thickness of 8% of the under-lying loose sand layer (D_r = 39%) shown in Fig. 3-11, and then slowly disappeared. Fig. 3-12 depicts typical time-dependent settlement curves at the surface as well as at interior points in the fine sand. The sand instantaneously liquefied by hammer impact at the benchmark b1 and the settlement started from the bottom. As may be observed from Fig. 3-12 the settlements increase with time linearly until kinks indicated by the benchmarks b2, b3 and b4, where the sedimentation of sand particles suspended in the water take place. Kokusho (1999) carried out a parameter study by varying the relative density of the lower layer. The maximum thickness of water film varied with sand relative density as depicted in Fig. 3-13. Kokusho & Kojima (2002) reported details of similar tests for three 3-layer systems (fine sand-silt-fine sand, coarse sand-fine sand-coarse sand, and coarse sand-fine sand-unsaturated fine sand crust) and a 2-layer system (coarse sand-fine sand). A stable water film was observed in all 3-layer system tests. In the 2-layer test fierce turbulence was observed at the layer interface, with larger void ratio near the bottom of the upper fine sand layer. A stable water film did not develop in the 2-layer test.

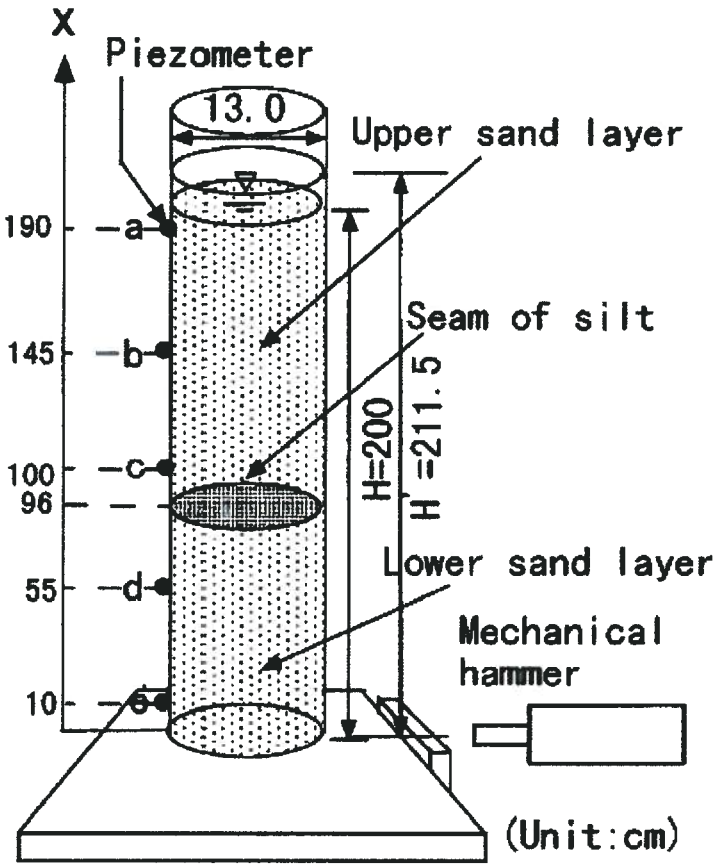

Fig. 3-10: Sketch of 1D tube test device (Kokusho, 1999, with permission from ASCE).

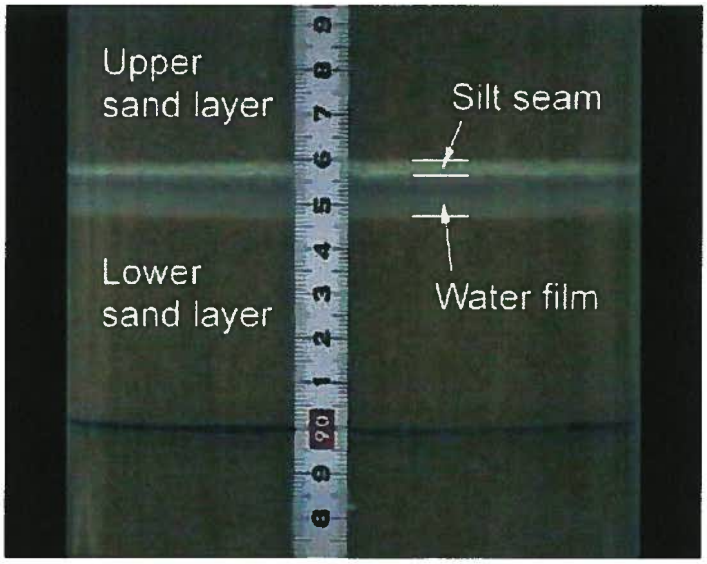

Fig. 3-11: Photograph of Water Film Consisting of Clear Water Formed beneath Silt Seam (Kokusho, 1999, with permission from ASCE).

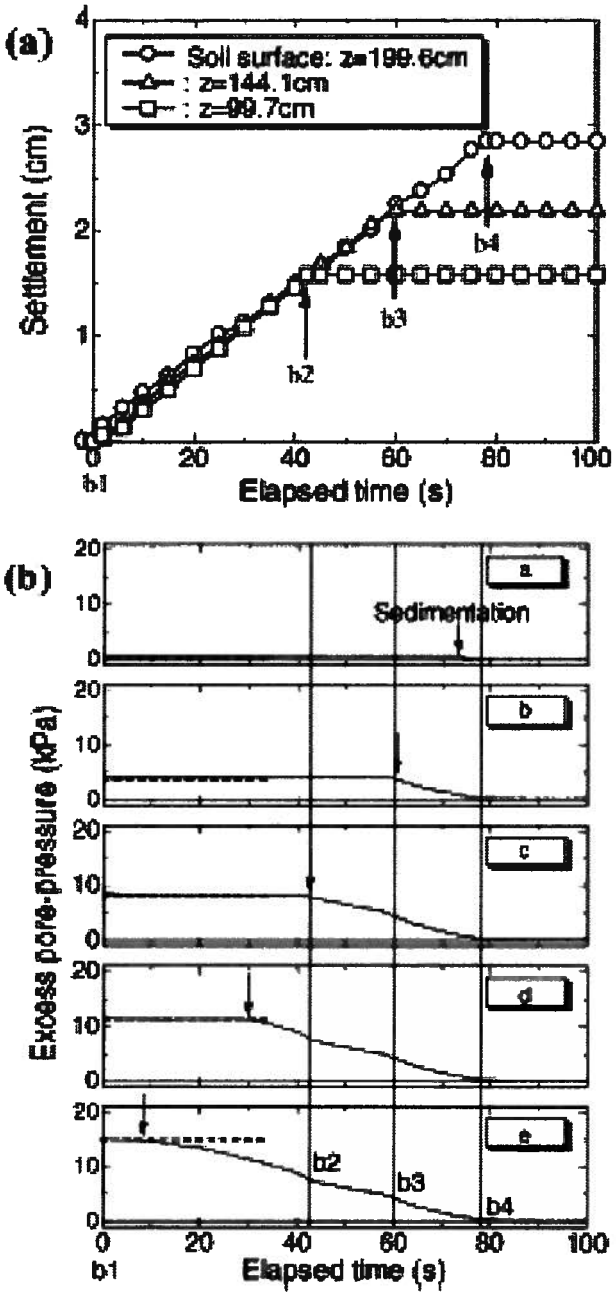

Fig. 3-12: Time-dependent variations in sand settlement (a) and pore pressure, (b) at different depths (Kokusho, 2003).

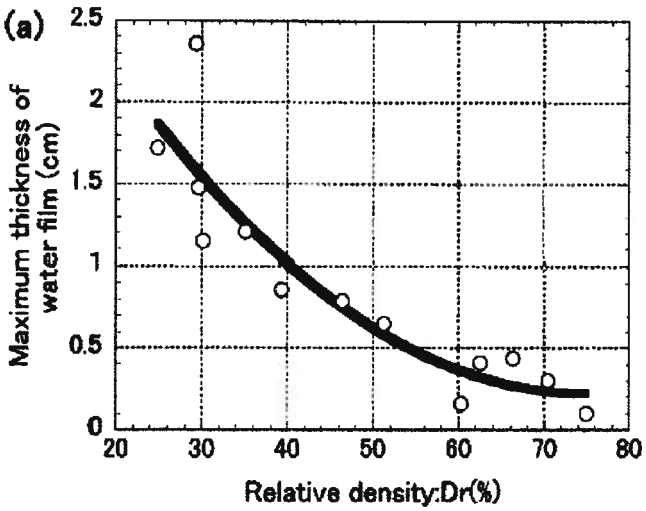

Fig. 3-13: Effect of sand relative density on water film thickness (Kokusho, 1999 with permission from ASCE).

Kokusho (1999, 2000) carried out two-dimensional model tests on the shake table to further investigate the water film mechanism and its effect on overall deformations. Fig. 3-14 shows the three different types of geometries tested. All models were prepared by water pluviation and had loose soils with *Dr* of 21%, 14%, and 35% for models in Fig. 3-14a, 3-14b, and 3-14c, respectively. For each of these tests, companion tests with the same geometry but without any silt seams were conducted to compare the behavior. The models were subjected to a very short duration motion applied in the transverse slope direction. This motion caused liquefaction and limited soil deformations during shaking. Deformations continued after shaking and caused flow failures for models with silt seams. Fig. 3-15 shows displacement time history for case "a" shown in Fig. 3-14 for certain representative points (see Fig. 3-15c for their positions) along with its corresponding case without a silt arc. As may be seen the deformation at the end of shaking for the case with silt arc is less than that of without silt arc case, whereas the former continues to deform after shaking. This deformation was mainly concentrated at the bottom of silt seam-sand interface. A hair-like water film was observed at the toe parts of this interface. In the case of sloping ground with horizontal seams of silt, breakage of the silt seams occurred followed by boiling of the overlying sand leading to a mudflow avalanche. This series of tests illustrates the important role of void redistribution in the failure mode and timing of lateral spreads and flow failures.

Kokusho (2003) reported results of a similar set of model test results with and without silt arc and their deformation patterns after failure are shown in Fig. 3-16 which indicates most of the deformation occurs at the silt-sand interface when the silt arc is present. These results are for an input acceleration of 0.31g. In Fig. 3-17c, the time histories of flow deformation of the same model subjected to weaker input acceleration of 0.18g are shown. Much larger post-shaking flow occurs in this case than when the acceleration was 0.34g; but minimal deformation takes place during shaking. This is because in the weaker motion, the slope remains steep during shaking and so the driving forces are larger during post-shaking flow along the interface.

Concurrently to the studies in Japan, several research model programs were conducted at University of California, Davis, U.S. to investigate low permeability sub-layer effects on seismic behavior of liquefiable soils namely, pile foundation, bridge abutments and sloping grounds using a small 1m and large 9m-centrifuge facilities. The results can be found in a number of reports and publications (e.g. Balakrishnan & Kutter, 1999; Gajan & Kutter, 2002; Kutter et al., 2004, and Malvick et al., 2006) that were interpreted in few PhD theses i.e. Kulasingam (2003)

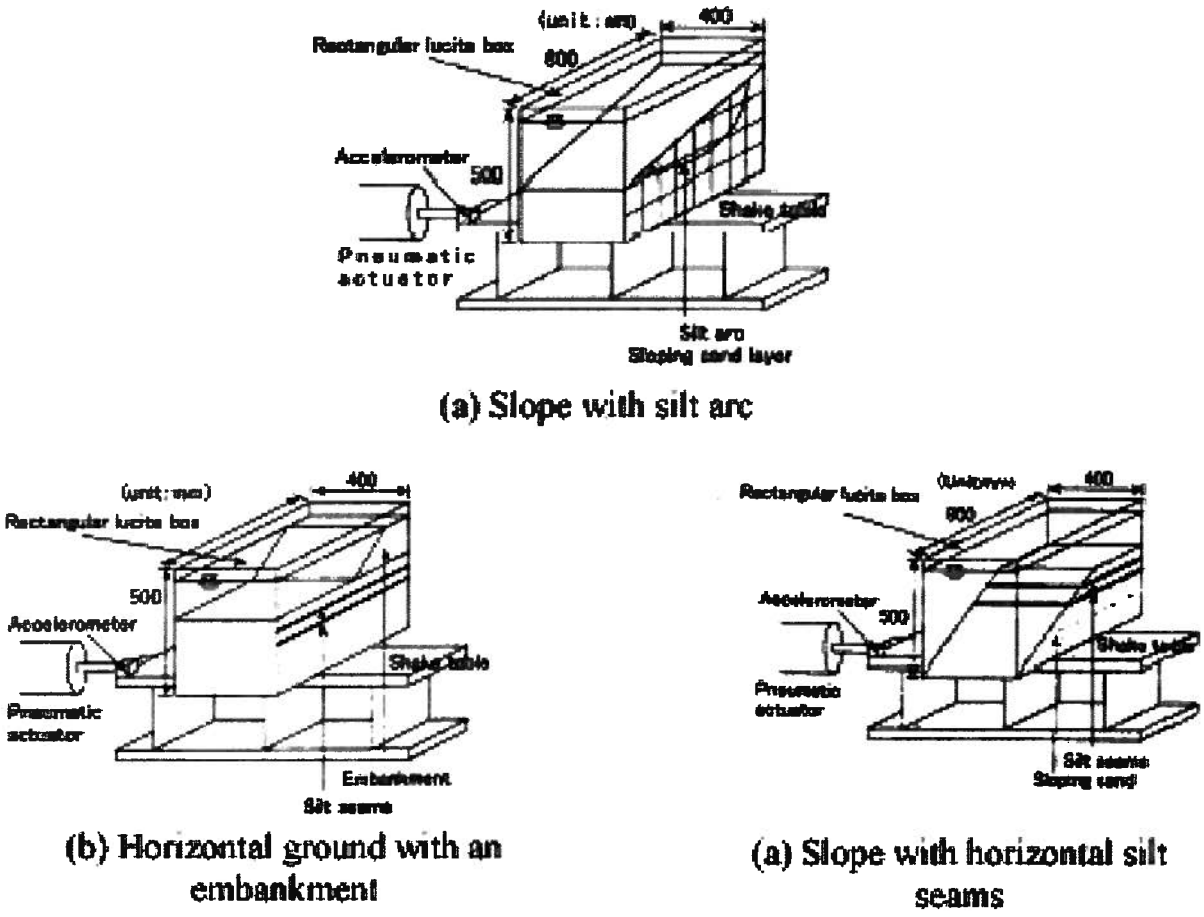

Fig. 3-14: 2-D model tests with silt layer (Kokusho, 1999, with permission from ASCE).

and Malvick (2005). Fig. 3-18 shows a test model of a river flood plain used to study the effect of relative density and thickness of sand layers on the amount of settlement and lateral spreading near bridge abutments. The models had a river channel with clay flood banks underlain by layers of sand with varying relative densities and thickness. The layers had a gentle slope with one of the banks having a bridge abutment surcharge. The models were constructed by air pluviating the sand and placing the clay in a slurry form consolidated at 1 *g* under a vacuum pressure of about 80 kPa. Water was used as the pore fluid. The models were subjected to three large shaking events. Discontinuous lateral deformations at the clay-sand interface (interface slip ≈ 1.2 m), with the clay layer moving more than the top of the sand layer, were observed for two of the models where the relative densities of the sand layer were high and/or the thickness of the looser layer was small.

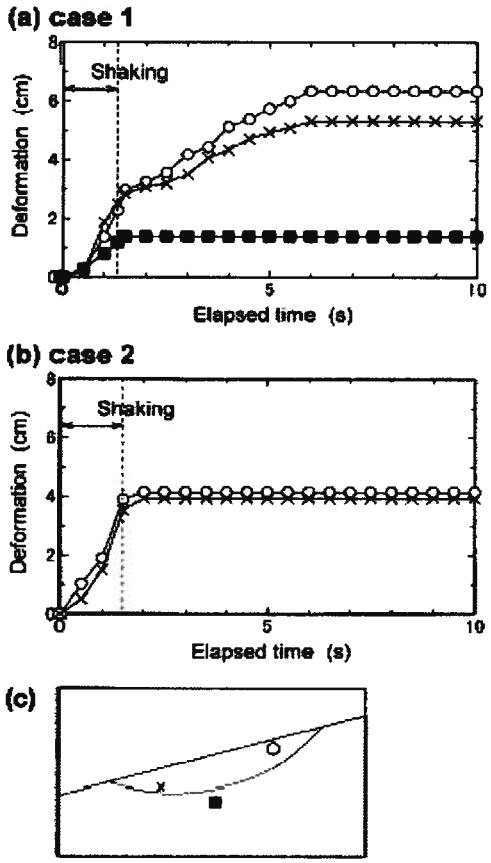

Fig. 3-15: Soil deformation vs. elapsed time for representative points in sloping ground (a) case 1, with silt arc; (b) case 2, without silt arc; (c) location of representative points (Kokusho, 1999 with permission from ASCE).

However, in cases where the sand layer was looser or thicker the deformation patterns appeared to be continuous or the clay appeared to move less than the sand. The clay layer seems to have moved by the same amount (1.5 – 1.8 m) for all the tests regardless of varying densities or thickness of the underlying sand layer (see details in Fig. 3-19 and Table 3-1). This may have been caused because of the deformations of the clay layer being limited by the river channel boundary.

The observations of discontinuous deformations at the interface in some tests and the fact that the clay layer had negligible strains (almost moved as a rigid block) indicate that void redistribution played an important role in the deformation mechanism.

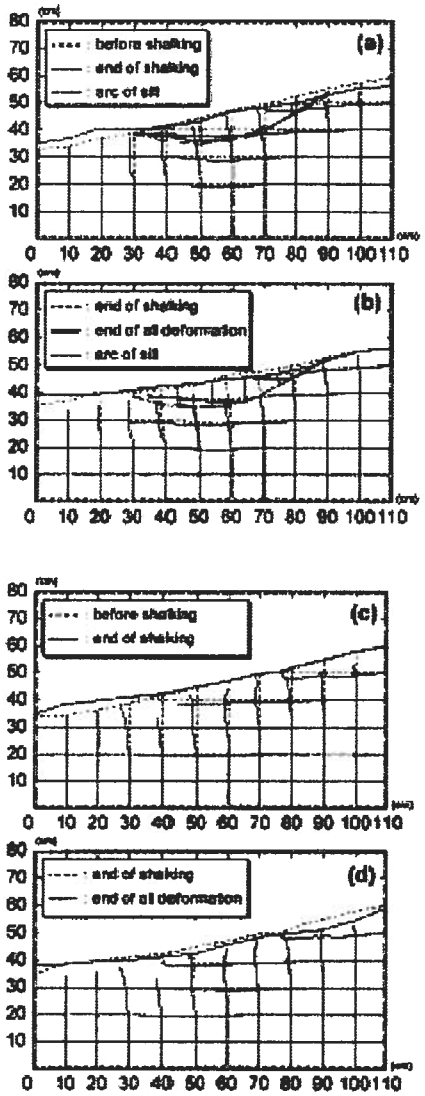

Fig. 3-16: Cross-sectional deformation for slopes (a) & (b): with buried silt arc. (c) & (d) without silt arc. (a) & (c) during shaking. (b) & (d) after the end of shaking (Kokusho, 2003).

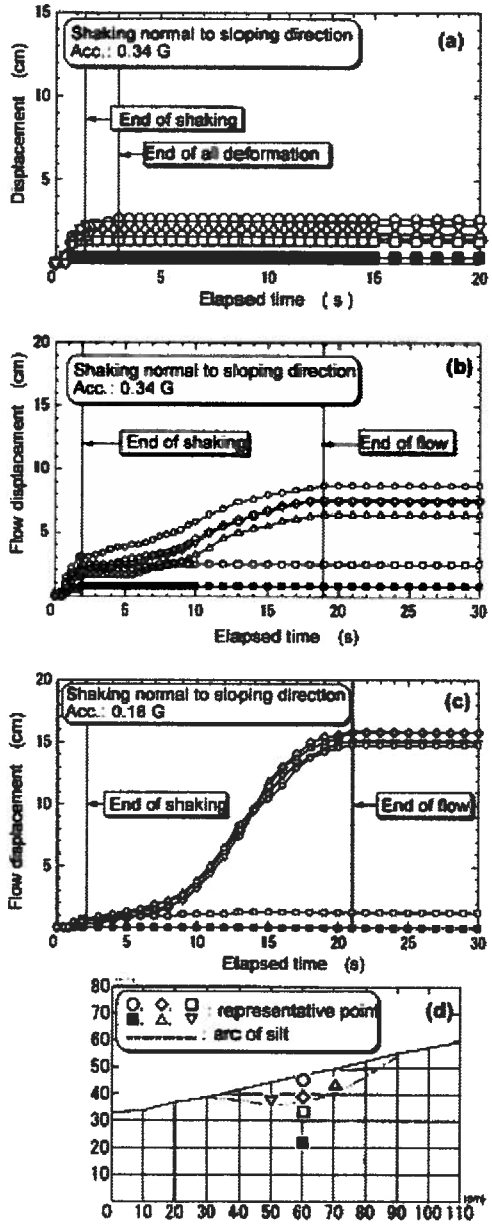

Fig. 3-17: Time-dependent flow displacement at target points shown in (d); a) without silt arc by PGA 0.34g. (b) with silt arc by PGA 0.34g. (c) with silt arc by PGA 0.18g. (Kokusho, 2003).

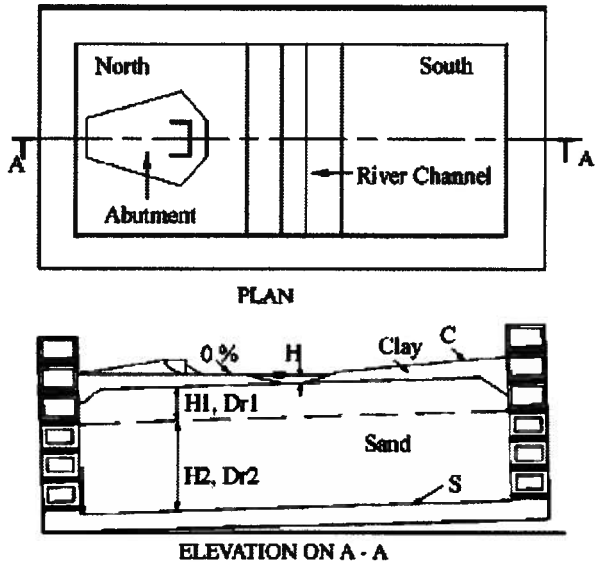

Fig. 3-18: General model configuration for lateral spreading study of bridge abutment (Kutter et al., 2004, with permission from ASCE).

Table 3-1: Model tests details for lateral spreads of bridge abutments (Kutter et al., 2004).

Model code	Model details	Slope of clay (*C*)	Slope of sand (*S*)	Height of water table (*H*) (m)
C80	$H1 = 0$ m $Dr_2 = 80\%$, $H2 = 15$	9.3%	3.3%	1.2
U50	$Dr_1 = 50\%$, $H1 = 9$ m $Dr_2 = 80\%$, $H2 = 6$ m	9.0%	3.0%	1.2
U50_4.5	$Dr_1 = 50\%$, $H1 = 4.5$ m $Dr_2 = 80\%$, $H2 = 10.5$ m	9.3%	3.3%	1.2
U50_4.5S	$Dr_1 = 50\%$, $H1 = 4.5$ m $Dr_2 = 80\%$, $H2 = 7.5$ m	3.0%	3.0%	1.2
U30_4.5	$Dr_1 = 30\%$, $H1 = 4.5$ m $Dr_2 = 80\%$, $H2 = 7.5$ m	9.3%	3.3%	1.2
U30_4.5M	$Dr_1 = 30\%$, $H1 = 4.5$ m $Dr_2 = 80\%$, $H2 = 7.5$ m	9.3%	3.3%	−0.3–1.3 (variable)

Note: U30_4.5M stands for Unimproved Dr=30% sand of 4.5 m thickness with input motion (*M*) varied. *C*, *S* and *H* are marked in Fig. 3-20.

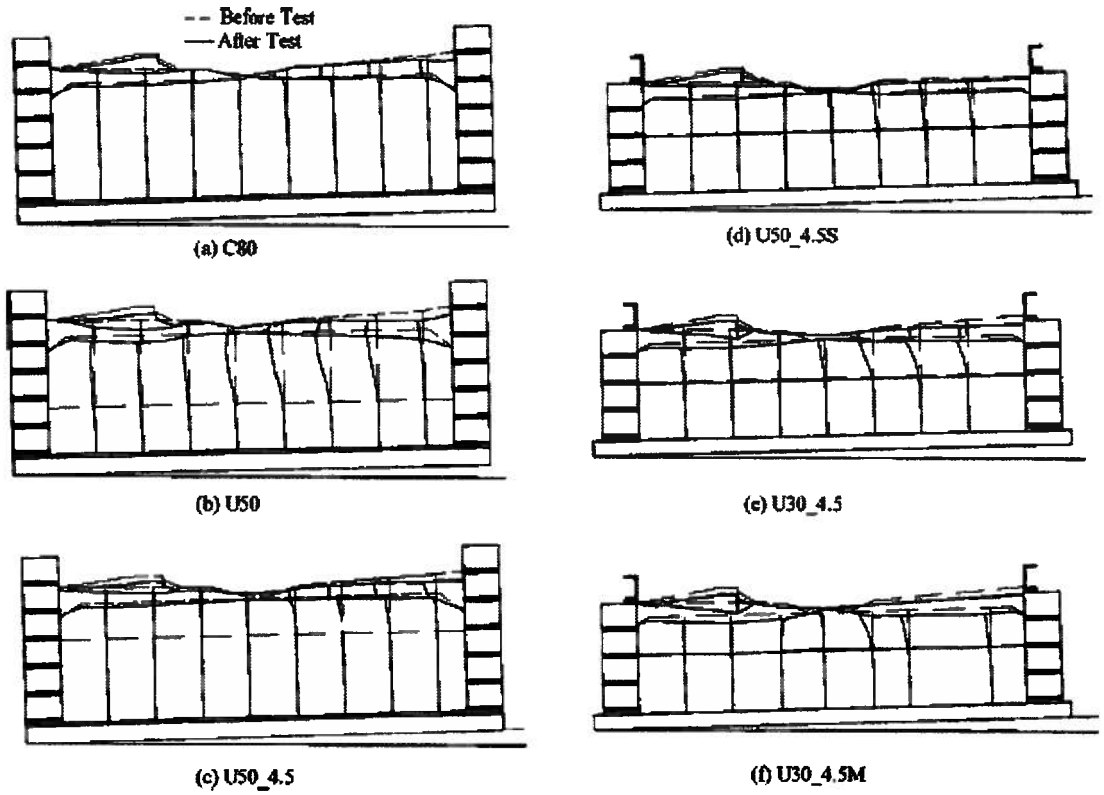

Fig. 3-19: Deformation pattern of tested models, see Fig. 3-18 and Table3-1 for details (Kutter et al., 2004, with permission from ASCE).

Kutter et al. (2004) also examined the empirical correlation proposed by Youd et al. (1999) for lateral spreading that only considers the thickness of soil layers that have $(N_1)_{60}$ <15; against their test results. They showed that thick soil layers with $(N_1)_{60}$ >15 (approximately Dr = 55%) can also produce significant lateral movement.

Davis U. research group reported results of another set of model tests to study the behavior of piles in laterally spreading ground (Singh et al., 2000, and 2001; Brandenberg et al., 2001). The models had a top, moderately over consolidated clay, layer underlain by a middle loose sand layer ($Dr \approx$ 20-30%) and a bottom dense sand layer ($Dr \approx$ 70-90%). Some models had a thin coarse sand layer on top of the clay layer. All layers had a 3° - 4.5° general slope. The clay had a 25° sloping river channel at one end. All models had single and group piles embedded in them. The models were constructed by air pluviating the sand and placing the clay in a slurry form consolidated at 1 *g* under a vacuum pressure of about 80 kPa. Water was used as the pore

Fig. 3-20: Discontinuous lateral deformations in the clay sand interface (adapted from Kulasingam, 2003).

fluid. The models were subjected to several (more than 3) large shaking events. Lateral deformation patterns after the shaking events show a clear discontinuity at the clay-loose sand interface as shown typically in Fig. 3-20 (photo taken by Brandenberg, 2001). This was attributed to loosening due to void redistribution driven by the upward hydraulic gradients produced by the excess pore pressures in the underlying sands.

Malvick et al. (2005) presented results of a U.S.-Japan cooperative research project conducted jointly at Chuo University in Tokyo, by Professor Kokusho and his coworkers and University of California at Davis to collaborate on a project studying the effects of void redistribution and water film formation on shear deformations due to liquefaction in layered soils. They employed 1g-shake table, small 1m-radius centrifuge and large 9m-radius centrifuge facility in a 2-D study of slopes with various relative density of liquefiable sand layer comprising silt sub-layer subjected to 1 to 3 subsequent events.

The typical shake table model had a 4H:1V slope that was 0.3m high and consisted of Tokyo Bay sand (see Fig. 3-14). Models were typically shaken transverse to the slope by a harmonic motion (Kokusho, 2003). The typical centrifuge model had a prototype 2H:1V slope that was 6m high and consisted of Nevada sand (shown in Fig. 3-21 and 3-22 for small and large centrifuge models, respectively). Models were typically shaken along the slope by a modified earthquake ground motion (Kulasingam et al., 2004). A few tests were performed at both institutions to control operation and procedures effects. Fig. 3-23 shows the shake table model configuration before and after shaking. This model consisted of a loose slope of Tokyo Bay sand with embedded silt arc. The model failed after being shaken transverse to the slope (normal to the

view shown) by a 3 Hz harmonic motion for 1 s with a peak base acceleration of 0.3 g. Approximately 50% of the deformations and localization occurred for 9 seconds after shaking stopped. This shake table test is similar to other tests completed at Chuo University and described in Kokusho (1999 and 2000), Kokusho & Kojima (2002), and Kokusho (2003). For comparison, some of the tests described in these references showed 50% to 85% of the movements occurring up to 20 s after shaking stops. The base acceleration during shaking for these models ranged from approximately 0.15 g to 0.35 g.

Fig. 3-24 shows typical centrifuge model configuration before and after shaking along with a close up of silt-sand interface showing localization. Kulasingam et al., (2004) demonstrated that a slope model of D_r = *20%* without a silt sub-layer can withstand the applied shaking event whereas a similar model with greater relative density e.g. 50% failed when a silt layer is present in the slope as shown in Fig. 3-24. Fig. 3-25 shows the initial states for the sand they used compared to the sand's *steady-state* line. The *steady-state* line is based on isotropically consolidated undrained and drained triaxial compression tests by Castro (2001). Initial states for the sand are shown for the confining stresses just below the silt arc near the middle of the slopes. This suggests that even the initial D_r = 20% models would be dense of critical and have sufficient undrained shear strength for stability. They inferred that water film formation is the extreme condition of localization that it may not be manifested during failure of a slope with barrier layer. Kulasingam (2003) back calculated shear strengths using limit equilibrium and Newmark (1965) sliding block method from test models experiencing localization and showed that they are much lower than that inferred from the *steady-state* condition. He also argued that the extent to which void redistribution affected the apparent residual strength, S_r in the few case histories that control current empirical procedures is unknown. Thus it is not clear whether these field-based correlations (e.g. Seed 1987; Seed & Harder and Olson & Stark, 2002) are conservative or unconservative in their implicit accounting for void redistribution effects. He concluded that numerical modeling is an appropriate approach to account for void redistribution effects in *post-liquefaction* strength.

Fig. 3-26 shows a typical displacement time history obtained in 1g-shaking table test and 80g-centrifuge test of the model with configuration given in Fig. 3-22 (Malvick et al. 2005). The authors concluded that timing of localization occurrence and the portion of post shaking displacement depend on model configuration and motion characteristics i.e. level of excitation and its duration.

Post-shaking failure also took place in centrifuge model of a submerged slope (with configuration given in Fig. 3-27) including a sub-layer silt barrier designed by UBC and tested at C-CORE, N.F. after end of shaking (Phillips et al., 2005 available at www.civil.ubc.ca/liquefaction).

Malvick et al. (2005) concluded that several key factors including: barrier shape, sand relative density, thickness/volume and permeability of liquefied layer, and earthquake characteristics control void redistribution and ground deformations. A summary of their findings is listed in Table 3-2 with a footnote for main references to specific factors. It indicates that looser materials experience larger displacements and more susceptible to localization. It also

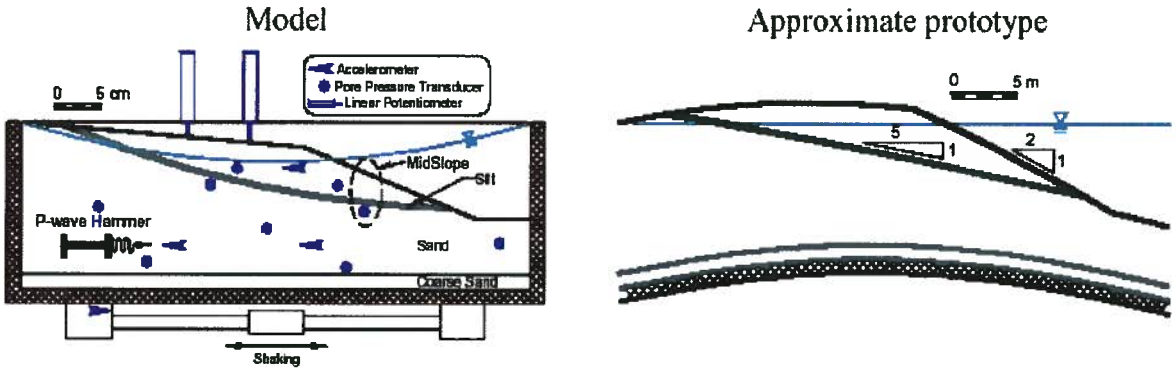

Fig. 3-21: Typical model configuration and prototype equivalent using 1m-radius centrifuge with rigid container of 560 × 280 × 180 mm tested at Davis U. (Kulasingam et al., 2004, with permission from ASCE). Note that the base of the model in prototype scale is curved due to great variation in revolution radius within the model.

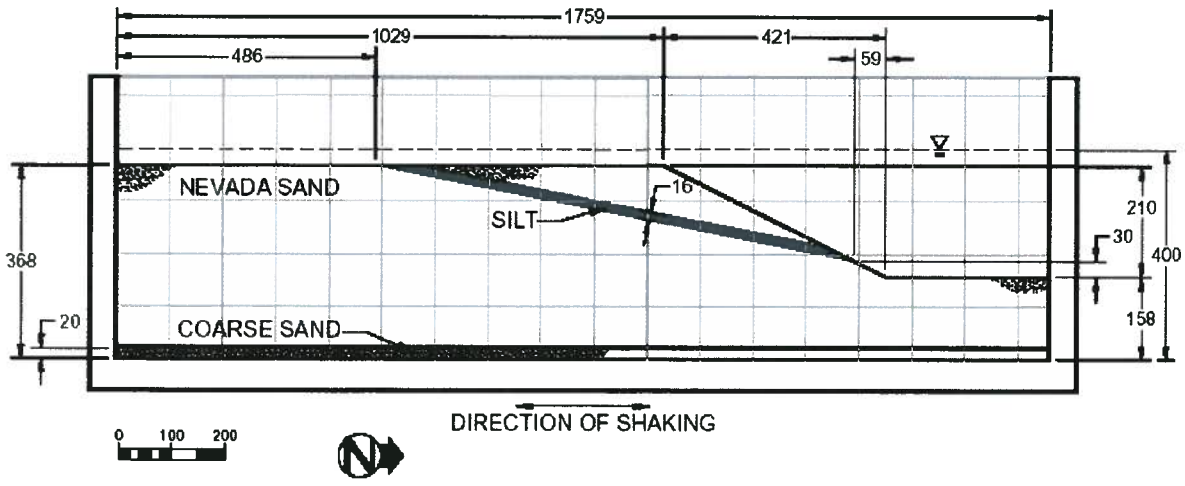

Fig. 3-22: Typical model configuration using 9m-radius centrifuge with rigid container of 1759 × 700 × 600 mm tested at Davis U. (Malvick et al., 2002).

shows that thicker liquefiable layers aggravate the effect of low permeability sub-layer.

The lower permeability of the liquefied layer can increase the potential for localization or water films to form after shaking. The delays of ground displacement until after shaking were most dramatic when the ground motion was small enough to minimize earthquake-induced deformations but strong enough to trigger high excess pore pressures throughout the slope. They also concluded that the residual shear strength of liquefied soil that would be appropriate for use in a stability analysis does not depend solely on the soil's pre-earthquake state (i.e. density and confining stress), because instability may form along a zone of soil that has become loosened during void redistribution or along interfaces that have trapped water films.

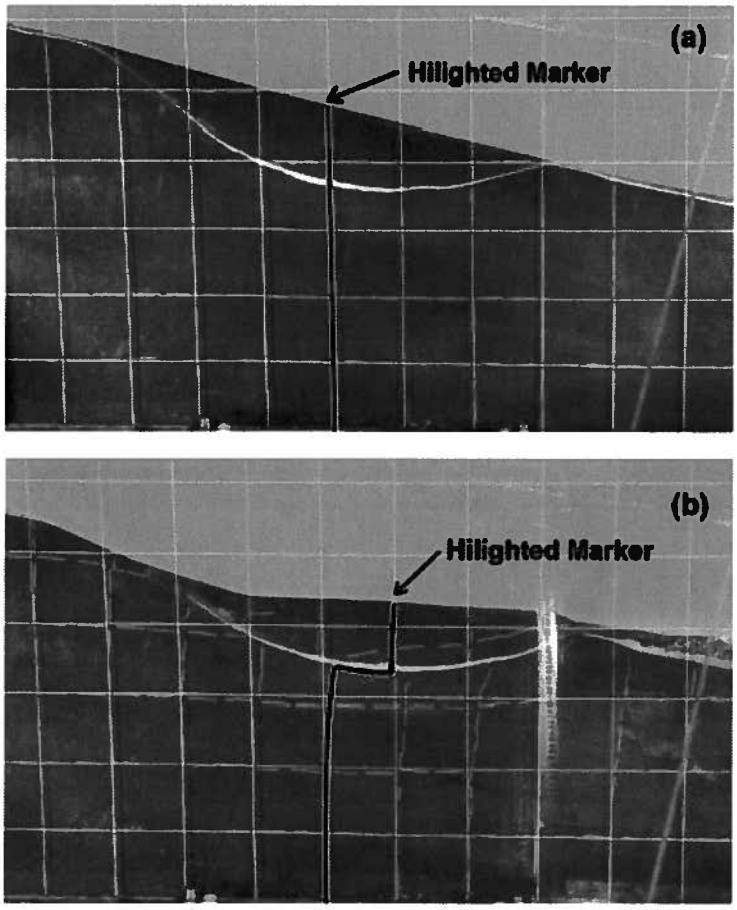

Fig. 3-23: Shake table model (a) before testing and (b) after testing (Malvick et al., 2005).

(a)

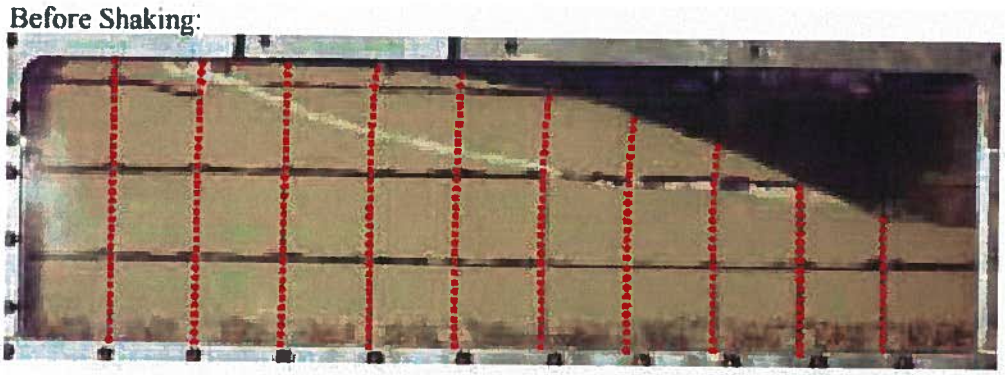

(b)

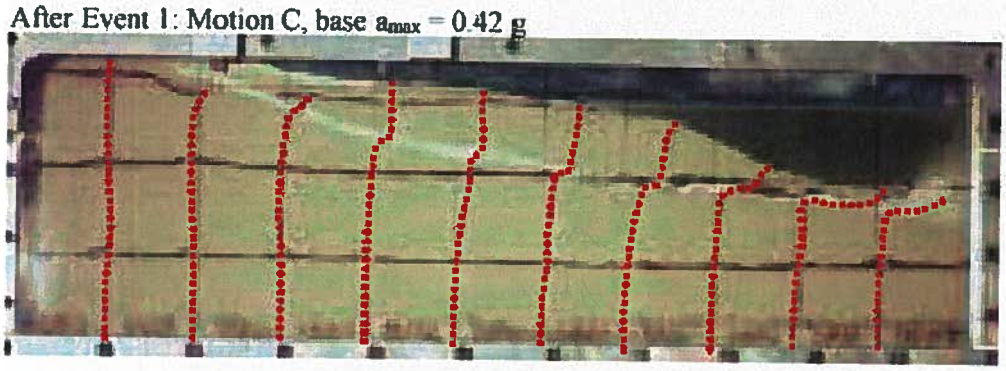

Photos from test RKS11 ($D_r \approx 50\%$, Sand with Silt Arc)

(c)

Fig. 3-24: Centrifuge model configuration (a) before shaking, (b) after shaking, (c) close up of silt-sand interface after shaking (Kulasingam et al. 2002).

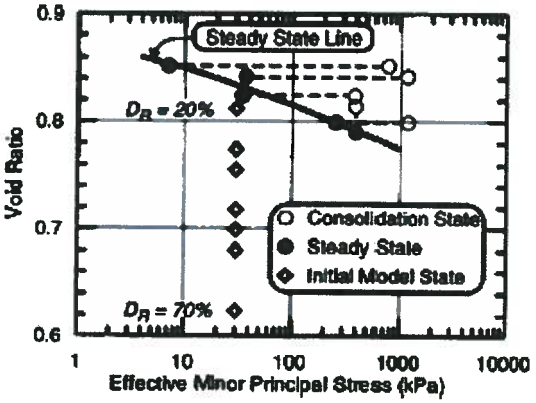

Fig. 3-25: Initial state of sand beneath silt arc at mid-slope relative to *steady-state* line for Nevada sand (Kulasingam et al., 2004).

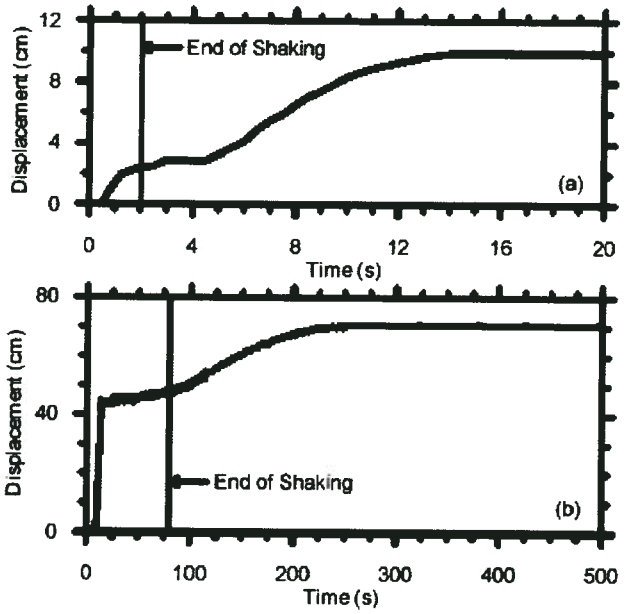

Fig. 3-26: Displacement time history above silt arc in models as shown in Fig. 3-22: (a) a 1-g shake table test and, (b) an 80-g centrifuge test (Malvick et al., 2005).

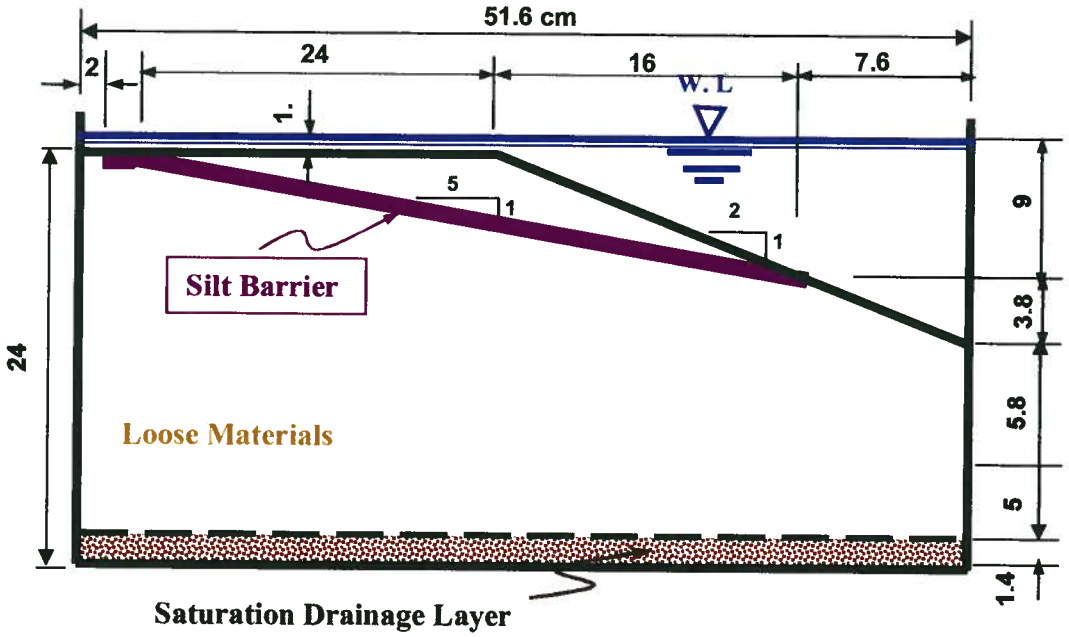

Fig. 3-27: UBC-CCORE model of submerged slope with barrier layer failed after end of shaking (prototype scale, Ng = 70g).

Table 3-2: Findings of Davis U. and Chou U. joint research program on void redistribution.*

Factor	Influence
Shape of low-permeability barrier[1,2,7,8,11]	• When the shape of the low-permeability layer coincides with a kinematically admissible failure surface, it is more likely to contribute to localization and large deformations.
Relative density of the liquefied layer[1,2,7,11,12]	• Looser soils trigger liquefaction sooner during shaking. • Looser soils experience larger consolidation strains, thereby expelling more water that can drive localization or water film formation elsewhere in the slope. • Looser soils require less water inflow (dilation) at the contact with a low permeability layer before they will localize and/or form a water film. • Looser soils develop larger shear strains during shaking and larger total displacements (includes displacements along localizations or water films). • The magnitude of ground displacement depends on whether or not localization forms with the transition between these cases occurring over a small range of relative density.
Thickness (volume) of the liquefied layer[1,5,7,9,11,12]	• Thicker layers expel more water to drive localization or water film formation beneath an overlying low-permeability barrier layer. • Thicker layers take longer to reconsolidate, which increases the potential for localization or water films to form after shaking.
Hydraulic impedance of barrier layer[1,2,3,6,9] • Permeability contrast between liquefied and barrier soils • Thickness of barrier layer	• The hydraulic impedance of the barrier layer increases with increasing thickness and decreasing permeability. • Greater hydraulic impedance restricts pore water flow across the interface between the liquefied soil and the overlying barrier soil. This allows more water to accumulate, thereby making localization or water film formation more likely.
Permeability of liquefying layer[1,6,7]	• A lower permeability for the liquefied layer reduces the rate of pore pressure dissipation and consolidation, which can increase the potential for localization or water films to form after shaking. • A lower permeability for the liquefied layer reduces the permeability contrast with the overlying barrier layer, and could reduce the potential for water to accumulate at the interface if the contrast is small enough.
Earthquake[1,2,4,5,6,7,9] • Frequency content • Amplitude and duration of motion • Direction of shaking • Shaking sequence and history	• The proportion of the total ground displacement that occurs after shaking depends on how much displacement is induced during shaking versus how much occurs due to pore water flow after shaking. • Delays of ground displacement until after shaking were most dramatic when the ground motion was small enough to minimize earthquake-induced deformations but strong enough to trigger high excess pore pressures throughout the slope. • Larger amplitude and/or duration motions increase shear strains, which increases volumetric strains in the liquefying layer, thereby making localization more likely. • Shaking transverse to the slope direction may reduce inertial stresses down slope which could reduce deformations during shaking. • Prior shaking can increase the cyclic resistance of the liquefying sand, thereby reducing the potential for localization. At the same time, prior shaking can cause loosening below the barrier layer, which increases the potential for localization in subsequent shaking events.

*Specific references for the factors are:

1. Kokusho (1999), 2. Kokusho (2000), 3. Kokusho & Kojima (2002), 4. Kokusho (2003), 5. Kulasingam et al. (2001), 6. Kulasingam (2003), 7. Kulasingam et al. (2004), 8. Kutter et al. (2002), 9. Malvick et al. (2002a), 10. Malvick et al. (2002b), 11. Malvick et al. (2003), 12. Malvick et al. (2004).

3.3 Laboratory Investigations on Void-Redistribution

Void redistribution was observed in laboratory sand specimens (Casagrande & Rendon 1978 and Gilbert, 1984). However, Casagrande (1980) suggested that void redistribution observed in the laboratory element tests are the result of test boundary conditions and may not reflect in-situ soil behavior. Recently, it was recognized that void redistribution can occur during an earthquake due to pore water flow (NRC, 1985), and a few investigators have attempted to simulate this condition by using element testing in partially drained condition (e.g. Vaid & Eliadorani, 1998 and Eliadorani, 2000) as discussed earlier.

Chu & Leong (2001) showed that instability occurs in both loose and dense sands when injection rate (called "imposed strain rate") is greater than their corresponding dilation rate.

Bobei & Lo (2003) reported strain softening behavior for silty sand under partially drained (strain-controlled) loading condition similar to that reported for sands (e.g. Eliadorani, 2000). Boulanger & Truman (1996) and Boulanger (1999) conceptualized the void redistribution mechanism in an infinite slope with a lower permeability top layer, by stress path testing in a triaxial apparatus.

Tokimatsu et al. (2001) conducted partially drained hollow cylinder torsional shear tests by controlling the amount of pore water injected into the specimens as a function of shear strains

The pore water migration from the underlying liquefied soil layer was modeled by pore water injection into these elements. They concluded that:

- Even dilative medium dense sand exhibits very low shear strength and may undergo flow failure if a sufficient amount of pore water is injected as noted by Eliadorani (2000). Such pore water migration is confirmed to be the major cause of liquefaction induced flow slides in dilative sands.
- If liquefied, saturated sand expands due to water injection; the mobilized shear stress tends to decrease, accompanied by large shear strain. The tendency becomes pronounced as the soil density decreases or the amount of injected pore water increases.
- If non-liquefied, saturated sand subjected to initial shear stress expands by only 0.3 – 0.5% due to inject flow, the shear strain tends to increase, irrespective of initial soil density.

Kokusho (2003) conducted a set of cyclic undrained hollow cylinder torsional tests with and without vertical constraint (no settlement) in an attempt to simulate low permeability sub-layer effects on a liquefiable soil layer behavior shown schematically in Fig. 3-28.

He tested clean sand samples of D_r = 40% consolidated under 98 kPa and cyclically sheared with τ_d/σ_c = 0.2 of 0.1 Hz under undrained conditions. The equipment had a shear strain limit of 25% double amplitude. Fig. 3-29 shows the test results in terms of shear stress, strain, excess pore water pressure, axial (total) stress fluctuation and water film thickness and/or settlement, respectively for case with and/or vertical constraint. In both tests the results are very similar in the earlier part. However, after the excess pore water pressure ratio reaches 100%, strain development is much more drastic in the case with vertical restraint and reaches the maximum strain limit earlier than in the case without the restraint because of void redistribution at the top of the sand specimen. Variation of total vertical stress can be measured in this case as on the fourth diagram in Fig. 3-29a, indicating the periodical fluctuation due to the dilatancy effect.

The water film formation is observed in the case with vertical constraint some time (i.e. at 60 s) after initial liquefaction, R_u = 100% (at the end of the 6th cycle) partly, where its thickness increases linearly in subsequent test period (see Fig.3-29a, fifth diagram). Obviously, the excess pore pressure and vertical stress cease to fluctuate after the formation of the water film in contrast with the case with no vertical restraint in Fig. 3-29b. The vertical settlement depicted on the 5th diagram of Fig. 3-29b indicates that the settlement after the onset of liquefaction occurs only at short periods of zero shear stress. This further suggests that the post-liquefaction settlement of sand particles suspended in pore water can occur at the moment of zero shear stress only. This is consistent with observation in centrifuge tests that the settlement of liquefied slopes decreases with ground inclination as reported by Taboada & Dobry (1998).

Kokusho (2003) reported results of another set of cyclic tests on a sand sample of Dr = 28% when consolidated under 98 kPa stress with static shear stress ratio of τ_o/σ'_c = 0.19 and cyclic stress ratio of τ_d/σ'_c = 0.20. Fig. 3-30 shows time histories of stress, strain, excess pore water pressure, axial total stress (change) and water film thickness for a test with vertical settlement constraint (clamped). Note that the excess pore water pressure has pak values when the shear stress is almost zero while it decreases considerably at all other times due to the dilatancy effect. Pore pressure builds up to 100% in the middle of the 3rd cycle, and the water film becomes visible 1.5 cycles later, increasing its thickness linearly up to 5 mm eventually. The residual strain increases in the direction of the initial shear stress while changing cyclically, arrives at the strain limit of 24%.

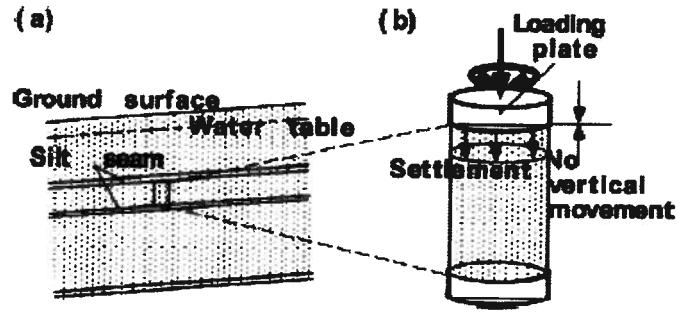

Fig. 3-28: Field condition of a stratified slope (a) sandwiched sub-layer silt, (b) laboratory simulation using torsional apparatus (Kokosho, 2003).

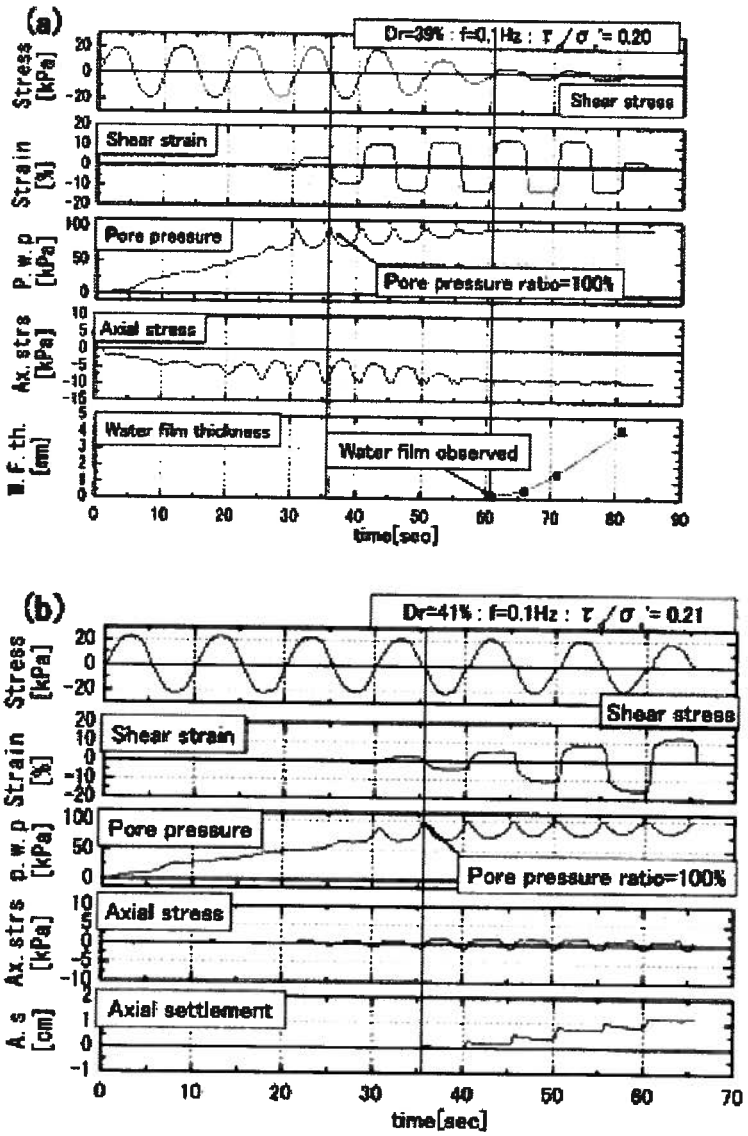

Fig. 3-29: Time histories of shear stress, strain, U_e, axial stress water film thickness/settlement for (a) with vertical restraint, and (b) without vertical restraint (Kokosho, 2003).

As may be noted, although the water film appeared after initial liquefaction in this test, this may not be the case in reality, since the sample was not allowed to displace freely due to equipment limitation (see the second graph in Fig. 3-30). The gap between liquefaction onset and water film appearance and then linearly increase in these tests may be attributed to inject flow.

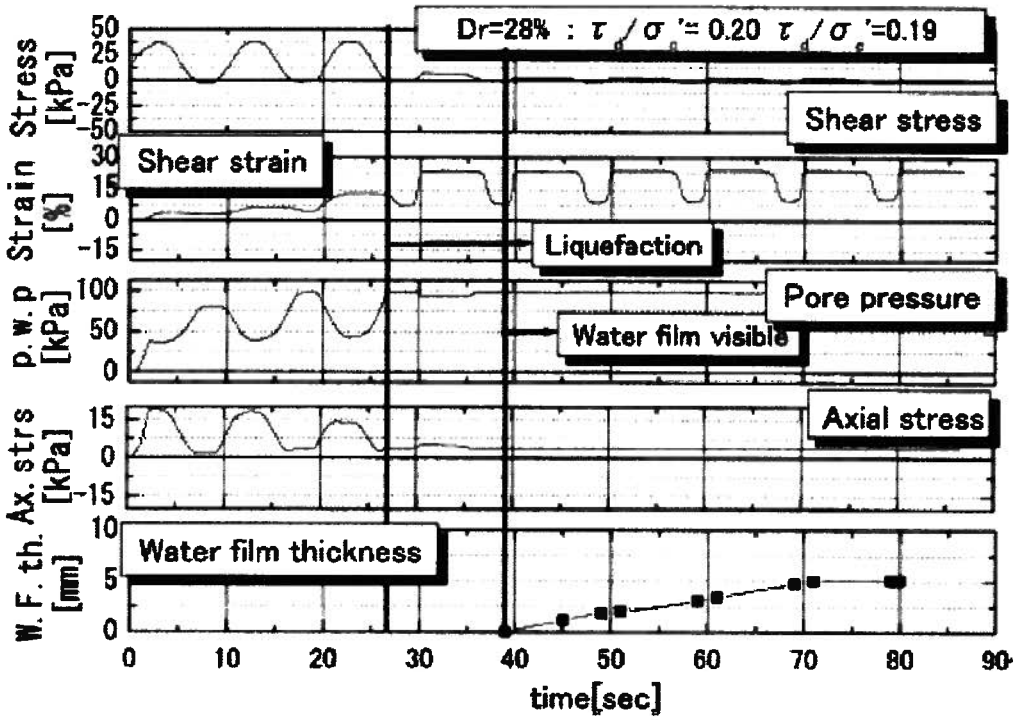

Fig. 3-30: Time histories of shear stress, strain, U_e, axial stress water film thickness for sample of D_r = 28% with static shear bias. (Kokusho, 2003).

3.4. Numerical Studies on Void Redistribution

Recently researchers have applied numerical methods to simulate the behavior of earth structures near the interface of a low permeability top layer and liquefiable bottom layer (e.g. Yoshida & Finn, 2000; Yang & Elgamal, 2002; Bastani, 2003; Uzuoka et al., 2003; Seid-Karbasi & Byrne, 2004a and Seid-Karbasi & Byrne, 2007). The computational formulations derived from fundamental soil mechanics principles and incorporated in a stress-flow coupled analysis procedure with an account for pore water redistribution can predict deformations in stratified grounds and resulted localized shear strains at the layers interfaces.

Yoshida & Finn (2000) presented initial results of a numerical work to model water film formation using a joint element technique. They applied their procedure to predict a centrifuge test model of liquefiable level ground with surface barrier (Liu & Dobry, 1993).

Yang & Elgamal (2002) employing an effective stress approach predicted large deformation in a mildly sloping ground of liquefiable soil with localization beneath the low permeability top layer. They noted that the analysis results are mesh size dependent and suggested further studies in this regard.

Bastani (2003) utilizing numerical analysis evaluated static centrifuge tests subjected to seepage forces similar to those that occur post-shaking. The model showed dilation characteristics, such as void ratio increases, consistent with void redistribution although the mechanistic explanation was not fully developed.

Uzuoka et al. (2003) with employing an effective stress approach demonstrated that localization may occur in a liquefiable sloping ground when an unsaturated soil layer above ground water table is present. They also addressed mesh size effects on the analysis results and needs for more studies.

These studies show that numerical modeling can be employed as a tool to shed more light on the mechanism of void redistribution and *flow-slides*.

3.5. Data from Case Histories

Researchers have speculated on the possible role of low permeability sub-layer (or void redistribution) in case histories of failures in earthquakes. These failures included both flow failures as well as large lateral spreads. The fact, that only very few case histories are well documented and it is very hard to find direct evidence of void redistribution during and after a failure, makes it difficult to directly observe the role of this mechanism in such failures. A comprehensive list of failed case histories with void redistribution involvement is provided in *Appendix III* of this thesis. Table *AIII-1* of *Appendix III* lists case histories of post shaking failures in a chronological order of occurrence based on information found in the literature (e.g. Hamada 1992; Kokusho, 2003 and Kulasingam, 2003). Details of geometry, soil conditions and shaking characteristics are given where available to evaluate whether void redistribution might possibly have played a role in the failure. Among them a case from Niigata 1964 earthquake,

Japan is described in the preceding section as a typical liquefaction induced failure in gentle slopes. Please consult with *Appendix III* for complete description for all cases listed in Table *AIII-1* along with some additional cases with less severe failure consequences. The compiled case histories are ones where large movements were known to have started after the end of shaking or where void redistribution would be expected to be important but the timing of failure initiation is unknown.

Case history records show that many post-earthquake failures took place from a few seconds after the end of shaking to days after the earthquake. In general some mechanisms, which could lead to delayed failure as noted by Kulasingam (2003), are:

- Loosening due to void redistribution.
- Pore pressure redistribution softening the non-liquefied portions.
- Shear strain accumulation due to small after shocks acting on liquefied soil (Meneses et al., 1998 and Okamura et al. 2001).
- Stress redistribution due to the failure of local regions of the slope during shaking, leading progressively to a global failure after shaking.
- Cracks formed during shaking, leading to piping and erosion.

It is also possible that more than one mechanism was active for any one case or other mechanisms e.g. mixing of layers with different gradation resulting in lower residual strength (Byrne & Beaty, 1997, Yoshimine et al., 2006 see *Appendix I* for more details) aggravated the resulted failure. Note that slide movements for steep slopes, which started during shaking, can continue after the end of shaking due to momentum effects.

Lateral Spreading in Kawagishi-cho and Hakusan, Niigata, Japan (1964)

The 1964 Niigata earthquake, of magnitude 7.5, caused widespread liquefaction in Niigata city, Japan (Kawakami & Asada, 1966). This event and Alaska earthquake in 1964 as benchmark events had a significant impact on geotechnical earthquake engineering. Since then a number of comprehensive investigations on liquefaction have been launched in Japan and North America.

Yoshida et al. (2005) noted that using aerial photos taken after earthquake and comparing conditions before and after the earthquake revealed earthen *flow-slides* or large lateral spreads at various nearly level-ground sites in Japan. It was found that liquefaction-induced flow is not an extraordinary phenomenon. They also argued that applying *steady-state* concept to evaluate residual strength of liquefied sand cannot explain the occurred *flow-slide* mechanism. It should be

noted that in the most relevant literature the *steady-state* strength of a liquefied sand layer refers to undrained strength of a sample of that layer at pre-earthquake in-situ void ratio (constant volume loading).

There were several lateral spreads along the banks of the Shinano River (Hamada, 1992) due to Niigata earthquake. Fig. 3-31 shows lateral displacement vectors at an area located a few hundreds meters from the river bank (insignificant free face effect). As may be noted in some locations (designated as 2b and 2c) large displacements (e.g. 4 m) occurred in the directions opposite to the river whereas the slope is less than 1% or less indicating that failure has occurred in a surface (possibly sub-layer interfaces) that does not follow the ground surface inclination. An area, located between the Echigo railway embankment and the left bank of the Shinano River in Kawagishi-cho, Hakusan district, suffered lateral displacements in the order of 7-11 m towards the river during that earthquake (Hamada 1992; Kawakami & Asada 1966; Kokusho 1999, 2000, 2003; Kokusho & Kojima, 2002, Yoshida et al., 2005). This area had a very gentle slope of less than 1%. The general soil profile in this area consisted of deep deposits of sands with a sandy clay layer sandwiched near the surface. The soil profile at the Hakusan transformer substation consisted of a 2m thick sandy clay sandwiched between a 4 m thick sand layer on top, and a sand layer (with sub-layers of silty to gravelly sands) extending for more than 25 m at the bottom. Trenching work reported by Kokusho & Fujita (2002) and Kokusho & Kojima (2002) showed the continuous nature of the sandy clay layer and additional micro layering within the top sand layer (see Fig. 3-32).

Liquefaction and lateral spreading caused the failure of several building foundations in Kawagishi-cho area. Kawakami & Asada (1966) described the case history as follows, "In the area where liquefaction of the ground had been occurred, many reinforced concrete buildings of multiple stories, which were settled or tilted with small breakage, were observed. The subsidence and the tilting of these buildings were not caused by the shear failure of soft ground, and slip plane in the ground or heaving of the ground around the structures could not be found. It took several minutes to overturn an apartment house in Kawagishi-cho, Niigata city, and the directions of the tilting of apartment houses in the area were the same, because this damage had no direct connection with vibration". A photo of Kawagishi-cho apartment buildings after the earthquake is shown in Fig. 3-33. Lateral spreading occurred in the nearby area, which included the Meikun High school and the Hakusan transformer substation, too (Kawakami & Asada 1966; Kokusho & Kojima 2002). The area of slide was measured to be 250 m by 150 m, and the maximum

displacement was about 7 m. The slide mass continued to move even after the shaking ended (Kokusho, 1999). Kokusho & Kojima (2002) reported pictures taken by a high school student indicated that muddy water started to come out of the ground, and fissures gradually expanded after the end of shaking. Kawakami & Asada (1966) also described the failure as quite a different phenomena from the usual slides of sloping ground in which the movement of upper part of the ground was due to the liquefaction of the lower part of the ground.

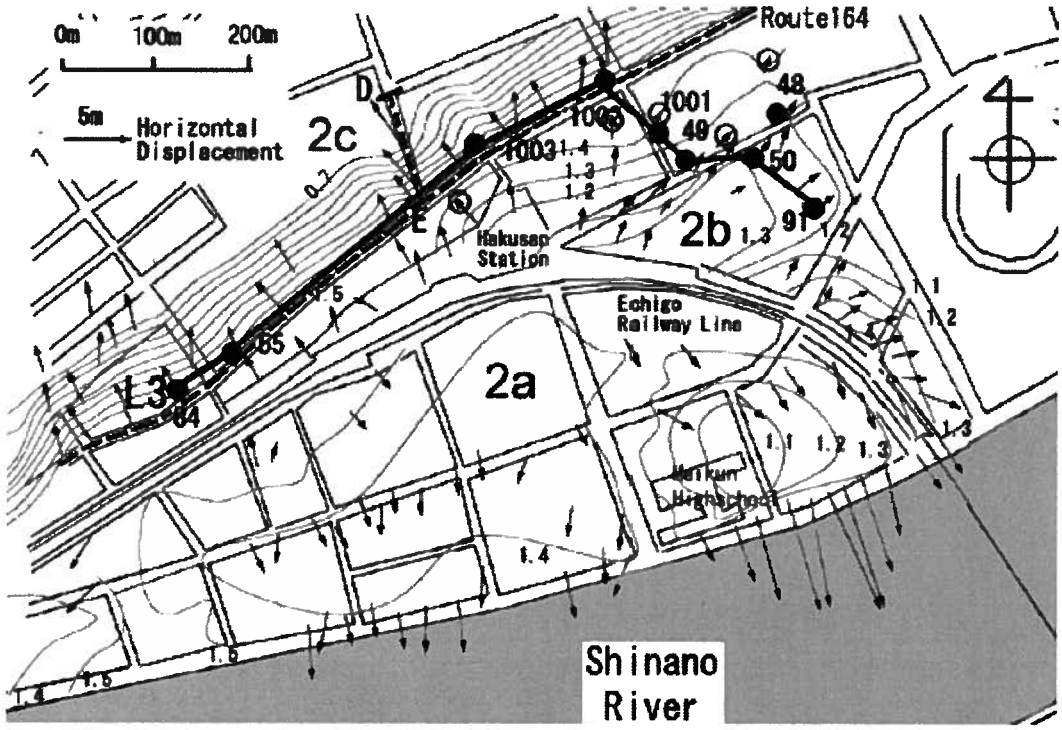

Fig. 3-31: Lateral displacement vectors at area few hundred meters from the Shinano River in Niigata (Hamada, 1992 and Kokusho, 2003).

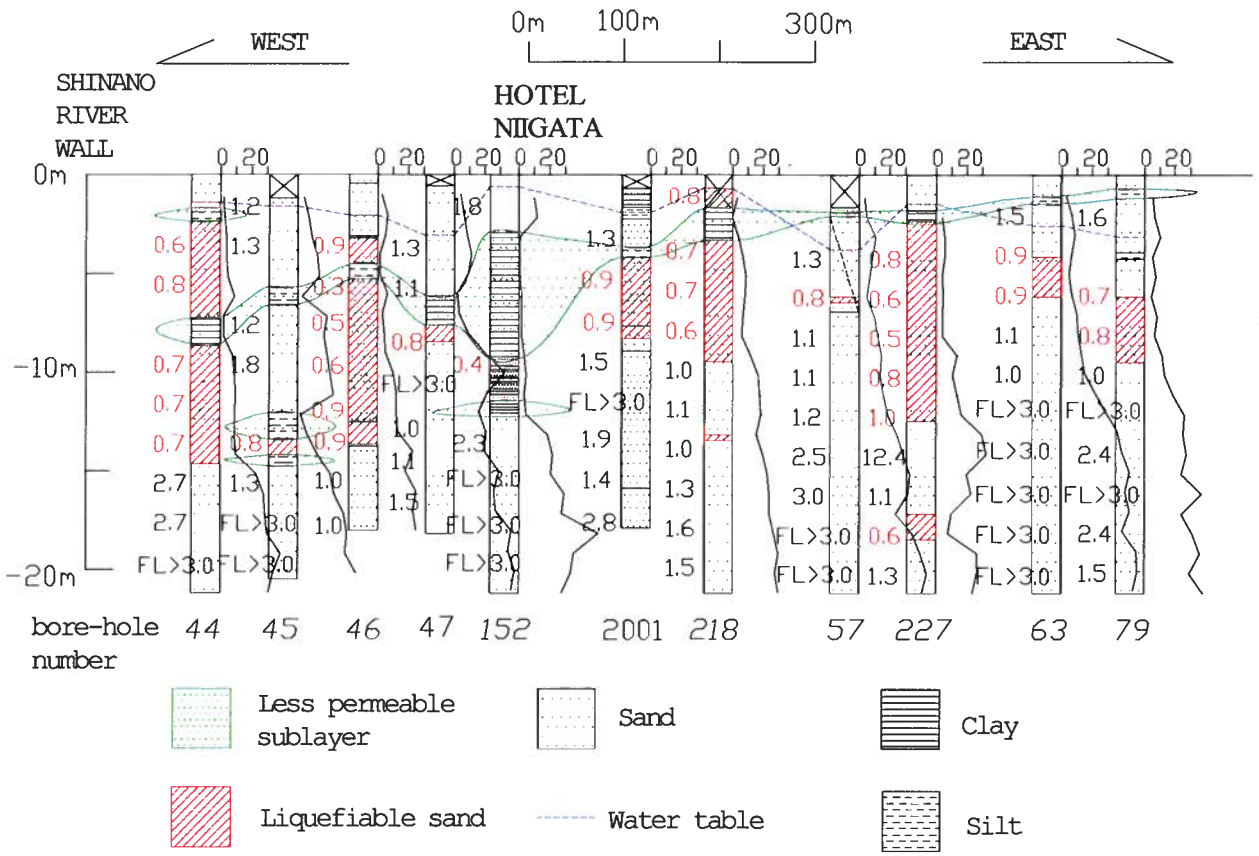

Fig. 3-32: Soil profile at Niigata Hotel area, Niigata (Kokusho & Fujita, 2002, with permission from ASCE).

Fig. 3-33: Liquefaction-induced bearing capacity failures of the Kawagishi-Cho apartment buildings (EERC, Un., Cal, Berkeley).

3.7 Summary and Main Findings

In this chapter, results of previous studies on void redistribution using physical model testing were first reviewed. Then, fundamentals of soil strength loss and instability due to injection flow under partially drained conditions based on element test data were discussed. A brief review of related numerical investigations carried out to date was presented. Finally, evidence from past earthquakes indicating the involvement of void redistribution were reviewed. The following are the main findings of this literature review:

- Liquefaction-induced flow slides have occurred in very gentle sloping ground conditions in past earthquakes.
- Most of these failures initiated during shaking or some time after the main shock of the earthquake motion from few seconds to days.
- Applying *steady-state* concepts in such cases to evaluate undrained residual strength of liquefied soils (at the pre-earthquake void ratio) suggests that failure should not occur.
- Residual strengths back calculated from case histories reflect implicitly the void redistribution effects on *flow-slides*. However, the extent of this influence remains unknown.
- Residual strengths during earthquakes are not solely controlled by pre-earthquake soil parameters.
- Field case histories do not have the information to prove whether void redistribution took place or not. However, the review of case histories of several cases where void redistribution could have possibly played a role in the failure, highlights the need for study of void redistribution and also site investigation techniques to detect thin sub-layers.
- In level ground condition after liquefaction onset, water film can occur beneath the barrier layer. Its occurrence is less likely in an (infinite) slope with shear stress bias as sand deforms in its path to *steady-state* condition before a water film can form.
- Physical model studies of slopes with and without low permeability sub-layer indicate that sand slopes as loose as 20% relative density are stable (with limited deformation) when subjected to earthquake shaking if no barrier layer is present. However, similar test models with silty sub-layers failed with localization in sand-silt interface, even in models of denser sand layers.
- Physical model data also suggests that the deformations of liquefied sloping ground conditions with a barrier are mainly controlled by pore water migration rather than the inertia effects of earthquakes. It is possible that a smaller earthquake that results in less displacement

during shaking (as a result of steeper slope at the end of shaking) causes larger post-shaking deformations due to greater driving static shear stress.

- It is difficult to determine the volume change (void ratio change) of expanding soil beneath the barrier in physical model testing. However, it is possible to observe water film formation in test models.
- Numerical methods can be a useful tool to provide insight into the void redistribution mechanism, especially regarding limitations involved in determining volume change within soil layers in physical tests.

CHAPTER 4

MODELING OF INJECTION FLOW AND VOID REDISTRIBUTION

4.1 Introduction

To investigate the effects of low permeability layers on ground deformations due to earthquake loading, predictions of the generation, redistribution, and dissipation of excess pore water pressures must be made during and after shaking. A fundamental approach requires a dynamic coupled stress-flow analysis, where the volumetric strains are controlled by the compressibility of the pore fluid and flow of water through the soil elements. To predict the instability and liquefaction flow-slide, an effective stress approach based on an elastic-plastic constitutive model (*UBCSAND*) is used in this study. The model is calibrated against laboratory element test data as well as centrifuge data and is described in this chapter. The *UBCSAND* model is incorporated in the commercially available computer code *FLAC* (***F**ast **L**agrangian **A**nalysis of **C**ontinua, Itasca*, 2000). In the analyses used in this investigation, version *IV* of the program was used in 2D plane-strain mode.

In general, three forms of soil-fluid mixture coupling formula are used in geomechanics, namely: (1) u - p, (2) u - U, and (3) u - p - U, as suggested by Zienkiewicz and Shiomi (1984) based on *Biot's* theory (1941). Here, the unknowns are the soil skeleton displacements u; the pore fluid (water) pressure p; and the pore fluid (water) displacements U. The u-p form captures the movements of the soil skeleton and change of pore water pressure, and is applicable when the relative fluid (water) acceleration is not important (in-phase movement). This relative acceleration is generally small in earthquake shaking (Zienkiewicz, et al., 1999). This approach is the most popular form of a coupling formulation used by many researchers in earthquake geotechnical engineering (e.g., Prevost, 1985, Dafalias, 1986, Zienkiewicz, et al., 1990, Byrne, et al., 1995, and Elgamal, et al., 1999, among others) and has been applied in this research.

In the first part of this chapter, to provide an insight into the computational process followed by the computer code, *FLAC,* and the constitutive model used in this study, the main features of the *FLAC* program and principles of the *UBCSAND* model are briefly described. Then, results of previous applications of this procedure related to partially drained condition (void redistribution) are presented. After demonstrating the capability of the model to capture element soil behavior, its use will be extended to analyze the response of a typical liquefiable soil profile with a low permeability sub-layer to earthquake excitation. Also, the significance of permeability of the liquefiable soils in seismic ground response is investigated and highlighted. In the following sections, the results of such studies are presented and discussed.

4.2 Principles of the *FLAC* Program

The solution of a stress-deformation (boundary-value) problem requires that equilibrium and compatibility be satisfied for the boundary and initial conditions using an appropriate stress-strain relationship. Finite element or finite difference techniques are routinely used to reasonably satisfy these conditions. The finite difference method is perhaps the oldest numerical technique used for the solution of sets of differential equations, given initial values and/or boundary values (see, for example, Desai & Christian, 1977). In the finite difference method, every derivative in the set of governing equations is replaced directly by an algebraic expression written in terms of the field variables (e.g., stress or displacement) at discrete points (nodes/gridpoints) in space; these variables are undefined within elements (*explicit method*). However, finite element programs often combine the element matrices into a large global stiffness matrix (*implicit method*), which is not normally done with finite difference programs since it is relatively efficient to regenerate the finite difference equations at each step.

The computer code *FLAC* uses the finite difference method and satisfies dynamic equilibrium using a step-by-step *explicit time domain* procedure. The dynamic approach used in *FLAC* has the advantages of achieving a numerically stable solution even when the problem is not statically stable, allowing for the examination of large strains and displacements prior to failure. Thus, even though for a static problem, *FLAC* uses the dynamic equations of motion in the formulation. Since it does not need to form a global stiffness matrix, it is a trivial matter to update coordinates at each *timestep* which is the case in the *large-strain* mode of the code. The incremental displacements are added to the coordinates so that the grid moves and deforms with the material it represents. This is termed a *"Lagrangian"* formulation, in contrast to an

"Eulerian" formulation, where the material moves and deforms relative to a fixed grid (*Itasca,* 2000). The constitutive formulation at each step is a *small-strain* one, but it is equivalent to a *large-strain* formulation over many steps. The geometric domain (continuum model) is discretized by the user into a finite difference mesh (grid) composed of quadrilateral elements (zones). An element should be small enough to be representative of material with the same properties and large enough so that the fluid and porous media system can be considered as a statistical homogenous porous medium. Internally, *FLAC* subdivides each element into two overlaid sets of constant-strain triangular elements (four triangular sub-elements), and calculations are carried out for these sub-elements to assure more reliable numerical results.

The general calculation sequence of the *explicit "time-marching"* scheme embodied in *FLAC* is illustrated in Fig. 4-1 for every cycle. This procedure can be summarized as follows:

1. The equations of motion are invoked to derive new nodal velocities and displacements from stresses and forces.
2. New strain-rates are derived from nodal velocities.
3. Constitutive equations (stress-strain laws) are used to calculate new stresses from strain-rates from previous calculation.

It takes one *timestep* for every cycle around the loop and the maximum out-of balance force in the model is monitored. This force will either approach zero, indicating the system is reaching an equilibrium state, or a constant, nonzero value, indicating that a portion (or all) of the system is at *steady-state* (plastic) flow of material. Importantly, each box in Fig. 4-1 updates all of its grid variables from *"known"* values that remain *"fixed"* while control is within the box. For example, the lower box takes the set of velocities already calculated and, for each element, computes new stresses. The velocities are assumed to be *"frozen"* for the operation of the box i.e., the newly calculated stresses do not affect the velocities. This can be done if the selected *timestep* is so small that physical information cannot pass from one element to another during that period. Of course, after several cycles of the loop, disturbances can propagate across several elements, just as they would propagate physically.

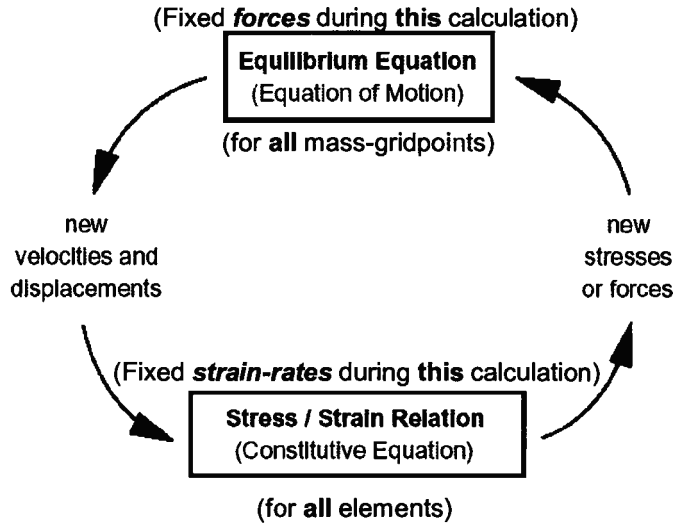

Fig. 4-1: Basic explicit calculation cycle used in *FLAC*.

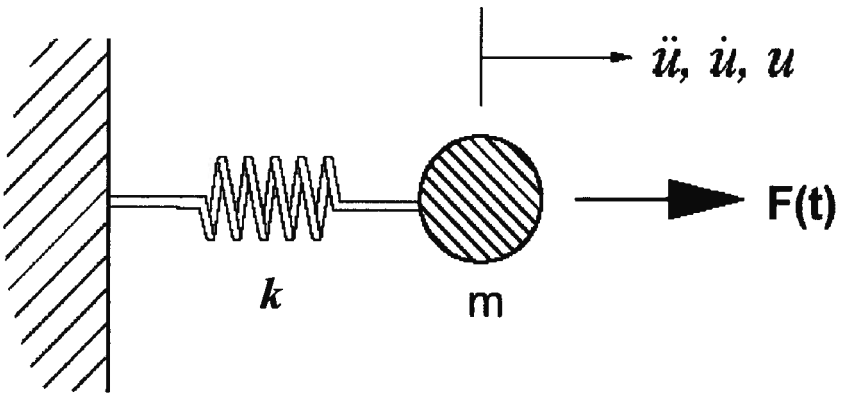

Fig. 4-2: Application of a time-varying force to a mass (concentrated in node), resulting in acceleration, velocity, and displacement (*FLAC* mass-spring system).

The central concept is that the *"computational wave speed"* always keeps ahead of the *"physical wave speed,"* so that the equations always operate on *known* values that are *fixed* for the duration of the calculation. Thus, no iteration process is necessary when computing stresses from strains in an element, even if the constitutive law is wildly nonlinear. In an *implicit* method (which is commonly used in finite element programs), every element communicates with every

other element during one solution step: several cycles of iteration are necessary before compatibility and equilibrium are obtained. This prediction is path-dependent if materials are not elastic. The disadvantage of the *explicit* method is in the small *timestep*, which means that large numbers of steps must be taken.

Fig. 4-2 illustrates a simple mass-spring system used in *FLAC* to solve the equation of motion with application of *Newton's law* of motion that relates the acceleration, $d\dot{u}/dt$ of a mass, m, to the applied force, $F(t)$, which may vary with time. The figure shows a force acting on a mass, causing motion described in terms of acceleration ($\ddot{u}$), velocity ($\dot{u}$) and displacement (u). *Newton's law* of motion for the mass-spring system is:

$$m\frac{d\dot{u}}{dt} = F(t) - ku \qquad [4\text{-}1]$$

where k is the spring stiffness and dt is the *timestep* which is selected by *FLAC* based on the problem specifications. When several forces act on the mass, *Eq.* 4.1 also expresses the static equilibrium condition when the acceleration tends to be zero i.e., $\Sigma F = 0$, where the summation is over all the forces acting. This property of the law of motion is exploited in *FLAC* when solving *"static"* problems. In a continuous solid body, *Eq.* 4.1 is generalized as follows:

$$\rho\frac{\partial \dot{u}_i}{\partial t} = \frac{\partial \sigma_{ij}}{\partial x_i} + \rho g_i \qquad [4\text{-}2]$$

where ρ, t, x_j, g_i and σ_{ij} are mass density, time, components of coordinate vector, components of gravitational acceleration (body forces); and components of stress tensor, respectively. By application of the *Gauss divergence theorem* to the quadrilateral elements (sub-elements), the derived velocities at each mass/gridpoint (node) are used to express the strain rates of the quadrilateral elements. To solve static problems, the equations of motion must be damped to provide static or quasi-static (non-inertial) solutions. *FLAC* uses a form of damping, called *"local damping"* (*non-viscous damping*) in which the damping force on a node is proportional to the magnitude of the unbalanced force. This form of damping has the following advantages (*Itasca,* 2005):

1. Only accelerating motion is damped; therefore, no erroneous damping forces arise from steady-state motion.

2. The damping constant, α, is non-dimensional.
3. Since damping is frequency-independent, regions of the assembly with different natural periods are damped equally, using the same damping constant.

For *"dynamic"* simulations, *"Rayleigh"* damping, as commonly used in the *time-domain* programs, is also available in *FLAC*. It is approximately frequency-independent over a restricted range of frequencies. Although *Rayleigh* damping embodies two viscous elements (in which the absorbed energy depends on frequency), the frequency-dependent effects are arranged to cancel out at the frequencies of interest (i.e., central/natural frequency). The reader is referred to consult with the *FLAC* users' manual for more details. For geological materials, damping commonly falls in the range of 2 to 5% of critical (Biggs, 1964). When using a plasticity-based constitutive model (e.g., *UBCSAND*) that captures material nonlinear behavior in cyclic loading, a nominal *Rayleigh* damping of 1% to 2% can be applied.

FLAC is capable of simulating groundwater flow problems, mechanical problems, and also coupled stress-flow problems (e.g., consolidation) when the program is configured to carry out this kind of analysis. The incremental formulation of coupled deformation-diffusion processes in *FLAC* provides the numerical representations for the linear quasi-static *Biot's* theory (*Itasca*, 2005). Two mechanical (coupling) effects related to the pore fluid/water pressure are considered: changes in pore water pressures induced by volumetric changes, and changes in effective stresses caused by pore water pressure changes. The first effect is captured through the fluid reaction to volume variations of the grid element. This volume change can be due to confining mean stress or deviatoric stress (shear induced) which is referred to as *"mechanical volume change"*. The second effect reflects the effective stress change when the pore water pressure is modified by the flow process (originated from mechanical or groundwater source). This is referred to *"flow volume change."*

The groundwater formulation of the program follows the same general scheme of finite differences and discretization of the grid for mechanical problem, and the governing equations are solved by applying *transport* law (*Darcy's* law), *balance* (*continuity*) law and *constitutive* law. *FLAC* considers pore water pressure and saturation as being associated with gridpoints/nodes. Furthermore, the groundwater equations are expressed in terms of pressures, P rather than hydraulic head, and hence, *Darcy's* law for anisotropic porous medium is written as (*Itasca*, 2005):

$$q_i = -k_{ij} \frac{\partial P}{\partial x_i} \qquad [4\text{-}3]$$

where q_i is the " *specific discharge vector*" (discharge in unit area), P the pressure, and k_{ij} is the *"FLAC permeability"* (k_{FLAC}) tensor. The program uses "*mobility coefficient*" (coefficient of the pore fluid/water pressure term in *Darcy's* law). The relation between "*hydraulic conductivity,*" k (e.g., in m/sec), commonly used when *Darcy's* law is expressed in terms of head, and k_{FLAC} (e.g., in [m^2/Pa-sec]) is as *Eq.* 4-4. Also, the property of *"intrinsic permeability,"* κ (e.g., in m^2) is related to k_{FLAC} and k, as shown by *Eq.* 4-5:

$$k_{FLAC} = \frac{k}{g\rho_w} \qquad [4\text{-}4]$$

where

g: the gravitational acceleration,

ρ_w: the fluid mass density,

FLAC allows the user to decide whether gravitational forces (stress/mechanical computation), flow effects (hydraulic/flow computation), or both (coupled stress-flow) should be taken into account. A "*Flow-on/Flow-off*" switch instruction is used for this purpose. Turning *"gravity"* on implies that body forces will be accounted for in the analysis. The gravitational acceleration, g is treated as a vector in *FLAC* formulation, so different vertical and horizontal components of g can be applied to a grid. In addition, the magnitude of g can be set to be equal to a value different from the actual Earth gravitational acceleration of 9.81 m/s^2. Therefore variation of g, like those in centrifuge testing, can be simulated.

Turning *"Flow-on"* (effective stress approach) implies that the fluid within a grid is allowed to move among the elements and the bulk modulus of the fluid increases the mechanical stiffness of a saturated zone. The effect of increased mechanical stiffness is incorporated in quasi-static analysis in the density-scaling scheme already in *FLAC* using *Biot's* theory (*Biot*'s coefficient, α is assumed 1, neglecting soil grains compressibility comparing to that of soil

skeleton, K_{ske}). The apparent mechanical bulk modulus of a saturated zone is modified by the presence of fluid as follows:

$$K = K_{ske} + \frac{K_f}{n} \qquad [4\text{-}5]$$

Depending on the boundary conditions with regard to the flow, the grid will be either an open or closed system. In an open system, fluid will enter or leave the grid, while in a closed system, no communication occurs with the outside world. In both cases, flow will occur within the geometric domain of the problem. Turning *"Flow-off"* (undrained condition) implies that the fluid will not enter or leave any of the elements comprising the grid, and thus, the fluid will not move at all.

Flow computations also require that the *timestep* be less than a critical value to assure that no physical (flow) process is transferred during a computation cycle. The *explicit flow timestep* can be derived by imagining that one node at the center of four zones is given a pressure of P^{old}. The resulting nodal flow is then given by *Eq.* 4-6. This relation has a stable and monotonic solution if the *timestep* is lower than a critical value as expressed by *Eq.* 4-7.

$$Q = P^{old} \sum M_{kk} \qquad [4\text{-}6]$$

$$\Delta t < \frac{nV}{K_f \sum M_{kk}} \qquad [4\text{-}7]$$

where:

ΣM_{kk}: the *permeability stiffness* sum over the four zones of the diagonal terms corresponding to the selected node;

K_f: bulk modulus of fluid (water);

V: element volume;

n: porosity;

FLAC uses this *timestep* for flow computations with applying a factor of safety of 1.25. In the same fashion, the *critical mechanical timestep* of a given model (of i × j zones) is determined by *FLAC,* which is controlled by element size and compression wave velocity, $V_p = \sqrt{\frac{K+\frac{4G}{3}}{\rho}}$ to assure that no physical (mechanical) effects are transferred during the time interval in one cycle of numerical calculation. A safety factor of 2 is used in this case.

Finally, *FLAC* uses the lowest *critical timestep* determined for the two types of computations for a given domain (of i × j zones), as expressed by *Eq.* 4-8 and *Eq.* 4-9, respectively for mechanical and flow calculations (see *Itasca,* 2005 for details):

$$\Delta t_{Mech.} = \min\left(\frac{\Delta x_{\min}}{\sqrt{\frac{K_{ske} + \frac{K_f}{n} + \frac{4}{3}G}{\rho}}} \right) \qquad [4\text{-}8]$$

$$\Delta t_{Flow} = \min\left(\frac{(\Delta x_{\min})^2 n}{k_{FLAC} K_f} \right) \qquad [4\text{-}9]$$

$$\Delta t_{FLAC} = \min(\Delta t_{Mech.}, \Delta t_{Flow}) \qquad [4\text{-}10]$$

where $\Delta t_{Mech.}$, Δt_{Flow} and Δt_{FLAC} are *critical mechanical timestep*, *critical flow timestep* and the *timestep* used by *FLAC,* respectively, and other parameters are as follows:

Δx_{min}: represents element minimum length (which is controlled by A, element area as $A/\Delta x_{max}$);

G: shear modulus;

ρ: unit density.

It may be seen that the *timestep* is controlled by size of the smallest element in the model and also, it decreases with an increase in compression wave velocity (denominator in *Eq.* 4-8 for Δt_{Mech}) and/or an increase in permeability and/or fluid bulk modulus, K_f (denominator in *Eq.* 4-9 for Δt_{Flow}).

Starting from a state of mechanical equilibrium, a coupled *stress-flow* (*hydro-mechanical*) static simulation in *FLAC* involves a series of steps. Each step includes one or more flow steps (*flow loop*), followed by enough mechanical steps (*mechanical loop*) to maintain quasi-static equilibrium. The increment of pore fluid/water pressure due to fluid flow is evaluated in the *flow loop*; the contribution from volumetric strain is evaluated in the *mechanical loop* as a zone value which is then distributed to the nodes. The total stress correction due to pore water pressure change arising from mechanical volumetric strain is performed in the *mechanical loop*, and from that arising from fluid flow in the *flow loop*. The total value of the pore water pressure is used to evaluate effective stresses and detect failure in plastic materials. In this context, the pore water pressure field may originate from different sources, e.g., a flow analysis or a *coupled stress-flow* (*hydro-mechanical*) simulation (*Itasca,* 2000).

Two *FLAC* executable codes are provided in two versions: a *single-precision* version and a *double-precision* version. The *single-precision* version is more efficient for most analyses and runs approximately 1.5 to 2 times faster than the *double-precision* version that also requires about 3 times more computer *RAM* (***R***andom ***A***ccess ***M***emory). The *double-precision* version provides more accurate solutions for cases in which (*Itasca,* 2000):

1. The accumulated value of a variable after many thousands of time steps is much larger than the incremental change in the variable (e.g., an accumulated value for displacement in a flow failure).
2. Model grids contain many zones with coordinates that are large compared to typical zone dimensions.
3. The third situation at which *double-precision* is recommended is related to flow computations. There is a limit to the amount by which fluid modulus may be reduced, and instability results when too much fluid enters or leaves a zone in one *timestep.*

An upper limit also exists to the fluid modulus. In this case, the amount of fluid exchanged with a zone in one *timestep* can be below the resolution of the computer arithmetic in *single-precision* (accuracy limit is around six decimal digits in *single-precision,* whereas, it is 15 digits for *double- precision*). However, computation speed in the *double-precision* mode is much slower compared to that of *single-precision.*

All analyses discussed in this thesis were carried out in "*Flow-on*" and '*single-precision*' modes, unless otherwise stated.

4.3 Stress-Strain Model for Sands – Principles of the *UBCSAND* Constitutive Model

Plasticity models are formulated along the lines of classical continuum mechanics, and a stress increment is specified by a strain increment. Therefore, the stress-strain relationship is incremental in form, and the total strain increment is separated into elastic and plastic strain increments (Hill, 1950). In addition, zones of elastic and plastic behavior are assumed to be separated by a boundary called a *yield surface* (or *yield locus* or *loading surface*). A classical plasticity model consists of four distinct components: (1) *yield surface,* (2) *flow rule,* (3) *hardening rule* (4) *hardening parameter,* which control stress-strain relationship. *Yield surfaces* are defined exclusively in stress space, and define the size of the *elastic region*. Any stress probe pushing outwards of the *yield surface* will cause *plastic strains* (known as *loading* process). The *flow rule* determines the directions of plastic shear and volumetric strain increments (plastic strain vectors). It could be *associated* (*yield surface* ≡ *plastic potential*) or *non-associated.* The *hardening rule* specifies the manner in which the *elastic region* evolves as yielding takes place (Prager, 1955). Two types of hardening are possible: i.e., *isotropic* (proportional expansion of *yield surface* in all directions) and *kinematic* (moving of the *yield surface* without change in orientation, size, or shape of the elastic region). The two types can also be combined and are known as *mixed hardening.* The *hardening parameter* is a scalar quantity used to record the plastic deformation history developed during the *loading process*. The *stress-strain* curve, generally nonlinear, describes the response of soil to loading.

The majority of classical plasticity models can be categorized into two types: (extended) *Mohr-Coulomb* model types and *Critical-State* model types (Puebla, 1999). More advanced models also exist: e.g., *bounding surface models* (Dafalias & Popov, 1975), *multi-yield* or *nested-surfaces* models (e.g., Prevost, 1985), advanced *general-plasticity* models (e.g., Pastor-Zienkiewicz Mark III, Pastor, et al., 1990), *multi-mechanism* models (e.g., Matsuoka & Sasakibara, 1978), and *multi-laminate* models (e.g., Pande & Pietruszezak, 1982). More discussion on constitutive models used for sands and liquefaction analysis can be found in the literature (e.g., Dafalias, 1994; Puebla, 1999; and Park, 2005, among others). In any case, the complicated models require more soil parameters that are not readily available in most cases and as a result they become less applicable for engineering purposes.

The *UBCSAND* constitutive model, as a *Mohr-Coulomb* type stress-strain model, is an elastic-plastic model proposed by Byrne, et al. (1995), and further developed by Beaty and Byrne

(1998) and Puebla (1999). The model has been successfully used in analyzing the *CANLEX* liquefaction embankments (Puebla, et al., 1997) and for predicting the failure of the Mochikoshi tailings dam (Seid-Karbasi & Byrne, 2004b). It has been validated against dynamic centrifuge test data (e.g., Byrne, et al., 2004) and has also been used to examine re-liquefaction effects (Seid-Karbasi, et al., 2005). The key aspects of the model are summarized as:

- *Yield loci* are lines of constant stress ratio ($\eta = \tau / \sigma'$), as shown in Fig. 4-3.
- The *flow rule* relating the plastic strain increment directions is *non-associated* (see Fig. 4-3a) and leads to a plastic potential defined in terms of dilation angle.
- Sand dilation property is accounted for, based on the Rowe (1962) dilatancy theory.
- *Hardening rule* is a *kinematic type.*
- *Hardening parameter* is plastic shear strain.
- The model is a *co-axial* constitutive model (i.e., coincidence of the directions of principal stresses with plastic strain increments). This is a widely-used assumption in plasticity models.
- The model in this version is developed for *2D*-condition and captures sand behavior under simple-shear test loading that better mimics the ground response to earthquake excitation.
- The elastic and plastic shear strains take place simultaneously (no strain threshold is assumed in the model).

The prime features of the model properties are briefly described in the following section (see Puebla, 1999 for more details).

4.3.1 Elastic Properties

The elastic component of response is assumed to be isotropic and specified by a shear modulus, G^e, and a bulk modulus, K^e, as follows:

$$G^e = k_G^e . P_a \left(\frac{\sigma'}{P_a} \right)^{n_e} \qquad [4\text{-}11]$$

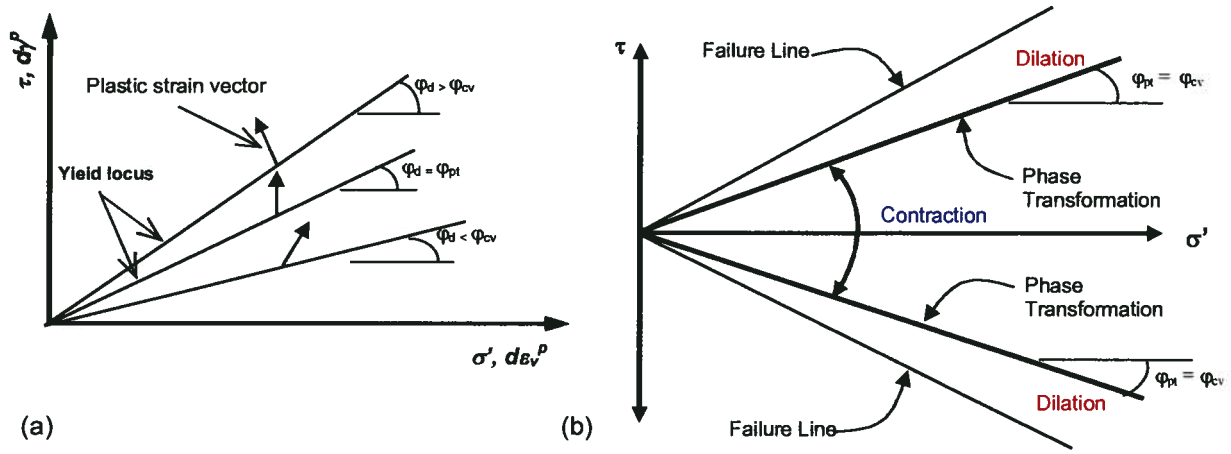

Fig. 4.3: Principles of *UBCSAND* model (a) moving yield loci and plastic strain increment vectors, (b) dilation and contraction regions.

$$K^e = \alpha \,.\, G^e \qquad [4\text{-}12]$$

where k_G^e is an elastic shear modulus number; P_a is atmospheric pressure; $\sigma' = (\sigma'_x + \sigma'_y) / 2$; n_e is an elastic exponent usually assumed to be approximately 0.5; α depends on elastic *Poisson's ratio*, μ, and ranges from 2/3 to 4/3 (μ controls K and G ratio as: $\mu = \frac{3\frac{K}{G}-2}{2\left(3\frac{K}{G}+1\right)}$). Small-strain drained *Poisson's ratio* for granular soils commonly varies from 0 to 0.2 (Hardin & Drnevich, 1972). Recent investigations (e.g., Burland, 1989; Tatsuoka & Shibuya, 1992; and Lehane & Cosgrove, 2000) using advanced techniques (i.e., local strain measurements with special internal high-resolution instrumentation) have confirmed that the value of drained μ ranges from 0.1 to 0.2 for all types of geomaterials at low strain levels, increasing to larger values as failure states are approached (Mayne, 2007).

4.3.2 Plastic Properties

The plastic shear strain increment $d\gamma^p$ is related to stress ratio, $d\eta$, where $\eta = \tau / \sigma'$, as shown in Fig. 4-4, and can be expressed as *Eq.* 4-24. Thus, under a constant shear stress, reduction in effective mean stress (due to mechanical or flow factors) results in plastic shear/volumetric strains.

$$d\gamma^p = \left(\frac{d\eta}{\left(\frac{G^p}{\sigma'} \right)} \right) \qquad [4\text{-}13]$$

where G^P is the plastic shear modulus, given by a hyperbolic function which is a common form to express the stress-strain curve for granular materials (e.g., Kondner & Zelasko, 1963, Duncan & Chang, 1970; and Matsuoka & Nakai, 1977) as:

$$G^p = G_i^p \left(1 - \frac{\eta}{\eta_f} R_f \right)^2 \qquad [4\text{-}14]$$

where $G_i^p = k_G^p \cdot P_a \left(\frac{\sigma'}{P_a} \right)^{n_p}$ is the maximum plastic shear modulus (at $\eta \approx 0$),

k_G^p: plastic shear modulus number,

n_p: plastic shear modulus exponent,

η_f: the stress ratio at failure and equals $\sin\varphi_f$, where φ_f is the peak friction angle, and

R_f: failure ratio ($= \eta_f / \eta_{ult}$), which is the ratio of the stress ratio at failure to that at the ultimate state. It is determined based on best-fit hyperbola, and generally ranges from 0.5 to 1.0.

$G^P{}_i$ in turn is related to G^e and the relative density of the sand. The associated increment of plastic volumetric strain, $d\varepsilon_v^P$, is related to the increment of plastic shear strain, $d\gamma^P$, through the *flow rule* as follows:

$$d\varepsilon_v^p = d\gamma^p . (\sin\varphi_{cv} - \eta) \qquad [4\text{-}15]$$

where φ_{cv} is the friction angle at *constant volume* (considered equal to *phase transformation*, φ_{pt}).

From Fig. 4-3, at low stress ratios, significant shear-induced plastic compaction is occurring (where plastic potential vectors slope to the right), while no compaction is predicted at stress ratios corresponding to φ_{cv} (where the plastic potential vector is vertical). For stress ratios greater than φ_{cv}, shear-induced plastic expansion or dilation is predicted as shown in Fig. 4-3b (where the plastic potential vectors slope to the left).

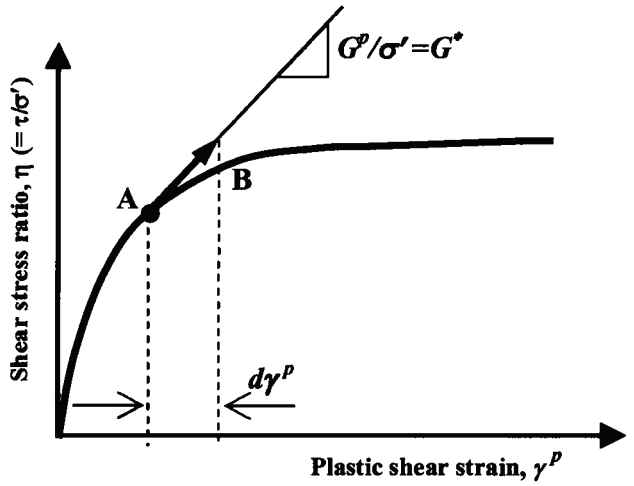

Fig. 4-4: Plastic shear strain increment and shear modulus.

This simple flow rule is in close agreement with the characteristic behavior of sand observed in drained laboratory element testing (discussed in *Chapter 2*). The response of sand is controlled by the skeleton behavior outlined above. The presence of a fluid (air-water mixture) in the pores of the sand acts as a volumetric constraint on the skeleton if drainage is fully or partially curtailed. This constraint causes the pore water pressure rise that can lead to liquefaction. Provided that the skeleton or drained behavior is appropriately modeled under monotonic and cyclic loading conditions, and that the stiffness of the pore fluid and drainage are accounted for, the liquefaction response can be predicted. Therefore, basically the model parameters should be determined based on laboratory drained tests.

This model is incorporated in the computer code *FLAC*. As mentioned before, the program models the soil mass as a collection of grid zones or elements and solves the coupled stress-flow problem using an explicit time-stepping approach. The program has a number of built-in stress-strain models, including an elastic-plastic *Mohr-Coulomb* model, and *UBCSAND* is a variation of this model, in which friction and dilation angles are varied to incorporate the *yield loci* and *flow rule* described earlier. Drainage conditions are built into *FLAC*, and drained, undrained, or coupled stress-flow conditions are specified by the user.

For practical purposes, the key elastic and plastic sand parameters can be expressed in terms of relative density, *Dr*, or normalized Standard Penetration Test values, $(N_1)_{60}$. Initial estimates of these parameters have been approximated from published data and model

calibrations. The response of sand elements under monotonic and cyclic loading can then be predicted and the results compared with laboratory data. In this way, the model can be made to match the observed response over the range of relative density or $(N_1)_{60}$ values. The model has also been calibrated to reproduce the NCEER 97 (Youd, et al., 2001) triggering chart (Byrne, 2003) which, in turn, is based on field experience during past earthquakes and is expressed in terms of the Standard Penetration Test resistance value, $(N_1)_{60}$. The model properties for obtaining such agreement are therefore expressed in terms of $(N_1)_{60}$.

4.3.3 Model Prediction of Laboratory Element Tests

The model was applied to simulate cyclic simple shear tests under undrained conditions. Fig. 4-5 shows model predictions along with test results on (air-pluviated) Fraser River sand. The test had an initial vertical consolidation stress $\sigma'_v = 100\ kPa$ and $Dr = 40\%$. The results in terms of stress-strain, stress path, and excess pore water pressure ratio, R_u compare reasonably well with the laboratory data. A comparison of model prediction with test results, in terms of required number of cycles to trigger liquefaction for different cyclic stress ratios, *CSR*, is shown in Fig. 4-5d and shows good agreement.

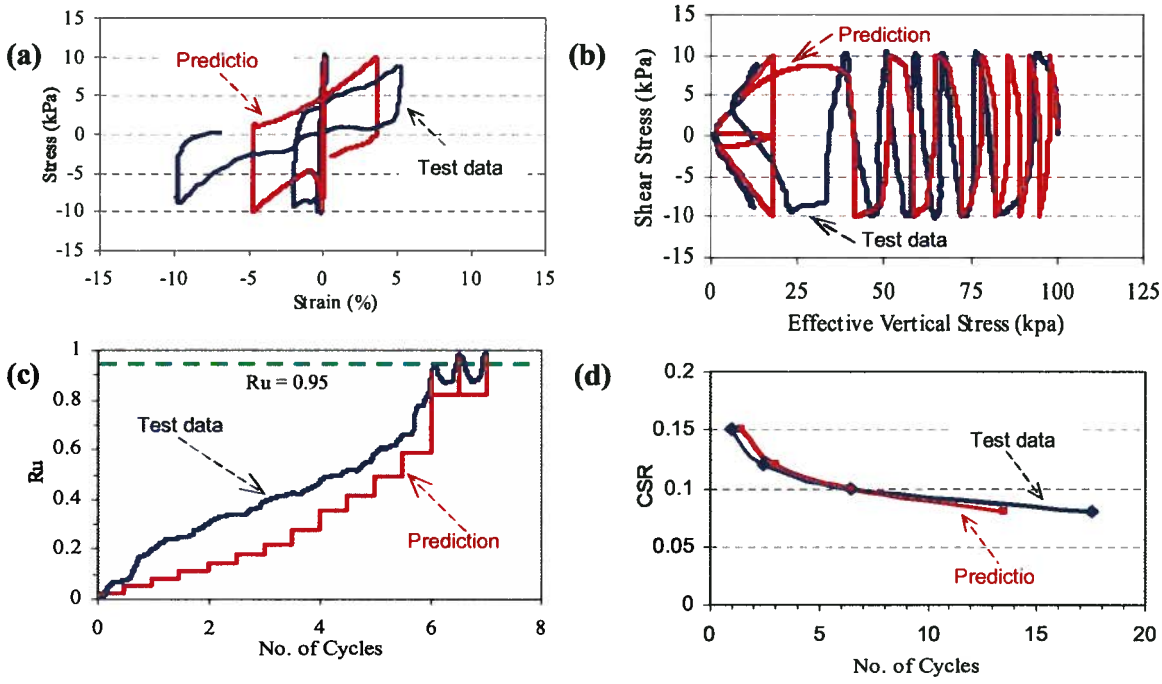

Fig. 4-5; Comparison of predicted and measured response for Fraser River sand, (a) stress-strain, *CSR* = 0.1, (b) stress path, (c) R_u vs. No. of cycles for liquefaction: $R_u \geq 0.95$, (d) *CSR* vs. No. of cycles for liquefaction (test data from Sriskandakumar, 2004).

The model was also used to predict the effect of both undrained and partial drainage as observed in triaxial monotonic tests. The partial drainage involved injecting the sample with water to expand its volume as it was sheared. The injection causes a drastic reduction in soil strength. In the numerical model, the same volumetric expansion was applied and the predicted results were compared to the test results shown in Fig. 4-6a to Fig. 4-6c (predictions and tests shown with solid and dotted lines, respectively). The test results conducted on Fraser River sand (D_r = 82%) are presented in terms of stress-strain, volumetric strain vs. mean effective stress, and stress path (Eliadorani, 2000). From Fig. 4-5, the predictions are in remarkably good agreement with the measured data.

The above simulations illustrate that the model can generate the appropriate pore water pressures and stress-strain response to undrained loading as well as account for the effect of volumetric expansion caused by inflow of water into an element.

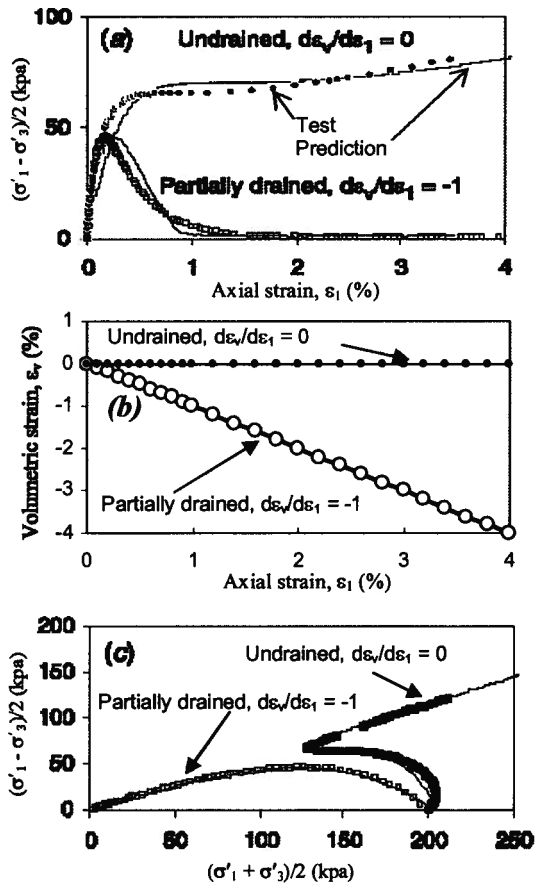

Fig. 4-6: Prediction of soil element response in undrained and partially drained (inflow) triaxial tests for Fraser River sand, D_r = *82%:* (a) stress-strain, (b) volumetric strain, and (c) stress paths (modified from Atigh & Byrne, 2004).

4.4 Soil Profile Used in the Analyses

The soil profile used throughout this study is a 10m thick deposit representing a sloping ground with 1° inclination (1.7% slope), with water level at ground surface, as shown in Fig. 4-7. It comprises a loose sand deposit resting on an impermeable base. The effect of a low permeability layer within the loose sand at a depth of 4m is examined. Fraser River sand, with relative density $Dr = 40\ \%$ is considered to represent the loose sand. Material properties are listed in Table 4-1, where ρ_d, n, and k are material dry density, porosity, and permeability respectively. The *UBCSAND* model was applied to the loose sand layer with an equivalent *UBCSAND* model $(N_1)_{60}$ value of 6.2 (see Table 4-1b for corresponding model properties). The low permeability silt layer barrier is simulated with a *Mohr-Coulomb* model with friction angle, $\varphi = 30^{\circ}$ and permeability, k =1000 times lower than that of the loose layer. Its stiffness in terms of bulk modulus and shear modulus was modeled as 1e4 kPa and 0.5e4 kPa, respectively. It is not considered to generate excess pore water pressure.

Input base motion, in terms of an acceleration time history, is shown in Fig. 4-8. It is a harmonic (sinusoid) excitation applied at the base of the soil layer, which ramps up to 2.5 m/s^2 within 1s and dies out in 2s, and lasts for 7s in total.

Analyses were conducted for two cases:

1. *Case I*: Sloping ground without low permeability sub-layer
2. *Case II*: Sloping ground with low permeability sub-layer

4.5 Analyses and Results

To model the free field condition, a mesh with 9 × 22 zones (as illustrated in Fig. 4-9) was used. Material types are recognized with different permeability values as shown in the figure. The nodes on the left and right boundaries were linked so as to force the soil column to deform as a shear beam. The earthquake motion was applied as a time history of acceleration at the base of the mesh.

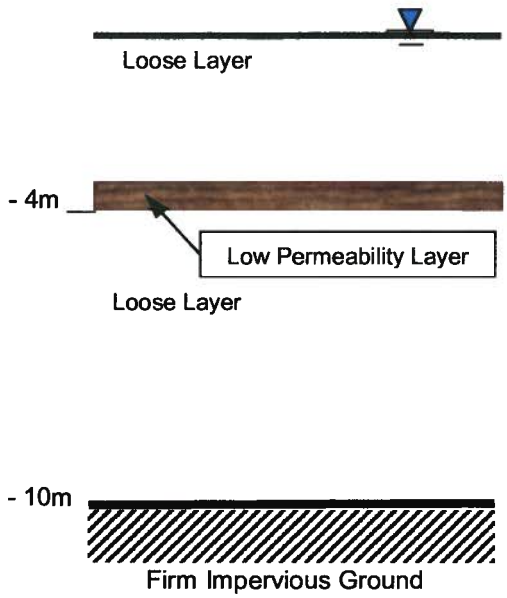

Fig. 4-7 Soil profile used in the analyses.

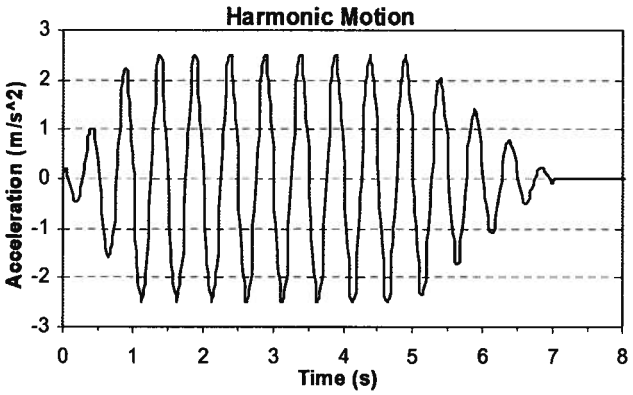

Fig. 4-8 Acceleration time history for base input motion.

Table 4-1a: Materials properties used in the analyses.

Material	ρ_d (kg/m^3)	Porosity (n)	UBCSAND $(N_1)_{60}$	k (m/s)
Loose sand layer	1500	0.448	6.2	8.81e-4
Silt barrier	1500	0.448	----	8.81e-7

Table 4-1b: Properties associated with *UBCSAND* model applied to sand layer.

Model parameter	Sand layer
Elastic shear modulus number, K_G^e	797
Elastic shear modulus exponent, n_e	0.5
Elastic bulk modulus coefficient, α_B ($B = \alpha_B.G^e$)	0.7
Plastic shear modulus number, K_G^p	115
Plastic shear modulus exponent, n_p	0.4
Peak friction angle, φ_f (deg.)	33.6
Constant-volume friction angle, φ_{cv} (deg.)	33.0
Failure ratio, R_f	0.94
Factor of anisotropy, F	1.0

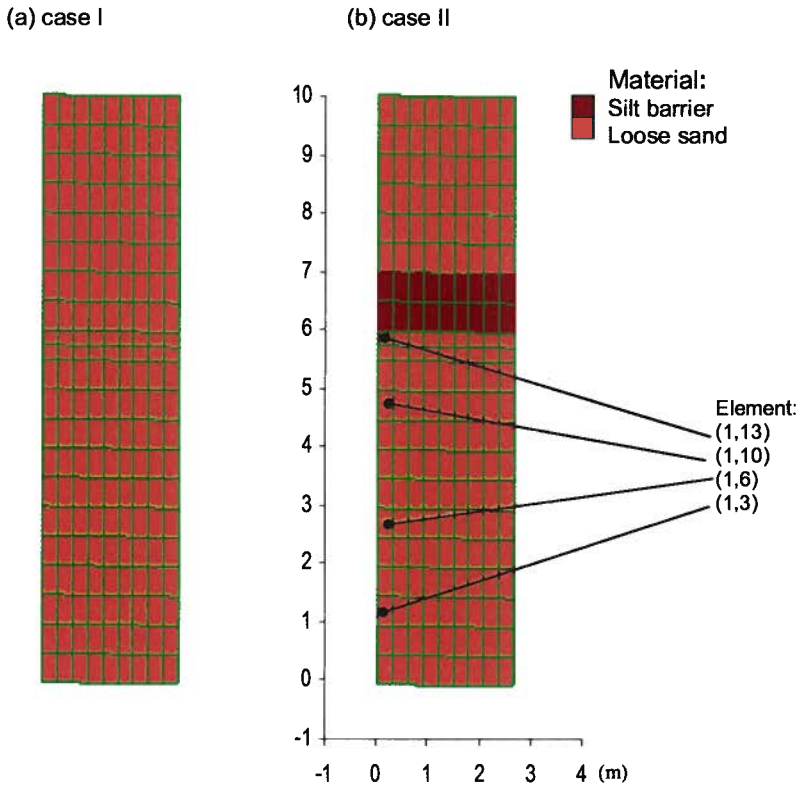

Fig. 4-9: Analyses meshes used in the two cases with different materials types, (a) *case I*, profile without low permeability sub-layer, (b) *case II*, profile with low permeability sub-layer.

4.5.1 Sloping Ground without Barrier, *Case I*

As the benchmark condition, a sloping ground condition with 1° inclination was analyzed without a low permeability layer. The results, in terms of time histories of excess pore water pressure ratio, R_u for selected depths, are shown in Fig. 4-10 (for position of the points refer to Fig. 4-9). The predicted patterns of excess pore water pressure indicate that essentially high excess pore water pressures build up within the soil profile during the strong shaking. Small dilation spikes, e.g., for element [1,3] are seen when $R_u \approx 1$ and are less pronounced in the upper parts as a result of upward inflow. Excess pore water pressures dissipate somewhat more rapidly at depth, e.g., R_u at 10s is 55% and 75% for element [1,3] and [1,13], respectively.

A similar trend has been observed in a number of centrifuge tests conducted for level and sloping grounds (e.g., Taboada & Dobry, 1993a; 1993b; 1998; Sharp, et al., 2003a, Phillips, et al., 2004).

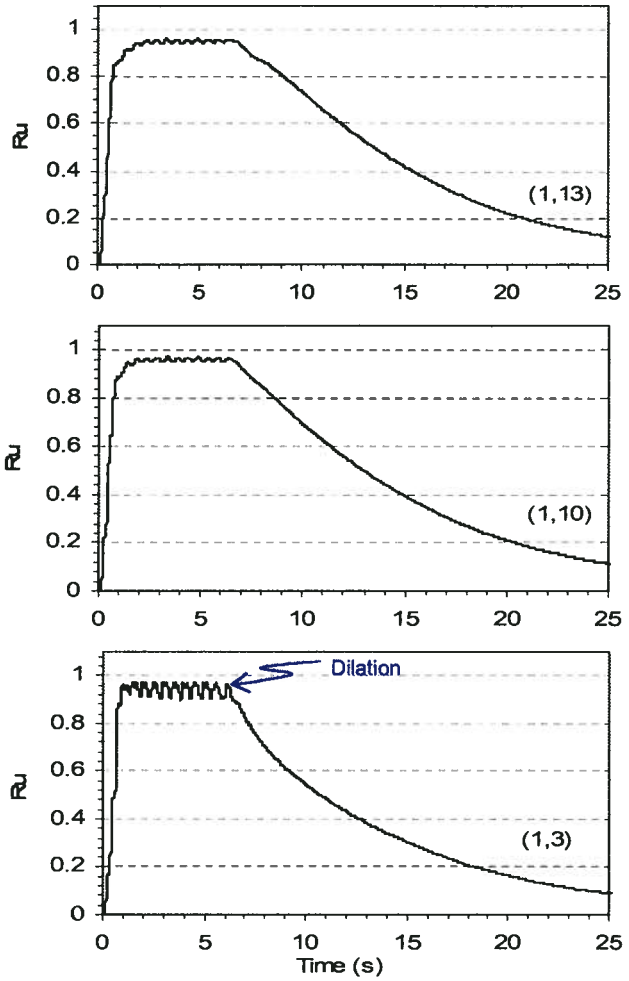

Fig. 4-10: Excess pore water pressure ratio *Ru* vs. time at selected points with increasing depth (*case I*).

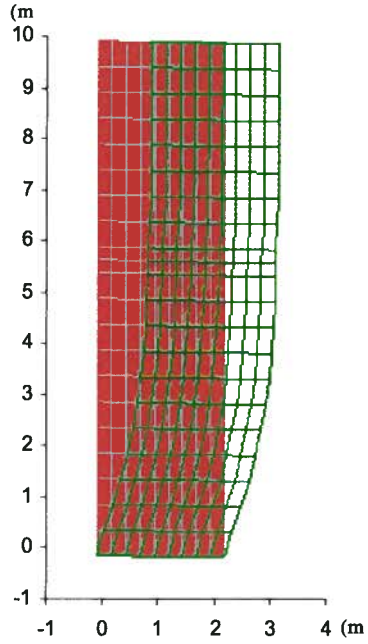

Fig. 4-11: Deformation pattern of soil profile without barrier, *case I* (with max. lateral displacement of 0.95m after 14 s).

Fig. 4-11 shows the predicted deformed mesh distortion occurring at the base and tapering off towards the surface resulting in a maximum displacement of 0.95m at the top surface. Fig. 4-12 shows isochrones of lateral displacement and excess pore water pressure at certain time intervals. It indicates that displacement gradually increases from the surface smoothly over time. It also shows that excess pore water pressure increases progressively along the soil profile while the motion is ramping up.

This predicted pattern compares well with reported dynamic centrifuge data (e.g., Sharp, et al., 2003a). The authors modeled a 10m uniform submerged liquefiable layer in a 50g field

using a viscous pore fluid 50-times more viscous than water. Fig. 4-13 shows the model configuration in the model scale with 2° inclination. The applied acceleration is not horizontal but parallel to the base of the model, thus also forming an angle of 2° with the horizontal. Accounting for the effects of the weight of the rings and the different hydrostatic pressures at both sides of the box caused by the water level being horizontal, the equivalent prototype slope angle being modeled becomes $\alpha_{field} = 5.16°$ (Taboada, 1995). As shown in Fig. 4-13b, the model was shaken with 22 cycles of harmonic motion with *PGA = 0.23g* at 2 *Hz*. The soil used in the tests was Nevada Sand 120, air pluviated at *Dr* = 45%. Fig. 4-13c and Fig. 4-13d show measured profiles of lateral displacement and excess pore water pressure, respectively, at different time intervals for the tested model. The majority of lateral displacements occurs after that excess pore water pressure approaches its high value (typically, $R_u \approx 0.9$).

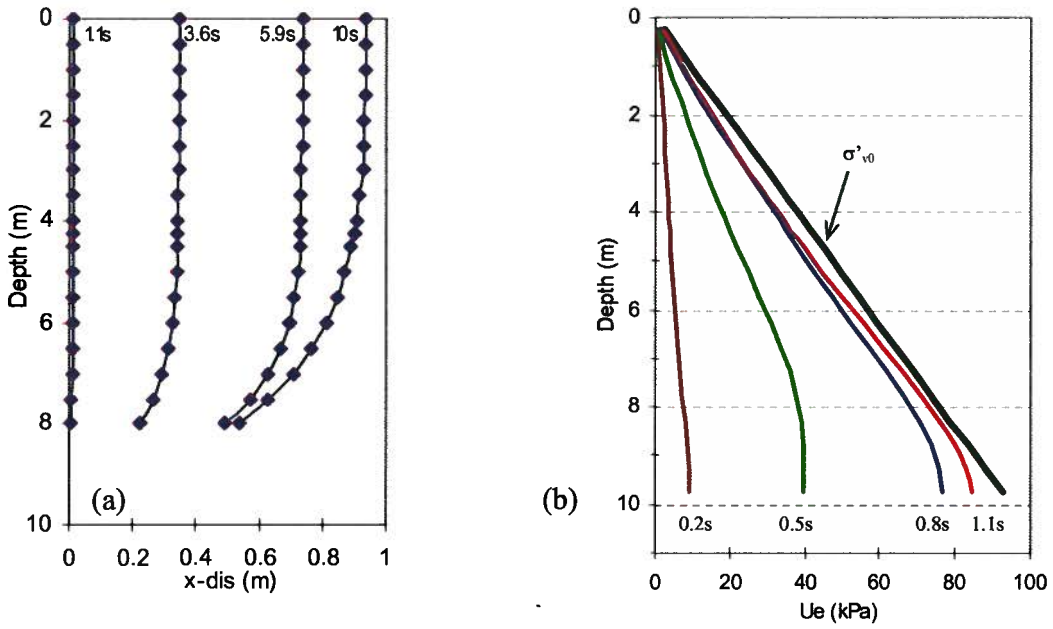

Fig. 4-12: Isochrones at certain time intervals for (a) lateral displacement, (b) excess pore water pressure (*case I*).

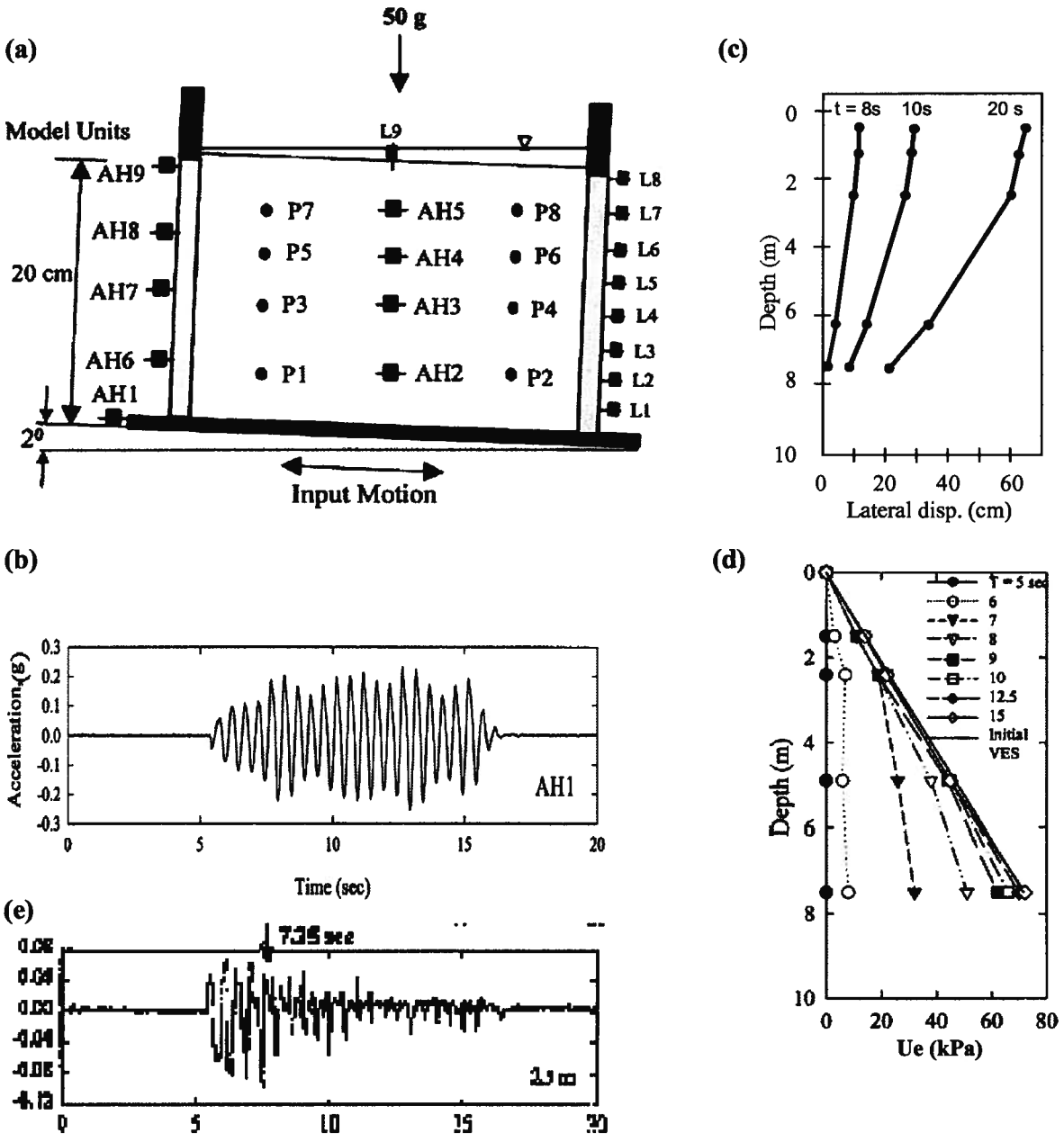

Fig. 4-13: Centrifuge model of a 10m infinite slope, (a) model configuration (model scale), (b) base motion, (c) & (d) isochrones of measured lateral displacement and excess pore water pressure at different time intervals, (e) acceleration time history measured at 2.5m depth with AH4 (modified from Sharp & Dobry, 2002 and Sharp, et al., 2003a, with permission from ASCE).

Fig. 4-14 shows the time histories of predicted volumetric strain at different depths of the soil profile. As may be seen all volumetric strains are essentially contractive and it is more

pronounced in deeper parts due to greater reconsolidation pressure. This indicates that soil volume change continues after shaking ceases.

The predicted time history of horizontal displacement of the top surface is shown in Fig. 4-15. For the case without the barrier, displacements mainly occur during shaking and cease shortly after the end of shaking.

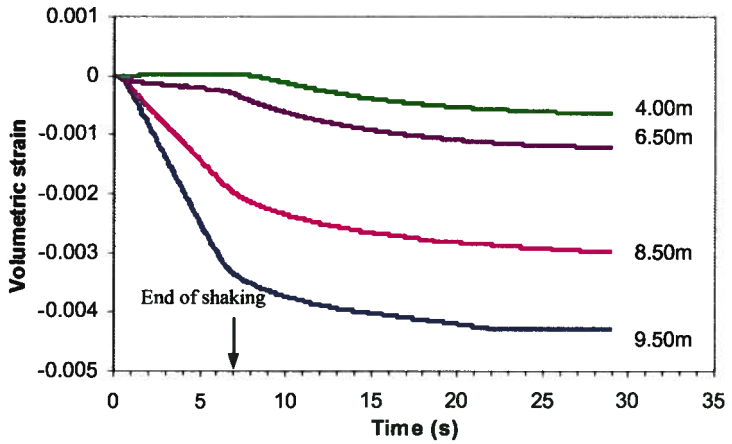

Fig. 4-14: Predicted time history of volumetric strain for various depths (*case I*).

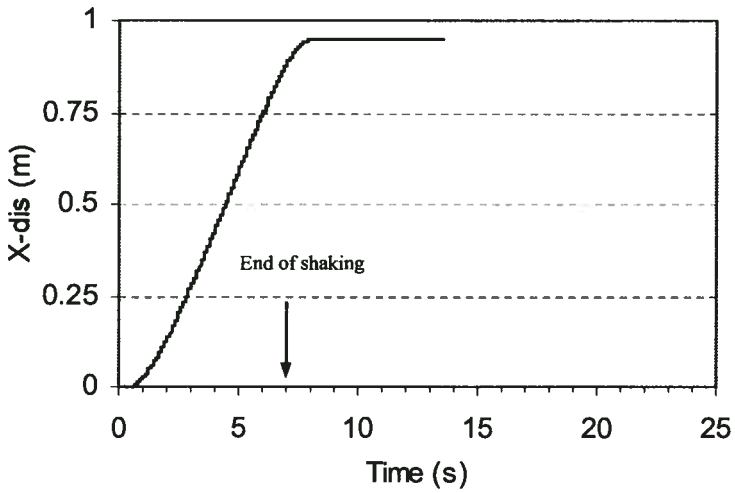

Fig. 4-15: Predicted time history of horizontal displacement at top surface (*case I*).

4.5.2 Sloping Ground with Barrier, *Case II*

Sloping ground with a low permeability layer was analyzed next. The layer was located at a depth of 4m and had a permeability 1000-times lower than that of the loose sand. The ground response in terms of excess pore water pressure ratio, R_u for different depths is shown in Fig. 4-16. Again, pore water pressure increases very rapidly; however, beneath the barrier layer, they remain high ($Ru \approx 100\%$) after the end of shaking, while dissipation occurs at greater depths. This indicates that water flows from the greater depths towards the layer beneath the barrier causing higher excess pore water pressure to last for a significantly longer time compared to the case without a barrier. The injected flow causes an expansion of the layer beneath the barrier to occur at essentially zero effective stress and leads to large deformation.

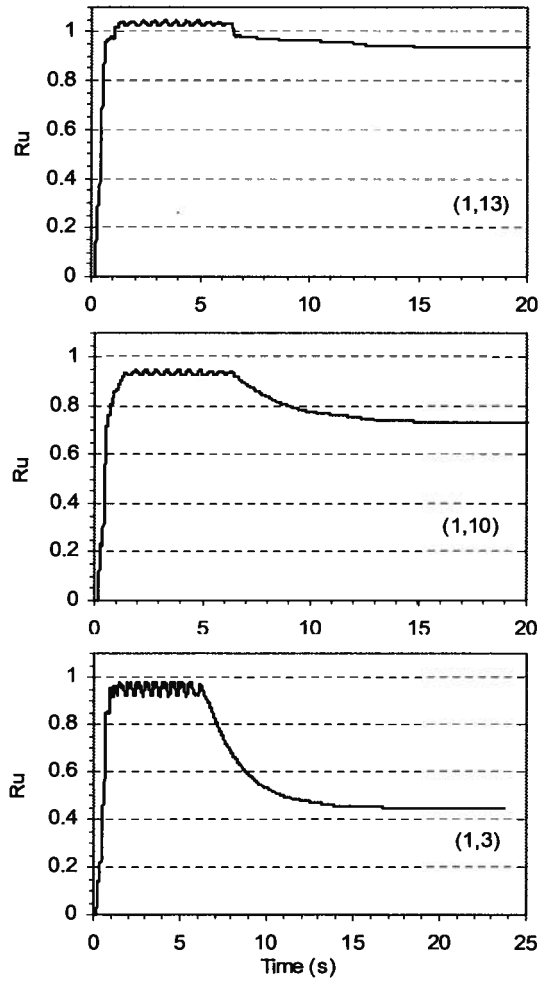

Fig. 4-16: Excess pore water pressure ratio Ru vs. time at selected points with increasing depth (*case II*).

The deformation pattern after 30s is shown in Fig. 4-17. Comparing the pattern and magnitude of lateral displacements with and without a barrier layer (Figs. 4-17 and 4-11), the magnitude is seen to increase from 0.95m to 1.75m and the pattern is quite different with a large slippage occurring at the base of the barrier layer that conforms well with the observations in physical testing, as discussed in *Chapter 3*. The time histories of horizontal displacement of the top surface are compared with the condition without a barrier layer in Fig. 4-18. The surface displacements are seen to be much larger when a barrier layer is present. They are larger during shaking and continue to increase after shaking ceases.

Fig. 4-19 shows a profile of volumetric strain beneath the barrier at different time stages. It shows the evolution of an expansion zone beneath the barrier that eventually leads to a practically stable situation of the lower 60% of the soil profile with contraction, while expansion occurs in the upper 40% of the profile with the highest rate of expansion in the vicinity of the barrier base. This also can be observed from the volumetric strain time history depicted in Fig. 4-20 for selected depths beneath the barrier. Comparing the pattern of volumetric strain change for the two cases (Fig. 4-14 and 4-20), the presence of the barrier results in expansion in the upper part of liquefiable soil and is the result of its loosening. Fig. 4-21 compares flow pattern for the two cases, revealing that the barrier impedes the drainage path of the pore water flow. Therefore, undrained conditions do not exist, especially locally within the soil deposit beneath the barrier. It also suggests that undisturbed samples taken prior to the earthquake will not represent the conditions during and shortly after the earthquake, due to void redistribution resulting from the upward flow of water.

Table 4-2 summarizes the effects of the low permeability layer on lateral displacements. It shows that a large portion of the surface displacements occurs after earthquake shaking due to the time required for water to flow into the layer beneath the barrier. Lateral displacements are concentrated in a thin zone beneath the barrier, and below this, the displacements are less than those in the condition without the barrier.

Similar analyses were also carried out for the same soil profile including a barrier layer with zero slope (level ground). In this case of level ground, no significant lateral displacements are predicted because of zero static driving force or shear stress bias for level ground conditions.

The preceding analyses reveals the impact of the presence of a low permeability sub-layer on a liquefiable soil layer behavior subjected to an earthquake in terms of pattern and the

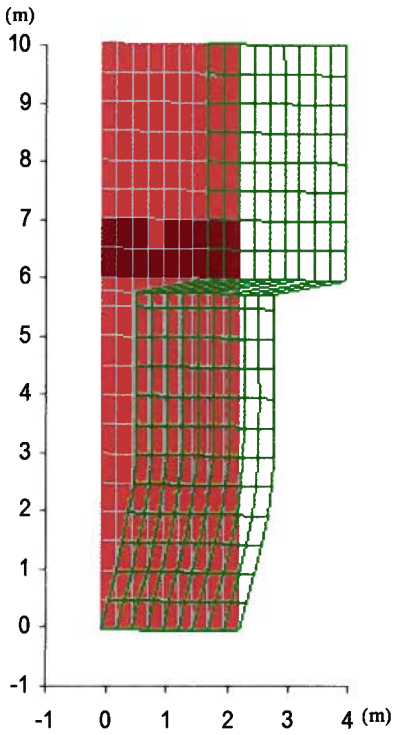

Fig. 4-17: Deformation pattern of soil profile with barrier, *Case II* (with max. lateral displacement of 1.75m after 30 s).

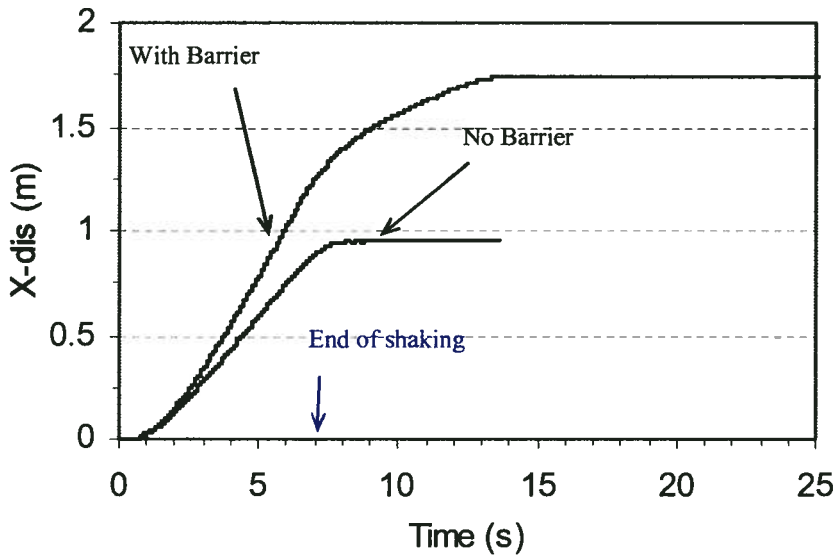

Fig. 4-18. Surface lateral displacement vs. time for profiles with and without barrier.

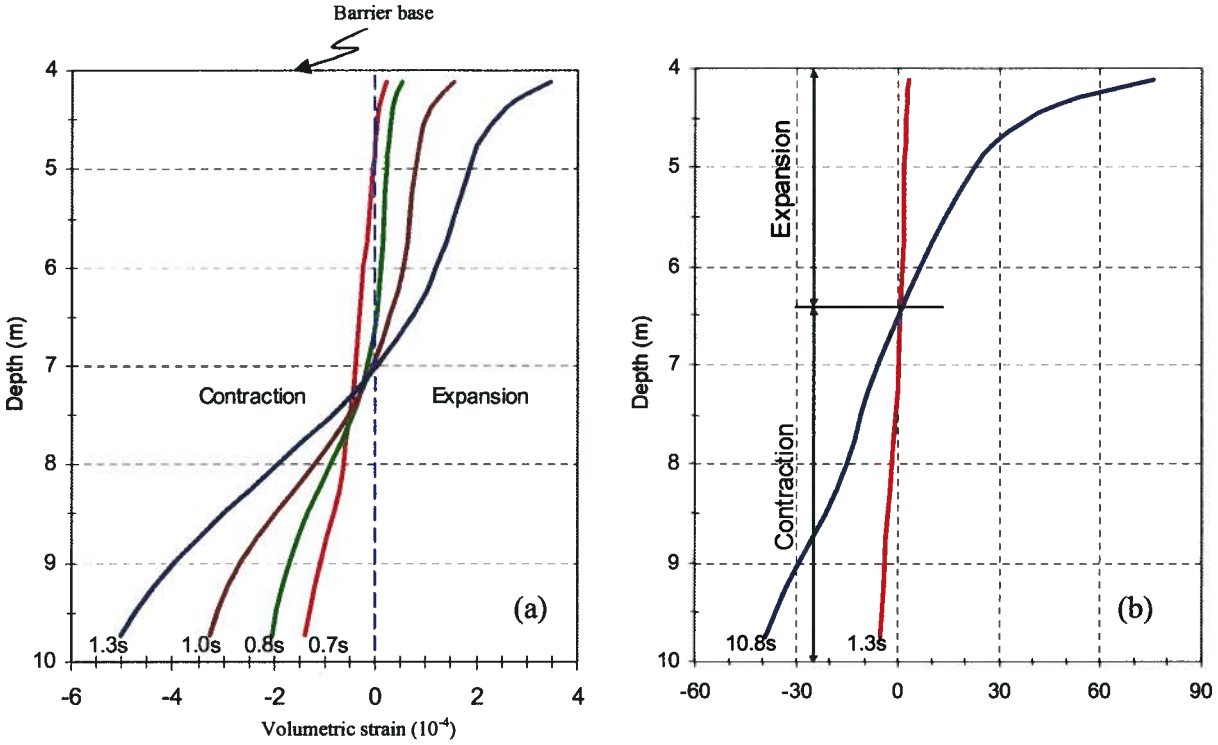

Fig. 4-19: Change of volumetric strain isochrones beneath the barrier over times, (a) initial stages, (b) longer time stages (*case II*).

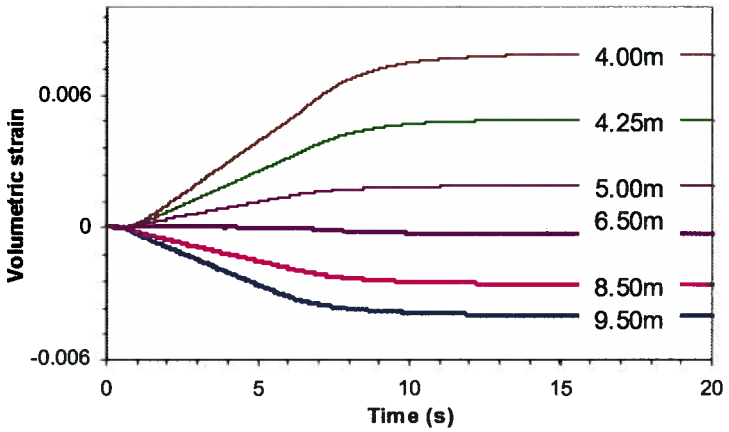

Fig. 4-20: Predicted time history of volumetric strain for various depths (*case II*).

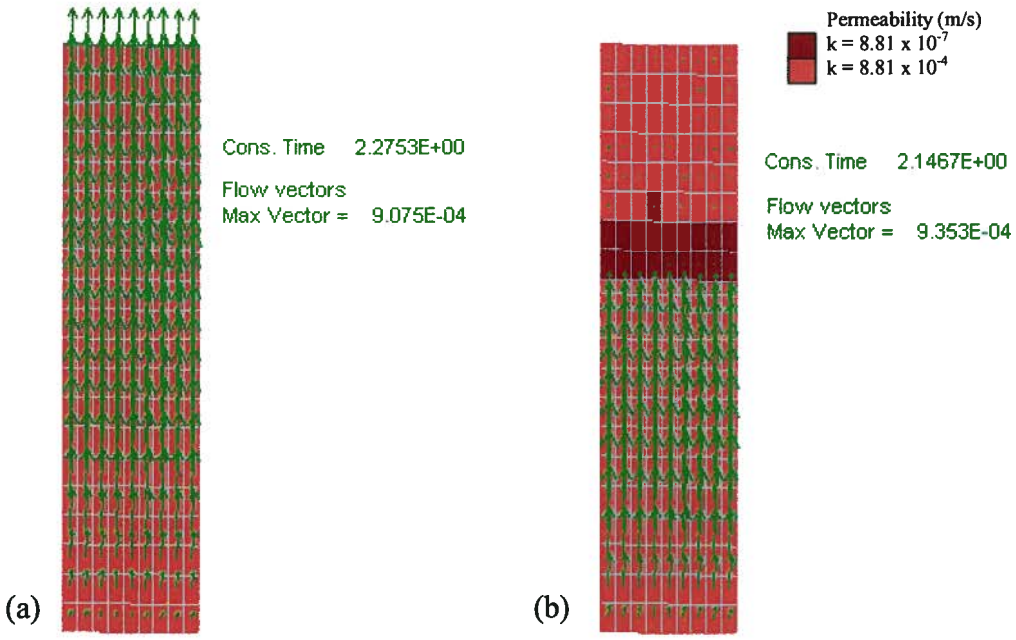

Fig. 4-21: Flow pattern after 2s shaking within (a) soil layer without barrier, *case I*, (b) soil layer with barrier, *case II*.

Table 4-2: Barrier effects on lateral displacements.

x-displacement	No barrier (case I)	With barrier (case II)
Top surface max. displacement (m)	0.95	1.75
Max. displacement at 4m depth (m)[a]	0.9	1.75
Top surface displacement at 7s (m)[b]	0.9	1.24
Displacement at 4m depth[a] at 7s (m)[b]	0.9	1.24
Ratio of displacement at 4m depth[a] to that of surface at 7s[b]	95%	100%
Ratio of post earthquake surface displacement to total	5.3%	30%

[a] Depth 4m lies just below the barrier base for the case II.
[b] The strong shaking ends at 7s (see Fig. 4-6).

order of magnitude of displacements, as well as delayed failure. The response of an earth structure to earthquake shaking is a coupled stress-flow problem and controlled by:

1. *Mechanical conditions:* soil strength (i.e., stress-strain characteristics) and the applied earthquake characteristics (i.e., amplitude, duration, etc.), and

2. *Flow conditions:* soil deposit permeability, permeability change within the soil layers (permeability contrast) and spatial distribution of different zones of various permeabilities.

The effect of liquefiable soil permeability, which has not been well appreciated in the literature, was recently addressed by Sharp, et al. (2003a) and by Seid-Karbasi & Byrne (2006b), and is discussed in the next section. The permeability contrast that results in void redistribution is the focus of this research and is treated in detail in subsequent chapters of this thesis. The permeability spatial distribution effects (that control the preferential dissipation path) should be accounted for when designing remedial measures and is further examined in *Chapter 8*.

4.6 Significance of the Permeability of Liquefiable Soil Layer

As discussed in *Chapter 2,* many researchers (e.g., Lee, 1965) have documented that sand contraction is a stress dependent characteristic in that it increases with confining stress (see Fig. 2-4). Cyclic element laboratory tests on sands also indicate that at higher confining stresses, the liquefaction resistance of sand decreases and liquefaction therefore is more likely to occur at depth. Fig. 4-22 shows *CRR* vs. relative density for Fraser River sand with different isotropic consolidation pressure. This suggests that for a given uniform sand layer the materials at greater depths (under higher confining pressure) are more susceptible to liquefaction triggering. To account for this overburden pressure effect, the conventional liquefaction triggering analysis (e.g., Youd, et al., 2001) involves a factor, K_σ that decreases with increasing effective overburden pressure and hence, depth, and predicts liquefaction occurs first at deeper parts. A more recent reevaluation of the K_σ effect, by Boulanger (2003) and Boulanger & Idriss (2004), based on a *critical-state* framework using *Bolton's* relative dilatancy index (1986) is presented in Fig. 4-23 and is compared to previous work of Hynes & Olson (1998). It indicates that shear induced contraction at high confining pressures is more pronounced for denser materials (K_σ equals 1 for a reference pressure of 100 kPa). Centrifuge testing data (e.g., Sharp & Dobry, 2002 and Taboada & Dobry, 1998) indicates that liquefaction ($R_u \approx 1$) initiates first at shallow depths and then extends toward deeper parts. This is not in agreement with the K_σ effect.

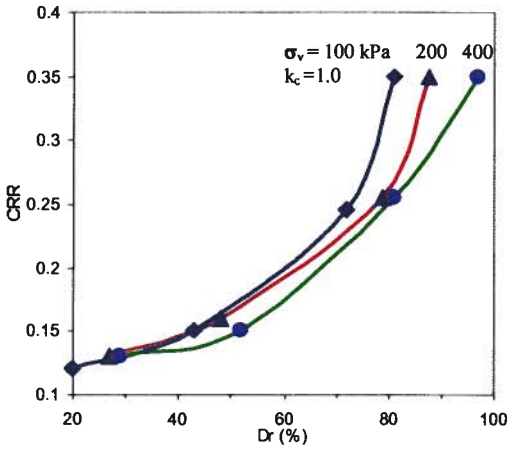

Fig. 4-22: CSR vs. relative density for Fraser River sand under different isotropic consolidation pressures (reproduced based on data from Vaid, et al., 2001).

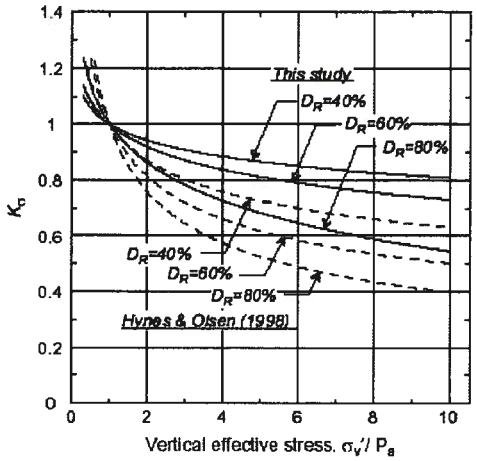

Fig. 4-23: Overburden reduction factor, K_σ for *CRR* (adapted from Idriss & Boulanger, 2006).

In the following section, the effects of soil permeability on liquefaction onset within a sand deposit are examined and the K_σ effect is addressed.

Consider the same 10m uniform layer of liquefiable soil (shown in Fig. 4-7) without barrier layer (uniform deposit modeled as single-column mesh with 20 elements, as shown in Fig. 4-24a) subjected to harmonic motion with PGA = 0.88 m/s^2, as depicted in 4-24b. The uniform sand layer is represented by constant $(N_1)_{60}$ = 12 in the analyses. The problem is analyzed for two conditions:

1) *Flow-on*
2) *Flow-off*

The first analysis represents a more realistic condition where pore water can flow during shaking (partially drained condition) due to hydraulic gradient. The permeability of sand is considered as k = 8.81 x 10^{-4} m/s. The second case represents an undrained condition where no water can flow,

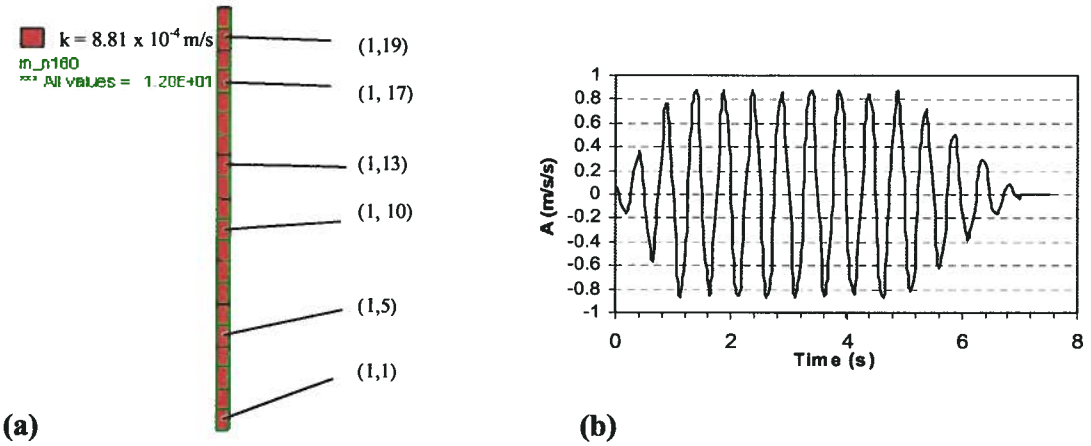

Fig. 4-24: (a) single-column mesh of 20 elements of 0.25m x 0.5m size, (b) Base acceleration time history.

thus the response of the sand layer is controlled solely by the mechanical properties of the materials. Fig. 4-25 shows the predicted time histories for surface acceleration compared with that of base motion. It indicates that no significant amplification takes place while the motion propagates to the surface. A similar response can be inferred from the centrifuge model shown in the Fig. 4-13 (compare Fig. 4-13b with Fig. 4-13e).

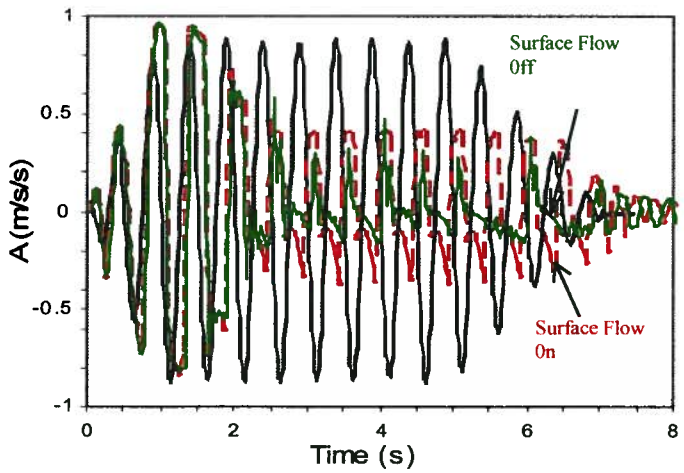

Fig. 4-25: Acceleration time history at surface for two cases compared to input base motion.

Fig. 4-26 compares the time history of excess pore water pressure ratio, R_u for various depths for both (partially) drained and undrained conditions. As may be seen, for the undrained condition, the R_u is higher at greater depths (e.g., element [1,3]) in accord with the K_σ effect, and lower R_u is observed at the surface. This pattern changes (in *Flow-on* condition) at the upper parts as for example in element [1,19] close to the surface, where $R_u \approx 0.9$ for partially drained condition compared to $R_u \approx 0.5$ for the undrained condition. The predicted higher R_u at shallow depths in *Flow-on* conditions is in agreement with centrifuge and field data (Sharp et al., 2003a and Youd et al., 2001). This unexpected result can be explained by examination of the net-inflow/outflow or volume change that occurs at various depths. This can be observed in Fig. 4-27 that shows time histories of volumetric strain at various depths in the liquefied layer depth (see Fig. 4-24 for position of elements). The figure indicates that in the (partially) drained condition, all volumetric strains at deeper parts are contractive over the time, whereas, at shallow depths, volume expansion is occurring in the elements as a result of pore water pressure redistribution. As may be observed, the volumetric strain at shallow depths (from element [1,17] to the ground surface) is expansive during shaking where inflow continues and results in high excess pore water pressure (see Fig. 4-26).

The water injection leads to soil loosening/weakening and decrease in its liquefaction resistance, and the analysis results are in accord with this observation. Fig. 4-28 & 4-29 show prediction for a soil element under undrained and inflow/outflow conditions for a typical liquefiable sand having $(N_1)_{60} = 10$. It is observed that high R_u and earlier liquefaction is predicted for inflow condition ($\varepsilon_v/\gamma = 0.01$) compared to that for outflow condition ($\varepsilon_v/\gamma = -0.01$). The undrained condition ($\varepsilon_v = 0$) is between these two cases. This suggests that more severe earthquake-induced damages at/near ground surfaces of uniform liquefied deposits are arising from soil loosening due to inflow during excitation. Also, the engineering design based on assumed undrained conditions for a uniform layers may not represent the condition in the field.

This finding on liquefaction onset at near surface conforms with centrifuge model test data. Fig. 4-30 shows excess pore water pressure time histories at different depths measured in the centrifuge testing described earlier (and shown in Fig. 4-13) (Sharp et al., 2003a). The liquefaction onset is shown with the arrow, and the same pattern of liquefaction initiation at the surface is seen, in agreement with the analysis and the flow condition.

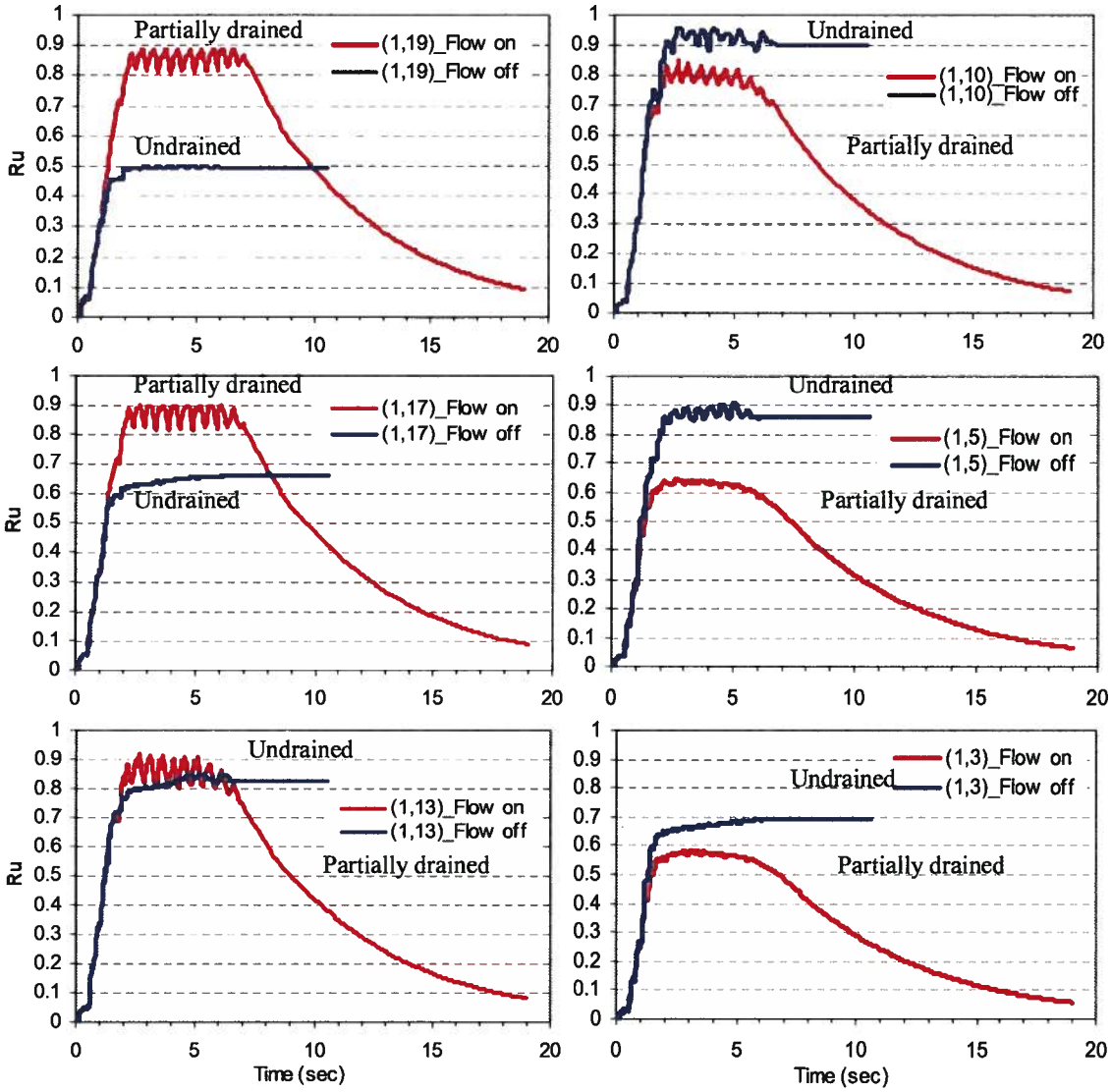

Fig. 4-26: Time history of excess pore water pressure ratio, R_u for *Flow-on* and *Flow-off* conditions analyses.

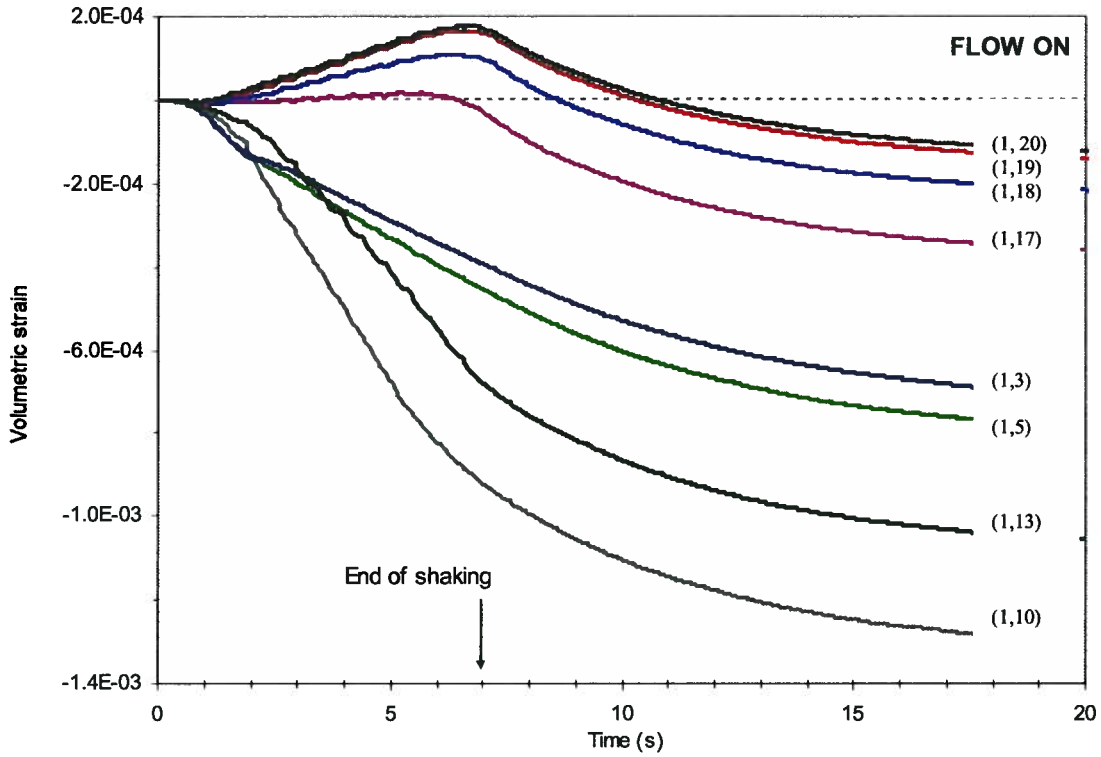

Fig. 4-27: Time histories of volumetric strain for *Flow-on* condition at various depths.

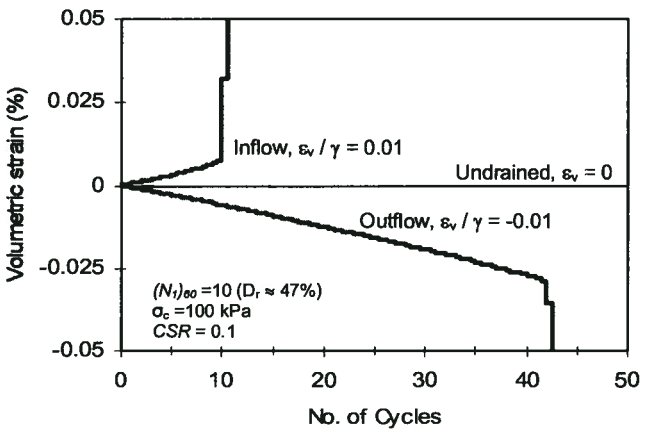

Fig. 4-28: Imposed volumetric strain paths with No. of cycles for a sample in cyclic simple shear test.

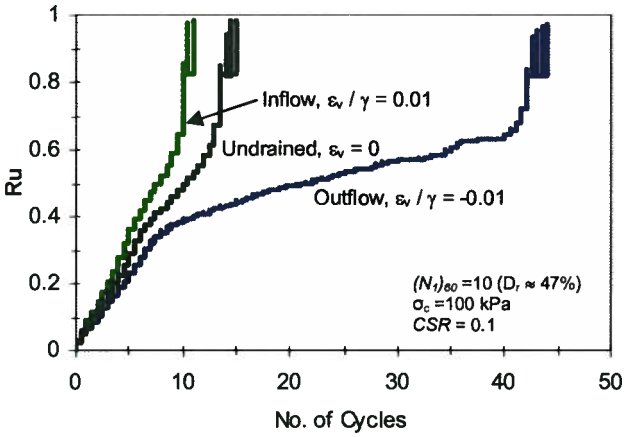

Fig. 4-29: Predicted excess pore water pressure ratio with No. of cycles for a sample in cyclic simple shear test.

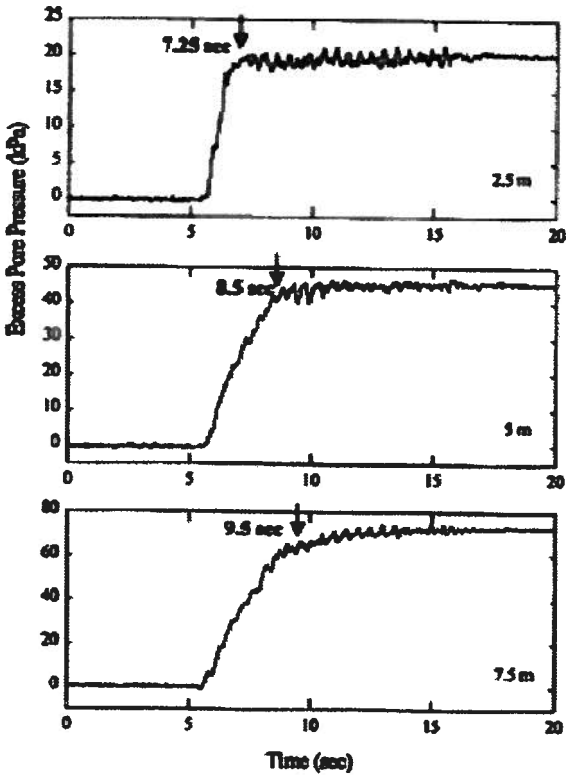

Fig. 4-30: Time history of excess pore water pressure at different depths measured in centrifuge test (Sharp & Dobry, 2002).

Another set of analyses (in the *Flow-on* condition) was conducted with 10 to 1000 times decrease in permeability of the liquefiable sand subjected to the motion given in Fig. 4-8. Responses are shown for these two extreme cases, in terms of excess pore water pressure increase rate, dissipation rate and timing, and displacements. Fig. 4-31 compares the time histories of R_u for soil permeabilities of $k = 8.81\times10^{-4}$ and $k = 8.81\times10^{-6}$ m/s. The permeability reduction results in a changed liquefaction tendency. It also causes a delay in excess pore water pressure dissipation. The results of further analyses with a range of permeabilities (from 8.81×10^{-4} to 8.81×10^{-8} m/s) in terms of R_u time histories for the ground surface (i.e., element [1,19]; Fig. 4-24) along with surface lateral displacement vs. soil permeability are shown in Fig. 4-32. For permeabilities of an order of magnitude typical of most sandy soils, flow effects speed up

liquefaction triggering at upper parts, which causes liquefaction to generally occur first near the top and work its way down.

Fig. 4-33 shows the model with displacement vectors for the undrained and (partially) drained condition (for the case with k = 8.81×10^{-4} m/s). The surface maximum lateral displacement is 0.30m and 0.23m in undrained and (partially) drained conditions, respectively. Thus, the undrained condition results in larger displacements that extend to greater depths.

The permeability effects on seismic behavior of earth structures have been recently investigated by a few researchers using centrifuge model testing (e.g., Taboada, 1995; Okamura, et al., 2001; and Sharp, et al., 2003a). Various authors also observed a similar trend of increasing displacements and liquefaction depth with soil permeability reduction. Fig. 4-34 and 4-35 show surface lateral displacement and liquefaction depth vs. sand layer permeability for the model shown in Fig. 4-13.

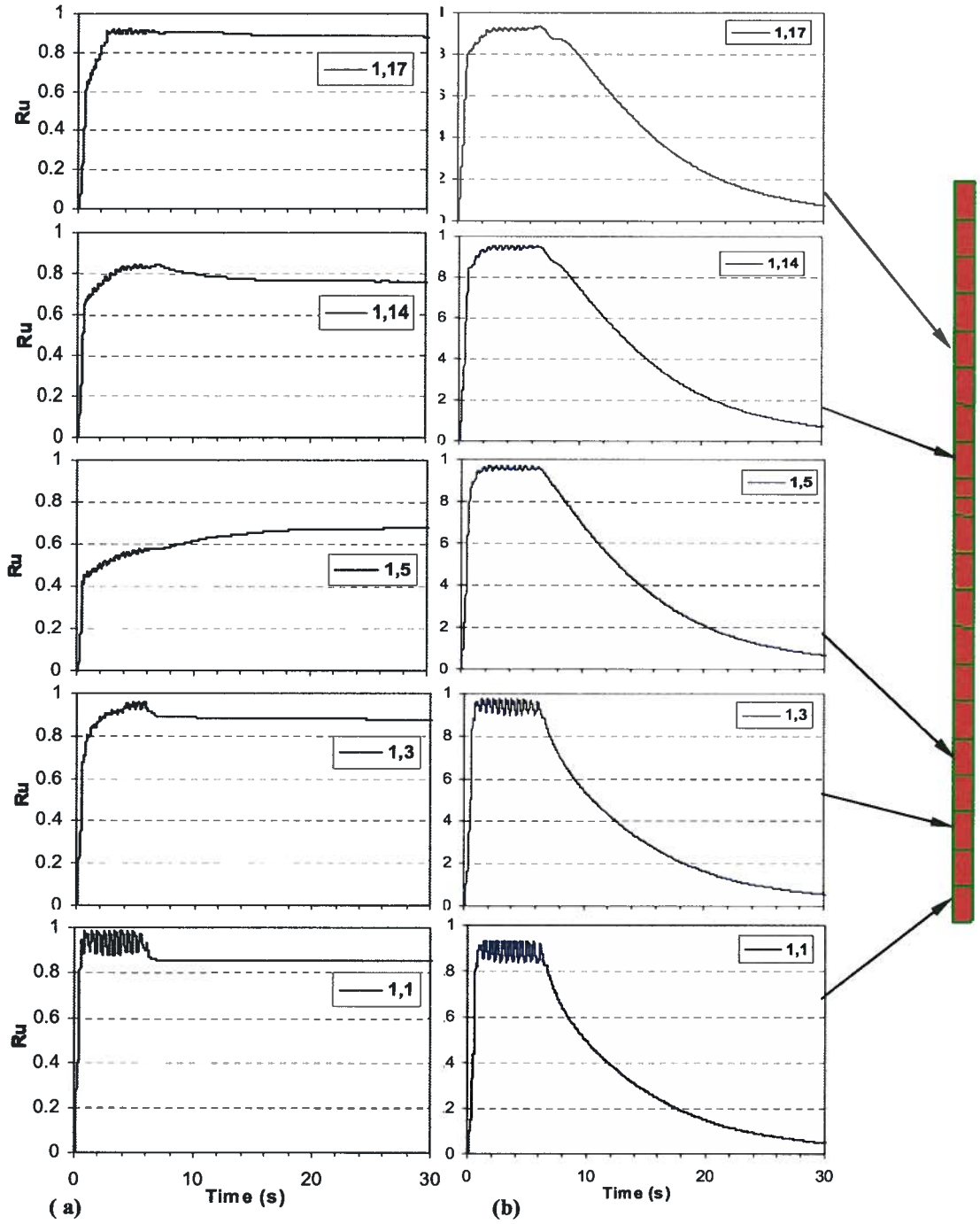

Fig. 4-31: Pattern of excess pore water pressure generation, (a) $k = 8.81 \times 10^{-6}$ m/s, and (b) 8.81×10^{-4} m/s.

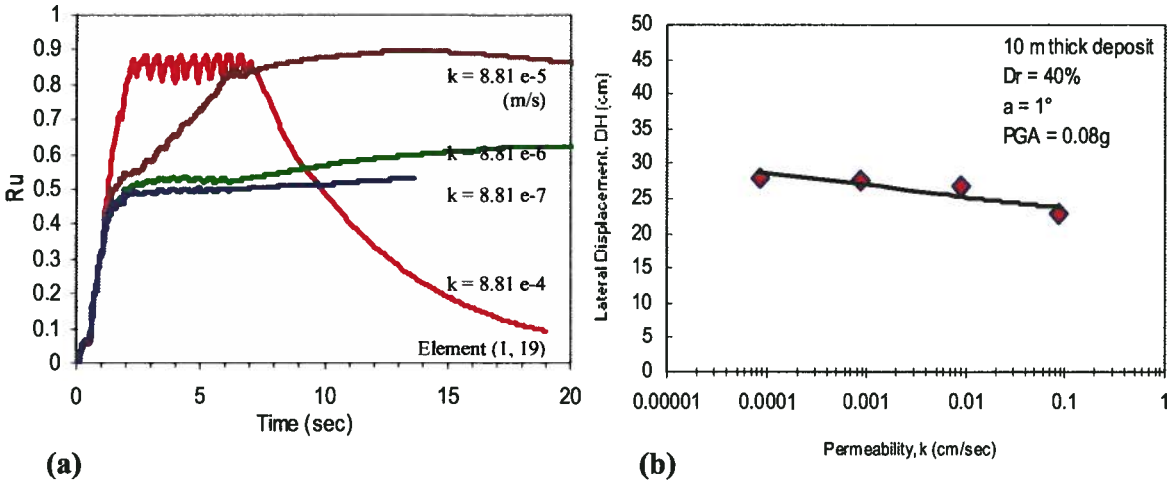

Fig.4-32: Effects of liquefied soil permeability reduction (a) time histories of R_u at shallow depth, and (b) ground surface lateral displacement.

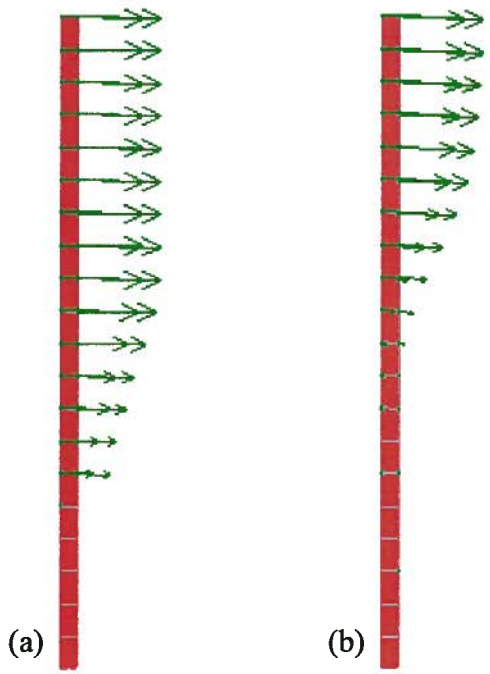

Fig. 4-33: Displacement vectors for (a) undrained condition (b) partially drained condition.

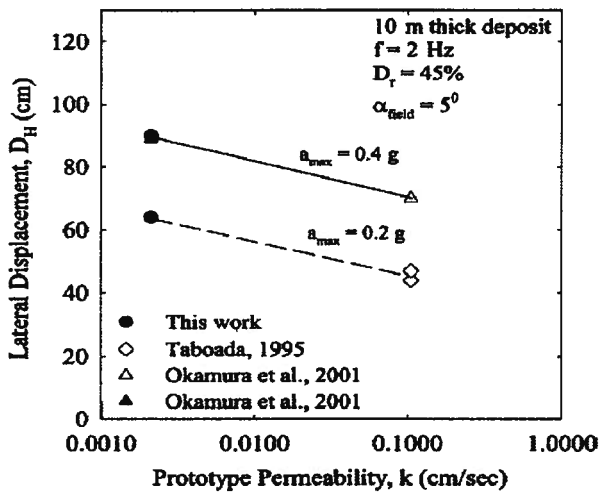

Fig. 4-34: Effect of soil permeability on lateral displacement in centrifuge tests (Sharp, et al., 2003a, with permission from ASCE).

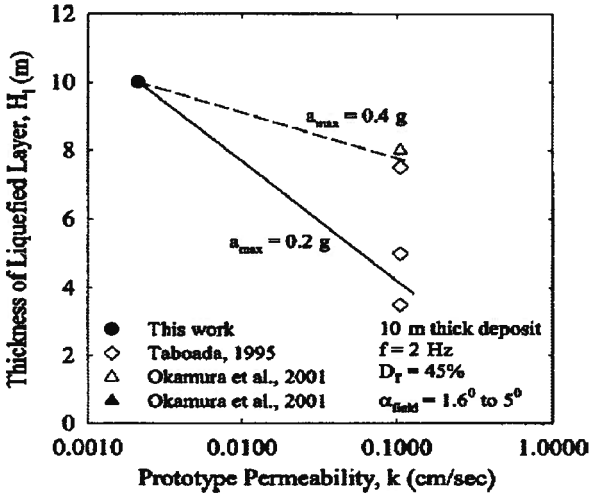

Fig. 4-35: Effect of soil permeability on liquefaction depth in centrifuge tests (Sharp, et al., 2003a, with permission from ASCE).

The significant effect of permeability reduction on deformations and applied loads in piled foundations was also reported from another study conducted at the Rensselaer Polytechnic Institute (RPI), NY, using centrifuge models. Gonzales (2005) and Gonzales et al. (2009) reported test results of the same models of piles (with single and group configuration), embedded in fine Nevada sand (D_r = 40%) of two different permeabilities (i.e., models saturated with water simulating coarse liquefiable sand, and models saturated with viscous fluid representing fine liquefiable sand of lower permeability). They observed that the lateral displacements and associated moments in the test models of lower permeability can reach as much as six-times those observed in the model of greater permeability.

This reveals that permeability of the liquefiable soil layer has a significant effect on the seismic response of the earth structures in controlling liquefaction onset. It also implies that the introduction of fine material (e.g., non-plastic silt) into a uniform sand deposit, regardless of its effects on sand mechanical properties (resistance to liquefaction triggering), leads to more deformations due to permeability reduction. As an example, Eigenbrod, et al. (2004) reported that the introduction of 30% silt into a clean concrete sand results in three-fold reduction in the mixture permeability (see Fig. 4-36).

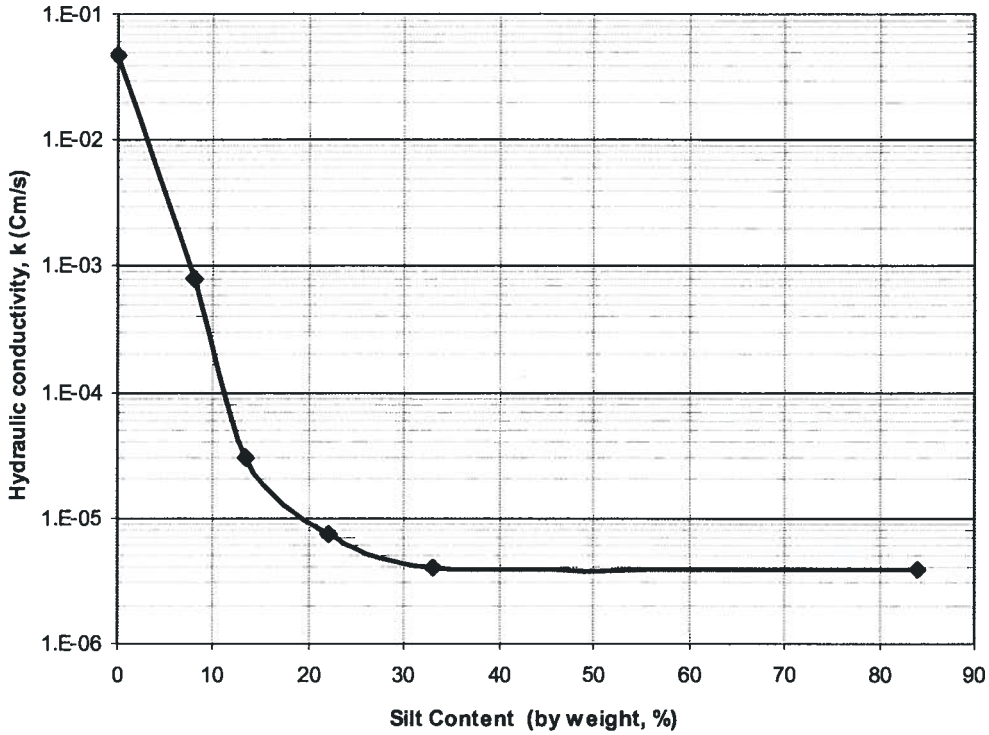

Fig. 4-36: Permeability reduction of concrete sand with silt content (data from Eigenbrod, et al., 2004).

4.7 Summary and Main Findings

In this chapter, fundamentals of the stress-flow coupled analysis and the computer code *FLAC,* used in this study, were briefly explained. The modeling procedure using the *UBCSAND* constitutive model was described and, with reference to other investigators, it was shown that the *UBCSAND* model can capture characteristic sand element behavior under different loading conditions, i.e., undrained, partially drained, and cyclic simple shearing.

This procedure was applied to analyze a typical response of a liquefiable soil layer with and without a low permeability sub-layer. The characteristic behavior of mildly sloping ground was examined in terms of deformation pattern, excess pore water pressure generation, and volumetric strain. The effects of permeability on seismic response of liquefiable soil were also investigated. From this study, the seismic response of earth structures was shown to be controlled by both mechanical and flow (hydraulic) conditions. Mechanical conditions control excess pore water pressure generation, and its dissipation and redistribution are controlled by flow conditions. This key observation is consistent with dynamic centrifuge model test data. The work presented in this chapter leads to the following conclusions:

1. *The typical characteristic response of gently sloping ground comprised of liquefiable soils without barrier in earthquakes can be described as follows:*
   - 1.1. The excess pore water pressure reaches a maximum value earlier, in the upper parts and lasts for a longer time.
   - 1.2. Excess pore water pressures start to dissipate in the deeper parts first.
   - 1.3. The volumetric strain near ground surface is essentially expansive during shaking, results in soil loosening and more surface damage in earthquakes.
   - 1.4. After shaking ceases, the volumetric strain within the soil layer is essentially contractive.
   - 1.5. Horizontal displacement is larger at the surface and it tapers smoothly with depth without any localization.

   These conclusions conform to physical model (centrifuge) testing data reported by other investigators.

2. *The presence of a low permeability sub-layer in a liquefiable soil layer has the following impacts on its characteristic seismic behavior:*
   - 2.1. The excess pore water pressure is generated with a similar pattern as that of a soil layer without barrier.
   - 2.2. The excess pore water pressure dissipation is affected significantly by the impedance of flow path, particularly at zones near the barrier base.
   - 2.3. The high excess pore water pressure at the base of the barrier lasts for a long time after the earthquake ceases.
   - 2.4. Volumetric strains are essentially contractive in the lower parts, whereas, they are expansive in the upper parts that are close to the barrier base.
   - 2.5. The deformation pattern is significantly different from that of the case without barrier. It has a greater magnitude at the surface with a larger post-shaking portion.
   - 2.6. The majority of the horizontal displacement is concentrated (localized) in a thin zone beneath the barrier base.
   - 2.7. The post-liquefaction strength with the presence of a sub-layer barrier cannot be determined solely as a material property based on its pre-earthquake state.

3. *The partially drained condition and permeability of liquefiable soil layers (without barrier) has a great impact on seismic response of earth structures:*

   3.1. Partially drained condition

   - 3.1.1. The initiation of liquefaction at shallow depths observed in the liquefied case histories and centrifuge tests are due to pore water migration driven by hydraulic conditions in the partially drained conditions.
   - 3.1.2. The K_σ effect in liquefaction triggering is offset by inflow/outflow in partially drained condition.

3.1.3. The excess pore water pressure redistribution mainly controls the volumetric strain within the liquefiable grounds, in terms of magnitude and induced expansion (contraction vs. dilation).

3.2. Significance of permeability of liquefiable soil

3.2.1. Liquefied soil layers with lower permeability experience high excess pore water pressure for a longer time and as a result greater displacements extend to deeper parts.

3.2.2. In liquefiable grounds of non-clean sands (with some fines content), the fines material, in addition to mechanical effects on sand liquefaction resistance, significantly influence the seismic sand layers' behavior as a result of permeability reduction.

CHAPTER 5

LOCALIZATION AND FLOW SLIDE FROM VOID REDISTRIBUTION

5.1 Introduction

The results presented in *Chapter 4* reveal that delayed large deformations in liquefiable gently sloping ground occur when a sub-layer with low permeability is present. However, two questions may arise in this regard:

1. In view of the deformation pattern localized in the element beneath the (hydraulic) barrier, to what extent is the predicted response affected by the model configuration (mesh size effects)?
2. What are the requirements for a *flow-slide*?

This chapter presents and discusses the results of analyses conducted to answer these questions. Further, based on the findings of this study, a practical approach to handling localization effects of a hydraulic barrier is developed.

5.2 Mesh Size Effects

The predicted deformation pattern for a liquefiable slope with a sub-layer barrier with strain localization implies that the computed results can be mesh-size dependent. This was also noted by Yang & Elgamal (2002a) and Uzuoka, et al. (2003). To investigate scale effects on predicted characteristic behavior, a separate series of analyses was conducted for the soil profile shown in Fig. 4-7, with 1° inclination and modeled as a single-column mesh subjected to (sinusoidal) harmonic base motion of PGA = 2.5 m/s^2 as given in Fig. 4-6. The purpose is to investigate whether any effect arising from the numerical approach might be involved with the predicted behavior. The problem was modeled in two different ways:

a) As a 10m-soil profile in 1g-field (prototype scale) and

b) As a 0.1m-soil profile in 100g-field (model scale) following appropriate conversion laws for modeling, as described by Schofield (1981) and Kutter (1995). The mesh size used in modeling (b) was one hundredth that used in modeling (a).

Fig. 5-1 illustrates the single-column mesh of 21 elements of 0.25m × 0.5m size used in the analyses along with the soil profile (the two elements beneath the barrier are of 0.25m × 0.25m size). The mechanical and flow properties of materials are the same as before (listed in Table 4-1). The displacement patterns were identical for both models when examined in prototype scale. Fig. 5-2 shows the (magnified) deformation pattern predicted in the analysis conducted in model scale that is similar to that obtained before (see Fig. 4-17). The surface displacement showed a very good agreement with the previous analysis results in terms of its magnitude and time history (e.g., Fig. 4-18). The time histories of excess pore water pressure ratio, R_u were also identical to that given in Fig. 4-16. The ground response, in terms of the profile of volumetric strain beneath the barrier layer, and time history for both models were also identical and as depicted in Fig. 4-19 and 4-20, respectively.

Thus, for a soil profile comprising a barrier layer, contraction at the lower parts and expansion at the upper parts, are characteristic behavior and controlled by flow conditions that occur due to pore water migration, which results in void redistribution regardless of layer size (the effect of liquefiable layer thickness on displacements is investigated in *Chapter VI*). These findings indicate that the phenomenon of pore water redistribution can be captured in centrifuge tests and that the actual physical size of the layers is not important. From a numerical modeling point of view, what matters is the size of the mesh in relation to the size of the liquefiable layer beneath the barrier.

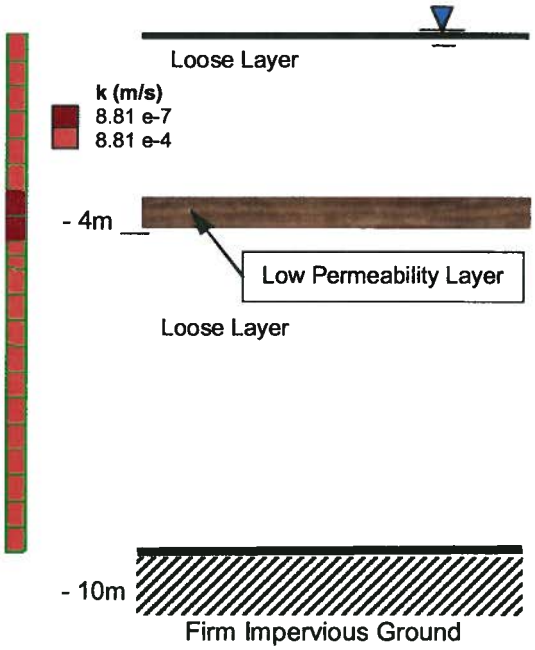

Fig. 5-1: Single-column model of the 10 m-layer profile.

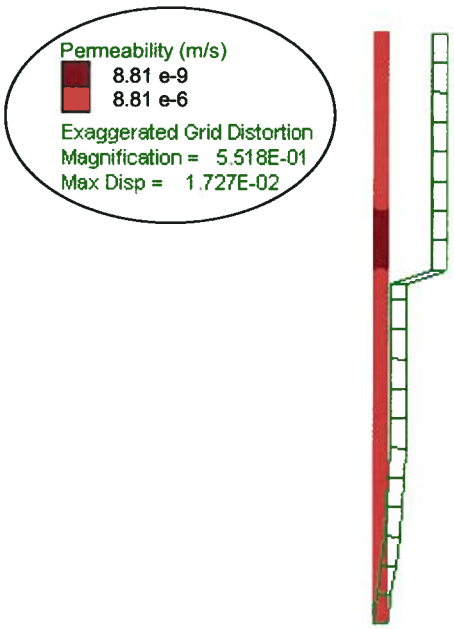

Fig. 5-2: (Magnified) deformation pattern of the 100g model. (Note: in model scale, the length and permeability are 1/100 that of the prototype).

5.2.1 Effects of Base Element Thickness

To study the effects of the element thickness ratio, *ETR* ($T_{Element}$/$T_{Layer\ thickness}$), further studies were undertaken to analyze the problem under the same conditions (1g-field) but using different meshes of decreased size (only) for the element beneath the barrier, as depicted in Fig. 5-3. The results, in terms of excess pore water pressure generation were the same as presented in Fig. 4-10. However, the results for surface lateral displacement, i.e., magnitude and time history (given in Fig. 5-4), were different and controversial, as a result of numerical error (low precision) due to element size. The corresponding displacement time histories for the models with 0.5m and 0.25m base elements coincide with each other, which indicates that the element thickness ratio, *ETR* (above a critical value) does not affect the predicted response. Fig. 5-5 shows the maximum expansion of the base element vs. *ETR,* i.e., the element thickness normalized with respect to liquefiable layer thickness beneath the barrier, 6m. A decrease in the element size ratio results in greater volumetric expansion for the very first element at the base of barrier layer.

To investigate the possible effects of the aspect ratio of the base element (height/width), the meshes in case c and d (Fig. 5-3) were replaced with combined meshes including fine square elements (as given in Fig. 5-6). The results were essentially similar to the corresponding analysis without embedded fine mesh, and no significant improvement was observed in the deformation prediction.

This suggests that the analysis results are mesh size-dependent due to numerical error. As the volumetric strain is mainly controlled by inflow/outflow (discussed in *Chapter* 4); however, the trend of increasing base element expansion with decreasing size can be real. To examine the validity of this conclusion, again, a series of analyses were conducted using the meshes shown in Fig. 5-3 as well as finer ones, with base element thicknesses of 0.031m and 0.015m, while *FLAC* was invoked in *double-precision* mode (as discussed in Section 4.2). Fig. 5-7 shows the maximum surface lateral displacement against the normalized base element thickness for *double-precision* analyses along with *single-precision* analysis. The deformation pattern in all analyses (in *double-precision* mode) was identical to that shown in Fig. 5-2. Thus, the *double-precision* mode provides consistent results (i.e., in terms of deformation pattern, displacement time history and magnitude) that are essentially identical to *single-precision* with large base element thickness (*ETR* > 0.04).

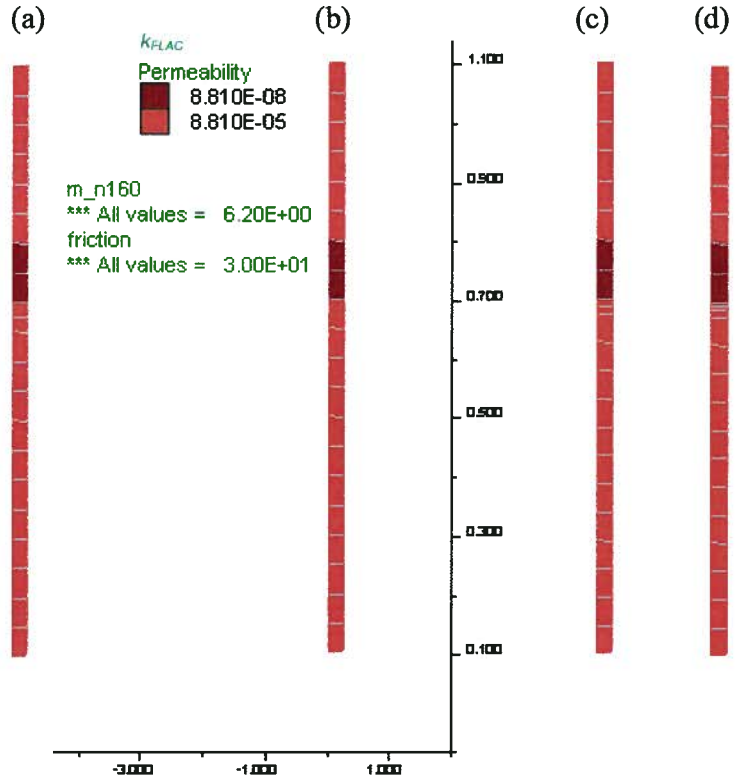

Fig. 5-3: Model of 10m soil profile with 0.25m width and different thicknesses for the base element, (a) 0.25m, (b) 0.5m, (c) 0.125m, and (d) 0.0625m.

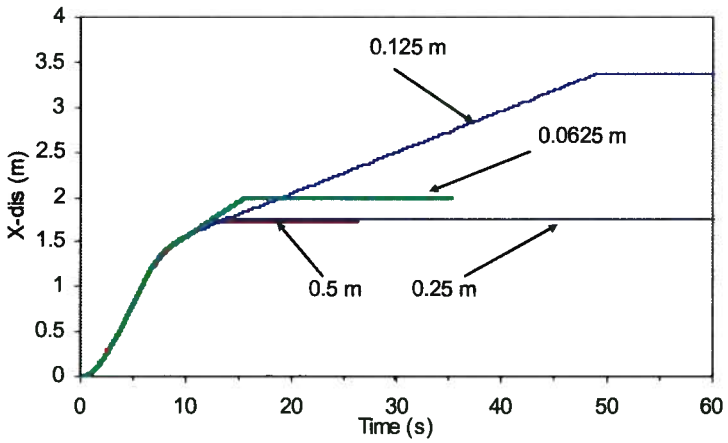

Fig. 5-4: Predicted time history of surface lateral displacement for models with various base element thicknesses.

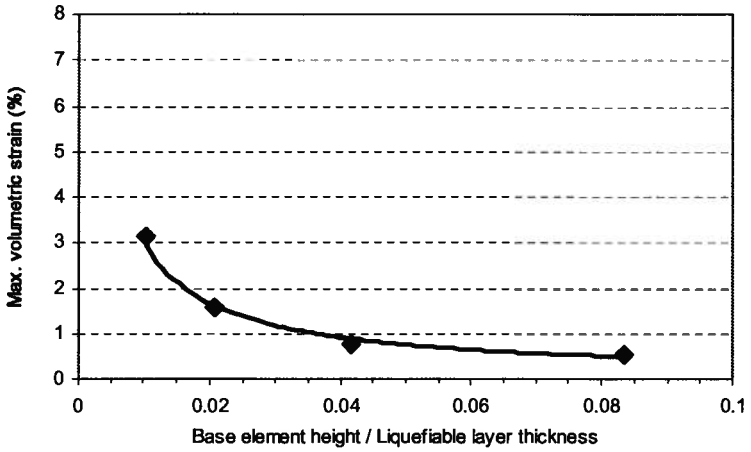

Fig. 5-5: Maximum volumetric strain of base element vs. its normalized thickness (*single-precision*).

Therefore, the inconclusive trend observed in the results (e.g., displacements) from the *single-precision* analysis is due to precision errors associated with numerical computations. Therefore, the study proceeded with use of the *double-precision* mode for analysis of the slope.

Fig. 5-8 shows maximum expansion of the base element vs. its normalized thickness. The figure indicates that a thin zone with large expansive volumetric strain (high void ratio) is formed beneath the barrier due to pore water pressure redistribution. Fig. 5-9 shows the profile of the volumetric strain of the soil layer beneath the barrier for different base element thicknesses from the *double-precision* analysis (at a stabilized time after shaking, with no further expansion). All profiles have essentially the same pattern except at the part that is close to the barrier base. Fig. 5-10 shows the same enlarged profiles at the vicinity of the barrier base. The predicted expansion beneath the barrier appears to vary with the thickness of the element immediately beneath the barrier.

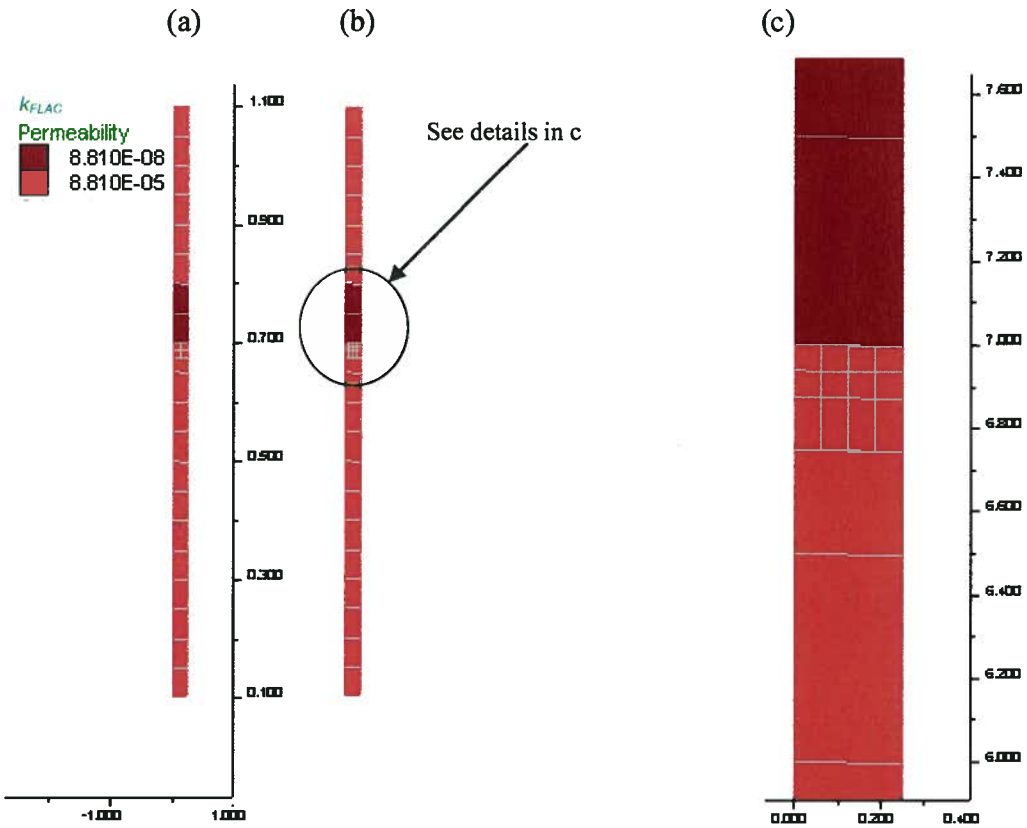

Fig. 5-6: Model of soil profile with embedment of a fine mesh of width/height = 1 beneath the barrier: (a) 0.125m, (b) 0.0625m, and (c) close-up of case b.

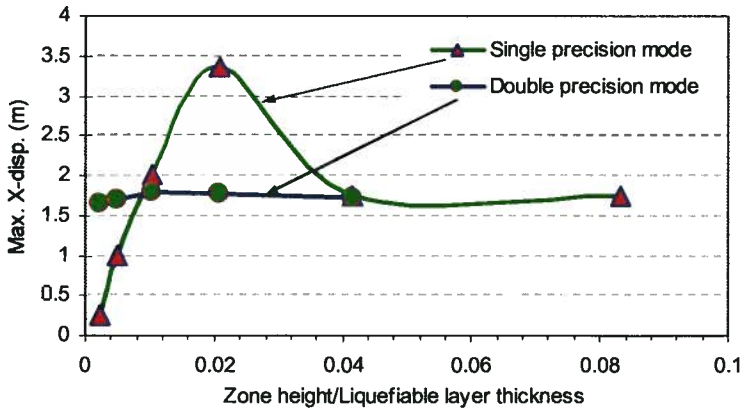

Fig. 5-7: Maximum surface lateral displacement vs. normalized base element thickness in two modes of analyses.

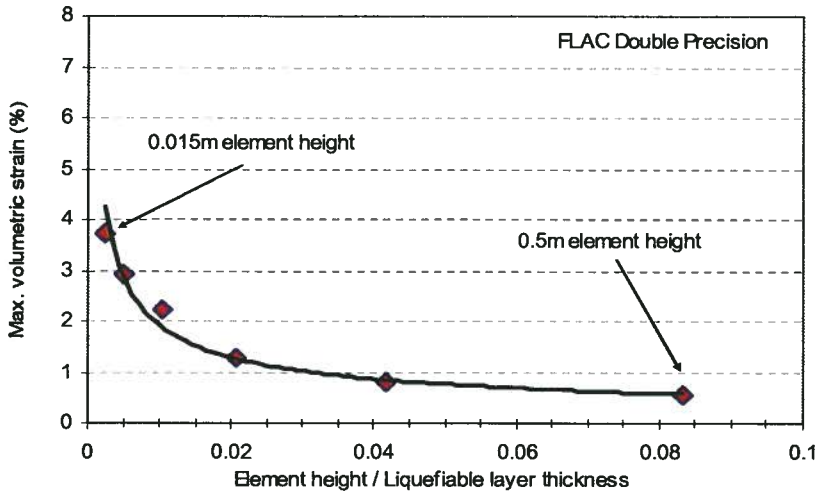

Fig. 5-8: Maximum volumetric strain of the base element vs. its normalized thickness (*double-precision*).

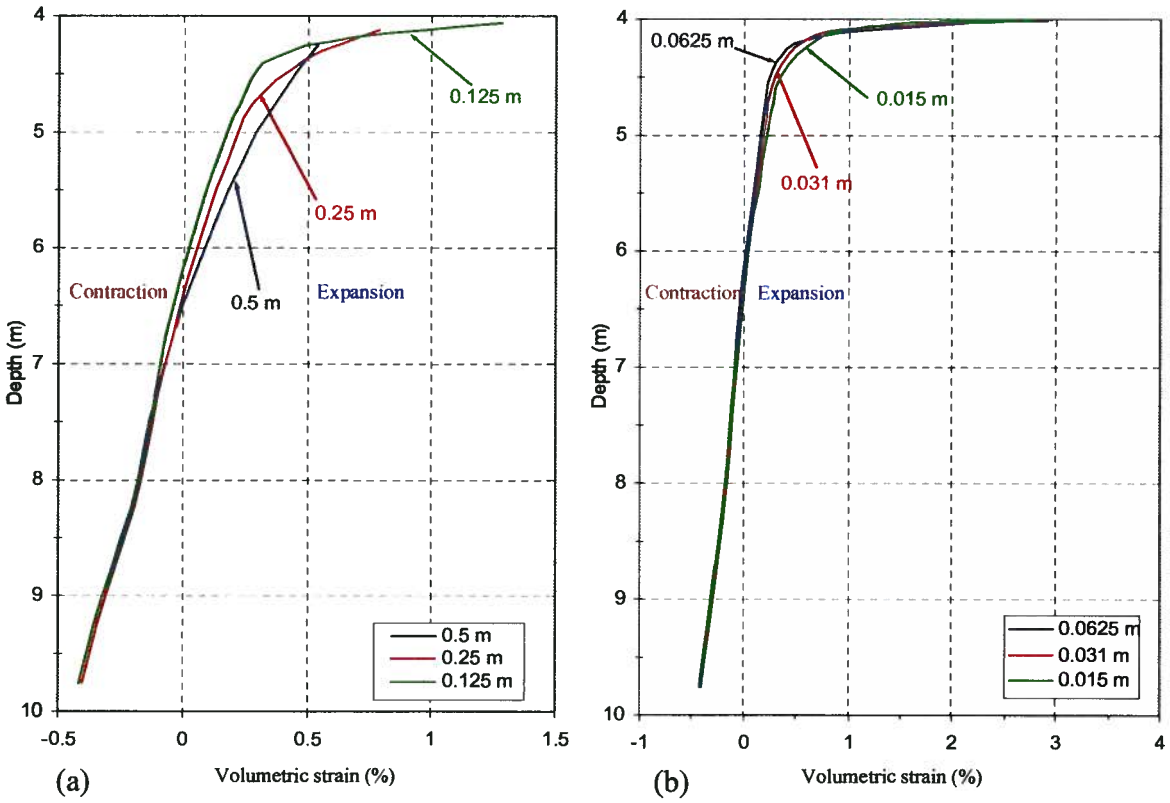

Fig. 5-9: Profile of volumetric strain for the meshes of different analyses: (a) 0.5m, 0.25m, and 0.125m base elements; (b) 0.0625m, 0.031m, and 0.015m base elements (*double-precision*).

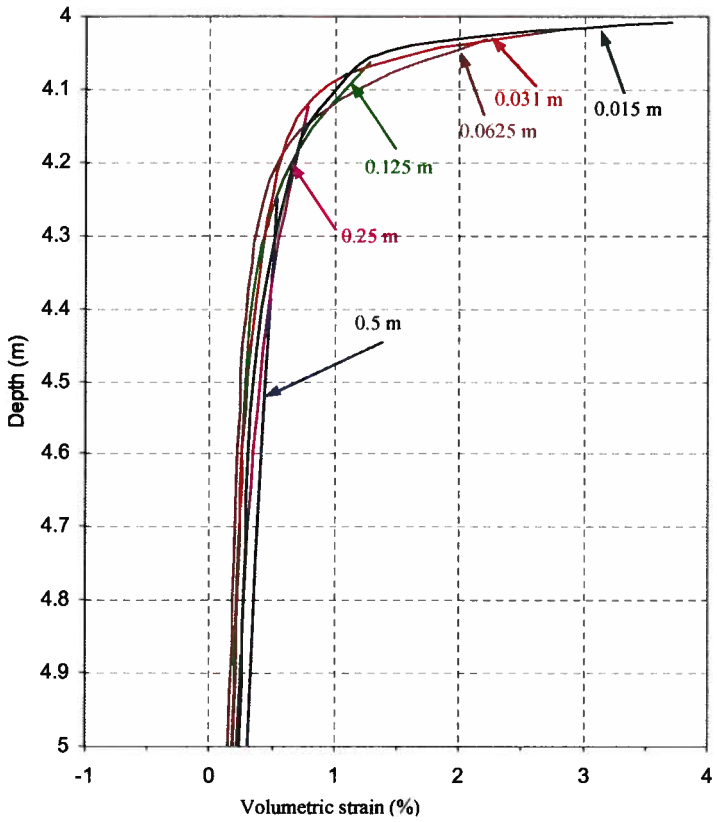

Fig. 5-10: Profile of volumetric strain for different analysis meshes close to the barrier base (*double-precision*).

Comparison of Fig. 5-5 and Fig. 5-8 (showing the maximum expansion for the base element predicted by *single* and *double-precision* analyses) suggests that the predicted expansion for a model of an *ETR* greater than about 4% is not affected by computation. *Double-precision* analysis, generally predicts less volumetric strain. This limit (*ETR* ≈ 4%). is also reflected in displacement predictions (see Fig. 5-7). This observation indicates that analysis precision not only affects the results controlled by mechanical computations (e.g., displacements) but also the flow computation results (e.g., volumetric strain essentially controlled by flow conditions).

These results suggest that void redistribution leads to a very thin water-rich zone at the base of the barrier as observed in the physical model testing discussed earlier in *Chapter III*. For example, Kulasingam (2003) and Malvick, et al. (2002 and 2005) reported the formation of localized shear zones, without evidence of water film formation, beneath silt arcs in simple slopes of sand at D_r of 20 to 50% in centrifuge tests. If enough water flows into the soil element,

it can expand until the *steady/critical-state* at zero effective stress is reached. This corresponds approximately to the maximum void ratio state. At this state, the skeleton can undergo no further expansion. Additional inflow can result in the formation of a water film at the interface and zero shear strength. The expelled water from the contractive zone must be in balance with that of the expansive zone, which depends on soil density, amplitude of cyclic shear strain induced in sand, and the number of cycles during excitation, as demonstrated by Silver and Seed (1971) and Martin, et al. (1975). This issue is discussed in more detail later in this chapter (Section 5-4).

The increasing trend of expansion of the base element (see Fig. 5-8) may lead to additional concerns, such as:

- Does the maximum expansion occur right at the barrier base?
- Does the maximum expansion approach infinity when the element thickness becomes minimal?
- To what extent is this pattern affected by the constitutive model used in the analyses?

To investigate these issues, an idealized model comprising a sand layer (instantaneously) liquefied with an impervious perfect barrier ($k = 0$) is used as the extreme case of such a response to pore water pressure redistribution. It will be shown that expansion and its rate for the base element reaches a finite value with decrease in the base element thickness and this is also the case for the slope subjected to cyclic liquefaction. The related analysis results and discussions are presented in the next section.

5.3 Characteristic Response of a Fully Liquefied Layer with Perfect Barrier

The predicted increasing trend in volumetric strain of the barrier base element shown in Fig. 5-8 suggests that volumetric strain of the base element becomes infinite as the base element size goes to zero. Thus, for a liquefiable layer with a sub-layer barrier, *flow-slide* occurs regardless of other factors, i.e., liquefied soil layer thickness, density, shaking level and duration, and ground slope. However, more detailed analyses suggests that this is not the case, as discussed below.

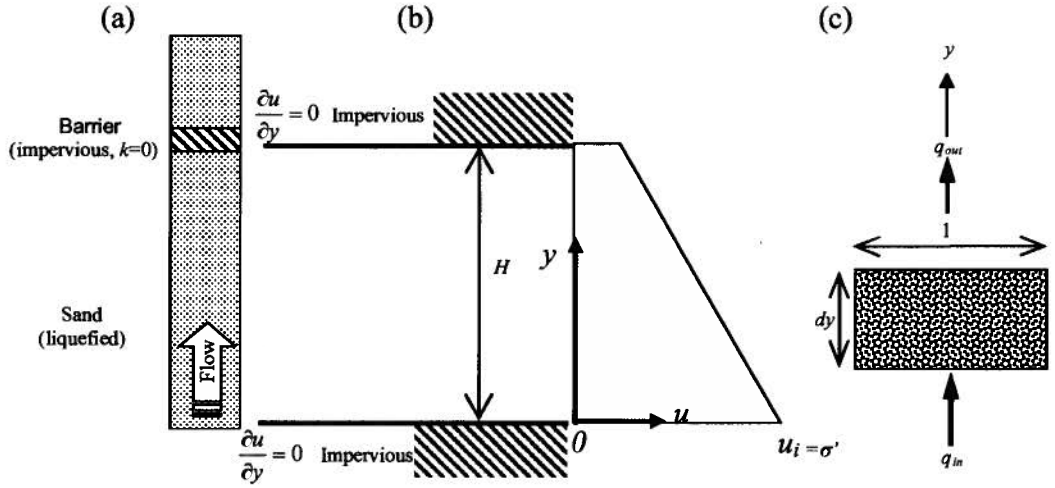

Fig. 5-11: (a) Fully liquefied sand layer with impervious barrier, (b) initial excess pore water pressure within the liquefied layer, and (c) inflow and outflow of an element.

Consider an idealized case of a fully liquefied soil layer (level-ground) comprising an impervious barrier ($k = 0$), as illustrated in Fig. 5-11a. The excess pore water pressure equals the initial effective stress at the onset of complete liquefaction and produces an excess pore water pressure that increases linearly with depth below the barrier (Fig. 5-11b). Note: this closed system case is different from the classical consolidation problem with drains at one or both boundaries (u = Const.). With reference to Fig. 5-11c and applying *Darcy's law*, the volume of stored/expelled water ($\Delta q = q_{out} - q_{in}$) per unit time for a saturated soil element becomes:

$$\Delta q = q_{out} - q_{in} = k\frac{\partial^2 h}{\partial y^2}dy \qquad [5\text{-}7]$$

where k, h, y, q_{in} and q_{out} are permeability, hydraulic head, elevation head, inflow and outflow rates, respectively. The rate of change of water volume for a saturated element equals its volume change rate, hence:

$$dq = \frac{dV_w}{dt} = \frac{d\varepsilon_v}{dt}dy \qquad [5\text{-}8]$$

where V_w, t and ε_v are pore water volume, time and volumetric strain, respectively. Hence,

$$\frac{\partial \varepsilon_v}{\partial t} = -\frac{k}{\gamma_w}\frac{\partial^2 u}{\partial y^2} = -\Delta q \qquad [5\text{-}9]$$

$d\varepsilon_v$ depends on the stress strain law used, and for the special case of an elastic skeleton:

$$\frac{\partial \varepsilon_v}{\partial t} = \frac{1}{M}\left(\frac{\partial \sigma}{\partial t} - \frac{\partial u}{\partial t}\right) \qquad [5\text{-}10]$$

where M, σ and u are constrained soil modulus, total stress and excess pore water pressure, respectively. From Eq. 5-9 and 5-10, the governing equation of one-dimensional flow for an elastic skeleton is:

$$\frac{k}{\gamma_w}\frac{d^2 u}{dy^2} = -\frac{1}{M}\left(\frac{d\sigma}{dt} - \frac{du}{dt}\right) \qquad [5\text{-}11]$$

This can be solved numerically and excess pore water pressures, volumetric strain, and flow rates examined in more detail. Computer programs such as *FLAC,* with coupled stress-flow analysis capability, can be used to solve the flow condition for elastic and elastic-plastic materials with and without tensile strength.

FLAC analyses were carried out for initial excess pore water pressure of R_u = 100% and impervious boundary conditions (k = 0 and i = 0), corresponding to Fig. 5-12. The elastic model was used for the case of materials with tensile strength. For the case without tensile strength,

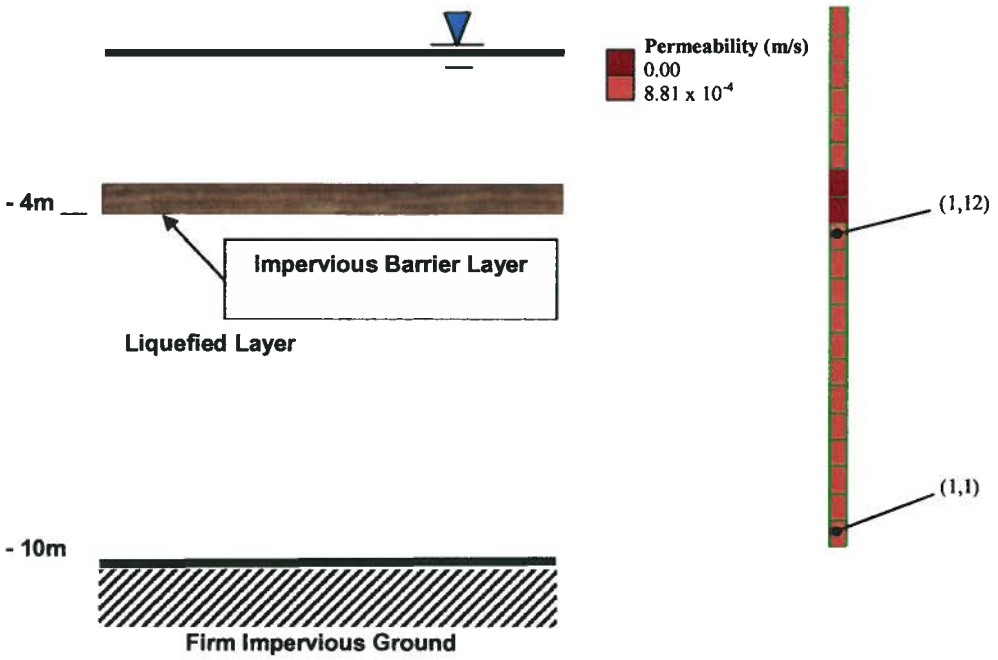

Fig. 5-12: Fully liquefied soil layer with perfect barrier and its model used in analyses (base element of 0.25m × 0.5m).

both *Mohr-Coulomb* and *UBCSAND* constitutive models were applied to the soil skeleton. Fig. 5-12 shows the soil profile, together with the single-column model used in this set of analyses. In addition, the analyses were conducted for two meshes, i.e., a coarse mesh of 0.5m × 0.25m base element size and a fine mesh of 0.0625m × 0.25m base element size (case b and d, shown in Fig. 5-3).

5.3.1 Elastic Materials with Tensile Strength

In this case, the medium was modeled as elastic with properties of ρ_d = 1500 kg/m^3, n = 0.448, B = 7.9e4 kPa, and G = 2.7e4 kPa; where, ρ_d, n, B, and G are soil dry density, porosity, bulk modulus, and shear modulus, respectively. The B and G values used correspond to a *Poisson's* ratio of 0.34.

The results in terms of profiles of excess pore water pressure, (accumulated) volumetric strain, and vertical specific discharge, *Y-Flow* (discharge per unit area), are shown in Figs. 5-13 and 5-14 for the coarse mesh. Fig. 5-14 shows that the excess pore water pressure stabilizes at an average pressure equal to the mid-depth initial effective stress if material has tensile strength. Fig.

5-14b indicates that specific discharge (*Y-Flow*) decreases from its maximum value at mid-depth of the layer, over time, with constant zero values at both boundaries, which results in a volumetric strain profile as given in Fig. 5-14a (at 1s.). Also, from Fig. 5-14b, the flow rate is seen to decrease as it approaches the barrier base. Again, the volumetric strain is seen to be contractive at mid-lower part and expansive at mid-upper part of the liquefied layer. This corresponds to the turning point of specific discharge that is at the mid-depth of the liquefied layer in this case. The small reduction in expansion seen near the impervious barrier (Fig. 14a) is attributed to water (fluid) compressibility as the excess pore water pressure difference with initial effective stress becomes larger (see Fig. 5-13). When the analysis was carried out with reduced fluid compressibility (by about 5 times), this reduction was not observed. Fig. 5-15a shows a similar profile of volumetric strain for the fine mesh with the same pattern but with larger volumetric strain at the barrier base vicinity. The time histories of the specific discharge for the base element (as a measure of its total volume change) are compared in Fig. 5-15b, for the two cases. As expected, the base element in *case II* (fine mesh) exhibits lower (in)-flow over time since it is closer to the impervious boundary (as discussed above). This suggests that in both cases the volume change of the base element is finite, and the volumetric strain is increasing with element thickness reduction. The following conclusions can be made from these results:

- Excess pore water pressure redistribution in material with tensile strength leads to a residual pore water pressure beneath the barrier that is greater than the initial effective stress (R_u>1). This is not a real case in sands
- Maximum specific discharge occurs at mid-depth corresponding to zero volumetric strain.
- Flow gradient decreases over time (with ultimate zero value when hydraulic gradient becomes zero) and, as a result, volumetric strain tends to descend with time and reach zero ultimately.
- Flow computations also depend on mesh-size, as the specific discharge (*Y-Flow*) is nonlinear (Fig. 5-14b).

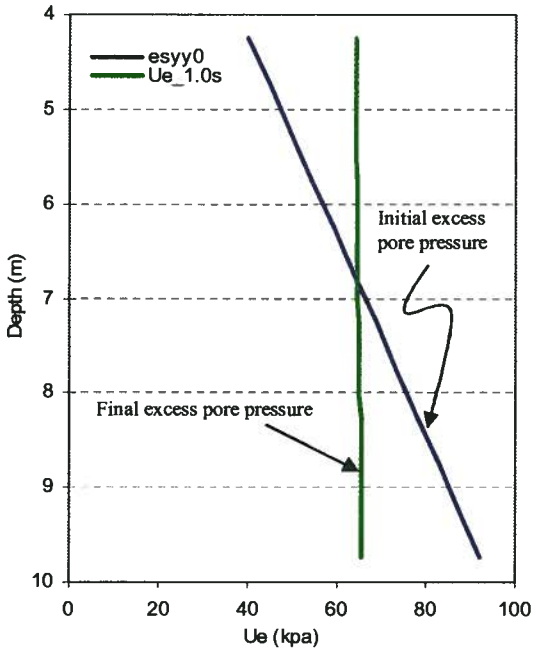

Fig. 5-13: Profile of excess pore water pressure after stabilization time (1.0 s).

5.3.2 Materials without Tensile Strength

The problem was also analyzed using the *Mohr-Coulomb* and *UBCSAND* models. For the *Mohr-Coulomb* model, the material properties were: dry density, ρ_d = 1500 kg/m^3, porosity, n = 0.448, and friction angle, $\varphi = 30°$; with stress-dependent stiffness: $B = G_{max}$, which is calculated by:

$$G_{\max} = 21.7 \times 20 P_a \left(\frac{P_m'}{P_a} \right)^{0.5} \times [(N_1)_{60}]^{0.333} \qquad [5\text{-}12]$$

where $(N_1)_{60}$ was assumed to be 6.2, representing (air-pluviated) Fraser River sand with D_r = 40%. Fig. 5-16 shows the excess pore water pressure isochrones for initial and final conditions along with those at various time intervals for the *Mohr-Coulomb* model (for coarse mesh). From the Figure, excess pore water pressure within the sand layer stabilizes at a value corresponding to *Ru* = 1 for the barrier base element as a result of zero-tensile strength material (compare this to Fig. 5-13). Fig. 5-17 and Fig. 5-18 show analyses results in terms of the isochrones of volumetric strain, ε_v and vertical specific discharge, and *YFlow* at different time intervals using coarse and

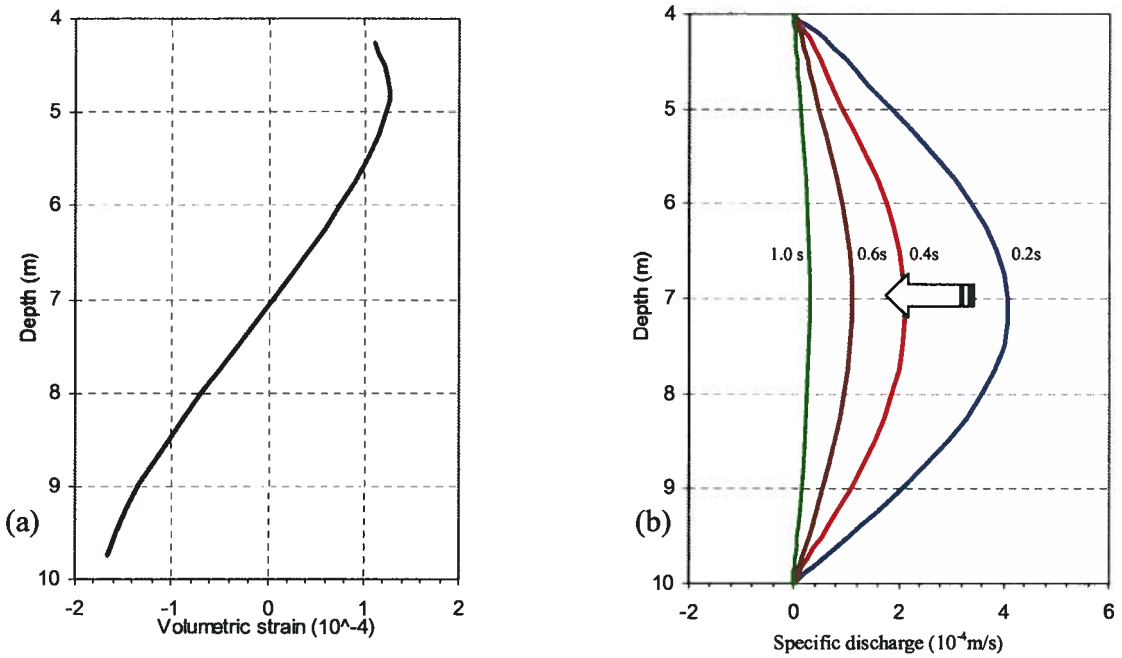

Fig. 5-14: Profile of (a) ε_v at 1 s, (b) vertical specific discharge at different time intervals (level-ground, instantaneously liquefied, elastic model).

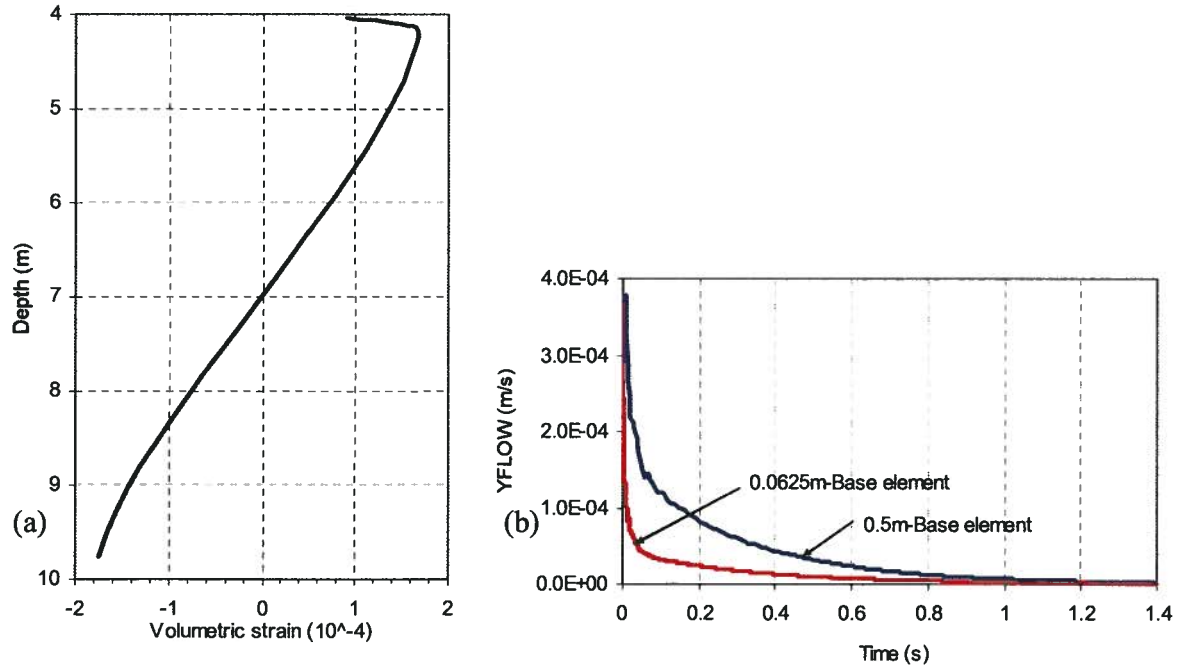

Fig. 5-15: (a) Profile of ε_v for mesh with base element height of 0.0625m (at 1s), (b) Specific discharge time histories for the base element of 0.5m and 0.0625m thickness (level-ground, instantaneously liquefied, elastic model).

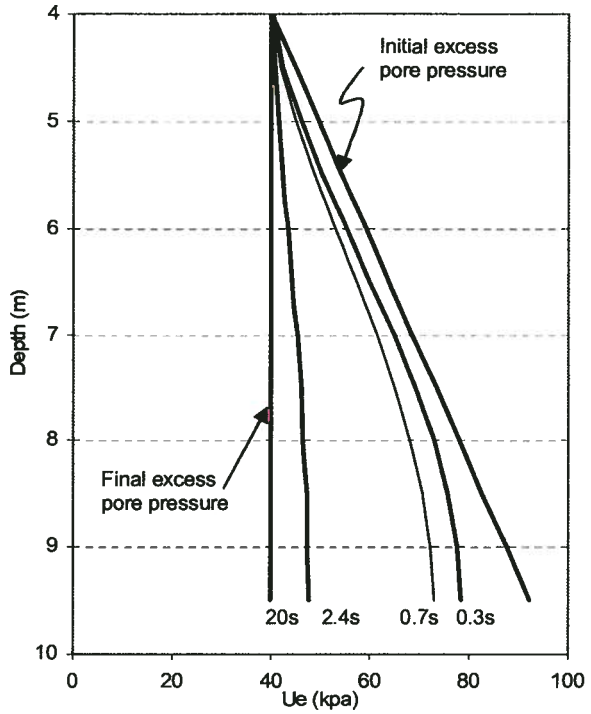

Fig. 5-16: Excess pore water pressure isochrones at various time intervals and after stabilization time (20s) for the *Mohr-Coulomb* model.

fine mesh, respectively. A similar descending trend for *YFlow* with time is observed. Fig. 5-19 shows the time histories of vertical specific discharge, (accumulated) volumetric strain and excess pore water pressure for various elements at different depths of the coarse mesh model (see Fig. 5-12 for elements' positions). The volumetric strain remains constant when the vertical specific discharge does not change. This is also clear from the excess pore water pressure time history where water flows upward within the soil layer from deeper parts over time and eventually the pore water pressure stabilizes at a pressure equal to the initial excess pore water pressure, U_e at the base of the barrier with constant U_e that corresponds with R_u =1 and zero effective stress. This is in accord with observations reported from centrifuge model tests (e.g. Dobry & Liu, see Fig. 3-8). Fig. 5-20 schematically shows the excess pore water pressure isochrones for materials with and without tensile strength, which is conceptually comparable to Fig. 5-13 and Fig. 5-16, respectively.

Fig. 5-21 and Fig. 5-22 show the isochrones of volumetric strain, ε_v and vertical specific discharge, *Y-Flow* for the *UBCSAND* model for coarse and fine mesh, respectively. As in the previous case (elastic model), volumetric strain at the lower parts is contractive while it is

expansive at the upper parts close to the barrier. Fig. 5-23 shows the enlarged isochrones for the fine mesh indicating more clearly that water accumulates (inflows) at the barrier base vicinity, while the discharge rate decreases over time. Similar results were obtained to those of the *Mohr-Coulomb* model in terms of time history for *Y-Flow*, ε_v, and U_e in this case. Fig. 5-24 shows the time history of ε_v for models of three different base element thicknesses. Initially, a smaller base element expands with greater rate (slope of expansion curve). Nevertheless, all the expansion curves level off (become horizontal with zero slope) when upward flow wanes. This can also be inferred from Fig. 5-25a, showing volumetric strain rate ($\Delta\varepsilon_v / \Delta t$) time histories for the elements at the bottom and the top (barrier base) of the liquefied layer. Thus, the onset of expansion cessation (with zero rate) for the base element at the top coincides with the time when the contraction of the bottom element (at the base of layer) stops. Fig. 5-25b shows that (total) in-flow into the base element decreases with element thickness reduction, as observed before for the elastic model case (Fig. 5-15b). The maximum rate of ε_v vs. base element thickness ratio, *ETR* (normalized by the liquefied soil layer thickness, i.e. 6m) is shown in Fig. 5-26 in natural and logarithmic scales. No indication of infinite strain rate is seen for this extreme case.

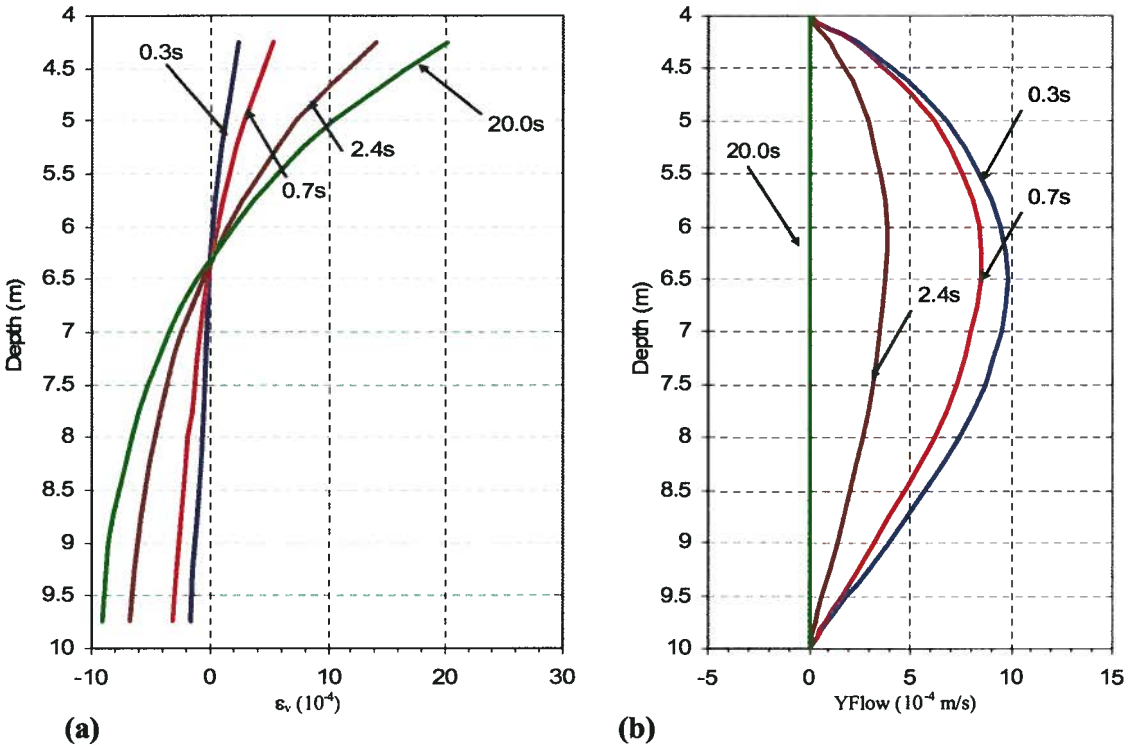

Fig. 5-17: Isochrones at different time intervals for the *Mohr-Coulomb* model with 0.5m base element thickness: (a) volumetric strain, (b) vertical specific discharge (level-ground, instantaneously liquefied).

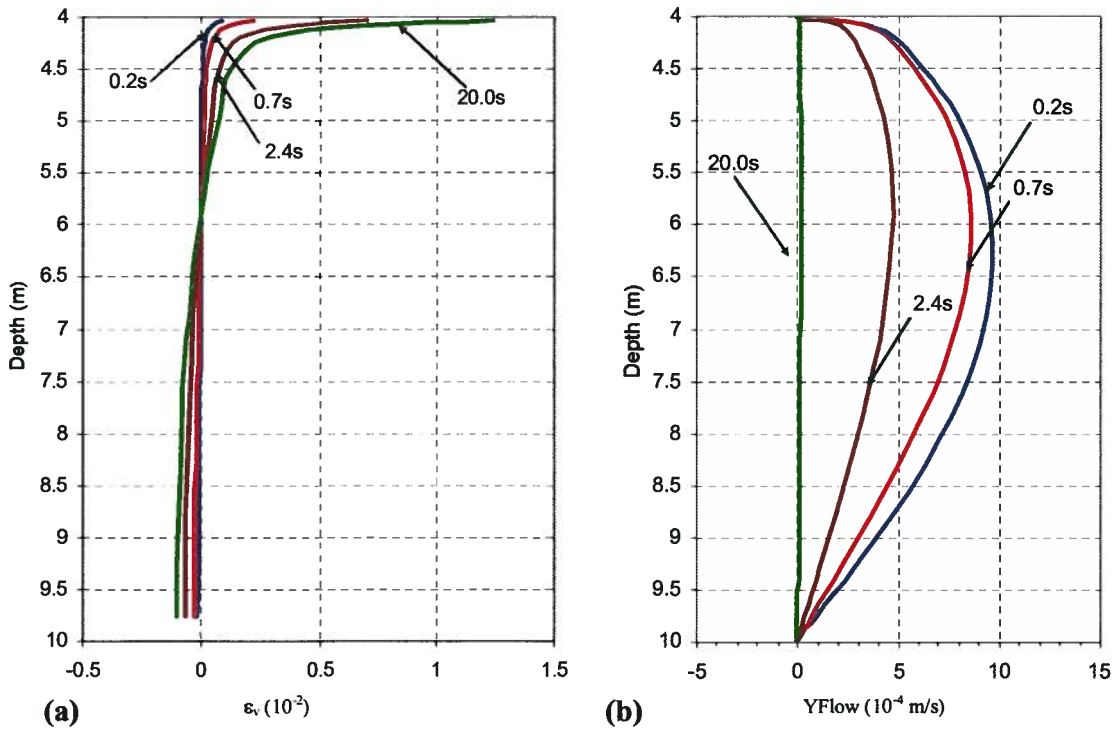

Fig. 5-18: Isochrones at different time intervals for the *Mohr-Coulomb* model with 0.0625m element thickness: (a) volumetric strain, (b) vertical specific discharge (level-ground, instantaneously liquefied).

.

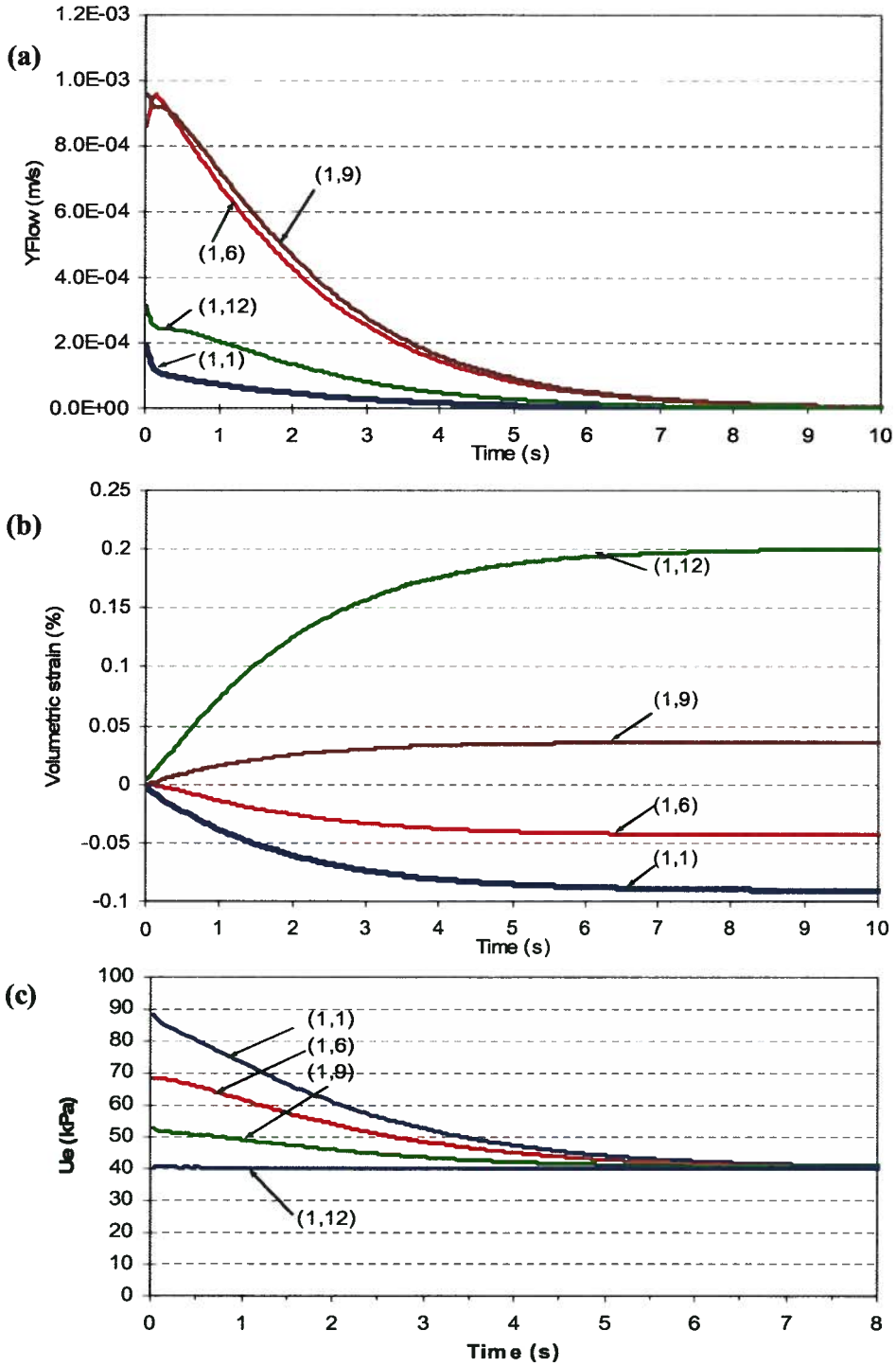

Fig. 5-19: Time history of (a) vertical specific discharge, (b) volumetric strain, and (c) excess pore water pressure ((level-ground, instantaneously liquefied, *Mohr-Coulomb* model).

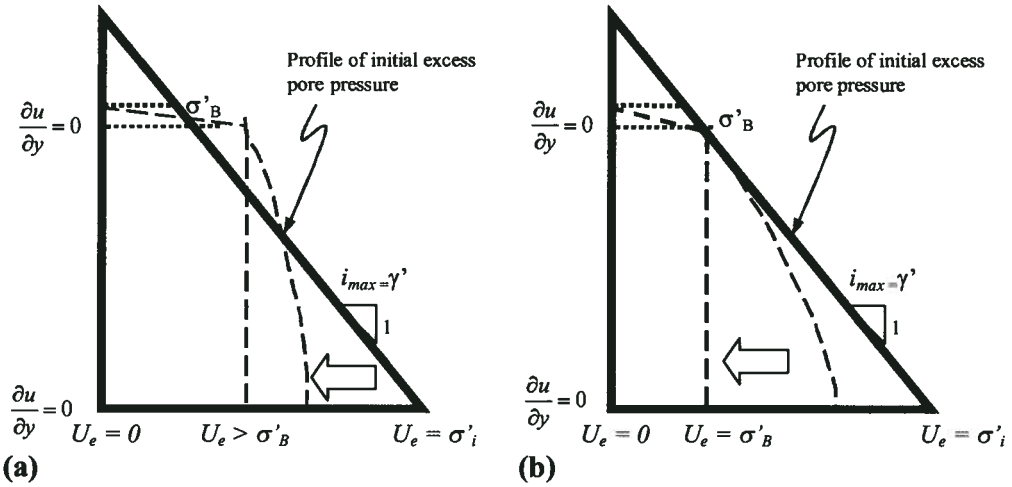

Fig. 5-20: Conceptual pattern for excess pore pressure isochrones at different time intervals: (a) materials with tensile strength, and (b) materials without tensile strength.

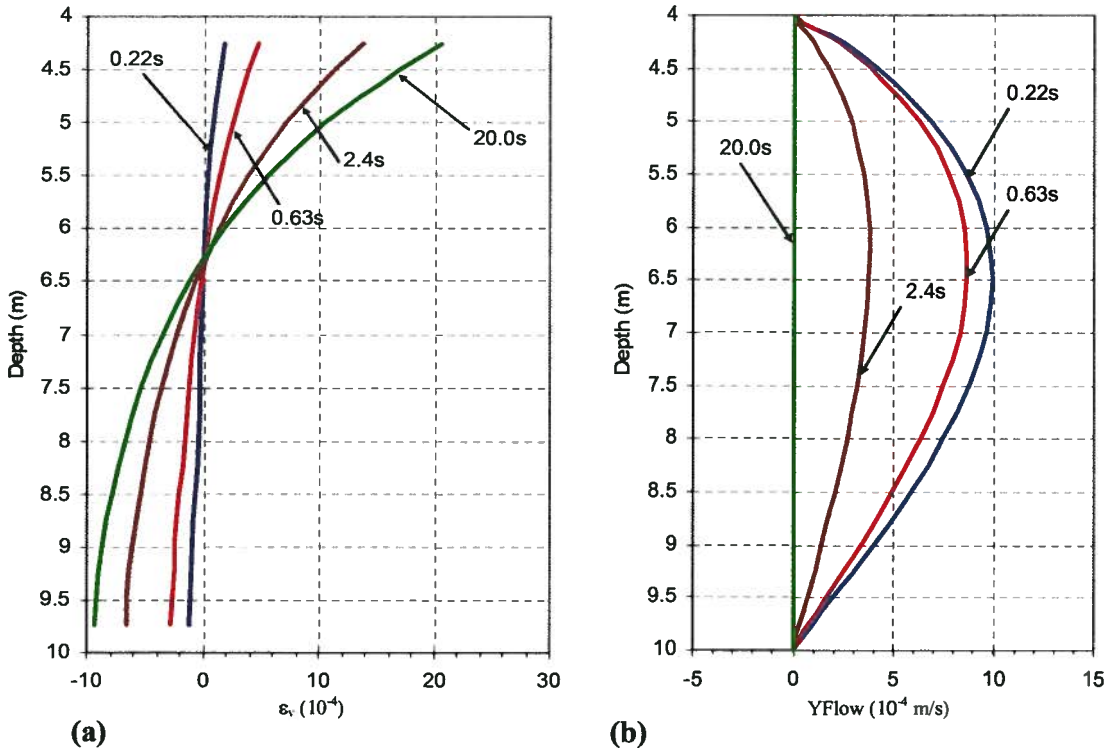

Fig. 5-21: Isochrones at different time intervals for *UBCSAND* model with 0.5m element thickness: (a) volumetric strain, (b) vertical specific discharge (level-ground, instantaneously liquefied).

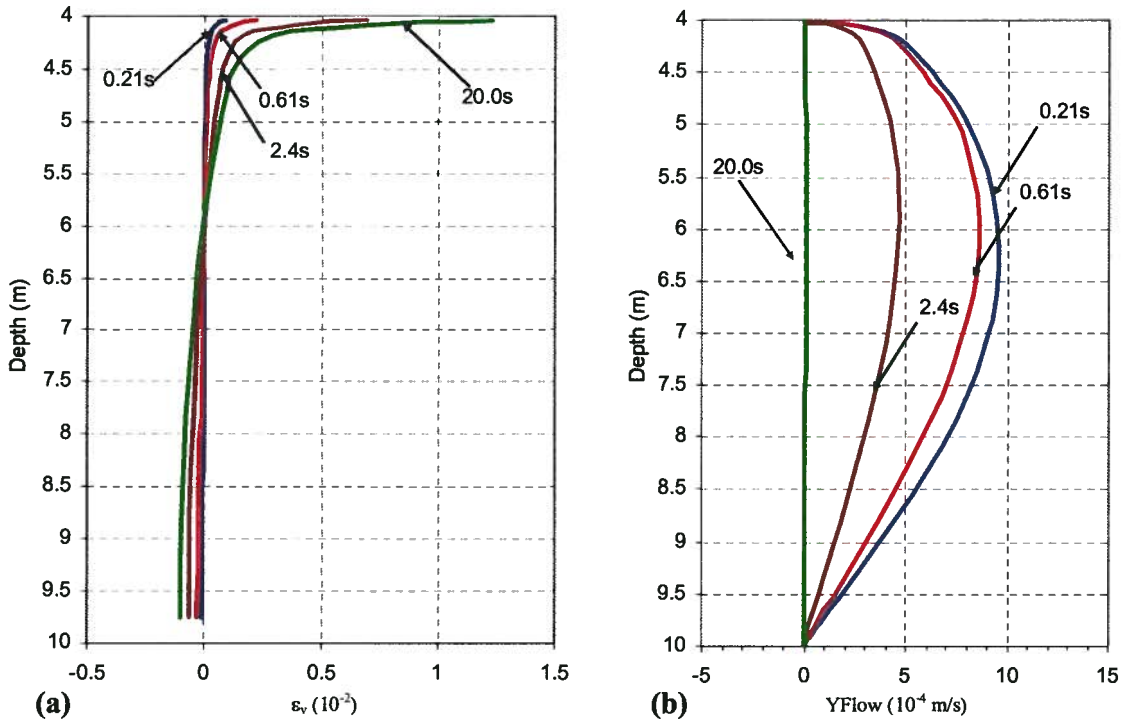

Fig. 5-22: Isochrones at different time intervals for the *UBCSAND* model with 0.0625m element thickness: (a) volumetric strain, (b) vertical specific discharge (level-ground, instantaneously liquefied).

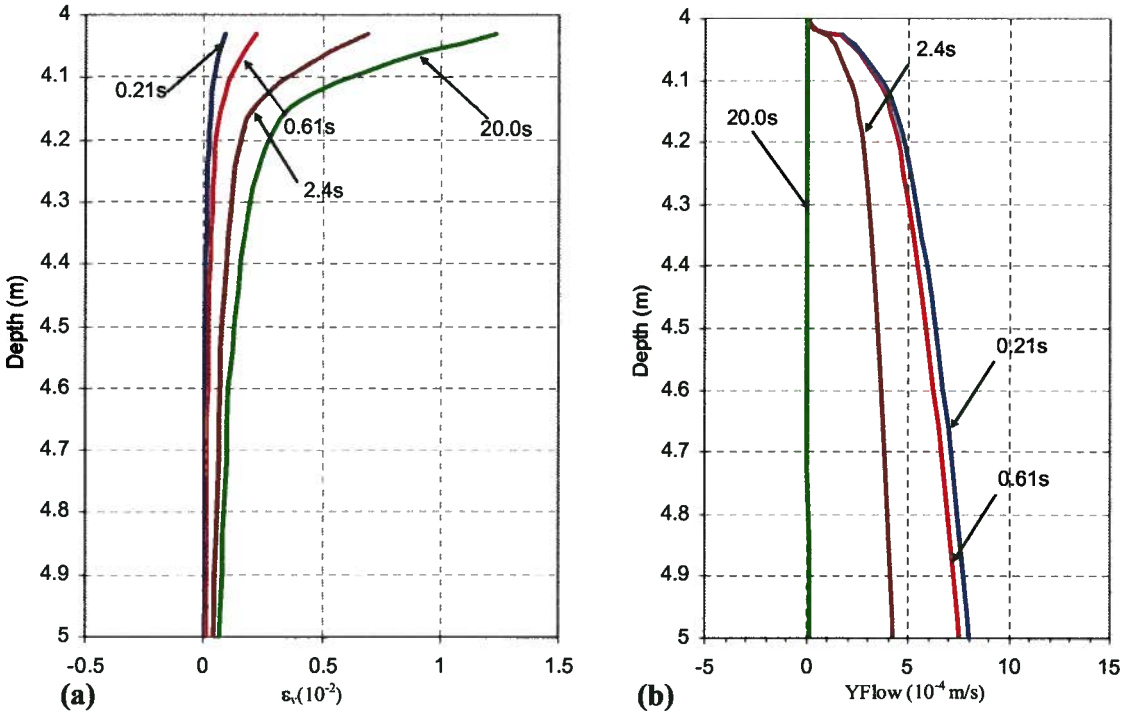

Fig. 5-23: Enlarged isochrones at different time intervals for the *UBCSAND* model with 0.0625m element thickness: (a) volumetric strain, (b) vertical specific discharge (level-ground, instantaneously liquefied).

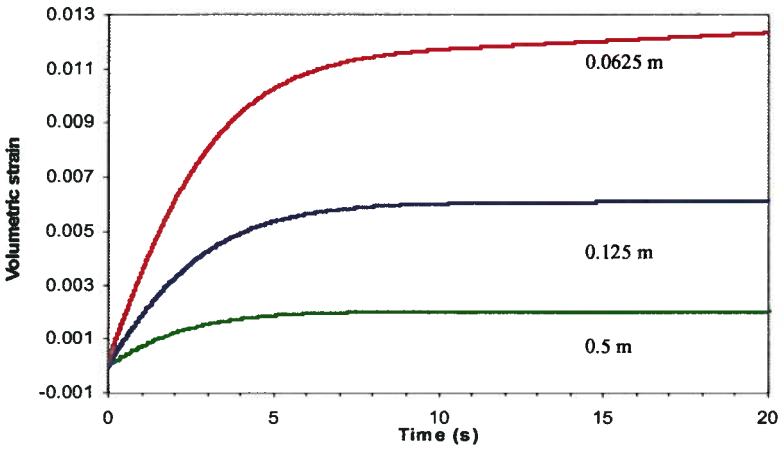

Fig. 5-24: Volumetric strain time history for the barrier base element having various thicknesses for level-ground condition with impervious barrier (level-ground, instantaneously liquefied, *UBCSAND* model).

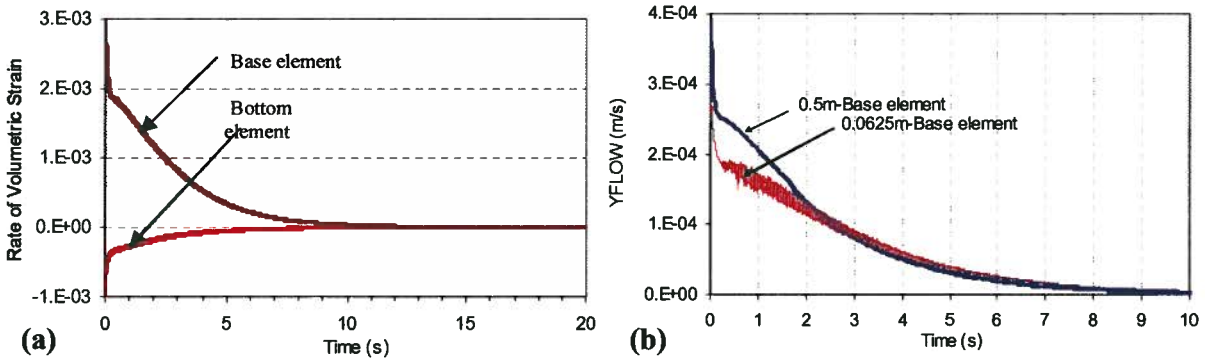

Fig. 5-25: Time histories of (a) volumetric strain rate for bottom and base elements showing zero value at stabilized time (no-hydraulic gradient) for the *UBCSAND* model of level-ground with 0.125m base element thickness: (b) specific discharge for the base element of 0.5m and 0.0625m thicknesses (level-ground, instantaneously liquefied, *UBCSAND* model).

The same approach has been applied to the 1°-inclined soil profile (subjected to cyclic loading) that results presented before (see Fig. 5-9). Fig. 5-27 shows time histories of ε_v for the base element with various normalized thicknesses, *ETR*, for the sloping ground using the *UBCSAND* model. It also shows that the expansion rate (slope of expansion curve) increases with decreases in element thickness, but eventually tends to be essentially zero. Fig. 5-28 shows the maximum expansion rate of the base element vs. its normalized thickness, *ETR*, in natural scale and semi-log scale based on five analyzed cases. Clearly, no indication is seen of an infinite value for the expansion rate. These results show that, though the expansion increases with reduced element thickness, its maximum value is finite.

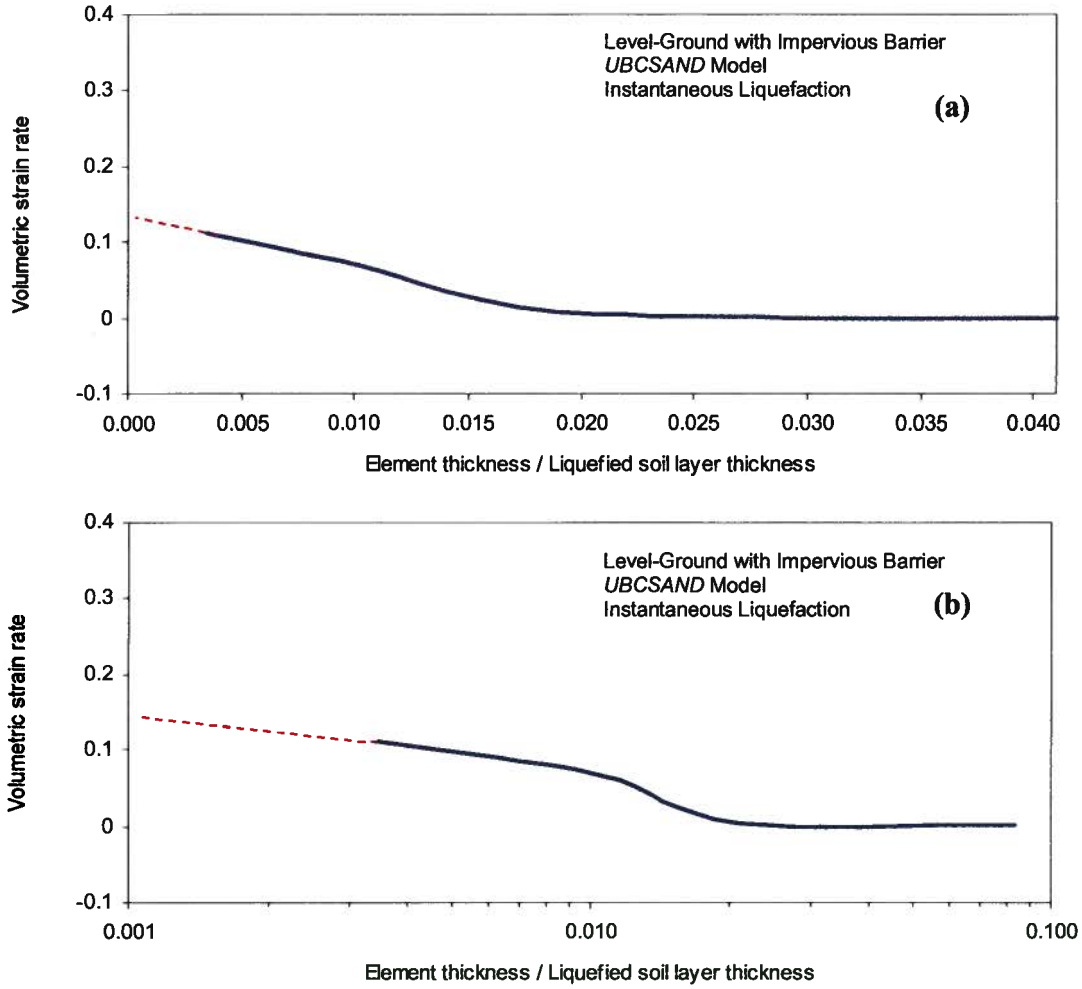

Fig. 5-26: Max. volumetric strain rate vs. base element thickness: (a) in natural scale, and (b) in logarithmic scale (*UBCSAND* model with impervious barrier).

As shown before, this pattern of volume change in the liquefied layer (level-ground) is predicted by the three constitutive models and is controlled by flow conditions (i.e., permeability contrast). Water flows upward from the lower parts that have the highest initial excess pore water pressures, towards the upper impervious boundary where the initial excess pore water pressure is the least. Maximum flow occurs at some point near the mid-depth of the soil layer. This is also the case for the slope subjected to cyclic loading.

This finding suggests that, though the expansion at the barrier base increases with reduced element thickness, its maximum value is finite.

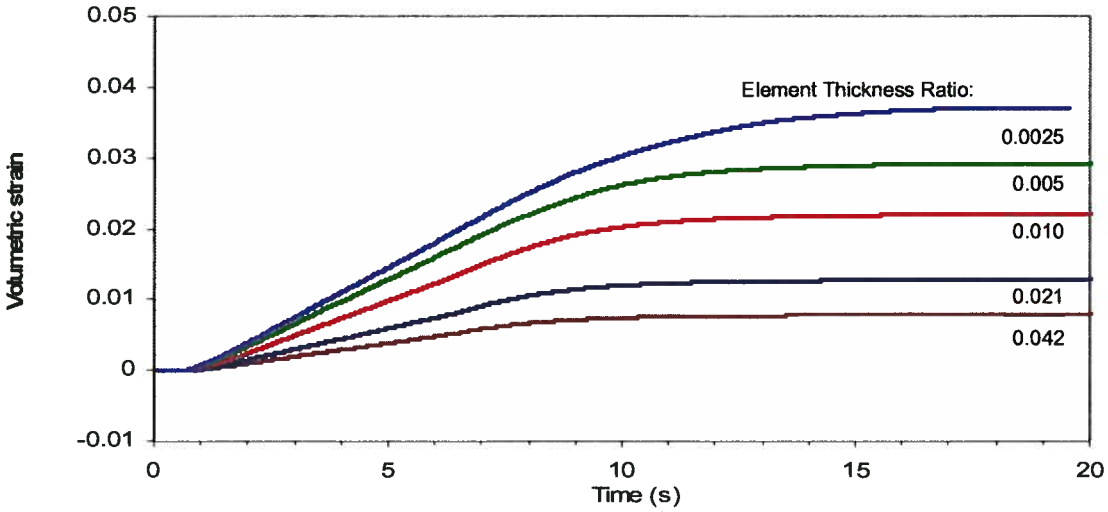

Fig. 5-27: Time histories of volumetric strain for the base element with various normalized thicknesses (*UBCSAND* model).

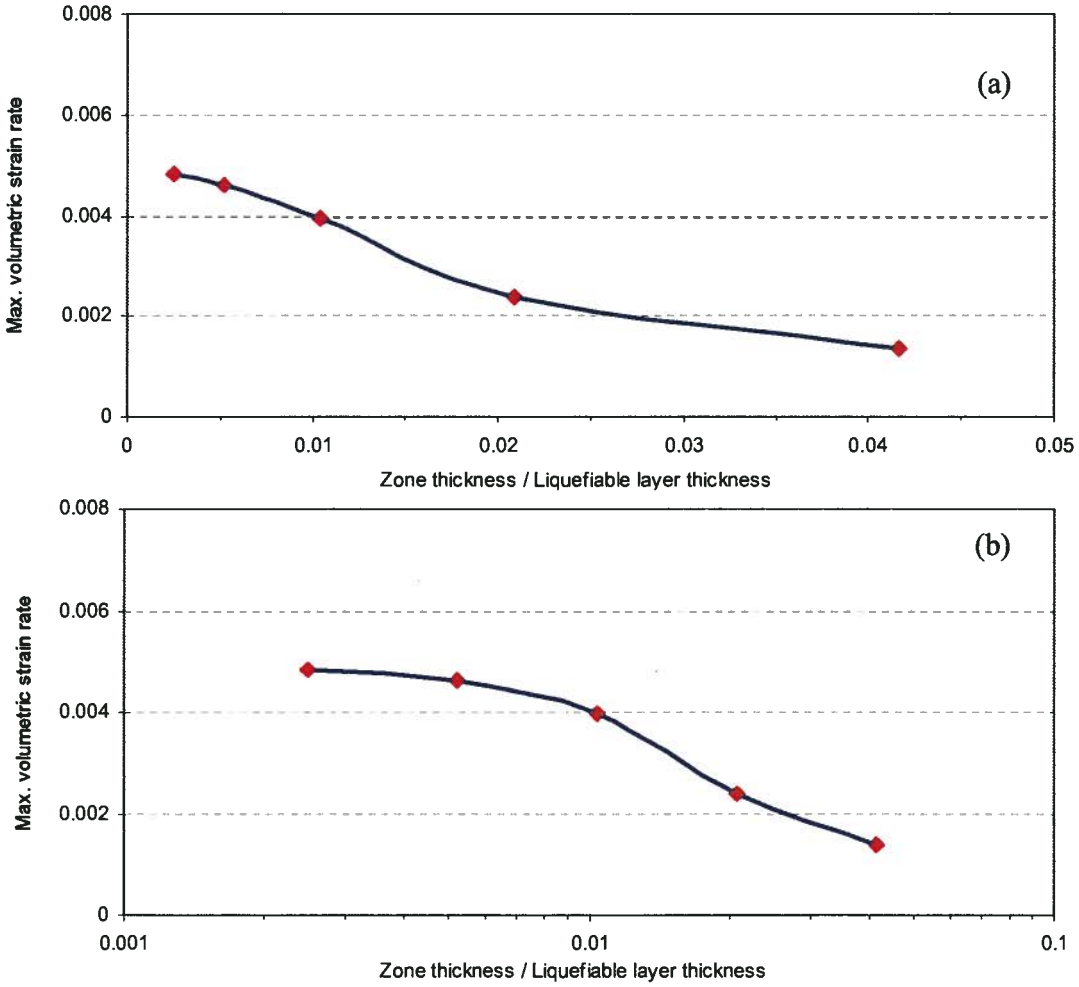

Fig. 5-28: Max. expansion rate vs. normalized base element thickness, (a) natural scale, (b) semi-log scale (*UBCSAND* model).

It also reveals that predicted volume change (contraction at the lower part and expansion at the upper part) is mainly controlled by the flow conditions and is essentially independent of the skeleton constitutive model used. This also confirms that the flow patterns are essentially the same for the three constitutive models.

As mentioned earlier, the pattern of volumetric strain profile is controlled by the flow condition, i.e., permeability contrast between the barrier and the soil layer. In the next section, the effect of permeability contrast on the observed response of level-ground with perfect barrier is discussed.

5.3.3 Effect of Permeability Contrast ($k_{Barrier} / k_{Sand}$) on Level-Ground Response

The effect of permeability contrast was investigated through increasing barrier permeability ratios, reaching that of the liquefiable soil layer, going from 10^{-3} to 10^{-1} times for the (liquefied) level-ground condition with perfect barrier (shown in Fig. 5-12). Fig. 5-29 shows the isochrones of volumetric strain, ε_v, at different time intervals for the *Mohr-Coulomb* model of coarse mesh for these cases. The volumetric strain profile for permeability contrast of 1000 (Fig. 5-29a) is essentially the same as that of the impervious case. Nevertheless, this pattern tends to complete consolidation contraction due to excess pore water pressure dissipation in the long-term (e.g., 20s) when the permeability contrast ($k_{Barrier} / k_{Sand}$) decreases by 10^{-1} (see Fig. 5-29b). This is also inferred from the flow isochrones shown in Fig. 5-30 that indicate an essentially constant upward hydraulic gradient in the long-term (e.g., 20s).

In the following section, the second question regarding the *flow-slide* conditions and maximum possible expansion that may take place in a sloping ground is discussed.

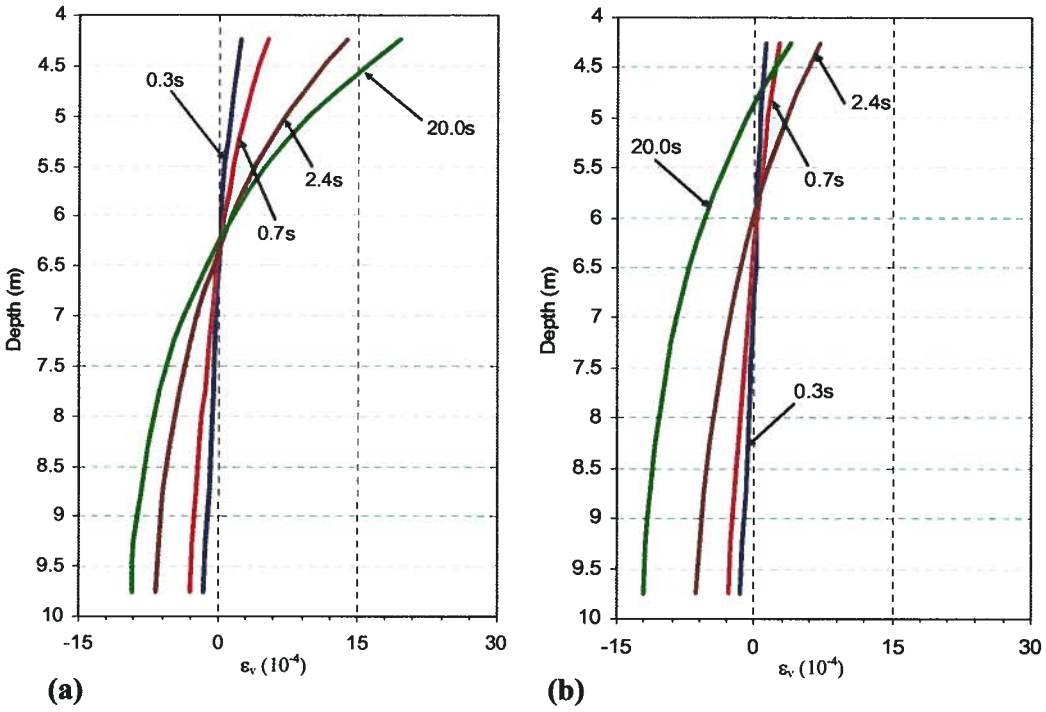

Fig. 5-29: Isochrones of volumetric strain at different time intervals for the *Mohr-Coulomb* model with 0.5m element thickness for (a) $k_{Barrier} = 10^{-3} \times k_{Sand}$, (b) $k_{Barrier} = 10^{-1} \times k_{Sand}$

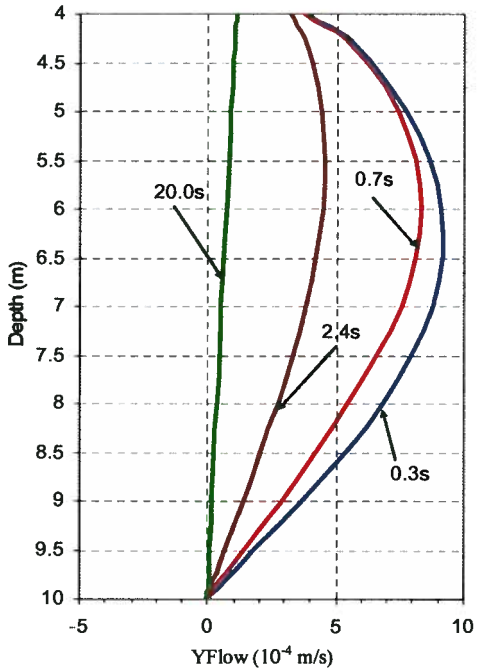

Fig. 5-30: Isochrones of vertical specific discharge at different time intervals for the *Mohr-Coulomb* model with 0.5m element thickness for $k_{Barrier} = 10^{-1} \times k_{Sand}$ condition (level-ground with impervious barrier, instantaneously liquefied).

5.4 Maximum Soil Expansion and Flow Failure Conditions

It has been demonstrated that the presence of a low permeability sub-layer in liquefied sloping ground results in large displacements with localization beneath the barrier due to excess pore water pressure redistribution. In this section, the typical behavior of an idealized infinite slope, comprised of a barrier sub-layer (water level at surface) (illustrated in Fig. 5-31) is first discussed in more detail, and then the conditions for a *flow-slide* are explored. In the Figure, point B and T represent typical points in the upper and lower parts of the liquefied soil layer, respectively.

Earthquake shaking generates excess pore water pressure (u_e) within the sand layer that results in an upward hydraulic gradient, i ($i = \Delta h / l$, $h = u_e / \gamma_w$ where h, l and γ_w are hydraulic head, flow path length, and water unit weight, respectively), as depicted by the u_e isochrones in Fig. 5-20. If the overlying low-permeability layer precludes any significant pore water drainage in the time of interest, then the volume of water expelled from the contracting (densifying) lower portion of the liquefied sand layer will all accumulate at the upper parts of the sand layer. Regarding Fig. 5-31, points B and T experience two different behaviors due to liquefaction and void redistribution. Point B has a larger flow exiting it (outflow) than entering it (inflow), and thus, the soil contracts (densifies). Point T expands (loosens) as a result of a net inflow of water due to the low permeability confining layer restricting outflow at that location. The overlying layer can restrict the sand layer to be globally undrained during the time of interest if it is thick enough and of sufficiently low permeability. Fig. 5-32 illustrates typical void ratio, e change vs. effective mean stress, σ', for points B and T with initial identical void ratio. The figure also denotes the effective stress reduction associated with earthquake shaking, where the soil layer at the upper parts (e.g., point T) becomes looser (e increases) driven by excess pore water pressure redistribution, while at the deeper parts it undergoes compression (e decreases) (e.g., at point B). The soil expansion may continue until it reaches the *steady-state* line, if enough net inflow is available and large displacements and/or *flow-slides* are caused due to static shear stress. If no shear stress bias exists (level-ground condition), the soil can expand beyond the *steady-state* void ratio, e_{ss}, even until reaching e_{max} (at zero effective stress), and further inflow leads to water film formation, as observed in physical model tests (Kokusho, 1999). For a given sand, the *steady-state* void ratio, e_{ss}, depends on stress at failure that varies with the ground slope.

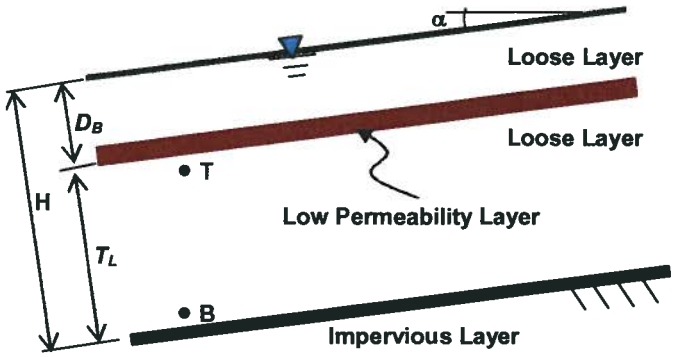

Fig. 5- 31: Idealized infinite slope with low permeability sub-layer.

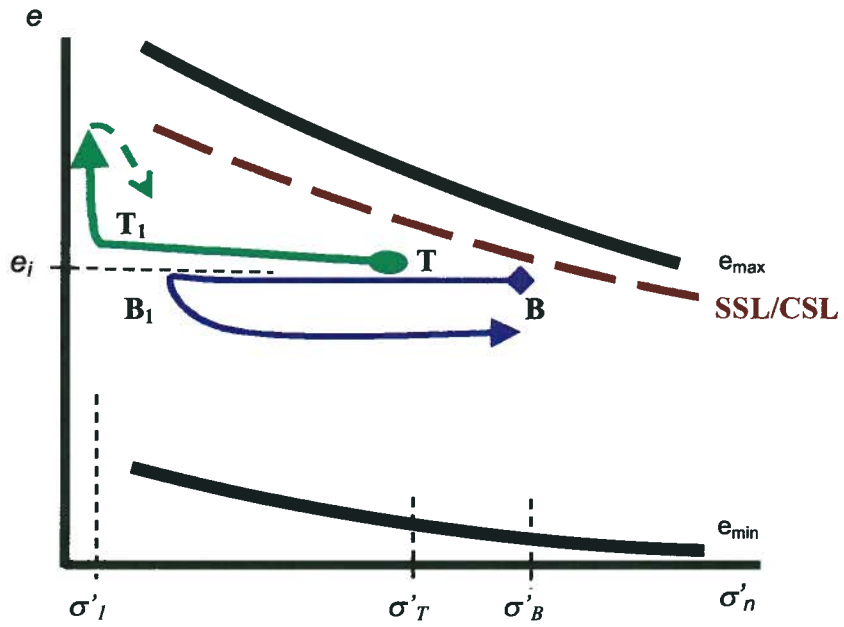

Fig. 5-32: Conceptual diagram of void ratio change due to excess pore water pressure redistribution in a liquefied layer beneath hydraulic barrier.

Figs. 5-33 and 5-34 show typical analysis results in terms of volumetric strain, $\varepsilon_v = \Delta e/(1+e_o)$ vs. effective vertical stress and corresponding stress paths predicted for a point close to the barrier base and bottom of the liquefied soil layer, respectively, for the model shown in Fig. 5-3a (with 0.25m × 0.25m base element). The same pattern as that of Fig. 5-32 is seen, and is as predicted from the analyses.

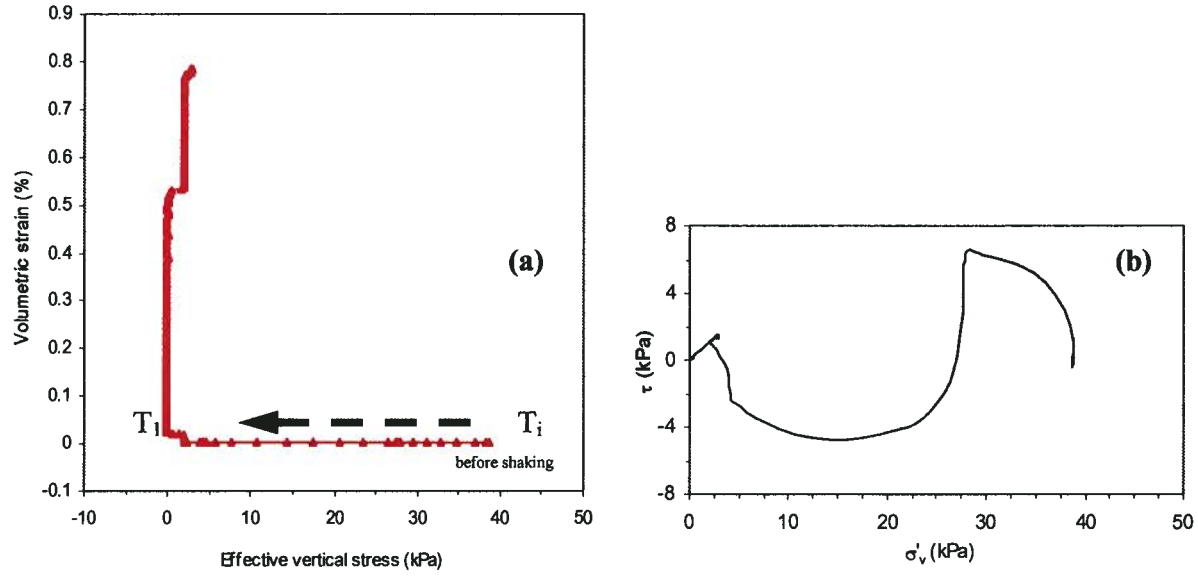

Fig. 5-33: Typical predicted response of sand at upper part of the liquefied layer in terms of: (a) volume change with vertical effective stress, and (b) effective stress path.

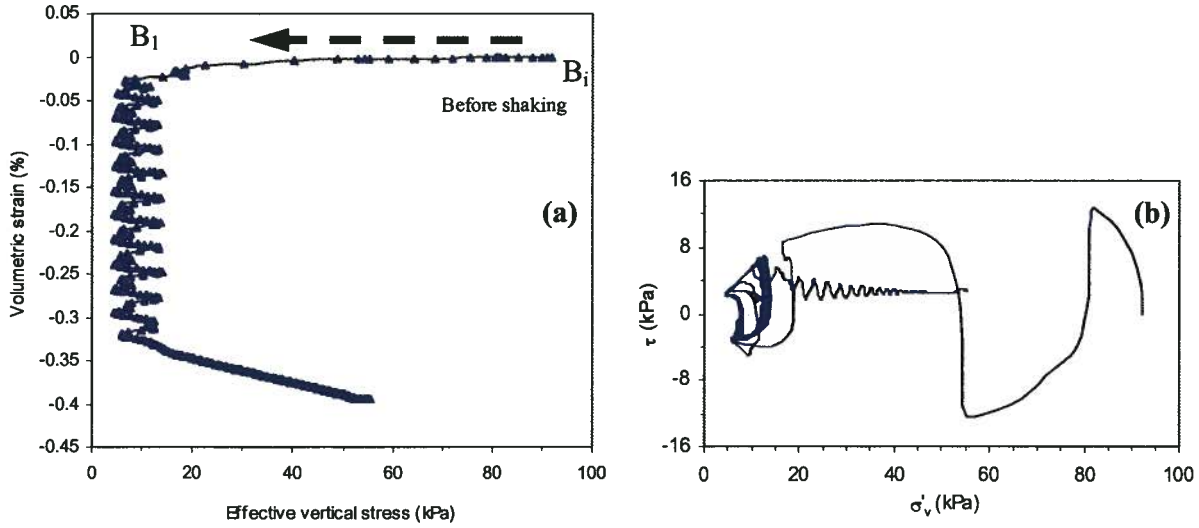

Fig. 5-34: Typical predicted response of sand at lower part of the liquefied layer in terms of: (a) volume change with vertical effective stress, and (b) effective stress path.

In general, the volume of expelled water depends on the liquefied soil (relative) density, applied amplitude of cyclic shear strain, and number of cycles during excitation, as demonstrated by several researchers using element testing (e.g., Silver & Seed, 1971; Youd, 1972; and Martin, et al., 1975). Recently, Tsukamoto, et al. (2004) and Sawada, et al. (2006) used cyclic element tests on saturated and partially saturated samples and concluded that for fully or partially saturated soil, the key factor determining volume change was maximum shear strain. This measure is a prominent index representing the level of disturbance to the soil structure, and the total induced settlement (including during shaking and post-shaking) is independent of saturation. A number of investigators suggested correlations for post-shaking settlement of level-grounds to soil relative density and liquefaction resistance (e.g., Tokimatsu & Seed, 1987; Nagase & Ishihara, 1988; Ishihara & Yoshimine, 1992; Wu, 2002; Stewart, et al., 2004; and Sawada, et al., 2006). As an example, Stewart, et al. (2004) and Duku, et al. (2008) proposed a model to predict volumetric strain following liquefaction for sand fills with various fine contents and plasticity. Based on data from laboratory element tests, centrifuge testing, and field experiences of past earthquakes, Dobry (1992) suggested a range for post-liquefaction volumetric strain of $\varepsilon_v \approx 1.5$ to 5% and 0.2% or less for loose sands and very dense sands, respectively. The post-liquefaction settlement in the sloping-ground condition is lower than that for the level-ground condition due to dilation effects (and as a result, less residual excess pore water pressure), which is more pronounced in the presence of shear stress bias. This is in conformity with the observations from centrifuge model tests (e.g., Taboada & Dobry, 1998) and laboratory element testing data (e.g., Dismuke, 2003).

In a liquefied layer with a hydraulic barrier, the volume of the expelled water from the contracting parts must be in balance with the volume of water absorbed (stored) by the expanding parts (negligible water seeps through the barrier if a non-perfect barrier is present). From the previous discussion, the expansion at the barrier base together with localized deformation of the liquefied layer does not necessarily result in a *flow-slide* as was the case in physical model tests reported by Malvick, et al. (2003; 2005). They noted that for a given 2-D configuration, occurrence of localization, in turn, is controlled by induced excess pore water pressure (ratio) and its duration. Therefore, the soil capacity to store water (to expand) before reaching the *steady-state* and probable large displacements and/or *flow-slide* are key factors that control liquefaction-induced ground failures. This concept is illustrated in Fig. 5-35 in terms of the *e-p* diagram. It shows a typical path for point T of the liquefied soil layer at the barrier base, to the steady–state,

as a result of shaking (T_0 to T_1) and pore water pressure redistribution (T_1 to T_2). As seen from the figure, the state parameter, ψ, corresponding to essentially zero effective stress, ψ_1, (at point T_1) controls the soil expansion potential and its capacity for water storing.

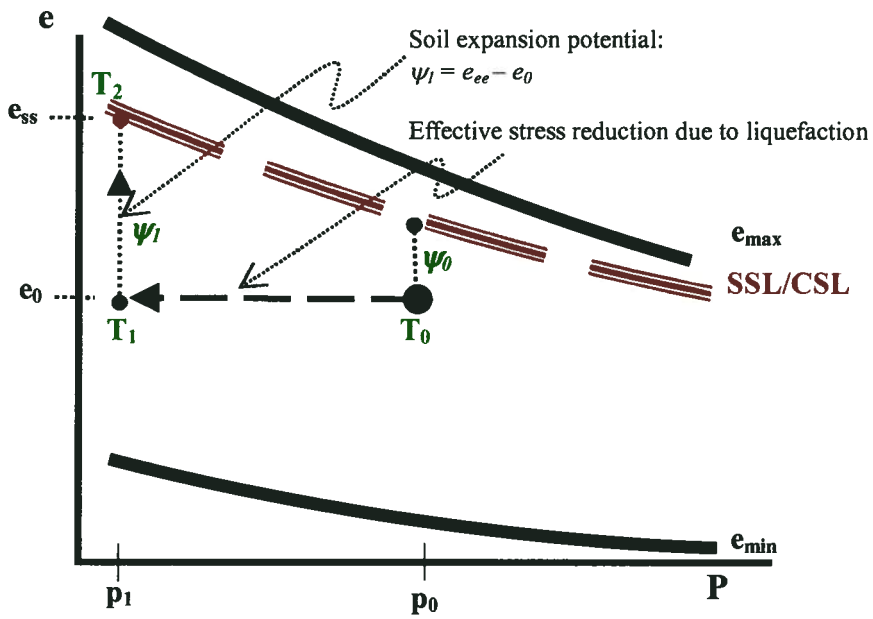

Fig. 5-35: Conceptual diagram showing increase in void ratio as a result of pore water migration due to liquefaction beneath the hydraulic barrier.

Experimental results of strain-controlled hollow cylinder tests (injection test) with constant shear stress, reported by Sento, et al. (2004), suggest that for Toyoura sand with 35%, 60%, and 85% relative density, a volumetric strain of 4.7, 6.4, and 10%, respectively, is required for a shear strain of 80% (see Fig. 2-27). In any case, these authors did not continue their tests further to include larger strains, presumably because of equipment constraints. Hence, even this amount of shear strain does not correspond to a *steady-state* for that material, and larger volumetric strains are required. Verdugo & Ishihara (1996) reported a void ratio of $e_{ss} = 0.93$ for Toyoura sand. Similar test results on Toyoura sand using triaxial injection tests with various initial consolidation stress ratios (shear stress bias) were reported by Yoshimine, et al. (2006). These test results, in terms of void ratio change and volumetric strain, are given in Figs. 5-36 and 5-37, respectively. Fig. 5-36 also compares their results (i.e., void ratio at the final stage, 30% axial strain) to the *steady-state* line of the material reported by Verdugo & Ishihara (1996). Data

in Fig. 5-37 (dot symbols) indicates that for a sample of 23% and 95% relative density, a volumetric strain of 2.5% and 13%, respectively, is required for reaching 30% axial strain. More experimental research is needed in this area.

Potential maximum volumetric strain can be estimated based on data from various soils, as reported in the literature. Table 5-1 lists a number of (relatively clean) sands with their minimum and maximum void ratio compiled mainly by Cubrinovski & Ishihara (2002) and Olson & Stark (2003) along with some other data. The potential maximum volumetric strain can be calculated as:

$$(\varepsilon_v)_{\max} = D_r \frac{e_{\max} - e_{\min}}{1 + e_i} \qquad [5\text{-}13]$$

where

$(\varepsilon_v)_{max}$: potential maximum volumetric strain

D_r: soil relative density

e_{max}: maximum void ratio

e_{min}: minimum void ratio

e_i: initial void minimum

In fact, the numerator of Eq. 5-13 should be $(e_{ss} - e_{min})$, where e_{ss} is the steady-state void ratio at zero effective stress, but it may be assumed to take a value of $(e_{max} - e_{min})$ for the sake of simplicity. A similar approach was adopted by Tsukamoto, et al. (2004) and Yoshimine, et al. (2006) to estimate potential maximum liquefaction-induced settlement and injection expansion, respectively. Furthermore, available data for *steady-state* void ratio, e_{ss}, of materials, e.g., Toyoura sand (Verdugo & Ishihara, 1996; see Fig. 2-29) and Nevada sand (Castro, 2001) suggest that the *steady-state* void ratio, e_{ss} and e_{max} are very close, and their difference corresponds to a relative density of less than 10% at low confining stresses. For example, application of Eq. 5-13 for Toyoura sand, results in less than 3% error in potential maximum volumetric strain. Therefore, regarding the loosest sands involved in engineering practice (commonly greater than 25%) this approximation is rational. In Table 5-1, potential maximum expansion is also provided for a typical medium dense state (D_r = 50%). Fig. 5-38 shows the upper and lower bounds for potential maximum expansion for a complete range of initial D_r, calculated based on Eq. 5-13.

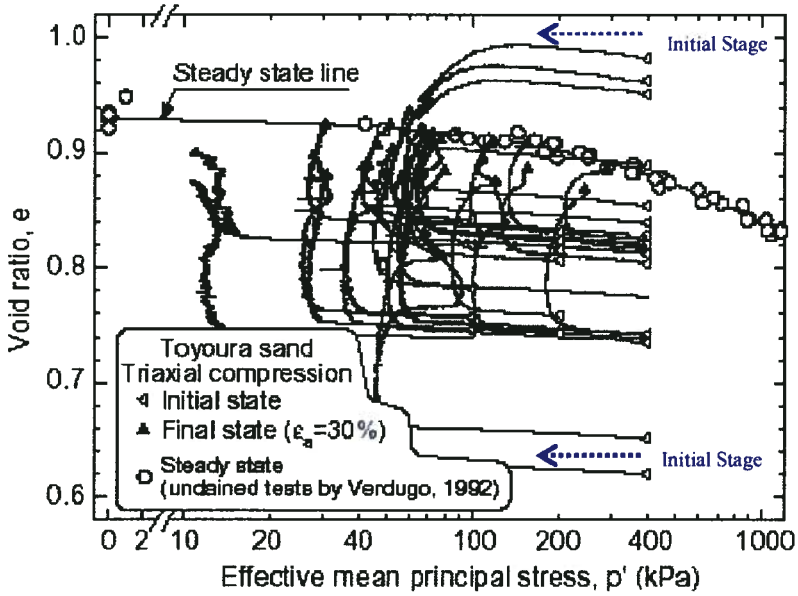

Fig. 5-36: Void ratio change due to water injection in triaxial compression test for Toyoura sand (modified from Yoshimine, et al., 2006).

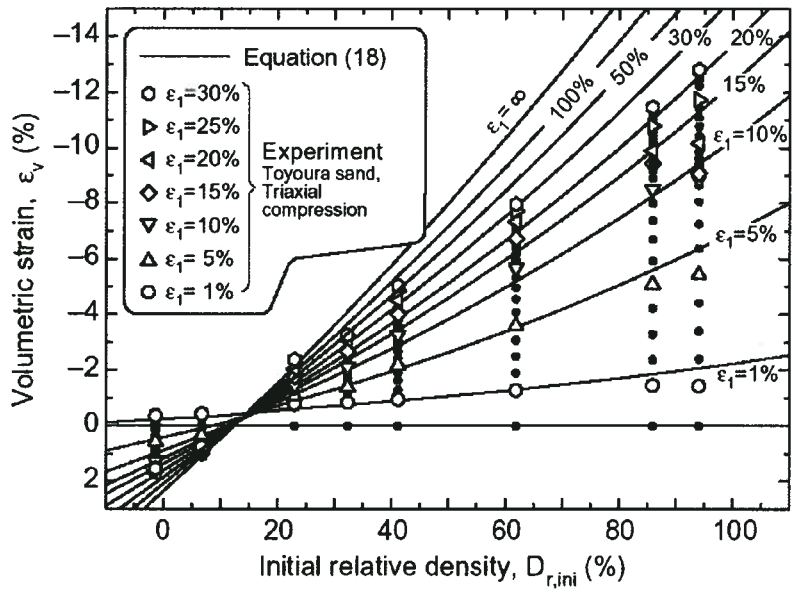

Fig. 5-37: Volumetric strain (expansion negative) vs. D_r to reach 30% axial strain in triaxial injection test for Toyoura sand (Yoshimine, et al., 2006).

A range of 25% to 80% for relative density is of interest from a practical point of view. A lower limit of D_r = 15% has been adopted in Fig. 5-38 to account for a loose state of the critical-state, where potential expansion could be negative (reaching steady-state from a contractive path). The application of Eq. 5-13 suggests that an expansion of 7.1%, 12.76%, and 19.09%, is required for samples of Dr = 35%, 60%, and 80%, tested by Sento, et al. (2004). These strains are greater than what the authors reported.

Table 5-2: e_{min}, e_{max} and potential maximum expansion (%) values of sands at D_r = 50%

Soil name	Void ratio		Expansion potential (%)	Reference
	e_{min}	e_{max}	$(\varepsilon_v)_{50}$	
Fraser River sand	0.596	0.9	8.76	Vaid & Eliadorani, 1998
Fraser River sand	0.62	0.94	8.99	Wijewickreme et al., 2005
Fraser River sand	0.68	1.00	8.69	Park & Byrne, 2004
Cambria sand	0.538	0.767	6.96	Lade et al., 1998
Nevada sand 50/80	0.581	0.858	8.05	Lade et al., 1998
Nevada sand 80/200	0.617	0.94	9.08	Lade et al., 1998
Nevada Fines	0.754	1.178	10.78	Lade et al., 1998
Ottawa sand 50/200	0.55	0.805	7.60	Lade & Yamamuro, 1997
Ottawa sand F-95	0.58	0.865	8.27	Lade & Yamamuro, 1997
Host sand A2	0.6	0.98	10.61	Thevanayagam, 1998
Toyoura sand	0.616	0.988	10.32	Zlatovic, 1994
Ottawa sand	0.48	0.78	9.20	Salgado et al., 2000
Ottawa sand C-109	0.5	0.83	9.91	Pitman et al., 1994
Quiou sand	0.78	1.2	10.55	Pestana & Whittle, 1995
Mine Tailings sand	0.69	1.06	9.87	Vaid et al., 1985
Brasted sand	0.48	0.79	9.48	Cornforth, 1974
Dune sand	0.54	0.91	10.72	Konrad, 1990
Well rounded silica sand	0.67	1.06	10.46	Konrad, 1990
Nerlek 0-2%	0.62	0.94	8.99	Sladen et al., 1985
Tottri sand	0.938	1.008	10.15	Takeshita et al., 1995
Monterey #9 sand	0.53	0.86	9.73	Reimer et al., 1990
Massey Tunnel sand	0.712	1.102	10.22	Konrad & Pouliot., 1997
Quebec sand	0.54	0.79	7.51	Konrad, 1998
Sand B	0.50	0.84	10.18	Castro, 1969
Sand C	0.66	0.99	9.04	Castro, 1969
Sand A	1.23	1.88	12.72	Castro, 1969

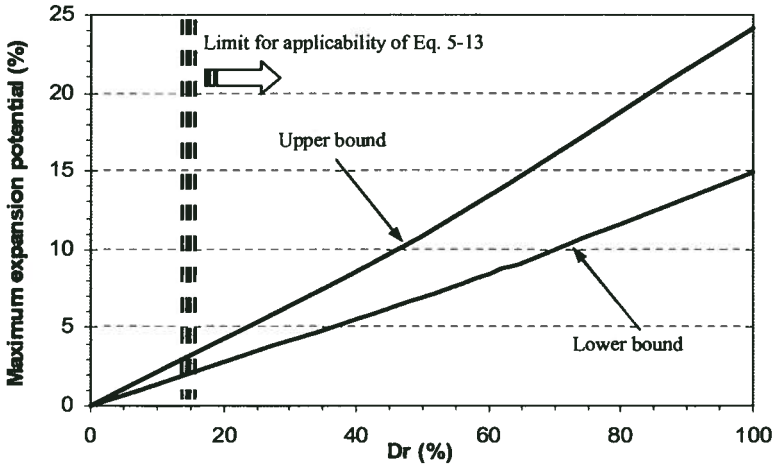

Fig. 5-38: Maximum expansion potential vs. initial relative density for sands (based on Table 5-1 data and Eq. 5-13).

5.5 Proposed Approach for Modeling Localized *Flow-Slides*

Roscoe (1970), in his experimental studies, observed that a shear band forms within a thin zone with a thickness 10 to 20 times that of the mean grain size of the soil, D_{50}, during its shear failure. Similar findings have been reported from further experimental and numerical (e.g., district element method, DEM) investigations by a number of researchers (e.g., Han & Vardoulakis, 1991; Han & Drescher, 1993; Finno, et al., 1997; Alshibli & Sture, 1999; Alshibli, et al., 2000a; 2000b; Nemat-Nasser & Okada, 2001; Wolf, et al., 2003; Desrues & Viggiani, 2004; Batiste, et al., 2004; Lu, et al., 2004; and Wu, et al., 2008).

These authors have shown that, under large shear deformations: 1) non-uniformity in terms of concentration of shear deformations (shear bands) and redistribution of pore fluid seem to be an *intrinsic* characteristic of soil response, and 2) the *critical-state/steady-state* soil response may only occur inside the shear bands, and not necessarily everywhere in a test sample. The direct consequence of strain localization is that traditional stress/strain measurements from soil samples in fact only results in nominal values of residual strength, which depend strongly on sample geometry and load pattern (Yang & Elgamal, 2002b).

Soil in the *critical-state/steady-state* deforms at constant volume without any further strain-hardening response, and shear-induced volume change is zero. Therefore, soil dilation does

not occur anymore and dies off. This can take place in a thin zone of liquefied sand at the barrier base when shearing takes place during a *flow-slide.*

Computationally, this localization, which is reflected by mesh size effects, can be approximately accounted for by specifying a dilation cut-off on skeleton expansion that is related to the initial relative density and the mesh size. This threshold volumetric strain, $(\varepsilon_v)_T$, can be specified based on $(\varepsilon_v)_{max}$, as defined in Eq. 5-13. Thus, a denser material would have more expansion capacity to reach the maximum void ratio at which point dilation would be set to zero. For a coarser mesh, less expansion is predicted for the element and the amount of expansion required to trigger dilation cut-off would be less. The mesh size should also be related to the particle size. Adopting Roscoe's concept, localization beneath the barrier base may occur within a thin zone with an order of magnitude of 10- to 20-times that of the mean grain size of the soil, D_{50}. A reasonable lower limit on mesh size could be based on this concept. For a soil profile comprising Fraser River sand of Dr = 40%, with D_{50} = 0.3 mm, shearing would occur within a zone with 3mm to 6mm in thickness.

Fig. 5-39 shows the data from Fig. 5-9 in semi-log format with the initial portion extrapolated to reach a value corresponding to a zone thickness of 3mm (3/6000 = 0.0005). From the figure, the maximum volumetric strain, $(\varepsilon_v)_{max}$, predicted for that element thickness ratio, *ETR* = 0.0005, is about 5.1%. If the base element with the thickness of the shear band zone (i.e., $10D_{50}$) can expand by 5.1% before reaching its *critical-state*, then it can retain some strength and prevent a *flow-slide.* Therefore, for this given condition (soil profile, level of shaking, and duration), flow failure does not occur since the induced expansion, 5.1% in the base element (with thickness of shear band width, $10D_{50}$) is smaller than the threshold value (i.e., $(\varepsilon_v)_{max} < (\varepsilon_v)_T$ that is, 6.9% for Fraser River sand of D_r = 40%). Also, water film does not appear beneath the barrier. When this cut-off is reached, the soil element deforms in the *steady-state* condition with essentially zero shear strength. If the predicted inflow causes the element to expand beyond its potential maximum volumetric strain, water film formation is likely taking place. This can be the case locally in a sloping ground condition since it should have already failed due to static shear stress, with e_{ss} at essentially zero effective confining stress.

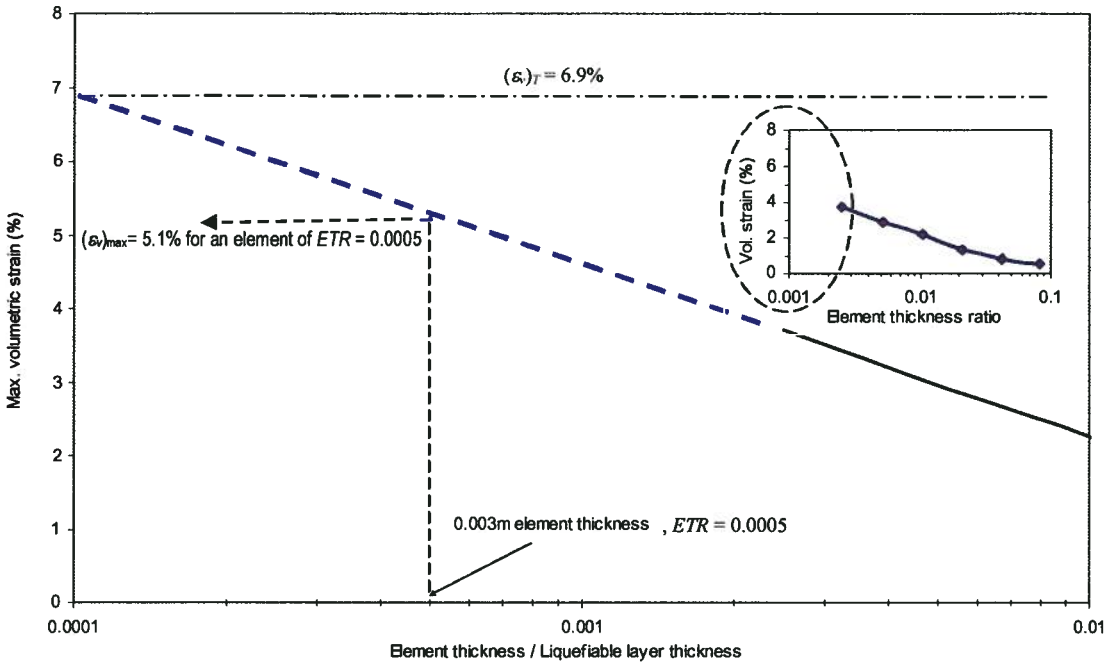

Fig. 5-39: Estimate of $(\varepsilon_v)_{max}$ for a base element with $10D_{50}$ (0.003m) thickness (ETR = 0.0005) for Fraser River sand using extended trend of $(\varepsilon_v)_{max}$ with element thickness ratio, ETR.

When the element thickness is chosen equal to the shear band thickness, $10D_{50}$, no correction is used for element size. Generally, it is not practical to make the element thickness this small and a correction for element size is then needed. To examine this approach, the sloping ground problem was re-visited using the mesh shown in Fig. 5-3a. This mesh has an element thickness ratio of 0.042, compared to a localized failure or shear band zone ratio of 0.0005. Based on Fig. 5-9, the predicted volumetric strain in the element beneath the barrier would be 0.79%, compared to 5.1% in the shear band. To account for this, the strain in the element must be modified to $(\varepsilon_v)^* = \varepsilon_v \times (5.1 / 0.79) = 6.4\varepsilon_v$, where 6.4 is a mesh size correction factor, MCF which is defined as:

$MCF = (\varepsilon_v)_{max}$ *for the base element with thickness of shear band zone,* $10\,D_{50} / (\varepsilon_v)_{max}$ *for the element with greater thickness.*

The analysis shows the computed $(\varepsilon_v)^*$ to be less than the threshold value of 6.9% and the results were identical to those predicted before (e.g., Figs. 4-16 to 4-18 and Fig. 5-4). When the duration of base motion was increased from 7s to 12s, the computed $(\varepsilon_v)^*$ was greater than 6.9%, at which time, dilation was suppressed and a *flow-slide* was predicted.

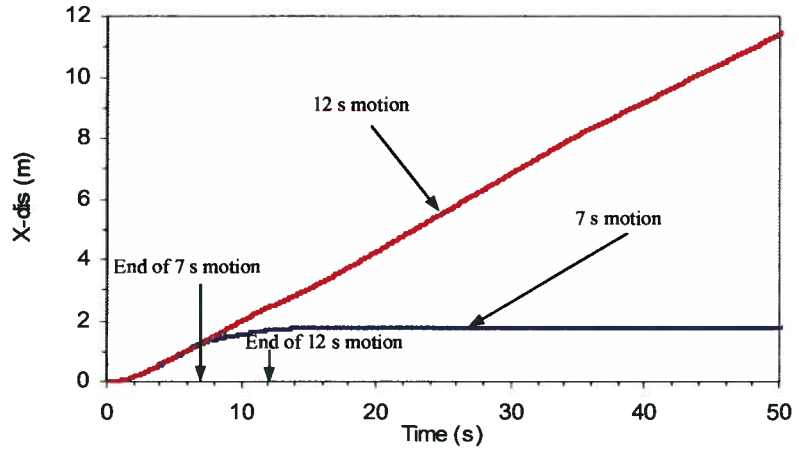

Fig. 5-40: Time histories of surface lateral displacement for two events.

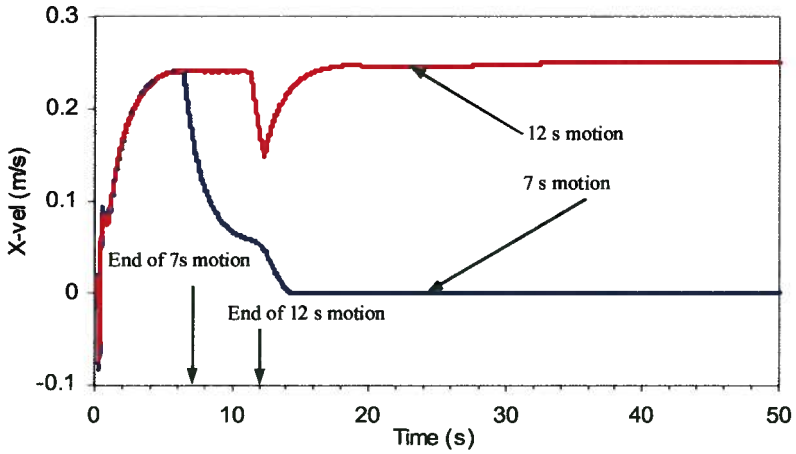

Fig. 5-41: Time histories of surface lateral velocity for two events.

Fig. 5-40 shows the surface displacement time histories for both cases. Surface displacement for 12s motion is seen to be ever-increasing, whereas displacements stop some time after the end of shaking in the 7s case. Ground surface velocity is a good indicator of flow failure. Fig. 5-41 shows ground surface velocity vs. time for the two events. It shows that for the 7s event surface velocity with descending trend, the ground surface velocity vanishes some time after the end of shaking, while in the 12s event it is essentially constant over that period. Thus, flow failure takes place in the second case when the dilation threshold is reached.

In practice, the analyses are commonly carried out for several earthquake records, and based on the results of this study, the process of handling localization can be shortened as follows:

1. Analyze the given model with a nominal *ETR* (e.g., 5%) for the base element with ε_v computation subjected to a certain earthquake.
2. Establish the corresponding $\varepsilon_v - ETR$ curve for the model using Fig. 5-41 or re-analyze the model with two lower *ETRs* (e.g., 3% and 2%) for the base element.
3. Determine the mesh size correction factor, *MCF*, for that particular model regarding liquefied soil specifications and shear band thickness (e.g., $10D_{50}$).
4. Re-analyze the model (*ETR* = 4%) with tracking $(\varepsilon_v)^* = MCF.\ \varepsilon_v$ for controlling *flow-slide* by applying dilation cut-off if $(\varepsilon_v)^*$ equals the threshold value, $(\varepsilon_v)_T$, corresponding to $(e_{ss} - e_i)$.
5. Analysis of the model, subjected to any other earthquake record, can be conducted in one step by applying the *MCF*, as determined for the first record using the procedure prescribed in Step 5.

5.6 Post-Liquefaction Strength Loss from Void Redistribution

Void redistribution was seen to result in localization and eventually *flow-slide* when enough inflow is provided to the barrier base zone. As mentioned earlier, the residual strengths, back calculated from case histories with *flow-slide*, are much lower than those obtained from undrained *steady-state* laboratory tests of undisturbed samples. In this section, void redistribution effects on post-liquefaction residual strength are explored in the light of findings from this study.

Fig. 5-42 shows the effective stress vs. void ratio path followed by an element located at point T beneath the barrier layer in a typical infinite slope, as depicted in Fig. 5-33. The initial *in situ-state* is defined as T_0 with void ratio e_0. If liquefaction is triggered in an undrained or constant volume condition, the element effective stress decreases to T_1 (with essentially a zero value) while its void ratio remains constant (i.e., e_0). At this *in-situ* void ratio, the element would have an undrained strength corresponding to point T_2 on the *critical-state* line (see Fig. 5-42). This strength would be greater than the drained strength. Thus, no danger is present of *flow-slide* during or following seismic loading if the element remained at the *in-situ* void ratio, e_0. If void redistribution occurs largely after liquefaction is triggered, then expansion takes place at approximately zero effective stress. When expansion is sufficient, the element may reach the *critical-state* at essentially zero effective stress and zero strength, corresponding to point T_3. At

this point, the skeleton has no further ability to expand, and further inflow to the element will result in the formation of a water film or bubble.

Not all elements along a potential failure surface of an earth structure will necessarily reach this state, and the low residual strengths back calculated from field experience are reflections of the average strength on the failure surface. Therefore, at the current state of knowledge, the use of strengths from case histories is prudent for engineering purposes, as Byrne, et al. (2006) noted.

On the other hand, if the inflow is not sufficient and expansion takes place to e_4, at this void ratio the element would have an undrained strength corresponding to point T_5 on the critical-state line. Thus, in stratified conditions of layered sands and silts, liquefied sand elements beneath the silt layer could have strengths ranging from the undrained strength to zero, depending on the density and severity of earthquake shaking.

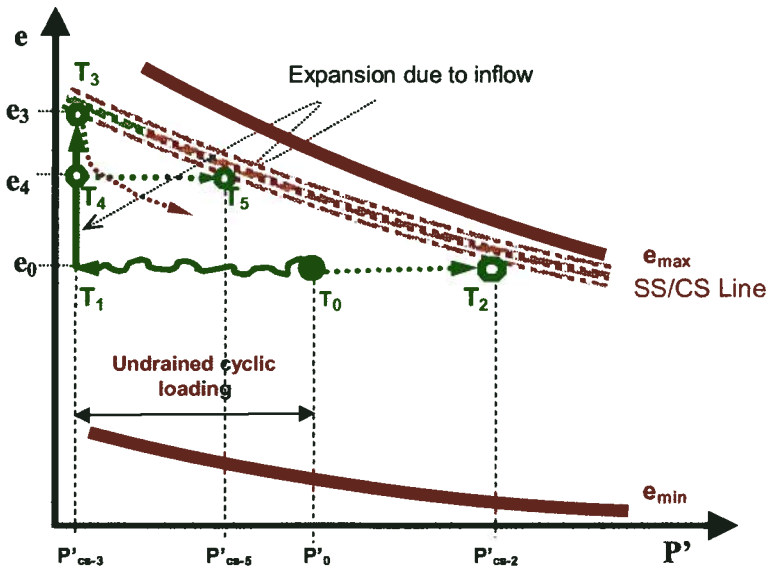

Fig.5-42: Void ratio and effective stress change at the barrier base due to undrained shaking and pore pressure redistribution.

Thus, strengths obtained from back analysis of failed case histories can be much lower than the undrained strengths from laboratory investigations. This also implies that the perfect undisturbed sample obtained prior to the earthquake will not represent the conditions during and

shortly after the earthquake, due to expansion that results from the upward flow of water in stratified deposits. Dissipation of excess pore water pressure, some time after the earthquake, will re-consolidate soil elements beneath the barrier so that the perfect sample, some time after the earthquake, will also not represent the critical conditions.

5.7 Summary and Main Findings

In this chapter the two main issues are: 1) difficulties in the numerical analysis of localized deformations (mesh size effect), and 2) requirements for liquefaction induced *flow-slide* of slopes. These issues are concerned with numerical modeling and sand behavior, respectively.

1) In the first part of this chapter:
   - Strain localization beneath the barrier layer was shown to lead to inconsistent results in the analysis using *FLAC* in *single-precision* mode if the base element thickness compared to the larger thickness is less than 5%. The issue can be resolved by increasing the computation precision, as demonstrated in this study.

2) In the second part of the chapter, the mechanism responsible for void redistribution and *flow-slide* was investigated based on fundamentals of sand behavior, and by applying different constitutive models. The following conclusions are presented:
   - In the presence of a low permeability sub-layer, pore water redistribution results in contraction in the lower 60% of the layer and expansion in the upper 40% of a liquefied infinite layer. This is a key characteristic behavior, regardless of the thickness of the liquefiable soil layer. This finding indicates that the phenomenon of pore water redistribution can be captured in centrifuge tests and that the actual physical size of the layers is not important.
   - Pore water migration, driven by a hydraulic gradient from zones with high excess pore water pressures is the key mechanism responsible for volume change and controls the behavior of a liquefied layer. The expansion in the upper 40% of the layer is not uniform but increases as the behavior is reached. This can result in a very thin, loose water-rich zone (expanded by water inflow) close to the barrier.
   - As the excess pore water pressure redistribution are controlled by flow conditions, this thin zone is predicted in the analyses regardless of the constitutive model used, since it occurs due to pore water pressure redistribution (flow condition).

- For a layer subjected to shaking, the pattern of volume change is controlled by flow conditions. However, the amount of expansion is affected by mechanical conditions.
- The maximum expansion for the minimal element at the barrier interface is not infinite, and is controlled by the net inflow into the minimal element.
- The void redistribution mechanism was shown to result in localized large lateral displacements. These can eventually lead to *flow-slide* if enough water is injected into that sheared zone to reach a *steady-state* at zero effective stress. Further inflow, beyond the *steady-state* (e_{ss}), can result in water film formation in a level ground condition, and locally in slopes. This conforms to observations by others (e.g. Kokusho, 2003) from physical model testing.
- The void redistribution mechanism is responsible for the low residual strengths calculated from failed case histories as also noted by other investigators. A liquefied soil layer with barrier sub-layer was shown to exhibit a wide range of (residual) strengths, even near-zero, when expansion exceeds the threshold expansion in the localized zone.
- This study indicates that the undisturbed sample obtained prior to an earthquake will not represent the conditions during and shortly after the earthquake in stratified earth structures. Such samples are quite useful to determine pre-earthquake properties (e.g. e_i) and the maximum expansion potential. The undisturbed sample, at some time after the earthquake, will also not represent the critical conditions, due to the re-consolidation that occurs during and after the earthquake.
- A practical approach to handle the strain localization (shear band) problem involved in numerical analysis was developed and its capability to predict a *flow-slide* was shown for the analyzed slope.

CHAPTER 6

FACTORS AFFECTING SEISMIC RESPONSE OF GENTLE LIQUEFIABLE SLOPES WITH HYDRAULIC BARRIER

6.1 Introduction

In this chapter, the effects of several factors influencing the magnitude of liquefaction-induced large displacements of a typical gentle infinite slope with low permeability sub-layer are investigated through a parametric study. The response of a typical sloping ground to earthquake (Fig. 6-1) is controlled by mechanical and flow conditions, namely:

a) Mechanical parameters, i.e.,
   1. Ground inclination, α.
   2. Depth of barrier layer, D_B.
   3. Relative density, D_r of the liquefiable soil layer.
   4. Motion characteristics, e.g., magnitude and acceleration amplitude.

b) Flow parameters, i.e.,
   5. Thickness of liquefiable layer, T_L.
   6. Permeability of the liquefiable soil layer, k_L.
   7. Soil/barrier permeability contrast, k_c ($k_c = k_L/k_B$).
   8. Barrier layer thickness.
   9. Shaking duration.

The factors associated with the generation of excess pore water pressure are accounted for as mechanical parameters, whereas, the pore water pressure redistribution and required time for its dissipation are mainly controlled by flow parameters. In this regard, the ground base shaking record is comprised of the two types of effects, i.e., mechanical effect in terms of

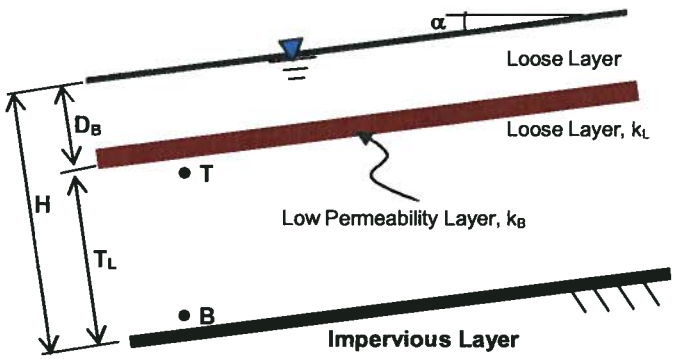

Fig. 6-1: Idealized infinite slope with low permeability sub-layer.

acceleration amplitude and earthquake magnitude (expressed as number of cycles) that affects the generation of excess pore pressure, and flow effect in terms of shaking duration.

The same 10 m soil profile, modeled with a single-column mesh, as shown in Fig. 4-7 and Fig. 5-1 was analyzed, and the results are discussed in the next sections.

6.2 Effects of Mechanical Conditions

In this section, the parameters that control the mechanical aspects of the seismic behavior of the soil profile are discussed. For the sake of comparison, the motion characteristic effects (i.e., amplitude and duration) are also presented in this section.

6.2.1 Effects of Ground Inclination

To study the effects of layer inclination, the 10 m soil profile (shown in Fig. 4-7) was analyzed for two conditions:

1) Soil profile without barrier,

2) Soil profile with barrier.

The *UBCSAND* model was applied to the liquefiable soil layer and the barrier layer was modeled as a *Mohr-Coulomb* material with $\varphi = 30^{\circ}$ and $C = 0$, assuming that no excess pore water pressure is built up in the low permeability sub-layer (see Table 4-1 for material properties).

6.2.1.1 Soil Profile without Barrier

For the uniform soil profile, the soil properties are represented by a constant $(N_1)_{60\text{-}UBCSAND}$ = 6.2 in the analyses with the *UBCSAND* model. The model was subjected to harmonic base motion with *PGA* = 2.5 m/s^2 (depicted in Fig. 4-8). The analyses were conducted for two ground inclinations: 1.0 and 2.0 degrees. Fig. 6.2 shows the surface lateral displacement vs. ground inclination and indicates that with an increase in ground inclination, the displacements become larger due to greater static shear bias. The same pattern has been observed in centrifuge model tests carried out at Rensselaer Polytechnic Institute, Troy, NY (Taboada & Dobry, 1998). Fig. 6-3 shows the centrifuge test results for the model depicted in Fig. 4-13 with various inclinations (water was used as the pore fluid).

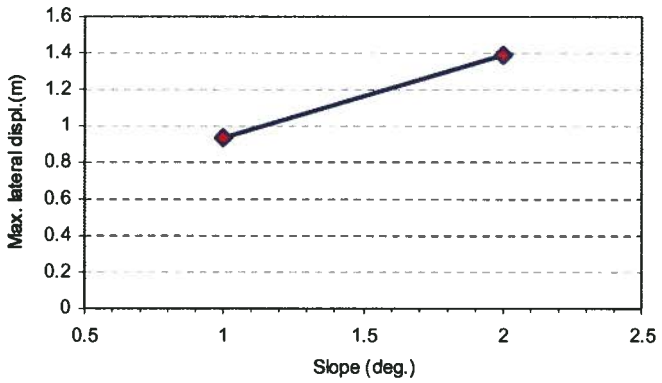

Fig. 6-2: Predicted surface lateral displacement vs. ground inclination (profile without barrier layer, 0.25g *PGA*).

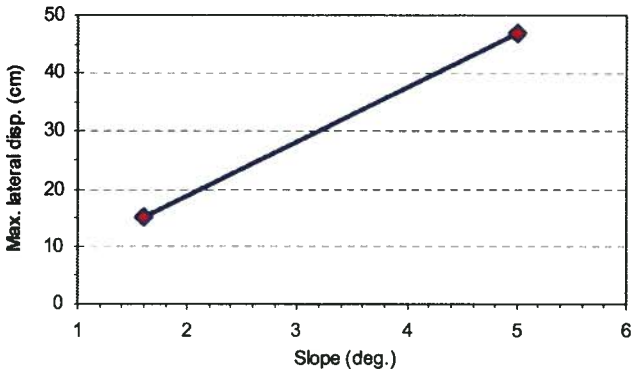

Fig. 6-3: Surface lateral displacement vs. ground inclination in centrifuge tests.

6.2.1.2 Soil Profile with Barrier Sub-Layer

The effects of inclination on seismic behavior of liquefiable infinite slopes with barrier sub-layers were investigated for the same soil profile shown in Fig. 4-5 with a constant $(N_1)_{60\_UBCSAND}$ = 6.2 in the analyses using the *UBCSAND* model (representing Fraser River sand with D_r = 40%), subjected to harmonic base motion with PGA = 2.5 m/s^2 with 7 s duration, as depicted in Fig. 4-6. The permeability of the liquefiable soil layer and the barrier layer were considered as 8.81 × 10^{-4} m/s and 8.81 × 10^{-7} m/s, respectively.

The change of maximum ground surface lateral displacement with its inclination is given in Fig. 6-4. The trend of displacement increases with ground slope similarly to that seen in the profile without barrier; however, a greater impact of inclination is observed. This is attributed to the pore water pressure redistribution mechanism, resulting in high R_U for a longer duration in this case. Corresponding time histories of surface lateral displacements are shown in Fig. 6-5, indicating that the rate of displacement is higher for steeper slopes.

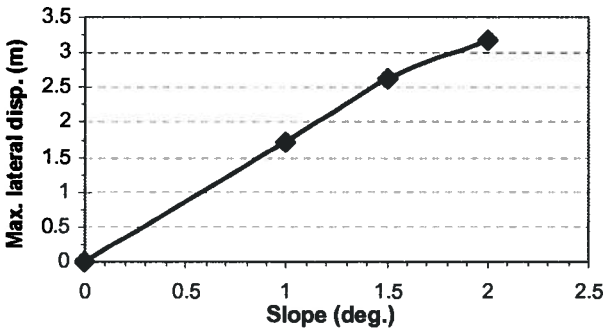

Fig. 6-4: Increase of surface lateral displacement with ground slope (profile with barrier layer).

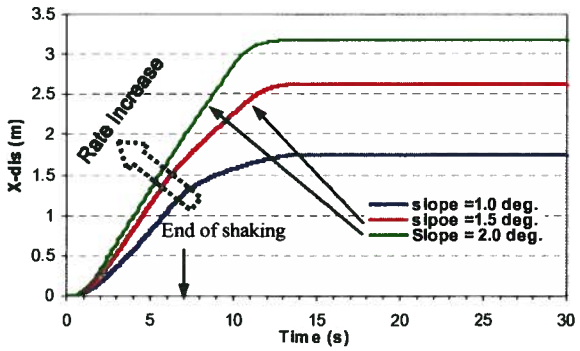

Fig. 6-5: Surface lateral displacement time histories for different ground slopes (profile with barrier layer).

Fig. 6-6 and Fig. 6-7 compare the time histories of ground surface lateral velocity and the base element excess water pore pressure (enlarged) for the 2°-slope and 1°-slope cases, respectively. At initial stages, the 2°-slope deforms with greater velocity; however, its velocity declines due to further reduction in excess water pore pressure. Fig. 6-7 shows that lower excess pore water pressure is induced in the base element of the 2°-slope case and the displacement is mainly controlled by mechanical conditions.

In general, earthquake-induced deformations are arising from two different causes, i.e., inertia effects (applied dynamic load) and soil strength reduction (due to excess pore water pressure generation) which interact with each other through the mechanical and flow conditions.

Fig. 6-8 and Fig. 6-9 show liquefaction evolution ($R_u \approx 1$) for Fraser River sand (air-pluviated) samples of $D_r = 40\%$, in terms of R_u vs. No. of cycles observed in cyclic simple shear

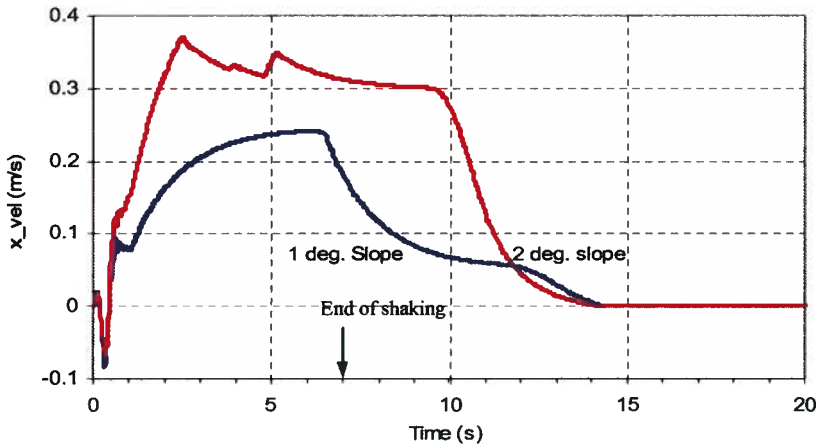

Fig. 6-6: Surface lateral velocity time histories for the two slopes.

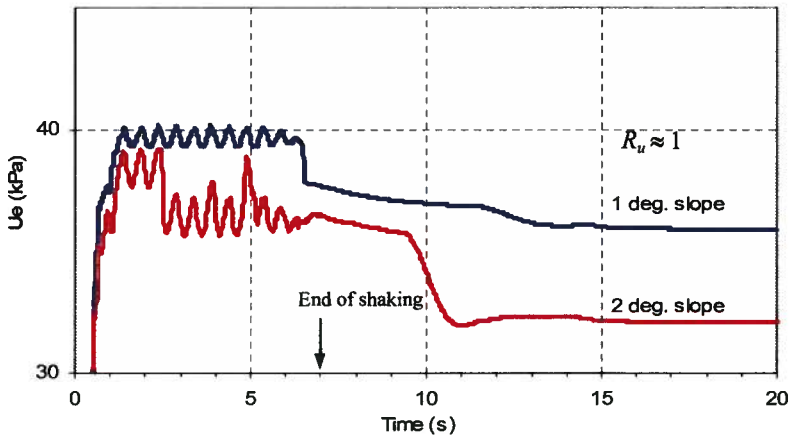

Fig. 6-7: Excess pore water pressure time histories for the barrier base element.

tests carried out under different loading conditions, i.e., static shear stress bias, τ_s and *CSR* (Sriskandakumar, 2004). In the figures, the minimum post-liquefaction excess pore water pressure ratios are indicated with dashed lines. After the first momentarily complete liquefaction ($R_u \approx 1$), the excess pore water pressure decreases whenever the sample dilates. This suggests that an increase in shear stress (including static and dynamic stresses) induces more dilation and as a result, lowers the post-liquefaction minimum excess pore water pressure.

Similar test results indicating reduction effects of shear stress (combined effect of static and cyclic stresses) on post-liquefaction R_u are observed in unidirectional and bi-directional undrained cyclic simple shear tests with pore water pressure measurement, reported by Wu (2002) and Kammerer (2002), respectively.

Fig. 6-10 schematically illustrates the stress path for a typical loose liquefied sand with shear stress bias. Before the onset of liquefaction, to point D at *PT* line (stage I), the sand behaves as a contractive material and the excess pore water pressure build-up has a progressive trend all the way. This results in increasing flow from zones with higher hydraulic gradient during stage I of shaking. After the stress path reaches point D (stage II), the flow conditions within the earth structure change due to alternating dilative and contractive soil behavior. This leads to a different effective stress condition from that of stage I and, as a result, the contribution of mechanical properties in the deformations is altered. Therefore, depending on the onset of stage II (point D), which is controlled by shear stress bias and loading amplitude, i.e., shaking level and the minimum post-liquefaction excess pore water pressure value (corresponding to point M), the contribution of mechanical and flow conditions in the deformations varies as the seismic excitation and induced excess pore water pressure regime change within a soil layer (see Fig. 6-11 for a typical cyclic stress change in an idealized level-ground case, modified from Kammerer, 2002). The issue of post-liquefaction reduction in excess pore water pressures affects the flow regime (hydraulic gradient) within the soil deposit.

Fig. 6-12 shows the time histories of the vertical specific discharge, *Y-Flow* for the base element in both cases. Water inflows into the base element more steadily (with less variation) in the 1°-slope case during shaking and *Y-Flow* in the 2°-slope case exhibits lower minimum values, compared to those of the 1°-slope, due to the excess pore water pressure reduction driven by soil dilation, as discussed above.

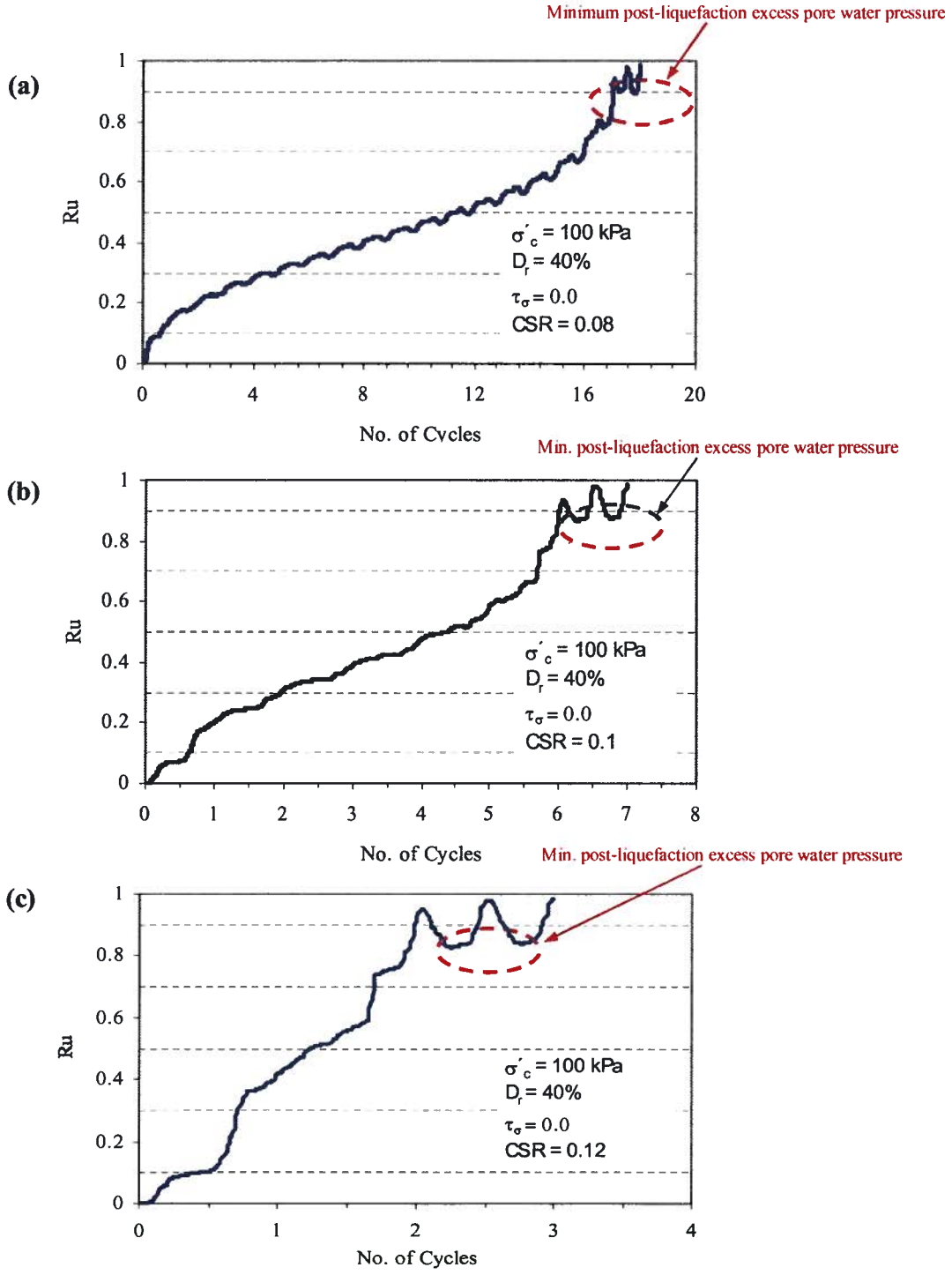

Fig. 6-8: *Ru* vs. No. of cycles for Fraser River sand of *Dr* = 40% without static shear stress indicating post-liquefaction excess pore water pressure for (a) *CSR* = 0.08, (b) *CSR* = 0.1 and (c) *CSR* = 0.12 (test data from Sriskandakumar, 2004).

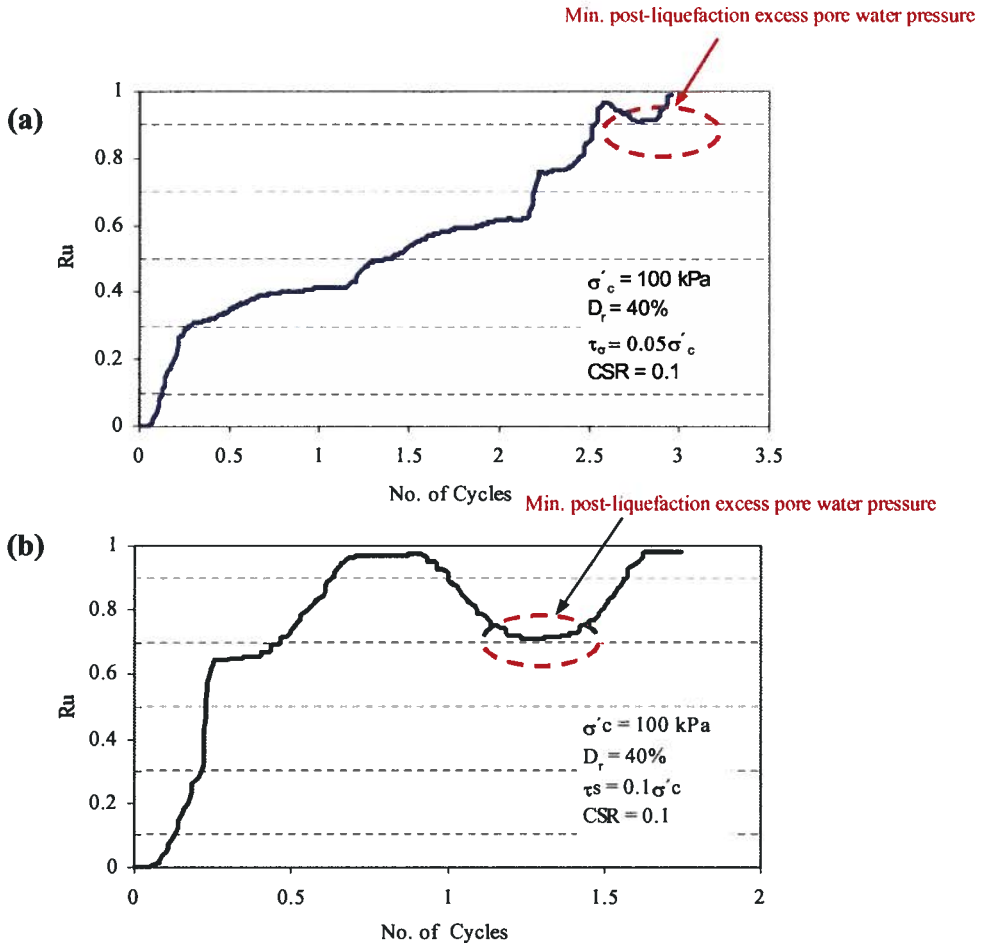

Fig. 6-9: *Ru* vs. No. of cycles for Fraser river sand of D_r = 40% with static shear bias indicating post-liquefaction excess pore water pressure for, (a) $\tau_s = 0.05\ \sigma'_c$ and (b) $\tau_s = 0.1\ \sigma'_c$.

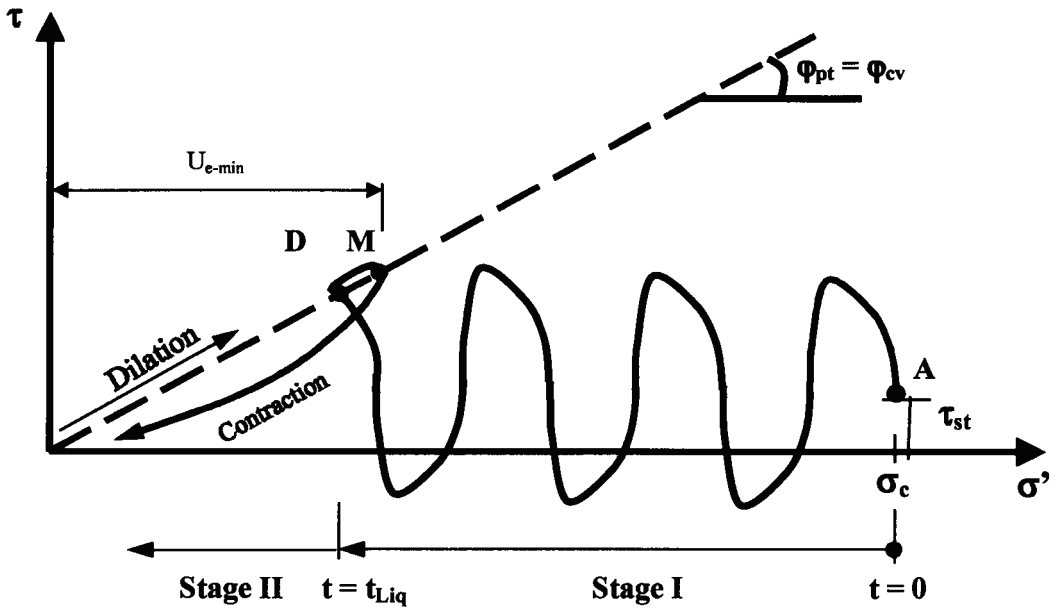

Fig. 6-10: Typical stress path of a soil element to liquefaction and subsequent dilation and contraction during loading and unloading, respectively.

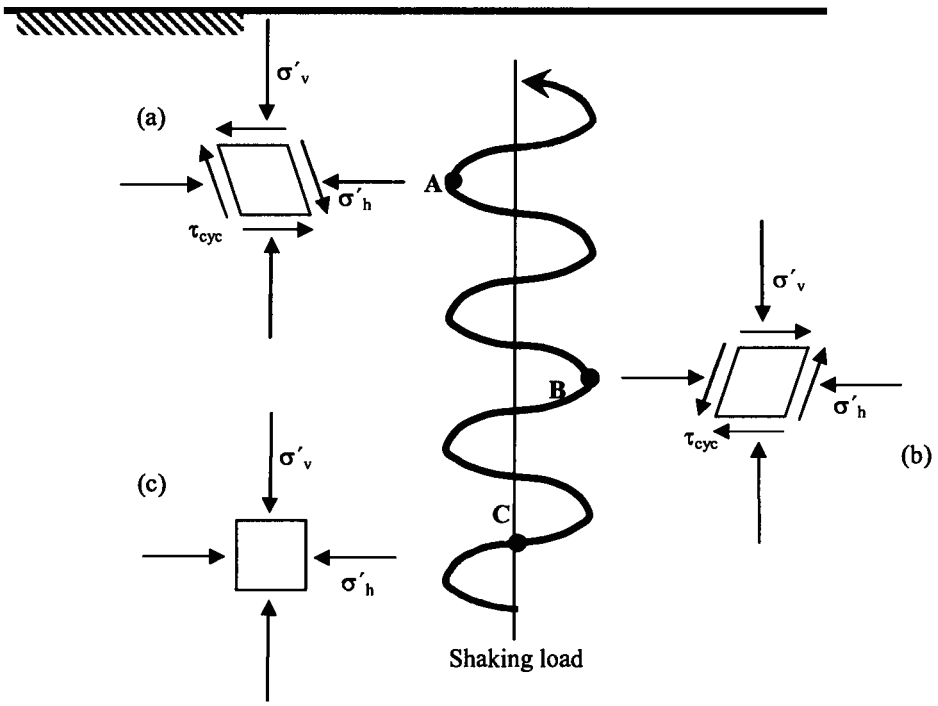

Fig. 6-11: Typical idealized seismic shear stress variation within an earth structure for level-ground condition.

6.2.2 Effects of the Barrier Depth, D_B

A set of analysis was conducted for the same soil profile of α =1° slope comprising liquefiable soil with thickness of T_L = 6 m and a barrier layer of variable depth, D_B (see Fig. 6-1) subjected to harmonic base motion of PGA = 2.5 m/s^2 (shown in Fig. 4-6). The soil properties were considered as listed before (Table 4-1). Generally, the driving shear stress (static shear bias) applied on the base element increases with the depth of the barrier layer.

Time histories of surface lateral displacements for various barrier depths, D_B are shown in Fig.6-13. The effects of the barrier depth are shown in terms of delayed deformation (compared to the uniform layer) and order of magnitude for different depths of the barrier, D_B. The rate of displacement is seen to increase with the barrier presence and is the same for the cases comprising barrier layer, until the shaking ceases (7 s), thereafter it is driven essentially by flow properties of the soil layer, i.e., permeability and flow path. This also implies that deeper barriers result in larger displacements due to greater static shear stress being applied at the barrier base. Fig. 6-14 shows the maximum ground surface displacement vs. barrier depth, indicating the increasing effect of barrier depth, D_B.

6.2.3 Effects of Soil Relative Density, D_r

To explore the effects of sand relative density on volumetric strains and lateral displacements, the same 10m-soil profile (1°-slope) was analyzed with material properties corresponding to dense sand subjected to the motion, as given in Fig. 4-8. The dense sand was accounted for with $(N_1)_{60\text{-}UBCSAND}$ = 26.05 in the analysis. It represents (air pluviated) Fraser River sand with D_r = 80% that liquefies (γ = 3.75%) at the 46th cycle under σ_c =100 kPa with CSR = 0.25 (Sriskandakumar, 2004). The dry density, permeability, and porosity were considered as ρ_d = 1610 kg/m^3, k = 6.4 × 10^{-4} m/s, and n = 0.406, respectively. The barrier layer properties were the same as those listed in Table 4-1, but with permeability contrast of 1000 relative to that of dense sand. The mesh shown in Fig. 5-1, with 0.25 m element base thickness, was used in this analysis.

The dense sand layer exhibited the same pattern of deformation as that of loose sand (with localization); however, with a lower order of magnitude of displacements (as shown in Fig. 6-15). Predicted variation of the excess pore water pressure ratio vs. time, for the bottom element

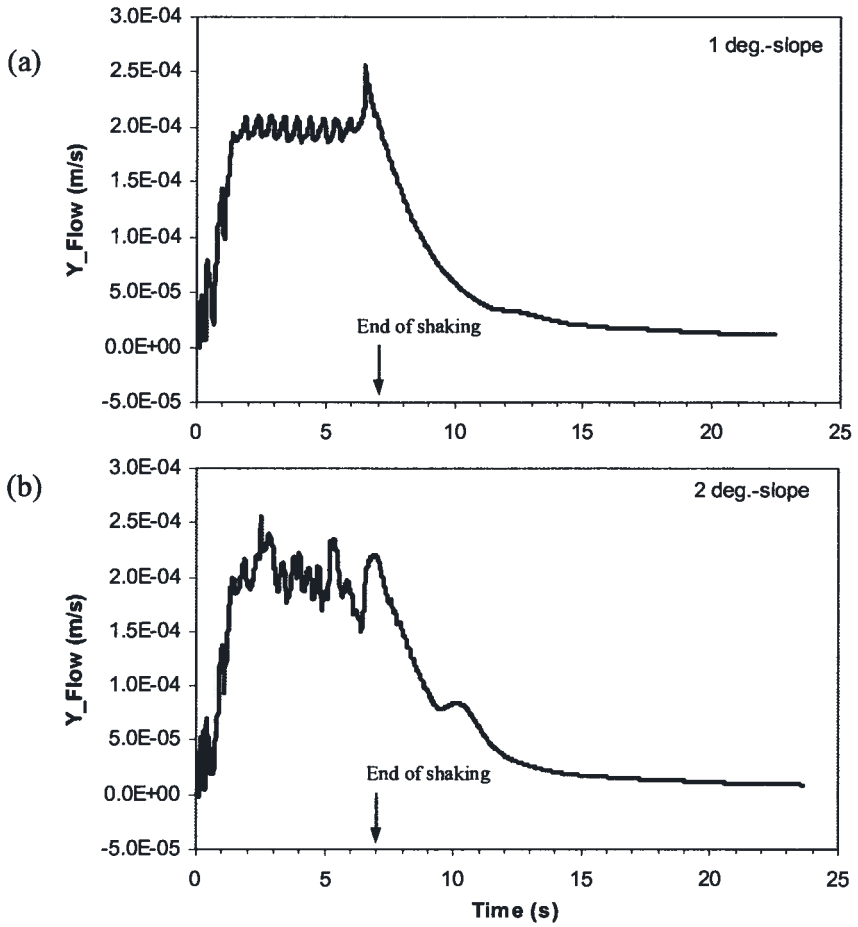

Fig. 6-12: Specific vertical discharge, *Y-Flow* for the base element, (a) 1°-slope and (b) 2°-slope.

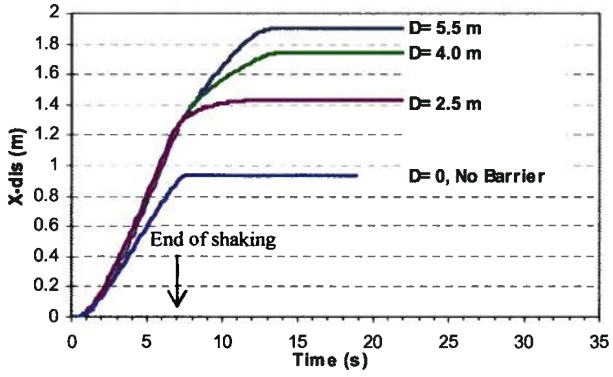

Fig. 6-13: Surface lateral displacement time histories for different barrier depths (1°-slope).

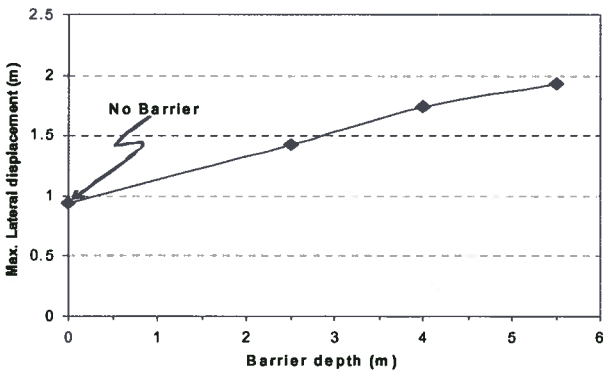

Fig. 6-14: Increase of surface lateral displacement with barrier depth (1°-slope).

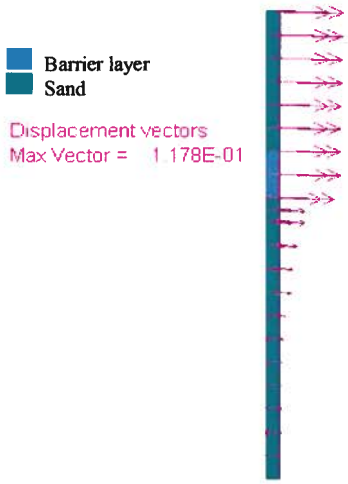

Fig. 6-15: Displacement vectors within the dense sand profile with barrier sub-layer.

(1,1) and the barrier base element (1,13) is shown in Fig. 6-16. Thus, the significant dilation results in relatively low minimum excess pore water pressure.

Fig. 6-17 shows the surface lateral displacement time history for the dense layer (with barrier sub-layer) with maximum value of 0.12 m. As observed, the dilation effect is also reflected in the ground surface displacement record by cyclic spikes. This suggests that the inertia effects on seismic displacements in dense layers are more pronounced and the post-shaking displacement is minimal. Fig. 6-18 shows the change of maximum surface lateral displacement vs. soil density. In the figure, data related to a medium dense case (i.e., D_r = 60%) is also shown.

Seismic behavior of dense sands, in terms of stiffness degradation and stress-strain response, has recently been of interest to several researchers (Elgamal et al., 2005). Laboratory investigations on dense sands (e.g., Ishihara, 1985; Kammerer, 2002; Wu, 2002; Seed et al., 2003; and Sriskandakumar, 2004) suggest that significant excess pore water pressure builds up (effective stress reduction) during the unloading phase of a cycle, compared to the counterpart loading phase, even in the first cycle of cyclic loading. This is in significant contrast to the response of loose samples. Fig. 6-19 shows a typical response of a dense sand, as reported by Ishihara (1985), for the undrained torsional condition for Fuji River sand (D_r = 75%). The loose samples do not develop any significant excess water pore water pressure during the unloading phase (almost elastic unloading, as considered in the current version of the *UBCSAND* model) of initial loading cycles. In the case of loose sands, the excess pore water pressure generation

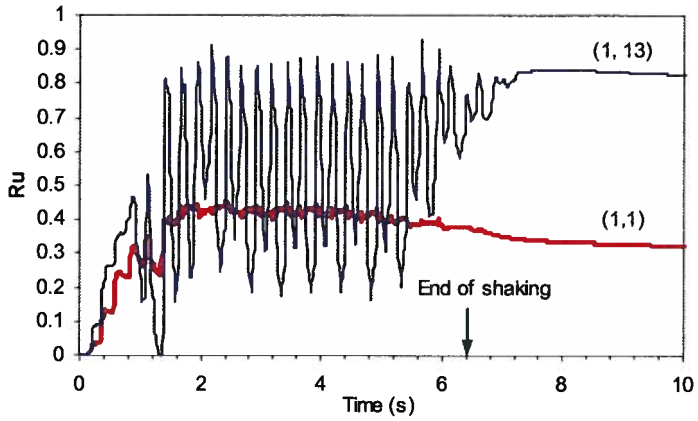

Fig. 6-16: Excess pore pressure vs. time for the bottom and the base element of the dense soil layer.

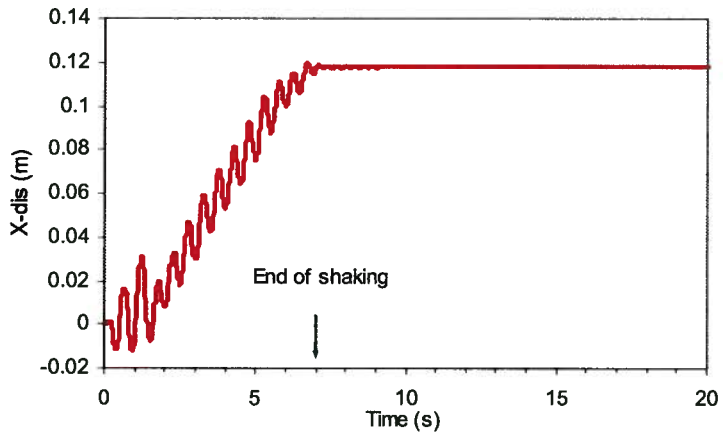

Fig. 6- 17: Time histories of surface lateral displacement for dense soil layer.

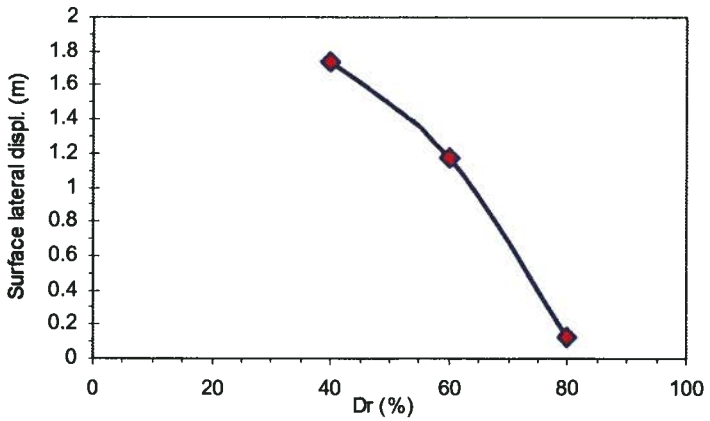

Fig. 6-18: Maximum surface lateral displacement vs. liquefiable soil layer D_r.

during unloading cycle becomes significant only when the stress path reaches the line of phase transformation (see Fig. 6-10). This relatively large excess pore water pressure generation during unloading in loose samples reflects the contractive tendency and "plastic unloading" after the development of phase transformation. The early plastic unloading in dense sands can be attributed to early development of phase transformation for dense sands.

In undrained loading conditions, dilation causes:

- Increase in effective confinement or reduction in excess pore water pressure, and
- A corresponding increase in shear resistance and stiffness as a stress-level dependent soil property. This increasing shear resistance may lead to the appearance of acceleration spikes during dynamic excitation, as observed in centrifuge tests (Kutter & Wilson, 1999; Kramer & Elgamal, 2001; Taboada et al., 2002; and Elgamal et al., 2005).

The unloading effect on excess pore water pressure generation has been accounted for in developing a two-plane mobilized model (Park, 2005). Considering this effect would lead to more generated excess pore water pressure, greater localized deformations in the dense layer will be predicted.

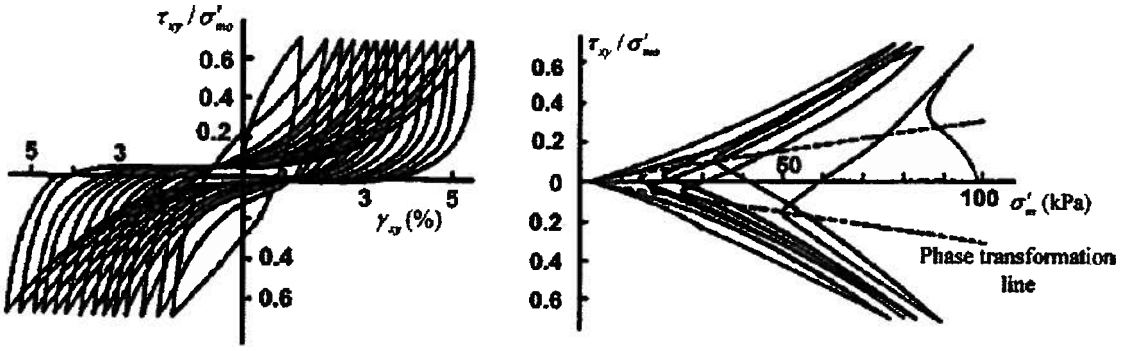

Fig. 6-19: Undrained torsional shear behavior of Fuji River sand at D_r = 75% (Ishihara, 1985) (σ'_m = mean effective confinement; σ'_{m0} = initial mean effective confinement; τ_{xy} and γ_{xy} in-plane shear stress and strain, respectively).

The same trend of decreasing displacements (as per Fig. 6-18) was observed in centrifuge model tests (shown in Fig. 3-23) conducted by Kulasingam et al. (2004). Nevertheless, the authors argued that localization did not occur in some of their 2-D model tests with materials denser than 45~50% relative densities, when subjected to particular earthquake records. In

another investigation, Kutter et al. (2004) studied the effects of relative density and thickness of the underlain soil layer of barrier sub-layers on lateral displacements of bridge foundations using centrifuge testing (see Fig. 3-18 and Fig. 3-19 for model configuration and deformation pattern, respectively). Their data suggest that localization occurs even in dense materials with D_r = 80% (see Fig. 3-19). They introduced a deformation index, *DI,* as Eq. 6-1 to account for soil layer thickness and its relative density in deformations, and correlated the surface lateral displacement to *DI* as given in Fig. 6- 20.

$$DI(z) = \sum_{z}^{rigidbase} H_i(1-Dr_i)^2 \qquad [6\text{-}1]$$

The analyses conducted in this study confirm that localization occurs regardless of the underlying layer density when a hydraulic sub-layer barrier impedes the flow path (practically) completely; however, denser materials, as discussed in *Chapter 5,* require more net inflow to reach a *steady-state* of deformation and exhibit greater *maximum expansion potential.* The analyses also indicated that the expansion occurs to a lesser degree for the dense profile due to lower expelled water as a result of stronger soil mechanical properties.

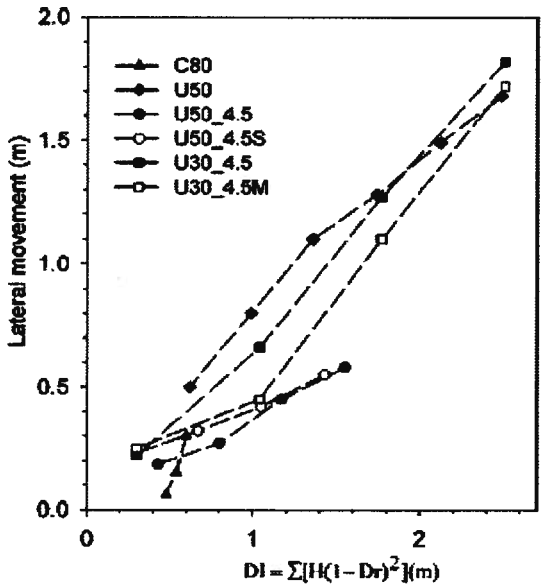

Fig. 6-20: Accumulated lateral displacement vs. deformation index (Kutter et al., 2004, with permission from ASCE).

6.2.4 Effects of Motion Characteristics

Shaking a granular soil mainly results in excess pore water pressure build-up which redistributes subsequently based on flow conditions. The excitation characteristics have two kinds of effects:

1. Amplitude: the amount of volume of the expelled water (excess pore water pressure) directly reflects the cyclic shear strain, and
2. Duration: this controls the continuation of high flow rate of the expelled water.

To explore the effects of shaking characteristics, the same 10 m soil profile with materials properties listed in Table 4-1 was analyzed by applying base harmonic motions of various *PGA*s and durations. The mesh shown in Fig. 5-1 with 0.25 m element base was used in this series of analyses. Fig. 6-21 shows three acceleration time histories of the applied base motions. The records are recognized as:

- Event 1: with $PGA = 2.5$ m/s^2 and 7 s duration (Fig. 6-21a) is the same motion used in the previous analyses.
- Event 2: with $PGA = 1.25$ m/s^2 and 7 s duration (Fig. 6-21b).
- Event 3: with $PGA = 1.25$ m/s^2 and 14 s duration (Fig. 6-21c).

6.2.4.1 Effects of Motion Amplitude, *PGA*

Effects of shaking level on the surface lateral displacements can be seen by comparing the results of event 2 with those of event 1. Fig. 6-22 shows surface displacement time histories for events 1 and 2 with maximum values of 1.74 m and 1.47 m, respectively. In both cases, the ground surface continues to deform until after shaking ceases, indicating the severity of the excitations for this given soil profile to cause significant excess pore water pressure. It demonstrates that an increase of shaking level by 100% results in about 18% in surface displacement for this given soil profile.

The rate of displacement for event 1 becomes greater than that for event 2, by the end of shaking (at 7 s), due to the greater induced shear strain that results in displacement difference, Δx_1 when shaking ceases. The displacement difference remains essentially constant ($\Delta x_1 \approx \Delta x_2$) after a stabilization time (about 15 s) as a result of similar post-shaking conditions. Fig. 6-23 shows maximum surface lateral displacement vs. motion amplitude. The same pattern of

increasing effect of motion amplitude has been reported from centrifuge testing by Malvick et al. (2005), as quoted in Table 3-3.

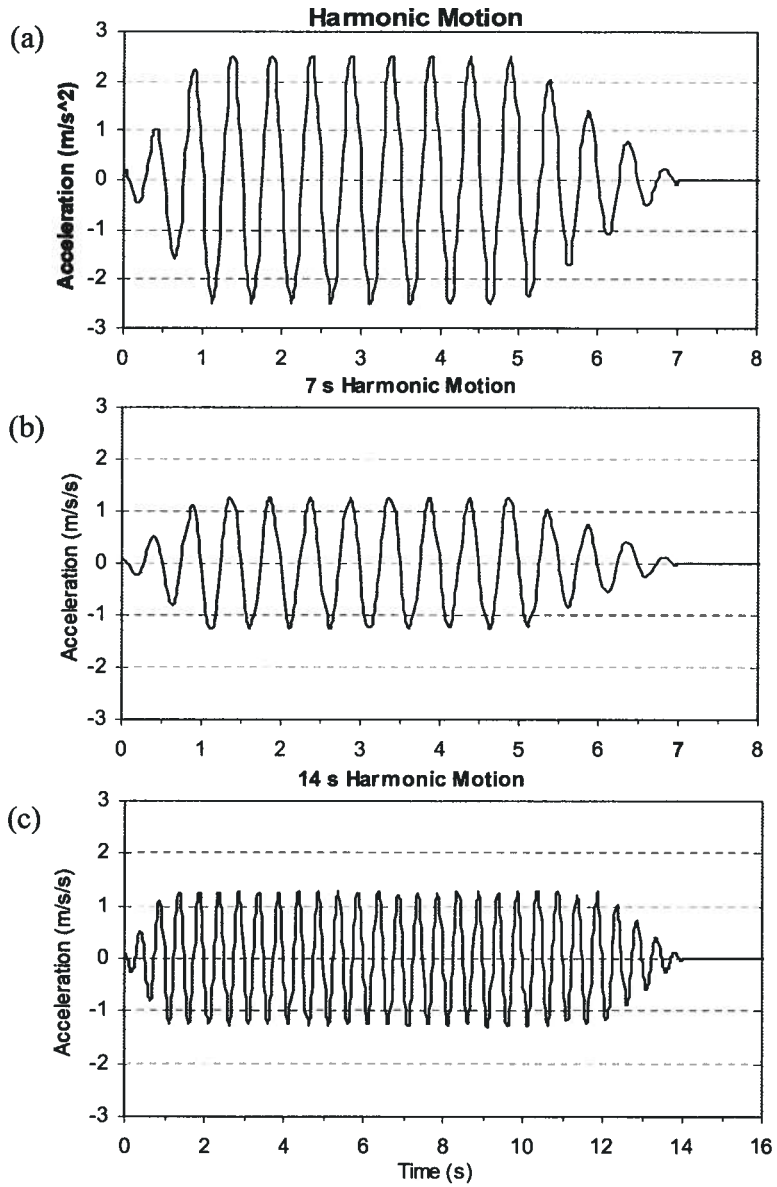

Fig. 6-21: Applied acceleration time history of (a) event 1, *PGA* = 2.5 m/s^2 of 7 s, (b) event 2, *PGA* = 1.25 m/s^2 of 7 s, (c) event 3, *PGA* = 1.25 m/s^2 of 14 s.

Fig. 6-24 shows the profile of volumetric strain for the two events. It indicates that volumetric strains at the vicinity of the barrier base for the two cases are essentially the same. Therefore, as mentioned earlier, for these given conditions (i.e., fully saturated) the main cause of different surface displacements is due to mechanical factors (i.e., cyclic shear strain). Event 2

(PGA = 1.25 m/s^2) resulted in lower volumetric strain (contraction) at deep parts (D ≥ ≈ 8.5 m) of the contraction zone. It indicates that the motion is strong enough to produce high excess pore water pressures and its redistribution towards the upper parts, as the contraction of the deeper points is more influenced by mechanical properties, whereas, expansion of the upper parts is mainly controlled by flow properties. Contractive volume change in the upper part of the contraction zone (D < ≈ 8.5 m) is higher in the event 2 case. This is attributed to relatively greater cyclic shearing stress transmitted to the upper parts. Fig. 6-25 shows the predicted acceleration time history for a point at a depth of 8 m for the two cases. In event 1, the acceleration de-amplifies, whereas, in event 2, it amplifies up to this depth. In the figure, an arbitrary line of $0.65A_{max}$ is shown for comparison purposes.

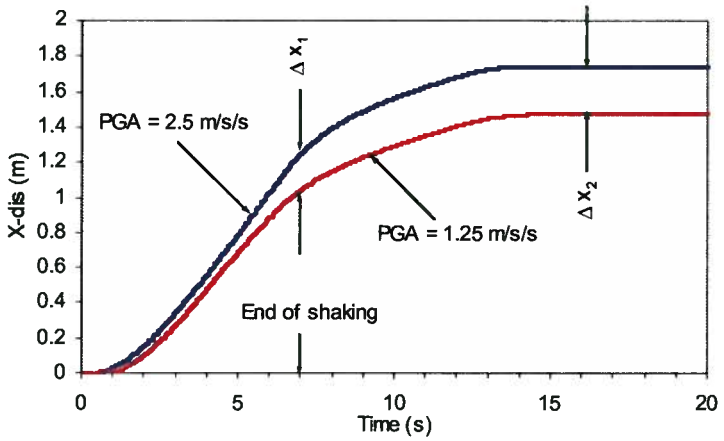

Fig. 6-22: Maximum surface lateral displacement vs. motion amplitude.

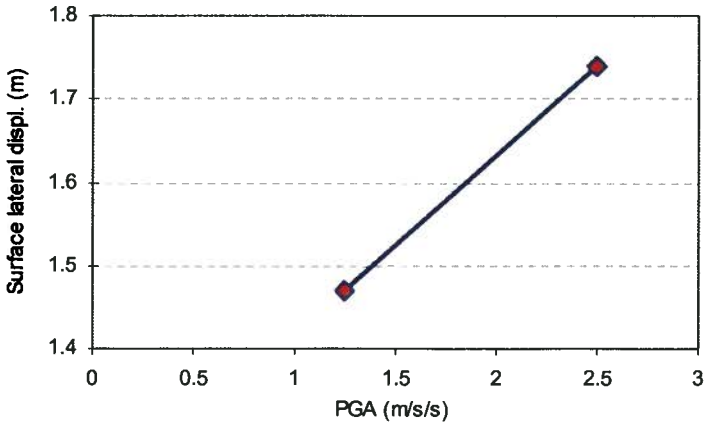

Fig. 6-23: Surface lateral displacement time histories for event 1, PGA = 2.5 m/s^2 and event 2, PGA = 1.25 m/s^2.

Kokusho (2003) conducted shaking table tests of a 2-D slope model with barrier sub-layer subjected to two motions of different amplitudes, *PGA*. He observed that the motion with higher *PGA* caused less final deformation since, during shaking, larger deformation had occurred and the post-shaking driving force was less, compared to that in the smaller event. In an infinite slope condition, the driving force remains constant, so that the event with larger *PGA* results in greater displacements.

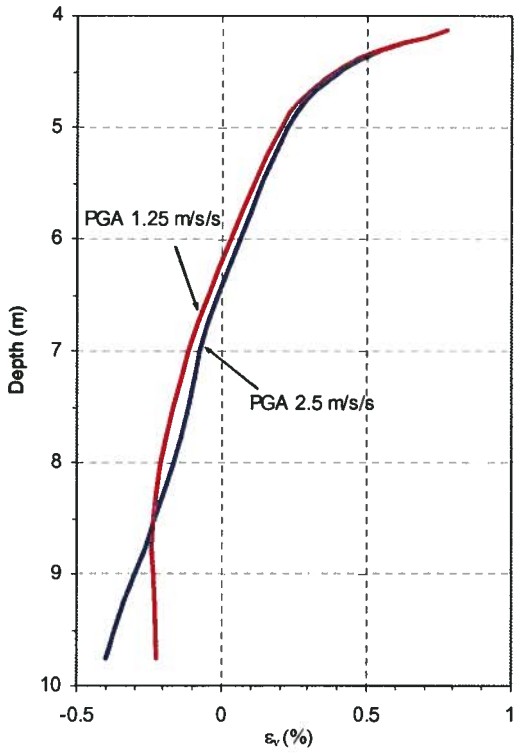

Fig. 6-24: Volumetric strain profile for event 1 and event 2.

6.2.4.2 Effects of Motion Duration

Comparison of the analyses results of event 2 and 3 reveal the effects of shaking duration. Fig. 6-26 shows the time histories of surface lateral displacement for two events. Fig. 6-27 shows maximum surface lateral displacement vs. base motion duration. By comparing the results shown in Fig. 6-22 and 6-26, the effects of motion duration are seen to be more significant if they are strong enough to produce excess pore water pressure. This implies that long moderate earthquakes can be more devastating in this regard.

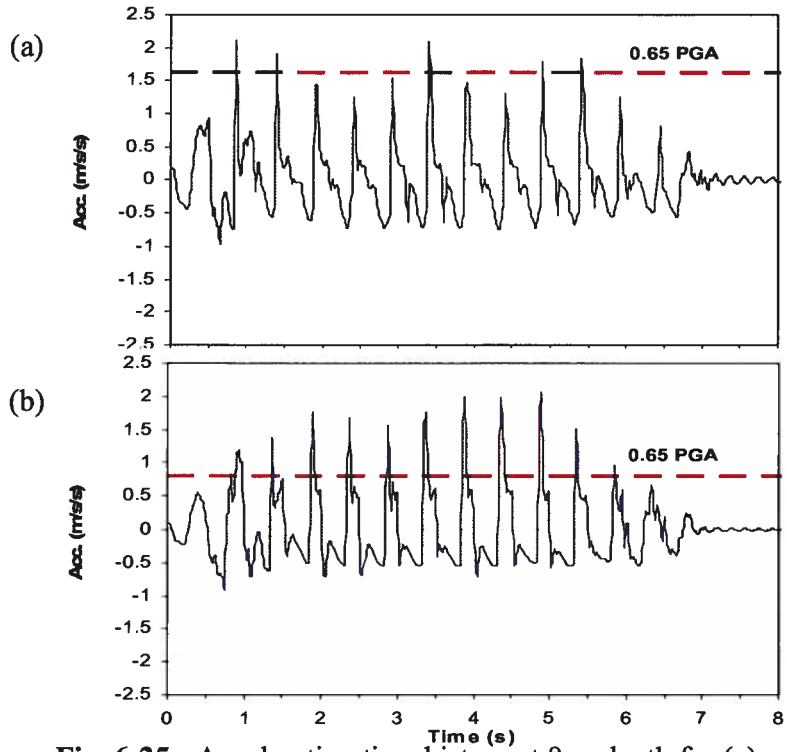

Fig. 6-25: Acceleration time history at 8 m depth for (a) event 1, *PGA* = 2.5 (m/s^2) and (b) event 2, *PGA* = 1.25 (m/s^2).

Fig. 6-28 shows the profiles of volumetric strain for the three events. A longer duration of motion results in more accumulated expelled water due to the higher No. of cycles and consequently greater expansion. As may be seen, event 3 with 14 s duration results in maximum expansion that is twice that of event 2, with 7 s duration time. Greater contraction from event 2 (PGA = 1.25 m/s^2), compared to that from event 1 (PGA = 2.5 m/s^2) is attributed to stronger transmitted motion, as observed in the previous section (Fig. 6-25). Again, that the thicknesses of the expansion zone and contraction zone in the soil profile are essentially independent of the applied motion (total volume of the expelled water) and are controlled by flow boundary conditions.

6.3 Effects of Flow Conditions

In this section, the factors that control the flow conditions involved in seismic behavior of the soil profile are discussed. These factors include: liquefiable layer thickness (flow path), permeability of the liquefied layer and barrier, permeability contrast, and barrier thickness.

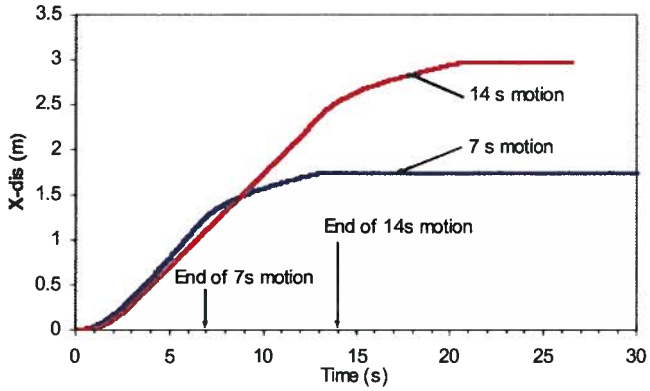

Fig. 6-26: Surface lateral displacement vs. time for event 2, and event 3.

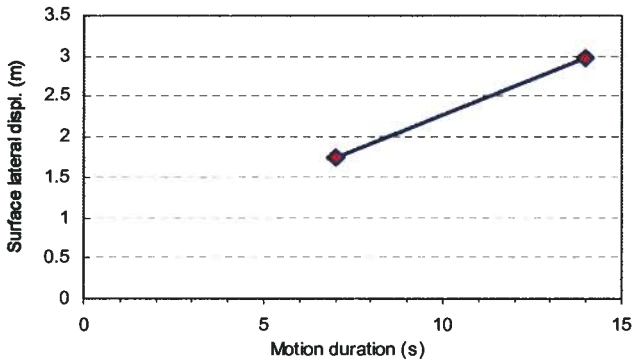

Fig. 6-27: Maximum surface lateral displacement vs. motion duration.

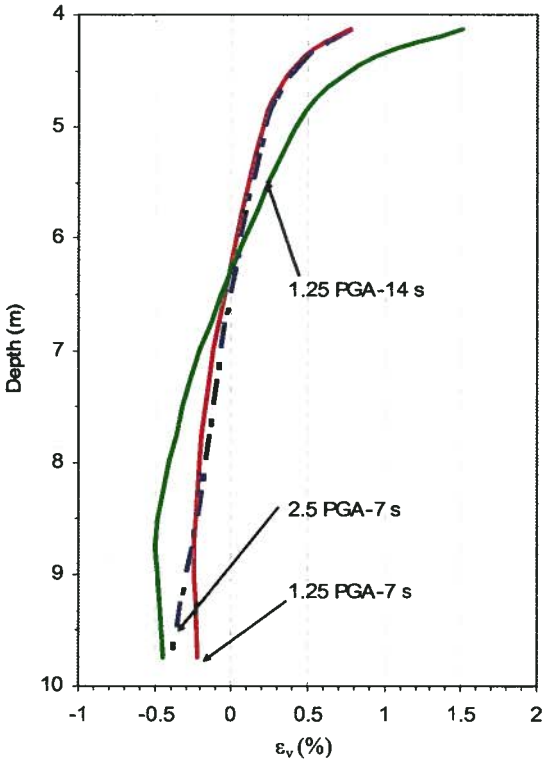

Fig. 6-28: Volumetric strain profiles for event 1, event 2 and event 3.

6.3.1 Effects of the Liquefiable Layer Thickness, T_L

The same soil profile with barrier layer at 4 m depth was analyzed while other parameters, i.e., inclination, $\alpha = 1°$, and base motion ($PGA = 2.5$ m/s^2) remained the same except for the thickness of the liquefiable soil layer, T_L, which was increased to 12 m (see Table 4-1 for soil properties). Fig. 6-29 shows the mesh used in this analysis along with the counterpart mesh (with the same base element thickness ratio) for the 6 m liquefiable soil layer. It also shows the positions of some selected elements for presenting the analysis results. Fig. 6-30 shows volumetric strain time histories for this case, together with its corresponding case from the previous analysis presented earlier (*Chapter 4*, Fig. 4-20) for discussion purposes. Essentially, they are the same, in terms of maximum values; however, they have different timing due to various flow paths. Note that the element thicknesses are twice for the 12 m soil layer. The flow path effect is also reflected in surface lateral displacement time histories, as shown in Fig. 6-31.

Thus, displacement continues for a longer time after shaking ceases (at 7 s) for the 12 m liquefiable soil layer, giving rise to larger displacements. Also, until the end of shaking, the mechanical properties mainly control the liquefiable layer response, as both time histories coincide. Afterwards, however, the flow properties are the main controlling parameters.

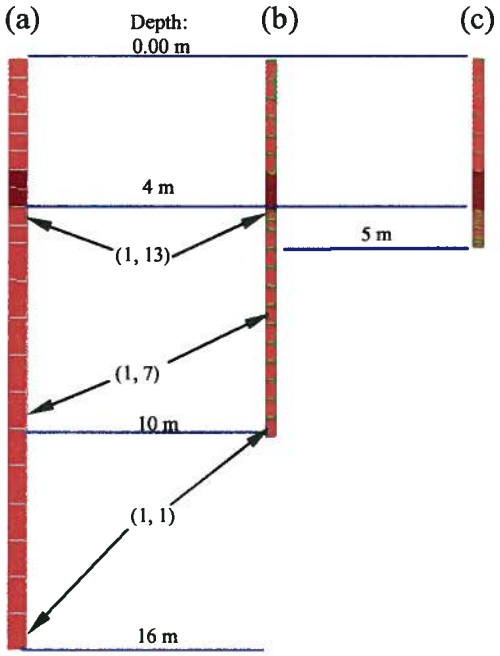

Fig. 6-29 Models used in analyses with position of elements for (a) 12 m liquefiable layer, (b) 6 m liquefiable layer, and (c) 1 m liquefiable layer.

Fig. 6-32 shows the time histories of excess pore water pressure, U_e for the bottom element (1,1) and the base element (1,13); specific vertical discharge, *Y-Flow,* for the bottom element (1,1); and the lateral surface velocity for the 12 m liquefiable soil layer case. In a companion figure (Fig. 6-33) the corresponding time histories for the 6 m liquefiable soil layer are shown. In this figure, the equalized condition for excess pore water pressure is reached after a longer time for the 12 m layer case, compared to the 6 m layer case. The same pattern is observed in the *Y-Flow* time history (the magnitude of *Y-Flow* for the 12 m layer is greater because of element size).

The surface lateral velocities are essentially the same in both cases at the end of shaking at 7 s (see Fig. 6-32c and Fig. 6-33c). Nevertheless, for the 12 m layer case, lateral movement lasts for a longer time due to the high excess pore water pressure in the barrier base element.

Another analysis was carried out for a 1 m liquefiable layer (shown in Fig. 6-29c), where the liquefied soil was modeled with 11 elements. Fig. 6-34 shows the results in terms of time histories of excess pore water pressure, *Y-Flow,* and surface lateral velocity. From the figure, that the induced excess pore water pressure in the base and bottom elements are essentially the same due to a small difference in effective stress and short flow path. The *Y-Flow is* small but sufficient to result in void redistribution. Fig. 6-35 shows the time history of volumetric strain for elements within the 1 m liquefiable layer which are similar to those of the 6 m layer and the 12 m layer. The time history of surface lateral velocity, given in Fig. 6-31c, indicates that displacement is mainly due to the inertia effect of shaking and controlled by mechanical conditions. Surface lateral displacement is much lower than in the 6 m layer, and the flow path is too short for delay deformation and inflow continuation.

Fig. 6-36 shows the profile of volumetric strain for the liquefiable layer with three thicknesses (at a stable time), where depth is normalized with respect to the liquefiable layer thickness, T_L, for comparison purposes. It indicates that all have the same pattern of expansion and contraction and also have (practically) essentially the same magnitude. The differences are attributed to the level of excitation transferred to corresponding depths of the liquefiable layers. Again, this reveals that the ratio of expansion zone to contraction zone is independent of T_L, as discussed in *Chapter 5*. This also implies that the expansion does not depend on the absolute volume of the expelled water; it is controlled by flow boundary conditions, as demonstrated in *Chapter 5* (Section 5.3.2, for the complete liquefaction case). This study suggests that large deformation is controlled by the base element expansion to a limited extent, but that the duration of expansion, which facilitates high excess pore water pressure at the barrier base, is a key factor in this regard.

Fig. 6-37 shows the variation of maximum surface lateral displacement with the square root of liquefiable soil layer thickness, T_L, and indicates a good correlation.

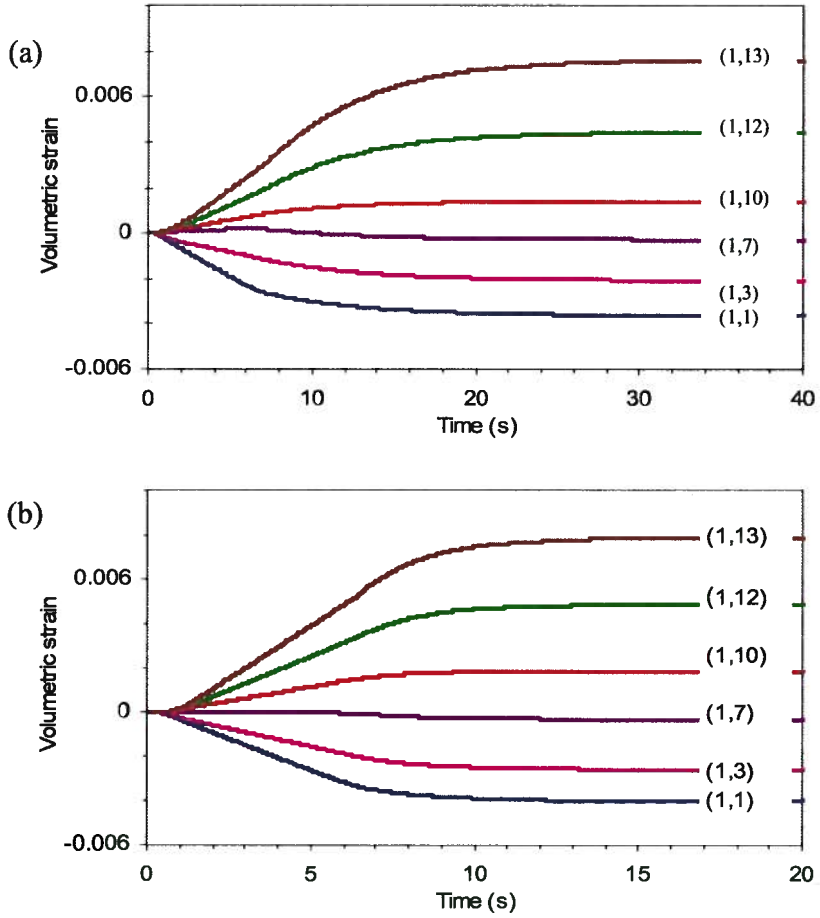

Fig. 6-30: Time histories of volumetric strain for elements at various depths (a) 12 m liquefiable layer, (b) 6 m liquefiable layer.

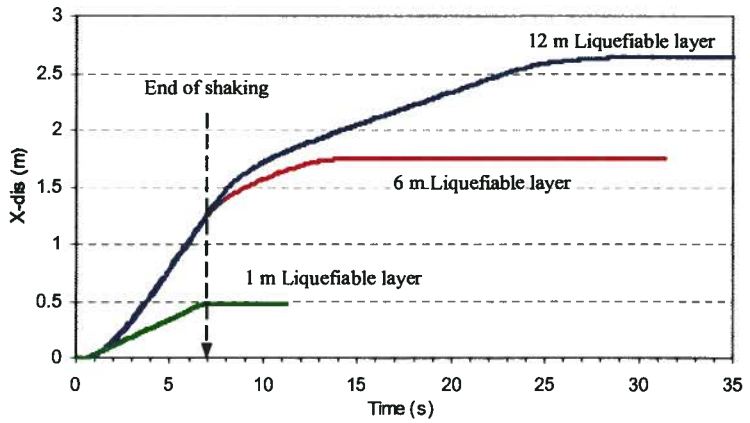

Fig. 6-31: Time histories of surface lateral displacements for 12 m, 6 m and 1 m liquefiable layer thicknesses.

The same trend of increasing displacement with the liquefiable layer thickness has been observed in centrifuge tests reported by Malvick et al. (2005). Although, these authors attributed this finding to the volume of expelled water, this is not supported by the results of the present study.

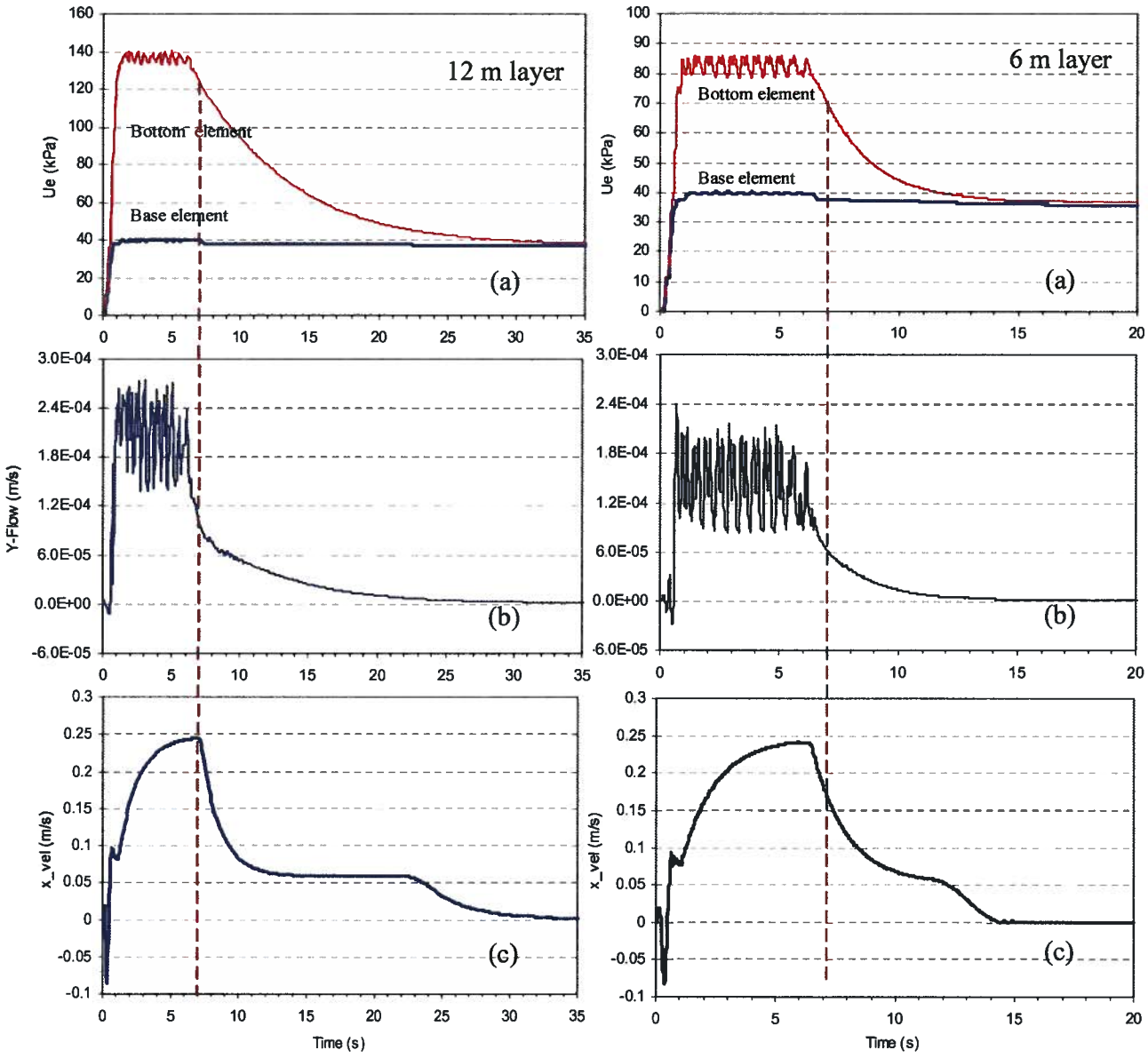

Fig. 6-32: Time history of (a) excess pore pressure, (b) specific discharge of bottom element, and (c) surface lateral velocity (12 m liquefiable layer case).

Fig. 6-33: Time history of (a) excess pore pressure, (b) specific discharge of bottom element, and (c) surface lateral velocity (6 m liquefiable layer case).

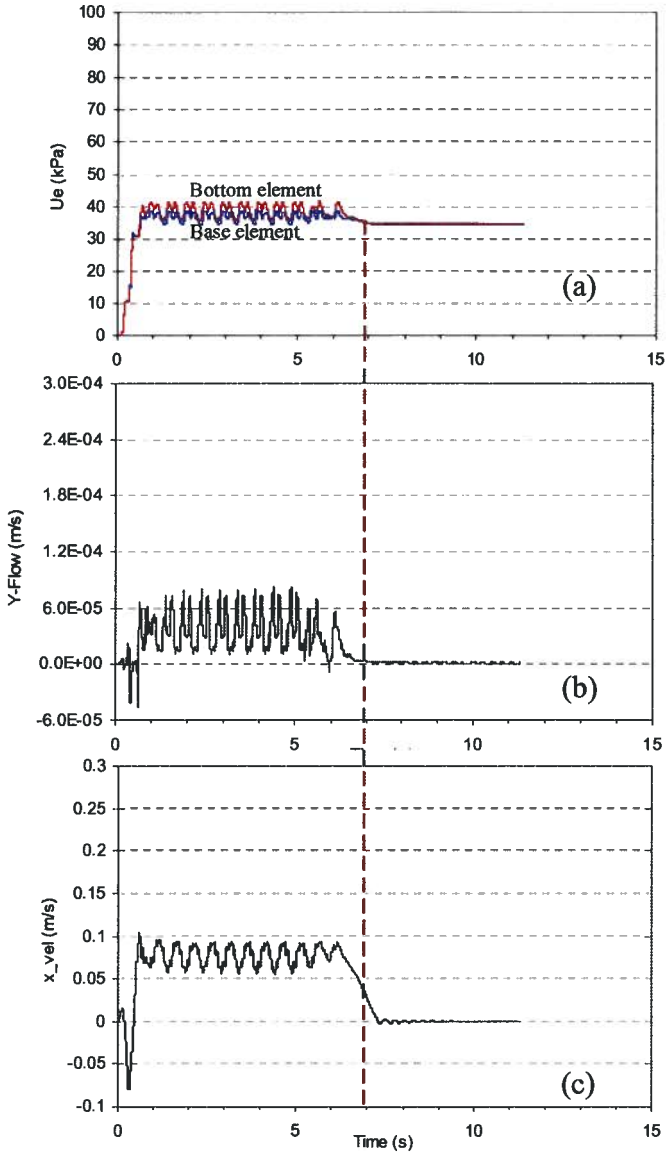

Fig. 6-34: Time history of (a) excess pore pressure, (b) specific discharge of bottom element, and (c) surface lateral velocity (1 m layer liquefiable case).

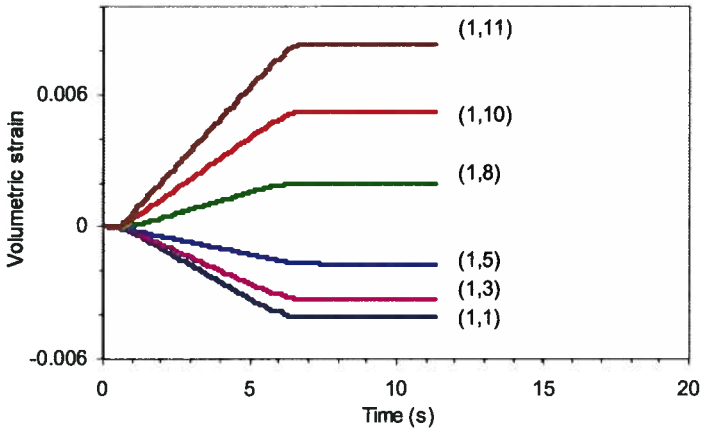

Fig. 6-35: Time history of volumetric strain for elements at various depths of the 1 m liquefiable layer.

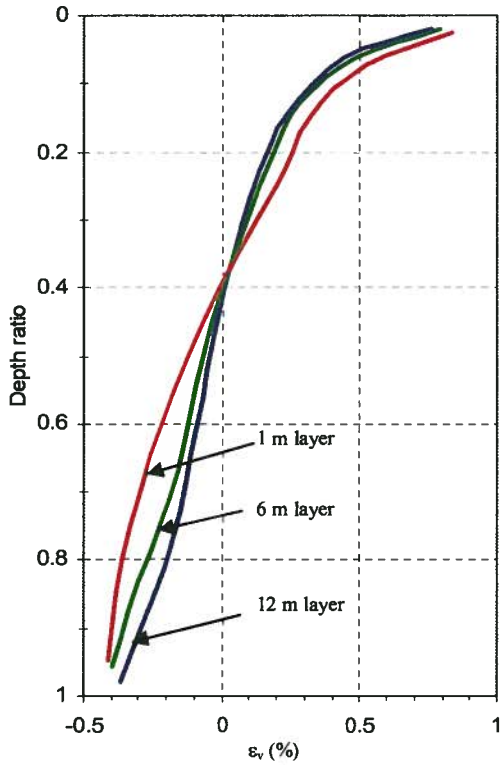

Fig. 6-36: Isochrones of volumetric strain along normalized liquefiable layer depth.

6.3.2 Effects of Decrease in Liquefiable Layer Permeability

The effects of permeability on seismic behavior of uniform liquefiable layers were discussed in *Chapter 4, S*ection 4.3. In this section, the effects of decrease in permeability of the liquefiable layer while the permeability contrast is constant (k_L/k_B = 1000) is presented. The 10 m soil profile, subjected to the harmonic base motion given in Fig. 4-7, was analyzed, with the same soil properties as in the benchmark case (listed in Table 4-1), except that the permeability; k was reduced by a certain value (e.g., 100 times). Fig. 6-38 shows the surface lateral displacement relative to the benchmark case vs. permeability, for the three analyzed cases. It indicates that the permeability reduction results in an increase in the deformations due to a lower flow rate, as in the case of the uniform layer (discussed in *Chapter 4,* Section 4.3), though the presence of the sub-layer barrier aggravates this impact.

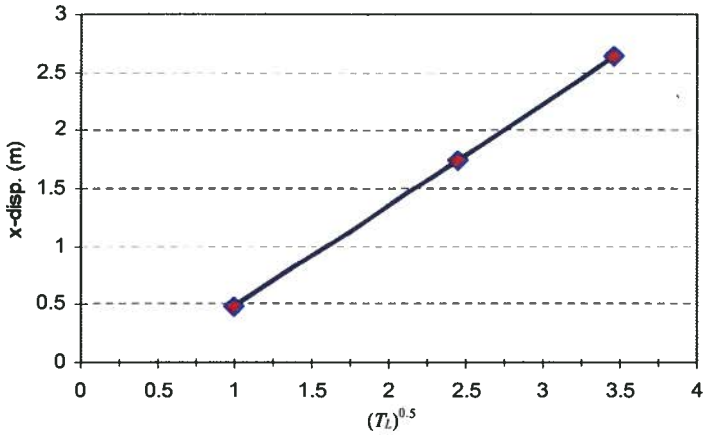

Fig. 6-37: Max. surface lateral displacement vs. $(T_L)^{0.5}$(in $m^{0.5}$).

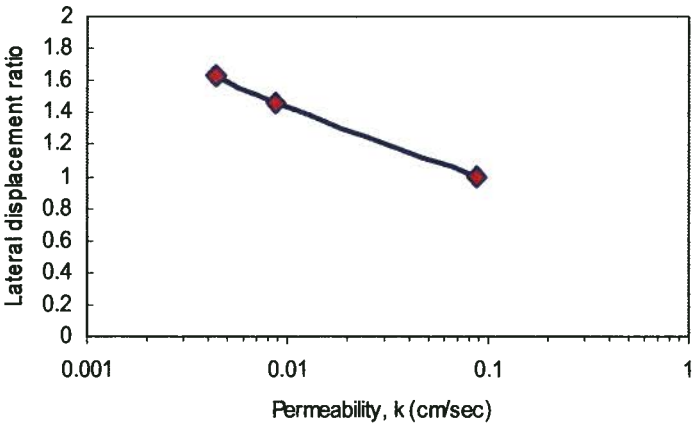

Fig. 6-38: Increase of surface lateral displacement with reduction in permeability of liquefiable soil (profile with barrier layer, PGA = 2.5 m/s^2).

6.3.3 Effects of Permeability Contrast within the Sand Layer, k_L / k_B

This section presents results of analyses that explore the effects of (hydraulic conductivity) permeability contrast between the liquefiable sand layer and the sub-layer barrier with regards to the characteristic response of the infinite slope. Permeability of the barrier layer was increased from 1000 times lower than that of the underlying sand layer (i.e. k_B/k_L = 0.001) to 10 times (i.e. k_B/k_L = 0.1) in a step-wise fashion. In addition, the thickness of the low permeability sub-layer at 4 m of the 10 m soil profile was reduced from 1 m to 0.1 m in the analyses. All other parameters, i.e., ground slope; α =1° and the base motion (i.e., harmonic with PGA = 2.5 m/s^2) were kept the same. The mesh given in Fig. 6-8b was used in the analyses.

The impacts of permeability of the barrier layer (relative to that of the liquefiable soil, permeability ratio), in terms of excess pore water pressure generation and surface lateral displacements, are presented in the following sections:

6.3.3.1 Effects of Permeability Contrast on Excess Pore Water Pressure

Fig. 6-39 demonstrates pattern changes in generation of excess pore water pressure, in terms of R_u time history, within the soil profile arising from a decrease in the permeability ratio; k_L / k_B (see Fig. 6-27b for the position of selected elements). As may be seen, excess pore water pressure is generated in the deep parts with almost the same pattern, regardless of permeability contrast. However, the dissipation rate is affected by the permeability ratio, which is more pronounced at shallower depths. This leads to high excess pore water pressures lasting for a longer time after shaking ceases, beneath the barrier, when the permeability contrast is relatively great ($k_L / k_B > 100$).

The flow condition effects on the effective stress path can be observed from Fig. 6-40, where the stress path for various k_L / k_B values are seen for the barrier base element (1, 13) in which most of deformations take place (and stabilize after 15 s). This indicates that higher k_L / k_B results in lower effective stress and consequently, lower strength.

These analyses show that permeability reduction has a substantial effect on the dissipation rate of the excess pore water pressure, particularly, for the upper parts near the barrier, and the same effect was observed earlier for a uniform layer (*Chapter 4*, Section 4.6). This impact; however, is exacerbated by the presence of the low-permeability sub-layer.

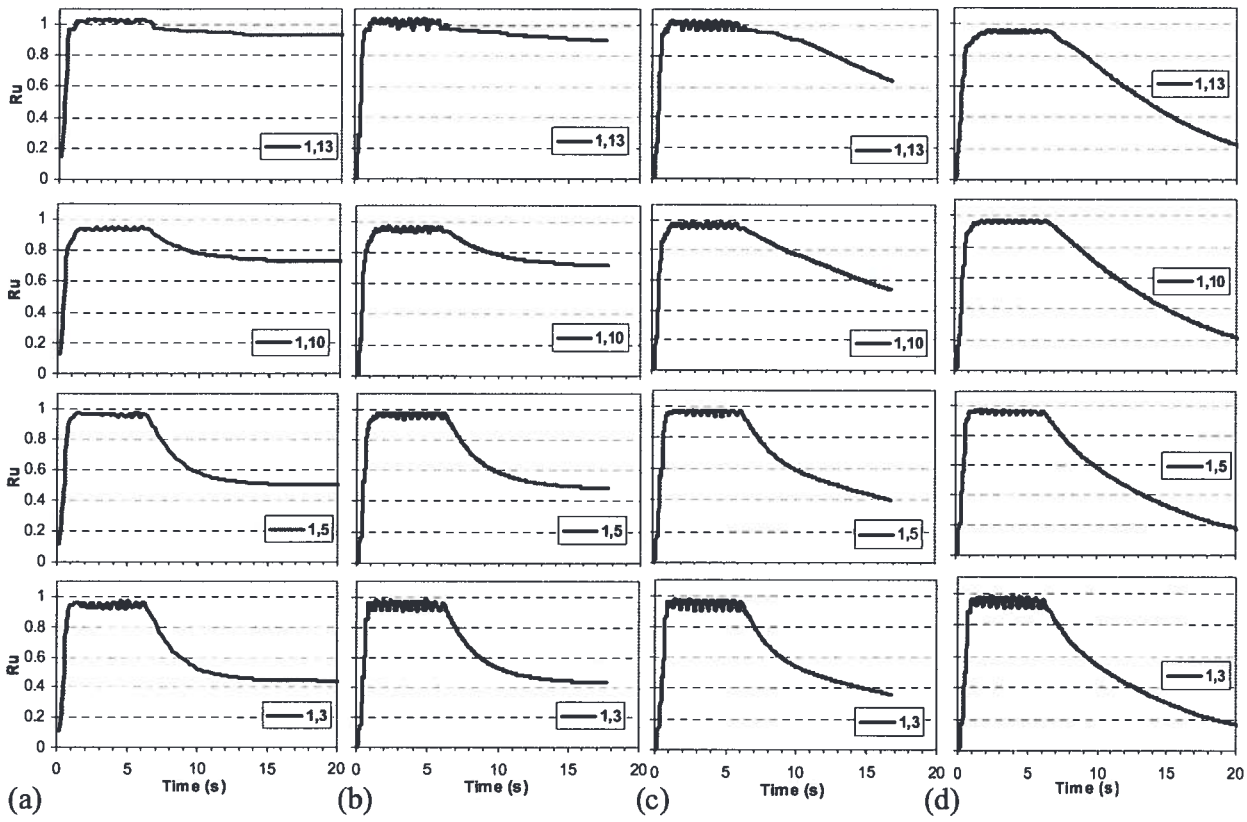

Fig. 6-39: Time histories of R_u at different depths of the soil layer for different permeability contrast, (a) k_L/k_B = 1000, (b) k_L/k_B = 100, (c) k_L/k_B = 10, and (d) k_L/k_B = 1 (no barrier).

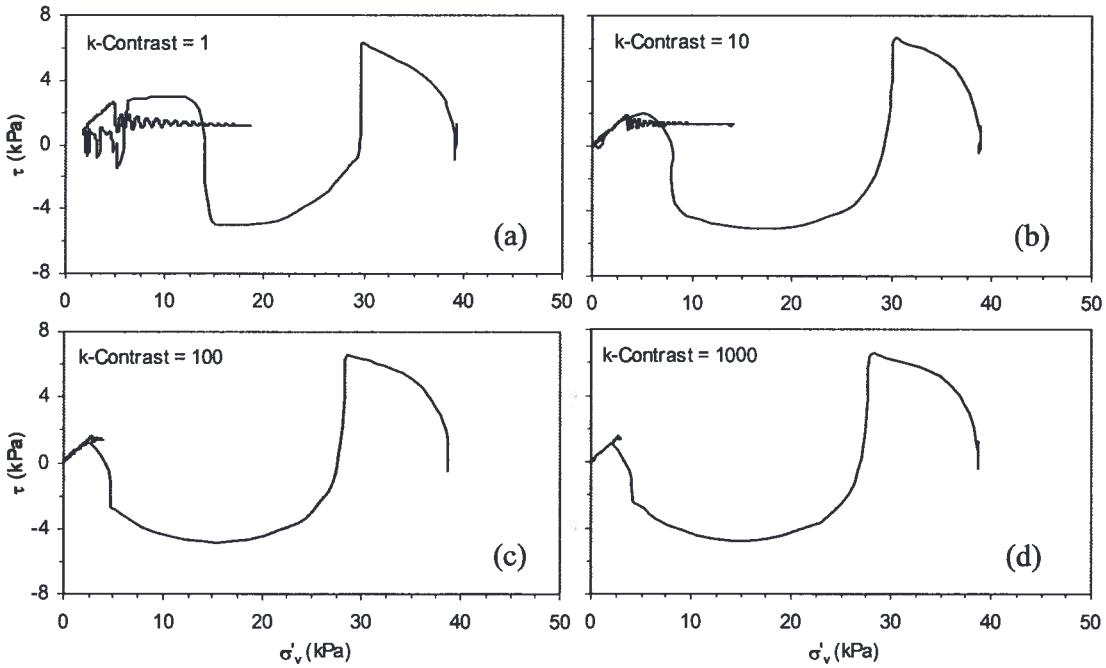

Fig. 6-40: Effective stress path for the base element for permeability contrast of (a) k_L/k_B=1, no-barrier, (b) k_L/k_B=10, (c) k_L/k_B=100, and (d) k_L/k_B=1000.

6.3.3.2 Effects of Permeability Contrast on Surface Displacements

Fig. 6-41 shows the time histories of surface lateral displacements (10 m profile) for different values for permeability contrasts, k_L / k_B. From the figure, displacements continue to increase for a longer time when the permeability ratio is higher. Also, the rate of displacement increases with the permeability ratio. Fig. 6-42 shows the effects of permeability contrast on the increase in maximum surface displacements, relative to that of uniform liquefiable soil (in percent). This suggests an essentially linear variation of displacements with logarithm of the permeability ratio.

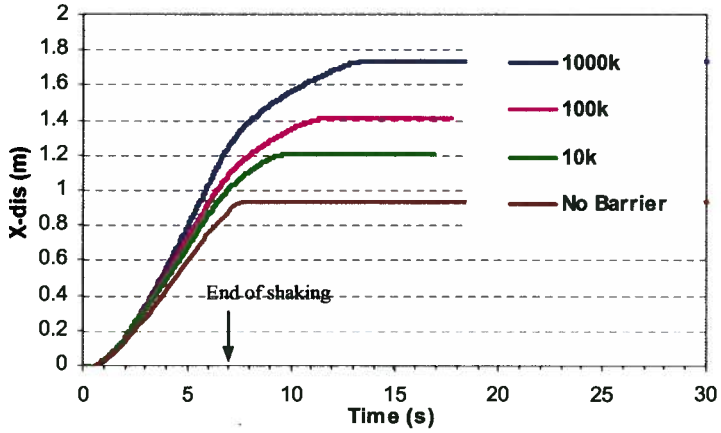

Fig. 6-41: Time histories of surface lateral displacements for different permeability contrasts (k_L/k_B).

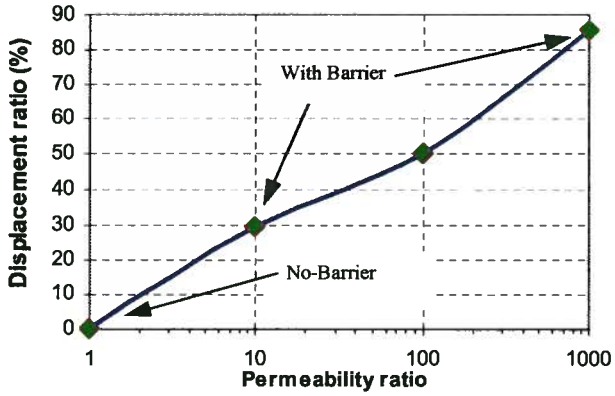

Fig. 6-42: Surface displacement difference relative to uniform soil profile (%) with permeability contrast (k_L/k_B).

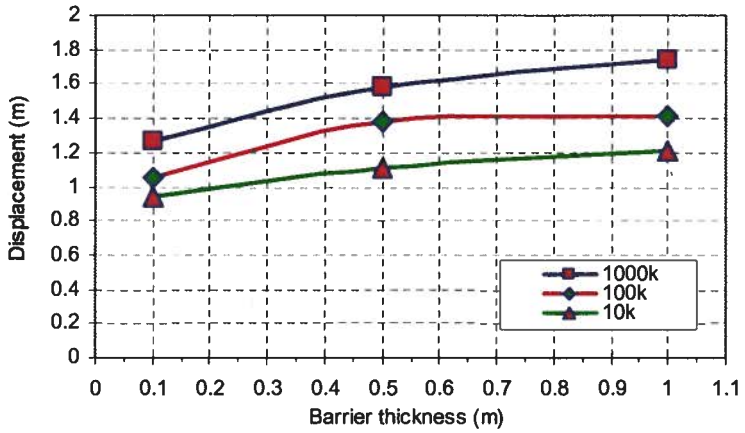

Fig. 6-43: Change of surface displacements with barrier layer thickness for different permeability contrast (k_L/k_B).

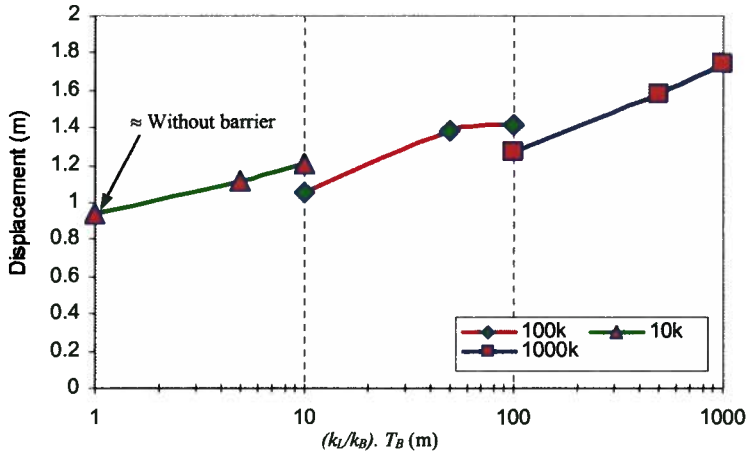

Fig. 6-44: Surface lateral displacement vs. product of permeability contrast (k_L/k_B) and barrier thickness.

6.3.4 Effects of Thickness of Barrier Layer, T_B

The effects of low permeability sub-layer thickness, in terms of surface displacements, are shown in Fig. 6-43 for different permeability ratios. An increase of barrier thickness, from 0.1 m to 1 m, results in about 40% increase in surface displacements. The rate of displacement increase with barrier thickness decreases when the barrier thickness is greater than 0.5 m for the soil profile. From the figure, the permeability ratio has almost a similar effect on displacements regardless of the barrier thickness. Fig. 6-44 shows the surface lateral displacement vs.

permeability contrast, times the barrier layer thickness. This suggests that the effect of permeability contrast is more significant.

6.4 Summary and Main Findings

This chapter presented the results of a parametric study on the effects of various mechanical and flow factors on seismic behavior of a typical liquefiable infinite slope with barrier sub-layer. According to the results, the main effects of these factors are summarized in Table 6-1:

Table 6-1: Effects of various factors on the response of liquefiable slopes with barrier sub-layer.

Factor	Influence
Ground slope	• Greater ground inclination results in larger displacements for gentle slopes due to higher driving forces (shear stress bias).
Barrier depth	• Lateral displacements increase with barrier depth due to larger shear stress bias.
Permeability contrast	• Higher permeability contrast causes stronger flow impedance and as a result greater displacements with more delay due to lower dissipation rate. • Lateral displacements increases linearly with log of permeability contrast.
Barrier thickness	• Displacements increase with barrier thickness practically linearly.
Liquefiable layer thickness	• Thicker liquefiable layer results in larger displacements due to longer duration of expansion occurring at the barrier base as a result of further flow path.
Liquefiable layer permeability	• Decrease in liquefiable permeability results in larger displacements due to lower flow rate.
Motion characteristics	• Displacements increase with motion amplitude due to greater inertia effects during shaking. • Motion duration has significant impact on increase of displacements if it is strong enough to produce excess pore water pressure leading to greater expansion.
Relative density	• Displacements decrease with increasing material relative density because of stronger mechanical properties and larger expansion potential (lower e_0).

The effects of some of these parameters were examined partly through physical model testing by other investigators (Malvick et al., 2005), and the results of this study are in agreement with those observations. In addition, the following principal findings were determined in this study:

- During the shaking period, the ground response is essentially controlled by mechanical properties. After shaking ceases; however, the flow properties control the liquefied soil layer behavior.

- Any reduction in permeability of liquefiable slopes results in displacement increase as a result of longer duration of high excess pore water pressures. Nevertheless, the presence of a barrier sub-layer exacerbates this effect due to longer times for volume expansion to occur and consequently larger expansion at the base of barrier.
- The deformation pattern with localization at the barrier base (including expansion at upper parts and contraction at lower parts) is controlled by flow boundary conditions. However, the displacement magnitude is mainly controlled by both mechanical properties (e.g., ground inclination, D_r) and flow properties (e.g., liquefiable layer thickness, T_L and permeability).
- Thicker liquefiable soil layers experience larger displacements with more delay due to the longer flow path and the continuation of net inflow at the base of barrier.
- Not only does the magnitude of expansion influence the liquefiable slope deformations but the onset time at which maximum expansion occurs is also a key factor affecting the displacements.
- For a given barrier permeability, surface lateral displacement increases linearly with barrier thickness. The analyses suggest that a minimum value for product of permeability ratio and barrier thickness is required for the manifestation of barrier effects in surface displacements.
- Shallow barrier layers result in smaller lateral displacements with less post-shaking deformations due to lower driving shear stresses.
- For a given soil, after reaching *PT,* further shaking leads to a reduction in excess pore water pressure causing a strain-hardening response during the loading phase of cyclic shearing that reduces displacement rate.
- Slopes comprising denser materials (i.e., stronger mechanical properties) exhibit a better performance during earthquakes due to higher liquefaction resistance (lower induced R_u) and also greater *maximum expansion potential.*

CHAPTER 7

BARRIER EFFECTS IN LIQUEFIABLE PARTIALLY SATURATED SOILS

7.1 Introduction

Previous chapters dealt with hydraulic barrier effects on the seismic response of liquefiable grounds under (full) saturation conditions. Recent field measurements indicate that a partially saturated condition may exist for some metres below the ground water level, hence the effects of saturation were also examined in this research. Fig. 7-1 schematically illustrates saturation variation in a typical soil layer with respect to the ground water table, along with profiles of shear wave and compression wave velocities. To date, the majority of investigations on liquefiable grounds have focused on fully saturated soils and assume that a complete saturation condition exists beneath the water table.

This chapter presents the results of an investigation on the effects of partial saturation (approximate saturation greater than 85%) on a typical liquefiable ground response. The soil layer response to seismic excitation was examined in terms of excess pore water pressure and deformations. The investigation was extended to soil layers comprising the low permeability sub-layer. Finally, the findings from this study are used to explain the behavior of the liquefiable soil layer at the Wildlife Experimental Array (WLA) site (California, US) during the 1987 Superstition Hill earthquake.

7.2 Facts pertaining to the Partially Saturated Condition

Recent field data, including compression wave velocity, V_p, measurements indicate that a partial saturation condition may exist below ground water level for a few metres (e.g., 5 m). This condition arises from the inclusion of air bubbles in on-land deposits (Ishihara et al., 2001; Nakazawa et al., 2004; Okamura et al., 2006; and Tsukamoto et al., 2007) or gas bubbles in

marine sediments and oil sands (Mathiroban & Grozic, 2004). For example, Ishihara et al. (2001) reported V_p = 1200 to 1300 m/s measured down to about 7 m below the water table in Niigata city. Fig. 7-2 shows field profiles of the compression wave velocity, V_p, measured in various types of soils in Japan.

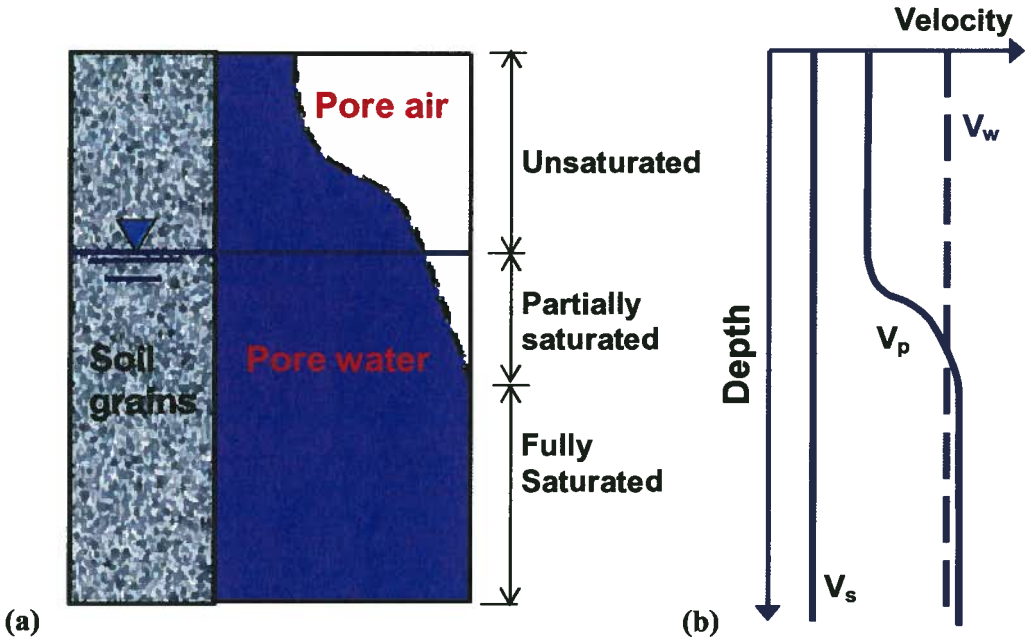

Fig. 7-1: (a) schematic profile of saturation condition in a typical soil layer, (b) profile of shear wave and compression wave velocity compared with that of water (V_w = 1500 m/s).

A few investigators (e.g., Yang & Sato, 2001; Pietruszczak et al., 2003; Atigh & Byrne, 2004; Mathiroban & Grozic, 2004; Yang et al., 2004; Sawada et al., 2006; and Seid-Karbasi & Byrne, 2006a) recently addressed the effects of a partial saturation condition on liquefiable ground response and its consequences.

In general, the condition of partial saturation can produce two major impacts on the seismic ground response, as noted by Yang (2002). The first, which is related to liquefaction, causes a greater resistance of soil to liquefaction onset. The other is that partial saturation can cause larger amplification in the vertical component of the ground motion, as demonstrated numerically by Yang & Sato (2001). The authors attributed the amplification in the vertical acceleration component, observed during the 1995 Kobe earthquake in Japan and recorded by an instrumented array (in a reclaimed island), to this effect (see Fig. 7-3). In the figure, the profile of recorded peak ground accelerations in three directions indicates amplification of surface ground

acceleration in the vertical direction, whereas, de-amplification occurs in the horizontal components (i.e., EW, NS).

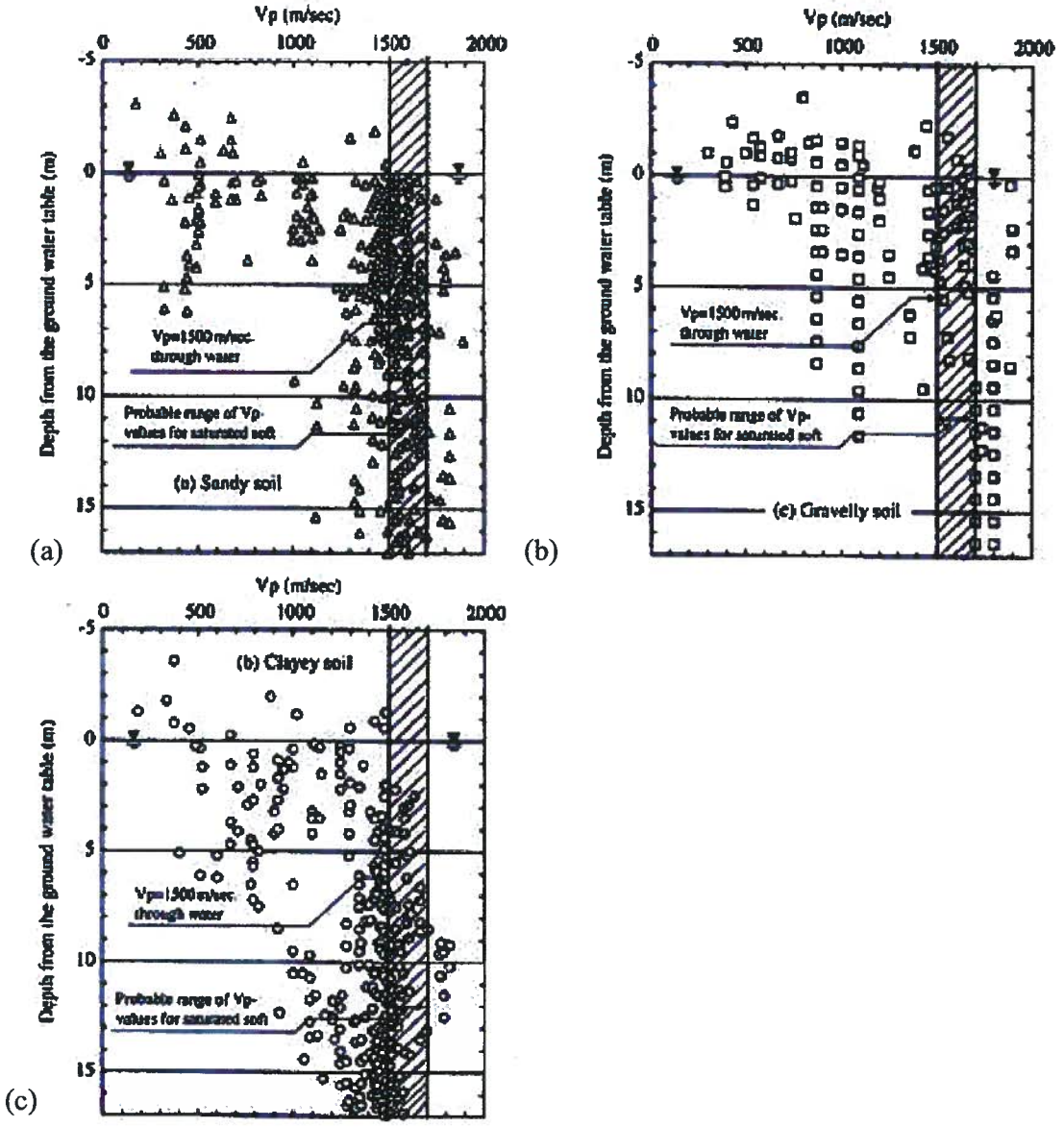

Fig. 7-2: Measured compression wave velocity in various soil types (Ishihara et al., 2004, reproduced by permission of Taylor & Francis Group, LLC, a division of Informa Plc.).

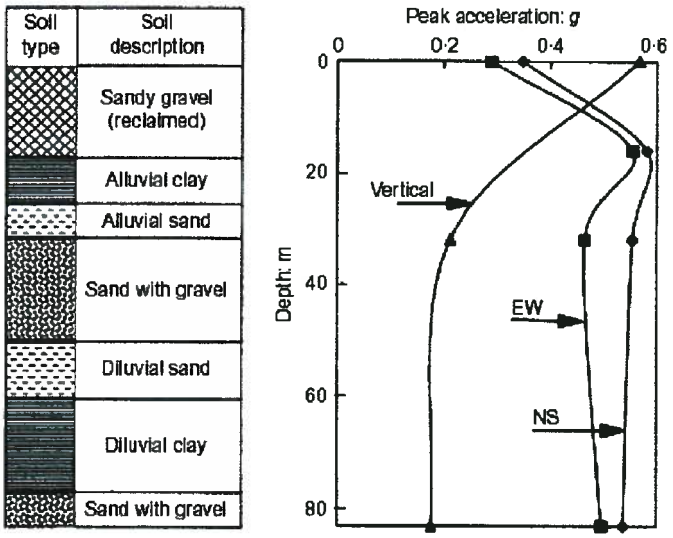

Fig. 7-3: Distribution of recorded peak accelerations with depth in three components (Yang & Sato, 2001).

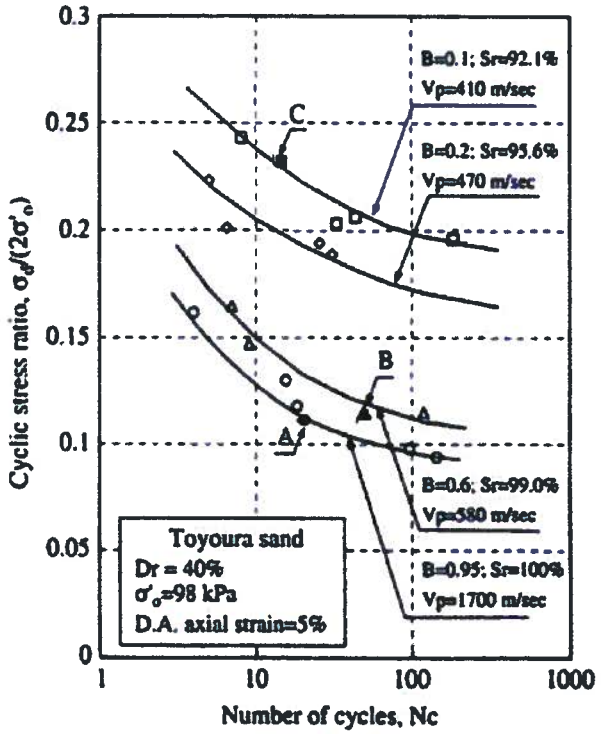

Fig. 7-4: Cyclic stress ratio vs. No. of cycles for Toyoura sand (Ishihara et al., 2004, reproduced by permission of Taylor & Francis Group, LLC, a division of Informa Plc).

Laboratory test data suggests that the resistance of sands to liquefaction onset increases as saturation decreases (e.g., Yoshimi et al., 1998; Ishihara et al., 2001 & 2004; Yoshimichi et al., 2002; Yang, 2002; and Yang et al., 2004). Fig. 7-4 shows cyclic stress ratio, *CSR*, vs. number of cycles required for liquefaction of Toyoura sand at different saturation states, S_r, that is evaluated in terms of *Skempton's B* value.

The saturation condition of soil samples in laboratory can be evaluated by measuring *Skempton's B* ($= \Delta u/\Delta\sigma_m$) value and/or the compression wave velocity, V_p. In the field, saturation is evaluated by measurements of the compression wave velocity V_p.

For an elastic dry soil, medium compression wave velocity, V_p and shear wave velocity, V_s are expressed as Eq. 7-1 and 7-2:

$$V_p = \sqrt{\frac{K_{ske} + 4G/3}{\rho}} \qquad [7\text{-}1]$$

$$V_s = \sqrt{\frac{G}{\rho}} \qquad [7\text{-}2]$$

where, K_{ske}, G, and ρ are material (skeleton) bulk modulus, shear modulus, and density, respectively. If the soil pores are filled with fluid, and assuming incompressible grains, (*Biot's* coefficient = 1) then the total bulk modulus of material ($K = K_{ske} + K_f/n$) should be used in Eq. 7-1 as given by Eq. 7-3.

$$V_p = \sqrt{\frac{4G/3 + K_{ske} + K_f/n}{\rho}} \qquad [7\text{-}3]$$

where K_f and n are fluid bulk modulus and porosity, respectively. Total soil density should be used in this condition. V_p can also be expressed in terms of *Skempton's B* value (Yang, 2002) as:

$$V_p = \sqrt{\frac{4G/3 + K_{ske}/(1-B)}{\rho}} \qquad [7\text{-}4]$$

Laboratory tests for Toyoura sand, reported by Tsukamoto et al. (2002) and Ishihara et al. (2004), imply that the *P-wave* velocity, V_p tends to increase from 500 m/s to about 1800 m/s when saturation varies from about 90% to 100%.

A large number of studies have been carried out to investigate the soil-water characteristic curve to quantify soil properties e.g., permeability in unsaturated conditions. Fredlund & Rahardjo (1993) and Lu & Likos (2004) provide a comprehensive catalogue in this regard. These studies suggest that sand permeability due to saturation decrease would be 70% at 80% saturation (e.g., Brooks & Corey, 1964). Therefore, regarding the uncertainty involved in permeability determination, the permeability change due to saturation variation was not considered in this study and its effects are postulated to be insignificant.

7.3 Modeling Pore Air Fluid

The effects of free air/gas within the soil voids are accounted for by considering the bulk stiffness of the air-water mix in the pores as a single entity. The stiffness of the water is known and constant, and the stiffness of the gas can be determined based on *Boyle's gas* law. The stiffness of the combined air-water mix can be computed by appropriately combining the components of stiffness. Fredlund & Rahardjo (1993) argued that for degrees of saturation higher than 85%, where free gas exists in occluded (bubble) form, *Terzaghi*'s effective stress concept can be applied; in other words, surface tension is neglected. The same approach was adopted by Atigh & Byrne (2004) and by Mathiroban & Grozic (2004) for analyzing submarine failures in gassy sands.

7.3.1 Bulk Modulus of Water-Air Mixture and its Pressure-Level Dependence

The amount of pore gas is related to *Skempton's B* value, and the stiffness of the fluid is related to the amount of gas present; hence, the *B* value. Pore gas pressure and volume change respond in accordance with *Boyle's law*, and *Henry's law* governs the dissolving of free gas into the water.

Assuming negligible volume change for the soil solid component ($\Delta V_s = 0$) and no escape of gas (air) from the water-gas mixture, the following equations for fluid mix stiffness can be derived (see *Appendix IV* for details).

$$K_{mix} = \frac{1}{\frac{1}{P_{abs}}(1-S_r)+\frac{1}{K_w}S_r} \qquad [7\text{-}5]$$

$$\frac{K_{mix}}{K_w} = \frac{1}{\frac{K_w}{P_{abs}}(1-S_r)+S_r} \qquad [7\text{-}6]$$

Where

U_{gas}, u and P_{abs} are: absolute pore gas pressure, (relative/gauge) pore water pressure, and atmospheric pressure, respectively.

K_w, K_{gas}, and K_{mix} are: bulk modulus of water, gas, and mixture, respectively.

The value of K_{mix}, based on Eq. 7-5, for two extreme cases of S_r = 100% and S_r = 0, are equal to K_w and P_{abs}, respectively. Eq. 7-6 expresses K_{mix} ratio to water, K_w, that is equal to 2 GPa. In fact, K_{mix} represents an equivalent fluid to the water-gas mixture. Fig. 7-5 shows the change of the ratio of mix bulk modulus to that of pure water with saturation degree, for different (absolute) pore air pressures. From the figure, the mix bulk modulus dramatically falls due to a small reduction in saturation.

It can readily be inferred from Eq. 7-6 that the contribution of water bulk modulus in K_{mix} magnitude is negligible ($1/K_w \approx 0$), and the K_{mix} value can be determined according to the (absolute) pore fluid pressure approximately, hence:

$$K_{mix} \cong \frac{P_{abs}}{1-S_r} < K_w \qquad [7\text{-}7]$$

Fig. 7-6 compares the variation of mix bulk modulus with saturation under a (gauge) pore fluid pressure of 100 kPa (P_{abs} = 200 kPa), derived from rigorous and approximate equations. It reveals that a small error (less than 10% for S_r = 99.9%) is involved in Eq. 7-7 (the deviation of triangle points from circle centers is an error measure).

Eq. 7-5 and Eq. 7-7 assume that no gas dissolution into water occurs as the gas pressure changes. If there is enough time for dissolution to occur, the effect can be considered using *Henry's law*. Since *Henry's law* will change S_r to (S_r + hS_r) in Eq. 7-7, h = ±0.02 for an air-water

mixture, where h is *Henry's* volumetric coefficient of solubility (Atigh & Byrne, 2004). The effect of *Henry's law* is very small, as shown by Jafari & Popescu (2007) and is not considered in this study.

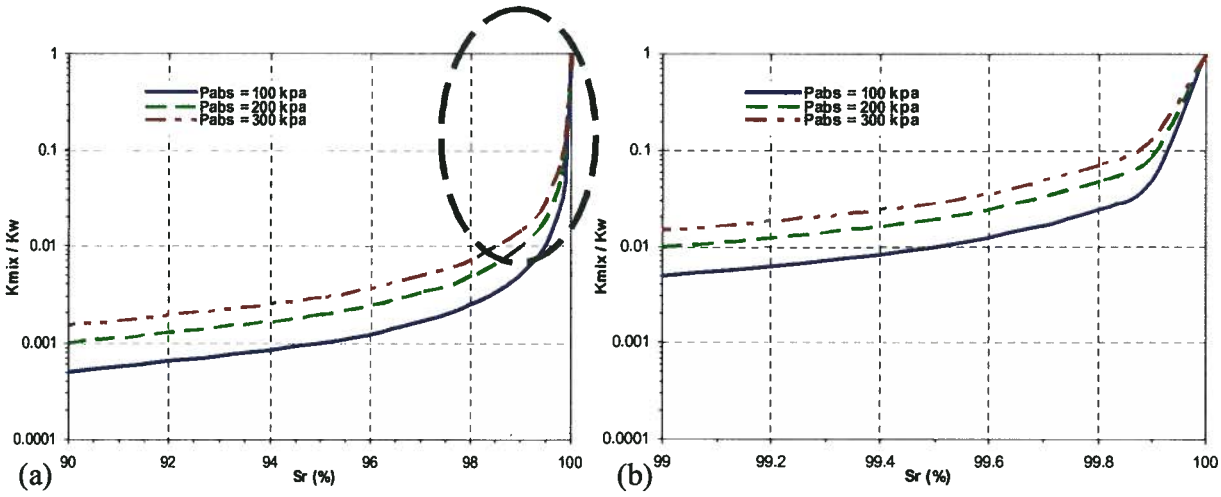

Fig. 7-5: Variation of air-water mix bulk modulus for different pore air pressures vs. saturation degree, (a) for saturation degree higher than 90%, (b) near fully saturation (> 99%).

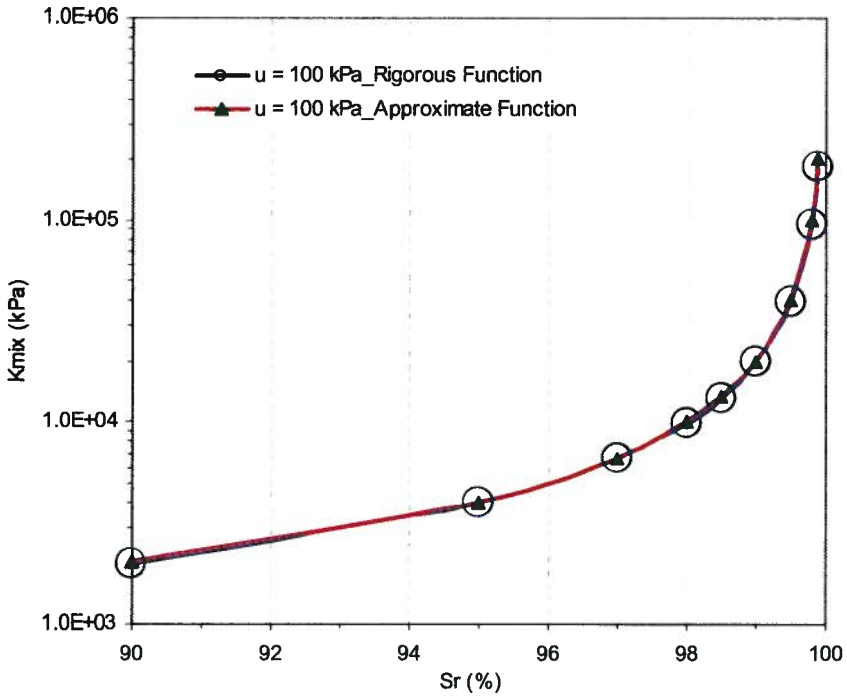

Fig. 7-6: Bulk modulus of water-air mix vs. saturation for 100 kPa pore fluid (gauge) pressure derived from rigorous and approximate relationships represented by circles and triangles, respectively.

The mix stiffness, K_{mix}, expressed in Eq. 7-7, will change as the pore water/gas pressure changes, which can be accounted by:

$$\frac{(K_{mix})_1}{(K_{mix})_0} = \frac{(P_{abs})_1}{(P_{abs})_0} \cdot \frac{(1-S_r)_0}{(1-S_r)_1} \qquad [7\text{-}8]$$

For a unit volume of soil, and neglecting porosity change, one can derive the volume of gas, V_a, at different absolute pore gas pressures, based on *Boyle's law* as follows:

$$P_1 \cdot V_1 = P_2 \cdot V_2 \qquad [7\text{-}9]$$

$$V_a = n\,.\,(1\text{-}S_r) \qquad [7\text{-}10]$$

$$P_0 \cdot n\ (1-S_r)_0 = P_1 \cdot n \cdot (1-S_r)_1 \qquad [7\text{-}11]$$

$$\frac{(1-S_r)_0}{(1-S_r)_1} = \frac{(P_{abs})_1}{(P_{abs})_0} \qquad [7\text{-}12]$$

$$\frac{(K_{mix})_1}{(K_{mix})_0} = \frac{(P_{abs})_1^2}{(P_{abs})_0^2} \qquad [7\text{-}13]$$

Eq. 7-13 reveals that the bulk modulus of the air-water mixture is (absolute pore) pressure level-dependent and the initial (absolute) pore air pressure strongly affects its magnitude. Hence, if the pore air/fluid pressure increases, as is the case during a seismic excitation, the pore-fluid bulk modulus increases accordingly.

7.3.2 *Skempton's B* Value for Partially Saturated Soils

Skempton's B value, which is a measure indicating soil pore fluid pressure response (Δu) to mean total stress change ($\Delta\sigma_m$), as defined by Eq. 7-14 (Skempton, 1954), can be expressed by Eq. 7-15. By substituting K_{mix} for partially saturated soil, one may derive Eq. 7-16 (see *Appendix V* for details):

$$B = \frac{\Delta u}{\Delta \sigma_m} \qquad [7\text{-}14]$$

$$B = \frac{1}{1 + n\dfrac{K_{ske}}{K_{mix}}} \qquad [7\text{-}15]$$

$$B = \frac{1}{1 + n\dfrac{K_{ske}}{K_w}S_r + n\dfrac{K_{ske}}{P_{abs}}(1 - S_r)} \qquad [7\text{-}16]$$

where:

Δu: pore fluid pressure change

$\Delta\sigma_m$: mean total stress change

n: porosity

S_r: Saturation

P_{abs}: absolute pore fluid pressure

K_{ske}: skeleton bulk modulus, and

K_w: water bulk modulus

Skempton's B value thus depends on the skeleton bulk modulus, K_{ske}, (absolute) pore air pressure, P_{abs}, and saturation, S_r (neglecting porosity change). From Eq. 7-15, the B value may be inferred to increase with pore mixture modulus, K_{mix}, that, in turn, rises with the absolute pore fluid pressure, P_{abs} (see Eq. 7-13). Therefore, a greater pore water/air pressure results in a higher B value.

Fig. 7-7 shows the typical variation of *Skempton's B* value with degree of saturation for different skeleton bulk modulus, K_{ske}, for a 100 kPa (relative) pore water/air pressure condition for *Poisson's ratio,* μ of 0.2. The effects of *Poisson's ratio* on *Skempton's B* value may be seen from Fig. 7-8, which shows its variation with saturation for different values of μ for a typical condition of G = 43830 kPa ($\approx V_s$ =150 m/s). Thus, a larger μ leads to a lower *Skempton's B* value; however, saturation has an increasing effect.

The above argument, for partially saturated sands, suggests that:

- The bulk modulus of pore fluid of a water-gas mixture increases with saturation; this feature is more pronounced near the fully saturated condition.
- The bulk modulus of pore fluid of a water-gas mixture increases with the rise in pore water/air pressure accordingly; this is the case during an earthquake shaking.
- *Skempton's B* value and soil saturation increase with the rise in pore water/air pressure.

7.4 Analyses Results

In the next sections, the effects of the partial saturation condition on liquefiable ground response is explored using water-air mix bulk modulus in the analyses. First, the capability of this procedure to capture the main features of a typical partially saturated sand response to cyclic loading is demonstrated by simulating cyclic element tests. Then, results for a partially saturated liquefiable soil layer are presented.

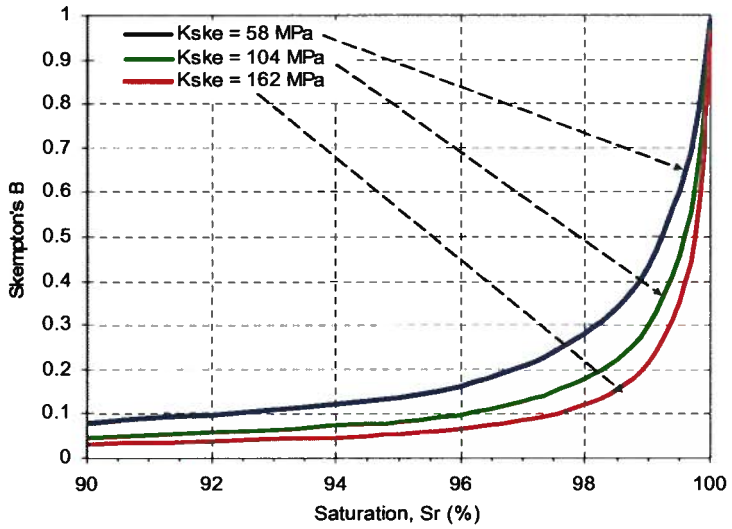

Fig. 7-7: Variation of *Skempton's B* value with saturation for different skeleton bulk modulus ($\mu = 0.2$, $u = 100$ kPa).

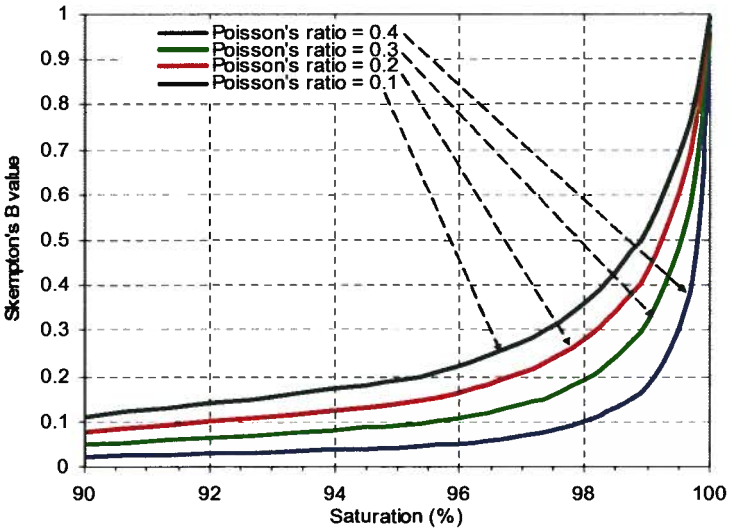

Fig. 7-8: Variation of *Skempton's B* value with saturation for different *Poisson's ratio,* μ ($G = 43830$ kPa, $u = 100$ kPa).

7.4.1 Element Tests

A set of analyses was conducted to simulate the response of a typical partially saturated sand in a cyclic simple shear test to examine the pattern of predicted liquefaction resistance. Fig. 7-9 shows results of the analysis to capture Toyoura sand behavior during cyclic loading. The results are presented in terms of *CSR* vs. number of cycles for liquefaction (onset of shear strain of 3.75% or R_u = 95%), assuming 98 kPa as the initial (back pressure/relative) pore water/air pressure. In the figure, test results for Toyoura sand (reported by Ishihara et al., 2004) are also shown. For the sake of comparison, *Skempton's B* value was used as a fundamental criterion for saturation, which is a direct measure of pore fluid response to applied load. The analyses results show a similar trend in *CSR* for the partially saturated condition.

Fig. 7-10 shows predicted variation of *Skempton's B* value and fluid bulk modulus with sample saturation, which indicates a similar trend of increase in both values during cyclic loading as a result of saturation increase. Fig. 7-11 shows a similar trend for change in K_{mix} as seen in Fig. 7-5.

Variation of pore (fluid) pressure ratio, R_u, saturation, *Skempton's B* value and fluid bulk modulus, K_{mix} during cyclic shearing (up to 100 cycles) predicted by *FLAC* analysis are shown in Fig. 7-11. All variables show the same trend of increase during cyclic loading. As expected, the partially saturated condition results in a drastic increase of liquefaction resistance. Regarding this effect, recently, a few researchers have suggested using partial saturation as a possible measure for liquefied ground improvement (e.g., Pietruszczak et al., 2003 and Yegian et al., 2007).

Fig. 7-12 shows variation of R_u, vs. number of cycles normalized with respect to number of cycles to liquefaction for different initial saturation conditions. At a given normalized No. of cycles, despite initial lower bulk modulus of pore fluid for samples with less saturation, rate of R_u rise is greater for cases with lower saturation due to greater increase in bulk modulus of pore fluid. Obviously, the required No. of cycles for samples with lower saturation is much greater.

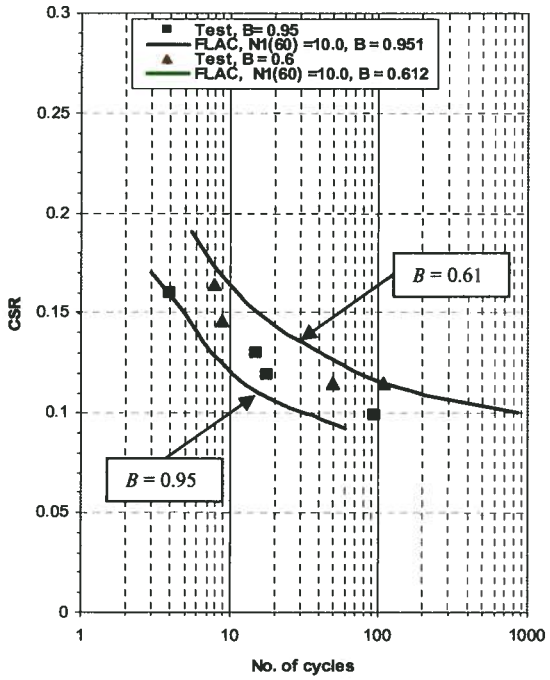

Fig. 7-9. Trend of model prediction for *CSR* with No. of cycles required for liquefaction for fully saturated ($B = 0.95$) and partially saturated Toyoura sand ($B = 0.61$) compared to test data.

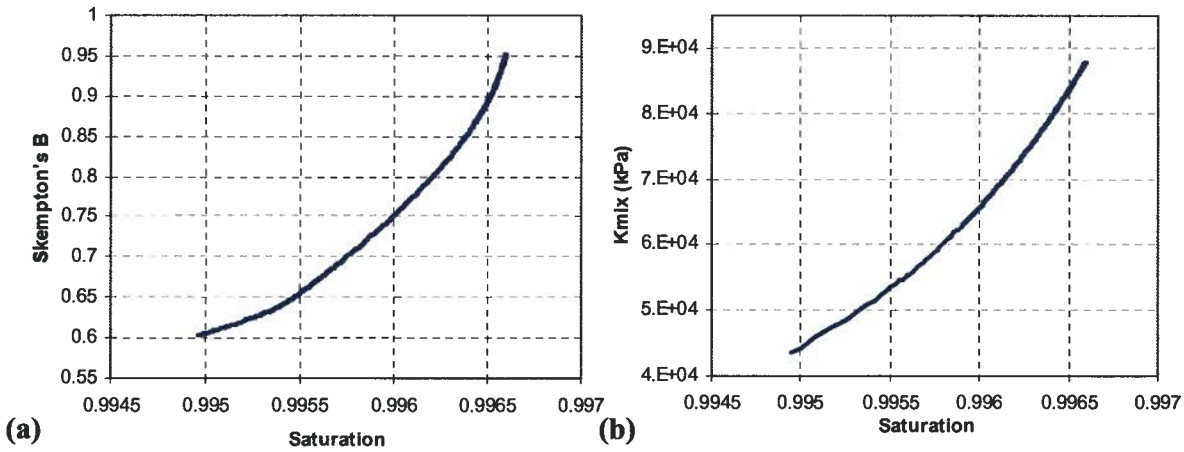

Fig. 7-10: Effect of saturation change during cycling on (a) *Skempton's B* value, (b) fluid bulk modulus (analysis results for sand element testing).

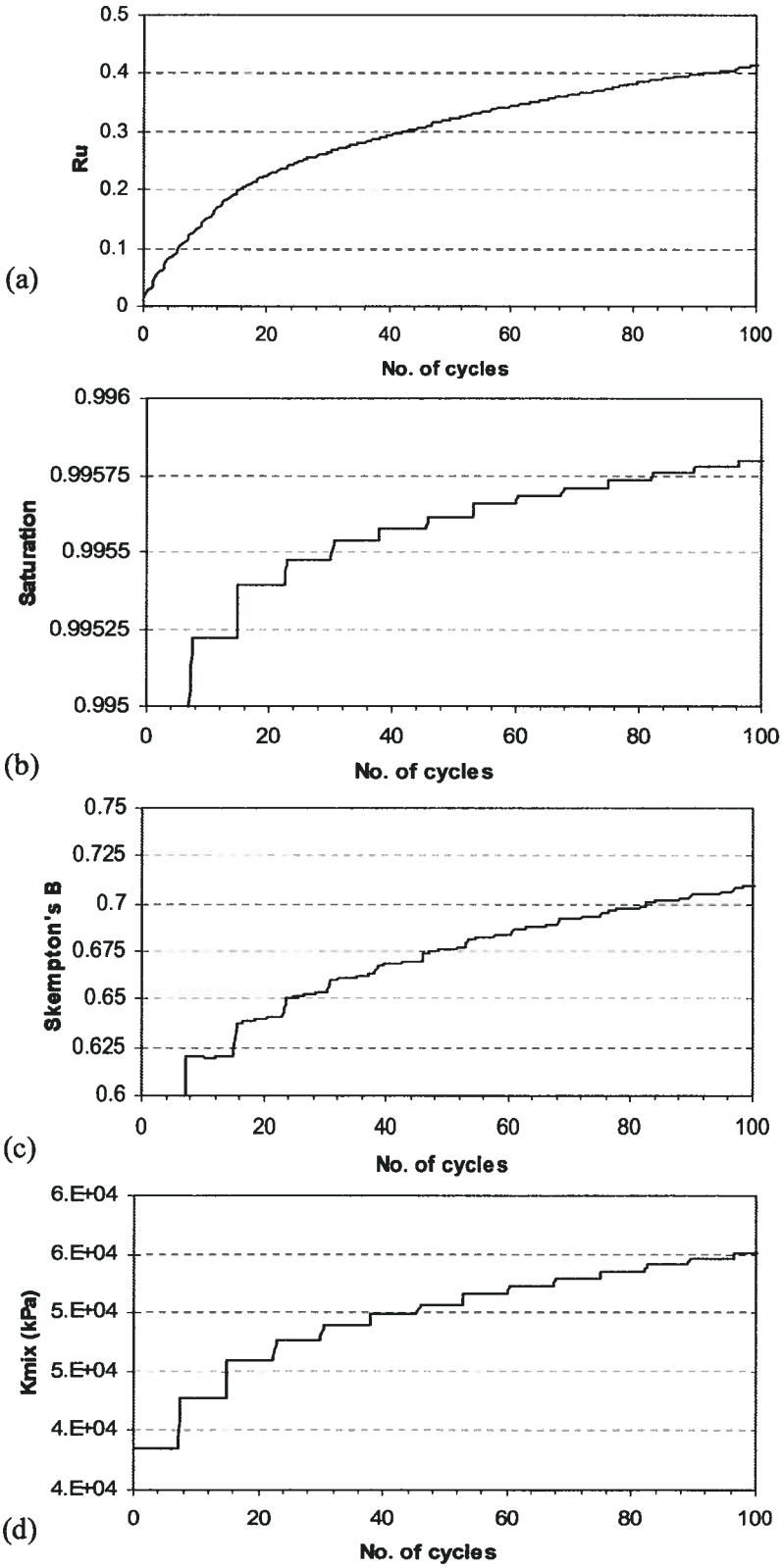

Fig. 7-11: Typical predicted response of partially saturated soil sample to cyclic shearing, (a) R_u, (b) saturation, (c) *Skempton's B* value, and (d) pore fluid bulk modulus.

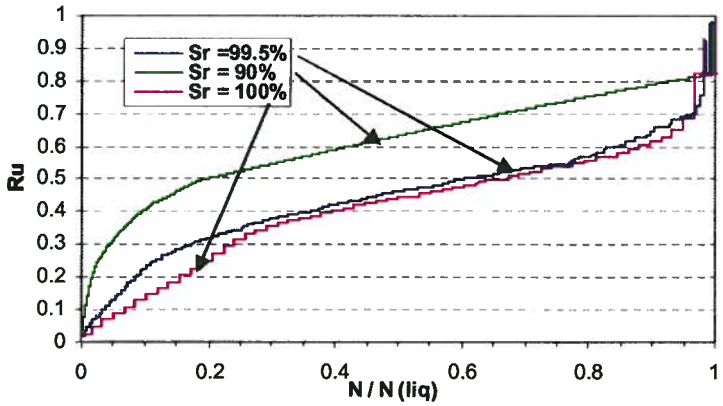

Fig. 7-12: R_u rise vs. normalized No. of cycles for different initial saturation conditions predicted by element test *FLAC* simulation.

7.4.2 Soil Profile without Barrier

The effects of the partial saturation condition were investigated for the 10 m-uniform soil layer with 1° inclination (without low permeability barrier) subjected to base motion, as shown in Fig. 4-7 considering different initial saturation degrees. The soil parameters given in Table 4-1 were used in the analyses (see Fig.7-13 for mesh details). Fig. 7-13 shows maximum surface lateral displacement vs. saturation. From the figure, displacement for the (fully) saturated condition is greater than twice that of the 90% saturation condition.

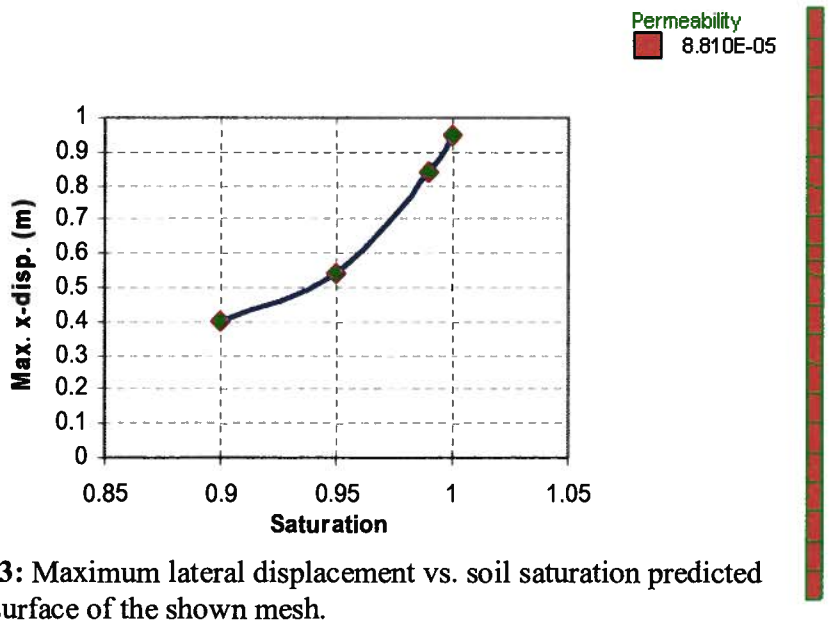

Fig. 7-13: Maximum lateral displacement vs. soil saturation predicted for top surface of the shown mesh.

Fig. 7-14 shows the time histories of excess pore pressure ratio, R_u (predicted) for different depths of the soil profile with different initial saturation conditions. The pattern of time history of pore fluid pressure buildup and dissipation also changes due to saturation effects as excess pore fluid pressure increases after excitation ceases and dissipates at a lower rate. The partial saturation condition causes a delay in the rise of pore fluid pressure. In addition, it lowers the magnitude of excess pore fluid pressure ratio, R_u (or u_e) compared to that of the fully saturated condition. These effects are more pronounced at shallower depths, suggesting that in the partial saturation condition, greater R_u occurs at deeper points with higher bulk modulus of pore fluid because of higher saturation during shaking, compared to that occurring in the fully saturated condition, where liquefaction takes place first at upper parts with constant and identical pore fluid modulus.

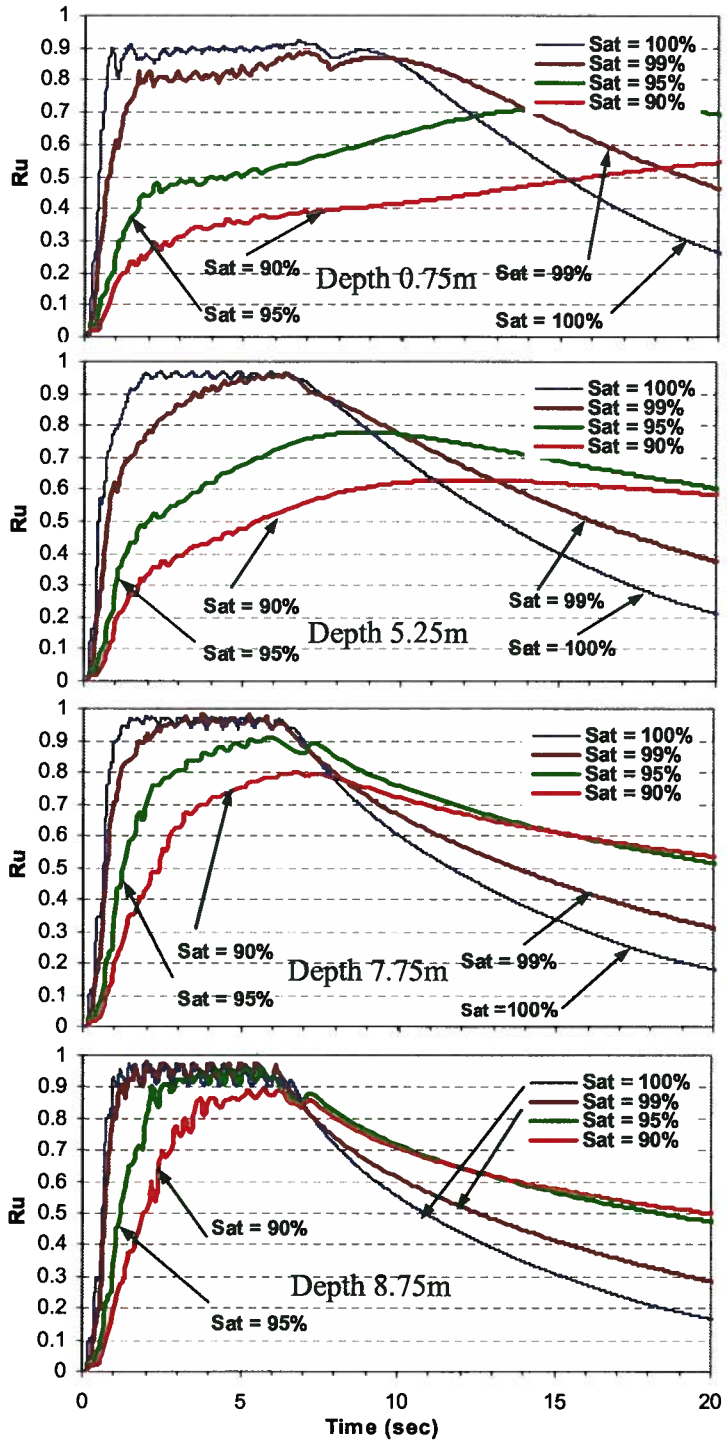

Fig. 7-14: Predicted time histories of excess pore fluid pressure ratio, *Ru* for different initial saturations at shallow to deep points in a uniform gentle slope.

7.4.3 Soil Profile with Barrier

The same procedure was used to analyze the 10 m-soil profile of 1° inclination with low permeability sub-layer at 4 m depth subjected to harmonic base motion (see Fig. 4-7, Fig. 4-8, and Table 4-1 for soil profile, input motion, and material properties, respectively).

As noted in *Chapter 4*, in the *FLAC* program, the amount of the fluid modulus variation within the model is limited, and instability results when too much fluid is expelled or absorbed by a zone in one *timestep* (controlled by void volume of the element; porosity). In this case (referred to as *hydraulic localization*), the amount of fluid exchanged with a zone in one *timestep* can be below the resolution of the computer arithmetic in *single-precision* (accuracy limit is around six decimal digits in this mode, whereas, in the *double-precision* mode, it is around 15 digits). This is the case for an unsaturated layer with hydraulic barrier. Due to this issue, the analyses results obtained from the *FLAC* in *single-precision* mode were inconclusive (see *Chapter 4* for more details about the *FLAC* program). Therefore, *FLAC* was used in *double-precision* mode for the analyses (despite its lower speed) and the results are presented here.

Fig. 7-15 shows the surface lateral displacement time histories for different initial saturation conditions. From the figure, saturation reduction can result in larger or smaller displacements at a later time depending on variable conditions (e.g., fluid bulk modulus, hydraulic gradient) beneath the barrier layer. The interplay of flow and saturation effects control the layer response. Fig 7-16 shows variation of the maximum lateral displacement with initial soil saturation. Fig. 7-17 depicts the predicted response of the soil layer with barrier layer in terms of the excess pore fluid pressure ratio, R_u time histories at different depths of the liquefiable soil beneath the barrier. The figure indicates that saturation reduction not only lowers the generated excess pore fluid pressures (with greater delay) but also postpones its dissipation to a later time. It causes the zone immediately beneath the barrier to deform for a longer time due to high R_u that leads to low shear strength. Fig. 7-17 implies that the delay in generation of excess pore fluid pressure occurring throughout the liquefied layer beneath the barrier is a direct effect associated with the partial saturation condition.

A comparison of Fig. 7-16 with Fig. 7-13 suggests that when a low-permeability layer is present in the soil profile, surface displacement does not show a consistent trend with saturation change, whereas, the trend is consistent if no barrier exists.

In the following section, in light of the findings from this study, the response in the Wildlife case history, observed during the 1987 Superstition earthquake is scrutinized and discussed.

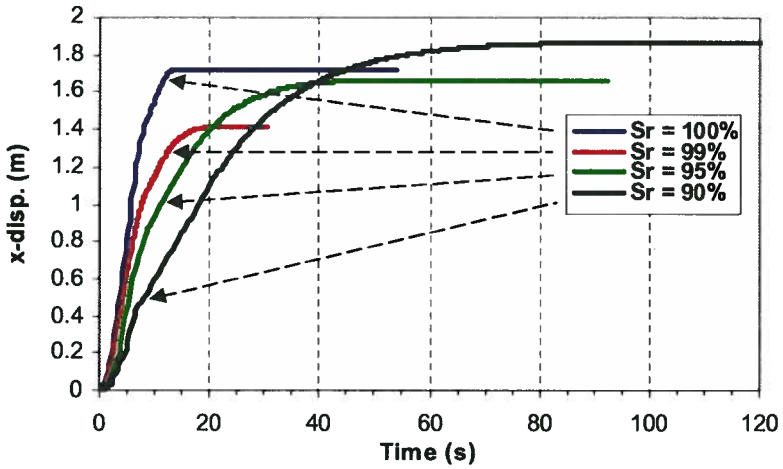

Fig. 7-15: Time histories of surface lateral displacement for different initial saturation condition for soil layer with barrier.

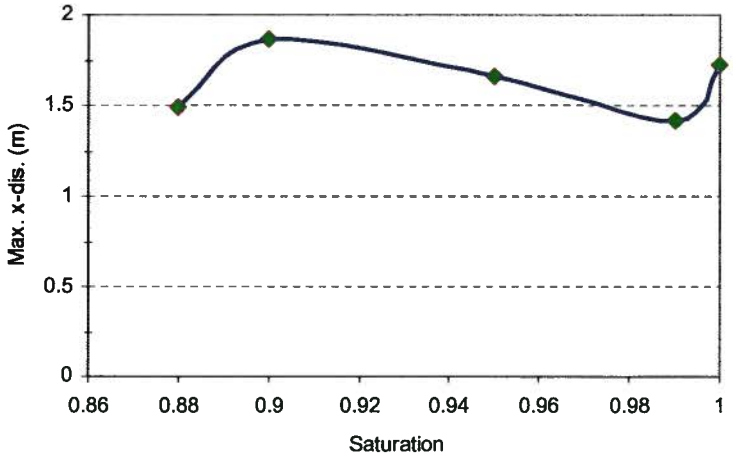

Fig. 7-16: Surface lateral displacement vs. initial saturation for soil layer with barrier.

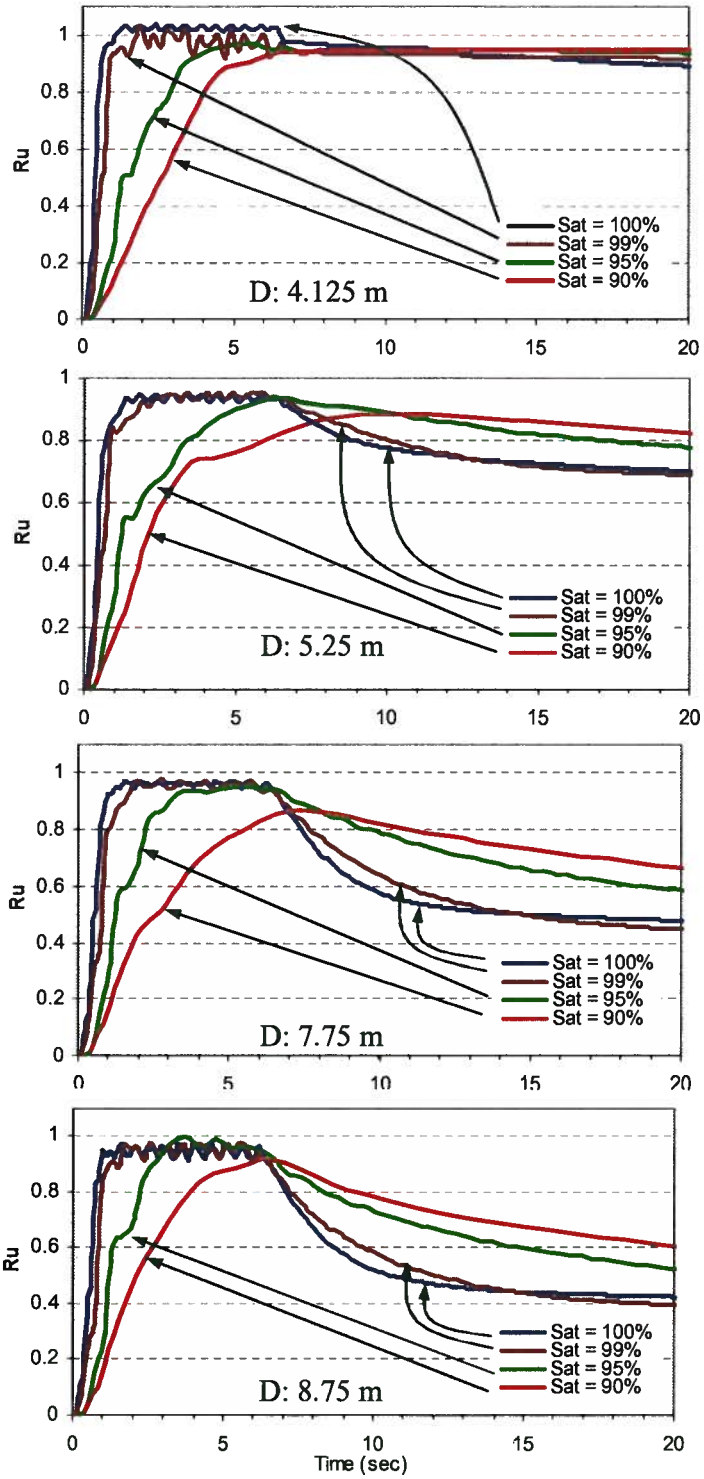

Fig. 7-17: Time histories for excess pore fluid pressure ratio, *Ru* for different initial saturation, from deep to beneath the barrier in a liquefied soil profile.

7.5 Observations from a Liquefied Site: Wildlife Liquefaction Array Case Study

For many years, liquefaction investigations were confined to laboratory element testing data. The need exists however, to study seismic behavior of a liquefiable soil in a real earthquake, which led to the design of instrumented liquefiable sites with continued monitoring programs. Today, down-hole arrays are deployed worldwide to record real seismic ground responses in near-surface strata. The information obtained from these arrays, increasingly, is becoming the basis for development, verification, and calibration of predictive tools and design procedures (e.g., Beaty & Byrne, 1998 and Arulanandan & Siva, 2000; among others). Future improvement in these areas can increase the convenience and accuracy of the data analysis and numerical modeling to facilitate more advanced applications. Currently, many instrumented sites have been developed in seismic regions; e.g., in the US, Japan, Taiwan, and elsewhere (Yoshida & Iai, 1998 and Elgamal et al., 2002). A comprehensive catalog of these sites can be found in Elgamal et al. (2001). These authors have listed more than 40 active sites that were monitored during seismic events. Recently, an international workshop was held to discuss the lessons gained from the data and other advances in the area. The workshop planned for further actions and conferences to provide a forum for on-going advancements in earthquake geotechnical engineering (de Alba et al., 2004).

As mentioned earlier, incomplete saturation, below the water table, is a common situation that may be occurring in many liquefiable grounds. In this section, the findings from the previous section are used to obtain an insight into the observed response of an instrumented site. One of the very first and well-documented sites instrumented to record ground response during a real earthquake is the Wildlife Liquefaction Array (WLA) site located in the Imperial Valley, California, US, which was developed in 1982 and has become a legend in this regard. This site experienced a few earthquakes; however, its response during the 1987 Superstition Hills earthquake became a benchmark in earthquake geotechnical engineering for use by a number of researchers for the validation of procedures over the years. The site was equipped with piezometers, accelerometers, and inclinometers that recorded the ground response during the earthquake. Still, some unanswered questions remain with regard to the site performance, measured data, and, in particular, the delayed excess pore water pressure rise and its post-shaking continuation. This issue has drawn attention from many researchers with controversial conclusions (e.g., Hushmand et al., 1992; Baziar et al., 1992; Zeghal & Elgamal, 1994; Youd et al., 1994; 2004b; Gu et al., 1994; and Soroush & Koohi, 2004; among others). In the following

sections, and in light of the findings on liquefaction of partially saturated soils, an attempt is made to clarify this problem.

7.5.1 General Information about the WLA Site

Fig. 7-18 shows the general location of the Wildlife Liquefaction Array (WLA) site and epicenters and magnitudes of the three important earthquakes that shook the site prior to and after its development (Holtzer et al., 1989). The magnitude 5.9 event is the 1981 Westmorland earthquake that generated numerous sand boils at the WLA site. Because of this liquefaction history, the WLA site was selected for instrumentation.

The instruments recorded responses during two significant earthquakes in 1987: the November 23 Elmore Ranch event (M_w = 6.2, PGA = 0.16g), which produced no significant rise in pore water pressure; and the November 24 Superstition Hills event (M_w = 6.6, PGA = 0.21g), which generated widespread liquefaction at the site. Because of the wealth of data obtained, and lessons learned from these responses, WLA is being re-instrumented at a locality of about 70 m downstream from the 1982 site, as part of the NSF Network (see Fig. 7-19 for the situation of these sites) for the US Brown Network Earthquake Engineering Simulation, NEES (Youd et al., 2004b). The new locality was chosen because of disturbances that occurred at the old site due to post-earthquake investigations and because of an increased potential for ground deformation at the new site. The amount of instrumentation at the site is also being enhanced.

7.5.2 WLA Ground Conditions and Instrumentation

The soil profile, as reported by Youd et al. (1994; 2004a; & 2004b) is comprised of a low permeability layer of 2.8 m silt to clayey silt material (PI = 9 to 19), underlain by 4 m loose sand to silty sand (SM in USCS) overlaying a clayey layer (PI =13 to 31). The clayey layers are expected to exhibit clay-like behavior when subjected to cyclic loading based on currently accepted practice (Boulanger & Idriss, 2004) that would respond as non-strain softening material with insignificant excess pore water pressure rise. The ground water table is at about 1.2 m depth. Fig. 7-20 shows the instrumentation plan and general stratigraphy at WLA and the locations of instruments placed in 1982. A forced balance accelerometer (FBA) was installed at ground surface (SM1) in an instrument shelter, while a companion down-hole FBA was wedged into the bottom of a casing (SM2) below the liquefiable layer at a depth of 7.5 m. Five electric

piezometers (transducers) were installed in the liquefiable layer (i.e., P1 to P5, and one was installed in the deep silt layer, P6). More details on the site development and its instrumentation, including special procedures undertaken to assure saturation condition of the piezometers, can be found in Bennett et al. (1984) and in Youd & Holzer (1994).

7.5.3 Ground Response in the 1987 Superstition Earthquake

Acceleration and pore water pressure records from the 1987 Superstition Hills earthquake are reproduced in Figs. 7-21 and 7-22. These records show ground accelerations recorded above and below the liquefiable layer and pore water pressures generated within that layer. Some notable aspects of the records were addressed by Youd et al. (1994; 2004) as follows:

- A sharp rise in pore water pressures began with the arrival of the peak acceleration pulse ($a_{max} \approx 0.21$g) that propagated through the site 13.6 s after instrumental triggering.
- Discordance developed between incoming acceleration pulses recorded by the down-hole FBA and those measured by the surface FBA as pore water pressures developed. Beyond about 15 s, the predominant period of the surface motions lengthened relative to the down-hole record. Also, compatibility between down-hole and surface motions degraded. Beyond 20 s, the surface motions were dominated by long period oscillations with periodic sharp acceleration spikes indicating abrupt negative acceleration and reversal of direction of the ground movement. These acceleration spikes were caused by dilative responses within the liquefied layer as also reflected in the pore pressure record (see Fig. 7-21).
- The continued rise of pore water pressures after cessation of strong ground shaking had not been seen before and led to considerable controversy and discussion of this issue. This unexpected delayed rise of pore water pressures led to some debate among researchers and to speculations about the occurrence of liquefaction and, in particular, the recorded pore water pressure data (e.g., Hushmand & Scott, 1992).

Youd & Holzer (1994) reported that 19 min after the main shock, an aftershock retriggered the monitoring system and providing a short record of pore water pressures at that time. Pore water pressures at the three uppermost piezometers (P1, P2, and P5) were still near R_u = 100%, while pressures measured by the lowest piezometer, P3 had dissipated to about R_u = 60%.

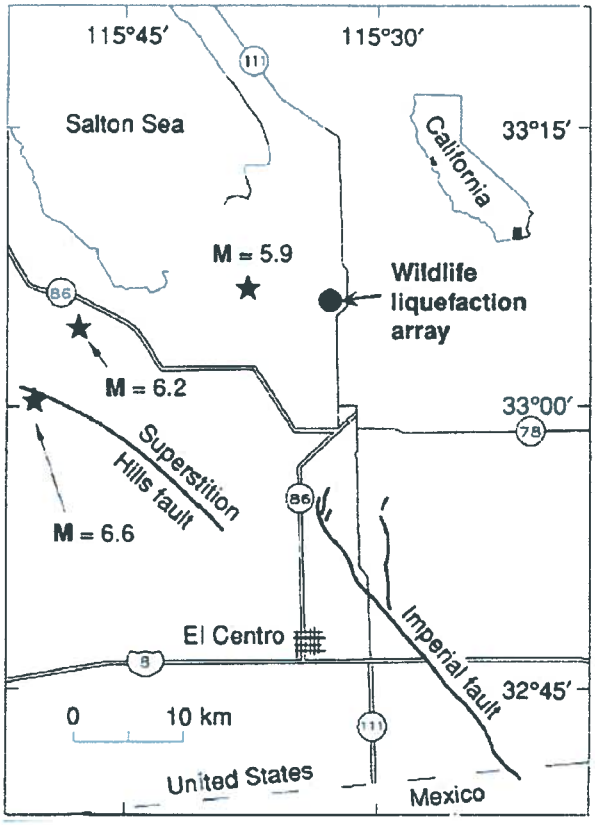

Fig. 7-18: Map of Imperial Valley with marked location of WLA site and epicenters of the following pertinent earthquakes: 1981 Westmorland (M = 5.9), 1987 Elmore Ranch (M_w=6:2) and 1987 Superstition Hills (M_w=6.6) (Holzer et al., 1989).

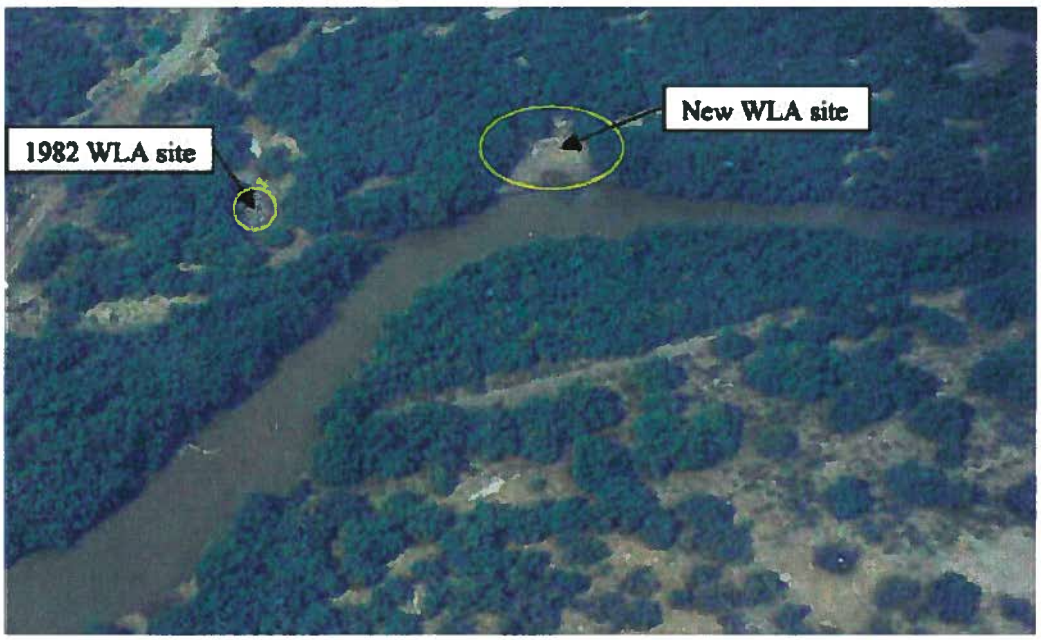

Fig. 7-19: Oblique photo of Wildlife area showing localities of 1982 and new WLA sites (Youd et al., 2004a, by courtesy of Professor Youd).

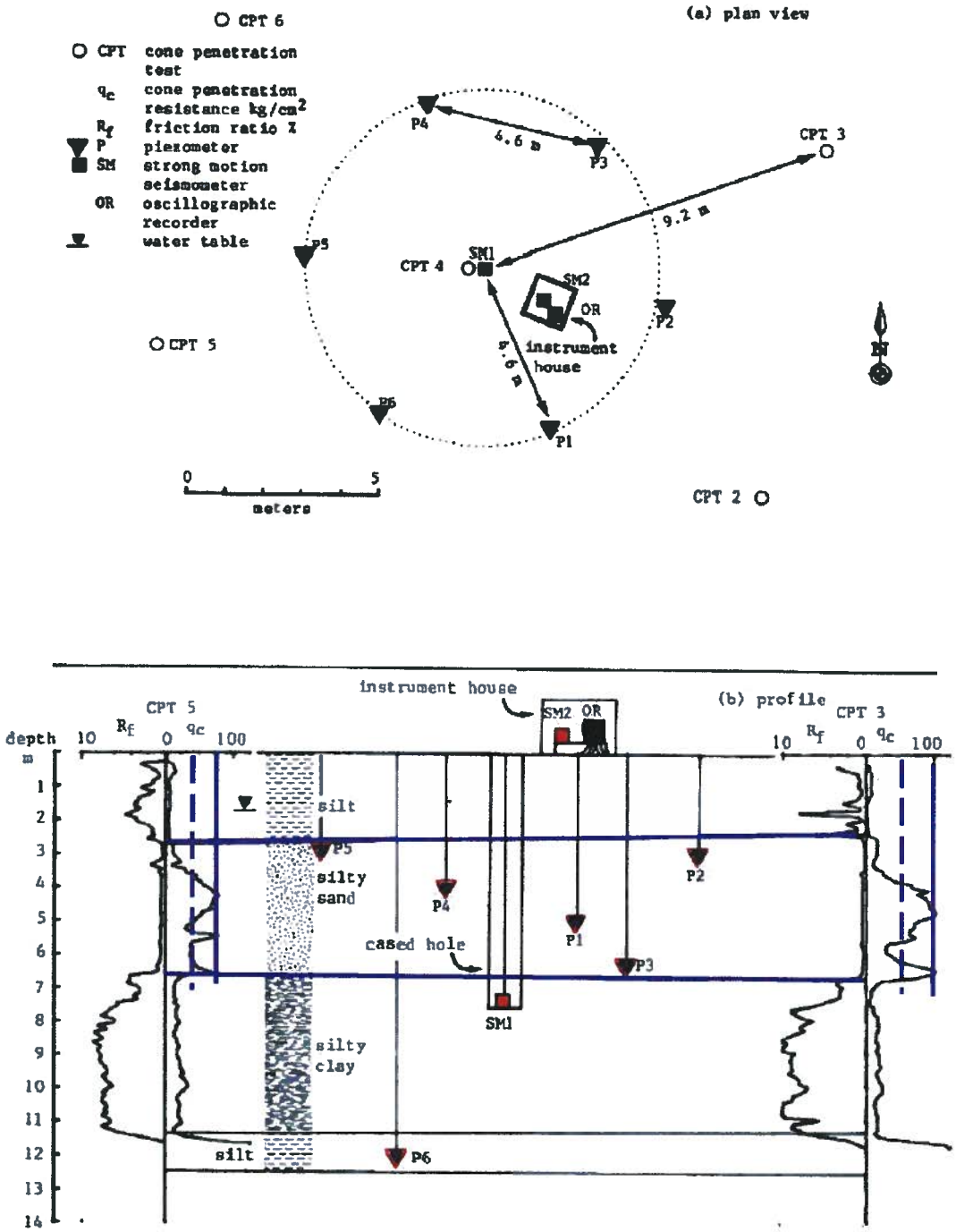

Fig. 7-20: WLA soil profile and instrumentation (modified from Bennett et al, 1984).

The authors demonstrated that the average stress-strain curve obtained for that layer represented a typical response of a liquefied soil to shaking. They inferred that liquefaction occurred during the 1987 Superstition earthquake in the sandy layer and spikes in acceleration could be attributed to sand dilation characteristics.

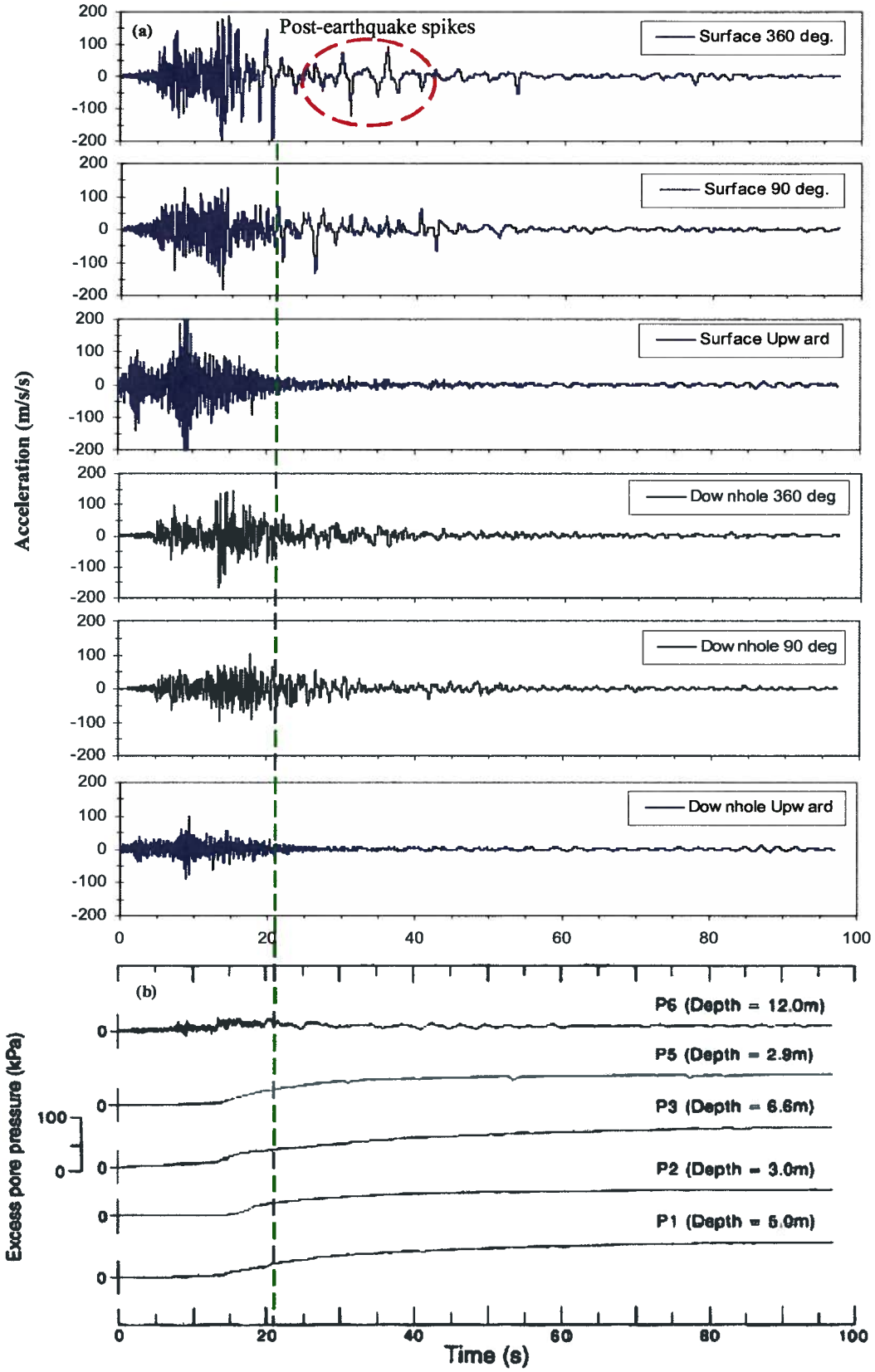

Fig. 7-21: Time histories of measured acceleration and excess pore pressure during the 1987 Superstition earthquake (modified from Holzer et al., 1994).

From Fig. 7-21, greater amplification is observed in the vertical component of acceleration rather than in the horizontal components in the WLA, that could be attributed to the partial saturation condition. As mentioned earlier, a similar observation was reported from the 1995 Kobe earthquake (Yang & Sato, 2001).

Nevertheless, the question regarding delay in excess pore (water) pressure rise has remained unanswered. This is pronounced in the excess pore water pressure ratio time histories, shown in Fig. 7-22, and especially for piezometer P5, installed close to the low permeability top layer.

Therefore, two issues are involved with the characteristic response of the WLA, measured during the 1987 Superstition Hill earthquake, namely:

- The delay in excess pore water pressure rise with regards to the strong ground shaking record that lasts about 20 s; and
- The long-lasting high excess pore water pressure at the top zones of the sandy liquefied layer.

The second issue is a typical behavior of a liquefiable layer with low permeability barrier, as addressed in the previous chapters of this thesis and as observed in centrifuge model tests (e.g., Phillips et al., 2004).

7.5.4 Characterization of the WLA Site

As shown in Fig. 7- 20, a number of Cone Penetration Tests, *CPT,* at the time of the WLA site development were conducted. In the figure, the corresponding results, in terms of cone friction ratio, R_f and tip resistance, q_c are shown, along with lines indicating the maximum and average values used for characterization (average q_c is 35 kPa to 50 kPa for sandy layer). Arulanandan & Sivathasan (2000) also reported a shear wave velocity of V_s = 137 m/s for that layer. Using the data, and applying available correlations for Cyclic Stress Ratio, *CSR* (e.g., Robertson & Wride, 1998; Andrus & Stokoe, 2000; and Youd et al., 2001), results in *CSR* = 0.075 to 0.085 for the sandy layer (see *Appendix VI* for more details). Thus, the sandy layer is implied to liquefy under this cyclic stress ratio within 15 cycles. In the analyses, this layer was modeled with the *UBCSAND* model, represented with $(N_1)_{60-UBCSAND}$ = 7.2 that exhibits the same

liquefaction resistance (*CRR*). The clayey layers were considered as non-liquefiable soil, based on currently accepted practice (e.g., Bray & Sancio, 2006; and Boulanger & Idriss, 2006).

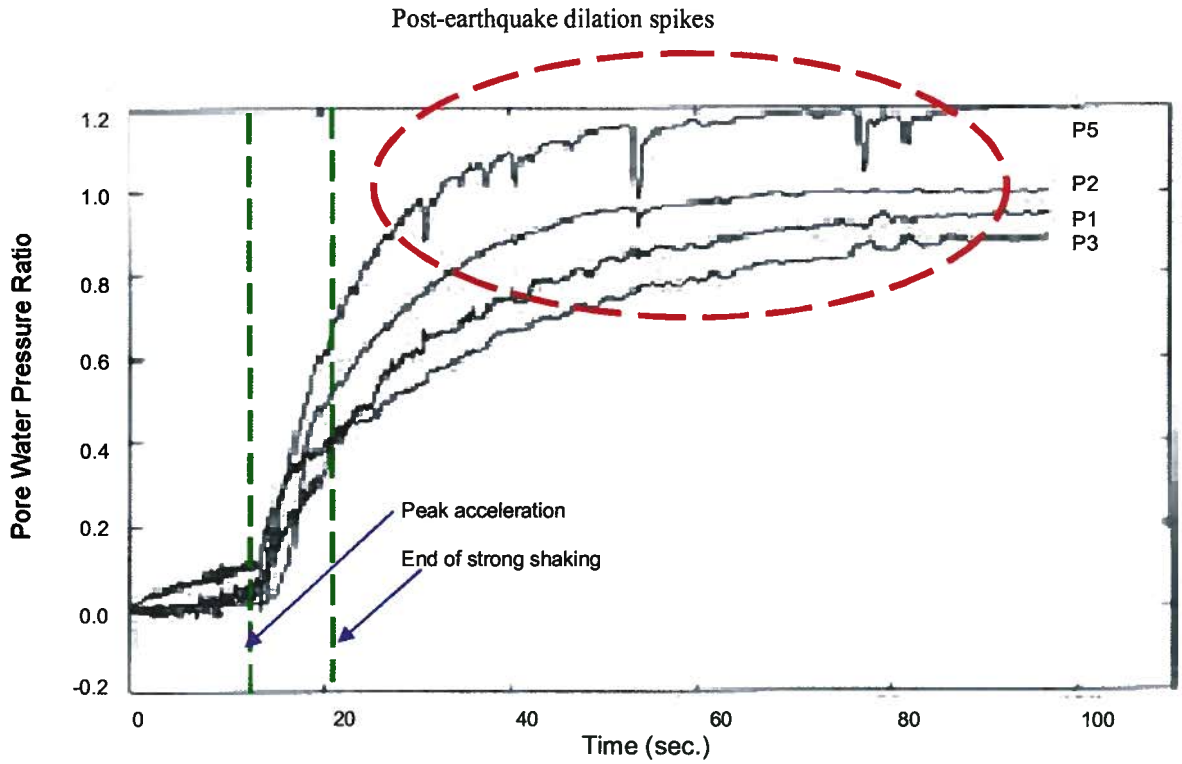

Fig. 7-22: Time histories of excess pore pressure ratio, R_u, recorded by piezometers in sandy layer of WLA site (data from Dobry et al., 1989).

As mentioned earlier, the WLA site, with the new NEES research program was recently upgraded and a new site was developed about 70 m downstream of the 1982 site (Youd et al., 2004b). During the program, geotechnical investigations including seismic wave measurement and in situ falling head permeability tests were conducted (Youd et al., 2004). Fig. 7-23a shows the results of compression wave, V_P measurements at the upper parts of the new site (see *Appendix VI* for a complete V_P profile). It shows that the V_P in the sand layer is generally low (compared to that in the saturation condition $\approx$ or $>$ 1500 m/s), ranging from about 500 m/s at the upper parts to around 1500 m/s at the zone close to the clay layer (averaging less than 1000 m/s). This suggests that a partial saturation condition in the WLA site is very likely, as Kokusho (2000) and Ishihara et al. (2004) also raised this point for some liquefied Japanese sites. Fig. 7-24 shows

typical (theoretical) variation of V_P in a porous medium for a wide range of *Poisson's ratio* and porosity for the saturation condition from 90% to 100%. The effects of porosity and *Poisson's ratio* are practically insignificant compared to those of saturation. A saturation of 99.2% was estimated as a representative value for the liquefiable sand layer at the WLA site, based on a trial and error method.

7.5.5 *FLAC* Model of the WLA Site

Fig. 7-23b shows a single column model of a level ground, comprised of 17 elements representing different soil layers in the WLA site. Table 7-1 lists material properties used in the analyses for the three layers. The *Mohr-Coulomb* and the *UBCSAND* models were applied to low permeability layers and the sandy layer, respectively.

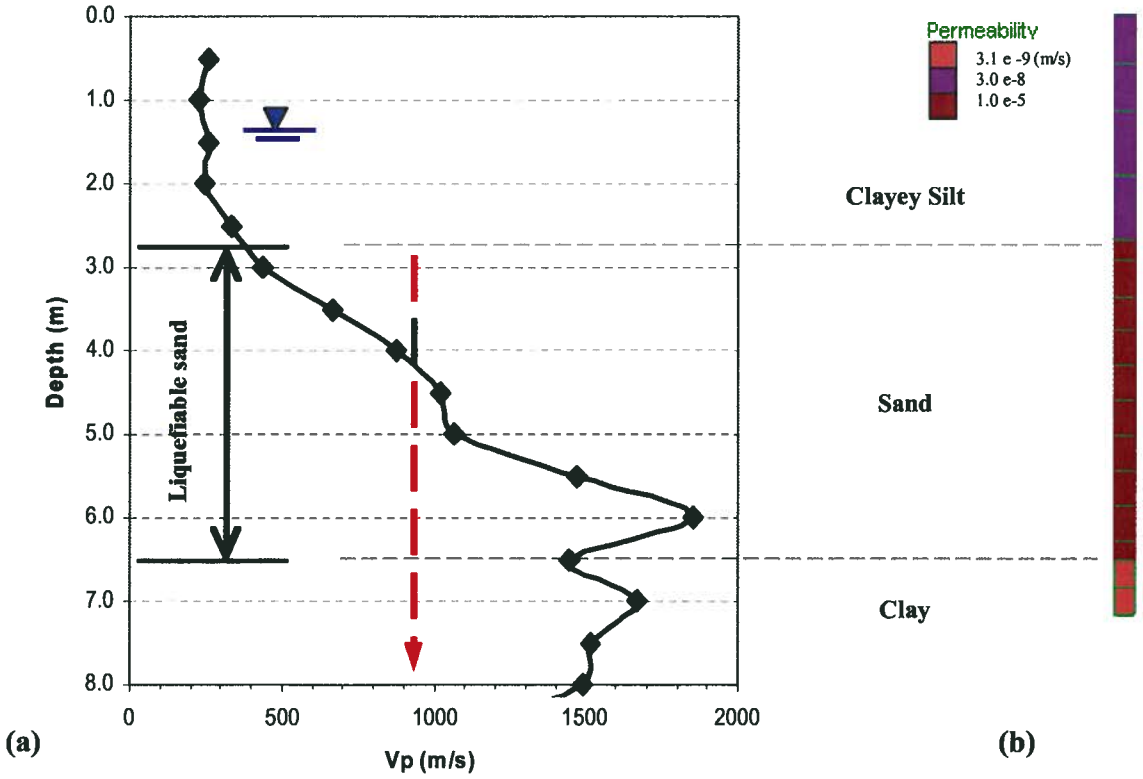

Fig. 7-23: (a) profile of *P*-wave velocity measured at the new WLA site (data from Youd et al., 2004), (b) model used in the analysis.

Table 7-1: Material properties used in the WLA analyses.

Layer	Material	ρ_d (1000kg/m^3)	n	UBCSAND $(N_1)_{60}$	k (m/s)	Model	φ *(deg.)*
1	**Clayey silt**	1.55	0.47	----	3.0e-8	Mohr-Coulomb	30.0
2	**Sand**	1.65	0.44	7.2	1.0e-5	UBCSAND	----
3	**Clay**	1.50	0.528	----	3.1e-9	Mohr-Coulomb	30.0

ρ_d, n, and k are dry density, porosity, and permeability, respectively.

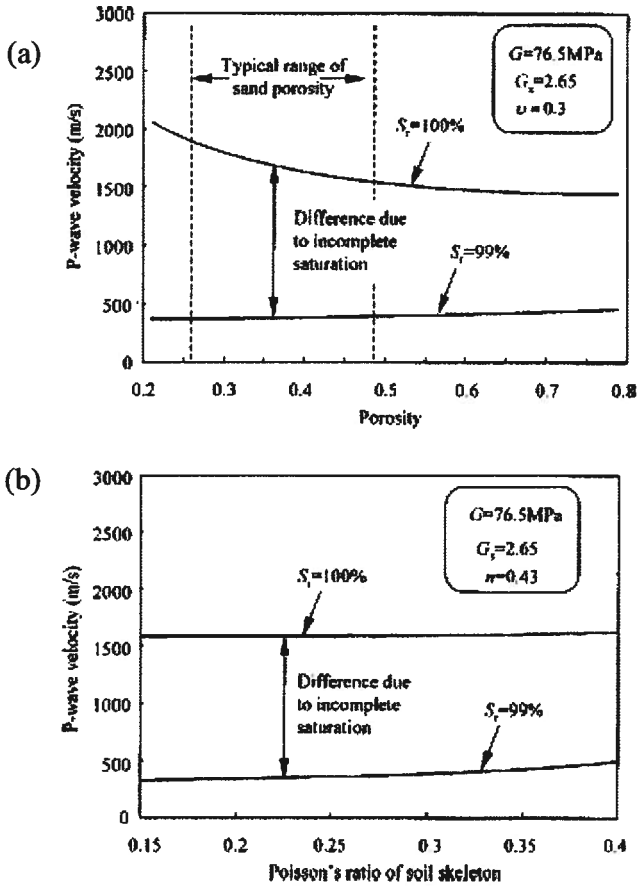

Fig. 7-24: Typical variation of V_P in a porous medium with a saturation range of 90% to 100% with (a) medium porosity and (b) *Poisson's* ratio (Yang et al., 2004)

7.5.6 Earthquake Input Motion

Acceleration time histories recorded at down-hole (depth of 7.5 m) and ground surface during the 1987 Superstition Hill earthquake in different directions are available from the COSMOS program, at the USGS website (http://db.cosmos-eq.org). The horizontal component of 360 deg. down-hole was selected as the input base motion in this study; its time history is shown in Fig. 7-25 along with the applied motion at the base of the *FLAC* model.

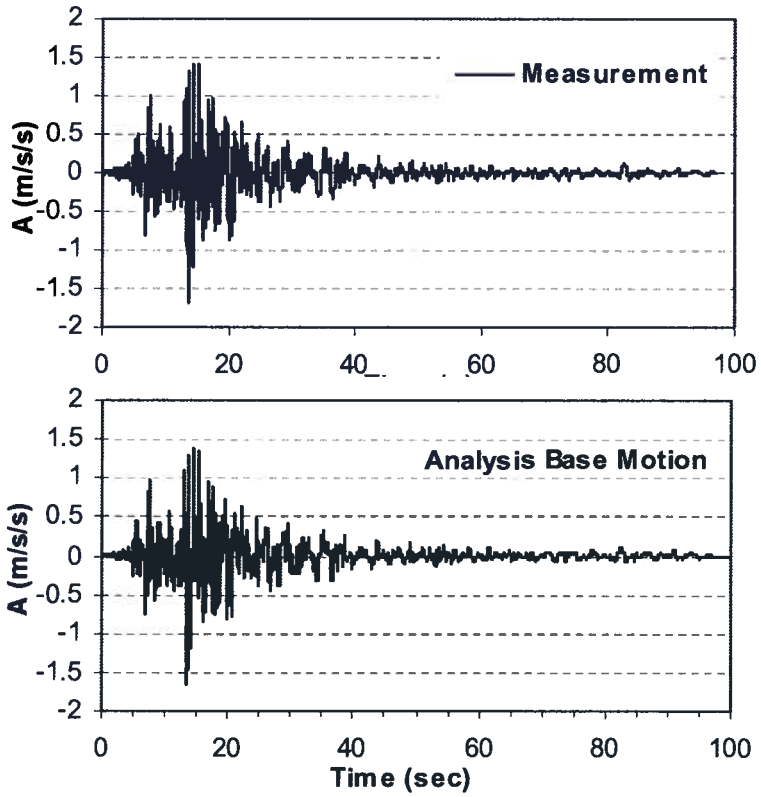

Fig. 7-25: NS component (360 deg.) of Superstition 1987 Earthquake acceleration time history recorded by SM1 in down-hole and input motion applied to the model base in the analysis.

7.5.7 Results of Analyses

A set of analyses was conducted for the fully saturated condition and partially saturated conditions with different degrees of saturation. The results for the fully saturation condition and initial saturation condition of S_r = 99.2%, in terms of time histories of acceleration and excess pore water pressure ratio, are presented here. Fig. 7-26 shows the predicted time history of acceleration at ground surface for fully (with *PGA* = 0.11 g) and partially saturated conditions

(with *PGA* = 0.19 g), compared with the measured record (with *PGA* = 0.20 g; represented as points on the graph). The predictions for the partially saturated condition show more agreement with the measurements, in terms of PGA (0.19 g vs. 0.20 g) and number of significant pulses ($0.65a_{max}$). This agreement can also be inferred from spectral acceleration for both conditions, as depicted in Fig. 7-27 (measurements represented by the dashed line).

The predicted time histories of R_u for the deepest piezometer, P3, and the upper piezometer, P5, in liquefiable sand are shown in Fig. 7-28. From the figure, excess pore water pressure rise continues until after the main shocks when the partial saturation condition is taken into account, which has a better match to the recorded trend during the event. Nevertheless, the predicted spikes after the main shock are smaller than the measured spikes. It is attributed to greater dilation effects in material under very low effective confining stress ($Ru \approx 100\%$) which is considered constant in the analyses.

The predicted time histories of the excess pore water pressure ratio for P5, installed at the upper part of the liquefiable layer, along with surface acceleration is shown in Fig. 7-29. The figure indicates that the pore pressure rise beneath the top low permeability layer continues for a longer time after the strong shocks (at 20 s).

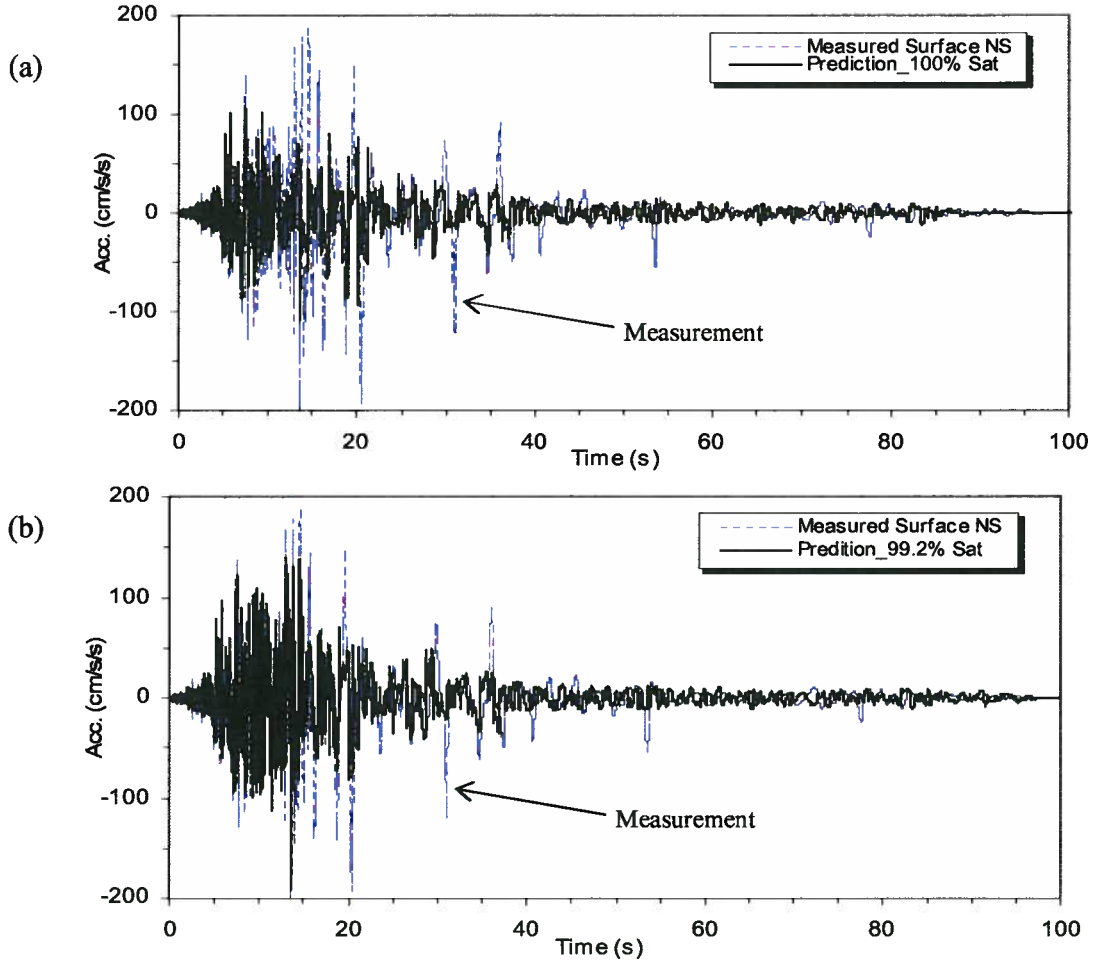

Fig. 7-26: Predicted surface acceleration time histories compared to the measured record for (a) fully saturated condition and (b) partially saturated condition.

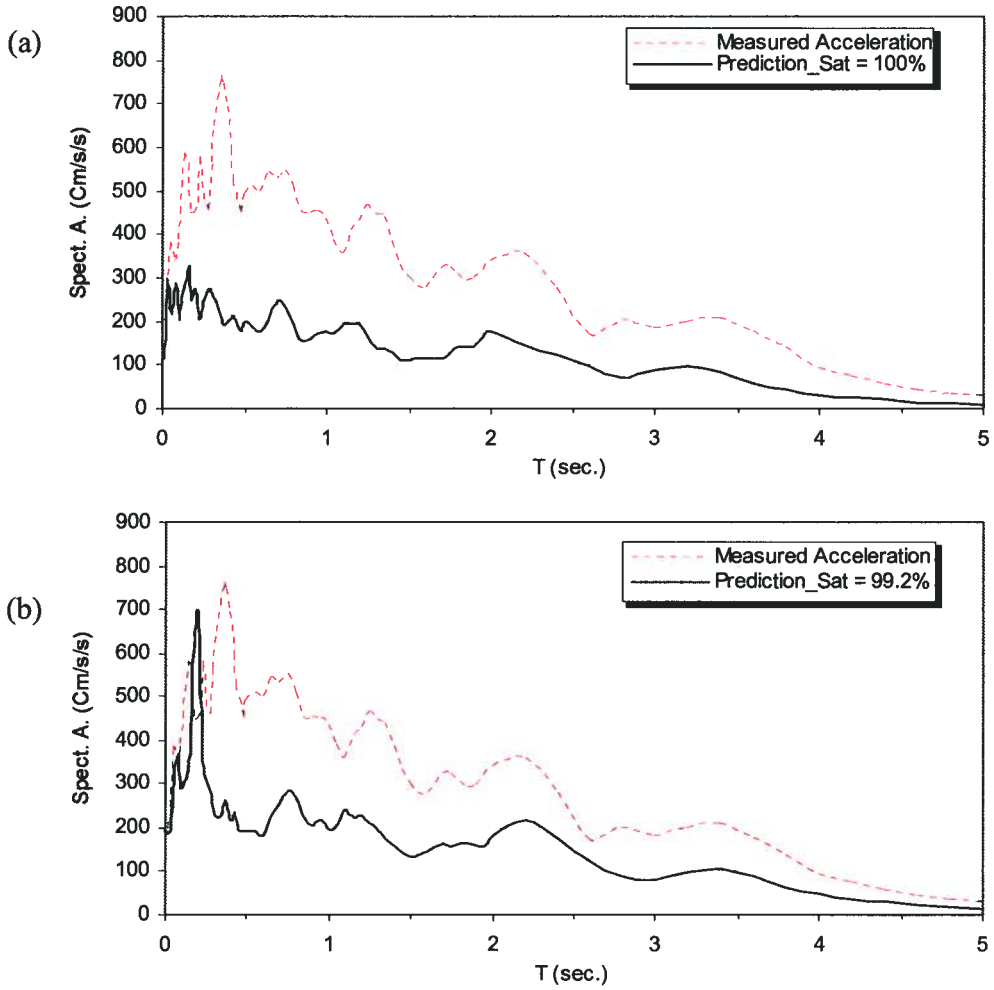

Fig. 7-27: Predicted surface spectral acceleration (D = 5%) compared to that measured for (a) fully saturated condition and (b) partially saturated condition.

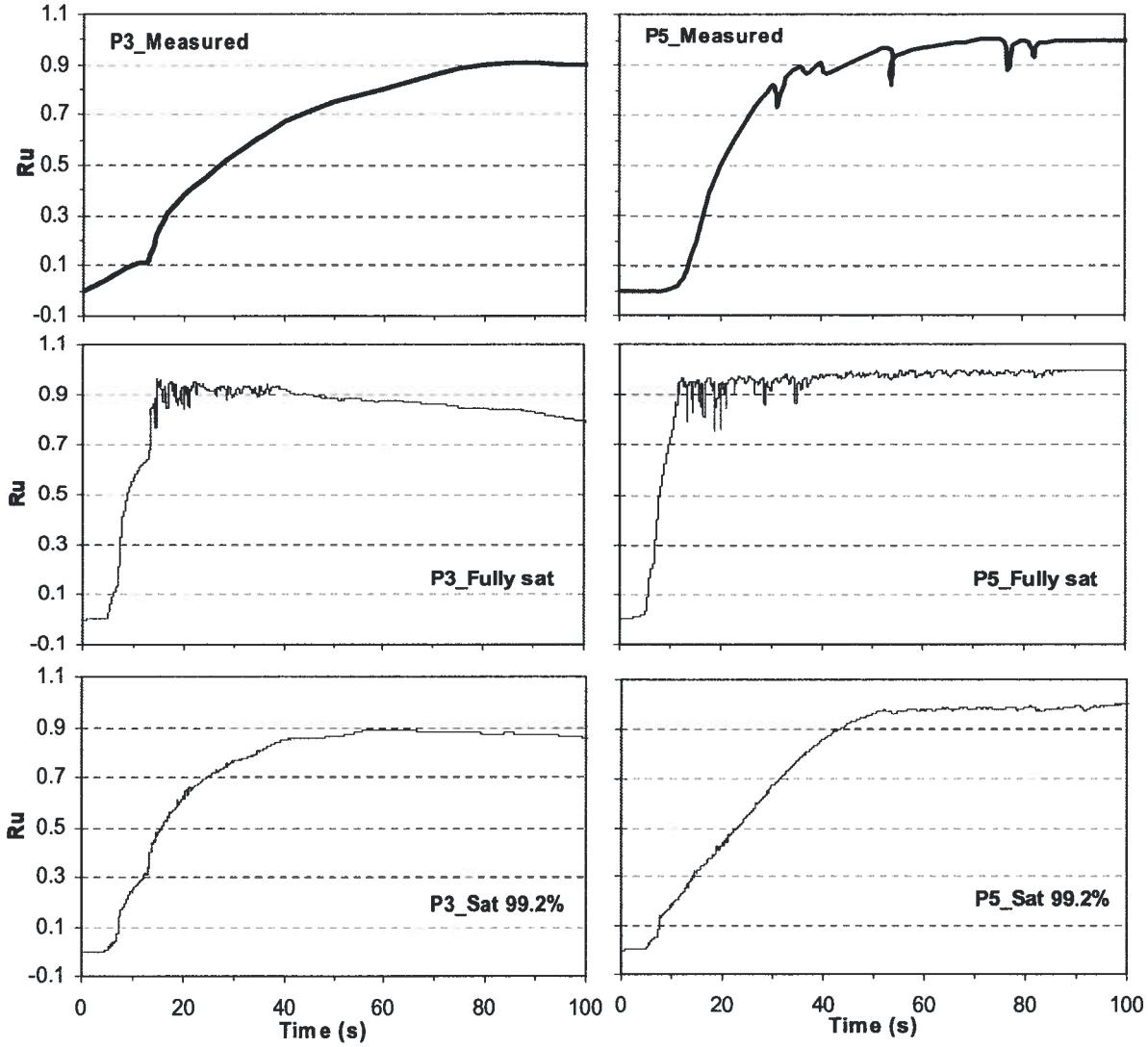

Fig. 7-28: Predicted excess pore pressure ratio, R_u for P3 and P5 piezometers along with measurements.

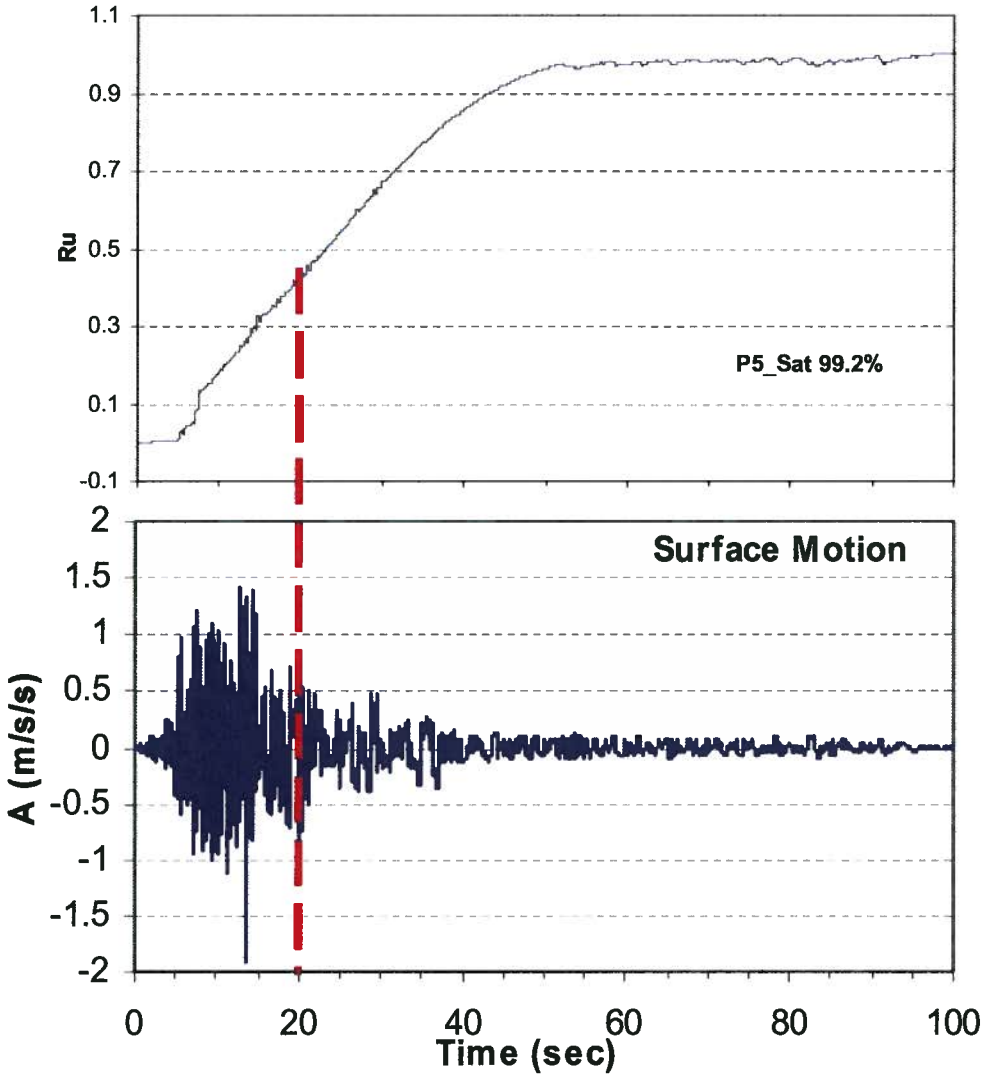

Fig. 7-29: Predicted excess pore pressure build-up after main shock for piezometer P5.

Fig. 7-30 shows the predicted long-term time histories of excess pore water pressure ratio, R_u for piezometer P3 and P5 for 20 min after the event that indicates high excess pore water pressure for P5 and about R_u = 55% for P3 at this time. This is in good agreement with the observations reported by Youd & Holzer (1994). Scott & Hushmand (1995), in their critique of the study by Youd and his coworkers, reported a performance test they conducted two years after the Superstition event where they inferred that the upper piezometers functioned properly while the other devices did not perform satisfactorily. Therefore, the records from the upper piezometers may be taken as reliable sources for data in this assessment.

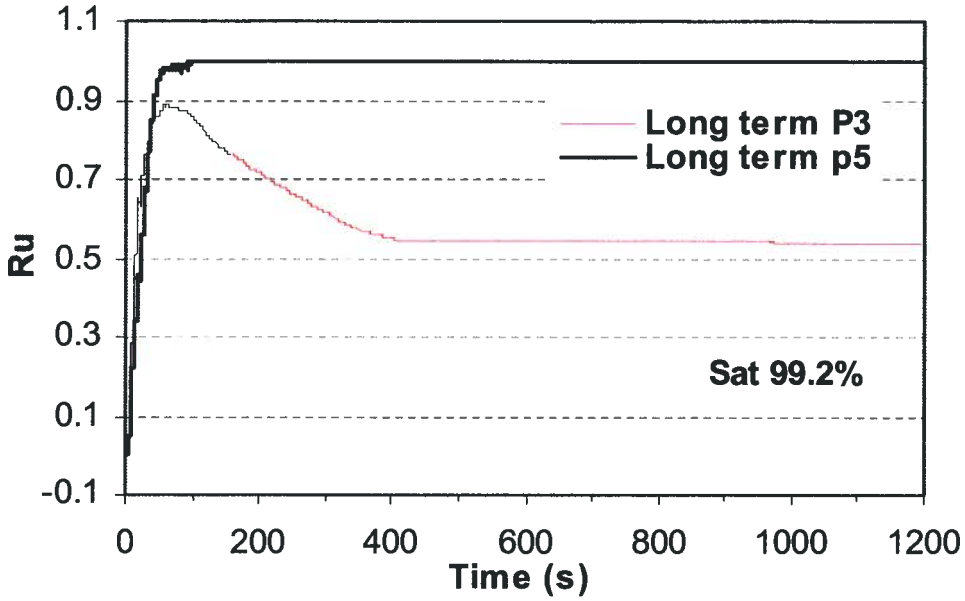

Fig. 7-30: Predicted long-term record of R_u for piezometers P5 and P3.

The continued rise of pore water pressures after cessation of strong ground shaking had not been reported before, and led to considerable debate among the experts (e.g., Holzer et al., 1988; Hushmand et al., 1992; Youd & Holzer, 1993; and Scott & Hushmand, 1995; among others). Some investigators disputed the occurrence of liquefaction within the sand layer during that event. Zeghal & Elgamal (1994) based their work on measured accelerations using a double integration technique, called System Identification Analysis (Abdel-Ghaffar & Scott, 1978; and Koga & Matsno, 1990) to evaluate the average shear stress-strain curve of the sandy layer (as given in Fig. 7-31b), indicating a typical behavior of liquefied sands. The analysis prediction of the (shear) stress-strain curve for an element in the liquefiable sand layer is shown in Fig. 7-31a. This is comparable to the (interpreted) average stress-strain curve (Zegal & Elgamal, 1994) and confirms that the sandy layer liquefied during the 1987 Superstition Hill earthquake.

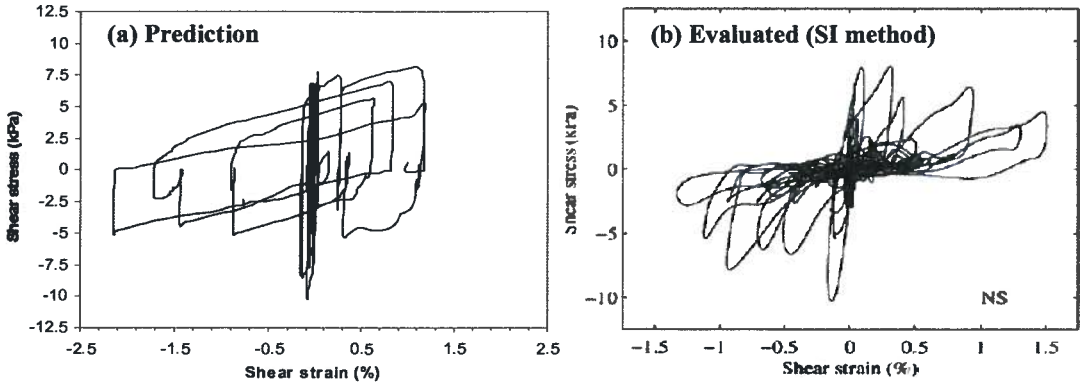

Fig. 7-31: Shear stress-strain curve, (a) prediction, (b) interpreted from measured data (Zeghal & Elgamal, 1994).

7.6 Summary and Main Findings

Recent field data indicates that a partial saturation condition below the water table is very likely in liquefiable grounds. In this chapter, a generic study was carried out to investigate the effects of partial saturation in the response of liquefied soil layers. The numerical procedure was shown to be able to predict the increase in liquefaction resistance of partially saturated samples as observed in cyclic laboratory tests. This was based on the following key points:

1. The bulk modulus of a water-air mixture is essentially controlled by the absolute pressure of the mixture.
2. A small reduction in sample saturation strongly influences the pore fluid stiffness, and consequently, the pore water pressure rise, during shaking and liquefaction resistance.

Other investigators have already addressed the above observations from experimental work. The principal outcomes from this study are summarized as follows:

- In liquefiable grounds with a partial saturation condition, the excess pore water pressure rises more slowly and also dissipates at a lower rate.
- This may result in a higher excess pore water pressure ratio at deeper zones of a liquefiable layer, compared to that in a fully saturated condition.
- The partial saturation condition results in lower displacements in uniform slopes during earthquakes.

- In a partially saturated liquefied layer with sub-layer barrier, a decrease in saturation does not necessarily result in lower displacements as a result of the interplay of variable flow and the saturation condition (fluid stiffness).
- This study reveals that the response of the WLA site during the Superstition Hill earthquake can be explained on the basis of seismic behaviour of partially saturated soils.
- The analyses suggest that the delay in excess-pore water pressure rise at the WLA site can be attributed to the partially saturated condition of the sandy layer.
- The long-lasting high excess pore water pressure at the interface of the overlying layer with the sandy layer in the WLA site exhibits a typical effect of a low permeability layer within liquefied grounds.
- The analyses indicated that the sandy layer at the WLA site was liquefied during the 1987 Superstition Hill earthquake, as inferred by the characteristics of the predicted stress-strain curve and by the excess pore water pressure rise. This is in accordance with measurements and observations by other investigators.

CHAPTER 8

MITIGATING LOCALIZATION EFFECTS OF HYDRAULIC BARRIERS IN LIQUEFIABLE GROUNDS: PRINCIPLES

8.1 Introduction

In previous chapters, the significant impact of the low permeability sub-layer on liquefiable sloping ground behavior in earthquakes was explored. The net results imply that the liquefaction response is strongly affected by the presence of low-permeability seams which impede flow, forming a water-rich zone beneath the barrier, leading to localization and large deformations. Such conditions can be treated with vertical seismic drains as discussed in this chapter.

Seismic gravel drains (stone columns), as a liquefaction mitigation measure, were initially studied by Seed & Booker (1977). As noted by Adalier & Elgamal (2004), since then, the gravel drain technique has received increased attention from a number of leading researchers (e.g., Ishihara & Yamazaki, 1980; Tokimatsu & Yoshimi, 1980; Baez & Martin, 1995; Boulanger, et al., 1998; Pestana, et al., 1999; Rollins, et al., 2004; Adalier & Elgamal, 2004; Seid-Karbasi & Byrne, 2004b & 2007; Chang, et al., 2004; Brennan & Madabhushi, 2005; and Shenthan, 2005).

The risk of liquefaction and associated ground deformation can be reduced by various ground-improvement methods, including: densification, solidification (e.g., cementation), and gravel drains or stone columns. Use of gravel drains is a rather recent development, when compared to the more traditional soil densification techniques. Based on performance, sites with seismic drains had better performance compared to unimproved sites during past earthquakes (e.g., Hausler & Sitar, 2001; Hausler, 2002; and Martin, et al., 2004). Some centrifuge test data, also suggests that the densification method is not an effective treatment technique for liquefiable soils with barrier layer (e.g., Balakrishnan, 2000). Various studies and guidelines on liquefaction remediation techniques and their design can be found in the literature (e.g., Mitchell, 1981;

Mitchell & Cooke, 1999; JGS, 1998; Mitchell, et al., 1995 & 1998; PHRI, 1997; and USACE, 1999).

Recently, a few investigations have been carried out to study the effects of seismic drains using physical model testing (e.g. UBC-CCORE work reported by Phillips, et al., 2005 and Cambridge U. work reported by Brennen & Madabushi, 2005, among others). Chang, et al. (2004) reported a field model test to induce liquefaction in a sand fill (see Fig. 8-1.for test set-up). They installed the drains before filling up the trench with liquefiable soil to exclude any densification induced by the insertion of drains. Fig. 8-2 shows the time histories of excess pore water pressure ratios, measured in the field tests within a liquefiable soil for a deposit without and with vertical drains, subjected to a harmonic surface excitation. The data shows that the rate of excess pore water pressure build-up is significantly slower with drains, which confirms their effectiveness as a remediation measure.

Most of the previous studies have focused on the application of drains in uniform liquefiable soils. This chapter presents the results of a numerical study exploring the measure needed to mitigate the large displacements in liquefiable slopes associated with void redistribution. In this respect, the application of seismic drains was examined for a liquefiable sloping ground including the barrier sub-layer. The purpose is to demonstrate the effectiveness of this technique in a conceptual framework, without providing a design monograph that would be conducted on a project-basis and optimized accordingly.

8.2 Implication of Seismic Drains and Analysis Approach

Drains have the potential to nullify the barrier effect and curtail or prevent the occurrence of lateral spread or *flow-slides* in the event of an earthquake. Gravel drains facilitate dissipation of excess pore water pressure and mitigate the effects of low permeability layers. The effects of seismic drains were examined for the same ground condition (shown in Fig. 4-7) with 1.0° inclination where it was treated with gravel drain penetrated through the low permeability sub-layer. The motion time history given in Fig. 4-8 (PGA = 2.5 m/s^2) was applied at the base of the model. The material properties were the same as listed in Table 4-1. The drain properties are identical to those of the surrounding sand layer except that the drain permeability is greater. Thus,

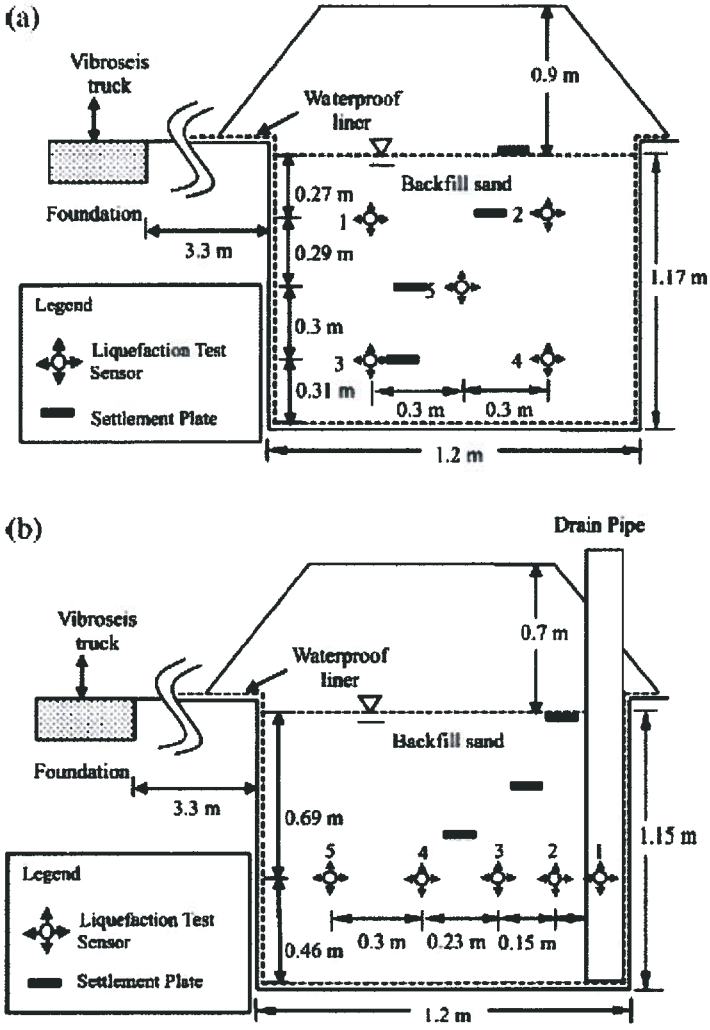

Fig. 8-1: Testing set-up for the: (a) no drain test and (b) drain test (Chang, et al., 2004).

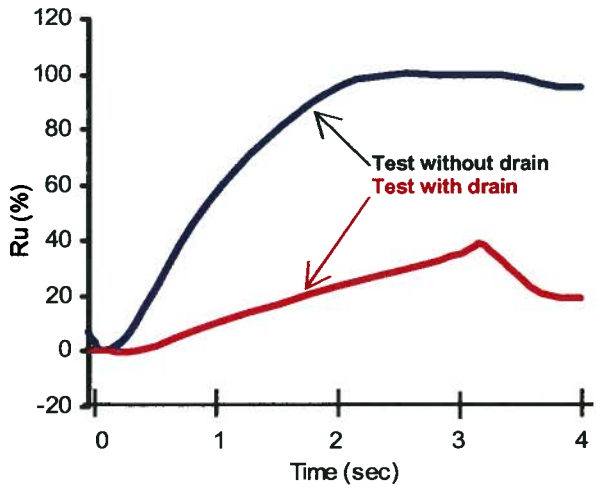

Fig. 8-2: Measured R_u in the field liquefaction test for the case without drain and with drain (data from Chang, et al., 2004).

the other promising effects of the stone (drain) columns, as noted by Alalier & Elgamal (2004), are not considered in this study. These include:

- Densifying surrounding soils during construction,
- Restricting shear deformation and offering containment of the 'encapsulated' soils, and
- Providing stiffening-matrix effects (i.e., reducing the stresses in adjacent soil).

This study was conducted in plane-strain condition, and the drains were represented by a column (curtain) of permeability 100-times greater than that of the native liquefiable soils in the analyses. For design purposes, the 3-D effects of drain columns installation-pattern can be treated in a plane-strain analysis by using an appropriate equivalent drain curtain approach suggested by a few investigators (e.g. Indraratna & Redana, 1997 & 2000).

To examine the influence of penetration depth of the drain on its mitigating effects, three cases were analyzed, i.e.:

1. Complete penetration (*Case I*)
2. Partial (half) penetration (*Case II*)
3. Minimum penetration (*Case III*)

Inclusion of a drain curtain in the current 1-D model converts it to a 2-D model, as the flow properties vary in the horizontal direction. This is also the case for an infinite slope (including drain). The effect of drain spacing in soil layer performance is well recognized; however, little information is available about penetration depth effects and in particular, where a barrier sub-layer presents.

The effect of decrease in drain permeability that may occur over time (e.g., due to biological causes), was accounted for in these cases by re-analyzing them with the condition of a 10-times reduced drain permeability. Fig. 8-3 shows the meshes used in the analyses for the three cases.

8.3 Analyses Results for Treated Models

The results of the analyses for the three cases are presented below, in terms of time history of surface lateral displacement, deformation pattern, and/or time histories of excess pore pressure:

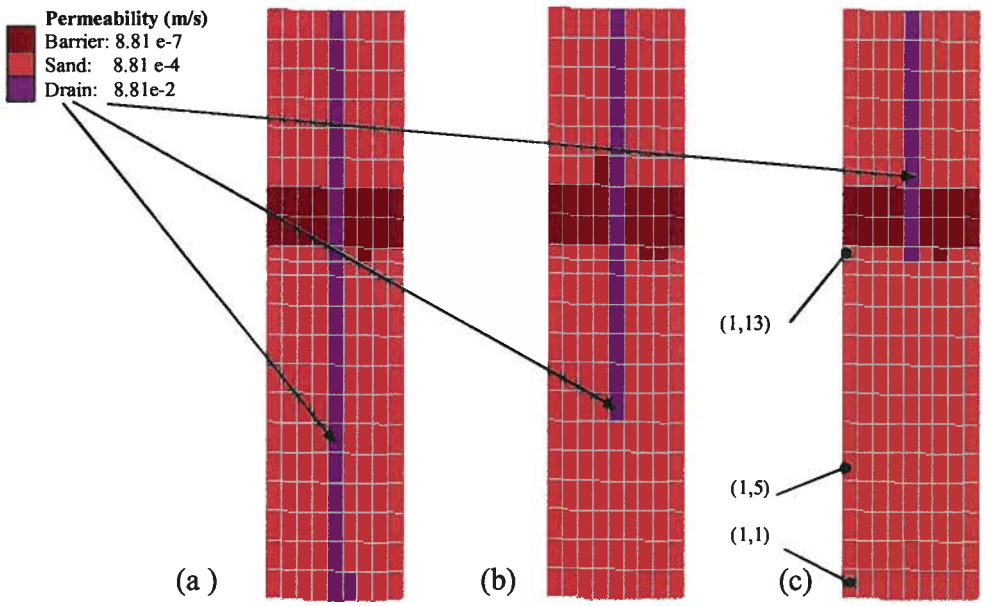

Fig. 8-3: Meshes used in analyses of drain effects with (a) full penetration, (b) half penetration, and (c) minimum penetration.

8.3.1 Fully Penetrated Drain, *Case I*

Fig. 8-4 shows distributions of maximum excess pore pressure ratio, $R_{u(max)}$ within the model, along with flow vectors after 3.5 s of shaking. From the figure, $R_{u(max)}$ increases with distance from the drain column. The drain curtain exhibits some excess pore pressure during shaking. The maximum predicted lateral displacement in this case was 0.7 m, which is even less than for the model without a low permeability sub-layer. Fig. 8-5 shows the time history of the surface lateral displacement along with that of the uniform layer.

A comparison of predicted time histories of excess pore water pressure build-up for a point at mid-depth of loose sand for the case without barrier and this case (with drain, fully penetrated) is shown in Fig. 8-6. This suggests that drains can reduce the excess pore water pressures rise and speed up its dissipation significantly. This is also inferred from the displacement time history (see Fig. 8-5) that indicates that displacements cease sooner than in the case of the uniform layer. Fig. 8-7 shows the mesh with displacement vectors at 12 s. The displacement decreases gradually with depth, without any localization at the barrier base. Fig. 8-8 shows the distribution of volumetric strain within the model treated with a fully penetrated drain (at 12 s). All volumetric strains are seen to be contractive (negative).

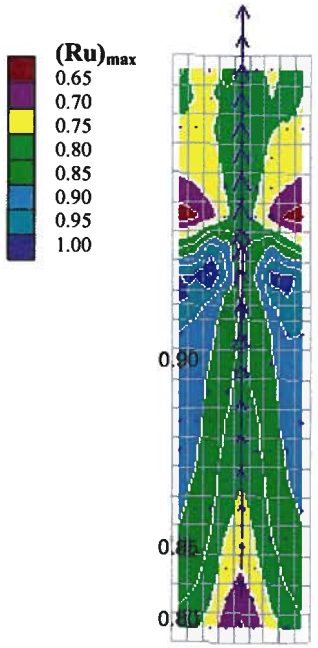

Fig. 8-4: Distribution of $(R_u)_{max}$ in the model with drain and flow vectors at 3.5 s.

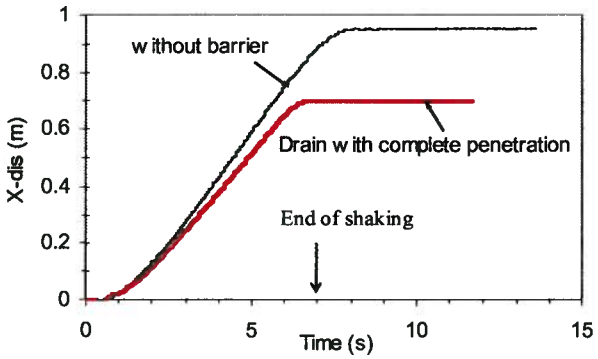

Fig. 8-5: Surface lateral displacement time history of the profile with barrier treated by drain compared to that of profile without barrier.

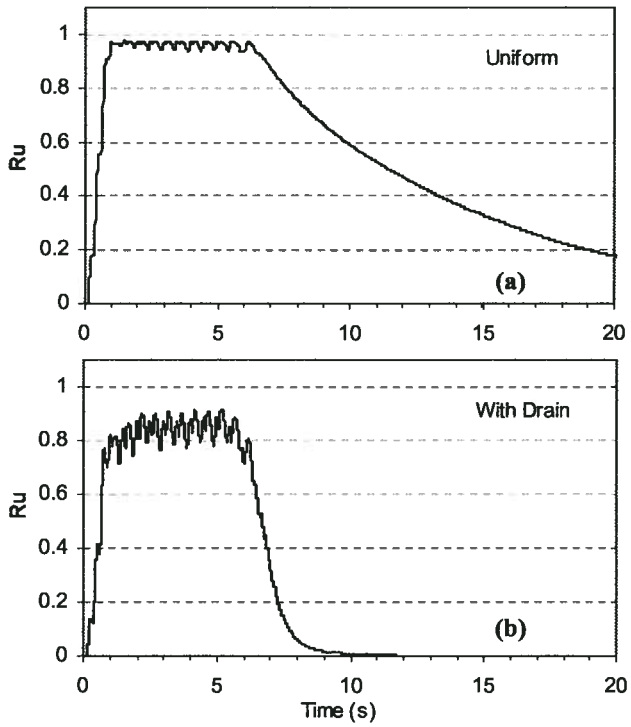

Fig. 8-6: Predicted time history of R_u at mid-depth of loose sand: (a) uniform profile, (b) treated with drain (fully penetrated).

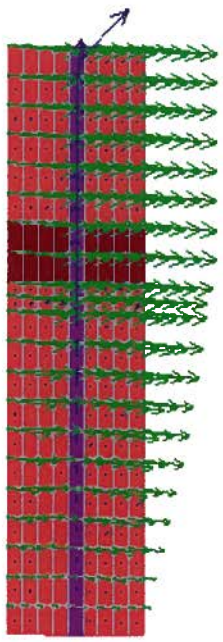

Fig. 8-7: Displacement and flow vectors within the model after 12 s (*case I*).

These analysis results demonstrate that the drain column is a promising measure to mitigate liquefaction induced deformations in liquefiable soil slopes comprised of barrier layers. The same effect of drain curtains in preventing post-shaking flow failures and displacement reduction was reported by Naesgaard, et al. (2005) from centrifuge model tests. In the next sections, the results of other cases with smaller penetration depths are discussed.

8.3.2 Partially Penetrated Drain, *Case II*

Partial penetration effects need to be investigated for the effect on the efficiency of drains, as they are traditionally implemented through the whole thickness of the liquefiable layer when used as a remedial measure (e.g., Rollins, et al., 2004 and Chang, et al., 2004). Fig. 8-9 shows the distribution of the maximum excess pore pressure ratio, $(R_u)_{max}$ within the model that occurs over the time until after shaking ceases (12 s). In the figure, the high excess pore pressures are limited to the deep zones in this case. The effect of drain implementation is well pronounced in the upper half of the liquefiable layer.

The displacement vectors and flow pattern are shown in Fig. 8-10. The deformation is more uniform compared to that seen in *case I* where it tapers off sharply close to the bottom of the model. The time history of the surface lateral displacement for *case II* (treated with partially penetrated drain) is shown in Fig. 8-11. The model with the partial penetration drain exhibits stronger response to oscillation during shaking, thus indicating lower isolation effect from liquefaction. Also, the lateral displacement is less than that in *case I* (with a fully penetrated drain). This issue is discussed in more detail later.

8.3.3 Minimum Penetrated Drain, *Case III*

Minimum treatment can be achieved by installing the drain just through the barrier base, as depicted in *case III* (Fig. 8-3).

Fig. 8-12 shows the contours of maximum excess pore water pressure ratio, $(R_u)_{max}$ that occur within the model with drain of minimum penetration depth over time (along with contours obtained for the other cases, discussed later). The figure shows that most of the layer experiences large excess pore water pressures (indicated by high R_u values). However, the flow conditions (soil permeability and drain presence) mitigate the induced displacements. Fig. 8-13 shows the mesh with displacement and flow vectors after 16 s, which is similar to that of the drain with

partial penetration depth (Fig. 8-10). Thus, a drain with minimum penetration can also prevent localized deformations. This situation may occur in a real condition with the propagation of a crack in the barrier which is manifest as sand boils at the ground surface. Fig. 8-14 shows the time history of the surface lateral displacement, which resembles *case I* with fully-penetrated drain.

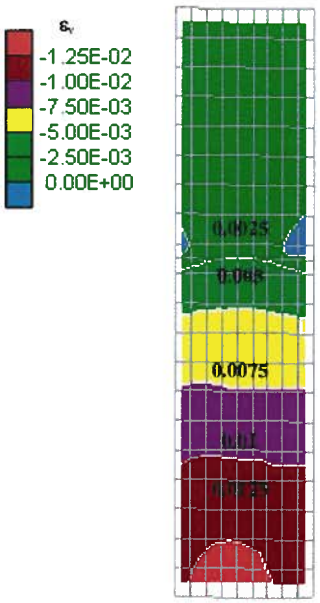

Fig. 8-8: Distribution of volumetric strain within the model, *Case I* (12 s).

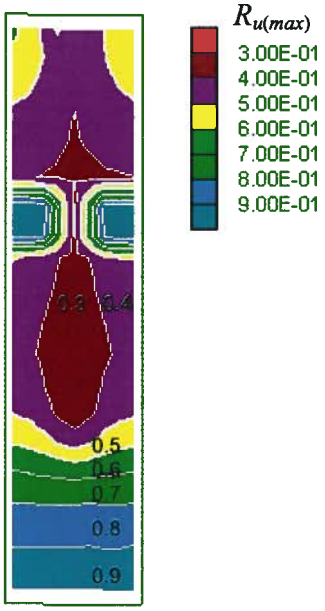

Fig. 8-9: Distribution of $(R_u)_{max}$ over time, during and after shaking (at 12 s), for the layer treated with the partially penetrated drain.

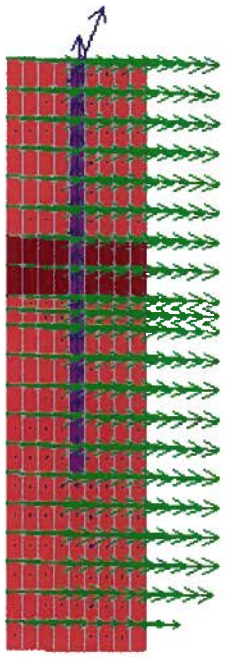

Fig. 8-10: Displacement and flow vectors within the model with partially penetrated drain after 10 s.

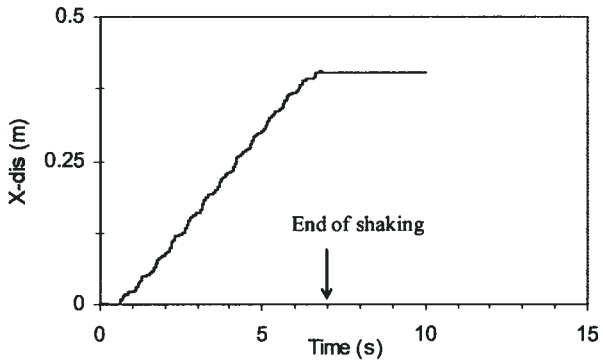

Fig. 8-11: Surface lateral displacement time history of the profile with partially penetrated drain (*case II*).

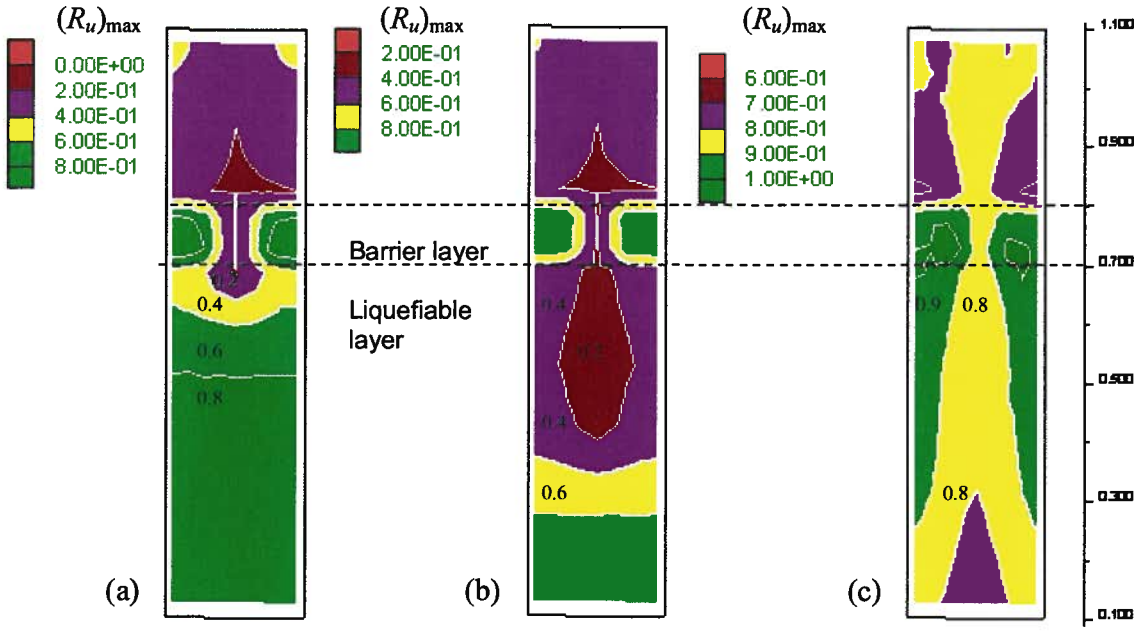

Fig. 8-12: Contours of $(R_u)_{max}$ within the model treated by drain with: (a) minimum penetration, (b) half penetration, and (c) complete penetration.

Fig. 8-15 compares surface lateral displacements of the three cases with that of the uniform layer, in terms of their time histories. It indicates that, essentially, the drains lower the deformations, compared to that of the layer without the barrier layer. This effect is attributed to a shorter duration of high excess pore water pressure within the liquefiable soil. The optimum solution; however, would not be full penetration of the drain through the liquefiable layer. Fig. 8-16 shows maximum surface lateral displacement vs. normalized drain penetration depth with regard to the liquefiable layer thickness (6 m). It reveals that the optimum solution is a drain with partial penetration. More discussion on the effects of penetration depth is presented in the following.

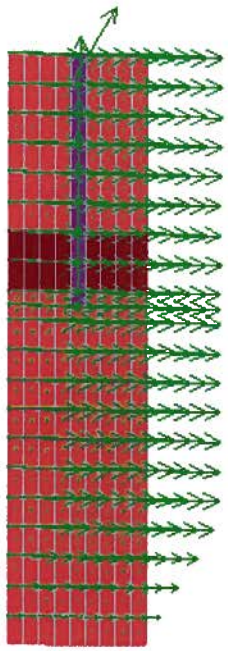

Fig. 8-13: Displacement and flow vectors within the model with minimum penetration drain after 16 s.

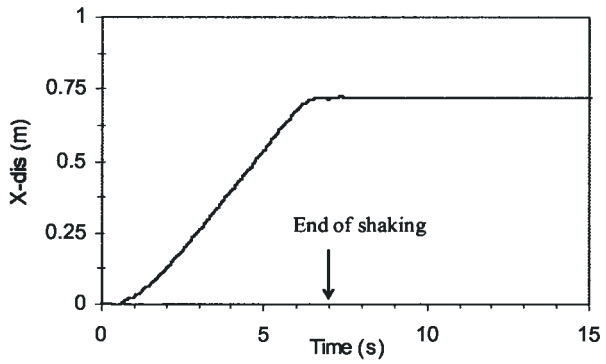

Fig. 8-14: Time history of surface lateral displacement for *case III* with minimum drain penetration.

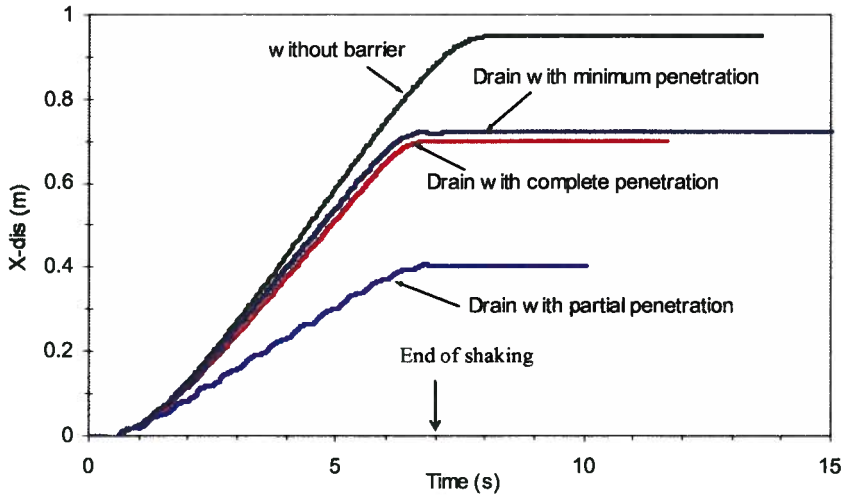

Fig. 8-15: Comparison of surface lateral displacement time histories with that of uniform layer.

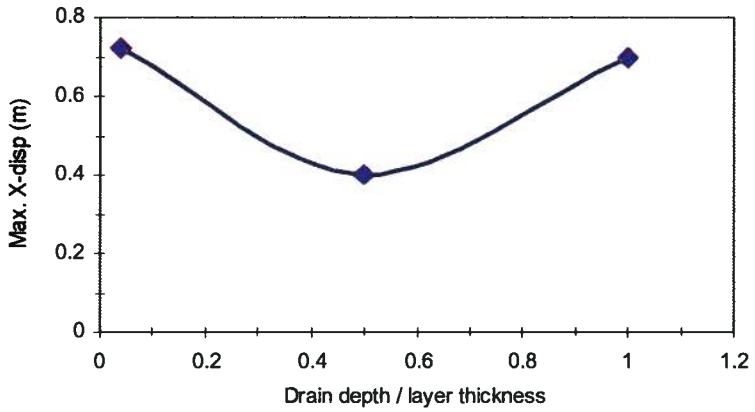

Fig. 8-16: Variation of maximum surface lateral displacement vs. drain penetration depth ratio.

8.3.4 Discussion on Drain Depth Effects

The results presented earlier imply that implementing drains with partial penetration depth results in a more desirable and economical solution for liquefiable slopes with barrier layers. In fact, the drains (or high permeability layers or dykes) also have some controversial effects, i.e.:

1. Dissipating effect by facilitating water passage of high pressures toward zones with lower pore water pressures.
2. Providing easier circulation of flow within the liquefied medium.
3. Alleviating the base isolation effect of the liquefied zones.

Deformation patterns (given in Fig. 8-7, Fig. 8-10, and Fig. 8-13) indicate that the insertion of drains in the liquefiable slope (with barrier layer) significantly influences its response to shaking. In all analyzed cases, the ground deformations are considerably lower than that of unimproved case that are controlled by an average (available) strength within the liquefiable layer. Contours of $(R_u)_{max}$ (given in Fig. 8-12) suggest that implementing a fully penetrated drain causes greater excess pore water pressure in the most parts of the liquefied layer. Fig. 8-17 shows the effects of drain depth on the time histories of excess pore water pressure, R_u in the mid-depth (element 1, 5) of the liquefiable layer, and the specific vertical discharge, *Y-Flow* beneath the barrier (element [1, 13]; see Fig. 8-3 for element positions). Fig. 8-17a shows that a drain with half penetration (*case II*) results in an average minimum R_u. Nevertheless, the dissipation rate is greater in *case I*, as expected. The figure also shows that the pore water pressure spikes become greater as the seismic drain extends to a greater depth. Fig. 8-17b shows the minimum inflow (or the least over-drainage) at the barrier base (for the farthest element i.e. [1, 13]), as occurs in *case II*. The minimum penetrated drain (*case III*) results in under-drainage as the inflow continues after shaking ceases, due to the low-capacity drainage system, whereas, the situation tends to become over-drainage, as in *case I*. In an ideal situation, with optimum drainage system, the rate of inflow and outflow are balanced and no expansion occurs at the barrier base. The over-drainage (inflow) is also reflected in the predicted stress-strain response of element [1,13] as shown in Fig. 8-18 for the 3 cases. It indicates that (high) inflow in full penetration case results in large strains (as discussed before in *Chapter 4*, Section 4.6) in the farthest element at the barrier interface. It shows that liquefaction occurs in earlier stage of shaking in this case as a result of water inflow through the full penetrated drain. Liquefaction in *case ii* occurs at late stages of shaking and in *case iii* the onset is between these two. This finding suggests that liquefaction and soil weakening can occur due to inappropriate drainage system because of easier water circulation within the model in earthquakes (issue 2). Fig. 8-19 compares the displacement profiles for the 3 cases with that of uniform layer and layer with barrier. It indicates that implication of drain causes a change in deformation pattern that increase from the fix base of the layer gradually.

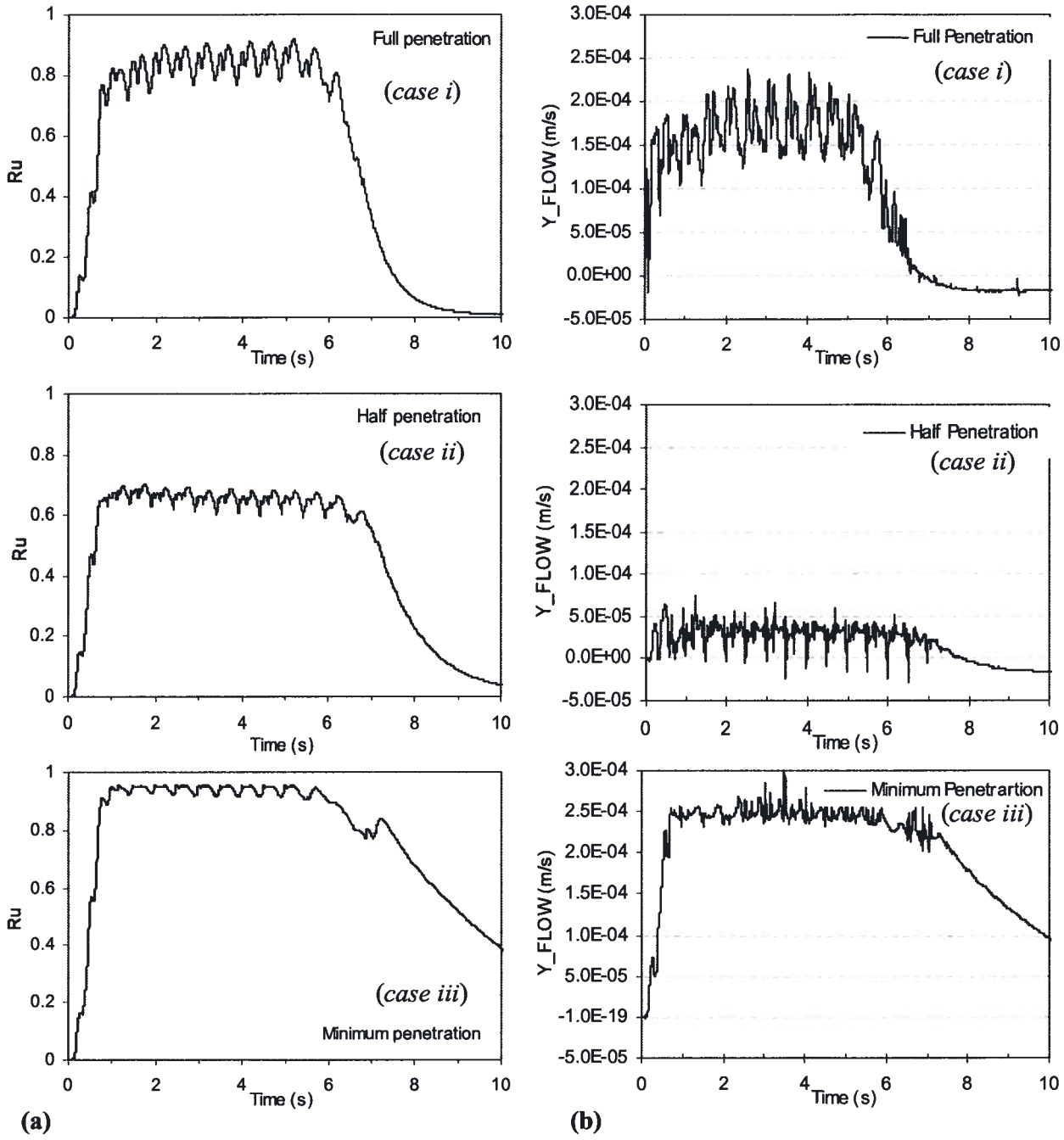

Fig. 8-17: Effects of penetration depth of the seismic drains in terms of time history of (a) R_u at mid-depth (element 1, 5), and (b) vertical specific discharge at barrier base (element 1, 13).

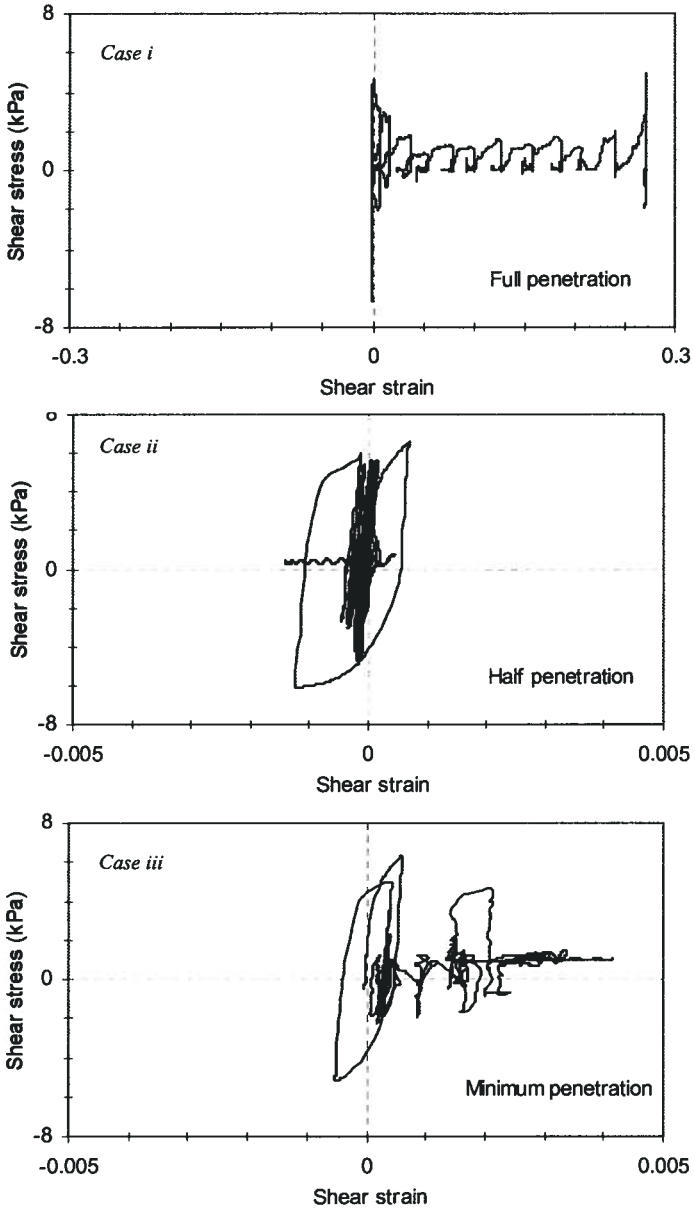

Fig. 8-18: Predicted stress-strain response for the barrier base element, [1,13] in the 3 cases.

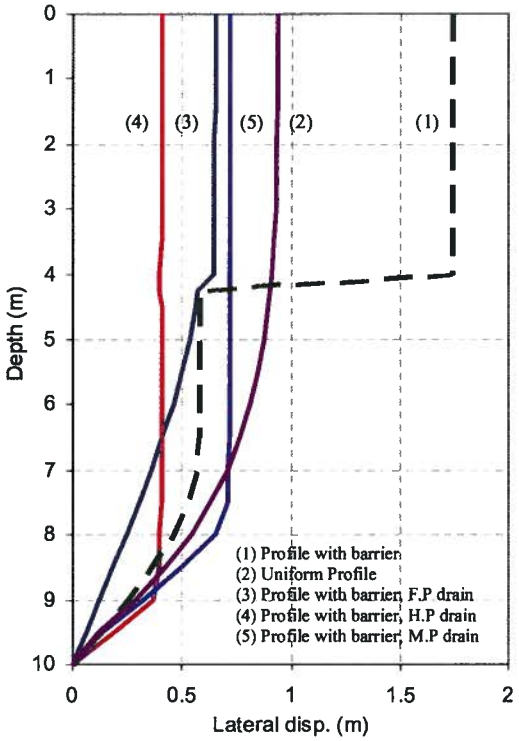

Fig 8-19: Deformation profile for the profile with/without barrier and with drain of various depths i.e. full penetration, half penetration, and minimum penetration.

The drain depth effect is also well pronounced in the acceleration records. Fig. 8-20 shows the acceleration time histories at the base of the barrier layer (node 1, 14) for the three cases. From the figure, some of the relatively smaller displacements in *case III* can be attributed to lower transmitted motion (base isolation effect) compared to those in *case I*. Thus, despite the greater motion in *case II*, the displacements are smaller due to the lower average R_u, driven by the (practically) optimum capacity of the drainage system. Deformations, in this case, show a

relatively greater influence over the excitation inertia effect, as reflected in the surface lateral displacement record (see Fig. 8-15). A similar observation regarding transmitted motion was considered for the densification improvement method, based on centrifuge model tests (Mitchell, et al., 1998). In general, the ground deformations take place because of the interplay of applied loads (transmitted motion), available average strength within the liquefiable medium (Fig. 8-12), and drainage capacity, as observed in these cases. Some of the above mentioned effects of a seismic drain application were noticed from centrifuge test models of liquefiable soils and foundations by a few researchers (e.g., Liu & Dobry, 1997; Cooke, 2000; Hausler, 2002; Ghosh & Madabhushi, 2003; Brennan & Madabhushi, 2005 and 2006). Likely, an inappropriate drain system only facilitates more net flow and exacerbates the situation, as the outcome of drain installation is controlled by various factors. In this regard, design optimization should consider seismic drain penetration depths along with drain spacing, in the engineering of seismic drain systems.

8.4 Effects of Drain Permeability Reduction

In practice the permeability of drains likely decreases over time due to fines migration or similar reasons. This was accounted for in the analyses by reducing the permeability of the drain 10-fold, compared to the previous analyses. Fig. 8-21 shows the time histories of surface lateral displacements for the three cases with reduced permeability of the drain. It shows that the deformations are essentially unaffected by this reduction in drain permeability. Thus, as long as the drain permeability is much greater than the barrier layer permeability, the drain can mitigate localized deformations and have an improved performance. Also, from the figure, penetration effects vanish with a decrease in drain permeability.

Another analysis was conducted to determine any lower bound for drain permeability reduction that might prevent localized deformation. Hence, the permeability of the drain curtain was reduced 100-times, which is the same as that of the liquefiable layer. This model also represents a liquefied deposit with the barrier layer that cracks (longitudinally) in the initial stage of shaking (or in a line of sand boils). In reality, at heterogeneity (e.g., small fissure, void, etc.) a fingering process may start within the barrier mass and make its way to the surface in the form of a sand boil, typically seen in a number of liquefied cases. Fig. 8-22 shows a long crack that was observed in a channel of the Salinas River, California, during the 1989 Loma Prieta earthquake (Yang & Elgamal, 2001).

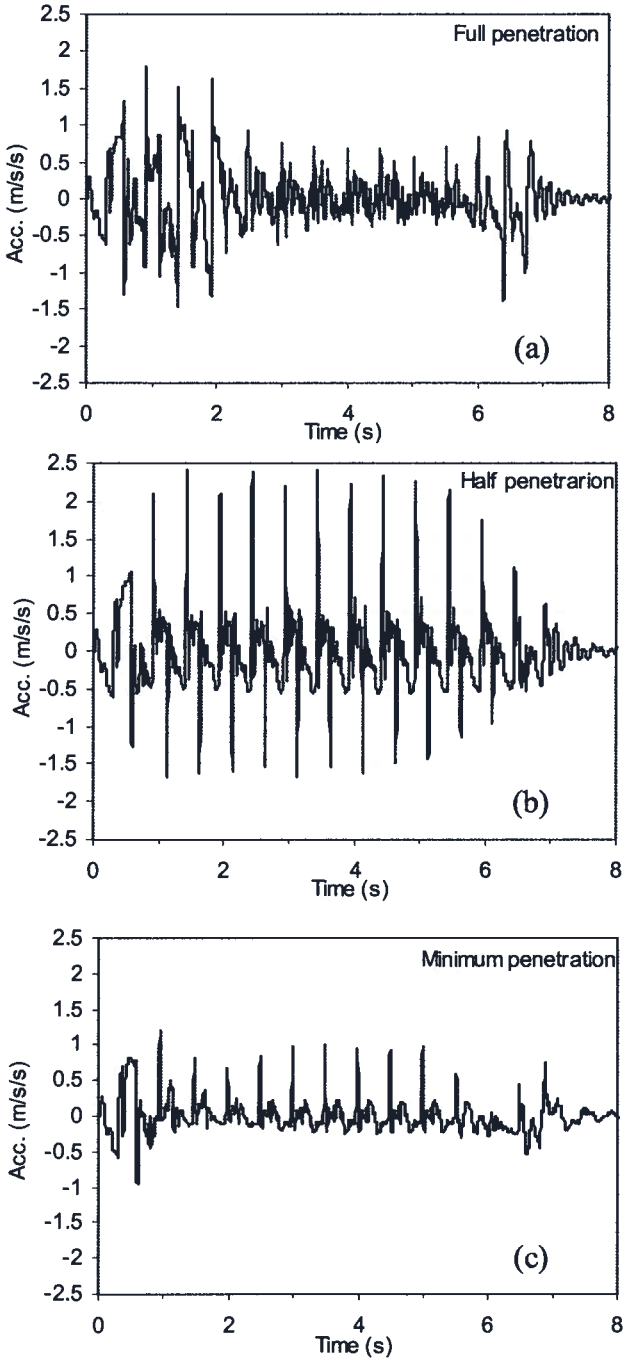

Fig. 8-20: Acceleration time history at the barrier base (1, 14) for model treated by drain of (a) full penetration, (b) half penetration and (c) minimum penetration.

The lateral surface displacement in this case increased to 1.3 m with localization beneath the barrier base. Fig. 8-23 shows the deformation pattern (displacement vectors) and contours of the maximum values of R_u, occurring over time. It suggests that a lower bound exists for the capacity of the drain curtain below which its performance is not satisfactory.

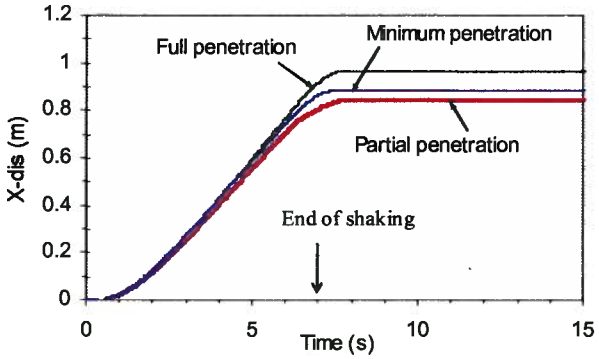

Fig. 8-21: Time histories for the three cases with reduced drain permeability.

Fig. 8-22: Open crack in liquefied soils in an abandoned channel of the Salinas River, Loma Prieta, California (earthquake: October 17, 1989) (adapted from Yang & Elgamal, 2001).

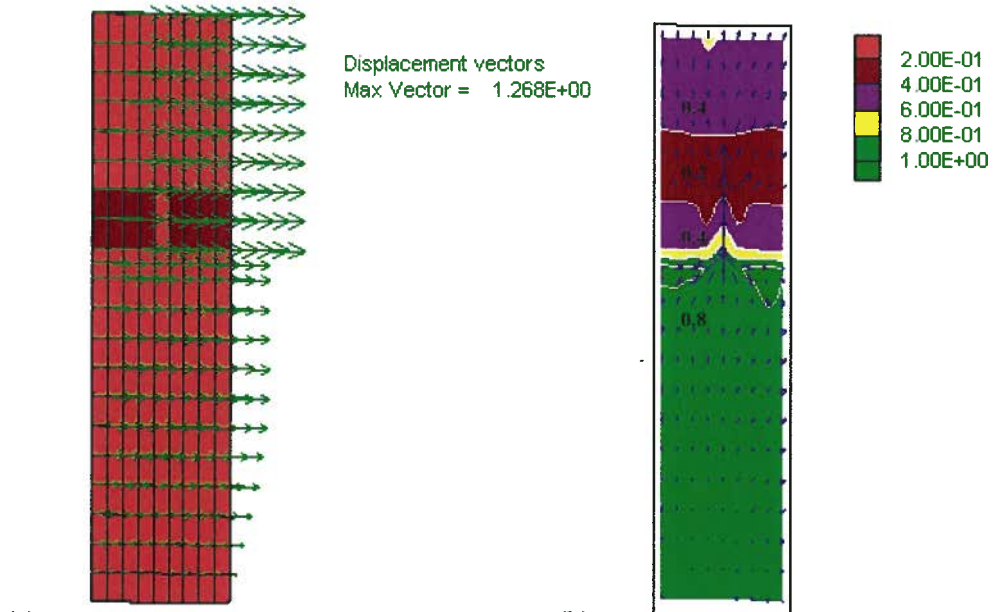

Fig. 8-23: Drain of minimum k (a) deformation pattern of the model with cracked barrier, maximum lateral displacement of 1.3 m, and (b) counters of $(R_u)_{max}$ within the soil profile.

The implementation of drains in liquefiable grounds mainly prevents the risk of localized deformations from the presence of the low permeability barrier layer with the consequent flow slide. However, the deformations can be larger than that can be tolerated by super-structures as the drains do not improve the mechanical properties of soil materials (passive treatment). From an engineering design point of view, this measure should also be combined with other treatment techniques, e.g., densification methods, as used in a few engineering projects such as the G. Massey Tunnel, BC (Yang, et al., 2003 and Seid-Karbasi, 2003). Based on centrifuge model tests and numerical analyses, Seid-Karbasi (2003) demonstrated that drains can provide more improvement than densification method for that submerged tunnel within liquefiable strata. A combination of densification and drain techniques, have been designed to lower the estimated deformations to minimum values that are tolerable (Yang, et al., 2003).

8.5 Summary and Main Findings

In this chapter, the effects of seismic drains in mitigating the destructive effects of the low permeability sub-layer were investigated. This study focused on the numerical modeling aspects of this improvement technique, which are summarized as follows:

i) Drains can alleviate the barrier layer effects and reduce the lateral deformations (shear failure).

ii) Installation of an appropriate seismic drain system results in lower deformations, even when compared to those of a uniform soil profile without the barrier layer. This agrees with physical modeling data and experience from past earthquakes, as noted by others.

iii) Seismic drains have multiple effects on the response of liquefiable soil layers to earthquakes i.e.,

   a) Dissipation effect,

   b) Facilitating flow within the medium.

   c) Alleviation of the base isolation effect of liquefied soil.

The extent of improvement from drain installation reflects the interplay of the above effects.

iv) Since the installation of drains essentially does not improve the mechanical properties of a liquefiable layer, other remedial measures (e.g., densification, combined with drains) should be considered to further lower deformations (particularly settlements).

The present research work showed that:

- Seismic drains with full penetration through the liquefiable layer are not the optimum measure in all cases. Drains with partial penetration are the optimum solutions for providing minimum deformations. They are also more cost-effective.

- Drains with minimum penetration can be a promising economic measure for providing improvement.

- A decrease in permeability of the drains has no significant influence on their performance, if the reduced permeability is sufficiently greater than that of liquefiable soil (more than 10 times). Development of sand boils through the barrier layer can also mitigate destructive effects on liquefied ground deformations to some degree.

- Systematic studies and numerical modeling, using a coupled stress-flow approach, can provide the optimum design solution for engineering projects.

CHAPTER 9

SUMMARY AND CONCLUSIONS

9.1 Introduction

The purpose of this research has been to understand and predict the effects of the void redistribution mechanism on deformations of liquefiable gentle slopes in earthquakes. Tasks performed in the study included the review of characteristic behavior of sands, past physical tests studies, and examination of case histories with possible void redistribution involvement. A numerical investigation was conducted to explore the mechanism arising from flow conditions. A comprehensive set of stress-flow coupled analyses was carried out to investigate the seismic behavior of a liquefiable gentle infinite slope with low permeability sub-layer. The findings presented here are not necessarily limited to these conditions.

In this study, a framework for a clear understanding of the void redistribution mechanism affecting the liquefaction-induced deformations and flow-slides was developed. The principal contributions of this study are:

- To provide an in-depth explanation for the occurrence of large deformations and/or failures which have been observed in very gentle liquefiable slopes following earthquakes. Based on this understanding supported by field data, physical models, and laboratory data, a simple and practical numerical approach was developed to model localized shear failures.
- This research also provides a basis for showing that the void redistribution mechanism is responsible for low residual strengths (S_r) back-calculated from failed case histories. Further, this research explains the reason for the inconsistencies between these values and the undrained *steady-state* strengths obtained from laboratory test data.

It was demonstrated that the applied coupled stress-flow dynamic analysis procedure can reproduce the seismic response of liquefiable soils, having a low permeability sub-layer. The presence of such sub-layers impede the upward drainage and can lead to the formation of water-rich zones with essentially zero shear strength causing the large ground deformations and flow slides. Based on the results of this study, seismic drains should be effective in alleviating the destructive effects of sub-layer hydraulic barriers.

For design implications, the main outcomes of this study are:

- Appropriate site investigation techniques should be applied to detect low-permeability thin layers (<1 m) within sand and/or gravel layers.
- If such layers are present and widespread liquefied zones are predicted, low residual shear strengths should be used that are consistent with field back-analyses, or a drainage/densification treatment method should be considered. The design of drains/densification can be optimized from coupled stress-flow dynamic analyses.
- Undisturbed samples, obtained prior to the earthquake, will not be representative of the conditions during, and shortly after the earthquake, due to the potential expansion or contraction from inflow or outflow of water. Such samples are quite useful to determine pre-earthquake properties (e.g. e_i) and the maximum expansion potential. Dissipation of excess pore water pressure some time after the earthquake, will re-consolidate soil elements beneath the barrier such that the undisturbed sample taken some time after the earthquake will also not be representative of the critical conditions.

In the following sections of this chapter, first a summary of the main features of the sands behavior and field observations related to void redistribution are addressed. Then the key findings of this research, along with recommendations for future investigations, are presented in the final sections.

9.2 Summary

In a seismic event, different types of deformations and mechanisms are involved in the liquefiable ground response and the failure. Observations from a number of case histories, where void redistribution may have played a role in the failure, suggests the need for field instrumentation of stratified ground to detect the void redistribution effects in future earthquakes (i.e., experimental arrays). Model tests and case histories provide valuable sources of information

for studies of void redistribution in earthquakes, and in particular model tests have shown that void redistribution occurs. Currently, no direct measurements are available to detect void changes within a physical model during shaking. Therefore, a numerical procedure developed based on fundamentals of Soil Mechanics that captures sand characteristic behavior can provide a very useful tool in understanding void redistribution and predicting response of liquefiable soils with barrier layers.

From laboratory tests, the behavior of sands is known to be affected by a number of factors (i.e., void ratio, stress and strain level, initial fabric, stress path, stress and strain history, fines content, aging, saturation, particle mineralogy and mixing). These data suggest that:

- Applied shear strain induces volume change in granular materials that results in dilation or contraction. This is a fundamental feature of the bahavior of granular materials.
- Laboratory test data indicate that partially drained conditions can provide the most severe condition compared to the conventional fully drained or undrained conditions.
- The liquefaction resistance of soils, in partially saturated conditions, is greater than that in fully saturated conditions.

Observations from case histories and previous physical model studies indicate that:

- Liquefaction-induced flow-slides have occurred in very gentle sloping ground in past earthquakes in many cases.
- Many of these failures were initiated some time after the main shock of the earthquake motion (from a few seconds to days).
- These failures cannot be explained by undrained residual strengths derived solely based on pre-earthquake soil void ratio.
- Physical model studies of slopes with, and without, low permeability sub-layers indicate that sand slopes as loose as 20% relative density were stable (with limited deformation) when subjected to earthquake shaking, if a barrier layer was not present. Similar tests of slopes of denser material, but with a silty sub-layer failed due to localization in the sand-silt interface.
- The void redistribution mechanism is a major factor affecting the response of earth structures in earthquakes.

9.3 Key Findings and Contributions

Most of the previous studies on seismic liquefaction have focused on mechanical properties of soils, with no account for flow properties. This investigation using a numerical coupled stress-flow procedure, based on effective stress approach, highlights the importance of flow conditions as a key issue in controlling the seismic behavior of earth structures.

The study's main contributions can be summarized as follows:

- *Typical seismic response of gentle slopes of liquefiable sands (without hydraulic barrier)*
  1. Excess pore water pressure reaches its maximum value (liquefaction onset) earlier at shallow depth, and lasts for a longer period, due to water migration from zones below with greater excess pore water pressures (the pore water pressure redistribution effect).
  2. Initiation of liquefaction at shallow depths, as observed in the case histories with liquefaction, and centrifuge tests, can essentially be attributed to pore water migration.
  3. Volumetric strain within the soil layer is generally contractive, after the end of shaking, due to dissipation of excess pore water pressure.
  4. Ground lateral deformation is larger at the surface and tapers off smoothly with depth, without any abrupt changes (no localization).
  5. A decrease in soil layer permeability results in higher excess pore water pressure lasting for a longer time, leading to greater displacements that extend to deeper parts.
  6. For given mechanical properties (e.g., *CRR* and earthquake) inclusion of fine-grained materials (e.g., silt) in a uniform liquefiable sand layer results in greater deformations due to the permeability reduction.

These findings are in agreement with observations from physical model testing data and case histories reported by other investigators.

- *Impacts of a hydraulic barrier on the above described response*
  1. Excess pore water pressure is generated with a similar pattern to that of the soil layer without barrier.
  2. Excess pore water pressure dissipation is affected significantly due to the impedance of flow path, particularly in zones near the barrier base.
  3. The high excess pore water pressure at the base of the hydraulic barrier lasts for a long time after the earthquake ceases.

4. Volumetric strains are essentially contractive at the lower parts whereas they are expansive at the upper parts close to the barrier base.
5. The deformation pattern is significantly different, in comparison to the case without a barrier. The magnitude at the ground surface is greater and has a larger post-shaking portion.
6. Most of the deformation is concentrated (localized) at a thin zone beneath the barrier.
7. Post-liquefaction strength loss, due to the (hydraulic) barrier presence explains the inconsistencies seen between the (*steady-state*/residual) strengths derived from back analysis of the *flow-slide* case histories and those derived from laboratory testing of samples at pre-earthquake void ratios. A given soil may exhibit a wide range of (residual) strengths, depending on the degree of expansion taking place because of the earthquake shaking.
8. Excess pore water pressure redistribution results in contraction in the lower parts (about 60% of the layer thickness) and expansion in the upper parts (about 40% of the layer thickness) of a liquefied loose layer in the presence of a low permeability sub-layer. This is a key characteristic behavior, regardless of the liquefiable soil layer thickness.
9. Void redistribution in sloping grounds can lead to two scenarios:
    a. Large lateral displacement, and
    b. *Flow-slide*, if enough water flows into the expansion zone.
10. Analyses of models with localized strains can lead to different results depending on the thickness of the barrier interface element (mesh-size effect).
11. A simple and practical approach to handle the strain localization problem involved in numerical analysis was proposed. The approach was shown to be capable of predicting a *flow-slide.*

➢ *Effects of various mechanical and flow factors*

1. Surface lateral displacements increase with barrier thickness, underlying liquefied layer thickness, ground slope, and motion amplitude.
2. A decrease in permeability contrast lessens the barrier effects
3. Shallower barrier layers results in lower lateral displacements with less post-shaking deformations due to the lower driving shear stresses.
4. Motion duration can have a significant impact on the increase of displacements.

5. Materials having higher relative density, and stronger mechanical properties, exhibit a better performance during earthquakes due to the lower excess water pressure rise, and the greater expansion potential.

The effects of some of these factors were examined by others using physical model testing, the results of this study are in agreement with those observations.

- *Partial saturation effects*
  1. In liquefiable grounds with a partial saturation condition, excess pore water pressure rises with a delay and dissipates at a lower rate. In such conditions, the displacements are reduced.
  2. The presence of a low permeability barrier within a partially saturated liquefiable layer can cause greater displacements, in comparison to those in a (fully) saturated condition.
  3. The response of Wildlife Liquefaction Array (WLA) site during the 1987 Superstition Hill earthquake can be explained on the basis of partial saturation effects on liquefied soil behavior.
- *Seismic drains as a remedial measure*
  1. Seismic drains can effectively alleviate the barrier layer effects and reduce the ground deformations and localization effects.
  2. Drains with full penetration through the liquefiable layer may not be an optimal measure for all cases. Seismic drains with partial penetration are optimal solutions that provide minimal deformations, and are also more cost-effective.

9.4 Recommendations for Further Studies

Even though this research has improved the understanding of liquefaction-induced ground failures and, in particular, the role of void redistribution in large deformations, more research is necessary to increase our understanding of liquefaction-related issues. Therefore, experimental studies including laboratory, field and physical test models and numerical analysis are needed to understand this complex phenomenon, specifically:

- To develop reliable and accurate measurements of in-situ initial states, including: magnitudes and history of stresses, soil stiffness, void ratio, hydraulic conductivity (permeability) and its spatial variation, flow pattern, and saturation.

- To develop a direct technique to measure soil void changes in physical model tests during simulated earthquake loading. So far, only inferences can be made about void redistribution, based on the deformation patterns and pore pressure measurements.
- Field instrumentation for experimental array sites that can detect the presence or absence of void redistribution during future earthquakes would be valuable to confirm its importance.
- To conduct physical model tests (centrifuge tests) of infinite slopes with a barrier layer, to explore the effects of different factors, i.e., barrier layer depth, ground inclination, liquefiable layer thickness, etc. on lateral spread and/or flow-slide.
- To conduct experimental studies on liquefiable level grounds, to directly monitor and quantify water film formation and the subsequent sedimentation/reconsolidation process, based on levels of liquefaction, with and without a barrier layer. This can provide reliable data for numerical modeling of post-liquefaction sedimentation. The investigation can also be extended to sloping grounds condition.
- To carry out centrifuge model tests of steep slopes subjected to different levels of excitation and magnitude, to study the effects of high shear stress bias.
- To conduct laboratory investigations (e.g., injection test under simple shear condition) on the volumetric expansion potential, to provide more reliable data in this regard.
- To refine the *UBCSAND* constitutive model to improve its performance under static shear stress bias (e.g., one-way loading) and post-liquefaction settlement prediction.
- To incorporate stress-level-dependent contraction to *UBCSAND* model to account for the K_σ effect directly and also upgrading the current 2-D version (plane-strain) *UBCSAND* model to a 3-D version.
- To improve the analysis procedure by updating the soil properties based on the current void ratio (accumulated volumetric strain) during the pore water pressure redistribution process.
- To perform a parametric study on the behavior of liquefiable layers with multiple barrier layers, to develop a rational approach for modeling the conditions as a single layer with one equivalent sub-layer barrier. This would provide an efficient and practical tool.
- To investigate the directional effects of shaking on sand element behavior (i.e. bi-directional/multi-directional loading) and its contribution in the observed behavior in

some case histories e.g., Mochikoshi tailings dams (the site comprised of two similar dams but they responded differently when subjected to a certain earthquake event).

- Availability of high capacity computers together with computational codes using Discrete Element Methods (DEM) provides a new area and opportunity to enhance the current numerical modeling techniques developed based on Continuum Mechanics concepts. This approach as an aid can be used to investigate the following issues to enhance plasticity models:
    i. Effective stress concept for various porous media.
    ii. Relationship of principal stress direction and principal strain direction (co-axiality).
    iii. Yield conditions and flow rules (i.e. normality) for granular materials.
    iv. Characteristics of shear bands e.g. initiation condition, thickness, direction etc.
    v. Fabric and anisotropy.

REFERENCES

Abdel-Ghaffar, A. M. and Scott, R. F. 1978. "Investigation of the Dynamic Characteristics of an Earth Dam", *Report No. EERL 78-02,* Earthquake Engineering Laboratory, Pasadena.

Alshibli, K.A., and Hasan, A. 2008. "Spatial Variation of Void Ratio and Shear Band Thickness in Sand using X-Ray Computed Tomography", *Geotechnique,* V. 58(4), pp. 249-257.

Alshibli, K.A., Sture, S., Costes, N.C., Frank, M.L., Lankton, M.R., Batiste, S.N., and Swanson, R.A. 2000a. "Assessment of Localized Deformations in Sand using X-ray Computed Tomography", *Geotechnical Testing Journal*, ASTM, V. 23(3), pp. 274-299.

Alshibli, K.A., Sture, S., and Batiste, S.N. 2000. "Experimental Evaluation of Bifurcation Phenomena in Sands", In *Proc., 8th Intl. Symposium on Plasticity and Its Current Applications,* July 16-20, Whistler, Canada, A.S. Khan, H. Zhang, and Ye Yuan (Eds.), NEAT Press, Fulton, MD, 276-278.

Adalier, K. 1996. "Mitigation of Earthquake Induced Liquefaction Hazards", *Ph.D. Dissertation,* Rensselaer Polytechnic Institute, Troy, New York, 659 p.

Adalier, K. 2001. "Liquefaction and Ground Failures during the 1998 Adana (Turkey) Earthquake and Lab Model Simulations", In *Proc. 4th Int. Conf., Recent Advances in Geotechnical Earthquake Engg. and Soil Dynamics and Symposium in Honor of Prof. L. Finn,* San Diego, CA., March 26-30, 2001, Paper No. 4.47.

Adalier K. and Elgamal, A. 2001. "Seismic Response of Dense and Loose Sand Columns", In *Proc. 4th Int. Conf., Recent Advances in Geotechnical Earthquake Engg., and Soil Dynamics and Symposium in Honor of Prof. L. Finn,* San Diego, CA., March 26-30, 2001, Paper No. 4.19.

Adalier K. and Elgamal, A. 2002. "Seismic Response of Adjacent Dense and Loose Saturated Sand Columns", *J., Soil Dynamics and Earthquake Engineering,* Elsevier Science Ltd., V. 22, pp. 115-127.

Adalier K. and Elgamal, A. 2004. "Mitigation of Liquefaction and Associated Ground Deformations by Stone Columns", *J., Engineering Geology,* Elsevier, V. 7, pp. 275-291.

Adalier K., Elgamal, A., and Martin, G. 1998. "Foundation Liquefaction Countermeasures for Earth Embankments", *ASCE J., Geotechnical and Geo-environmental Engineering,* V. 124(6), pp. 500-517.

Alba, P. and. Ballestero, T. 2006. "Residual Strength after Liquefaction: A Rheological Approach", *J., Soil Dynamics and Earthquake Engineering,* Elsevier Science Ltd., V. 26, pp. ??.

Alba, P., Stepp, C., Nigbor, R. and Steidl, J. 2004. "Summary of Workshop Discussions and Workshop Recommendations", In *Proc., Int. Workshop for Site Selection, Installation and Operation of Geotechnical Strong-Motion Arrays*", COSMOS, Los Angeles, Cal., Oct 2004.

Akiba, M., and Semba, H.1941. "The Earthquake and its Influence on Reservoirs in Akita Prefecture", *J. Agricultural Engineering Soc.* Japan, V. 13(1), pp. 31-59.

Amini, F., and Chakraverty, A. 2004. "Liquefaction Testing of Layered sand-gravel Composites", Geotechnical Testing J., ASTM, V. 27 (1), pp. 1-11.

Amini, F., and Qi, G. Z. 2000. "Liquefaction Testing of Stratified Silty Sands", *ASCE J. Geotechnical and Geoenvironmental Engg.,* V. 126(3), pp.208-217.

Amini, F., and Sama, K.M. 1999. "Behavior of Stratified Sand-Silt-Gravel Composites under Seismic Liquefaction Conditions", *J., Soil Dynamics and Earthquake Engg.,* Elsevier Science Ltd., V.18, pp. 445-455.

Anderson, D.G and Stokoe, K.H. 1978. "Shear Modulus, A Time–Dependent Soil Property", In *Dynamic Geotechnical Testing,* ASTM Special Technical Publication, 954, pp. 66-90.

Andrews, D. C. A. 1997. "Liquefaction of Silty Soils; Susceptibility, Deformation, and Remediation", *Ph.D. Dissertation.* University of Southern California, Los Angles. 374p.

Andrew, D. C. A., and Martin, G. R. 2000. "Criteria for Liquefaction of Silty Soils ", In *Proc., the 12th World Conf., Earthquake Engg.,* Auckland, New Zealand, Jan., 30-Feb., 4, 2000, Paper No. 0312.

Anubhav, & Rao, N. S. K. 2001. "Liquefaction Studies on Silty Clays Using Cyclic Triaxial Tests", In *Proc. 4th Int. Conf., Recent Advances in Geotechnical Earthquake Engg. and Soil Dynamics and Symposium in Honor of Prof. L. Finn,* San Diego, CA., March 26-30, 2001, Paper No. 4.55.

Andrus, R. D., Stokoe II, K. H., and Rosset, J. M. 1991. "Liquefaction of Gravelly Soil at Pence Ranch during the 1983 Borah Peak, Idaho Earthquake", In *Proc. 5th Intl. Conf.Soil Dynamics and Earthquake Engineering*, Kalsruhe, Germany, pp. 251-262.

Arulanandan, K., and Scott, R. F., (Editors), 1993. "Verification of Numerical Procedures for the Analysis of Soil Liquefaction Problems", *International Conference Proceedings on VELACS Project,* Two Volumes, A.A. Balkema, the Netherlands.

Arulanandan, K. and Sivathasan, K. 2000. "Evaluation of Dynamic Site Response and Deformation of Instrumented Site: El Centro", In *Proc., Computer Simulation of Earthquake Effects,* Geo Denver, ASCE, pp. 166-200.

Atigh, E. and Byrne, P. M. 2004. "Liquefaction Flow of Submarine Slopes under Partially Undrained Conditions: An Effective Stress Approach", *Canadian Geotechnical Journal,* V. 41, pp. 154-165.

Atukorala, U., Wijewickreme, D., and Mc Cammon, N. 2000. "Some Observations related to Liquefaction Susceptibility of Silty Soils", In *Proc., the 12th World Conf., Earthquake Engg.*, Auckland, New Zealand, Jan., 30-Feb., 4, 2000, Paper No. 1324.

Balakrishnan, A. 2000. "Liquefaction Remediation for a Bridge Site", *PhD. Dissertation,* Un. California, Davis, California. 261p.

Bardet, J. 1997. "Laboratyory Data Files from the Verfication of Liquefaction Analysis and Centrifuge Studies (VELACS)", Geotechnical Earthquake Egineering Server [on lines data files], available at: *http://rccg01.usc.edu.edu/ GEES/celacs/labdata.html.*

Bardet, J., Oka, F., Sugito, M. and Tashima, A. 1995. "The Great Hanshin Earthquake Disaster", *Preliminary Investigation Rep.*, Dept. of Civil Engg., Un., Southern California, Los Angeles, CA.

Bastani, A. 2003. "Evaluation of Deformations of Earth Structures due to Earhtquakes", *PhD. Dissertation,* Un. California, Davis, California. 305p.

Baziar, M. H., and Dobry, R. 1995. "Residual Strength and Large Deformation Potential of Loose Silty Sands", *ASCE J., Geotechnical and Geo-Environmental Engg.,* V. 121(12), pp. 896-906.

Beaty, M. H. 2001. "A Synthesized Approach for Estimating Liquefaction-Induced Displacements of Geotechnical Structures", *Ph.D. Dissertation*, Un., British Columbia, Vancouver, BC., 328 p.

Beaty, M. H. and Byrne, P. M. 1998. "An Effective Stress Model for Predicting Liquefaction Behavior of Sand", In *Proc., Specialty Conf., Geotechnical Earthquake Engg. and Soil Dynamics III, Seatle,* ASCE GSP No. 75, Edited by Dakouluas, M. and Holtz, R.D., V. 1, pp. 766-777.

Beaty, M. H. and Byrne, P. M. 1999. "A Synthesized Approach for Modeling Liquefaction and Displacements", In *Proc., Conf., FLAC and Numerical Modeling in Geomechanics,* Edited by Detourneay and Hart, R., A. A. Balkema, Rotterdam, pp. 339- 347.

Beaty, M. H. and Byrne, P. M. 2001. "Observations on the San Fernando Dams", In *Proc. 4th Int. Conf., Recent Advances in Geotechnical Earthquake Engg. and Soil Dynamics and Symposium in Honor of Prof. L. Finn,* San Diego, CA., March 26-30, 2001, Paper No. 4.27.

B.C-Hydro, 1992. "Report on Laboratiory Testing on Foundation Soils, Appendix to Report, V. 2", *Hydroelectric Engineering Division, Geotechnical Department,* Report No. Geo 1/91. Updated June 1992.

Been, K., Jefferies, M. G. and Hachey, J. 1991. "The Critical State of Sands", *J., Géotechnique,* V. 41(3), pp. 365–381.

Been, K., and Jefferies, M.G. 1985. "A State Parameter for Sands", *Geotechnique,* V. 35(2), pp. 99-112.

Been, K., and Jefferies, M.G. 2004. "Stress-Dilatancy in Very Loose Sands", *Canadian Geotechnical Journal,* V. 41, pp. 972-989.

Bennett, M. J., Mclaughlin, P. V., Sarmiento, J. S., and Youd, T. L. 1984. "Geotechnical Investigation of Liquefaction Sites, Imperial Valley, California", *Open-file Report 84–252,* U.S. Geological Survey, Washington D.C.

Berrill, S. A., Christensen, S. A., Keenan R. J., Okada, W. and Pettinga, J. R. 1997. "Lateral-Spreading Loads on a Piled Bridge Foundation", In *Proceedings, Discussion Session, Seismic Behavior of Ground and Geotechnical Structures,* ICSMGE, Humburg, pp. 173–83.

Berrill, S. A., Christensen, S. A., Keenan R. J., Okada, W. and Pettinga, J. R. 2001. "Case Study of Lateral Spreading forces on piled Foundation", *Geotechnique,* V. 51 (6), pp. 501-517.

Bishop, A. W. 1954. "Shear Characteristics of a Saturated Silt, Measured in Triaxial Compression", *Correspondence, Geotechnique,* V. 4, pp. 43-45.

Biggs, J. M. 1964."*Introduction to Structural Dynamics*. New York: McGraw-Hill.

Bishop, A. W. 1971. "Shear Strength Parameters for Undisturbed and Remolded Soil Specimens", In *Proc. of the Roscoe Memorial Symposium,* Cambridge University, Cambridge, Mass., pp. 3–58.

Biot, M.A. 1941. "General Theory of Three dimensional Consolidation", *Journal of Applied Physics,* V. 12, pp. 155-164.

Bobei, D. C. 2004. Static Liquefaction with Small Amount of Fines", *Ph.D. Dissertation,* School of Aerospace, Civil & Mech. Engg., NSW University, Australia.

Bobei, D. C. and Lo, S. R. 2003. "Strain Path Influence on the Behavior of Sand with Fines", In *Proc., 12th Pan-American Conf., Soil Mechanics and Geotechnical Engineering,* Soil and Rock America 2003, V.1, pp. 583-588.

Bolton, M. D. 1986. "The Strength and Dilatancy of Sands", *Geotechnique*, V. 36(1), pp. 65-78.

Bopp, P. and Lade, P. 2005a. "Relative Density Effects on Drained Sand Behavior at High Pressure", *Soils and Foundations,* V. 45(1), pp. 1-15.

Bopp, P. and Lade, P. 2005b. "Relative Density Effects on Undrained Sand Behavior at High Pressure", *Soils and Foundations,* V. 45(1), pp. 16-26.

Bouckovalas, G. D., Gazetas, G. and Papadimitriou, A. G. 1999. "Geotechnical Aspects of the 1995 Aegion (Greece) Earthquake", In *Proceedings, 2nd Inernational, Earthquake Geotechnical Engineering,* Lisbon, Portugal, 21-25 June, pp. 739-748

Boulanger, R.W. 1990. "Liquefaction Behavior of Saturated Cohesionless Soils Subjected to Uni-Directional and Bi-Directional Static and Cyclic Loads", *Ph.D. Thesis,* University of California, Berkeley.

Boulanger, R. W. 1999. "Void Redistribution in Sand Following Earthquake Loading", In *Proc., Physics and Mechanics of Soil Liquefaction,* A. A. Balkema, Rotterdam; pp 261-268.

Boulanger, R. W. 2003a. "Relating K_α to Relative State Parameter Index", *J. Geotechnical and Geo-Environmental Engineering*, ASCE, V. 129(8), pp.770-773.

Boulanger, R. W. 2003b. "High Overburden Stress Effects in Liquefaction Analyses", *J. Geotechnical and Geoenvironmental Engineering*, ASCE, V. 129(12), pp. 1071-1082.

Boulanger, R. W., Arulnathan, R., Harder, L. F., Torres, R. A., and Driller, M. W. 1998. "Dynamic properties of Sherman Island Peat", *ASCE J., Geotechnical and Geoenvironmental Engg.*, V. 124(1), pp.12-20.

Boulanger, R. W., and Idriss, I. 2004. "Evaluation the Potential for Liquefaction or Cyclic Failure of Silts and Clays", *Report No. UCD/CGM-04/01,* Un. Cal., Davis.

Boulanger RW, and Idriss I.M. 2004. "State Normalization of Penetration Resistance and the Effect of Overburden Stress on Liquefaction Resistance", In *Proc., 11th Int. Conf., Soil Dynamics and Earthquake Engineering* and 3rd International Conference on Earthquake Geotechnical Engineering, Univ. of California, Berkeley, CA, 2004.

Boulanger, R. W., and Idriss, I. 2006. "Assessing the Potential for Strength Loss and Deformations in Low Plasticity Silts and Clays during Earthquakes", In *Proc., 3th Int. Conf., Urban Earthquake Engineering* , Tokyo Institute of Technology, Tokyo, pp. 77-84.

Boulanger, R. W., and Idriss, I. 2006. "Liquefaction Susceptibility Criteria for Silts and Clays", *ASCE J., Geotechnical and Geoenvironmental Engg.*, V. 132(11), pp.1413-1426.

Boulanger, R. W., Stewart, D., Idriss, I., Hashash, Y., and Schmidt, B. 1997 ", Notes for Seismic Short Course: (1) In-Ground Walls for Mitigation of Liquefaction Hazards, (2) Drainage Capacity of Stone Column or Gravel Drains*", the Third Seismic Short Course on Evaluation and Mitigation of Earthquake Induced Liquefaction Hazards.* Cal. Un., Berkeley.

Boulanger, R. W., and Truman, S. P. 1996. "Void Redistribution in Sand under Post-Earthquake Loading", *Canadian Geotechnical J.*, V. 33. pp 829-833.

Brandon, T., Rose, A., and Duncan, J.M. 2006. "Drained and Undrained Strength Interpretation for Low-Plasticity Silts", *ASCE J. Geotechnical and Geoenvironmental Engineering,* V. 132(2), pp. 250-257.

Bray, J. D. and Sancio, R. B. 2006. "Assessment of the Liquefaction Susceptibility of Fine-Grained Soils", *ASCE J. Geotechnical and Geoenvironmental Engineering,* V. 132(9), pp. 1165-1177.

Bray, J. D., Sancio, R. B., Durgunoglu, T., Onalp, A., Youd, T. L., Stewart, J. P., Seed, R. B., Cetin, O. K., Bol, E., Baturay, M. B., Christensen, C., and Karadayilar, T. 2004. "Subsurface Characterization at Ground Failure Sites in Adapazari, Turkey", *ASCE J. Geotechnical and Geoenvironmental Engineering,* V. 130(7), pp. 673-685.

Bray, J. D., Sancio, R. B., Riemer, M. F., and Durgunoglu, T. 2004. "Liquefaction Susceptibility of Fine-Grained Soils", In *Proc. 11th Int. Conf. on Soil Dynamics & Earthquake Engineering & 3rd Int. Conf. on Earthquake Geotechnical Engineering*, Stallion Press, V. 2, pp. 655-662.

Brennan, A. J. and Madabhushi, S. P. 2005."Liquefaction and Drainage in Stratified Soil", *ASCE J. Geotechnical and Geoenvironmental Engineering,* V. 131(7), pp. 876-885.

Brennan, A. J. and Madabhushi, S. P. 2006. "Liquefaction Remediation by Vertical Drains with Varying Penetration Depths", *J., Soil Dynamics & Earthquake Engineering,* V. 26, pp. 469-475.

Brooks, R. and Crey, A. 1964. "Hydraulic Properties of Porous Media", *Colorado State University,* Hydrology Paper No. 3.

Burland, J.B. 1989. "Small Is Beautiful: The Stiffness of Soils at Small Strains," *Canadian Geotechnical Journal*, Vol. 26, No. 4, pp. 499–516.

Butterfield, K., and Bolton, M. D. 2003. "Modeling Pore Fluid Migration in Layered, Liquefied Soils", In *Proc., Pacific Conf. on Earthquake Engineering*, N.Z Society for Earthquake Engineering, Christchurch, New Zealand, Paper No. 131.

Byrne, P. M. 1991. "A Model for Predicting Liquefaction Induced Displacements due to Seismic Loading", In *Proc., Second Int. Conf., Recent Advances in Geotechnical Earthquake Engg., and Soil Dynamics, March 11-15, 1991, St. Louis, Missouri,* V. 2, pp. 1027-1035.

Byrne, P. M. 1991. "A Cyclic Shear-Volume Coupling and Pore Pressure Model for Sand", In *Proc., Second Int. Conf., Recent Advances in Geotechnical Earthquake Engg., and Soil Dynamics,* March 11-15, 1991, St. Louis, Missouri, V. 2, pp. 47-55.

Byrne, P. M. 2003. "Personal Communications".

Byrne, P. M. 2007. "Personal Communications".

Byrne, P. M., Cheung, H. and Yan, L. 1987. "Soil Parameters for Deformation Analysis of Sand Masses", *Canadian Geotechnical J.,* V. 24, (3), pp. 366-376.

Byrne, P. M., Debasis, R., Campanella, R.G., and Hughes, J. 1995. "Predicting Liquefaction Response of Granular Soils from Self-Boring Pressuremeter Tests", In *Proc., Conf., Static and Dynamic Properties of Gravely Soils, ASCE National Convention,* San Diego, Calif., 23–27 Oct. 1995, Edited by Evans, M. D. and Fragaszy, R. J., ASCE, GSP No. 56, pp. 122–135.

Byrne, P.M. and Beaty, M. 1998. "Post-Liquefaction Shear Strength of Granular Soils: Theoretical/ Conceptual Issues", In *Proc., Workshop on Post-Liquefaction Shear Strength of Granular Soils*, University of Illinois at Urbana-Champaign.

Byrne, P. M., and Beaty, M. H. 1999. "Assessment of Residual Strength for Embankments", In *Proc., Second Int. Conf., Earthquake Geotechnical Engg.*, Lisboa, edited by Pinto, A. A. Balkema, the Netherlands, V. 3, pp. 1069-1075.

Byrne, P.M., Imrie, A. S., and Morgenstern, N. R. 1994. "Results and Implications of Seismic Performance Studies for Duncan Dam", *Canadian Geotechnical J.,* V. 31(6), pp. 979-988.

Byrne, P.M., and Seid-Karbasi, M. 2003. "Seismic Stability of Impoundments", In *Proceedings, 17th VGS Symposium on Geotechnical Engineering for Geoenvironmental Applications,* Vancouver, British Columbia, pp. 77-84.

Byrne, P.M., Park, S., Beaty, M., Sharp, M., Gonzalez, L., Abdoun, T. 2004. "Numerical Modeling of Liquefaction and Comparison with Centrifuge Tests" *Canadian Geotechnical J.*, V. 41, pp. 193-211.

Byrne, P.M., Naesgaard, E. and Seid-Karbasi, M. 2006. "Analysis and Design of Earth Structure to Resist Seismic Soil Liquefaction", *Hardy Lecture* In *Proc., 59th Canadian Geotechnical Conf.,* Vancouver, pp. 1-24.

Byrne, P. M. and Wijewickreme, D., 2006. "Liquefaction Resistance and Post-Liquefaction Response of Soils for Seismic Design of Buildings in Greater Vancouver", In *Proc. 59th Canadian Geotechnical Conference,* Vancouver.

Castro G. 1969. "Liquefaction of Soils", *Ph.D. Dissertation,* Harvard Un., Cambridge, Mass., 231 p.

Castro G. 1975. "Liquefaction and Cyclic Mobility of Saturated Sands", *ASCE J., Soil Mechanics and Foundation Engineering Division,* V. 101, pp. 551-569.

Castro, G. 1998. "Post-Liquefaction Shear Strength from Case Histories", In *Proc. National Science Foundation Workshop on Shear Strength of Liquefied Soils.* pp 53-57.

Castro, G. 2001. "Steady State Testing for Nevada Sand", *Memorandum to Void Redistribution Research Team by GEI Consultants Inc.,* University of California, Davis.

Castro, G., Keller, T. O., and Boynton, S. S. 1989. "Re-Evaluation of the Lower San Fernando Dam. Report 1: An Investigation of the February 9, 1971 Slide." *Rept. No. GL-89-2, U.S. Army Corps of Engineers, WES.*

Cetin, K.O., Seed, R.B., Kiureghian, A.D., Tokimatsu, K., Harder, L.F., Jr., Kayen, R.E., and Moss, R.S. 2004. "Standard Penetration Test-Based Probabilistic and Deterministic Assessment of Seismic Soil Liquefaction Potential." *J. Geotechnical & Geoenvironmental Engg.*, ASCE, V. 130 (12), pp.1314–1340.

Chameau, J. L. and Sutterer, K. 1994. "Influence of Fines in Liqurefaction Potential and Steady State Considerations", In *Proc., 13th Int. Conf., Soil Mechnics and Foundation Engg.*, New Delhi, India, A.A. Balkema, Rotterdam, The Netherlands, V. 5, pp. 183-194.

Chang, N. Y. 1990. "Influence of Fines Content and Plasticity on Earthquake-Induced Soil Liquefaction", *Contract Report DACW3988-C-0078,* U.S. Army Waterways Experiments Station, Vicksburg, Miss.

Chang, W. J., Rathje, E., Stokoe II, K. H., and Cox, B. R. 2004. "Direct Evaluation of Effectiveness of Prefabricated Vertical Drain in Liquefiable Sand", *Soil Dynamics and Earthquake Engineering Journal,* V. 24, pp. 723-731.

Chu, J., and Leong, W. K. _2001_. "Pre-Failure Strain Softening and Pre-Failure Instability of Sand: A Comparative Study", *Geotechnique*, V. 51(4), pp. 311–321.

Chu, J. 2006. "Discussion of Possibility of Postliquefaction Flow Failure due to Seepage by Sento et al., 2004", *ASCE J. Geotechnical and Geoenvironmental Engineering,* V. 133(3), pp. 425-426.

Clare, D. G., Lubkowski Z. A., and Bird, J. F. 2002. "Factors Affecting Liquefaction Susceptibility of Fine Grained Soils and the Use of Dewatering and Suction to Mitigate Liquefaction Risk", In *Proc., 12th European Conf., Earthquake Engineering,* the Elsevier Science Ltd., Paper No. 562.

Coduto, D. P. 1999. *"Geotechnical Engineering, Principles and Practices",* Printice-Hall Inc., 655p.

Cole, E.R.L. 1967. "The Behaviour of Soils in the Simple Shear Apparatus. *Ph.D. Thesis,* University of Cambridge.

Cooke, H. G. 2000. "Ground Improvement for Liquefaction Mitigation at Existing Highway Bridges", *PhD Thesis,* Virginia Polytechnic Institute and State University, Blacksburg, VA. 372p.

Cooke, H. G. and Mitchell, J. K. 1999. "Guide to Remedial Measures for Liquefaction Mitigation at Existing Highway Bridge Sites", *MCEER Technical Report*, MCEER-99-0015.

Cornforth, D. H. 1974. "One-Dimensional Consolidation Curves of a Medium Sand", *J., Géotechnique*, V. 24, pp. 678–683.

Coulter H. W, and Migliaccio R. R. 1966. "Effects of the Earthquake of March 27, 1964 at Valdez, Alaska", *Geological Survey Professional Paper 542-C,* US Department of the Interior, p. 36.

Cubrinovski, M. and Ishihara, K. 1999. "Emperical Correlation between SPT N-Value and Relative Density of Sandy Soils", *Soils and Foundations,* JSSMFE, 39(5), pp. 61-71.

Cubrinovski, M. and Ishihara, K. 2001. "Correlation between Penetration Resistance and Relative Density of Sandy Soils", In *Proc., the 15th Int., Conf., Soil Mechanics and Geotechnical Engineering,* ISSMGE, Istanbul (Turkey) 2001, A.A. Balkema, The Netherlands, V. 1, pp. 393-396.

Cubrinovski, M. and Ishihara, K. 2002. "Maximum and Minimum Void Ratio Characteristics of Sands", *Soils and Foundations,* JSSMFE, V. 42(6), pp. 65-78.

Das, B., Puri, V., and Prakash, S. 1999. "Liquefaction of Silty Soils", In *Proc., Second Int. Conf., Earthquake Geotechnical Engineering,* Lisboa, Portugal, 21-25 June 1999, Edited by Pinto., P. S., V. 2, pp. 619-623.

Dafalias, Y.F. 1986. "Bounding Surface Plasticity. I: Mathematical Foundation and the Concept of Hypoplasticity", *Journal of Engineering Mechanics,* ASCE, V. 112(9): 966–987.

Dewoolkar, M., Ko, H., and Pak, R.1999. "Centrifuge Modeling of Models of Seismic Effects on Saturated Earth Structures", *Geotechnique,* V. 49, No. 2, pp. 247-266.

Dismuke, J. N. 2003. "Aspects of the Cyclic Loading Behavior of Saturated Soils", *M.S. Thesis,* University of California, Davis, Calif.

Desrues, J. and Viggiani, G. 2004. "Strain Localization in Sand: An Overview of the Experimental Results obtained in Grenoble using Stereo-Photogrammetry", *Int. J., Numerical and Analytical Methods in Geomechanics,* V. 28, pp.279–321.

Desai, C. S., and Christian, JT. 1977. *"Numerical Methods in Geomechanics", New* York: McGraw-Hill.

Dobry, R. 1989. "Some Basic Aspects off Soil Liquefaction during Earthquakes", In *Proc., Earthquake Hazards and the Design of constructed Facilities in Eastern US,* New York, N.Y., Part IV, pp. 172-182.

Dobry, R., Baziar, M. H., O'Rourke, T. D., Roth, B. L., and Youd, T. L. 1992. "Liquefaction and Ground Failure in the Imperial Valley, Southern California during the 1979, 1981, and 1987 Earthquakes", *Case Studies of Liquefaction and Lifeline Performance During Past Earthquakes.* V. 2: United States Case Studies. Technical Rep. NCEER-92-0002, pp. 4.1-4.85.

Dobry, R., Elgamal, A. W., Baziar, M. H., and Vucetic, M. 1989. "Pore Pressure and Acceleration Response of Wildslife Site during the 1987 Earthquake", In *Proc. 2nd U.S.-Japan Workshop on Liquefaction, Large Deformation and Effects on Buried Pipelines*, Niagara Falls, New York, pp. 145-160.

Dobry, R., and Liu, L. 1992. "Centrifuge Modeling of Soil Liquefaction." In *Proc., 10th World Conf. on Earthquake Engineering.*, Madrid, Spain, pp. 6801–6809.

Duncan J. M., Byrne, P. M., Wong. K. S. and Marbry, P. 1980. "Strength, Stress-Strain and Bulk Modulus Parameters for Finite Elements Analysis of Stresses and Movements in Soil Masses", *Report No. UCB/GT/80-01,* Un., Cal., Berkeley.

Duncan, J. M. and. Chang, C. Y. 1970. "Nonlinear Analysis of Stress and Strain in Soils", *ASCE J., Soil Mechanics and Foundation Engineering Division,* V. 96(SM 5), pp. 1629-1653.

Duku, P.M., Stewart, J.P., Whang, D.H. and Yee, E. 2008. "Volumetric Strains of Clean Sands Subject to Cyclic Loads", *ASCE J., Geotechnical and Geoenvironmental Engg.*, V. 134(8), pp. 1073-1085.

EERI (1995). "Guam Earthquake of August 8, 1993 Reconnaissance Report", *J., Earthquake Spectra*, EERI 95-02.

Eigenbrod, K. D., Kjartanson, B. H. and Vanapalli, S. 2004. "Influence of Silt Content on the Engineering Properties of Saturated and Unsaturated Granular Soils", In *Proc., the 57th Canadian Geotechnical Conf.,* Quebec, Session 6E, pp. 25-32.

Elgamal, A. W., Dobry, R., and Adalier, K. 1989. "Small Scale Shaking Table Tests of Saturated Layered Sand-Silt Deposits", In *Proceedings, 2nd U.S.-Japan Workshop on Soil Liquefaction,* Buffalo, N.Y., NCEER Rep. No. 89-0032, pp. 233–245.

Elgamal, A., Lai T. Yang, Z and He, L. 2001. "Dynamic Soil Properties, Seismic Down-Hole Arrays and Applications in Practice", In *Proc. 4th Int. Conf., Recent Advances in Geotechnical Earthquake Engg. and Soil Dynamics and Symposium in Honor of Prof. L. Finn,* San Diego, Cal., March 26-30, 2001, SOAP-6.

Elgamal, A., Parra, E., Yang, Z., Dobry, R., and Zeghal, M.1999. "Liquefaction Constitutive Model". In *Proceedings of International Workshop on Physics and Mechanics of Soil Liquefaction,* Baltimore, Md., 10–11 Sept. 1998. Edited by P.V. Ladeand J.A. Yamamuro. A.A.Balkema, Rotterdam, the Netherlands. pp. 269–279.

Elgamal, A., Yang, Z. and Parra, E. 2001."Computational Modeling of Cyclic Mobility and Post-Liquefaction Site Response", *J., Soil Dynamics & Earthquake Engineering,* V.22, pp. 259-271.

Elgamal, A., Yang, Z. and Stepp. J. 2004. "Seismic Down-Hole Arrays and Applications in Practice", In *Proc., the Int. Workshop for site Selection, Installation and Operation of Geotechnical Strong-Motion Arrays,* Los Angeles Cal. COSMOS, Edited by C. Stepp, P. De Aalba, J. Steidl and R. Nigbor,.

Eliadorani, A. 2000. "The Response of Sands under Partially Drained States with Emphasis on Liquefaction", *Ph.D. Dissertation,* Un., British Columbia, Vancouver, BC. 221p.

Eliadorani, A. 2001. "The Effect of Drainage Conditions on Liquefaction Response of Sands", In *Proc., the 54th Canadian Geotechnical Conf.*, Calgary, pp. 1022-1028.

Elkateb, T., Chalaturnyk, R., and Robertson, P. K. 2003. "Simplified Geostatistical Analysis of Earthquake-Induced Ground Response at Wildlife Site, California, USA", *Canadian Geotechnical Journal,* V. 40, pp. 16-35.

Elorza, O., and Machado, M. R. 1929. "Report on Causes of Failure of Barahona Dam", *Boletin del Museo Nacional de Chile* (in Spanish).

Erten, D. and Maher, M. H. 1995. "Cyclic Undrained Behavior of Silty Sands", *J., Soil Dynamics and Earthquake Engineering,* Elsevier Science Ltd., V. 14, pp. 115-123.

Evans, M. D. and Zhou, S. 1995. "Liquefaction Behavior of Sand-Gravel Composites," *Journal of Geotechnical Engineering*, ASCE, V. 121(3), pp. 287–298.

Ferritto, J. 1997. "Seismic Design Criteria for Liquefaction", *Technical Report, TR-2077-SHR,* U.S. Naval Facilities Engineering Services Center, Port Hueneme, CA.

Fiegel, G. L., and Kutter, B. L. 1994a. "Liquefaction Mechanism for Layered Soil", *J., Geotechnical Engineering, ASCE,* V. 120(4), pp. 737-755.

Fiegel, G.L., and Kutter B.L. 1994b. "Liquefaction-Induced Lateral Spreading of Mildly Sloping Ground", *J. Geotechnical Engrg., ASCE,* V. 120(12), pp 2236-2243.

Field M. E., Gardner J. V., Jennings A. E., and Edwards B. D. 1982. "Earthquake Induced Sediment Failures on a 0.258 Slope, Klamath River Delta", *Journal of California Geology,* V. 10, pp. 542–546.

Finn, W. D. L., Emery, J. J., and Gupta, Y. P. 1971. "Liquefaction of Large Samples of Saturated Sand Excited on a Shaking Table", In *Proc. 1st Canadian Conference on Earthquake Engineering*, Univ. of British Columbia, Vancouver, B.C., Canada. pp. 97-110.

Finn W. D, L. 1990. "Analysis of Post-Liquefaction Deformations in Soil Structures (Invited Paper). *In* Proc., Seed Memorial Symposium, University of California, Berkeley, Bi-Tech Publishers, Vancouver, V. 2. pp. 291-311.

Finn, W. D. L., Bransby, P. L., and Pickering, D. J. 1970. "Effect of Strain History on Liquefaction of Sand. *J. Soil Mech. and Found. Div.*, ASCE, V. 96(6), pp. 1917–1934.

Finn, W. D. L., and Vaid, Y. P. 1977. "Liquefaction Potential from Drained Constant Volume Cyclic Simple Shear Tests", *In* Proceedings of the 6th World Conference on Earthquake Engineering. Sarita Prakashan Publishers, Meerut, India. Vol. III, pp. 2157-2162.

Finn, W.D.L., Vaid, Y.P., and Bhatia, S.K. 1978. Constant Volume Simple Shear Testing. *In* Proceedings of the 2nd International Conference on Microzonation for Safer Construction, Research and Application, San Francisco, U.S.A., Vol. II, pp. 839-851.

Finno, R.J., Harris, W.W., Mooney, M.A., and Viggiani, G. 1997. "Shear Bands in Plane Strain Compression of Loose Sand", *J., Géotechnique,* V. 47(1), pp.149-165.

Florin, V. A., and Ivanov, P. L. 1961. "Liquefaction of Saturated Sands", In *Proc., 5th Int. Conf. on Soil Mechanics and Foundation Engineering*, Dunod, Paris, 1, 107–112.

Fredlund, D.G., and Rahardjo, H. 1993. "Soil Mechanics for Unsaturated Soils", *John Wiley,* New York.

Fukushima, S. and Tatsuoka, F. 1984. "Strength and Deformation Characteristics of Saturated Sand at extremely Low Pressures", *Soils and Foundations,* V. 24, No. 4, pp. 30-48.

Furnas, C.C. 1928. "Relations between Specific Volume, Void Ratio, and Size Composition in Systems of Broken Solids of Mixed Sizes", *US. Bureau of Mines*, Report of Investigations 2894, V. 7, pp. 308-314.

Gajo, A., Bigoni, D., and Muir Wood, D. 2004. "Multiple Shear Band Development and related Instabilities in Granular Materials", *J. Mech. Phys. Solids,* V. 52, No. 12, pp. 2683–2724.

Gajo, A., Muir Wood, D. and Bigoni D. 2007. "On Certain Critical Material and Testing Characteristics affecting Shear Band Development in Sands", *Geotechnique*, V. 57(5), pp. 449-461.

Ghosh, B. and Madabhushi, S.P. 2003. "Effect of Localized Soil Inhomogenity in Modifying Seismic Soil Structure Interaction", In *Proc., ASCE 16th Engineering Mechanics Conference,* Seattle 16-18th July 2003.

Gonzalez, L. 2005. "Centrifuge Modeling of Permeability and Pinning Reinforcement Effects on Pile Response to Lateral Displacements", *PhD Dissertation,* Civil Engineering Department, Rensselaer Polytechnic Institute, N.Y., 464p

Gonzalez, L, Abdoun, T. and Dobry, R. 2009. "Effect of Soil Permeability on Centrifuge Modeling of Pile Response to Lateral Spreading", *Journal of Geotechnical and Geoenvironmental Engineering, ASCE,* V. 135(1), pp. 62–73.

Gonzalez, L., Abdoun, T. and Sharp, M. 2002. "Modeling of Seismically Induced Liquefaction under High Confining Stress", *Int., J., Physical Modeling in Geotechnics,* V. 3, pp. 1-15.

Gu, W. H., Morgenstern, N. R., and Robertson, P. K. 1994. Post-earthquake Deformation Analysis of Wildlife Site", *Journal of Geotechnical Engineering, ASCE,* V. 120(GT2), pp. 274–289.

Guo, T., and Prakash, S. 2000. "Liquefaction of Silt-Clay Mixtures", In *Proc., the 12th World Conf., Earthquake Engg.,* Auckland, New Zealand, Jan., 30-Feb., 4, 2000, Paper No. 561.

Gutierrez, M. 2003. " Mixture Theory Characterization and Modeling of Soil Mixtures", In *Proc., the first Japan-US Workshop on Testing, Modeling, and Simulation in Geomechanics, MIT, Boston, MA.*

Gutierrez, M., Ishihara, K., and Towhata, I. 1991. "Flow Theory for Sand during Rotation of Principal Stress Direction", *Soils and Foundations,* JSSMFE, V. 31(4), pp. 121-132.

Hadley, J. B. (1964). "Landslides and Related Phenomena Accompanying the Hebgen Lake Earthquake of August 17, 1959", *Geological Survey Professional Paper 435, The Hebgen Lake Montana Earthquake of August 17,* U.S. Dept. of the Interior.

Hamada, M. 1992. "Large Ground Deformations and their Efffects on Lifelines: 1964 Niigata Earthquake", *Chapter 3 of Hamada and O'Rourke (eds.),1992,* NCEER 92-0001, p. 3-1 to p. 3-123.

Hampton, M. A. and Lee H. J. 1996. "Submarine and Landslides", *Journal of Review of Geophysics,* V. 34, pp. 33-39.

Han, C. and Vardoulakis, I. 1991. "Plane Strain Compression Experiments on Water-Saturated Fine-Grained Sand", *J., Géotechnique,* V. 41(1), pp. 49-78.

Han, C. and Drescher, A. 1993. "Shear Bands in Biaxial Tests on Dry Coarse Sand", *Soils and Foundation,* V. 33(1), pp.118-132.

Harder, L., 1988. "Use of Penetration Tests to Determine the Cyclic loading Resistance of Gravelly Soils during Earthquake Shaking", *PhD. Dissertation,* University of California, Berkeley.

Harder, L., and Stewart, J. 1996. "Failure of Tapo Canyon Tailings Dam", *Journal of Performance Construction Facilities,* V. 10, pp. 109-114.

Hara, T., Kokusho, T., and Hiraoka, R. 2004. "Undrained Strength of Gravelly Soils with Different Particles Gradations", *In Proc., 13th World Conf., Earthquake Engineering,* Vancouver, Canada, Aug. 1-6, 2004, Paper No. 144.

Hardin, B. O., and Drenvich, V. P. 1972. "Shear Modulus and Damping in Soils: Design Equations and Curves", *ASCE J., Soil Mechanics and Foundation Engg. Division,* V. 98(SM7), pp. 667-692.

Hasiotis, T., Papatheodorou, G., Bouckovalas, G., Corbau, C. and Ferentinos, G. 2002. "Earthquake-Induced Coastal Sediment Instabilities in the Western Gulf of Corinth, Greece", *J., Marine Geology,* Elsevier, V. 186, pp. 319-335.

Hausler, E. 2002."Influence of Ground Improvement on Settlement and Liquefaction: A Study based on Field Case History Evidence and Dynamic Geotechnical Centrifuge Tests", *PhD. Thesis,* Civil & Environmental Engg. Dept., U. Cal., Berkeley, 364p.

Hausler, E. and Sitar, N. 2001a. "Performance of the Soil Improvement Techniques in Earthquakes", In *Proc. 4th Int. Conf., Recent Advances in Geotechnical Earthquake Engg. and Soil Dynamics and Symposium in Honor of Prof. L. Finn,* San Diego, Cal., March 26-30, 2001, Paper No. 10.15.

Hausler, E. and Sitar, N. 2001b. "Dynamic Centrifuge Testing of Improved Ground", In *Proc., the 15th Int., Conf., Soil Mechanics and Geotechnical Engineering,* ISSMGE, Istanbul 2001, A.A. Balkema, The Netherlands, V. 3, Section 4.3, also available at http://www.ce.berkeley.edu/~hausler/reports.html.

Hausmann, M. R. 1990. "Engineering Principles of Ground Modification", *McGraw Hill, 632p.*

Hoeg, K., Dyvik, R., and Sandbaekken, G. 2000. "Strength of Undisturbed vesus Reconstituted Silt and Silty Sand Specimens", *ASCE J., Geotechnical and Geoenvironmental Engg.*, V. 126(7), pp. 606-617.

Holzer, T. L., Youd, T. L., and Hanks, T. C. 1989. "Dynamics of Liquefaction during the 1987 Superstition Hills, California Earthquake", *Science*, 244, pp. 56-59.

Horrii, N., Toyosawa, Y., Tamate S., and Hashizume, H. 2001, "Centrifuge Model Tests on the Stability of A Clayey Ground Improved by Deep Mixing Method with a Low Improvement Ratio", *In Proc. 4th Int. Conf., Recent Advances in Geotechnical Earthquake Engg. and Soil Dynamics and Symposium in Honor of Prof. L. Finn,* San Diego, Cal., March 26-30, 2001, Paper No. 9.36.

Howie, J., Shozen, T. and Vaid, Y. 2002. "Effect of Ageing on Stiffness of very Loose Sand", *Canadian Geotechnical Journal,* V. 39, pp. 149-156.

Hushmand B, Scott R. F, and Crouse C. B. 1992. "In-place Calibration of USGS Transducers at Wildlife Liquefaction Site, California, USA", In *Proceedings, 10th World Conference on Earthquake Engineering, Rotterdam:* Balkema, pp. 1263–1268.

Huishan, L., and Taiping, Q. 1984. "Liquefaction Potential of Saturated Sand Deposits underlying Foundation of Structure", In *Proceedings, 8th World Conference, Earthquake Engineering*, Prentice–Hall, Englewood Cliffs, N.J., V. III, pp. 199–206.

Hyde, M, Higuchi, T. and Yasuhara, K. 2006. "Liquefaction, Cyclic mobility, and Failure of Silt", *ASCE J., Geotechnical and Geoenvironmental Engg.*, V. 132(6), pp. 716-735.

Hyodo, M., Yoshimoto, N., Hyde, F. L. and Okabayashi, T. 2002. "The Role of Fines in the Liquefaction of a Volcanic Soil Shirasu", In *Proc. The 12th European Conf., Earthquake Engg.,* Paper No. 529.

Hynes, M. E., and Olsen, R. S. 1999. "Influence of Confining Stress on Liquefaction Resistance", In *Proc., Int. Workshop on Phys. and Mech., Soil Liquefaction*, Balkema, Rotterdam, The Netherlands, pp.145–152.

Idriss, I. M. 1990. "Response of Soft Soil Sites during Earthquakes", In *Proc., Seed Memorial Symposium, May 1990,* Edited by J. M. Duncan, Bi Tech Publishers Ltd, Vancouver, V. 2, pp.273-289

Idriss, I. M. 1998. "Evaluation of Liquefaction Potential, Consequences and Mitigation: An Update", *Handout Provided by I. M. Idriss to the Vancouver Geotechnicasl Society,* Vancouver B.C., Feb. 17, 1998.

Idriss I. M, and Boulanger R. 2004."Semi-Empirical Procedures for Evaluating Liquefaction Potential during earthquakes", In *Proc., 11th International Conference on Soil Dynamics and Earthquake Engineering, and 3rd International Conference on Earthquake Geotechnical Engineering,* V. 1., pp. 32–56.

Idriss, I. M. and Boulanger, R. 2006. "Semi-Empirical Procedures for Evaluating Liquefaction Potential during Earthquakes", *J., Soil Dynamics and Earthquake Engineering,* V. 26, pp.115-130.

Idriss, I. M., 2006. "Field-Based Liquefaction Evaluation Procedures, A Critical Review", *Lecture Presented at University of British Columbia,* Vancouver B.C, Sept. 21, 2006.

Idriss, I. M. and Boulanger, R. 2007. "SPT- and CPT-Based Relationships for the Residual Shear Strength of Liquefied Soils", In *Proc., 4th Int. Conf., Earthquake Geotechnical Engineering,* Greece, Ishihara Lecture, pp. 1-22.

Indraratna, B., and Reana, I. W. 1997. "Plane Strain Modeling Smear Effects Associated with Vertical Drains", *Journal of Geotechnical Engineering, ASCE,* V. 119, pp.1321-1329.

Indraratna, B., and Reana, I. W. 2000. "Numerical Modeling of Vertical Drains with Smear and Well Resistance Installed in Soft Clay", *Canadian Geotechnical Journal,* V. 37, pp. 132-145.

Ishihara, K. 1971. "On the Longitudinal Wave Velocity and Poison's Ratio in Saturated Soils", In *Proc., 4th Asian Regional Conf., Soil Mechanics and Foundation Engineering,* Bangkok, V. 1, pp. 197-201.

Ishihara, K. 1984. "Post-Earthquake Failure of a Tailings Dam due to Liquefaction of the Pond Deposit", In *Proceedings of International Conference of Case Histories in Geotechnical Engineering,* Rolla, Missouri, V. 3, pp. 1129-1143.

Ishihara, K. 1985. "Stability of Natural Deposits during Earthquakes", Theme Lecture, In *Proc., 11th Int. Conf., Soil Mech. & Foundation Engineering,* Balkema, Rotterdam, V. 2, pp. 321–376.

Ishihara, K. 1993. "Liquefaction and Flow Failure during Earthquakes", *J., Géotechnique,* V. 43(3), pp. 351–415.

Ishihara, K. 1996. "Soil Behavior in Earthquake Geotechnics", *Oxford Science Publications,* 350p.

Ishihara, K., Tatsuoka, F., and Yasuda, S. 1975. "Undrained Deformation and Liquefaction of Sand under Cyclic Stresses", *Soils and Foundations,* V. 15(1), pp. 29-44.

Ishihara, K., Tsuchiya, H., Huang, Y. and Kamada, K. 2001. "Recent Studies on Liquefaction Resistance of Sand-Effect of Saturation", In *Proc. 4th Conf. Recent Advances in Geotech. Earth. Engg. and Soil Dynamics and Symposium in Honor of Prof. L. Finn,* San Diego, Cal., March 26-30, 2001,, Keynote Lecture.

Ishihara, K., Tsukamoto, Y., and Kamada, K. 2004. "Undrained Behavior of Near-Saturated Sand in Cyclic and Monotonic loading", In *Proc. Conf., Cyclic Behavior of Soils and Liquefaction Phenomena,* pp. 27-39.

Ishihara, K. and Yamazaki, F. 1980. "Cyclic Simple Shear Tests on Saturated Sand in Multi-Directional Loading", *Soils and Foundations,* V. 20(1), pp. 45-59.

Ishihara, K., Yasuda, S., and Yoshida, Y. 1990. "Liquefaction-Induced Flow Failure of Embankments and Residual Strength of Silty Sands", *Soils and Foundations*, V. 30(3), pp. 69-80.

Ishihara, K., and Yoshimine, M. 1992. "Evaluation of Settlements in Sand Deposits following Liquefaction during Earthquakes", Soils *and Foundations,* V. 32(1). pp. 173-188.

ITASCA, 2000 & 2005. "Fast Lagrangian Analysis of Continua (*FLAC*), Version 4, User's Guide", *Itasca Consulting Group, Inc.,* Thrasher Square East, 708 South Third Street, Suite 310, Minneapolis, Minnesota.

Jacka, M. E. 2001. "Delayed Liquefaction-Induced Failure of Embankments: A Case Study", *M.S. Thesis,* University of Canterbury, N.Z.

Jafari, A., Abedi, M. and Popescu, R. 2007. "Analysis of Liquefaction Susceptibility of Nearly Saturated Sands", *Int. J. Numer. Anal. Meth. Geomech.* V.31, pp. 691–714.

Japanese Geotechnical Society (JGS). 1996. "Geotechnical Aspects of the January 17, 1995 Hyogon-nambu Earthquke", *Soils and Foundations, Special Issue,* JSGE.

Japanese Geotechnical Society (JGS). 1998. "Remedial Measures against Soil Liquefaction, from Investigation and Design to Implementation", *Japanese Geotechnical Society*, A. A. Balkema, Rotterdam, the Netherlands.

Japanese Geotechnical Society (JGS). 1999. "Investigations of the 1999 Kocaeli Earthquake". *Reports on the Investigations of the 1999 Kocaeli Earthquake in Turkey and the 1999 Chi Chi Earthquake in Taiwan,* (in Japanese).

Jitno, H. and Byrne, P.M. 1995. "Predicted and Observed Liquefaction Response of Mochikoshi Tailings Dam", In *Proc., the First Inter. Conf., Earthquake Geotechnical Engineering*, Tokyo, Nov. 14-16, 1995, V. 2, pp. 1085-1090.

Kammerer, A. M. 2002. "Undrained Response Monterey 0/30 Sand under Multidirectional Cyclic Simple Shear Loading Conditions". *PhD Dissertation,* Civil & Environmental Engineering Department, Un., California, Berkeley, 443p.

Kammerer, A.M., Pestana, J., and Seed, R. 2003. "Behavior of Monterey 0/30 Sand under Multidirectional Loading Conditions", In *Proc., ASCE Geomechanics 2003 Conf.,* Massachusetts, USA, June 27–29, 2003 (GSP 143), pp. 154-173.

Kawakami, F., and Asada, A. 1966. "Damage to the Ground and Earth-Structures by the Niigata Earthquake of June 16, 1964", *Soils & Foundations,* V. 1, pp. 14–30.

Ko, H., Dewoolkar, M. 1999. "Modeling Liquefaction in Centrifuges", In *Proc., Int. Workshop on the Physics and Mechanics of Liquefaction,* John Hopkins Un., Baltimore, Sept. 10-11, 1998, A.A. Balkema, The Netherlands, pp. 307-318.

Koester, J. P. 1994. "The Influence of Fine Type and Content on Cyclic Strength", In *Proc., ASCE Conf. Ground Failures under Seismic Conditions,* ASCE, GSP No. 44, New York, pp. 17-33.

Koga, Y. and Matsuo, O. 1990. "Shaking Table Tests of Embankments resting on Liquefiable Sandy Ground", *Soils and Foundations,* JSSMFE, V. 4. pp. 162-174.

Kokusho, T. 1999. "Water Film in Liquefied Sand and its Effect on Lateral Spread", *J., Geotechnical and Geo-Environmental Engg.*, ASCE, V. 125(10), pp. 817–826.

Kokusho, T. 2000a. "Mechanism for Water Film Generation and Lateral Flow in Liquefied Sand Layer", *Soils & Foundations*, JGS, V. 40, pp. 99–111.

Kokusho, T. 2000b. "Correlation of Pore Pressure B-Value with P-wave Velocity and Poison's Ratio for Imperfectly Saturated Sand or Gravel", *Soils and Foundations*, JGS. V. 4 (4), pp. 95-102.

Kokusho, T. 2003. "Current State of Research on Flow Failure Considering Void Redistribution in Liquefied Deposits", *Journal of Soil Dynamic and Earthquake Engineering,* V. 23, pp. 585–603.

Kokusho, T., and Fujita, K. 2002. "Site Investigations for Involvement of Water Films in Lateral Flow in Liquefied Ground", *ASCE J., Geotechnical and Geoenvironmental Engg.*, V. 128(11), pp.1090-0241.

Kokusho, T., and Kojima, T. 2002. "Mechanism for Post-Liquefaction Water Film Generation in Layered Sand", *ASCE J., Geotechnical and Geoenvironmental Engg.*, V. 128(2), pp.129-137.

Kokusho, T., and Kojima, T., Nonaka, N. 2000. "Emergence of Water Film in Liquefied Sand and its Role in Lateral Flow", In *Proc., the 12th World Conf., Earthquake Engg.,* Auckland, New Zealand, Jan., 30-Feb., 4, 2000, Paper No. 946.

Konder, R. L., and Zelzska, J. S. 1963. "A Hyperbolic Stress-Strain Formulation for Sands", *In Proc., Second Pan-American Conf., Soil Mechanics and Foundation Engineering,* V. 1, pp. 289-324.

Konrad, J. M. 1990. "Minimum Undrained Strength of Two Sands", *Journal of Geotechnical Engineering, ASCE,* V. 116, pp. 932–947.

Konrad, J. M. 1988. "Interpretation of Flat Plate Dilatometer Tests in Sands in terms of the State Parameter", *Geotechnique,* V. 38(2), pp. 263–277.

Konrad, J. M. 1998. "Sand State from Cone Penetration Tests: A Framework Considering Grain Crushing Stress", *J., Géotechnique,* V. 38(2), pp.201–215.

Konrad, J. M. and Pouliot, N. 1997. "Ultimate State of Reconstituted and Intact Samples of Deltaic Sand", *Canadian Geotechnical Journal,* V. 34, pp. 737–748.

Koseki, J., Yoshida, T. and Sato, T. 2005. "Liquefaction Properties of Toyoura Sand in Cyclic Tortional Shear Tests under Low Confining Stress", *Soils and Foundations,* JSG., V. 45(5), pp. 103-113.

Kramer, S. L. 1996. "Geotechnical Earthquake Engineering", *Prentice Hall,* Upper Saddle River, N.J., 953p.

Kramer, S. L., and Elgamal, A.W. 2001. "Modeling Soil Liquefaction Hazards for Performance-Based Earthquake Engineering", *Rep. No. 2001/13*, Pacific Earthquake Engineering Research Center, Univ. of California, Berkeley, Calif.

Kuerbis, R.H., and Vaid, Y.P. 1989. "Undrained Behavior of Clean and Silty Sands", In *Proc., 12th Int. Conf. of Soil Mechanics and Foundation Engg., Session 27,* Rio de Janeiro, Aug. 13–18. Edited by K. Ishihara. Vol. 1, pp. 91–100.

Kuerbis, R., Nagussey, D., and Vaid, Y. P. 1988. "Effect of Gradation and Fine Content on the Undrained Response of Sand", In *Proc., Conf., Hydraulic Fill Structures,* ASCE, GSP No. 21, New York, pp. 330-345.

Kulasingam, R. 2003. "Effects of Void Redistribution on Liquefaction-Induced Deformations", *PhD Thesis,* Civil and Environmental Engineering Department, U.C., Davis. Cal.

Kulasingam, R., Malvick E. J., Boulanger, R. W. and Kutter, B. L. 2001. "Void Redistribution and Localization of Shear Strains in Model Sand Slopes with Silt Seams, Report on First Year Activities", In *Proceedings, US -Japan workshop,* Seattle, WA., pp. 117-128.

Kulasingam, R., Malvick E. J., Boulanger, R. W. and Kutter, B. L. 2002. "Effects of Void Redistribution on Liquefaction Behavior of Layered Soils: Centrifuge Data Report for Tests RKS01 - RKS11", *Center for Geotechnical Modeling,* Civil & Environmental Engg. Dept., U., C., Davis. Cal, Report No. UCD/CGMDR-02/01.

Kulasingam, R., Malvick E. J., Boulanger, R. W. and Kutter, B. L. 2004. "Strength Loss and Localization at Silt Inter-Layers in Slopes of Liquefied Sand", *Journal of Geotechnical and Geo-Environmental Engineering,* ASCE, V. 130, pp. 1192-1202.

Kulhawy, F. H., and Mayne, P. W. 1990. "Manual on Estimating Soil Properties for Foundation Design", *EPRI EL-6800, Final Report,* Electric Power Research Institute, 3412 Hillview Avenue, Palo Alto, CA, USA, 94303.

Kutter, B. L. 1995. "Recent Advances in Centrifuge Modeling of Seismic Shaking", In *Proc., 3rd Int. Conf., Recent Advances in Geotechnical Earthquake Engineering and Soil Dynamics,* University of Missouri–Rolla, Mo., V. 2, pp. 927–942.

Kutter, B., Gajan, S., Manda, K., and Balakrishnan, A. 2004. "Effects of Layer Thickness and Density on Settlement and Lateral Spreading", *ASCE, J., Geotechnical Engineering and Geo-Environmental Engineering,* V. 130, pp. 603-614.

Kutter, B. L., and Wilson, D. W. 1999. "De-Liquefaction Shock Waves", In *Proc., 7th U.S.–Japan Workshop on Earthquake Resistant Design of Lifeline Facilities and Countermeasures Against Soil Liquefaction, Rep. MCEER-99-0019*, Seattle, T. O'Rourke, J. P. Bardet, and M. Hamada. eds., pp. 295–310.

Lancelot, L., Shahrour, I. and Al Mahmoud, M. 2004. "Instability and Static Liquefaction on Proportional Strain Paths for Sand at Low Stresses", *ASCE, J., Engineering Geomechanics,* V. 130 (11), pp. 1365-1372.

Lade, P. V, Liggio, Jr. C. D and Yamamuro. J. A. 1998. "Effects of Non-Plastic Fines on Minimum and Maximum Void Ratios of Sand", *ASTM Geotechnical Testing J.* V. 21, pp.336–47.

Lade, P. V, and Yamamuro. J. A. 1997. "Effects of Non-Plastic Fines on Static Liquefaction of Sands", *Canadian Geotechnical Journal,* V. 34, pp. 918–928.

Lemke, R. W. 1967. "Effects of the Earthquake of March 27, 1964 at Seward, Alaska", Geological *Survey Professional Paper 542-E,* US Department of Interior.

Lee, K. L. 1965. "Triaxial Compressive Strength of Saturated Sands under Seismic Loading Conditions", *PhD Dissertation,* Civil Engg. Dept., Un., Cal., Berkeley, 521 p.

Lee, I. K, White, W. and Ingles, O. G. 1983. *"Geotechnical Engineering", Pitman Pub. Inc., 509p.*

Lehane, B. and Cosgrove, H. 2000. "Applying Triaxial Compression Stiffness Data to Settlement Prediction of Shallow Foundations," *Geotechnical Engineering J.,* V. 142 , Oct. 2000, pp. 191–200.

Leon, E., Gassman, S. and Talwani, P. 2006. "Accounting for Soil Aging When Assessing Liquefaction Potential", *ASCE, J., Geotechnical Engineering and Geo-Environmental Engineering,* V. 132 (3), pp. 363-377.

Liang, R. W., Bai, X. H., and Wang, J. C. 2000. "Effect of Clay Particle Content on Liquefaction", In *Proc., the 12th World Conf., Earthquake Engg.,* Auckland, New Zealand, Jan., 30-Feb., 4, 2000, Paper No. 1560.

Liu, H. and Qiao, T. 1984. "Liquefaction Potential of Saturated Sand Deposits underlying Foundation of Structure", In *Proceedings of 8th World Conf., Earthquake Engineering, San Francisco,* pp. 199-206.

Liu, H, and Dobry R.1997. "Seismic Response of Shallow Foundation on Liquefied Sand", *ASCE J., Geotechnical & Geoenvironmental Engineerinng,* V. 123(6), pp. 557–567.

Lu, N. and Likos, W. 2004. "Unsaturated Soil Mechanics", *J. Wiley & Sons,* N.J., 556p.

Lu, X., Shuyun, W., Yihua, W. and Cui, P. 2004. "An Approximate Method for Evaluating the Shear Band Thickness in Saturated Sand", *Int. J., Numerical and Analytical Methods in Geomechanics,* V 28, pp.1533-1541.

Malvick, E. J. 2005 "Void Redistribution-Induced Shear Localization and Deformation in Slopes", *PhD. Dissertation,* Civil & Environmental Engineering Department, Un., California, Davis, 285p.

Malvick, E. J., Kutter, B. L., Boulanger, R. W. 2008. "Postshaking Shear Strain Localization in a Centrifuge Model of a Saturated Sand Slope", *Journal of Geotechnical and Geoenvironmental Engineering,* ASCE, V. 134, pp. 164-174.

Malvick E. J., Kulasingam, R., Boulanger, R. W. and Kutter, B. L. 2002. "Effects of Void Redistribution on Liquefaction Behavior of Layered Soils: Centrifuge Data Report for Tests EJM01", *Center for Geotechnical Modeling,* Civil & Environmental Engg. Dept., U., C., Davis. Cal, Report No. UCD/CGMDR-02/02.

Malvick, E. J., Kulasingam, R., Boulanger, R. W., and Kutter, B. L. 2003. "Analysis of a Void Redistribution Mechanism in Liquefied Soil", In *Proceedings 12th Panamerican Conference on Soil Mechanics and Geotechnical Engineering*, Cambridge, MA. pp. 955-961.

Malvick, E. J., Kutter, B. L., Boulanger, R. W., and Feigenbaum, H. P. 2004. "Post-Shaking Failure of Sand Slope in Centrifuge Test", In *Proc., 11th Intl. Conf. Soil Dynamics and Earthquake Engrg., and 3rd Intl. Conf. Earthquake Geotechnical Engrg.*, D. Doolin et al., eds., Stallion Press, V. 2, pp. 447-455.

Malvick, E. J., Kutter, B. L., Boulanger, R. W., Kabasawa, K. and Kokusho, T. 2005. "Void Redistribution Research with 1-g and Centrifuge Modeling", *In Proceedings of 16th Int. Conf., Soil Mech. and Geotechnical Engg.,* ISSMGE. Osaka, V. 4, pp. 2543-2546.

Malvick, E. J., Kutter, B. L., Boulanger, R. W., Kulasingam, R. 2006. "Shear Localization due to Liquefaction-Induced Void Redistribution in a Layered Infinite Slope", *Journal of Geotechnical and Geoenvironmental Engineering,* ASCE, V. 132, pp. 1293-1303.

Malvick, E. J., Kulasingam, R., Kutter, B. L., and Boulanger, R. W. 2002. "Void Redistribution and Localized Shear Strains in Slopes during Liquefaction.", In *Proc. Intl. Conf., Physical Modeling in Geotechnics*, ICPMG '02, St. John's, Newfoundland, Canada, pp. 495-500.

Marcuson, W. F., III .1978. "Definition of Terms Related to Liquefaction", *J. Geotechnical Engineering. Div.*, ASCE, V. 104(9), pp. 1197–1200.

Marcuson, W.F., III. 1979. "Visit to Japan to Observe Damage which Occurred during the Near Izu Oshima Earthquakes January 14 and 15, 1978", *Miscellaneous Paper GL-79-20,* U.S. Army Corps of Engineers Waterways Experiment Station, Vicksburg, MS.

Marcuson, W. F., III, and Bieganousky, W. A. 1977a. ''Laboratory Standard Penetration Tests on Fine Sands'', *J. Geotech. Engrg. Div.*, ASCE, V. 103(6), pp. 565–588.

Marcuson, W. F., III, and Bieganousky, W. A. 1977b. ''SPT and Relative Density in Coarse Sands'', *J. Geotechnical Engineering Div.,* ASCE, V. 103(11), pp.1295–1309.

Marcuson III, W. F., Ballard, Jr. R. F., and Ledbetter, R. H. 1979. "Liquefaction Failure of Tailings Dams resulting from the Near Izu Oshima Earthquake, 14 and 15 January 1978", *Proc. 6th Pan-American Conference on Soil Mechanics and Foundation Engineering.* V. II, pp. 69-80.

Marcuson, W.F., Hadala, P. and Ledbetter, R. 1996. "Seismic Rehabilitation of Earth Dams", *ASCE J., Geotechnical Engg.,* V. 122 (1), pp. 7-20.

Marcuson, W.F., and Silver, M. L. 1987. "Shake-Proof Dams", *J., Civil Engineering,* V. 57(12), pp. 44-47.

Martin, G. R., Finn, W. D. L. and Seed, H. B. 1975. "Fundamentals of Liquefaction under Cyclic Loading," *ASCE, J., Geotechnical Engineering Division,* V. 101(GT5), Proc. Paper 11284, pp. 423-438.

Martin, J. R., Olgun, G., Mitchell, J. and Durgunoglu, T. 2004. (High-Modulus Columns for Liquefaction Mitigation", *ASCE, J., Geotechnical and Geoenvironmental Engineering,* V. 130 (1), pp. 561-571.

Masih, R. 2000. "Formula to Get Desired Soil Density", *J., Geotech. and Geoenviron. Engg.,* ASCE, V. 126(12), pp. 1145-1150.

Mathiroban S., and Grozic, J. 2004. "A Model to Predict the Undrained Behavior of Loose Gassy Sand", In *Proc 57th Geotech. Conf.*, Session 6G, pp.16-22.

Matsuoka, H. and Nakai, T. 1977. "Stress-Strain Relationship of Soil based on S.M.P", In *Proc., Specialty Session 9; Constitutive Equations of Soils, the Ninth Int. Conf., Soil Mechanics and Foundation Engineering,* Tokyo, pp. 153-162.

Mayne, P. 2007. "Cone Penetration Testing: A Synthesis of Highway Practice", *NCHRP Synthesis 368,* Transportation Research Board, National Cooperative Highway Research Program, 118p.

Mejia, L. H., and Yeung, M. R. 1995. "Liquefaction of Coralline Soils during the 1993 Guam Earthquake", *ASCE National Convention*, San Diego, California.

Meneses J, Ishihara K, and Towhata I. 1998. "Effects of Superimposing Cyclic Shear Stress on the Undrained Behavior of Saturated Sand under Monotonic loading", *Soils and Foundations* V.38(4), pp.115–27.

Miyamoto, J., Sassa, S. and Sekiguchi, H. "Progressive Solidification of a Liquefied Sand Layer during Continued Wave Loading", *Geotechnique,* V. 54(10), pp. 617-629.

Ministry of Transportation, Japan, 1997. "Handbook on Liquefaction Remediation of Reclaimed Land", *Port and Harbour Reseach Institute Publication,* A. A. Balkema, Amsterdam, the Netherlands, 312p.

Mitchell, J. K. 1981. "Soil Improvement-State-of–the-Art Report" In *Proc., 10th ICSMFE,* Stockholm, V. 4, pp. 509-565.

Mitchell, J. K. and Cooke, H. G. 1995. "Assessment and Mitigation of Liquefaction Risk for Existing Highway Bridge Foundations," *Proc., National Seismic Conference on Bridges and Highways*, San Diego, CA, December 10-15.

Mitchell, J. K., Baxter, C. D. P., and Munson, T.C. 1995 "Performance of Improved Ground during Earthquakes", In *Proc., ASCE Soil Improvements for Earthquake Hazard Mitigation,* ASCE GSP No. 49, pp. 1-36.

Mitchell, J. K., Cooke, H. G., and Schaeffer, J. A. 1998. "Design Considerations in Ground Improvement for Seismic Risk Mitigation", In *Proc., ASCE Conf., Geotechnical Earthquake Engg., and Soil Dynamics III,* ASCE, GSP No. 75, pp. 580-613.

Mulilis, J. P., Seed, H. B., Chan, C. K., Mitchell, J.K., and Arulanandan, K.1977!. ''Effects of Sample Preparation on Sand Liquefaction.'' *J. Geotech. Eng. Div., Am. Soc. Civ. Eng., V.* 103(2), pp. 91–108.

Naeini, S.a. and Baziar, M.H. 2004. "Effect of Fines Content on Steady-Satate Strength of Mixed and Layered Samples of a Sand", *J. Soil Dynamics and Earthquake Engineering,* V. 24, pp. 181-182.

Naesgaard, E., Byrne, P. M., Seid-Karbasi, M., and Park, S. 2005. "Modeling Flow Liquefaction, its Mitigation, and Comparison with Centrifuge Tests", In *Proc. of ICSMGE TC4 Satellite conf. on Recent Developments in Earthquake Engineering,* Osaka, Japan, pp. 95-103.

Naesgaard, E., Byrne, P.M., and Seid-Karbasi, M. 2006. "Modeling Flow Liquefaction and Pore Water Redistribution Mechanisms", In *Proc. of 8th U.S. National Conf., Earthquake Engineering, EERI,* San Francisco. U.S.

National Research Council (NCR), 1985. "Liquefaction of Soils during Earthquakes", *NRC Report CETS-EE-001,* National Academy Press, Washington, D.C.

Nagase, H. and Ishihara K. 1988. "Liquefaction-Induced Compaction and Settlement of Sand during Earthquake", *Soils and Foundations,* V. 28(1), pp.66–76.

Nagase, H., Ko, Y., Law, H., and Pak, R. 1994. "Permanent Displacement of Sloping Ground due to Liquefaction", In *Proc. Int., Conf. Centrifuge 94,* A.A. Balkema, The Netherlands, pp. 239-244.

Nakazawa, H., Ishihara, K., Tsukamoto, Y., and Kamata, T. 2004. "Case Studies on Evaluation of Liquefaction Resistance of Imperfectly Saturated Soil Deposits", In *Proc., Conf., Cyclic Behavior of Soils and Liquefaction Phenomena,* Germany.

Negussey, D., Wijewickreme, D., and Vaid, Y.P. 1988. "Constant Volume Friction Angle of Granular Materials", *Canadian Geotechnical Journal,* V. 25(1), pp. 50-55.

Nemat-Nasser, S. and Okada, N. 2001. "Radiographic and Microscopic Observation of Shear Bands in Granular Materials", *Geotechnique,* V. 51(9), pp. 753-765.

Newmark, N. M. 1965. "Effects of Earthquakes on Dams and Embankments", *Geotechnique,* V. 15(2), pp. 139-160.

Nova, R. 2004. "The Role of Non-Normality in Soil Mechanics and some of its Mathematical Consequences", *J., Computers and Geotechnics,* Elsevier, V. 31, pp. 185-191.

Oda, M. 1972. "Initial Fabric and their relation to the Mechanical Properties of Granular Material", *Soils and Foundations, Japan,* V. 12(1), pp. 17-36.

Oda, M., Koishikawa, I., and Higuehi, T. 1978. "Experimental Study of Anisotropic Shear Strength of Sand by Plane Strain Test", *Soils and Foundations,* JSSMFE, V. 18(1), pp. 25–38.

Oda, M., Kawamoto, K., Suzuki, K. Fujimori, H., and Sato, M. 2001. "Microstructural Interpretation on Re-Liquefaction of Saturated Granular Soils under Cyclic Loading", *J., Geotech. and Geoenviron. Engg.,* ASCE, V. 127(5), pp. 416-423.

Olson, S. M. 2001. "Liquefaction Analysis of Level and Sloping Ground using Field Case Histories and Penetration Resistance", *Ph.D. Thesis,* University of Illinois at Urbana-Champaign, Urbana, Illinois.

Okamura, M., Ishihara, M., and Tamura, k. 2006. "Degree of Saturation and Liquefaction Resistances of Sand Improved with Sand Compaction Pile", *J., Geotech. and Geoenviron. Engg.,* ASCE, V. 132(2), pp. 258-264.

Okamura, M., Abdoun, T. H., Dobry, R., Sharp, M. K., and Taboada, V. M. 2001 "Effects of Sand Permeability and Weak Aftershocks on Earthquake-Induced Lateral Spreading", *Soils Foundations,* V. 41(6), pp. 63–78.

Olson, S. M. and Stark, T. D. 2002. "Liquefied Strength Ratio from Liquefaction Flow Failure Case Histories", *Canadian Geotechnical Journal,* V.39, pp. 629–647.

Olson, S. M. and Stark, T. D. 2003. "Use of Laboratory Data to Confirm Yield and Liquefied Strength Ratio Concepts", *Canadian Geotechnical Journal,* V. 40, pp. 1164–1184.

Park, S. S. 2005. A Two-Mobilized Plane Model and its Application for Soil Liquefaction Analysis", *Ph.D. Thesis,* Civil Engineering Department, University of British Columbia, BC. 215p.

Pastor, M., Zienkiewicz, O.C. and Chan, A.C. 1990. "Generalized Plasticity and the Modeling of Soil behavior", *Int. J. Num. Anal. Meth. Geomechanics*, V.14, pp. 151-190.

Papatheodorou, G. and Ferentinos, G. 1997. "Submarine and Coastal Sediment Failure Triggered by the 1995, M=6.1 R Aegion Earthquake, Gulf of Corinth, Greece", J., Marine Geology, Elsevier, N. 137, pp. 287-304.

Peck, R. B. 1967. "Stability of Natural Slopes", *J. Geotechnical Engineering*, ASCE, V. 93(4), pp. 403-417.

Pestana, J. M., and Whittle, A. J. 1995. "Compression Model for Cohesionless Soils", *Géotechnique,* V. 45, pp. 611–631.

Pestana, J. M., Hunt, C., Goughnour, R. and Kammerer, A.1999. "Effect of Storage Capacity on Vertical Drain Performance in Liquefiable Sand Deposits", In *Proc., 2nd Int. Conf., Ground Improvement Techniques,* Singapore, pp. 373-380.

Phillips, R. and Coulter, S. 2005. "COSTA-E, Centrifuge Test Data Report", *C-CORE Report R-04-084-075*. C-Core, St. John's, Newfoundland, Canada. 103 pp.

PIANC, 2001. "Seismic Design Guidelines for Port Structures", *Working Group No. 34 of the Maritime Navigation Commission,* Int. Navigation Association, A.A. Balkema, 474 p.

Pietruszczak, S., Pande, G. and Oulapour M. 2003. "A Hypothesis for Mitigation of Risk of Liquefaction", *Geotechnique,* V. 53(9), pp. 833-838.

Pillai, V.S. and Byrne, P. M. 1994. "Effect of Overburden Pressure on Liquefaction Resistance of Sands", *Canadian Geotechnical J.,* V. 31, pp. 53-60.

Pitman, T. D., Robertson, P. K., and Sego, D. C. 1994. "Influence of Fines on the Collapse of Loose Sands", *Can. Geotechnical J.*, V. 31(5), pp.728-739.

Phillips, R., Tu, M. and Coulter, S. 2004. "Data Report of test CT1, Earthquake Induced Damage Mitigation from Soil Liquefaction", prepared by *C-CORE* for UBC available at http://www.civil.ubc.ca/liquefaction.

Phillips, R., Tu, M. and Coulter, S. 2005 "Data Report of test CT7, Earthquake Induced Damage Mitigation from Soil Liquefaction", prepared by *C-CORE* for UBC available at http://www.civil.ubc.ca/liquefaction.

Phillips, R., Tu, M. and Coulter, S. 2005. "Data Report of test CT8, Earthquake Induced Damage Mitigation from Soil Liquefaction", prepared by *C-CORE* for UBC available at http://www.civil.ubc.ca/liquefaction.

Polito, C.P., 1999. "The Effects of Non-Plastic and Plastic fines on the Liquefaction of Sandy Soils", PhD Theis, Virginia Polytechnic Institute and State Un., Blacksburg, Va.

Polito, C.P., 2001. "Plasticity Based liquefaction Criteria', In *Proc. 4th Int. Conf., Advances in Geotechnical Earthquake Engineering and Soil Dynamics,* P. No. 1.33.

Polito, C.P., and Martin, II, J. R. 2001. "Effects of Nonplastic Fines on the Liquefaction Resistance of Sands", *ASCE J., Geotechnical and Environmental Engg.*, V. 127(5), pp. 408-415.

Poorooshasb, H. B. 1961."The Properties of Soils and Other Granular Media in Simple Shear", *Ph.D. Thesis*, Cambridge University. U.K.

Poorooshasb, E B. 1989. "Description of Flow of Sand using State Parameters," *J., Computers and Geotechnics,* Vol. 8. pp. 195-218.

Porbaha, A., Zen, K., and Kobayashi, K. 1999. "Deep Mixing Technology for Liquefaction Mitigation", *ASCE J., Infrastructures Systems*, V. 5, No. 1, pp. 21-34.

Porbaha, A. 2000. "State of the Art in Deep Mixing Technology, Part IV: Design Considerations", *J., Ground Improvement,* Thomas Telford, London, pp.111-125.

PHRI (Port and Harbor Research Institute) 1997. *"Handbook on Liquefaction Remediation of Reclaimed Land",* PHRI, A. A. Balkema, Rotterdam, the Netherlands.

Poulos, S. J. 1981. "The Steady State of Deformation'. *ASCE J., Geotechnical Engineering Division,* V. 107(GT5), pp. 553-562.

Poulos, S. J., Castro, G., and France, J. W. 1985. "Liquefaction Evaluation Procedure", *ASCE J., Geotechnical Engg.,* V. 111(6), pp. 772-792.

Puebla, H., Byrne, P.M., and Phillips, R. 1997. "Analysis of CANLEX Liquefaction Embankment: Prototype and Centrifuge Models", *Canadian Geotechnical J.*, V.34, pp. 641-657.

Prevost, J.H. 1985. "A Simple Plasticity Theory for Frictional Cohesionless Soils", *J., Soil Dynamics & Earthquake Eng.,* V. 4(1), pp. 9–17.

Prevost, J.H. 1989. "DYNAID: A Computer Program for Nonlinear Site Response Analysis", *Technical Report NCEER-89-0025,* National Center for Earthquake Engineering Research, State University of New York (SUNY) at Buffalo, N.Y.

Ragheb, A. 1994. "Numerical Analysis of Seismically Induced Deformations in Saturated Granular Soil Strata", *PhD Thesis,* Dept. of Civil Engineering, Rensselaer Polytechnic Institute, Troy, NY.

Rauch, A. F. 1997. ''EPOLLS: An Empirical Method for Predicting Surface Displacements due to Liquefaction-Induced Lateral Spreading in Earthquakes'', *PhD Thesis,* Virginia Polytechnic Institute and State Univ., Blacksburg, Va.

Rauch, A. F., and Martin, J. R.2000. "EPOLLS Model for Predicting Average Displacements on Lateral Spreads", *J. Geotechnical Geo-Environmental Eng.,* ASCE, V. 126(4), pp. 360–371.

Reynolds, O. 1885. "On the Dilatancy of Media Composed of Rigid Particles in Contact", With experimental illustrations. *Phil. Magazine*, V. 20, pp. 469–482.

Riemer, M. F., and Seed, R.B. 1997. "Factors Affecting Apparent Position of the Steady State Line", *ASCE, J., Geotechnical Engineering,* V.123 (3), pp. 281–288.

Riemer, M. F., Seed, R. B., Nicholson, P. G., and Jong, H. L. 1990. "Steady State Testing of Loose Sands: Limiting Minimum Density", *Journal of Geotechnical Engineering,* ASCE, V. 116, pp. 332–337.

Rollins, K., Anderson, J., Goughnour, R. and Mccain, A. 2004. "Liquefaction Hazard Mitigation Using Vertical Composite Drains", In *Proc., 13th World conf., Earthquake Engineering*, Vancouver, Canada, p. No. 2880.

Roscoe, K.H., 1970. "The Tenth Rankin Lecture: The Influence of Strains in Soil Mechanics", *Geotechnique,* V. 20, pp.129-170.

Roscoe, K. H. & Burland, J. B. 1968. "On the Generalized Stress–Strain Behavior of Wet Clay", *In Engineering Plasticity.* Edited by J. Heyman and Leckie, F. A., pp. 535–609. Cambridge: Cambridge University Press.

Roscoe, K. H., Schofield, A.N. and Wroth, C.P. 1958. "On the Yielding of Soils", *Geotechnique,* V. 8(1), pp. 22-52.

Rowe, P. W. 1962."The Stress–Dilatancy Relation for Static Equilibrium of an Assembly of Particles in Contact", *Proc. R. Soc. London Ser.* A 269, pp.500–527.

Ryan, C. and Jasperse, B. 1989. "Deep Soil Mixing at the Jackson Lake Dam", In *Proc., ASCE Conf., Foundation Engineering: Current Principles and Practices,* ASCE, New York, V. 1, pp. 354-367.

Salgado, R. Bandini, P., and Karim, A. 2000. "Shear Strength and Stiffness of Silty Sand", *Journal of Geotechnical and Geoenvironmental Engineering.,* ASCE, V. 126, pp. 451-462.

Saito, A., Taghawa, K., Tamura, T., Oishi, H., Nagayama, H. and Shimaoka, H. 1987. "A Countermeasure for Sand Liquefaction: Gravel Drain Method", *Nippon Kokan Technical Report,* Overseas No. 51, Japan.

Sanin, M. and Wijewickreme, D. 2004. "Applicabilty of Emperical Criteria for Liquefaction Suceptibility of Evaluation of Fraser River Delta Silt" In *Proc. 57th Canadian Geotechnical Conf.*, Session 2E, p. 8.

Sanin, M. and Wijewickreme, D. 2006. "Cyclic Shear Response of Channel-Fill Fraser River Delta Silt", *J. Soil Dynamics and Earthquake Engineering,* V. 26, pp. 854-869.

Sasaki, Y., Ohbayashi, J., and Ogata, Y. 2000. "Compressibility of Liquefied Sand." In *Proc., Fourth Int. Conf. on Recent Advances in Geotechnical Earthquake Engineering and Soil Dynamics*, Paper No. 1.62, Univ. of Missouri-Rolla, Rolla, Mo.

Sassa, K., Fukuoka, H., and Sakamoto, T. 1995. "The Rapid and Disastrous Nikawa Landslide", *Landslide News*, Japan Landslide Society, No. 9, pp. 6-9.

Sawada, S., Tsukamoto, Y. and Ishihara, K. 2006. "Residual Deformation Characteristics of Partially Saturated Sandy Soils Subjected to Seismic Excitation", *J. Soil Dynamics and Earthquake Engineering,* V. 26, pp. 175-182.

Schofield, A. N. 1981. "Dynamic and Earthquake Geotechnical Centrifuge Modeling", In *Proc., Int. Conf., Recent Advances in Geotechnical Earthquake Engineering and Soil Dynamics,* University of Missouri–Rolla, Mo., V. 3, pp 1081–1100.

Schofield, A. N. 1959, "The Development of Lateral Force during the Displacement of Sand by the Vertical Face of a Rotating Mode/Foundation", *Ph.D. Thesis,* Cambridge University, UK.

Schofield, A. N. and Wroth, P. 1968. *"Critical State Soil Mechanics",* McGraw-Hill, Maidenhead, U.K, also available at www.vulcanhammer.org.

Scott, R. 1986. "Solidification and Consolidation of a Liquefiable Sand Column", *Soil & Foundations,* V. 26, No. 4, pp. 23-31.

Scott, R. F. and Hushmand, B. 1995."Discussion of Piezometer Performance at Wildlife Liquefaction Site, California, by T. Leslie Youd and Thomas L. Holzer, GT June 94, pp. 975-995), *Journal of Geotechnical Engineering*, ASCE, V. 121 (12), pp. 912-919.

Scott, R., Hushmand, B., and Rashidi, H. 1993. "Model No.3 Primary Test Description and Test Results", In *Proc., Int. Conf., Verification of Numerical Procedures for the Analysis of Soil Liquefaction Problems (VELACS),* Un., Davis 1993, A. A. Balkema, The Netherlands, V.1, pp. 435-462.

Scott, R. F., and Zuckerman K. A. 1972. "Sand Blows and Liquefaction in the Great Alaskan Earthquake of 1964", *Engineering Publication 1606;* National Academy of Sciences, Washington, D.C., pp 170-189.

Seed, H. B. 1968. "Landslides during Earthquakes due to Soil Liquefaction", *J. Soil Mechanics and Foundation Engineering*, ASCE, V. 94(5), pp. 193-259.

Seed, H. B. 1979. "Considerations in the Earthquake-Resistant Design of Earth and Rockfill Dams", *Geotechnique*, V. 29(3), pp 215-263.

Seed, H. B. 1987. Design Problems in Soil Liquefaction", *Journal of Geotechnical Engineering,* ASCE, V. 113, pp. 827-845.

Seed, H. B. and Booker, J. R. 1977. "Stabilization of Potentially Liquefiable Sand Deposits using Gravel Drains", *ASCE Journal of Geotechnical Engineering Division,* V. 103 (7), pp.757– 768.

Seed H. B., and Harder, L. F. 1990. "SPT-Based Analysis of Cyclic Pore Pressure Generation and Undrained Residual Strength", In *Proc., Seed's Memorial Symposium,* May 1990, Edited by Duncan, J., Bi Tech Publishers Ltd, Vancouver, BC., V. 2, pp. 351-376.

Seed H. B., and Idriss, I. M. 1970. "Soil Muduli and Damping Factors for Dynamic Response Analyses", *Report No. EERC 70-10,* Earthquake Engineering Research Center, Un., Calf., Berkeley.

Seed, H. B., and Idriss, I. M. 1971. "Simplified Procedure for Evaluating Soil Liquefaction Potential", *J. Soil Mechanics and Foundations Div.*, ASCE, 97:SM9, 1249-1273.

Seed, H. B., Idriss, I. M., Makdisi, F., and Banerjee, N. 1975. "Representation of Irrigular Stress Time Histories by Equivalent Uniform Stress Series in Liquefaction Analyses", *Report No. EERC 75-29,* Earthquake Engineering Research Center, Un., Calf., Berkeley.

Seed, H. B., and Lee, K. L. 1966. "Liquefaction of Saturated Sands during Cyclic Loading", ASCE *J., Soil Mech. & Found. Engg. Division,* V. 92, (SM6), pp. 105-134.

Seed, H. B., Makdisi, F. I., and DeAlba, P. 1978. "Performance of Earth Dams during Earthquakes", *J. Geotechnical Engineering*, ASCE, V. 104(7), pp. 967-994.

Seed, H. B., Martin, P. P., and Lysmer, J. 1976. "Pore-Water Pressure Changes during Soil Liquefaction", *ASCE J., Geotechnical Engg. Division,* V. 102(GT4), pp. 323-346.

Seed, H. B., Pyke, R. M., and Martin, G. R. 1975. "Effect of Multi-Directional Shaking on Liquefaction of Sands", *Rep. No. EERC 75-41*, University of California, Berkeley.

Seed, H. B., Tokimatsu, K., Harder, L. F., and Chung, R. M. 1984. "The Influence of SPT Procedures in Soil Liquefaction Resistance Evaluations", *Report No. UCB/EERC-84-15,* Earthquake Engineering Research Center, Un., Calf., Berkeley.

Seed, H. B., Tokimatsu, K., Harder, L. F., and Chung, R. M. 1985. "Influence of SPT Procedures in Soil Liquefaction Resistance Evaluations", *ASCE J., Geotechnical Engg. Division,* V. 111(GT12), pp. 1425-1445.

Seed, H. B., Wong, R. T., Idriss, I. M., Tokimatsu, K. 1986. "Moduli and Damping Factors for Dynamic Analyses of Cohesionless Soils", *ASCE J., Geotechnical Engg.,* V. 112(GT11), pp. 1016-1032.

Seed, R. B. 1999. "Engineering Evaluation of Post-Liquefaction Residual Strength", *In Proc., TRB Workshop on New Approaches to Liquefaction Analysis,* Jan.10, 1999, Washington D.C.

Seed, R. B., Cetin, K. O., Moss, R.E. , Wu, J., Pestant, J. M., and Riemer M. F. 2001. "Recent Advances in Soil Liquefaction Engineering and Seismic Site Response Evaluation", In *Proc. 4th Int. Conf., Recent Advances in Geotechnical Earthquake Engg., and Soil Dynamics and Symposium in Honor of Prof. L. Finn,* San Diego, Cal., March 26-30, 2001, Paper No. SPL-2.

Seed, R. B., Cetin, K. O., Moss, R.E. , Kammerer E., Wu, J., Pestant, J. M., Riemer M. F., Sancio, J. D., Bray, J. D., Kayan, R. E. and Faris, A. 2003. "Recent Advances in Soil Liquefaction Engineering: A Unified and Cosistent Framework", *26th Annual ASCE Los Angeles Geotechnical Spring Seminar,* Keynote Presentation, H.M.S. Queen Mary, Long Beach, California, April 30, 2003.

Seed, R. B., Dickenson, S. E., Riemer, M. F., Bray, J. D., Sitar, N., Mitchell, J. K., Idriss, I. M., Kayen, R. E., Kropp, A., Harder, L. F., and Power, M. S., 1990. "Preliminary Report on the Principal Geotechnical Aspects of the October 17, 1989 Loma Pietra Earthquake", *Rep No. UCB/EERC-90/05,* Earthquake Engineering Research Center, Un., California, Berkeley, CA.

Seed, R. B., and Harder, L. F., Jr. 1990. "SPT-Based Analysis of Cyclic Pore Pressure Generation and Undrained Residual Strength", In *Proc., Seed Memorial Symposium,* Berkeley, Bi Tech., Ltd., Vancouver, B.C., V. 2, pp. 351-376.

Seed, H.B., Seed, R. B., Harder, L. F., and Jong, H. L. 1989. "Re-Evaluation of the Slide in the Lower San Fernando Dam in the 1971 San Fernando Earthquake", *Rept. No. UCB/EERC-88/04*, Univ. of California, Berkeley.

Seid-Karbasi, M. 2003. "A Numerical Study on Liquefaction Mitigation using Densification and Drainage Methods" A report prepared for BC-Hydro, 178 p.

Seid-Karbasi, M. and Byrne, P.M. 2004a. "Embankment Dams and Earthquakes", *Hydropower and Dams J.*, V. 11(2), pp. 96-102.

Seid-Karbasi, M. and Byrne, P.M. 2004b. "Liquefaction, Lateral Spreading and Flow Slides" In *Proc. 57th Canadian Geotechnical Conf.*, p. G13.529.

Seid-Karbasi, M., Byrne, P.M., Naesgaard, E., Park, S., Wijewickreme, D., and Phillips, R. 2005. "Response of Sloping Ground with Liquefiable Materials during an Earthquake: A Class A Prediction", In *Proc., 11th Int. Conf., IACMAG,* Int. Association for Computer Methods and Advances in Geomechanics, V.2, pp. 313-320.

Seid-Karbasi, M., and Byrne, P.M. 2006a. "Effects of Partial Saturation on Liquefiable Ground Response", In *Proc., ASCE 2006 Geo Congress,* Geotechnical Engineering in the Information Tech. Age, Atlanta, Ga. Paper No. 11803.

Seid-Karbasi, M., and Byrne, P.M. 2006b. "Significance of Permeability in Liquefiable Ground Response," *In Proc. 59th Canadian Geotechnical. Conf.*, pp. 580-587.

Seid-Karbasi, M., and Byrne, P.M. 2007. "Seismic Liquefaction, Lateral Spreading and Flow Slides: A Numerical Investigation into Void Redistribution", *Canadian Geotechnical Journal.* V. 44 (7), pp. 873-890.

Seid-Karbasi, M., Ji, J., Atukorala, U. and Byrne, P.M. 2008. "Prediction of Post-Earthquake Failure for a Near-Shore Slope in a Low Seismic Region", In *Proceedings of the 6th Int. Conference on Case histories in Geotechnical Engineering, Arlington,* VA., Paper # 3-02.

Sento, N., Kazama, M., Uzuoka, R., Hirofumi Ohmur H., and Makoto Ishimaru, M. 2004. "Possibility of Post Liquefaction Flow Failure due to Seepage", *Journal of Geotechnical and Geo-Environmental Engineering,* ASCE, V. 130, pp. 707-716.

Sesev, V., Talaganov, K., and Towhata, I. 2002. "Application of a Model for Mitigation of liquefaction-Induced Hazard", In *Proc., 12th European Conf., Earthquake Engineering,* the Elsevier Science Ltd., Paper No. 185.

Shenthan, T., 2005. "Liquefaction Mitigation in Silty Soils using Stone Columns supplemented with Wick Drains", *PhD Thesis,* State University of New York at Buffalo, N.Y., 342p.

Sharp, M., Steedman, S. Peters, J., Hynes, M. and Ledbetter, R. 2001. "Cyclically–Induced Pore Pressure at High Confining Stress", *ASCE Journal of Geotechnical and Geoenvironmental Engineering,* V. 127, pp.

Sharp, M, and Dobry, R. 2002. "Sliding Block Analysis of Lateral Spreading based on Centrifuge Results", *Int. J., Physical Modeling in Geotechnics,* V. 1, pp. 13-32.

Sharp, M, Dobry, R., and Abdoun, T. 2003a. "Liquefaction Centrifuge Modeling of Sands of Different Permeability", *ASCE Journal of Geotechnical and Geo-environmental Engineering,* V. 129, pp. 1083–1091.

Sharp, M, Dobry, R., and Abdoun, T. 2003b. "Centrifuge Modeling of Liquefaction and Lateral Spreading of Virgin Overconsolidated and Pre-Shaken Sand Deposits", *Int. J., Physical Modeling in Geotechnics,* V. 2, pp. 11-22.

Shigemura, S. and Tokue, T. 2005. "Failure Mechanism and Characteristics of Soil subjected to Interaction between Soil Elements in Simple Shear", In *Proc., 16th Int. Conf., Soil Mechanics and Geotechnical Engineering,* ISSMGE, Osaka, Japan, V. 4. pp. 2575-2578.

Silver, M. L. and Seed, H. B. 1971. "Volume Change in Sands during Cyclic Loading", *Journal of Soil Mechanics and Foundation Engineering Division,* ASCE, V. 97, pp. 1171-1182.

Singh, S. 1996, "Liquefaction Characteristics of Silts", *J., Geotechnical and Geological Engineering,* Kluwer Academic Publishers, The Netherlands, V.14, pp. 1-19.

Sitar, N. (Editor), 1996. "Geotechnical Reconnaissance of the Effects of the January 17, 1995 Hyogonken-Nanbu Earthquake, Japan", *UCB/EERC Rep. 95/01*, Earthquake Engineering Research Center, Un., California, Berkeley, CA.

Sivathayalan, S. 2000. "Fabric, Initial State and Stress Path Effects on Liquefaction Susceptibilty of Sands", *Ph.D. Dissertation,* Un., British Columbia, Vancouver, BC., 307p.

Sivathayalan, S. 1994. "Static, Cyclic and Postliquefaction simple Shear Response of Sands", *M.A.Sc. Thesis,* Un., British Columbia, Vancouver, BC., 139p.

Sivathayalan, S. and Vaid, Y. P. 2002. "Influence of Generalized Initial State and Principal Stress Rotation on the Undrained Response of Sands", *Canadian Geotechnical J.*, V. 39, pp. 63-76.

Sivathayalan, S. and Logaswaran, P. 2007. "Behavior of Sands under Generalized Drainage Boundary Conditions", *Canadian Geotechnical J.*, V. 44, pp. 138-150.

Skempton, A. W. 1954. "The Pore-Pressure Coefficients A and B", *Geotechnique,* V. 6, pp. 143-147.

Sladen, J. A., D'Hollander, R. D., and Krahn, J. 1985. "The Liquefaction of Sands, a Collapse Surface Approach", *Canadian Geotechnical Journal,* V. 22, pp. 564–578.

Sladen, J. A., D'Hollander, R. D., Krahn, J., and Mitchell, D. E. 1985. "Back Analysis of the Nerlerk Berm Liquefaction Slides", *Canadian Geotechnical Journal,* V. 22, pp. 579–588.

Soroush, A. and Koohi S. 2004. "Numerical Analysis of Liquefaction–Induced Lateral Spreading", In *Proc., 13rd World Conf., on Earthquake Engineering,* Vancouver, BC, P. No. 2123.

Sriskandakumar, S. 2004. "Cyclic Loading Response of Fraser River Sand for Numerical Models Simulating Centrifuge Tests", *M.A.Sc. Thesis,* University of British Columbia, Vancouver, B.C, 159p.

Stark, T. D., and Mesri, G. 1992. "Undrained Shear Strength of Liquefied Sands for Stability Analysis", *ASCE J., Geotechnical Engg.,* V. 118(11), pp. 1727-1747.

Stark, T. D., Olson, S. M., Kramer, S. L., and Youd, T. L. 1998. "Shear Strength of Liquefied Soils", In *Proc., Workshop, April 17-18, 1997, Urbana. Illinois*, NSF, Grant CMS-95-31678.

Steedman, S., Ledbetter, R. and Hynes, M. 2000. "The Influence of High Confining Stress on the Cyclic Behavior of Saturated Sand", In *Proc., ASCE Conf., Geo Denver 2000,* ASCE GSP No. 107, pp. 35-57.

Stewart, J., Whang, D., Moyneur, M. and Duku, P. 2004. "Seismic Compression of As-Compacted Fill Soils with variable Levels of Fines Contents and Fines Plasticity", *Earthquake Damage Assessment and Repair Project Report No. EDA-04,* Civil Engg. Dept., University of California, Davis.

Stokoe, K. H., Darendeli, M. B., Andrus, R. D., Brown, L. T. 1999. "Dynamic Soil Properties: Laboratory, Field and Correlation Studies", In *Proc., Second Int. Conf., Earthquake Geotechnical Engg.*, Lisboa, edited by Pinto, A. A. Balkema, V. 3, pp. 811- 845.

Sun J. I., Golesorkhi, R., and Seed, H. B. 1988. "Dynamic Moduli and Damping Ratios for Cohesive Soils", *Report No. UCB/EERC-88/15, Earthquake Engineering Research Center,* Un. Cal., Berkeley.

Sawada, S., Tsukamoto, Y. and Ishihara, K. 2006. "Residual Deformation Characteristics of Partially Saturated Sandy Soils subjected to Seismic Excitation", *J., Soil Dynamics and Earthquake* Engg. Elsevier, V. 26, pp. 175-182.

Taboada-Urtuzuastegui, V. 1995. "Centrifuge Modeling of Earthquake-Induced Lateral Spreading in Sand using a Laminar Box", *PhD Thesis,* Civil Engineering Dept., Rensselaer Polytechnic Institute, Troy, N.Y.

Taboada-Urtuzuastegui, V. and Dobry, R. 1993a. "Experimental Results of Model No.1 at RPI", In *Proc., Int. Conf., Verification of Numerical Procedures for the Analysis of Soil Liquefaction Problems (VELACS),* Un., Davis 1993, A. A. Balkema, the Netherlands, V. 1, pp. 3-17.

Taboada-Urtuzuastegui, V. and Dobry, R. 1993b. "Experimental Results of Model No.2 at RPI", In *Proc., Int. Conf., Verification of Numerical Procedures for the Analysis of Soil Liquefaction Problems (VELACS),* Un., Davis 1993, A. A. Balkema, the Netherlands, V. 1, pp. 277-294.

Taboada-Urtuzuastegui V. and Dobry, R. 1998. "Centrifuge Modeling of Earthquake-Induced Lateral Spreading in Sand", *ASCE J. Geotechnical and Geoenvironmental Engineering,* V. 124(12), pp. 1195-1206.

Taboada-Urtuzuastegui, V, Martinez-Ramirez, G. and Abdoun, T. 2002. "Centrifuge Modeling of Seismic Behavior of a Slope in Liquefiable Soil", *J. Soil Dynamics and Earthquake Engineering,* V. 22, pp. 1043-1049.

Takeshita, S., Takeishi, M., and Tamada, K. 1995. "Static Liquefaction of Sands and its Liquefaction Index", In *Proceedings of the 1st International Conf., on Earthquake Geotechnical Engineering,* Tokyo, Japan, 14–16 Nov. 1995. V. 1. *Edited by* K. Ishihara, Balkema, Rotterdam, the Netherlands. pp. 177–182.

Tamura, S., Tokimatsu, K., Abe, A. and Sato, M. 2002. "Effects of Air bubble on B-Value and P-Wave Velocity of a Partly Saturated Sand", *Soils and Foundations*, JGS, V. 42(1), pp. 121-129.

Tani, S. 1996. "Damage to Earth Dams", *Soils and Foundations,* Special Issue on Geotechnical Aspects of the January 17, 1995 Hyogoken-Nambu Earthquake", JGS, Tokyo, pp. 263-272.

Tani, S. 2000. "Behavior of Large Fill Dams during Earthquake and Earthquake Damage", *J., Soil Dynamics and Earthquake Engineering,* Elsevier, V. 20, pp., 223-229.

Tatsuoka, F. and S. Shibuya, 1992. "Deformation Characteristics of Soils and Rocks from Field and Laboratory Tests", *Report of the Institute of Industrial Science,* University of Tokyo, Japan, Vol. 37, No. 1, 1992, 136 p.

Terzaghi, K., and Peck, R. B. 1967. *"Soil Mechanics in Engineering Practice"*, John Wiley and Sons, Inc. New York.., 729p.

Taylor, R. N. 1995. *"Geotechnical Centrifuge Technology"*, Blackie Academic & Professional, an imprint of Chapman and Hall, 296 p.

Taylor, D. W. 1948. *"Fundamentals of Soil Mechanics"*, John Wiley and Sons, Inc. New York.

TC4, S. 2001. "Case Histories of Post-Liquefaction Remediation. Report", *Technical Committee for Earthquake Geotechnical Engineering TC4,* International Society of Soil Mechanics and Geotechnical Engineering ISSMGE. The Japanese Geotechnical Society, Tokyo, Japan.

Thevanayagam, S. 1998. "Effect of Fines and Confining Stress on Undrained Shear Strength of Silty Sands", *ASCE J. Geotechnical and Geoenvironmental Engg.,* V. 124(6), pp. 479-491.

Thevanayagam, S. 1999. "Liquefaction and Shear Wave Velocity Characteristics of Silts/Gravelly Soils", In *Proc., 15 U.S.-Japan Workshop on Bridge Engg.* , Public Works Research Institute, Tsukuba City , Tokyo, pp. 133-147.

Thevanayagam, S. 2000. "Liquefaction Potential and undrained Fragility of Silty Soils", In *Proc., the 12th World Conf., Earthquake Engg.,* Auckland, New Zealand, Jan., 30-Feb., 4, 2000, Paper No. 2383.

Thevanayagam, S., Fiorillo, M., and Liang, J. 2000. "Effect of Non-Plastic Fines on Undrained Cyclic Strength of Silty Sands", In *Proc., ASCE Conf., Soil Dynamics and Liquefaction",* ASCE GSP No. 107, pp. 77-91.

Thevanayagam, S., Martin, G. R., Shenthan, T., and Liang, J. 2001. "Post-Liquefaction Pore Pressure Dissipation and Densification in Silty Soils", In *Proc. 4th Int. Conf., Recent Advances in Geotechnical Earthquake Engg. and Soil Dynamics and Symposium in Honor of Prof. L. Finn,* San Diego, Cal., March 26-30, 2001, Paper No. 4.28.

Thevanayagam, S., and Mohen, S. 2000. "Intergranular State Variables and Stress-Strain Behavior of Silty Sands", *Geotechnique,* V. 50(1), pp. 1-23.

Thevanayagam, S., Shenthan, T., Mohen, S., and Liang, J. 2002. "Undrained Fragility of Clean Sands, Silty Sands, and Sandy Silts", *ASCE J., Geotechnical and Geoenvironmental Engg.,* V. 128(10), pp. 849-859.

Tokimatsu, K., Tata, Y, and Zhang, J. M. 2001. "Effects of Pore Water Redistribution on Post-Liquefaction Deformation of Sands", In Proc. 15th International Conference on Soil Mechanics and Geotechnical Engineering, Istanbul, Turkey. V. 1, pp 289-292. 240

Toyota, H., Towhata, I., Imamura, S. and Kudo, K. 2004. "Shaking Table Tests on Flow Dynamics in Liquefied Slope", *Soils and Foundations*, JGS, V. 44(5), pp. 67-84.

Troncoso, J. H., Vergara, A., and Avendano, A. 1993. "The Seismic Failure of Barahona Tailings Dam", In *Proc. 3rd International Conference on Case Histories in Geotechnical Engineering,* St. Louis, Missouri, pp. 1473-1479.

Tsuchida, H. 1970. "Prediction and Countermeasaure Against Liquefaction in Sand Deposits", *Abstract of the Japan Seminar in Port and Harbor Institute* (in Japanese), 3.1-3.33.

Tsukamoto, T. Y., Ishihara, K., Nakzzawa, Kamada, K., and Huang, Y. 2002. "Resistance of Patially Satuarated Sand to Liquefaction with Reference to Longitudinal and Shear Wave Velocities.", *Soils and Foundations*, JGS, V. 42(6), pp. 93-104.

Tsukamoto, Y., Ishihara, K. and Sawada, S. 2004. "Settlement of Silty Sand Deposits Following Liquefaction during Earthqauke", *Soils & Foundations,* JGS, V. 44(5), pp. 135-148.

Tsukamoto, Y., Kamata, T., Fumio Tatsuoka, F. and Ishihara, K. 2007. "Undrained Flow Characteristics of Partially Saturated Sandy Soils in Triaxial Tests". In *Proc., 4th Int. Conf., Geotechnical Earthquake Engineering,* Greece, P. No. 1239.

U. S. Army Corps of Engineers. 1999. "Guidelines on Ground Improvement for Structures and Facilities", *USACE Report*, ETL-110-1-185.

Uthayakumar, M., and Vaid, Y.P. 1998. "Liquefaction of Sands under Multi-Axial Stresses", *Canadian Geotechnical J.,* V. 35, pp. 273–283.

Uzuoka, R., Sento, N. and Kazama, M. 2003. "Numerical Analysis on Liquefaction-Induced Progressive Deformation with Pore Water Pressure Migration", In Proceedings of 3rd Int. Symposium on Deformation Characteristics of Geomechanics, Lyon, pp. 1095-1101.

Vaid, Y.P. 1994. "Liquefaction of Silty Soils", In *Proc., Conf., Ground Failures under Seismic Conditions",* ASCE GSP No. 44, New York, pp. 1-16.

Vaid, Y.P., and Chern, J.C. 1985. "Cyclic and Monotonic Undrained Response of Sands", In *Proceedings of the Advances in the Art of Testing Soils under Cyclic Loading Conditions,* ASCE Convention, Detroit, pp. 171-176.

Vaid, Y.P., Chern, J.C., and Tumi, H. 1985. "Confining Pressure, Grain Angularity, and Liquefaction', *Journal of Geotechnical Engineering,* ASCE, V. 111, pp. 1229–1235.

Vaid, Y.P., Uthayakumar, M., Sivathayalan, S., Robertson, P. K., and Hofmann, B. 1995. "Laboratory Testing of Syncrude Sand", In *Proceedings of the 48th Canadian Geotechnical Conference,* Vancouver, V. 1, pp. 223–232.

Vaid, Y.P., and Sivathayalan, S. 1999. "Fundamental Factors Affecting Liquefaction Susceptibility of Sands (Keynote Lecture)", In *Proc., Int. Workshop on the Physics and Mechanics of Liquefaction,* John Hopkins Un., Baltimore, Sept. 10-11, 1998, A.A. Balkema, pp. 105-120.

Vaid, Y.P., and Sivathayalan, S. 2000. "Fundamental Factors Affecting Liquefaction Susceptibility of Sands", *Canadian Geotechnical J.,* V. 37, pp. 592–606.

Vaid, Y.P., Stedman, J.D., and Sivathayalan, S. 2001. "Confining Stress and Static Shear Effects in Cyclic Liquefaction", *Canadian Geotechnical J.,* V. 38, pp. 580–591.

Vaid, Y.P., and Thomas, J. 1995. "Liquefaction and Post-Liquefaction Behavior of Sand", *ASCE J., Geotechnical Engineering,* V. 121(2), pp. 163–173.

Vallejo, L. E. 2001. "Interpretation of the Limits in Shear Strength in Binary Granular Mixtures", *Canadian Geotechnical J.,* V. 38, pp. 1097–1104.

Verdugo R. and Ishihara K. 1996. "The Steady State of Sandy Soils. *Soils and Foundations*, V. 36(2), pp.81–92.

Wang, W. S. 1979. "Some Findings in Soil Liquefaction", *Water Conservancy and Hydroelectric Power,* Scientific Research Institute, Beijing, China.

Wang, C. H., 2003. "Prediction of the Residual Strength Liquefied Soils", *PhD. Dissertation,* Un., Washington, WA. 457p.

Wang, F. W., and Sassa, K., and Fukuoka, H. 2000. "Geotechnical Simulation Test for the Nikawa Landslide Induced by January 17, 1995 Hyogoken-Nambu Earthquake", *Soils and Foundations*, V. 40(1), pp. 35-46.

Wang, F. W., and Sassa, K., 2002. "Post-Failure Mobility of Saturated Sands in Undrained Load-Controlled Ring Shear Tests", *Canadian Geotechnical J.,* V. 39, pp. 821–837.

Warner, S., (editor), 1998. "Seismic Guidelines for Ports", *ASCE Technical Council on Lifelines Earthquake Engineering, Monograph No. 12,* Reston, VA.

Wickland, B. Wilson, W., Wijewickreme, D. and Klein, B. 2006, "Design and Evaluation of Mixtures of Mine Waste Rock and Tailings", *Canadian Geotechnical J.,* V. 43, pp. 928-945.

Wijewickreme, D. and Vaid, Y. P.1993. "Behavior of Loose Sand under Simultaneous Increase in Stress Ratio and Principal Stress Rotation", *Canadian Geotechnical J.,* V. 30(6), pp. 953-964.

Wijewickreme, D., Sriskandakumar, S., and Byrne, P. M. 2005. "Cyclic Loading Response of Loose Air-Pluviated Fraser River Sand for Validation of Numerical Models Simulating Centrifuge Tests", *Canadian Geotechnical J.,* V42, pp.550-561.

Wolf, H., Konig, D. and Triantafyllidis, T. 2003. "Experimental Investigation of Shear Band Patterns in Granular Material", *Journal of Structural Geology,* V. 25, pp.1229–1240.

Wride, C. E., Mc Robertson, P. K. 1999. "Reconsideration of Case Histories for Estimating Shear Strength in Sandy Soils", *Canadian Geotechnical J.,* V. 36(5), pp. 907-933.

Wu, J. 2002. "Liquefaction Triggering and Post Liquefaction Deformations of Monterey 0/30 Sand Under Uni-Directional Cyclic Simple Shear Loading", *PhD Dissertation,* University of California, Berkeley, Calf.

Wu, P.K, Matsushima, K. and Tatsuoka, F. 2008. "Effects of Specimen Size and Some Other Factors on the Strength and Deformation of Granular Soil in Direct Shear Tests", *ASTM Geotechnical Testing Journal,* V. 31 (1), Paper ID GTJ100773.

Yamamuro, J. A., and Covert, K. M. 2001. "Monotonic and Cyclic Liquefaction of Very Loose Sands with High Silt Content", *ASCE J., Geotechnical and Geoenvironmental Engg.,* V. 127(4), pp. 314-324.

Yamamuro, J. A., and Lade, P. V. 1997. "Static Liquefaction of Very Loose Sands", *Canadian Geotechnical J.,* V. 34(6), pp. 905-917.

Yamamuro, J. A., and Lade, P. V. 1998. "Steady-State Concepts and Static Liquefaction of Silty Sands", *ASCE J., Geotechnical and Geoenvironmental Engg.,* V. 124(9), pp. 868-877.

Yamamuro, J. A., and Wood, F. 2004. "Effect of Depositional Method on the Undrained Behavior and Microstructure of Sand with Silt", *Soil Dynamics and Earthquake Engineering J.,* V. 24, pp. 751-760.

Yang, J. 2002. "Liquefaction Resistance of Sand in Relation to P-wave Velocity", *Geotechnique,* V. 52(4), pp. 295-298.

Yang, Z., and Elgamal, A. 2001. "Sand Boils and Liquefaction-Induced Lateral Deformation," (CD-ROM), Lessons Learned From Recent Strong Earthquakes, In *Proc., 15th Intl. Conf. on Soil Mechanics and Geotechnical Engineering*, Istanbul, Turkey.

Yang, Z., and Elgamal, A. 2002a. "Influence of Permeability on Liquefaction-Induced Shear Deformation", *J., Engineering Mechanics,* ASCE, V. 128, pp. 720-729.

Yang, Z., and Elgamal, A. 2002b. "Challenges in Computational Modeling of Liquefaction-Induced Ground Deformations", In *Proc., NSF Int. Workshop on Earthquake Simulation in Geotechnical Engg.*

Yang, E and Ko, H. 1998. "Reduction of Pore Pressure by the Gravel Drainage Method during Earthquakes", In *Proc., Int., Conf., Centrifuge 98,* Tokyo, A. A. Balkema, the Netherlands, pp. 301-306.

Yang, D., Naesgaard, E., and Gohl, B. 2003. "Geotechnical Seismic Retrofit Design of George Massey Tunnel", In *Proc. 12th Pan-American Conf. on Soil Mechanics and Geotechnical Engg., Cambridge*, USA, pp. 2567 – 2574.

Yang, D., Naesgaard, E., Byrne, B., Adalier, K and Abdoun, T. 2004. "Numerical Model Verification and Calibration of George Massey Tunnel using Centrifuge Models", *Canadian Geotechnical J.,* V. 41, pp. 921-942.

Yang, S.L, Sandven, R. and Grande, L. 2006. "Steady-State Line of Sand-Silt Mixture", Canadian *Geotechnical J.,* V. 43, pp. 1213-1219.

Yang, J., and Sato, T. 2001. "Analytical Study of Saturation Effects on Seismic Vertical Amplification of A Soil Layer", *Geotechnique,* V. 51(2), pp. 161-165.

Yang, J., Savidis, S. and Roemer M. 2004. "Evaluating Liquefaction Strength of Partially Saturated Sand", *J., Geotechnical and Geoenvironmental Engg., ASCE,* V. 130(9), pp. 975-979.

Yasuda, S., Ishihara, K., Harada, K., and Shinkawa, N. 1996. "Effect of Improvement on Ground Subsidence due to Liquefaction", *Soils and Foundations,* JSSMFE, V. 36 (1), pp. 99-107.

Yazdi, A. M. 2004. "Post-Liquefaction Behavior of Sands under Simple Shear and Triaxial Loading Modes", *Master Thesis,* Carleton University, Ottawa, 119p.

Yegian, M.K., Esseler-Bayat, E., Alshawabkeh, A. and Ali, S. 2007." Induced-Partial Saturation for Liquefaction Mitigation: Experimental Investigation", *J., Geotechnical and Geoenvironmental Engg., ASCE,* V. 133(4), pp. 372-380.

Yoshida, N. and Iai, S. 1998. "Nonlinear Site Response and its Evaluation and Prediction", In Proc., 2nd Int. Symposium on the Effect of Surface Geology on Seismic Motion, Yokosuka, Japan, pp. 71-90.

Yoshida, N., Yasuda, S. and Ohya, Y. 2005. "Two Criteria for Liquefaction-Induced Flow", In *Proc., Performance Based Design in Earthquake Geotechnical Engineering: Concepts and Research*, Satellite Conf., Osaka, Japan, pp. 109-116.

Yoshimi, Y. 1967. "An Experimental Study of Liquefaction of Saturated Sands", *Soils and Foundations*, JSSMFE, V. 2 (2), pp. 20-32.

Yoshimi, Y., Tanaka, K., and Tokimatsu, K. 1989. "Liquefaction Resistance of a Partially Saturated Sand", *Soils and Foundations*, JSSMFE, V. 29 (3), pp. 157-162.

Yoshimi, Y., Tokimatsu, K., and Hosaka Y. 1989. "Evaluation of Liquefaction Resistance of Clean Sands based on High-Quality Undisturbed Samples", *Soils and Foundations*, JSSMFE, V. 29 (3), pp. 93-104.

Yoshimine, M. and Koike, R. 2005. "Liquefaction of Clean Sand with Stratified Structure due to Segregation of Particle Size", *Soils and Foundations,* JGS, V. 45 (4), pp. 89-98.

Yoshimine, M., Nishizaki, H., Amano, K. and Hosono, Y. 2006. "Flow Deformation of Liquefied Sand under Constant Shear Load and its Application to Analysis of Flow Slide of Infinite Slope', *J. Soil Dynamics and Earthquake Engineering,* V. 26, pp. 253-264.

Youd, T. L. 1984. "Recurrence of Liquefaction at the Same Site", In *Proc. 8th World Conference on Earthquake Engineering*, V. 3, Prentice-Hall, Inc., Englewood Cliffs, N.J., pp. 231-238.

Youd, T. L., Bartholomew, H. and Proctor, J. 2004a. "Geotechnical Logs and Data from Permanently Instrumented Field Sites: Garner Valley Down-Hole Array (GVDA) and Wildlife Liquefaction Array, WLA", *Report to the Network for Earthquake Engineering,* Simulation (NEES), Civil and Environmental Engg. Dept., Brigham Young University, UT.

Youd, T. L., and Gilstrap S. D. 1999. "Liquefaction and Deformation of Silty and Fine-Grained Soils", In *Proc., Second Int. Conf., Earthquake Geotechnical Engg.*, Lisboa, edited by Pinto, S., A. A. Balkema, the Netherlands, V. 3, pp. 1013-1020.

Youd, T. L., Hansen, C. M., and Bartlett, S. F. 1999. "Revised MLR Equations for Predicting Lateral Spread Displacement", In *Proc., 7th US-Japan Workshop on Earthquake Resistance Design of Lifelines Facilities and Countermeasures Against Soil Liquefaction,* Edited by O'Rourke, T. D., Bardet, J. P., and Hamada, M., MCEER-99-0019, Buffalo, New York, Multidisciplinary Center for Earthquake Engineering Reseach.

Youd, T. L., Hansen, C. M., and Bartlett, S. F. 2002. "Revised Multi-linear Regression Equations for Prediction of Lateral Spread Displacement", Journal of Geotechnical and Geoenvironmental Engineering, Vol. 128, No. 12, pp. 1007-1017.

Youd, T. L., Harp, E.L., Keefer, D. K., and Wilson, R. C. 1985. "The Borah Peak, Idaho Earthquake of October 28, 1983 – Liquefaction", Earthquake Spectra, V. 2 (4), pp. 71-89.

Youd, T. L. and Holzer, T. L. 1994. "Piezometer Performance at the Wildlife Liquefaction Site", *Journal of Geotechnical Engineering*, ASCE, V. 120, No. 6, p. 975-995.

Youd, T. L. and Holzer, T. L. 1995. "Closure to Discussion by Scott and Hushmand on Piezomerter Performance at Wildlife Site, California", *Journal of Geotechnical Engineering*, ASCE, V. 121 (12), pp. 919-919.

Youd, T. L., and Idriss, I. M. 1998. "Proceedings of the NCEER Workshop on Evaluation of Liquefaction Resistance of Soils", *Report No. NCEER-97-0022,* Multidisiplinary Center for Earthquake Engineering Research.

Youd, T. L., Idriss, I. M., Andrus, R., Arango, I., Castro, G., Christian, J., Dobry, J., Finn, L., Harder Jr., L., Hynes, H. M., Ishihara, K., Koester, J., Liao, S. S., Marcuson III, W. F., Martin, G., Mitchell, J. K., Moriwaki, Y., Power, M. S., Robertson, P. K., Seed, R. B., and Stokoe II, K. H. 2001. "Liquefaction Resistance of Soils: Summary Report from the 1996 NCEER and 1998 NCEER/NSF Workshops on Evaluation of Liquefaction Resistance of Soils", *Journal of Geotechnical and Geoenvironmental Engineering,* ASCE, V. 127, pp. 817-833.

Youd, T. L, Steidl, J., and Nigbor, R. L. 2004b. "Ground Motion, Pore Water Pressure and SFSI Monitoring at NEES Permanently Instrumented Field Sites", In *Proceedings, 11thInternational Conference on Soil Dynamics and Earthquake Engineering and 3rd International Conference on Earthquake Geotechnical Engineering,* Berkeley, California.

Youd, T. L., Steidl, J. H. and Nigbor, R. L. 2004c. "Lessons Learned and Need for Instrumented Liquefaction Sites", *J., Soil Dynamics and Earthquake Engineering, Elsevier*, V. 24, p. 639-646.

Youd, T. L., and Wieczorek, G. F. 1982. "Liquefaction and Secondary Ground Failure, in the Imperial Valley, California, Earthquake of October 15, 1979." *U.S. Geological Survey Professional Paper 1254*, USGS, Menlo Park, California, pp. 223-246.

Yu, H. S., Yang, Y. and Yuan, X. 2005. "Application of Non-coaxial Plasticity Models in Geotechnical Analysis", In *Proc.,16th Int. Conf., Soil Mechanics and Geotechnical Engineering,* ISSMGE, Osaka, Japan, V. 1. pp. 993-996.

Zeng, Z. 1999. "Several Important Issues related to Liquefaction Study Using Centrifuge", In *Proc., Int. Workshop on the Physics and Mechanics of Liquefaction,* John Hopkins Un., Baltimore, Sept. 10-11, 1998, A.A. Balkema, the Netherlands, 283-293.

Zeng, X., Arulanandan, K. 1995. "Modeling Lateral Sliding of Slope due to Liquefaction of Sand Layer", *J., Geotechnical Engineering,* ASCE, V. 121(11), pp.814–816.

Zeghal, M. and Elgamal A. W. 1994. "Analysis of Site Liquefaction using Records", *J., Geotechnical Engineering,* ASCE, V. 120(6), pp.96–1017.

Zienkiewicz, O. C. and Shiomi, T. 1984. "Dynamic Behavior of Saturated Porous Media; The Generalized Biot formulation and its Numerical Solution", *International Journal for Numerical Methods in Engineering*, 8, 71–96.

Zienkiewicz, O.C., Chan, A.C., Pastor, M., Paul, D.K., and Shiomi, T. 1990. "Static and Dynamic Behavior of Soils: A Rational Approach to Quantitative Solutions. Part I: Fully Saturated Problems", In *Proceedings of the Royal Society of London, Mathematical and Physical Sciences,* Series A, 429: 285–309.

Zienkiewicz, O.C., Chan, A., Pastor, M., Schrefler, B., and Shiomi, T. 1999. "*Computational Geomechanics with Special Reference to Earthquake Engineering*", John Wiley and Sons Ltd. U.K.

Zlatovic, S. 1994. "Residual Strength of Silty Soils", *Doctor of Engineering Thesis,* University of Tokyo.

Zlatovic, S., and Ishihara, K.1997. "Normalized Behavior of Very Loose Non-Plastic Soils: Effects of Fabric", *Soils and Foundations,* JSSMFE, V. 37(4), pp. 47-56.

APPENDIX I:

CURRENT PRACTICE FOR LIQUEFACTION ASSESSMENT

AI.1 Introduction

This appendix deals with the current practice for liquefaction assessment and also some factors influencing sand behavior that were not covered in *Chapter 2*. It provides a detail treatment of fines content effect in sand liquefaction.

AI.2 Liquefaction Triggering Assessment, Current Practice

Currently, majority of engineering design regarding liquefaction assesment are mainly based on in-situ tests results and in particular Standard Pentration Test (*SPT*) and to a lesser extent Cone Penetration Test (*CPT*) worldwide. This approach was first introduced by Seed & Idriss (1971) and then extended by Seed et al. (1984). Recently, two workshops were held by US. National Center for Earthquake Engineering Research (NCEER) to update the approach that its outcome was published by Youd et al. (2001). The approach is basically developed based on previous case studies and correlates Cyclic Resistance Ratio (*CRR*) for a reference condition (i.e. an *M7.5* earthquake, σ'_v =100 kPa and level-ground) to corrected SPT blow count for a clean sand, $(N_1)_{60}$. An earthquake with magnitude of 7.5 in considered to be equivalent to approximately 15 significant cycles of loading (Seed et. al., 1975). Figure I-37 shows the updated curve recommended by NCEER workshop that suggests a minimum *CRR* of 0.05 for very low N value (Youd et al., 2001). This value of *CRR* using correction factors as K_σ, K_α and K_m should be modified to account for the effects of overburden pressure, static shear bias and earthquake magnitude respectively per Eq. AI-1. In this respect NCEER recommends using correction factors as Seed & Harder (1990) suggested.

$$CRR = K_\sigma . K_\alpha . K_m . CRR_1 \qquad \text{[AI-1]}$$

Where:

CRR_1 and CRR are cyclic resistance ratio at the reference and real conditions respectively.

K_σ, K_α and K_m : Correction factor for overbuden pressure, shear stress bias and earthquake magnitude, respectively. NCEER does not recommend correction factors for ground inclination (i.e. $K\alpha = 1$). The same suggestion has been made by VGS Liquefaction Task Force (VGS, 2007).

Recently, Idriss & Boulanger (2004 & 2006) suggested some modificaiton to the NCEER recommendations as shown in Fig. AI-1 and AI-2 for K_σ and K_α respectively. Also, Fig. AI-3 shows charts for K_m proposed by various investigators in comparison with NCEER suggestion. Cetin et al. (2003) re-evaluated the data base of used by Seed et al. (1984) and extended them with post-dated case histories mainly from Kobe earthquake, Japan through a deterministic and probabilistic approach. Their suggestions in terms of CSR^* (an equivalent cyclic stress ratio normalized by a weighting factor for earthquake magnitude) and N value are shown in Fig. AI-5. As may be seen typically they predict a lower liquefaction resistance comparing to that of NCEER.

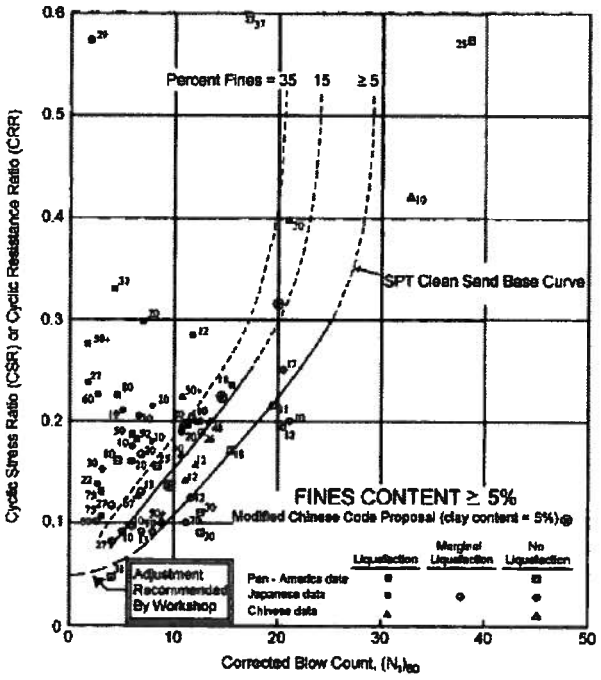

Fig. AI-1: MCEER Recommended chart for CRR evaluation based on $(N_1)_{60}$ (Youd et al., 2001).

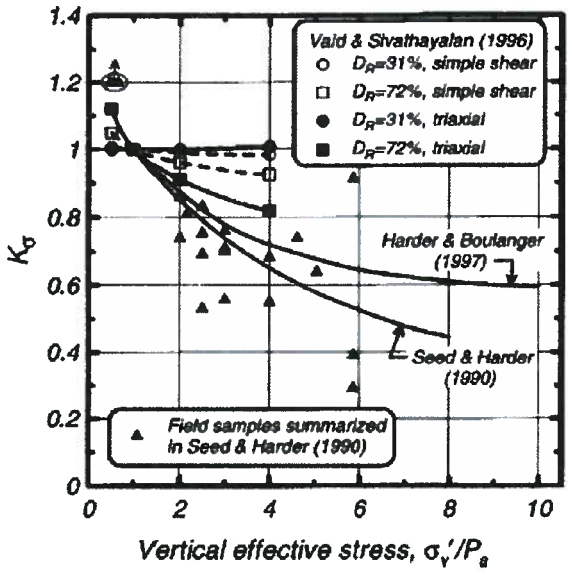

Fig. AI-2: K_σ vs. normalized confining stress for different values of relative density (Boulanger, 2003b).

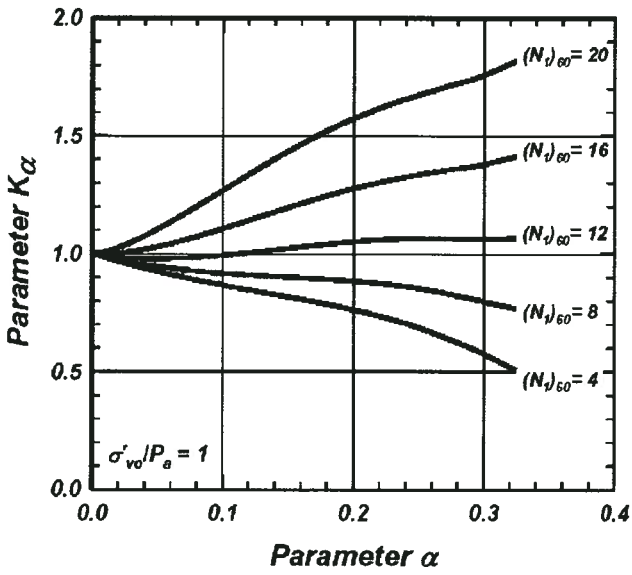

Fig. AI-3: Correlation of K_α with α derived based on relative state parameter at σ'_o = 100 kPa (Boulanger, 2003a).

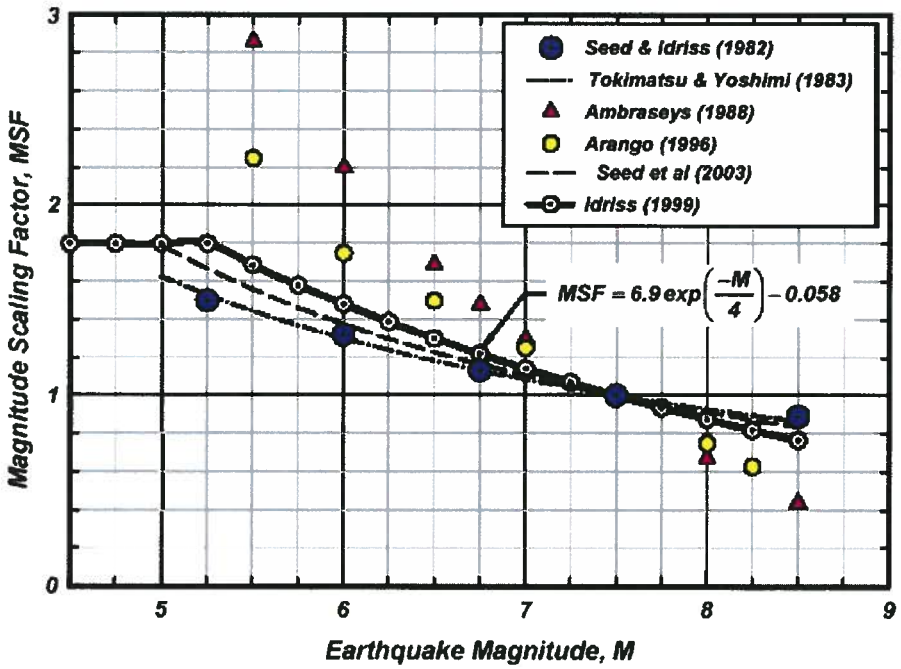

Fig. AI-4: Recommended charts for K_m by various investigators with MCEER suggestion (Idriss & Boulanger, 2004).

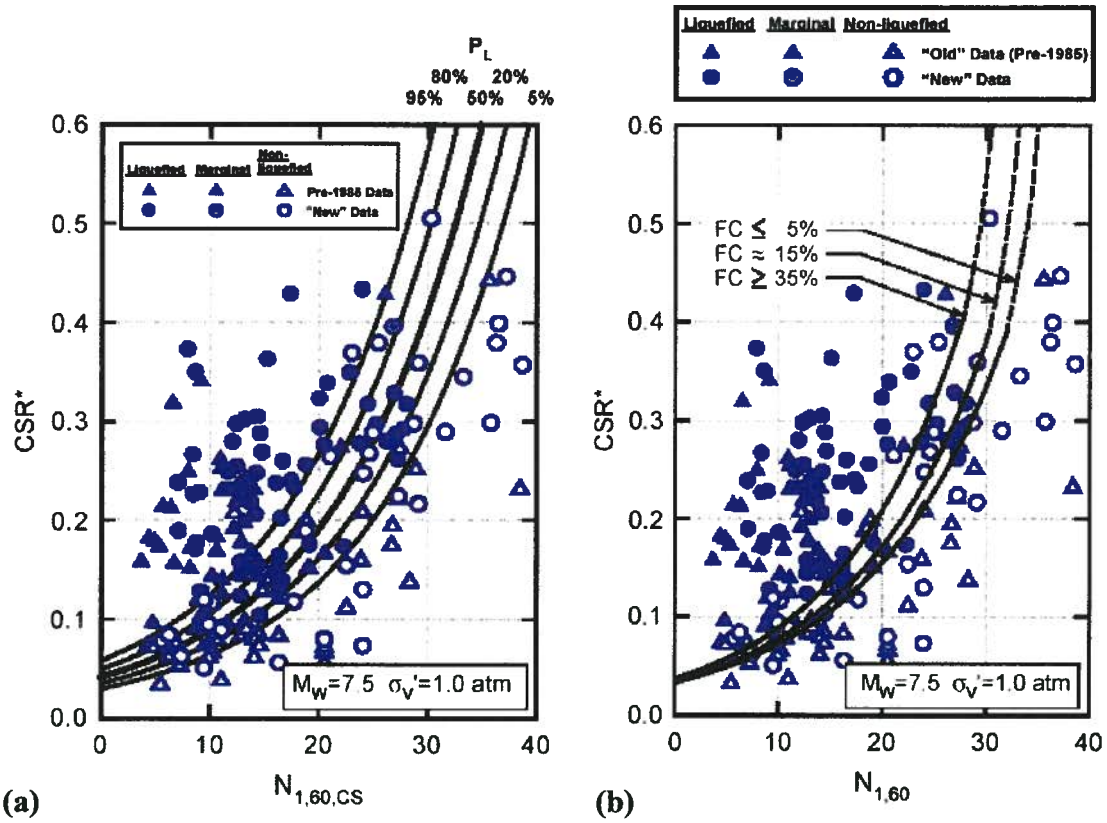

Fig. AI-5: Evaluation of CSR^* based on $(N_1)_{60}$ using (a) probabilistic and (b) deterministic approach (Cetin et al., 2004).

AI.2 Stress Path, Anisotropy and Fabric

Stress-strain response and strength of sand depend on loading path and direction of principal stresses as addressed by many researchers (Arthur & Menzies, 1972; Bishop, 1971; Kuerbis & Vaid, 1989; Vaid & Thomas, 1995; Riemer & Seed, 1997). Different response of sand can be due to inherent material properties or anisotropic consolidation loading (Wijewickreme & Vaid, 1993).

Traditionally soil samples are tested under compression triaxial condition in which major principal stress is applied in vertical direction (parallel to gravity direction) and maximum shear stress plane is inclined with 45° regarding horizontal bedding plane whereas, in extension test the major principal stress is horizontal (perpendicular to deposition alignment). In simple shear test the maximum shear stress occurs in horizontal plane while the major principal stress

direction varies during shearing (shear stress change). The relevance of testing condition to real situation is illustrated in Fig. AI-6.

Fig. AI-7 shows results of hollow-cylindrical torsion, HCT test results on Fraser River sand with different major principal stress direction. It suggests that shear strength of sand in triaxial compresion and extension test represents the upper and lower bound of shear strength, respectively, while simple shear test condition results in between (Vaid & Sivathayalan, 1999). The direction-dependent undrained behavior of sand is an expression of its inherent anisotropy.

To account for the effects of principal stress direction on undrained cyclic liquefaction resistance of sands Seed & Harder (1990) suggested a correction coefficient, K_α in similar fashion of K_σ to convert *CRR* to the reference level-ground condition ($\alpha = 0$) however, studies by Vaid et al. (2001) demonstrated that Seed and Harder suggestions understimates the effects as shown in Fig. AI-6 (in which α denotes static shear stress bias as $|\tau_0|/\sigma'_{v0}$). As mentioned earlier Boulanger (2003a & 2003b) using critical state concept developed a correlation for K_α as shown in Fig. AI-2 and Fig. AI-3.

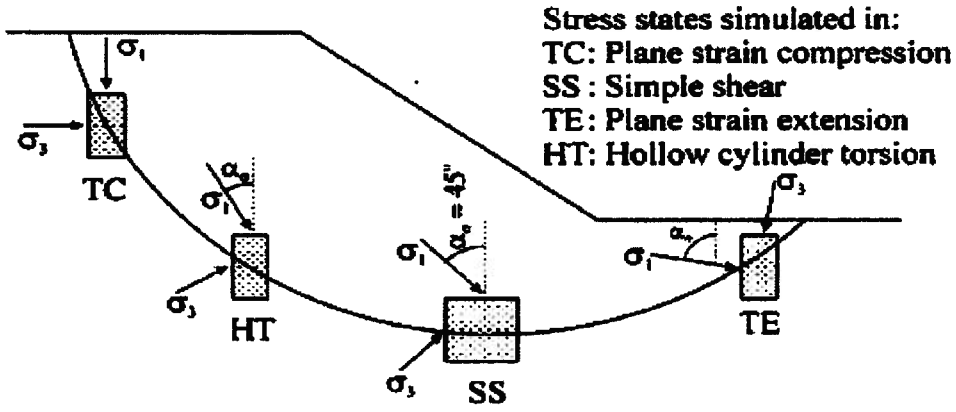

Fig. AI-6: Change of major principal stress orientation in a slope.

Particle orientation and particle contacts within sand matrix is called the fabric (Oda, 1972, Oda et.al., 1978). The effect of fabric on the stress-strain response of Syncrude sand in simple shear test is depicted in Fig. AI-8. The specimens with identical void ratio ($e = 0.76$, $Dr \approx$ 40%) after consolidatin ($\sigma'_c = 200$ kPa) were constituted with different techniques ie. moist

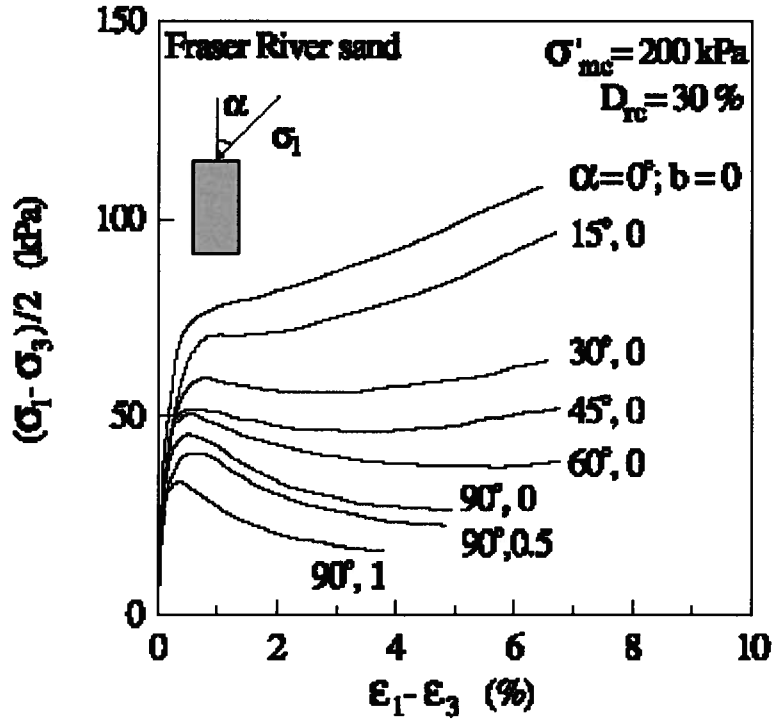

Fig. A-7: Sand respose change due to major principal stress rotation in undrained HCT test, $b = (\sigma_2 - \sigma_3)/(\sigma_1 - \sigma_3)$ (Vaid & Sivathayalan, 1999).

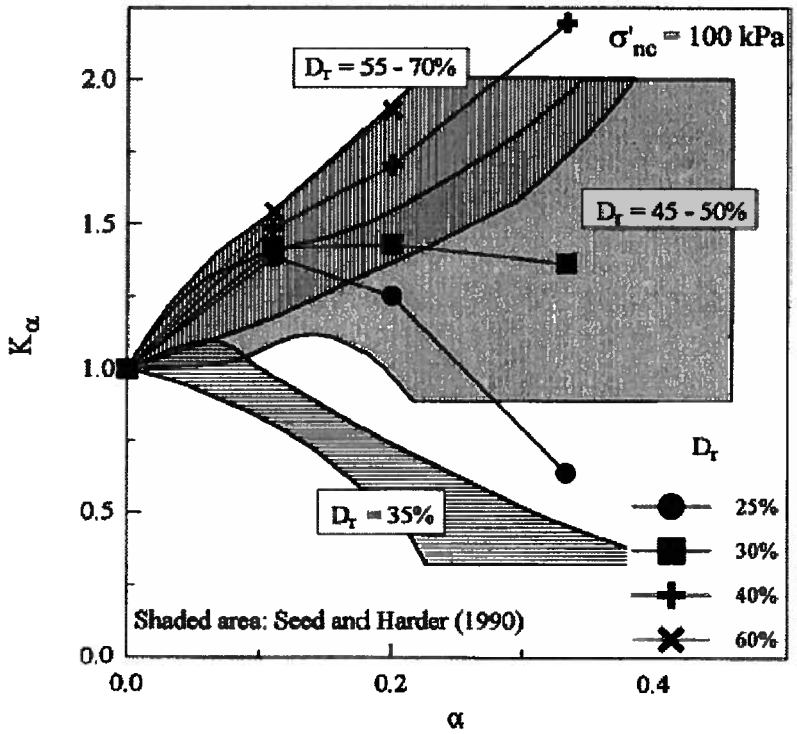

Fig. AI-8: K_α vs.α for Fraser River sand at different relative densities, compared to Seed & Harder (1990) suggestion, $\sigma'_o = 100$ kPa (Vaid et al., 2001).

tamping (MT), air pluviation (AP) and water pluviation (WP). As is evident, stress-strain behavior for these samples vary considerably, with the moist tamped sample having the lowest strength and the water tamped sample the highest strength. The effect of fabric should vanish with more straining. However, such strain is to be very large and untolerable for structures. The same observation has been reported by Japanese reseachers for different constitution techniques: moist placement; dry deposition; and water sedimentation. Ishihara (1996) observed that the change in void ratio of the densest state of sample during consolidation is generally very small over the wide range of the mean principal stress used in the test. Ishihara conlcluded that isotropic compression curve for the densest state is practically independent of sample preparation technique whereas the widest and smallest range in void ratio can be attained by moist tamping and water pluviation method, respectively. It implies that the effects of constitution method on sand compression are more pronounced in loose sands.

Water pluviated samples can simulate several types of earth structures such as hydraulic fill dams, some tailings impoundments, water dumped backfill behind quay walls, natural alluvial and/or delta deposits. A lightly compacted fill (e.g. in an embankment dam) may be liquefiable and have a structure similar to that of moist tamping. The air-pluviation method apprears to represent condition of deposits in aird areas irrigated with water (Ishihara, 1996). The fabric of landslide deposits or residual soils may be unique.

Vaid & Sivathayalan (1999) compared test results from undisturbed frozen samples obtained from alluvial deposits and those from water-pluviated constituted samples of the same materials and concluded that water pluviation technique seems to closely replicate the fabric of undistubed water-deposited sands response. However, againg effects should also be taken into consideration in this regard. Yoshimi et al. (1989) reported a ratio of more than 2 for *CRR* of undistrubed samples to that of freshly deposited samples.

The effects of sand fabric on cyclic undrained strength can be seen from Fig. AI-9 for Monterey sand in CT testing (Mulilis et al., 1977), as seen liquefaction resistance of moist tamped samples is higher compared with that of air pluviation ones . Other studies support this conclusin (Ishihara, 1996).

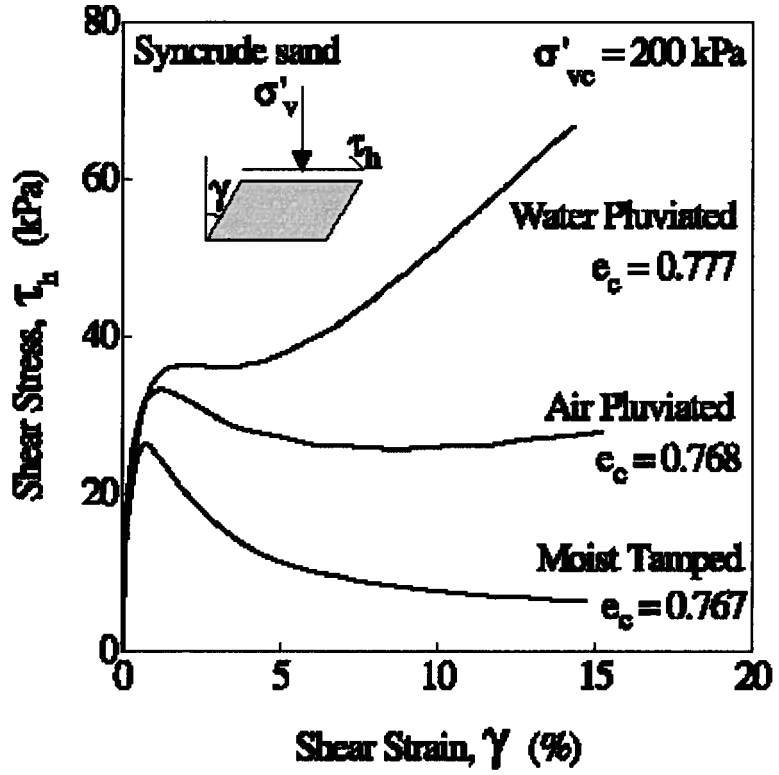

Fig. AI–8: Effect of fabric on undrained monotonic response of Fraser River sand with nominal D_r = 40% in simple shear test (Vaid et al., 1995).

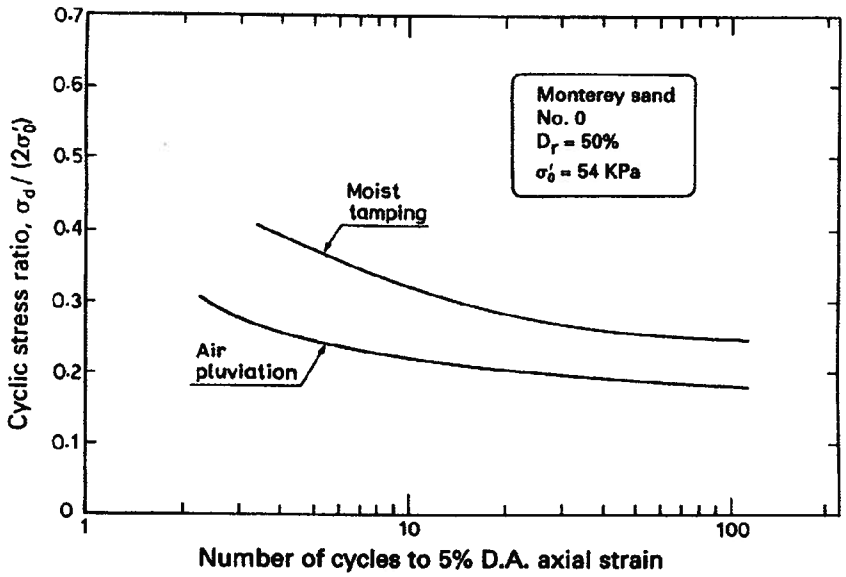

Fig. AI-9: Effects of sample constitution technique on *CRR* of sand (Mulilis et al., 1977).

AI.3 Rotation of Principal Stresses

Rotation of principal stresses at constant deviator stress can lead to a strain-softening response that may culminate in limited or unlimited flow deformation (Vaid & Sivathayalan, 2002). Significant plastic shear strains and pore pressures may occur during the rotation of principal stresses even if the shear stress or stress ratio is held constant (Gutierrez et.al, 1991). As it is shown in Fig. AI-10 sand response during monotonic shearing and pore pressure build up are function of both consolidation stress rario, $K_c (= \sigma'_{1c}/\sigma'_{3c})$ and direction of stress ($\alpha = 0°$; major principal stress in vertical direction and $\alpha = 90°$; major principal stress in horizontal direction). The resulting strains can be large for some stress paths, such as compression direction ($\alpha = 0°$) to extension ($\alpha = 90°$) at large stress ratio. A complication involved in developing a constitutive model to capture this effect is non-coaxiality; the increment of plastic strains are not in the same direction as the principal stresses (Gutierrez et.al, 1991; Wijewickreme & Vaid, 1993). The co-axiality is a common assumption in plasticity theory. Park (2005) with introducing a horizontal plane in a classical plasticity framework captured the effect of principle stress rotation in liquefied ground behavior during shaking.

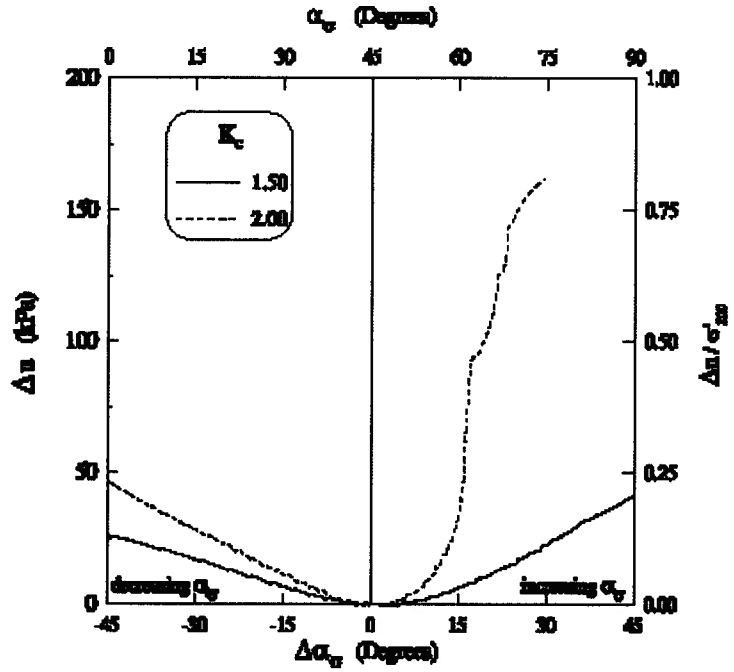

Fig. AI–10: Effect of major principal stress direction and K_c on undrained response of sand in HCT test (Sivathayalan & Vaid 2002).

AI.4 Mixing

Granular materials are generally heterogeneous in nature comprising both loose and dense, as well as, fine and coarse layers together. Each layer in itself may have adequate residual strength. Howevere, if strains are large enough, or shaking occurs these layers may mix to form a broadly graded material under globally constant volume. The void ratio (or relative density) of the layers will reflect the state of the premixed components but mixing results in volume change as illustrated in Fig. AI-11 that yields different strength characteristics e.g compressibility and residual strength. The mixed material contract while mixing and they may exhibit more contractiveness and as a result a flow failure. Recently results of element laboratory experiments on stratified granular materials have been reported by a few researchers (e.g. Amini & Sama, 1999; Amini & Qi, 2000; Amini & Chakraverty, 2004: and Yoshimine & Koike, 2005).

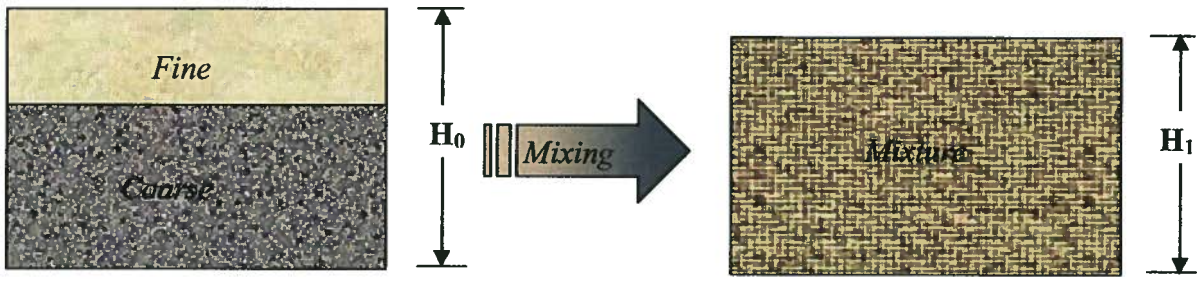

Volume Change: $(H_0 - H_1) / H_0 = \Delta\varepsilon_v^p$

Fig. AI-11: Volume reduction due to mixing.

Byrne & Beaty (1998) demonstrated that mixing was a critical component of the flow failure at the Muflira Mine in Zambia in 1970. Mixing of sand and silt layers under undrained conditions can lead to very large reduction in residual strength as shown in Fig. AI-12. Similar behavior for mixed materials was reported by Yoshimine & Koike (2005). They concluded that liquefaction resistances of sand, both in monotonic and cyclic triaxial tests are considerably affected by layering. The stratified sand was much more dilative and stiffer compared to the uniform sand (mixed) of the same density. This suggests that the in situ liquefaction resistance of

natural deposits with graded bedding could be highly less after mixing. Such effect may be significant in hydraulic fill dams and tailings deposits due to their layered stratigraphy. Despite, large strains required for mixing soils, it may be a crucial factor in progressive instability or in situations where liquefied sands have flowed for great distances e.g. natural beaches. During an eathquake shear deformations can be triggered by mechanisms such as void redistribution that results in mixing of two layers and as a result subcequent mixing aggravates the liquefaction-induced failures.

A few researchers e.g. Masih (2001), Vallejo (2001), and Gutierrez (2003) have tried to characterize a soil mixture properties based on its constituent properties. Fig. AI-12 shows a model prediction proposed by Gutierrez (2003) for undrained cyclic strength ratio of a mixture of sand and silt that comapres well with tests results. Mixing entails more experimental and modeling investigations.

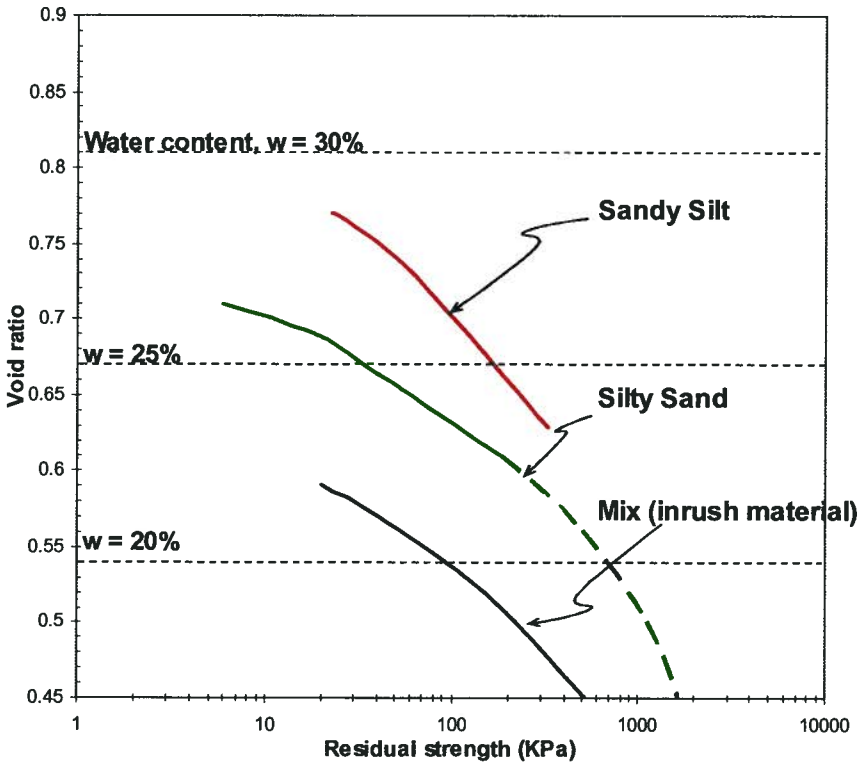

Fig. AI-12: Reduction of residual strength due to mixing.

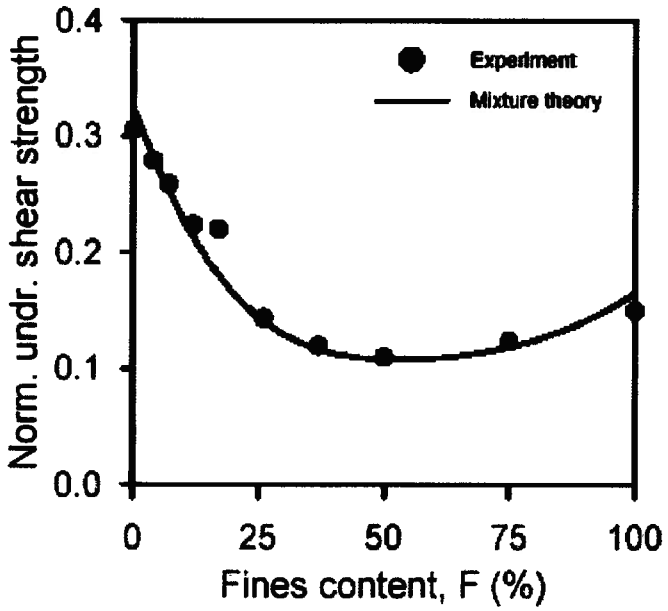

Fig. AI-13: Measured and predicted normalized cyclic undrained shear strength of Yatesville sand-silt mixtures at constant mixture void ratio of $e(F) = 0.76$ as function of fines content F (Gutierrez, 2003).

AI.5 Post-Liquefaction Volume Change

Apart from shear strength and stiffness loss, one of the consequeces of liquefaction which endanger the stability of structures is volume reduction (reconsolidation) due to excess pore pressure dissipation that initiates during and after shaking. Silver & Seed (1971) and Martin et al. (1975) demostrated that shear induced volumetric strain depends on relative density, shear strain magnitude and number of cycles. Based on data from laboratory element tests, dynamic centrifuge testing and field experiences of past earthquakes, Dobry (1992) suggested a range of 1.5 to 5% and 0.2% or less for post-liquefaction volumetric strain for loose sands and very dense sands respectively. There are some simple methods that can be applied in engineering practice e.g. Tokimatsu & Seed (1987); Ishihara & Yoshimine (1992) and Shamoto et al. (1998). All of these methods produce reasonably good predictions of actual field case history observations of post-liquefaction site settlements for sites where lateral site displacements were small (Level ground). Fig. AI-14 presents recommended chart by Seed et al. (2003) to estimate expected volumetric strains after liquefaction, or after at least significant cyclically induced pore pressure generation. The solid (from Cetin et al., 2002) line in this figure is the "triggering" boundary for probability

of P_L = 50%, and represents the approximate boundary for "triggering" of liquefaction. The strain contours represent expected values of volumetric strain due to post-earthquake dissipation of cyclically generated excess pore pressures. This is based on recent laboratory cyclic simple shear testing data, as well as previously available laboratory and field data from other researchers (Wu, 2002). This chart has also been adopted by liquefaction task force for Vancouver, B.C (Byrne & Wijewickreme, 2006).

Stewart et al. (2004) based on a review of compacted fills performance and cyclic simple shear tests of clean sands and mixed with fines developed models for settlement estimate as depicted in Fig. AI-15 in which Rc, S, γ_{tv}, a and b are modified Proctor compaction, saturation, shear strain threshold for settlement and a and b are correlation coefficients, respectively. They noted that silty sands exhibit larger post liquefaction settlements. Similar finding on silty sands behavior reported by Tsukamoto et al., (2004) support that volumetric strain of such materials is greater than that of clean sands due to larger void ratio range.

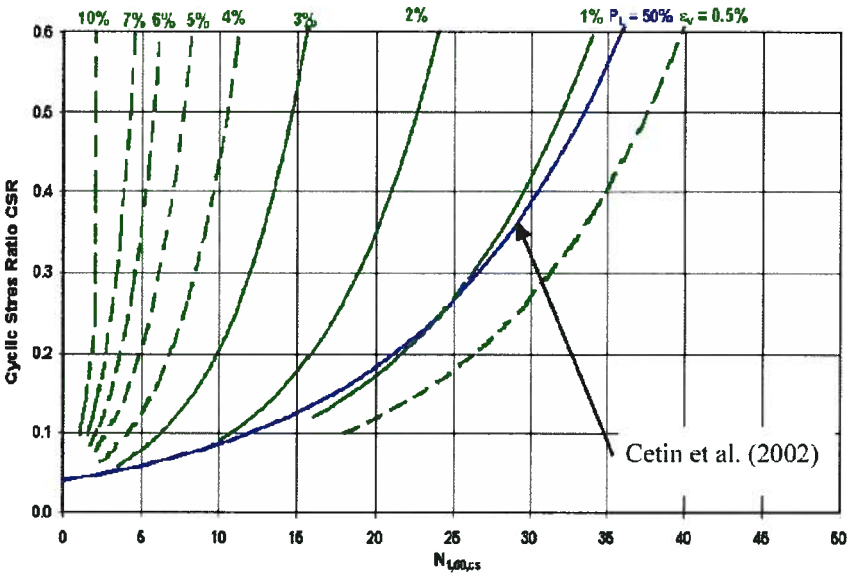

Fig. AI-14: Post-liquefaction volumetric strain (Wu, 2002).

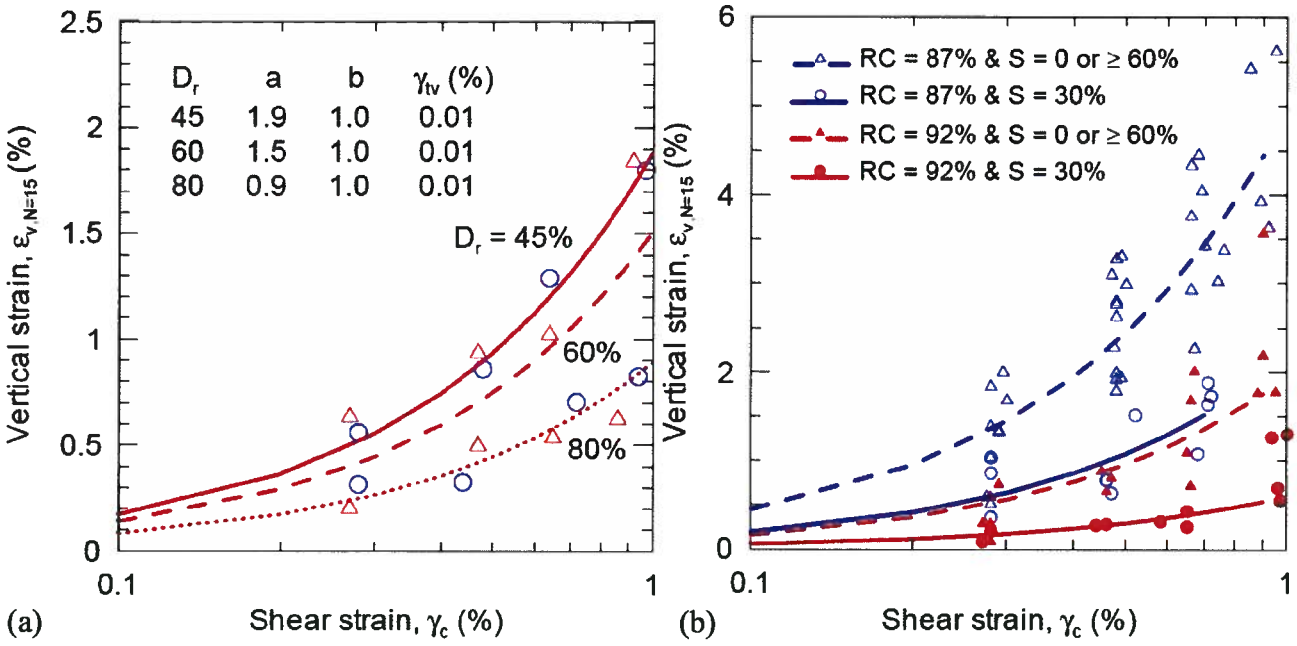

Fig. AI-15: Estimate of volumetric strain following 15 cycles of shearing for (a) clean sands, and (b) sand-silt mixture, 50% by weight, PI = 0 (Stewart et al., 2004).

There are a few experimental data (e.g. Florin & Ivanov, 1961; Scott, 1986; Ragheb, 1994; Butterfield & Bolton, 2003 and Miyamoto et al., 2004) that suggest that post liquefaction settlement is occurring due to two phenomena i.e. sedimentation and reconsolidation in level ground condition. Sedimentation occurs at a quiescent condition after full suspension of soil grains. It initiates from deeper zones of the liquefied layer under zero effective stress condition. After sedimentation completion with dissipation of excess pore pressure, the process of reconsolidation initiates and continues over the time. Test data reported by Sasaki et al. (2001) indicate that the sedimentation settlement is greater than that of consolidation.

More research works including experimental and numerical models are needed to quantify this phenomenon.

AI.6 Strain History

It is very likely the occurrence of earthquake in a soil deposit with previous history of seismic liquefaction. The cyclic resistance to liquefaction has also been noted to be significantly influenced by past liquefaction, or pre-shearing, effects (Finn et al., 1970; Seed et al. 1977;

Ishihara and Okada, 1978, 1982; Suzuki and Toki, 1984; Vaid et al., 1989). Finn et al. (1970) and De Alba et al. (1975) showed that once pore pressure ratio reaches 0.5, the soil weakens significantly, and the seismic strains and excess pore pressure increase rapidly during further earthquake loading. Ishihara and Okada (1978, 1982) have distinguished between the small and large pre-shearing by the location of the effective stress state with respect to the "line of phase transformation". Vaid et al. (1989) have suggested the line of critical stress ratio (CSR) as the demarcation between the small and large pre-shearing because larger deformations start to occur after CSR in true and limited liquefaction types of responses. Results from triaxial tests by Ishihara and Okada (1978) and Vaid et al. (1989) have shown that the small pre-shearing would significantly reduce the excess pore water pressure generation during subsequent cyclic loadings. On the other hand, large pre-shearing would significantly increase or decrease the pore pressure generation in next loading depending on the loading direction. If a sample is loaded in the same direction as the direction of pre-shearing (i.e. no strain reversal) then the pore pressure generation was noted to be less than that observed during the previous loading, and vice versa. Table 2-6 summarizes the laboratory cyclic simple shear test results reported by Sriskandakumar (2004) on Fraser River sand of 40% relative density constructed with air-pluviation method for the two loading stages. It may be seen that first stage loading results in sand densification and increased number of cycles to cause liquefaction on the second stage provided the sample did not liquefy on the first stage. However, if the sand liquefied during the first stage the number of cycles to cause liquefaction decreased on the second stage. Oda et al. (2001) also explained this behavior based on a micro-structural interpretation. Seid-Karbasi et al. (2005) reported a two-staged centrifuge testing of a sloping ground model shaken by two subsequent events. They presented a successful numerical prediction of the model behavior during the second event with consideration of re-liquefaction phenomenon.

AI.7 Ageing

Although the effect of secondary compression in sands has not been considered as an important issue, the ageing effect in sands has been reported (e.g. Mitchell & Solymar, 1984; Mesri et al. 1990), from field observation. While significant laboratory investigations have been undertaken to assess the effects of ageing on the soil response under monotonic loading (Anderson and Stokoe, 1978 and Howie et al., 2002), not much work has been reported with regard to the effect of ageing on liquefaction resistance (e.g. Leon et al., 2006). Howie et al.

(2002) reported the results of a laboratory study on very loose Fraser River sand under monotonic loading. Their data showed that stiffness is very dependent on the time of confinement prior to shearing and the stress ratio at which the sample is aged. This suggests that ageing effects should be accounted for in interpretation of laboratory tests results. Seed (1979) indicated that the cyclic resistance would increase with ageing based on results from tests on samples that had been subjected to sustained loads for periods ranging from 0.1 to 100 days prior to testing. Samples that had been subjected to longer periods of sustained pressure showed an increased resistance to liquefaction by about 25% in comparison to the un-aged samples. Similar finding was reported by Yoshimi et al. (1989) as mentioned earlier.

AI.8 Multi-Directional Loading

Conventionally in siesmic stability assessment of earth structures two assumptions are made:

- Earthquake inertia force is applied with constant axis (with changing direction).
- The greater earthquake component is parallel to slope and controls the soil behavior.

Fig. AI-16 illustrates different situations regarding earthquake loading direction that can occur during the event. A few experimental research have been conducted to study the multi-directional effects of cyclic loading (e.g. Seed et al., 1975; Ishihara & Yamazadi, 1980; Boulanger, 1991 and Kammerer, 2002). Recent studies by Kammerer (2002) highlights the complexity of the condition and a need for further work. She concluded that the CSR-based multi-direction reduction factors developed by Seed et al. (1975) and Ishihara & Yamazaki (1980) may not adequately represent actual changes in liquefaction triggering resistance. Her data suggested a range of *CSR*-based multi-direction reduction factor of 0.6 to 1.3. This is in contrast to the 0.8 to 1.0 values recommended by the previous studies. The difference in results is due, in part, to the wider range of stress paths incorporated into her study.

Having said that, in a sloping ground conditions, it is likely the larger earthquake component is applied perpendicular to the slope direction (with no shear stress bias) causing higher excess pore pressure rise and resulting in failure in the slope direction due to static shear stress bias as occurred in a test model conducted by Kokusho (1999).

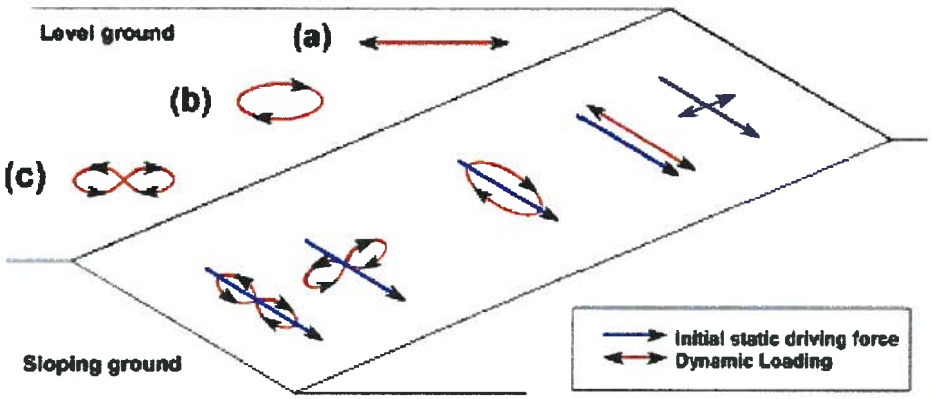

Fig. A-16: Schematic illustration of idealized multi-directional loading conditions (Kammerer, 2002).

AI.9 Gradation and Fines Content

It has long been recognized that relatively "clean" sandy soils, with few fines, are potentially vulnerable to seismically induced liquefaction. Tsuchida (1970) suggested a gradation range for soils vulnerable to liquefaction that indicates sands as mostly prone to liquefaction There has, however, been significant controversy and confusion regarding the liquefaction potential of silty soils (and silty/clayey soils), and also of coarser, gravelly soils and rockfills.

Coarser, gravelly soils are the easier of the two to discuss. The cyclic behavior of coarse, gravelly soils differs little from that of "sandy" soils, as Nature has little or no respect for the arbitrary criteria established by the standard #4 sieve (Seed et al., 2003). Coarse, gravelly soils are potentially vulnerable to cyclic pore pressure generation and liquefaction. There are now a number of well-documented field cases of liquefaction of coarse, gravelly soils (e.g. Evans, 1987; Harder, 1988; Hynes, 1988 and Andrus, 1994; JGS, 1996). These soils do, however, often differ in behavior from their finer, sandy brethren in two ways:

1. They can be much more pervious, and so can often rapidly dissipate cyclically generated pore pressures, and

2. Due to the mass of their larger particles, the coarse gravelly soils are seldom deposited "gently" and so do not often occur in the very loose states more often encountered with finer

sandy soils. Sandy soils can range from very loose to very dense, while the "very" loose state is relatively uncommon in gravelly deposits and coarser soils (Seed et al., 2003).

The apparent drainage advantages of coarse, gravelly soils can be defeated if their drainage potential is circumvented by either:

1. Their being surrounded and encapsulated by finer, less pervious materials,

2. If drainage is internally impeded by the presence of finer soils in the void spaces between the coarser particles (it should be noted that the D_{10} particle size, not the mean or D_{50} size, most closely correlates with the permeability of a broadly graded soil mix), or

3. If the layer or stratum of coarse soil is of large dimension, so that the distance over which drainage must occur (rapidly) during an earthquake is large. In these cases, the coarse soils should be considered to be of potentially liquefiable type, and should be evaluated accordingly (Seed et al., 2003). Some experimental studies on liquefaction of gravelly soils can be found in Evans & Zhou, 1995; Amini & Chakravrty, 2004 and Hara et al., 2004).

Questions regarding the potential liquefaction susceptibility of, "cohesive" soils (especially "silts" and "silty clays") have begun to receive attention in earthquake geotechnical profession. There is considerable new field data regarding this issue from recent major earthquakes, and this is an area in which major changes in both understanding and practice are occurring. This is treated in more detail in the following section.

AI.9.1 Liquefaction of Soils with Fine Grained Materials

Existence of fine materials (<74 μm, or # 200 ASTM seive size) in sand can results in significant impact on sand response. Most of the research carried out so far has been focused on pure sand (clean sand with FC < 5%). Recently, the behavior of granular mixes has drawn attention of a number of researchers (Kuerbis et.al., 1988; Chang, 1990; Chameau & Sutterer 1994; Pitman et.al, 1994; Vaid, 1994; Koester, 1994; Thevanayagam, 1998; Zlatovic & Ishihra, 1997; Yamamuro & Lade, 1998; Thevanayagam, 1999; Høeg et.al., 2000; Thevanayagam et.al., 2000; Thevanayagam & Mohen, 2000; Amini & Qi, 2000; Amini & Chakraverty, 2004; Yamamuro & Covert, 2001; Polito & Martin, 2001; Hyodo et.al., 2002; Thevanayagam et.al., 2002).

There is controversial and uncertain conclusion on the matter that ranges from:

1) Little or no effects of fines content on liquefaction resistance (Ishihara,1993),

2) Increase in liquefaction resistance due to the presences of fines (e.g., Chang et al., 1982; Kuerbis et al., 1988; and Yasuda et al., 1994),

3) Decrease in liquefaction resistance by the introduction of fines (e.g. Troncoso and Verdugo, 1985; Sladen et al. and 1985; Vaid,1994),

4) A reduction in liquefaction resistance until a certain threshold fines content then an increase in liquefaction strength with increasing fines.

A few reseachers have attemped to quantify the fines content effects on all aspects of soil properties based on mixture theory as a general framework (e.g. Gutierrez, 2003).

In the majority of studies on sand behavior, relative density D_r have been used as a measure for characterization. However, adding fine materials to sand more than a certain amount may change texture of native soil. So, the conventional definition for relative density may not be applicable. Thevanayagam (2000a) intruduced other measures to quantify the dominant behavior in the mix matrix. As shown in Fig. AI-17, Thevanayagam (1998) defined an equivalent intergranular contact index $(e_c)_{eq}$ based on intergranular void ratio e_c (Vaid, 1994) and interfine void ratio e_f (Thevanayagam, 1998) indices:

$$e_c = (e + f_c)/(1 - f_c) \qquad \text{[AI-2]}$$

$$e_f = e / f_c \qquad \text{[AI-3]}$$

$$(e_c)_{eq} = (e + (1-b) f_c)/(1 - (1-b) f_c \qquad 0 < b < 1 \qquad \text{[AI-4]}$$

Where $f_c = FC/100$ and b denotes the portion of the fine grains that contributes to the intergrain contacts: $b = 0$ could mean that none of the fine grains actively participates in supporting the coarse-grain skeleton; $b = 1$ would mean that all of the fine grains actively participate in supporting the coarse grain skeleton. He defined threshold fine content FC_{th} and limiting fine content FC_L to predict soil response .Thevanagam et.al., (2002) according to an experimental study on undrained strength of mix material concluded that:

- At low fines contents [see Fig. AI-17 for definition i.e. cases (i)-(iii), $FC < FC_{th}$], the mechanical response of the mixture is controled by the host sand.
- The dominant mechanisms for sandy silt [case (iv), $FC > FC_{th}$], are interfine material properties. The strength of sandy silt is typically higher than that of pure silt at the same

e_f. At the same $(e_c)_{eq}$, the behavior of all sandy silt specimens is similar to that of the host silt at $e = (e_c)_{eq}$.

- Silty sand and sandy silts can be deceptive in that they may have low global void ratios (or high relative density) while having high susceptibilty to undrained collapse.

Another experimental study on the effects of fines content on sand response to monotonic loading has been reported by Yamamuro and co-workers (e.g. Yamamuro & Covert, 2001; Yamamuro & Lade, 1997; Yamamuro & Lade, 1998). Their tests were conducted in a wide range of silt content regarding void ratio range (e_{max} - e_{max}). They argued that loose dry deposited sand sample exhibit opposite behavior pattern compared to that of clean sand. Complete static liquefaction may occur at low confining pressures and increasing stability and suppressed

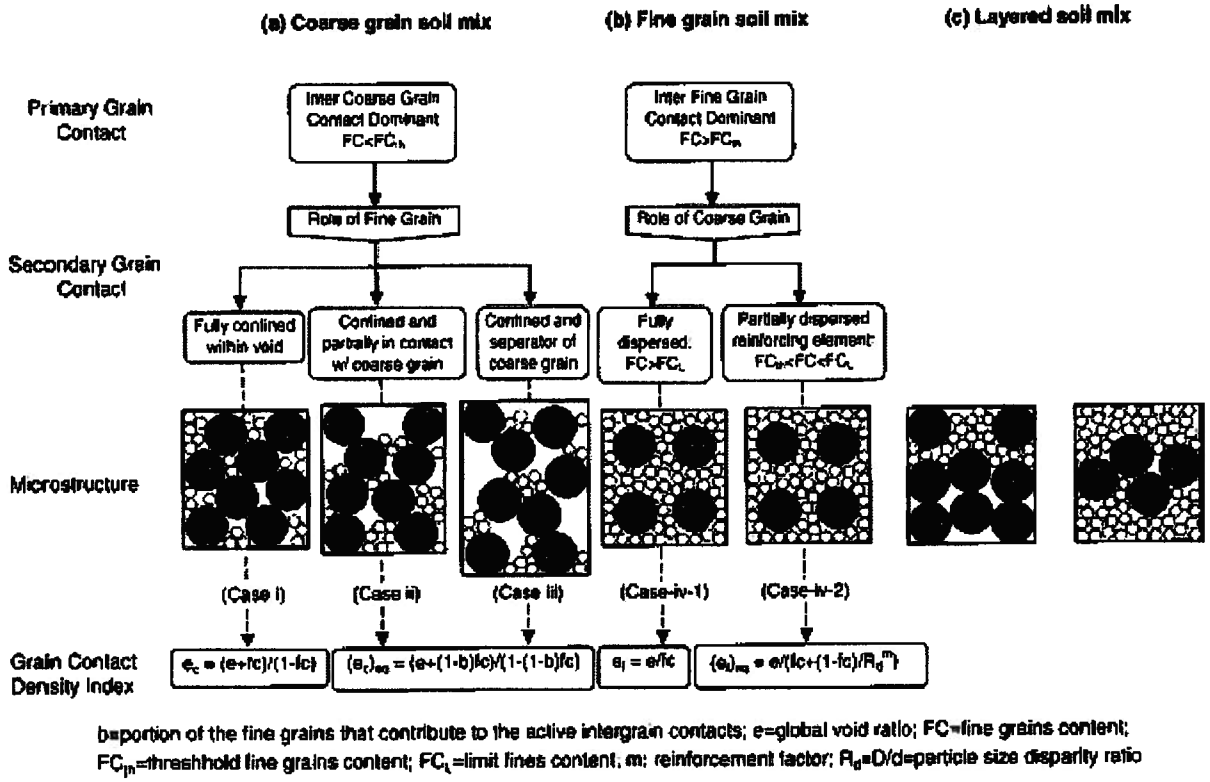

Fig. AI-17: Inter granular soil mixes classification (Thevanayagam et.al., 2002).

dilatancy can happen at high confining stress σ'_c.Yamamuro & Woods (2004) made an attempt to explain this behavior based on microstructure of the mixture constituted with a variety of

deposional methods including slurry deposition, water sedimentation, air pluviation, mixed dry deposition, and dry funnel deposition.

There are some attempts e.g. Åberg (1996) to derive a theoretical equation for optimum mixture gradation required for mimimum void ratio. Lade et al. (1998) investigated the effects of non-plastic fines on minimum and maximum void ratios of sands using a theoretical framework from packing theory of spherical beads. Their finding is consistent with previous works (e.g. Furnas, 1928). Fig. AI-18 shows porosity change with coarse grains percent for various particle sizes. Lade et al. (1998) demonstared that minimum void ratio generally varies with fines content, $F.C$ in such a way illustrated on Fig. AI-19 (assuming same specific gravity for all particles). It shows that attainable minimum void ratio decreases with $F.C$ to a certain value and then increases with $F.C$. They postulated the same trend for the maximum void ratio and presented a conceptual framwork for void ratio range variation with $F.C$ as depicted on Fig. AI-20. It suggests that the lowest value for e_{min} is obtained at about $F.C = 30\%$ (as is also inferred from Fig. AI-18) for a perfect mix that can be produced with coarse grains of a diameter of 7 times (or more) that of fine grains. It indicates that e_{min} of mix may increase or decrease depending on $F.C$ whereas void ratio range increases with $F.C$.

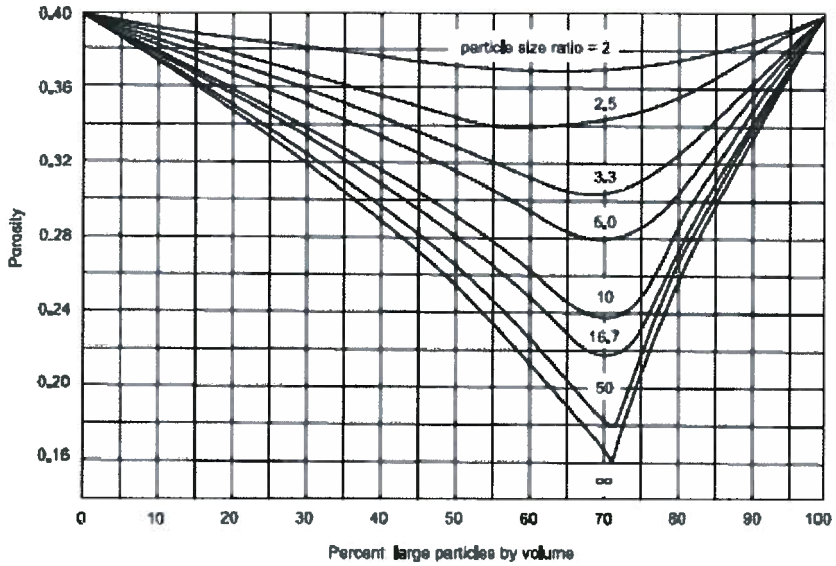

Fig. AI-18: Theoretical porosity change of binary mixture with large particles ratio (Wickland et al, 2006).

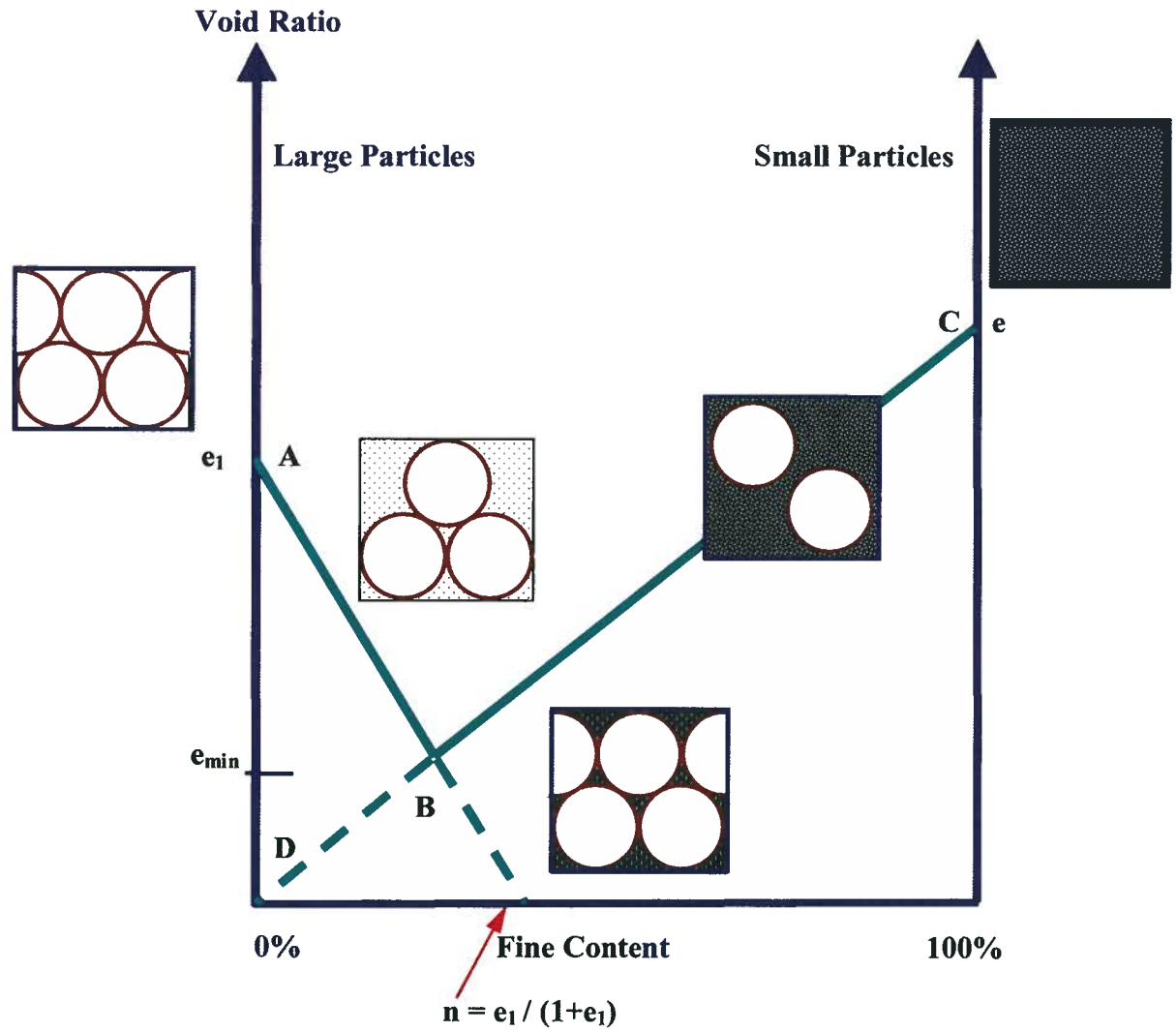

Fig. AI-19: Change of minimum void ratio of a binary pack and its matrix with fines content (modified from Lade et al., 1998).

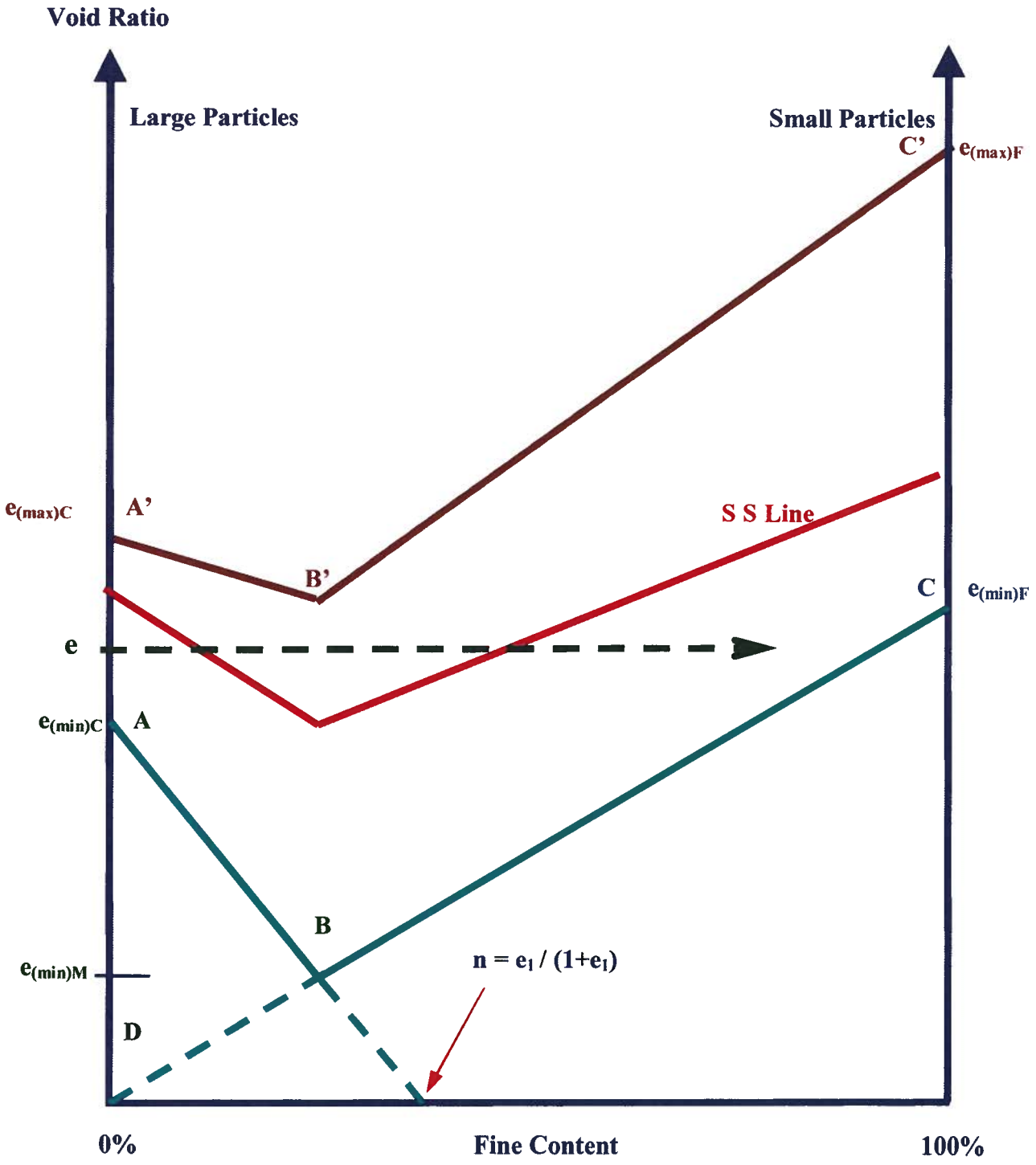

Fig. AI-20: Change of void ratio range of a binary pack with fines content (modified from Lade et al., 1998).

Experimental data also supports this conclusion as shown in Fig. AI-21 for Ottawa sand and Nevada sand with various proportions of fines. This reveals that relative density of the native sand does not represent as a state parameter for the mixure as noted by others (e.g. Vaid, 1994). They also demonstrated that fines content has a significat influence on the compressibility and static liquefaction of the mixture .

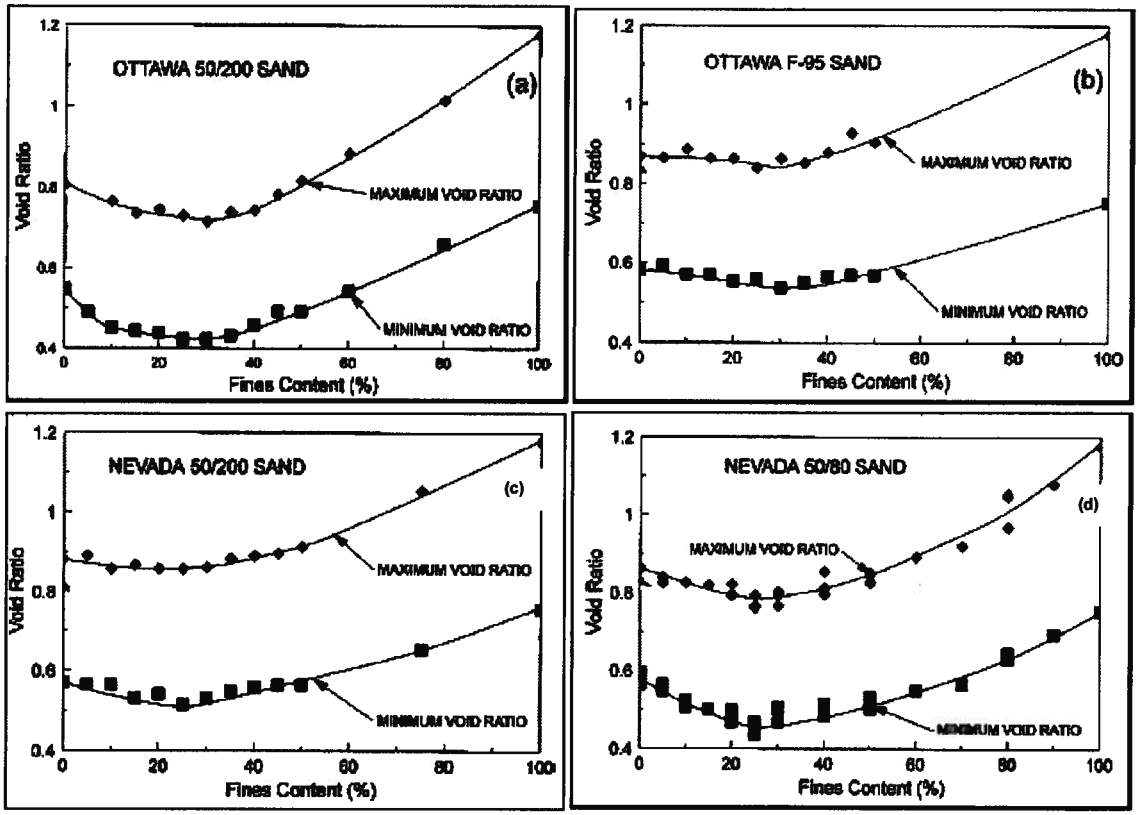

Fig. AI-21: Void ratio range vs. *F.C* for (a) Ottawa 50/200 sand, (b) Ottawa F-95 sand, (c) Nevada 50/200 sand, and (d) Nevada 50/80 sand (Lade & Yamamuro, 1997).

Verdugo & Ishihara (1996) introduced a parameter called contraction ratio, R_c to quantify the situation of steady state line regarding the loosest and densest states of a sand as illustrated on Fig. 2- 54a. It is defined at a reference effecteive mean stress of 100 kPa as Eq. AI-5.

$$R_c = \left(\frac{e_{\max} - e_{ss}}{e_{ss} - e_{\min}} \right)_1 \qquad \text{[AI-5]}$$

where R_c is contration ratio and e_{max}, e_{min}, and e_{ss} are minimum, maximum and steady state void ratio respectively at 100 kPa. Variation of R_c with fines content for Toyoura sand is shown in Fig. AI-22. It indicates that increase of (non-plastic) fines content shifts the steady state line towards the loosest state and causes more contractive behavior. Others data (e.g Naeini & Baziar, 2004 and Yang et al., 2006) support this conclusion. Therefore, it is reseanable to postulate the position of steady state line changes with fines content as illustrated in Fig. AI-20 It shows that at a given (global) void ratio, the mixture is likely to exhibit contractive or dilative behavior depending on fines content and its relative position to steady state line. This conceptual framework reveals the reason why that there is no consistent conclusion on fines content effects on sand liquefaction in literature. It should be noted that this conclusion applies to non-plastic fine materials as soil plasticity plays an important role in the mixture behavior.

Recently, cyclic response of silty or clayey sands have also drawn attention of a number of researchers e.g. Erten & Maher (1995); Kuerbis et al. (1988); Guo & Prakash (2000); Singh (1996); Liang et al. (2000); Anubhav & Rao (2001); Das et al. (1999); Hyodo (2002); Sanin & Wijewickreme (2006); Brandon et al. (2006); Bray & Sancio (2006), and Hyde et al. (2006) among others.

In coductiong cyclic triaxial tests on sands with different silt content Singh (1996) observed a lower rate of excess pore pressure build-up for silts at initial load cycles contrary to high rate of excess pore pressure build up in clean sands.

Polito (1999) and Polito & Martin (2001) reported the results of a systematic study on fines content on sand cyclic liquefaction resistance using non-plastic silt and two host sands, Yatesville sand and Monetery sand. Fig. AI-23 shows the *CRR* vs. No of cycles for liquefation for clean Yatesville sand along with that of the silt at relative density of 50% also variation of *CRR* with *F.C* at constant (total) relative density of 25% is depicted in Fig. AI-24. It indicates that generally sand exhibits greater resistance and that of mixture does not correlate to its relative density . Fig. AI-25 and Fig. AI-26 show void ratio range and *CRR* vs. *F.C* for Yatesville sand and Monterey sand at constant (gross) void ratio respectively (mixture relative density is recognized as gross, overal or total relative density by different investigators).

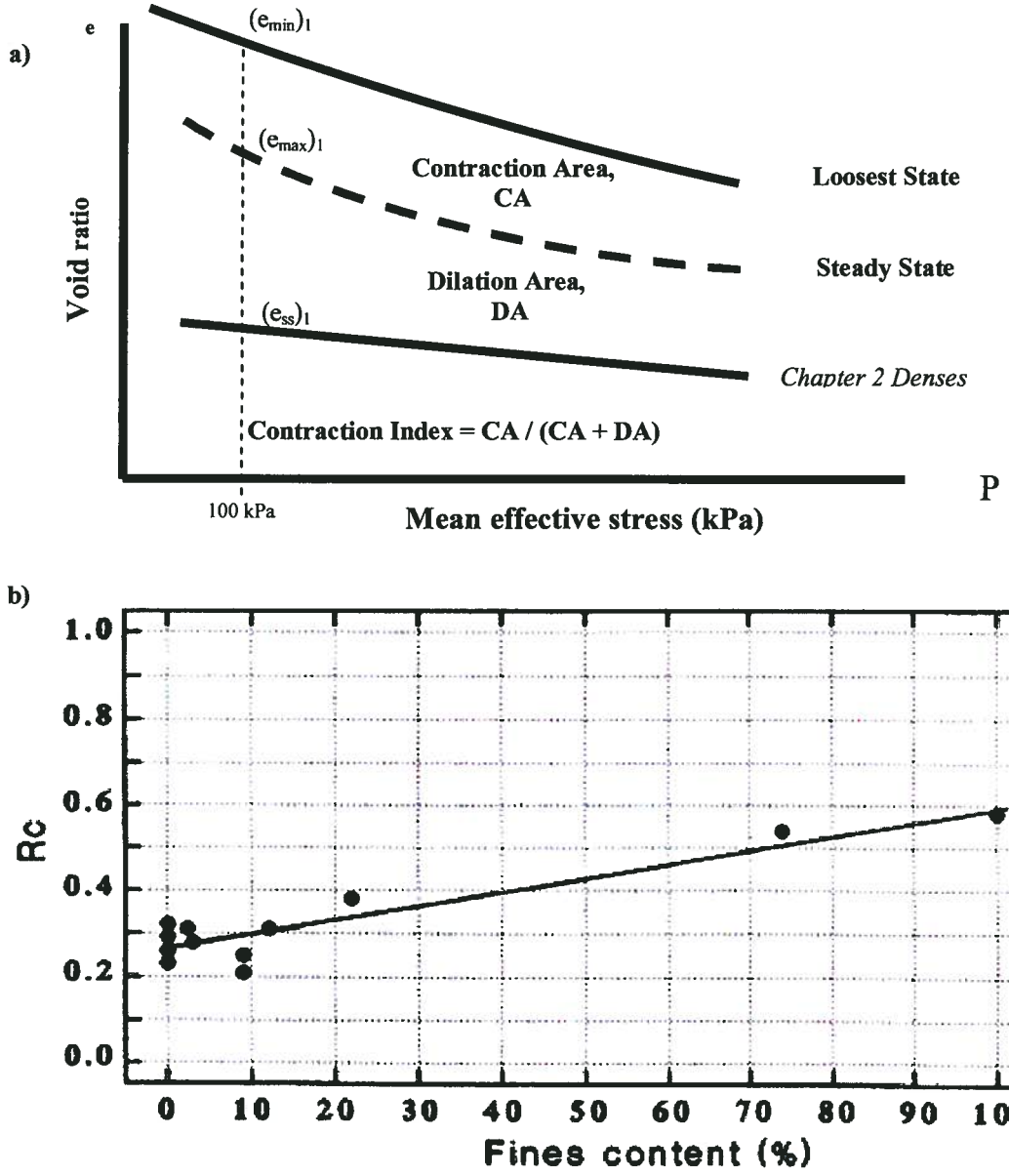

Fig. AI-22: (a) Definition of contraction ratio, R_c, (b) contraction ratio vs. F.C. for Touyora sand (Verdugo & Ishihara, 1996).

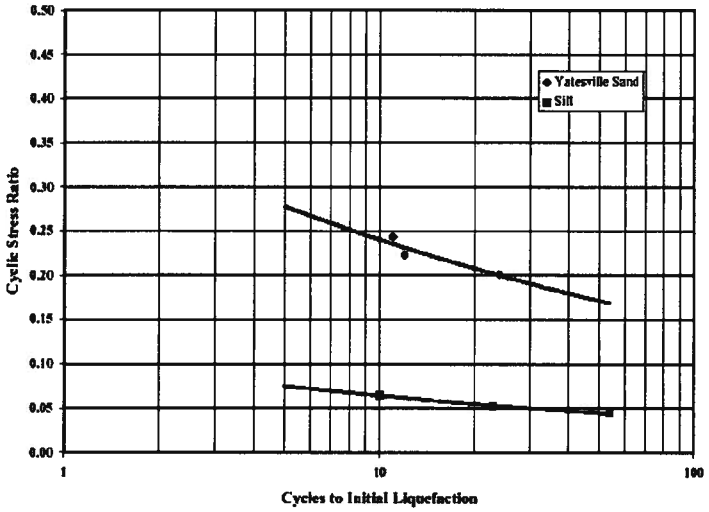

Fig. AI-23: *CSR* vs. No. of cycles for liquefaction for Yatesville sand and silt at *Dr* = 50% (Polito, 1999).

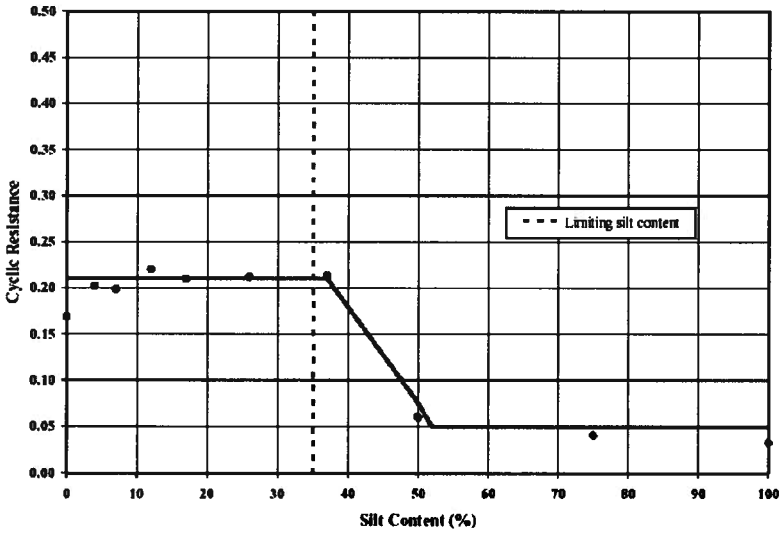

Fig. AI-24: *CSR* vs. F.C for Yatesville sand with *Dr* =25% (% (Polito, 1999).

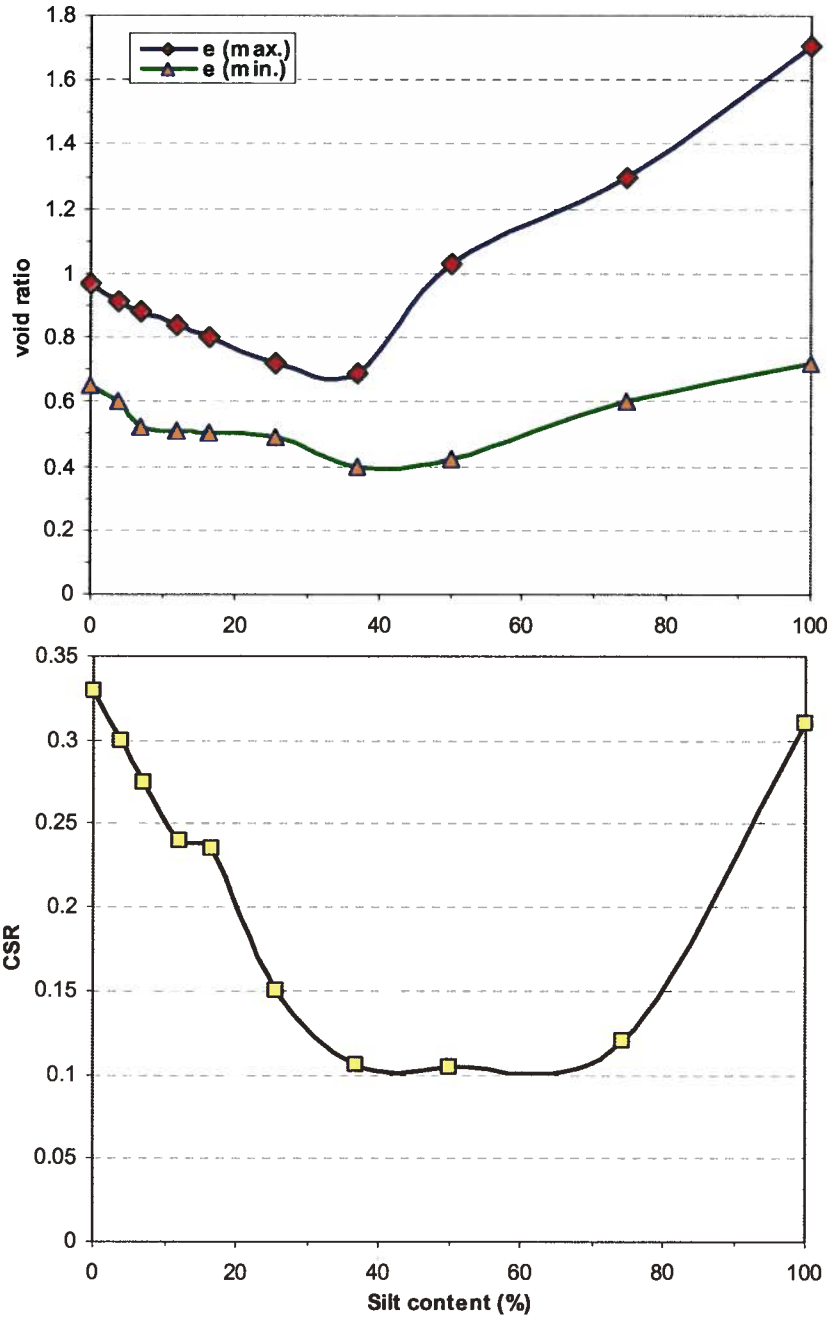

Fig. AI-25: *CSR* vs. *F.C* for Yatesville sand at gross *Dr* =76% (Polito, 1999).

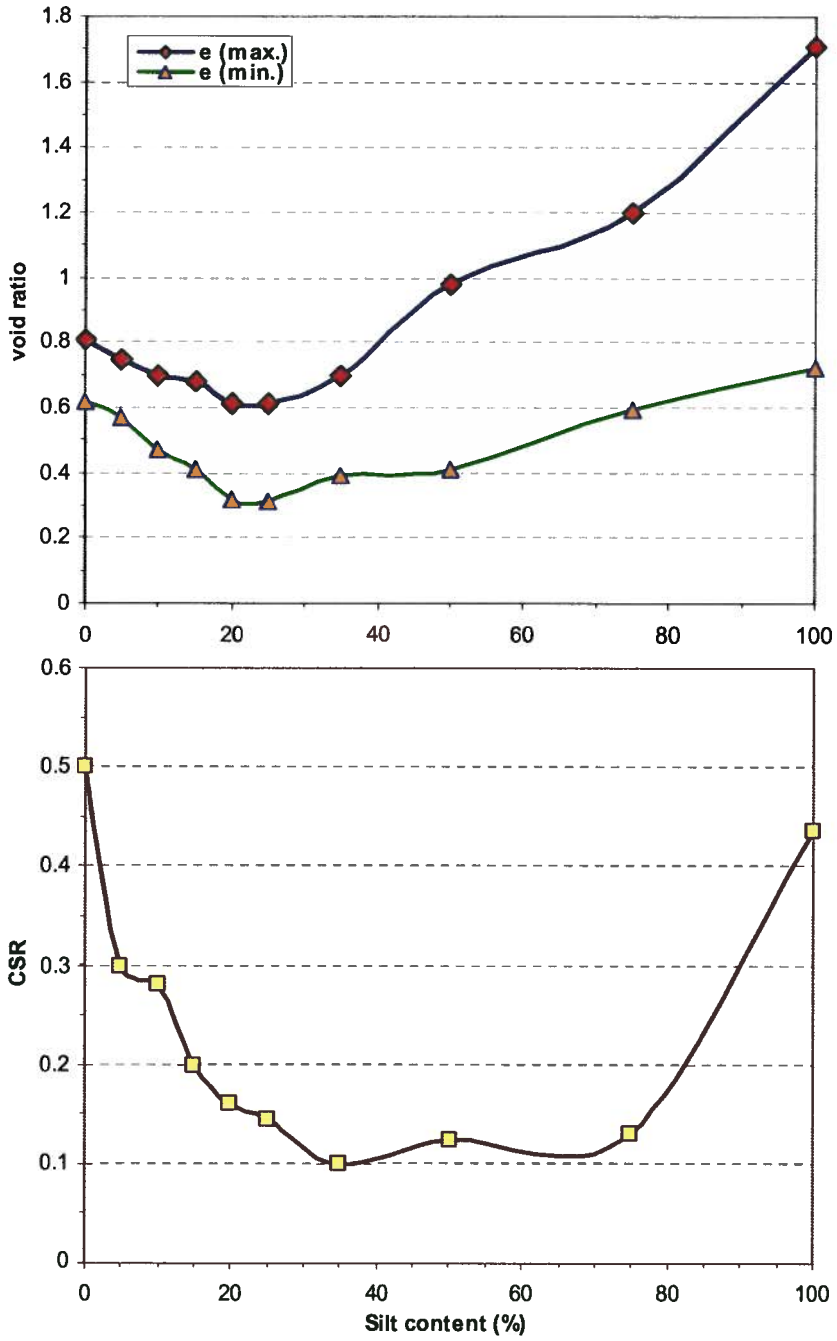

Fig. AI-26: *CSR* vs. *F.C* for Monterey sand at gross *Dr* = 68% (Polito, 1999).

It reveals that the pattern of *CRR* change with *F.C* is similar to that of void ratio range and this behavior can be explained using the framework outlined in Fig. AI-20. As may be seen initially *CRR* decreases with *F.C* till a certain limit (about 40% and 30% for Yatesville sand and Monterey sand respectively) then it tends up to that of pure silt. In other words, the pattern of *CRR* change is a reflection of mixure contractiveness which can be represented by the state parameter, ψ of the mixture as may be inferred from Fig. A1-20. They commented that the trend of increasing cyclic resistance with increasing silt content, which has been reported in the literature, does not appear to occur in non-plastic silts and is likely due to the plasticity of the fines used in those studies. They recommended an overall revision of penetration tests-based procedures used in practice for liquefaction assessment of sands with fines materials. In engineering practice, the liquefaction assessment of fine grained soils are approached using different criteria based on soil composion, geology etc. A number of investigators have suggested different criteria that are mainly based on case histories. Table AI-1 summerizes the different proposed criteria for liquefaction assessment of fine materials (Clare et.al., 2002).

Table AI-1: Criteria for soils prone to liquefaction (modified from Clare et.al, 2002).

Reference	Max. Clay Content	PI (%)	Remarks
El Horsi et. al., 1984	0.002 mm < 20%	< 10%	---
Tokimatsu & Yoshimi, 1984	0.005 mm < 20%	< 10%	---
Cao & Law, 1991	0.002 mm < 20%	---	---
Architectural Ins. of Japan, 1998	Clay fraction < 10%	<15%	Liquefies if either criterion is met
Wang, 1981	0.005 mm < 15%	<15%	LI > 0.75, LL <35%, Wc >0.9LL
Finn et. al., 1994	0.005 mm < 10%	<15%	LL <36%, Wc >0.9LL +2%

These suggestions are mainly founded on the so-called Chinese Criteria which is originally published by Wang (1979). It encompasses four index soil properties i.e. liquid limit (*LL*), liquidity index (*LI*), water content and clay content. The liquid limit of a soil is an indirect measure of the water content or void ratio (density) that corresponds to a specified undrained shear strengths of 2 to 2.5 kPa, while the liquidity index is an indirect measure of the sensitivity of the soil. The first three criteria, therefore, identify weak sensitive fine-grained soils. The fourth criterion, which is a measure of the clay content of the soil, eliminates the medium to high plastic soils that do not have the ability to undergo volume change during repeated application of cyclic loads. Since exclusively based on index properties and grain size data, the Chinese criteria are

independent of the intensity and duration of the applied loads. There are a number of examples indicate that using empirical criteria could sometimes lead to incorrect or non-conclusive determinations (e.g. Atukorala et.al., 2000 and Sanin & Wijewickreme, 2004& 2006).

Recently, a few researchers e.g. Polito & Martin (2001), Andrew & Martin (2000), Seed et al. (2003) and Bray et al. (2004) based on laboratorty investigations and recent case histories (e.g. 1999 Kocaeli, Turkey and 1998 Chi-Chi, Taiwan earthquakees) have proposed some modifications to the Chinese criteria and (see Fig. AI-27). Andrews & Martin (2000) suggested revised criteria based on *LL* and minus 2 μm fraction, while Seed et al. (2003) and Bray et al. (2004a,b) suggested criteria based on Plasticity Index (*PI*), *LL*, and w_c. The criteria by Bray et al. (2004b), for example, are that fine-grained soils with *PI* of 12 and w_c>0.85*LL* are susceptible to liquefaction, while soils with 12<*PI*<18 and w_c>*0.8LL* are "systematically more resistant to liquefaction but still susceptible to cyclic mobility". They enhanced their conclusion with further studies (Bray & Sancio, 2006). The criteria by Seed et al. (2003) are similar to Bray et al.'s, but with slightly different w_c/*LL* limits and additional constraints on the *LL*.

It should be noted that definition of clay fraction and consistency testing method can also influence on interpretation of the results (2 μm vs. 5 μm and Fall Cone vs. Cassagrande device respectively). Table AI-2 lists a comparison of these methods presented by Sanin & Wijewickreme (2004) regarding the factors controlling the respose of soils to cyclic loading. They also examined the applicability of such methods based on cyclic simple shear test data of undisturbed silty sand samples and noted that the empirical criteria that use plasticity parameters and water content (e.g. Bray et al. 2004) has a better ability to capture liquefaction susceptibility.

In practice, usually the susceptibility of soils are evaulated based on SPT-based methods proposed for clean sands (e.g. by Youd et al., 2001 and Bray & Sancio, 2006) and then some correction factors are applied for fines content (< 0.074mm). The 1997 MCEER workshop recommended a fines content correction to $(N_1)_{60}$ value given by Eq. AI-4 for using Fig. AI-1.

$$(N_1)_{60\text{-}cs} = \alpha + \beta . (N_1)_{60} \qquad \text{[AI-6]}$$

where $(N_1)_{60\text{-}cs}$ is equivalent N value for clean sand and α and β are factors presented in Table AI-3. Similar increase in N value was suggested by Seed & Harder (1990) to account for *F.C* in estimating residual strength as Table AI-4. Ministry of Transportation, Japan (1997)

recommends a combination of gradation criteria and SPT for assessment. It suggests a reduction factor for the critical N value (varying from 1 to 0.5 for 5% to 15% fines content). Apparently there is no comment concerning plasticity of fine materials.Ishihara (1993) recommended a modification in CRR with coefficient F to account for fines effects as:

$PI < 10\%$ $\quad F = 1.0$ [AI-7]

$PI > 10\%$ $\quad F = 1.0 + 0.022(PI - 10)$ [AI-8]

Boulanger & Idriss (2005 & 2006) suggested that fine-grained soils can be grouped into soils that behave more fundamentally like sands in monotonic and cyclic undrained loading, and soils that behave more fundamentally like clays. In this regard, a key aspect is that monotonic and cyclic shear strengths of clay exhibit a relatively unique dependence on consolidation stress and consolidation stress history (e.g. Ladd, 1991), and the soil's cyclic shear resistance is closely related to its monotonic undrained shear strength (see Fig. AI-28), while the strengths of sands do not. They suggested using Fig. AI-29 to predict the response type of a fine-grained soil to cyclic loading. Fine-grained soils that exhibit clay-like behavior include ML soils with PI values as low as 9 and CL-ML soils with PI values as low as 4. Intermediate behavior is predicted for samples classifying as CL-ML and ML with PI values of 4 to 5. Sand-like behavior is expected only for ML soils (below the A-line). Boulanger & Idriss (2004 & 2006) recommend that a plasticity index, *PI*, value of 7 be used as the demarcation between coarse and fine-grained liquefaction response for engineering purposes. They also reserved the term "liquefaction" for sand-like soils and conversely "cyclic failure" for clay-like soils. They suggested that liquefaction assessment of sand-like soils could be carried out based on method developed for clean sands e.g. (Youd et al., 2001). They developed a similar procedure and relationship as clean sands (Eq AI-1) for cyclic failure of clay-like soils (>50% for sieve #200) with corresponding factors for clay-like soils. Their proposed charts for magnitude scaling factor MSF, initial static shear factor K_α are depicted in Fig. AI-30 and Fig. AI-31.

Table AI-2: Factors controlling the response of soils to cyclic loading and their consideration by different empirical criteria for liquefaction assessment (Sanin & Wijewickreme, 2004).

Factors	Chinese criteria[1]	Andrew & Martin (2000)	Polito (2001)	Bray et al. (2004)
Mineralogy/plasticity	Yes	Yes	Yes	Yes
Grain size	Yes	Yes	No	No
Packing density	Yes[2]	No	No	Yes[2]
Microstructure	No	No	No	No
Fabric	No	No	No	No
Age	No	No	No	No
Stress level	No	No	No	No
Level of cyclic loading	No	No	No	No
Initial static shear	No	No	No	No

[1] Wang (1976), Seed et al. (1983), Finn et al (1994), Koester (1992)
[2] In terms of water content.

Table AI-3: Fines content correction factors for $(N_1)_{60\text{-}cs}$ (Youd et.al., 2001).

F.C (%)	α	β
F.C ≤ 5%	0	1
5% < F.C < 35%	$e^{(1.76-190/F.C^{\wedge}2)}$	$0.99+ F.C^{1.5}/ 1000$
35% ≤ F.C	5	1.2

Table AI-4: F.C. correction for N value for S_r estimate (Seed & Harder, 1990).

F.C (%)	ΔN
10	1
25	2
50	4
75	5

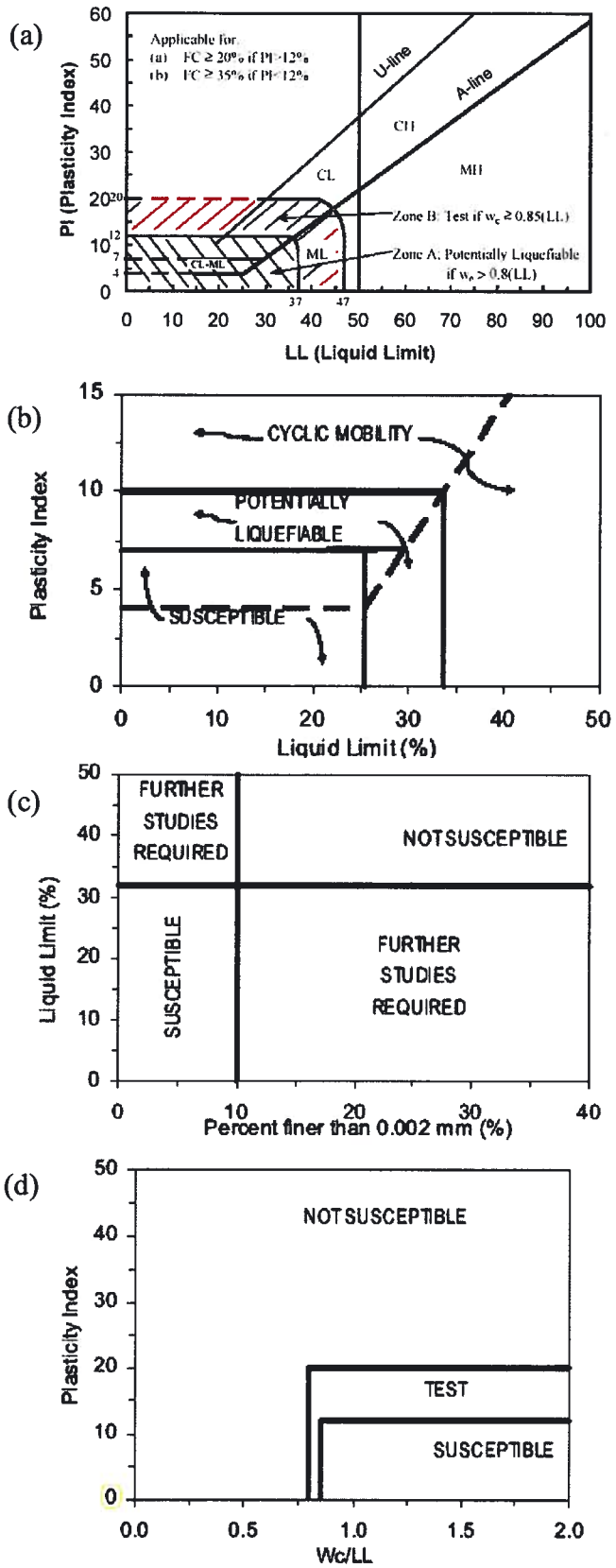

Fig. AI-27: Proposed chart for liquefaction assessment of fine grained soils by (a) Seed et al (2003), (b) Polito (2001), (c) Andrew & Martin (2000), and (d) Bray et al. (2004).

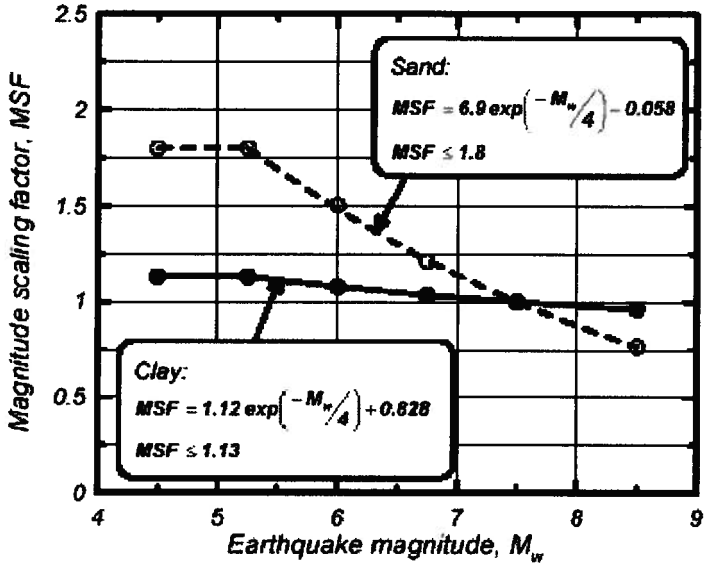

Fig.AI-28: Magnitude scaling factor for clay-like soils comparing to that of sands (Boulanger & Idriss, 2004).

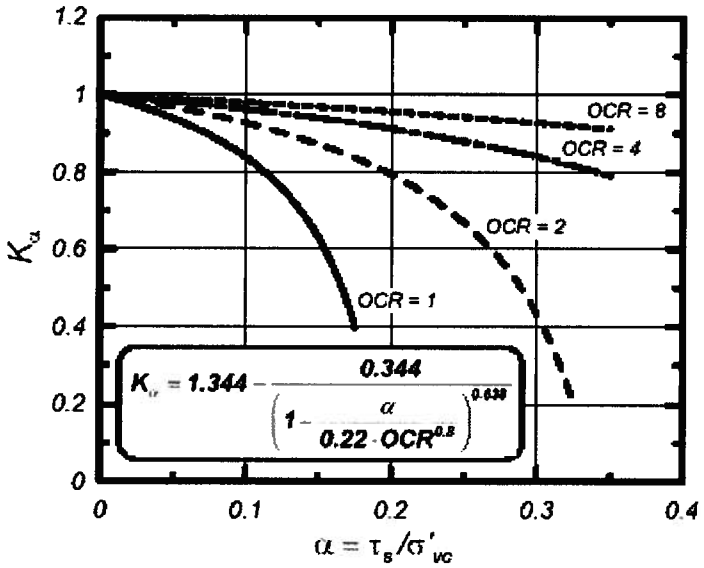

Fig.AI-29: Correction factor for initial shear stress on *CRR* for clay-like soils (Boulanger & Idriss, 2004).

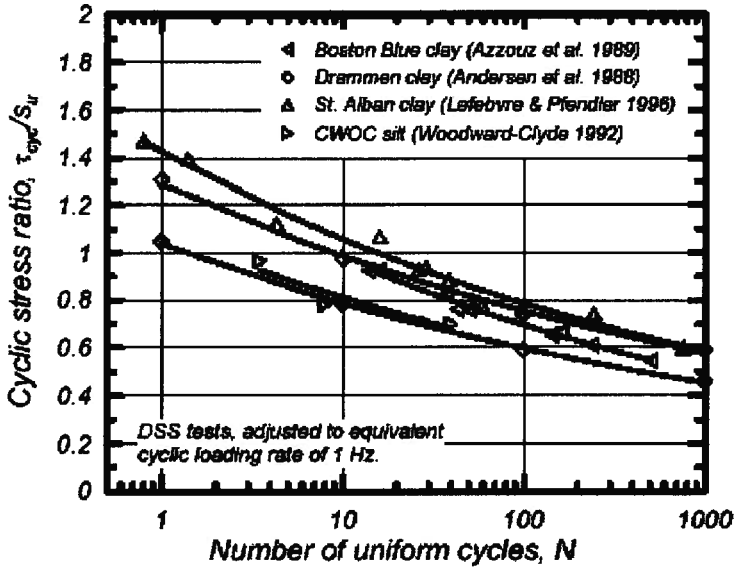

Fig. AI-30: Cyclic resistance ratios, CRR vs. No. of uniform loading cycles to failure (3% shear strain) for four clay soils in direct simple shear tests (Boulanger & Idriss, 2005).

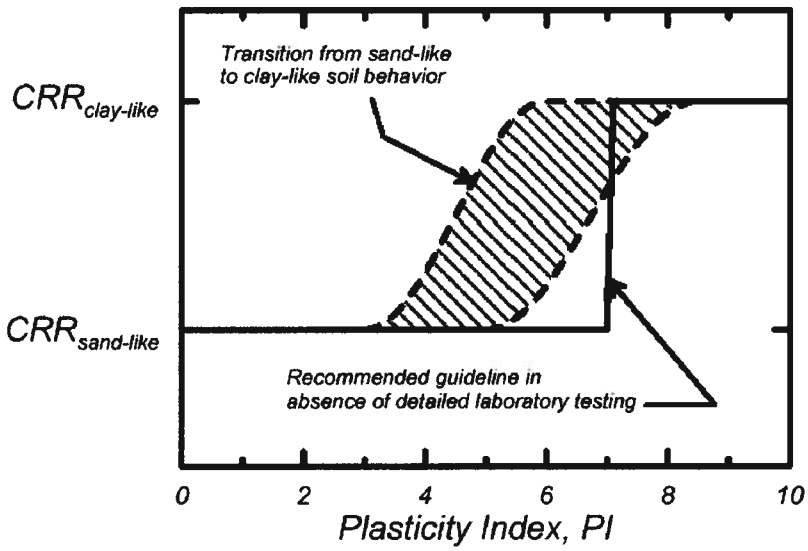

Fig. AI-31: Proposed chart by Boulanger & Idriss (2004 & 2006) to predict cyclic behavior of fine-grained soils.

Therefore, the available data on fines content effects on sand behavior suggest that:

1) Apparently, the statement of Seed et.al. (1985) "if a sand-fine mixture has the same N value as clean sand the addition of fines increases its liquefaction resistance" has led to erroneous belief that addition of fines to sands increases their liquefaction resistance.
2) Two factors are playing concurrently:
   a) Amount of fine materials,
   b) Consistency of fine materials.
3) Those methods e.g. NCEER (Youd et.al., 2001) and Japanese practice (PIANC, 2001) use just a modification factor and do not account for plasticity of fine materials.
4) There is a critical value for fines content (e.g. 25 - 40%) above which pattern of sand-silt mixture behavior is controled by fines fraction.
5) There are some indications suggesting that introducing non plastic fines in sands results in more contractive behavior.
6) At a certain (total) void ratio the mixture can exhibit more contractive or dilative behavior depending on $F.C$ and its position regarding the corresponding void ratio range and state parameter, ψ.
7) It is prudent to classify cyclic behavior of fine grained soils (>50% for sieve #200) into two types i.e. sand-like and clay-like.
8) Materials with low plasticity (e.g. CL-ML with PI = 4) can exhibit clay-like response to cyclic loading.
9) Non-plastic silt materials may exhibit lower cyclic strength comparing sand with greater volumetric strain.
10) As residual strength of silt is lower than that of sand, in general sense, catastrophic flow failure in non-plastic silt would be more likely.
11) Using emprical criteria i.e. the Chinese-based methods that only account for materials plasticity regardless of earthquake magnitude results in erroneous conclusions and should not be used in practice.
12) Regarding the existing confusion on the matter, the stress-strain behavior of soils containing fine material entails more comprehensive and detailed research works. To exclude other involved factors (e.g. grain miralogy) it is useful to produce fine materials from the same parent sand to study gradation effects.

AI.10. Current Practice for Estimating Residual Strength

The undrained shear strength S_u available following the liquefaction triggering is often considered as residual strength, S_r (Seed & Harder, 1990 and Stark et al., 1998). Some researchers suggest the minimum undrained shear strength at steady state (or quasi-state) obtained from laboratory element tests as residual strength (Vaid & Sivathayalan, 2000).

Liquefaction of soil foundation can result in global instability in level ground and sloping ground conditions if post-liquefaction strength is lower than initial static shear stress. Therefore, determination of post-liquefaction soil strength is a key issue for deformation assessment of earth structures and remedial measures undertaken accordingly. Byrne & Beaty (1997) examined the following three approaches to determine the post-liquefaction soil strength:

1. Laboratory-based approach; from laboratory testing of undisturbed samples,
2. Field-based approach; from back analysis of case histories, and
3. Analytical approach; based on a postulated theory of soil behavior.

Using Critical State Soil Mechanics framework one may derive steady state strength S_{ss} as Eq. *AI*-9:

$$S_{ss} = \sigma'_f \,.\, tan(\varphi_{cv}) \qquad [AI\text{-}9]$$

Where φ_{cv} is the friction angle at constant volume, often ranges between 29 to 33° for sands. Based on Critical State Soil Mechanics σ'_f, effective normal stress at failure depends merely on void ratio. The large shear strains as required for strength mobilization in the laboratory tests (e.g. more than 30%) may not be achieved in the field.. This approach results in relatively larger values for strength as noted by a few investigators (e.g. Harder, 1988 and Seed, 1999). Fig. AI-34 is another example of large difference of laboratory and field-based data for residual strengths as mentioned earlier (see Fig. 1-3). It compares labortory residual strengths with that of poroposed based on case studies (shaded area) revealing that lab-based data are much greater than case histories-based values. It should be noted that unsteady undrained conditions and change of void ratio (void redistribution) are main issues that strongly make this appraoch unjustifialbe.

The second approach as a case history-based approch is the most commonly accepted procedure in engineering practice at the current state of knoweledge (Byrne et al., 2006). Fig. AI-35 shows a correlation for residual strength, S_r with N-value suggested originally by Seed & Harder (1990) based on 17 shallow liquefied sites and then modified by Idriss (1998) according

to data base extension. He suggested a trend line based on the median value of $(N_1)_{60\text{-}cs}$, the value of $(N_1)_{60}$ converted to clean sand. To do this, a correction value, ΔN regarding fines content for N-value that is different from what used for triggering assessment was applied.

As shown before laboratory tests data suggest that minimum undrained shear strength S_{ss} normalizes with respect to effective vertical stress (see Fig. 2-30) following this rationale, a few investigators (e.g. Stark & Mesri, 1992 among others) have attempted to correlate residual strengths back calculated from case histories to prefailure effective vertical stress (σ'_v). Olson & Stark (2002) suggested Fig. AI-36 to estimate normalized residual strength of liquefied sand. They did not consider any adjustment for fines content. They argued that the data reveal no trend in liquefied strength ratio with respect to fines content and also effect of greater compressibility of soils with fines content is likely compensated by lower permeability effect and as a result, longer undrained condition.

A number of uncertainity regarding key factors such as prefailure earth structure conditions; geometry, layering, water table, failure surface, and soil properties e.g. gradation, void ratio, drainage, mixing and stress conditions are involved in this approach. Therefore a few investigators (e.g. Wang, 2003) have attempted to refine the approach by employing probability methods (e.g. Monte Carlo method) to get a more reliable correlation. Wang (2003) porposed the chart shown in Fig. AI-37 for residual strength estimation in terms of absolute and normalized value based on clean-sand N value, $(N_1)_{60\text{-}cs}$. This method also provides a level of probability associated with the available strenght after liquefaction as depicted in Fig. AI-38. As may be seen from Fig. AI-38 the back calculated residual strengths show a better correlation when they are not normalized. In fact, Fig. AI-38b reveals that strength ratio is essentially constant in contrast to laboratory results. On the other hand, Olson & Stark (2003) presented a comparison of their proposed chart to laboratory data to advocate about normalization. However, their data showed much lower scatterness (variability) for the field data than that of the laboratory data whereas the uncertainities involved in field data are definitely greater. They also mentioned that the large majority of the **flow failure case histories involve sands with some silt.**

More recently, a few researchers with recognition of void redistribution effects have suggested different correlation for such conditions. Kokusho & Kabasawa (2003) based on shake

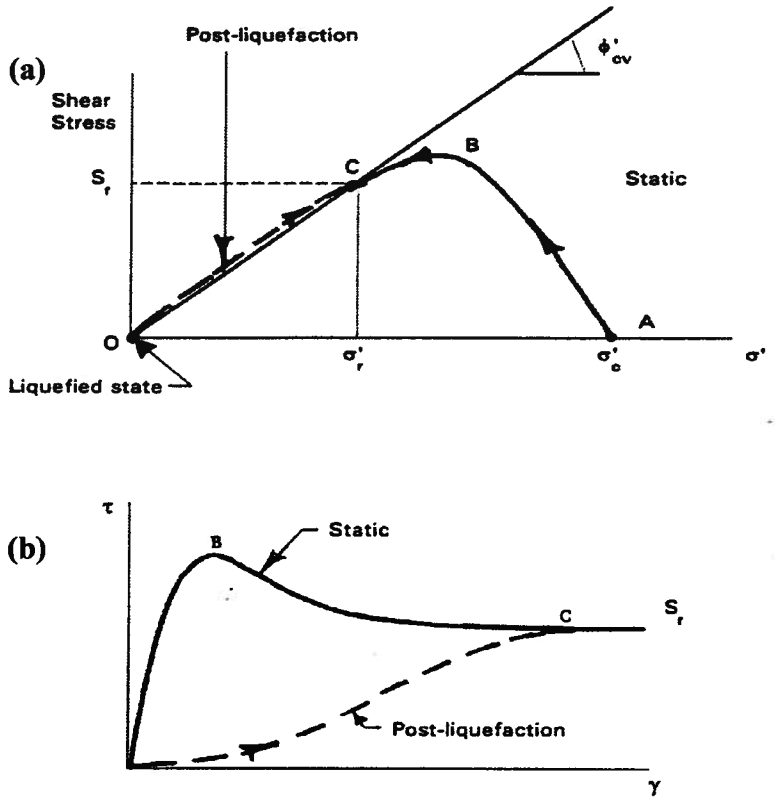

Fig. AI-32: Post-liquefaction sand behavior following satic and cyclic liquefaction, (a) stress path, (b) stress-strain and residual strength (Byrne & Beaty, 1997).

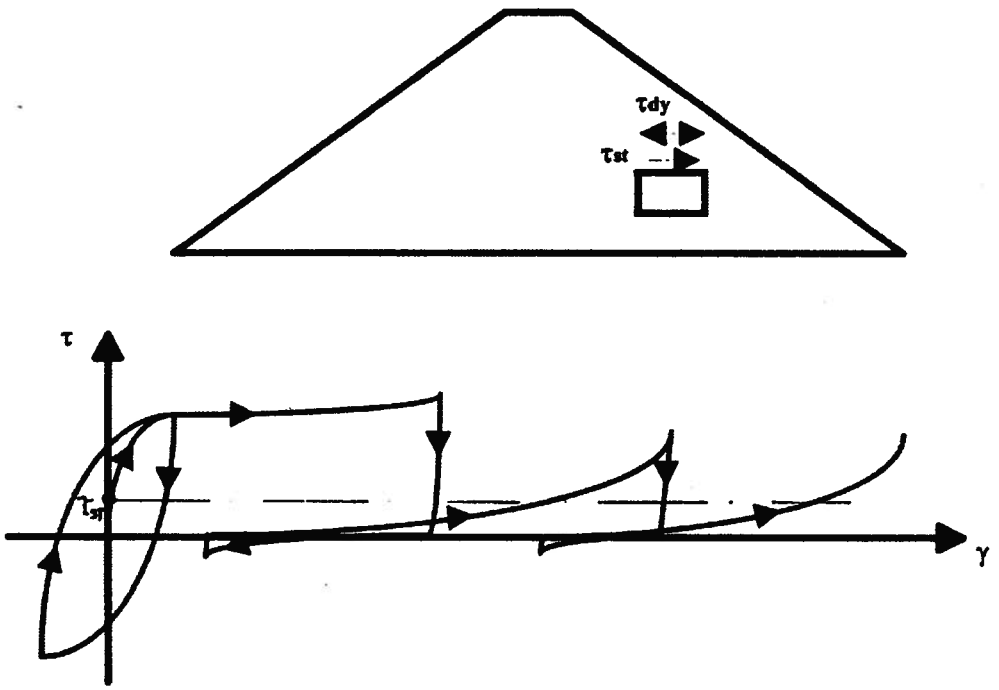

Fig. AI-33: Progressive deformation during undrained cyclic loading with a static shear bias (Byrne & Beaty, 1997).

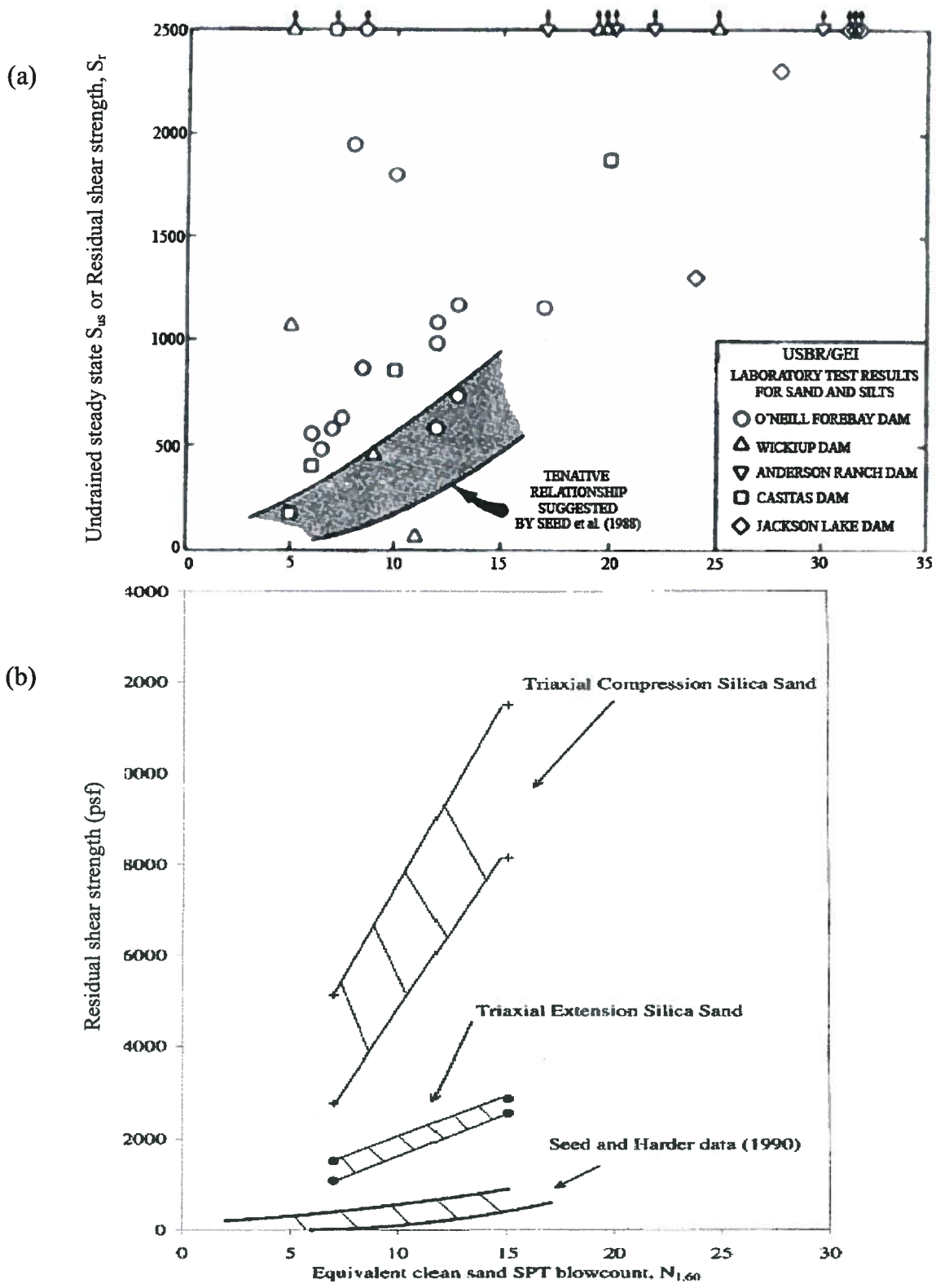

Fig. AI-34: Comparing laboratory residual strength with that inferred from failed case histories (a) undisturbed samples results (adapted from Seed, 1999 based on data from Harder, 1988 and Von Thun, 1986), (b) constituted sample results (Yazdi , 2004).

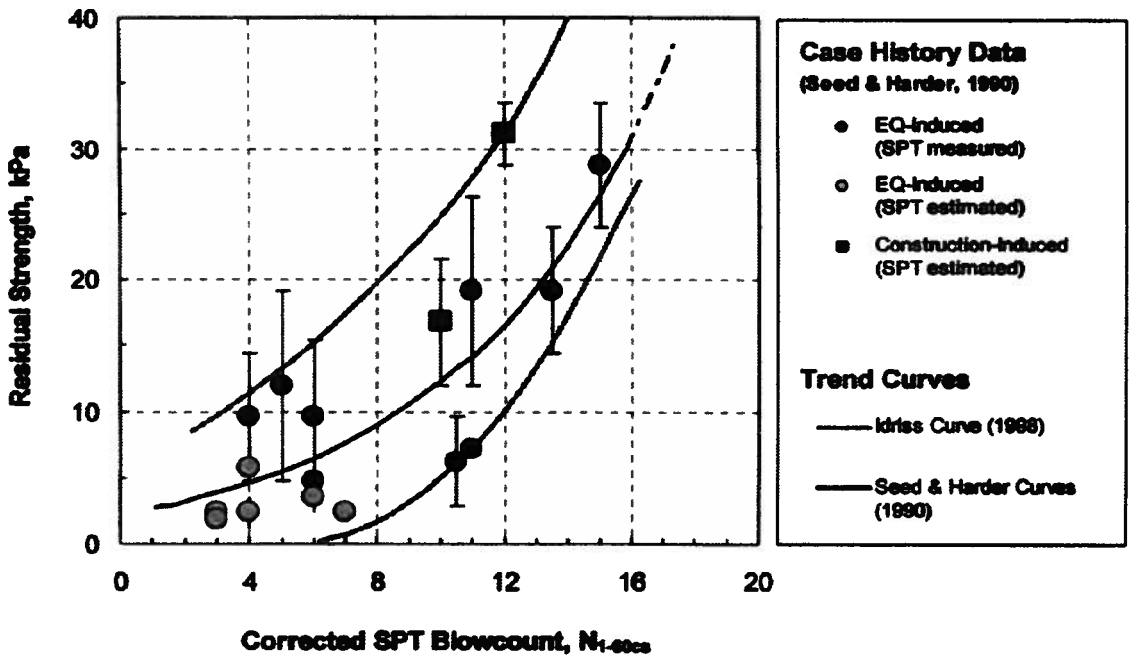

Fig. AI-35: Seed & Harder chart for residual strength, S_r, updated by Idriss (1998) (adapted from Beaty, 2001).

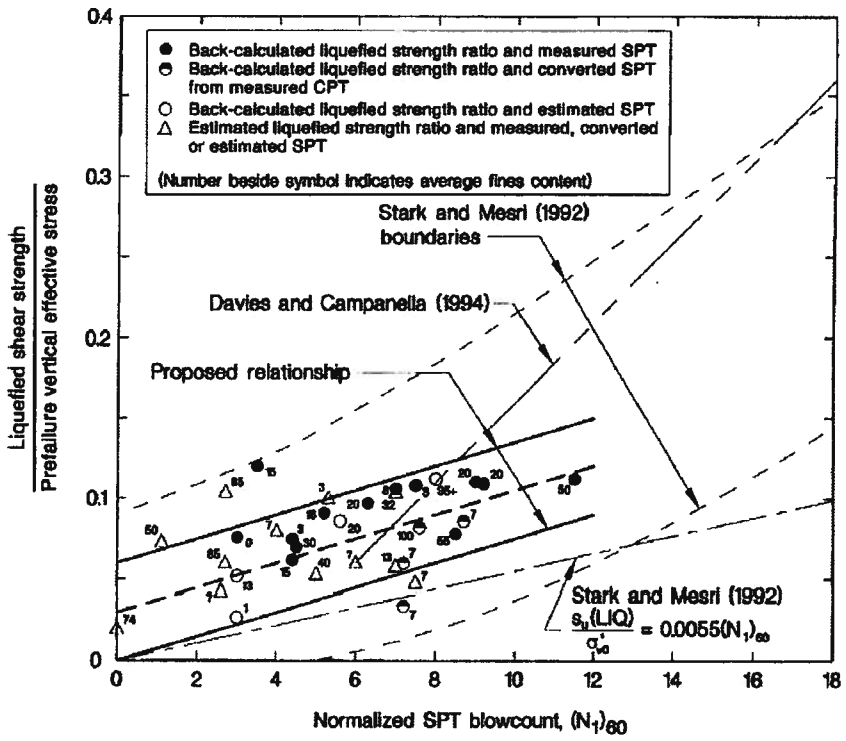

Fig. AI-36: Normalized residual strength for liquefied sand vs. $(N_1)_{60}$ (Olson & Stark, 2002).

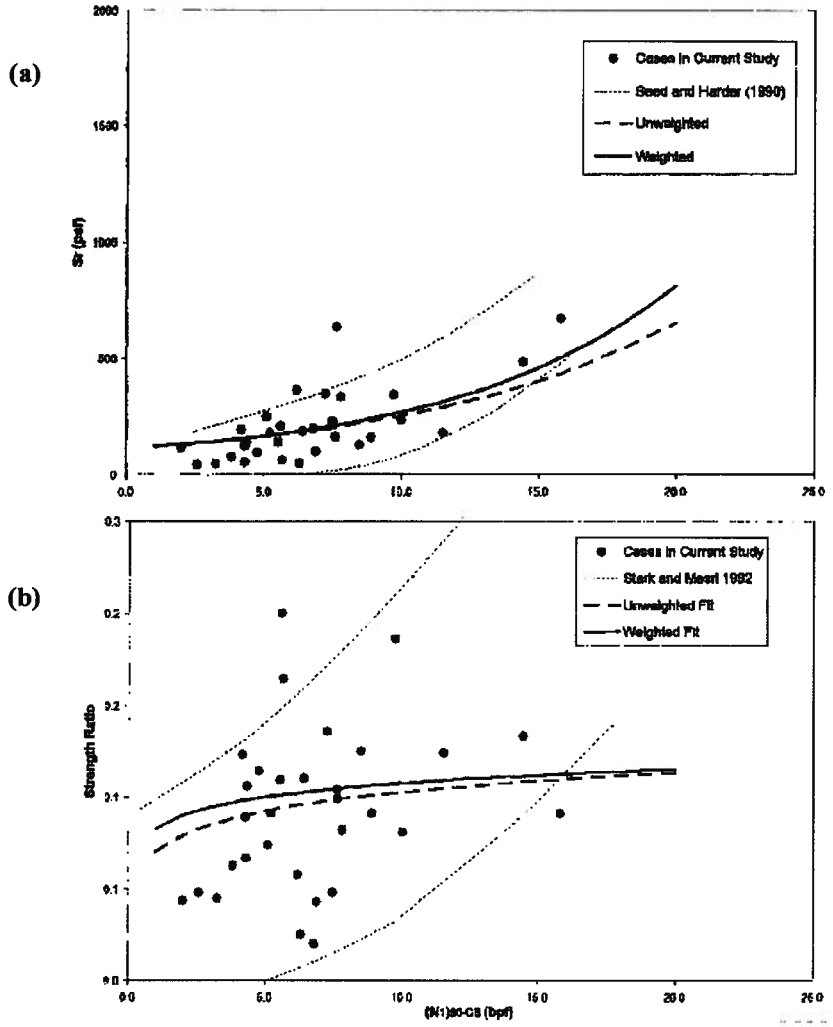

Fig. AI-37: Residual strength vs. $(N_1)_{60\text{-}cs}$ using probabilistic approach (a) without normalization, (b) with normalization (Wang, 2003).

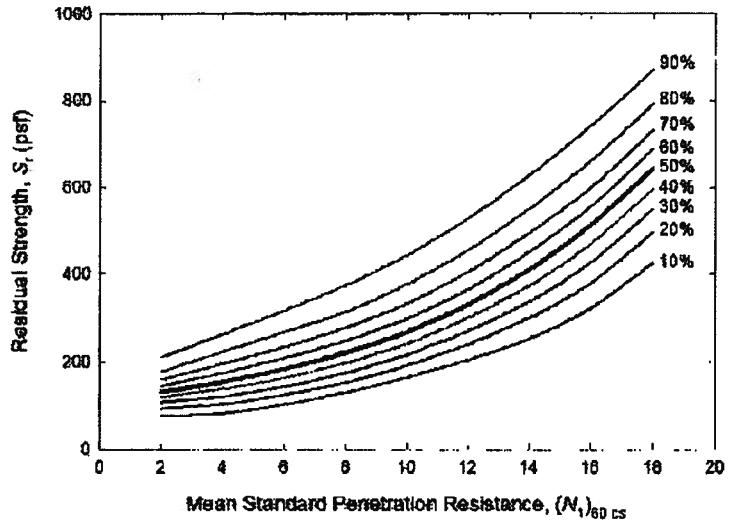

Fig. AI-38: Residual strength vs. $N_{1(60)cs}$ with various level of probability. (Wang, 2003).

table model tests of slopes with barrier layer proposed an equivalent friction angle along failure surface as depicted on Fig. AI-39.

Therefore, it is reasonable to postulate that field-based strengths represent a reflection of all factors involved in previous failures that might also be the case in future other probable failures and they can be recommended for engineering design as noted by Byrne et al. (2006) at the current state of knowledge. Boulanger & Idriss (2007) suggested Fig. AI-40 for estimating residual strength for conditions where void redistribution mechanism is involved and for those situations without void redistribution effects. The issue of post liquefaction strength of deposits comprising barrier layers needs more reseach works.

A1.11 Post-Liquefaction Stiffness

Liquefied soil deformation is controlled by its shear stifness. The sand after liquefaction onset behaves as a strain hardening material and tends to dilate as it deforms. Sand can support additional stress with strain due to the resulting drop in pore pressure and increase in normal effective stress. S_{ss} is reached when the sand does not have a tendency to dilate, although redistribution of pore pressure or cavitation of the pore fluid may occur before this steady state strength is reached. The mechanism of strain hardening results in a shear modulus that can be much softer than the preliquefaction condition. Thus drop in stiffness is much significant than undrained strength loss. An approximation of the post-liquefaction stiffness G_{liq} of a liquefied sand was proposed by Byrne & Beaty (1999) as Eq. *AI*-10.

$$G_{liq} = B^e \,.\, \sin(\varphi_{cv}) \,.\, \sin(\psi) \qquad [AI\text{-}10]$$

where

B^e : elastic bulk modulus, (a stress-dependent parameter)

φ_{cv}: constant volume friction angle

ψ : dilation angle

Eq. *AI*-10 implies that the post-liquefaction stress-strain response should be concave upward as B^e increases with the rising effective stress. This behavior is seen in test data reported by Vaid &

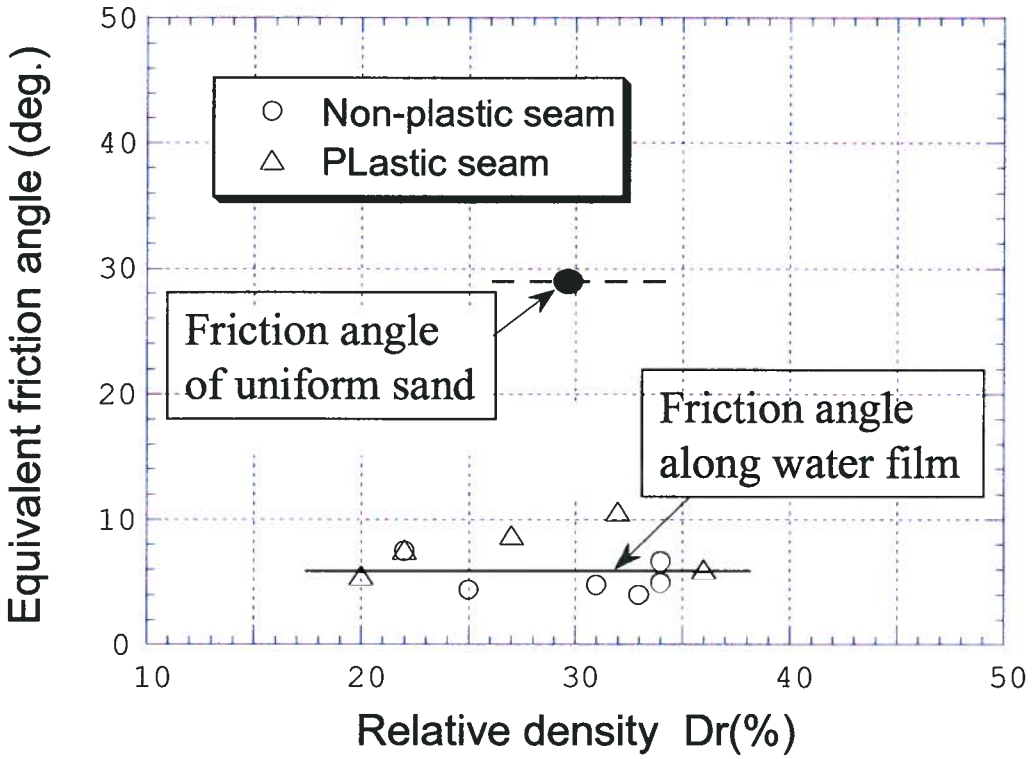

Fig. AI-39: Equivalent friction angle for failure surface of a slope with barrier layer suggested by Kokusho & Kabasawa (2003).

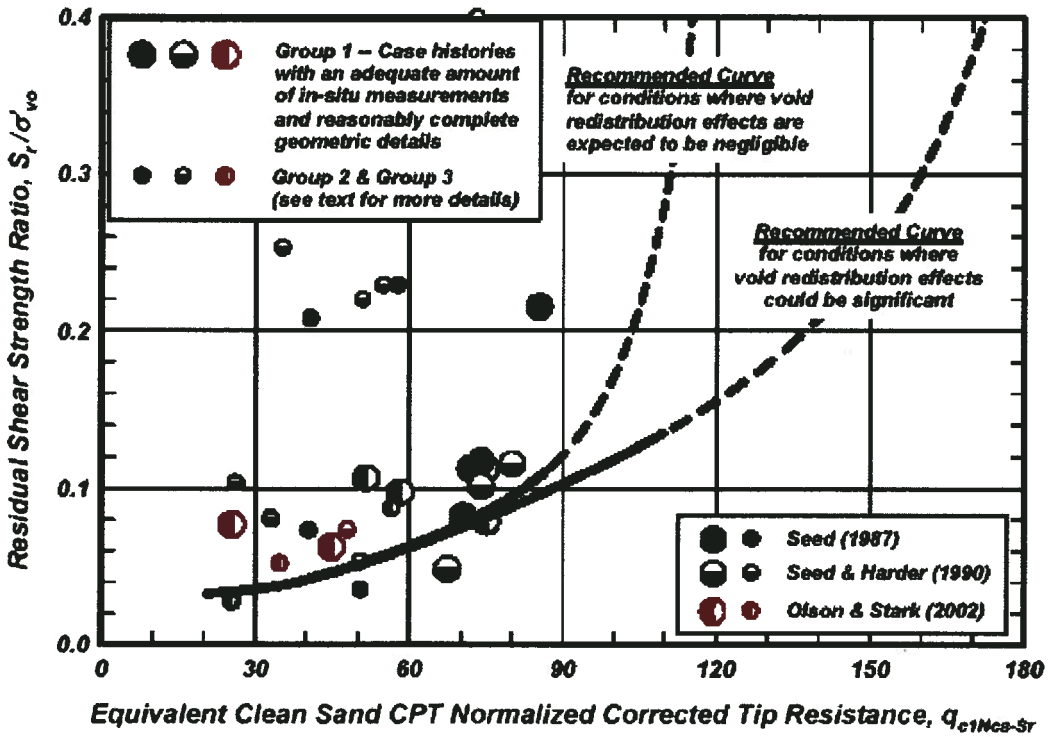

Fig. AI-40: Normalized residual strength with and without void redistribution involvement (Boulanger & Idriss, 2006).

Sivathayalan (1997) shown on Fig. AI-41 This also indicates the postliquefaction modulus depends on relative density (void ratio) and mode of shearing (anisotropy effect).

It seems that if significant zones beneath the barrier layer expand to a limit that flow failure occurs normalization of residual strength, which is essentially inferred from laboratory-undrained element test data cannot be applied to field back-analyzed values. Furthermore, the mechanism responsible for flow failure case histories cannot be explained based on behavior of a uniform liquefiable soil in undrained condition with pre-earthquake state.

Vaid & Thomas (1995) presented test results that suggest the type of loading that causes liquefaction (R_u = 100%), either cyclic loading or monotonic loading followed by unloading, does not affect the sand post-liquefaction stiffness. Vaid & Sivathayalan (1997) demonstrated that the tangent shear modulus in the dilative portion of a monotonic test is essentially the same as the shear modulus obtained from loading a sample from an R_u = 100% state following cyclic loading (see Fig. AI-41 and Fig. AI-42). Although the loading modulus of liquefied soils is low, the unloading modulus is relatively high.

As mentioned earlier sand under static shear stress bias does not experience R_u = 100% when liquefies, it suggests that its post liquefaction stiffness as a stress-level dependent parameter is greater than that of without shear stress bias depending on the stress bias.

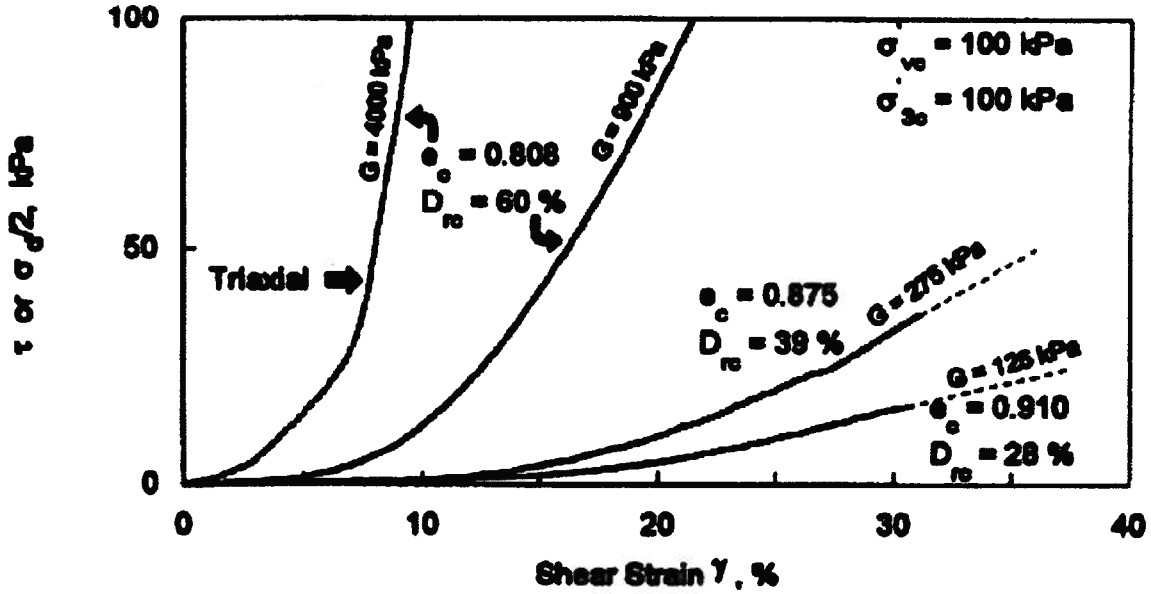

Fig. AI-41: Dependence of postliquefaction shear modulus on strain and relative density in simple shear test (Vaid & Sivathayalan, 1997).

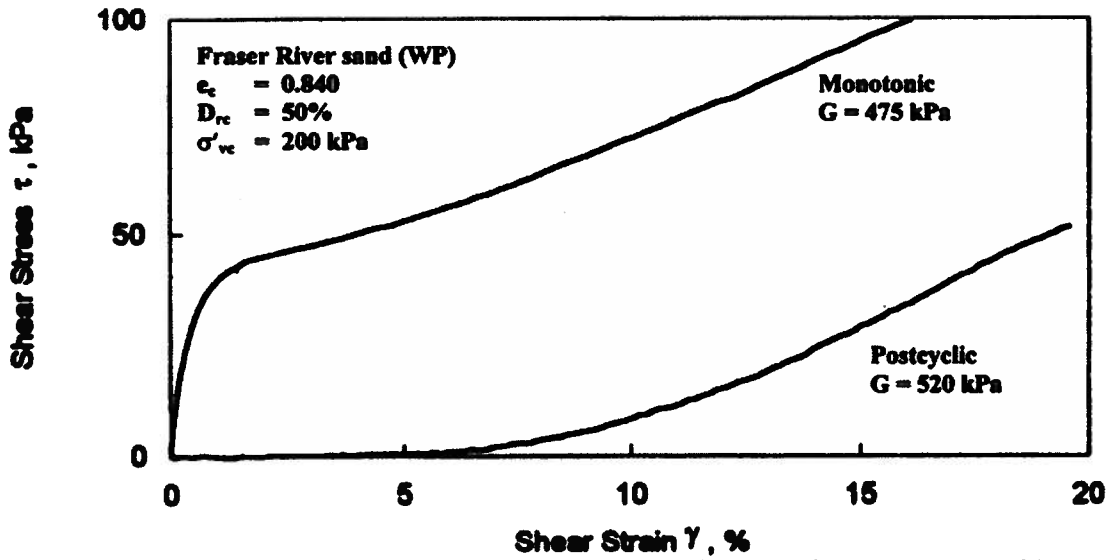

Fig. AI-42: Monotonic vs. postcyclic behavior of sand in simple shear test (Vaid & Sivathaylan, 1997).

APPENDIX II

PREVIOUS PHYSICAL MODEL STUDIES ON VOID-REDISTRIBUTION

AII.1 Introduction

This Appendix provides complete description of previous studies mentioned in *Chapter 3* carried out to study void redistribution mechanism involved in liquefaction induced-slides.

Table AII-1 summarizes the results of the past model tests that will be expressed in more detail in the following.

Table AII-1: Previous studies on void redistribution using physical testing procedure (Kulasingam, 2003).

No.	Investigator	Test Type and Container	Soil Geometry	Model Preparation	Soil Properties	Initial State	Shaking	Observation
1	Yoshimi (1967)	Shake table. Rigid box (50x25x27cm)	Horizontal sand layer covered by a membrane	Water pluviation with an upward flow of water Pore fluid water)	Niigata sand (D_{10} ≈0.11 mm, D_{60} ≈0.21 mm, Gs ≈ 2.66) Zircon sand (D_{10} ≈0.10mm, D_{60} ≈0.17 mm)	D_r ≈45% -50% D_r ≈ 45% - 52%	0.13g –0.96g sinusoidal motions at 4 –8 Hz for long duration	A water layer (≈16 mm thick) forms below the membrane. This is approximately 6% of the initial height of the sand.
2	Finn et al. (1971)	Shake table. Rigid box (183x26x18cm)	Horizontal sand layer covered by a membrane	Water pluviation (Pore fluid water)	Wedron silica sand (Gs = 2.66, D50 = 0.55 mm)	D_r ≈ 27%	0.1g – 0.5g sinusoidal at 2Hz, continuous for long duration	A water layer (≈6.3 mm thick) forms below the membrane. A loose surface sand layer inferred from the spreading of the colored sand column.
3	Scott & Zuckerman (1972)	Vibrational shock. Glass beaker (10x16cm diameter)	7.6 cm thick coarse sand layer overlain by fine sand (0.64 cm - 2.86 cm)	Not clear (Pore fluid water)	Ottawa sand	Loose (γ_d ≈ 1.5g/cm3)	Vibrational shock	Slow motion photos revealed that the fine and coarse sand layers instantaneously separated because of the settlement of the coarse sand layer.
4	Huishan & Taiping (1984)	Shake table. Rigid box (150x50x30cm)	Stratified sand deposit with approximately 1cm thick alternating layers of coarser and finer fractions of the same sand. A model foundation on top of this horizontal deposit.	Water pluviation and vibration (Pore fluid water)	D10 = 0.053mm D60 = 0.114mm	D_r ≈ 14%, 28%	0.3g sinusoidal at 3-5 Hz, continuous until evidence of liquefaction	Water inter-layers formed and grew to maximum thickness (≈2.5 cm for Dr =14% model and 1.5 cm for Dr = 28% model) and eventually resulted in boiling and disappearance of the water inter-layers.

Table AII-1: Previous studies on void redistribution using physical testing procedure (Cont.).

No.	Investigator	Test Type and Container	Soil Geometry	Model Preparation	Soil Properties	Initial State	Shaking	Observation
5	Elgamal et al. (1989)	Shake table. Rigid box (30.48x 60.96 m in cross section)	(1) Silty sand layer (15. 24 cm thick) underlying a silty clay blanket (1.91 cm thick). (2) Inter-layered clay (1.78cm) – clean sand (7.62cm) stratum	Water pluviation (Pore fluid water)	k in ft/s Silty sand ≈ $1.7x10^{-2}$ Clean sand ≈2.7x10-2 Clay ≈1x10-7, PI ≈18.1	Silty sand loose. Clean sand loose.	Periodic waves of 0.1g – 0.2g applied for over 100s.	Water inter-layers formed below the low permeability layers, continued to grow (to about 5% of the underlying sand thickness) and after about 100 s gradually shrunk after boiling.
6	Kutter and Fiegel (1991); Fiegel and Kutter 1994a)	Centrifuge. Rigid box (56 X 28 X 17.8 cm)	Nevada sand layer (≈2.5 m) beneath a non plastic silt top layer (≈1.3 m).	Sand air pluviated Silt placed as slurry and consolidated in-flight (Pore fluid water)	Nevada sand (k = 5 X 10-3 cm/s) Silica flour (k = 3 X 10-6 cm/s)	Sand Dr ≈60%	a_{max} ≈0.5 g and duration ≈30 s; a sinusoidal motion also applied.	Formation of a water gap or a very loose zone of soil at the interface between the two soil layers was inferred based on acceleration, pore pressure and settlement time histories.
7	Dobry and Liu (1992)	Centrifuge. Rigid box (43.2 X 24 cm in cross section)	(1) Nevada sand layer (≈ 3.0 m) beneath a non-plastic silt top layer (≈3.0 m). (2) Similar model (sand ≈ 5.0 m, silt ≈1.0 m) with a model foundation on top.	Not clear (Pore fluid water)	Nevada sand Silica flour (same soils as in 6)	Dr ≈40% - 45%	5 s duration motion with about 10 cycles with peak accelerations of .2g.	Based on the pore pressures and accelerations measured in these tests, four stages of behavior, which included the formation of a water interlayer was inferred.
8	Arulanandan et al. (1993)	Centrifuge. Rigid box (56 X 28 X 17.8 cm)	Clay embankment with an enclosed sand zone (thickness ≈0.8 m) in the upstream.	Clay (Yololoam) compacted at RC ≈90%. Sand water pluviated (Pore fluid water)	Yolo loam k = 2 X 10-10 m/s Nevada sand k = 1.09 X 10-4 m/s	Dr ≈45% - 50%	Sinusoidal motion of 0.47g at 1 Hz for 20 s	Loosening due to void redistribution inferred based on deformation pattern, lab tests and Newmark analysis. However, Castro (1995) pointed out several limitations in the interpretations.

Table AII-1: Previous studies on void redistribution using physical testing procedure (Cont.).

No.	Investigator	Test Type and Container	Soil Geometry	Model Preparation	Soil Properties	Initial State	Shaking	Observation
9	Fiegel & Kutter (1994b)	Centrifuge. Rigid box (56x28x17.8 cm)	Nevada sand layer (≈2.1 m) beneath a non plastic silt top layer (≈2.1 m). Both layers had a 2.6° slope.	Sand air pluviated Silt placed as slurry and consolidated in-flight (Pore fluid water)	Nevada sand Silica flour (same soils as in 6)	Sand Dr ≈60%	a_{max} ≈0.7 – 0.9 g and duration ≈ 30s	Photos clearly show lateral displacement was concentrated along the interface between layers. Loosening due to void redistribution inferred based on instrument recordings and Newmark analysis.
10	Kokusho (1999, 2000); Kokusho & Kojima (2002)	Instant shock. Lucite tube (13 cm diameter and 211.5 cm height)	A thin non plastic silt seam (2 – 8 mm) sandwiched between a looser upper sand layer (104, 60 cm) and a varying density lower sand layer (96, 140 cm)	All soils water pluviated (Pore fluid water)	Toyoura sand ($k \approx 10^{-2}$ cm/s) Non plastic silt ($k \approx 1 \times 10^{-4}$ cm/s)	Upper layer Dr ≈14 –23% Lower layer Dr ≈25 –70%	Instant shock (strong enough to cause about 3% liquefaction settlements)	A water film started developing below the silt layer, reached a maximum thickness and then slowly disappeared. The maximum thickness (0.1 – 2 cm) and duration (10 – 700 s) of this water film varied for different combinations of parameters.
11	Kokusho (1999 , 2000); Kokusho & Kojima (2002)	Shake table. Rigid box (80 x 40 x 50 cm)	(1) Slope (s ≈30%) with an arc shaped seem of silt (average thickness 6 mm) embedded. (2) Horizontal ground with 2 horizontal seams of silt (4 mm) loaded by an embankment (coarse sand). (3) Sloping ground with 2 horizontal seams (5 mm) of silt.	All soils water pluviated (Pore fluid water)	Same soils as in 10	Dr ≈ 20% Dr ≈ 15% Dr ≈ 35%	3 cycles of 0.3 g applied in 1 s. The shaking direction was transverse.	Very large deformations with large discontinuous movements at the bottom of silt – sand interface. A very thin water film was observed at some parts. Most of the movements occurred after shaking was over. In the third case after the breakage of the silt seams, boiling of the overlying sand resulted in a mud-flow avalanche.

Table AII-1: Previous studies on void redistribution using physical testing procedure (Cont.).

No.	Investigator	Test Type and Container	Soil Geometry	Model Preparation	Soil Properties	Initial State	Shaking	Observation
12	Balakrishnan & Kutter (1999); Gajan & Kutter (2002)	Shake table. Rigid box (80 X 40 X 50 cm)	(1) Slope (s ≈30%) with an arc shaped seem of silt (average thickness 6 mm) embedded. (2) Horizontal ground with 2 horizontal seams of silt (4 mm) loaded by an embankment (coarse sand). (3) Sloping ground with 2 horizontal seams (5 mm) of silt.	All soils water pluviated (Pore fluid water)	Same soils as in 10	Dr ≈20% Dr ≈15% Dr ≈35%	3 cycles of 0.3 g applied in 1 s. The shaking direction was transverse.	Very large deformations with large discontinuous movements at the bottom of silt – sand interface. A very thin water film was observed at some parts. Most of the movements occurred after shaking was over. In the third case after the breakage of the silt seams, boiling of the overlying sand resulted in a mud-flow avalanche.
13	Singh et al. (2000, and 2001); Brandenberg et al. (2001)	Centrifuge. Flexible shear beam container (170 x 80 x 50 cm)	A top clay layer (≈4.5 m), middle loose sand layer (≈2.5 – 5.0 m) and a bottom dense sand layer (≈12.5 – 10.0 m). Some models had a thin coarse sand layer on top of the clay. All layers had a 3° general slope. The clay had a 25° river channel at one end. All models had piles embedded.	Sand air pluviated. Clay placed as slurry and consolidated in a press. (Pore fluid water)	Nevada sand and Clay San Francisco bay mud (same as in 12).	Loose Sand Dr ≈20 - 30% Dense Sand Dr ≈70 -90% Clay OC.	More than 3 big shake events. a_{max} ≈0.3 – 1.6 g.	Discontinuous lateral deformations at the clay sand interface. Clay layer appears to slide on the loose sand layer.

Yoshimi (1967) conducted shaking table tests to study qualitatively the factors influencing liquefaction in a saturated mass of loose sand within impervious boundaries. Niigata sand ($D_{10} \approx 0.11$ mm, $D_{60} \approx 0.21$ mm) and Zircon sand ($D_{10} \approx 0.10$ mm, $D_{60} \approx 0.17$ mm) were tested in rigid sample boxes with glass windows. The samples were prepared by water pluviating while maintaining an upward flow of water. A rubber membrane was used to cover the sample and a surcharge pressure was applied. The initial relative densities ranged from 45% to 52% for different tests. A horizontal vibration was applied to the model. Yoshimi (1967) observed the formation of a water layer between the rubber membrane and the surface of the sand, thus making the surcharge literally float on the layer of water. The average thickness of the surface water layer was 1.6 cm, which is approximately 6% of the initial thickness of the sand. The average relative density of the sands after shaking increased due to consolidation, and ranged from 72% - 107% in different tests. These observations agree with Yoshimi's comment, "the test should really be called a "constant total volume test" rather than an undrained test".

Finn et al. (1971) conducted liquefaction studies of large saturated sand samples excited on a shaking table. A sample box with Plexiglas viewing windows was used for the tests. The sample was prepared by water pluviation. After leveling the surface, the sample was sealed by placing a thin rubber membrane and a lid. Wedron silica sand ($G_s = 2.66$, $D_{50} = 0.55$ mm) was used for all tests at an initial relative density of 27%. A backpressure and a total surcharge pressure were applied to the sample. The soil was liquefied by the application of sinusoidal shaking motions. A vertical black sand column in the sample was used to observe the horizontal movement of sand grains during and after shaking. The authors reported, "In some tests, particularly those at low surcharge pressures, there appeared to be some spreading of the column near the surface which would indicate the formation of a looser surface layer. After the initial liquefaction, the sand grains 'settle' to give a lower void ratio, the pore water pressure drops to the surcharge pressure and a layer of water approximately 0.25" in depth forms on the surface of the sample. There is no longer any contact between the surface sand grains and the membrane, so it is quite possible that these surface sand grains may move at this point and a non-uniform surface layer is formed". They also noted that for higher acceleration amplitudes, there was a definite spreading of the column of black sand at the surface and this would indicate that a loose layer was being formed.

Scott & Zuckerman (1972) performed qualitative experiments to study the mechanism of sand boil formation. They carried out tests on saturated layered soils on a small glass beaker. Different types of soils, liquefaction methods and pore fluids were used in the testing program. Observations during a test carried out on a 3"thick loosely placed coarse sand layer overlain by a fine sand layer (thickness range for different tests 0.25"– 1.125") is of particular interest. This sample was liquefied by the application of vibrational shock. Scott and Zuckerman (1972) expressed that "...no sand boils developed. The expulsion of pore fluid from the soil was uniformly distributed over the soil surface. The source of ejected fluid was determined to be the pore water in the uppermost region of the fine sand layer. Slow motion photography of the interface between the fine and coarse soil layers revealed a nearly instantaneous separation between these layers, caused by the settling of the coarse grained layer after the shock. Immediately afterward the fine-grained layer began to settle onto the coarse grained soil. This settling took the form of a liquefaction interface traveling upward in the fine grained layer, and dying out as it moved towards the surface". Based on these observations and other tests in the same program they conclude, that even though directly liquefied layers become denser after shaking it is possible that those layers in which liquefaction is induced due to the adjacent liquefied zones would be looser after shaking.

Huishan and Taiping (1984) performed shaking table tests on homogeneous deposits and horizontally stratified deposits in the presence or absence of a model foundation. A rigid model container with Plexiglas sidewalls was used. The sand was water pluviated and brought to the desired density by vibration. The sand had a D_{10} of 0.053 mm and a D_{60} of 0.114 mm. Two of the models were prepared by pluviating sand in about 2 cm layers and waiting for it to consolidate before pluviating the next layer in order to form stratified deposits. This resulted in each of these layers having a coarser bottom layer and a finer top layer. The relative densities of these stratified sand models were 14% and 28%. A sinusoidal excitation of 3 – 5 Hz frequency was applied to the models and continued until evidence of liquefaction was observed. The sinusoidal motion applied to the stratified models had a 0.3 g acceleration. The observations for the 14% relative density test are shown in Fig AII-1. Huishan and Taiping (1984) described the observations as follows, "When the pore pressure increases, the small horizontal fissures filled with water appear symmetrically or asymmetrically outside the foundation. If vibration continues, the fissures grow up rapidly to form water inter-layers or water lens. With further build up of pore pressure water lens located at the same elevation will be interconnected to form a long

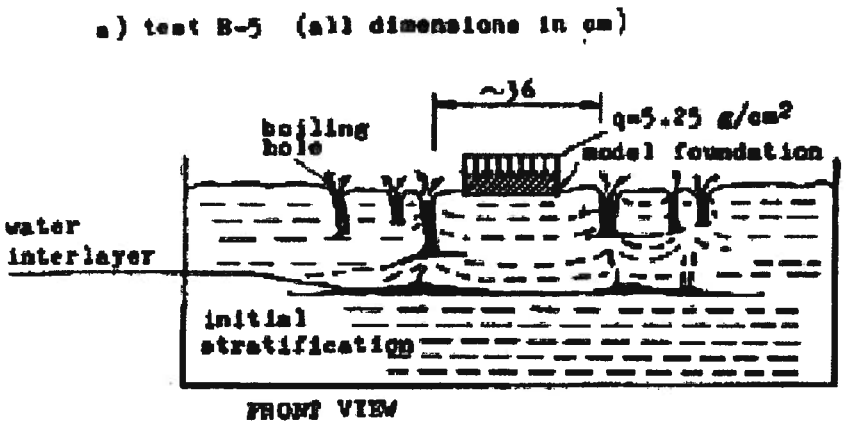

Fig. AII-1: Observation of water interlayers on shaking table tests of stratified sand deposits (Huishan and Taiping 1984).

water interlayer. Meanwhile, the other fissures may appear somewhere. With increasing thickness of water interlayer the ground surface is uplifted. Once the first water interlayer reaches its maximum thickness, the water burst out with a noise through the overburden stratum and boiling occurs. After boiling the water interlayer soon disappears and the fissure is closed". The maximum thickness of the observed water inter-layers for the 14% and 28% relative density sands were 2.5 cm and 1.5 cm respectively.

Elgamal et al. (1989) performed a series of qualitative 1-g shake table tests to investigate the effect of stratification of soil deposits on liquefaction. Three different models, a uniform silty sand layer, a silty sand layer underlying a silty clay blanket and an inter-layered clay–loose sand stratum were tested. The models were prepared by water pluviation. Water inter-layers were observed to form below the less permeable layers in the second and third models. These water inter-layers continued to grow as the dynamic excitation progressed and reached a maximum thickness of about 5% of the underlying sand layer. Finally after about 100 seconds of continued dynamic excitation the water inter-layers gradually shrunk and a combination of sand and clay boils erupted to the surface. They addressed two points in this regard i.e. the relatively large thickness of the water inter-layers and the long time duration during which this thickness is sustained following the end of dynamic excitation. Fig. AII-2 depicts their observation from the test.

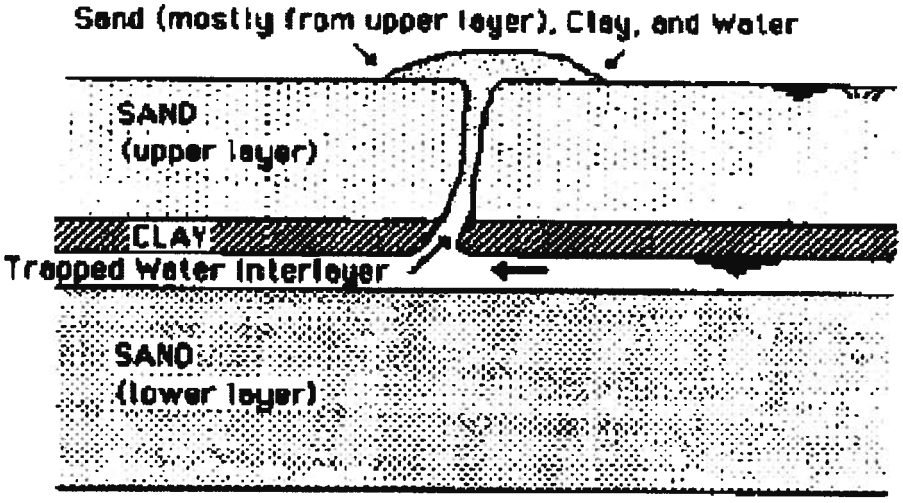

Fig. AII-2: Formation of trapped water interlayer, and delayed sand boil following a hydraulic fracture-mechanism (Elgamal et al. 1989).

Fiegel and Kutter (1991 and 1994a) reported results of centrifuge model tests carried out to study the liquefaction mechanism for layered soils. Four models were tested with the first model having homogeneous Nevada sand ($k = 5 \times 10^{-3}$ cm/s) air pluviated at 60% relative density and the next three models with a non-plastic silt layer ($k = 3 \times 10^{-6}$ cm/s) on top of the Nevada sand. The silt was placed in a slurry form and consolidated in-flight. Water was used as the pore fluid. During the last three tests the accelerations in the silt layer followed the base shaking (and the acceleration in the sand layer) only for a few cycles and then damped out, indicating that the silt layer became isolated from the base. Pore pressure records showed that pore pressure ratio remained at 100% at the sand-silt interface for a relatively long time. Surface settlement recordings indicated that the silt surface bulged first before finally settling. These observations were not seen for the homogeneous Nevada sand test. Based on these test results they concluded that an overlying, relatively impermeable soil tends to restrict the escape of pore water produced by the settlement of an underlying liquefiable sand layer. This can result in the formation of a water gap or a very loose zone of soil at the interface between the two soil layers.

Dobry & Liu (1992) presented two centrifuge tests results done on layered soil deposits. In the first test, sand was placed at a relative density of 40% with a silt layer on top. These soils were the same used by Fiegel & Kutter (1991 and 1994a) for their tests. Based on the pore pressures and accelerations measured in these tests, they inferred four stages of behavior, which

included the formation of a water interlayer. These are shown in Fig. AII-3. The first stage lasted 2 s where the pore pressure generation towards initial liquefaction took place with resulting upward water flow. The second stage lasted from 2 seconds to the end of shaking at 5 seconds, and extended a little bit beyond shaking (initial part of consolidation). Initial liquefaction had been reached at the upper part of the sand layer and a water film at the sand-silt interface grew during this stage. The third stage lasted for about 4 minutes during which the only point of the whole profile that had a pore pressure ratio of 100% was the interface of the two layers. During this stage the water film was shrinking. After this the fourth (last) stage took place where there was no water film and coupled consolidation of the two layers took place. The second test had a model with a very similar two-layer horizontal soil deposit. The main difference was that a shallow foundation was placed on the soil surface. The relative density of the sand was also 45%. Dobry & Liu (1992) reported that a water interlayer formed in this case also. The thickness of the water interlayer was thought to be larger in the free field than under the structure, since the weight of the structure was forcing the water out towards the free field. Water was used as pore fluid in the two tests described above.

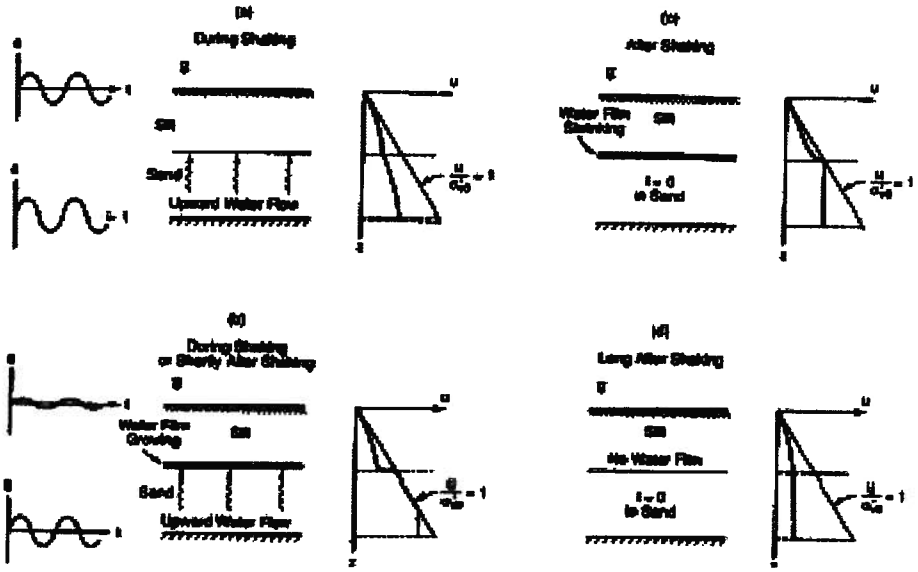

Fig. AII-3: Four stages inferred in centrifuge test of two-layer deposit (Dobry & Liu 1992).

Arulanandan et al. (1993) reported loosening due to void redistribution within a globally undrained sand layer, confined by clay layers, within a model embankment shaken in a centrifuge. The sand layer was only present in the upstream side. The clay, which made up most

of the embankment, was Yolo loam compacted at a relative compaction of 90%. Nevada sand was water pluviated with resulting relative density range of 45% - 50%. A sinusoidal motion of 0.47g at 1 Hz was applied for 20 s. The model was observed to deform during the shaking. The failure mechanism was inferred by the authors as loosening due to void redistribution in the sand–clay interface. This was based on the deformation pattern, and the comparison of the shear strength from lab tests with the one found by back-calculation using Newmark analysis. The authors estimated that the sand initial void ratios of 0.77 got loosened to 0.70 during shaking. However, regarding this test, Castro (1995) brought up several limitations in these interpretations such as the estimation of a high shear strength value for the clay in the centrifuge model, similar magnitudes of displacements for the upstream side with the sand and the downstream side without the sand and acceleration records in clay not supporting the inference that uncoupling of the layers took place due to loosening at the interface due to void redistribution.

Fiegel and Kutter (1994b) reported details of two centrifuge model tests done to study the liquefaction-induced lateral spreading of mildly sloping ground (slope angle 2.6 degrees). The first model consisted of homogenous Nevada sand and the second consisted of a layer of Nevada sand overlain by a layer of non-plastic silt. The Nevada sand was air pluviated at a relative density of 60%. Silt was placed in a slurry form and consolidated in-flight. Water was used as the pore fluid. Both models were subjected to a base motion with a 30 s duration. The homogenous and layered models had maximum base accelerations of 0.9 g and 0.7 g respectively. Pore pressure records during the test indicate that they remained high for a longer duration for the layered model than for the homogeneous model. In both tests approximately 0.8 m of prototype lateral displacement was measured at the surface. As shown in Fig. AII-4 in the homogeneous sand model this lateral displacement was distributed throughout much of the layer whereas in the layered model displacement was concentrated along the interface between layers. Almost all the lateral displacement occurred during shaking for both the tests. Based on Newmark sliding block calculation and previous lab tests (Kutter et al. 1994) they pointed out that the undrained steady state strength of the sand far exceeds the strength required to prevent lateral displacement of a 2.6 degree slope, even with 0.7g of lateral acceleration. This provides support to their argument "the concentration of displacement is consistent with a reduction in the sliding resistance between the silt and the sand layers due to the redistribution of voids at the interface".

(a) (b)

Fig. AII-4: Lateral displacement patterns in centrifuge tests models of mildly sloping layered grounds, (a) homogenous sand, (b) layered soil (Fiegel & Kutter, 1994).

In an attempt to investigate the mechanism involved in the extensive lateral slides reported from the 1964 Alaska earthquake (e.g. Seed, 1968), Zeng & Arulanandan (1995) conducted a centrifuge model of silty slope with a seam of liquefiable sand. They demonstrated that liquefaction of the sand led to slope failure.

AII.2 Studies done in Chuo U. and Davis U.

An initiative experimental studies lounged by professor Kokusho at Chuo University in the late 90s to investigate the mechanism involved in liquefaction-flow slide and in particular in gently sloping grounds. Kokusho (1999) reported results of layered soil column liquefaction tests done to study the mechanism of water film formation in level-ground condition. An instant shock was used to liquefy a tube of a water sedimented soil. The test was conducted for a uniform soil with and without a thin non-plastic silt seam (of 4cm thick at z = 96cm) sandwiched between sand layers (see Fig. AII-5). A water film started developing below the silt layer, reached a maximum thickness of 8% of under-laying loose sand (D_r = 39%) layer shown on Fig. AII-6 and then slowly disappeared. Fig. AII-7 depicts typical time-dependent settlement curves at the surface as well as at interior points in the fine sand. As soon as the sand instantaneously liquefies by hammer impact at the benchmark b1, the settlement starts from the bottom. The settlement is remarkably linear with time until kinks indicated by the benchmarks b2, b3 and b4 appear, where the sedimentation of sand particles suspended in the water takes place.

A parameter study was carried out by varying the relative density of the lower layer. The maximum thickness of water film varied with sand relative density as depicted on Fig. AII-8. Kokusho & Kojima (2002) reported details of similar tests for three 3-layer systems (fine sand-

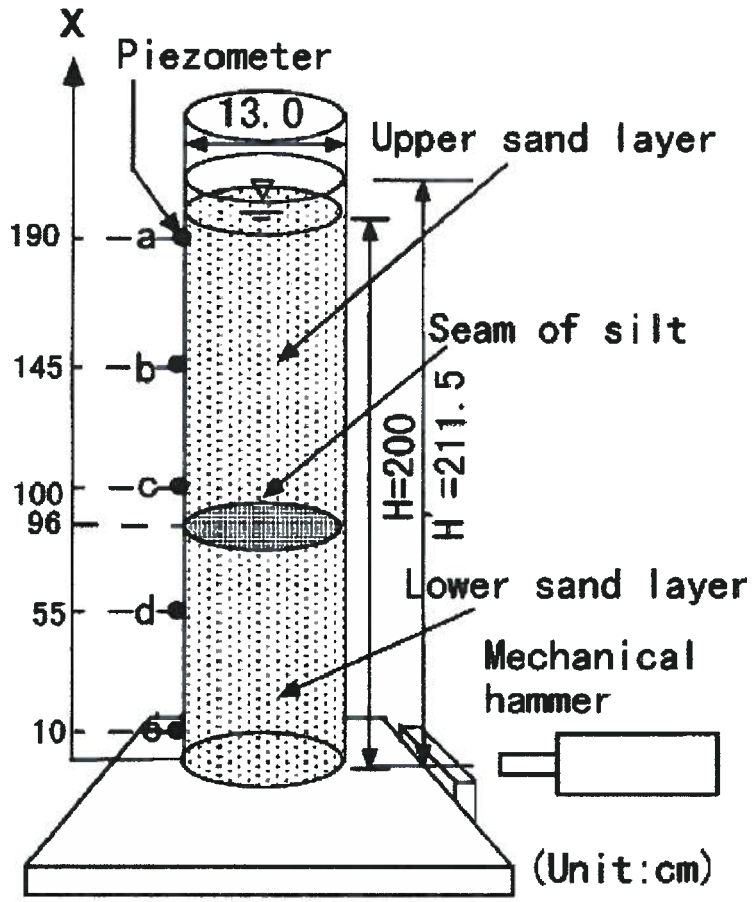

Fig. AII-5: Sketch of 1D tube test device (Kokush, 1999).

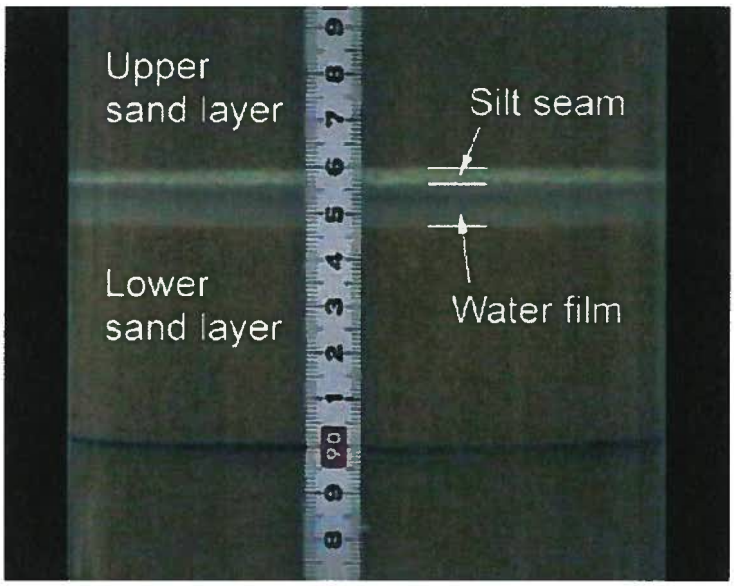

Fig. AII-6: Photograph of Water Film Consisting of Clear Water Formed beneath Silt Seam (Kokosho, 1999).

silt-fine sand, coarse sand-fine sand-coarse sand, and coarse sand-fine sand-unsaturated fine sand crust) and a 2-layer system (coarse sand-fine sand). A stable water film was observed in all 3-layer system tests. In the 2-layer test fierce turbulence was observed at the layer interface, with larger void ratio near the bottom of the upper fine sand layer. A stable water film did not develop in the 2-layer test.

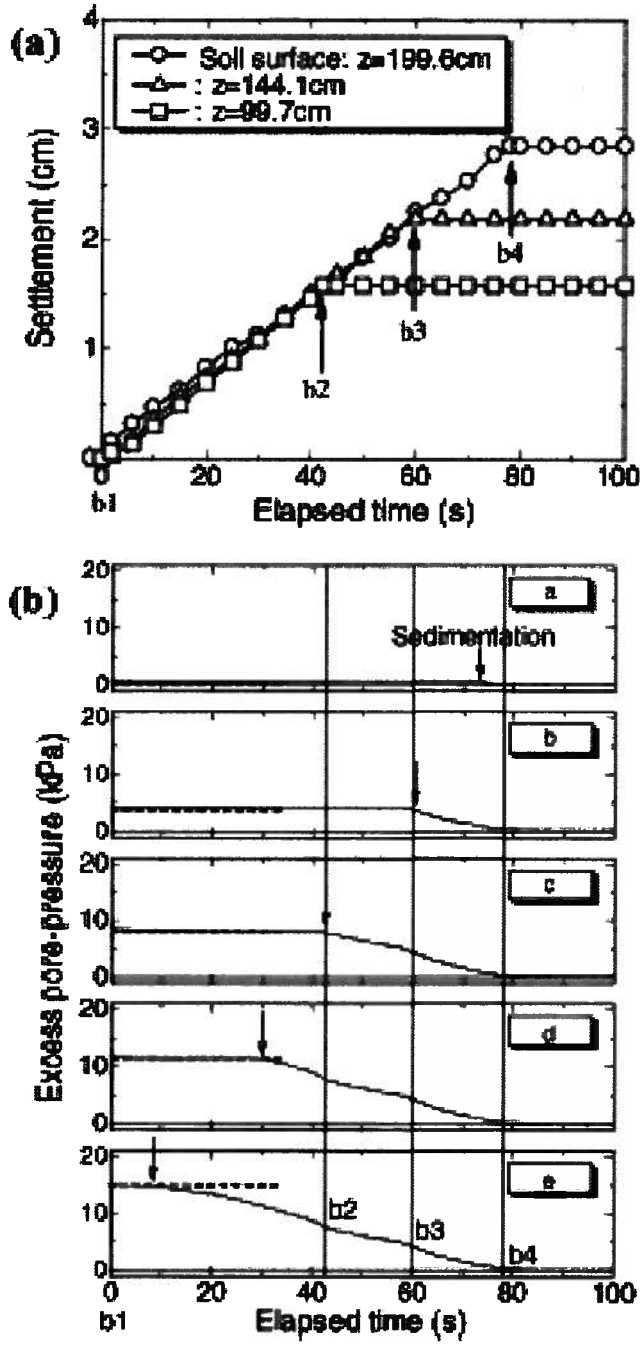

Fig. AII-7: Time-dependent variations in sand settlement (a) and pore pressure, (b) at different depths (Kokosho 2003).

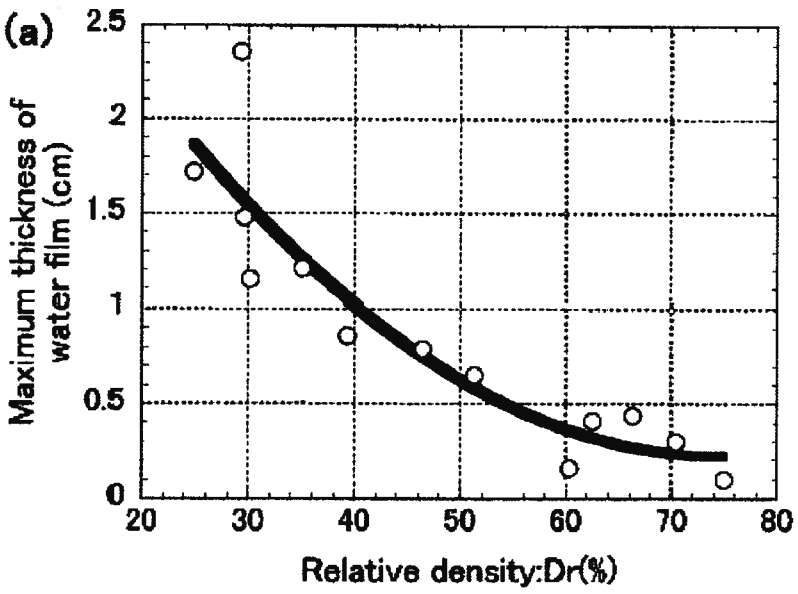

Fig. AII-8: Effect of sand relative density on water film thickness (Kokosho, 1999).

Kokusho (1999, 2000) carried out two-dimensional model tests on the shake table to further investigate the water film mechanism and its effect on overall deformations. Fig. AII-9 shows the three different types of geometries tested. All models were prepared by water pluviation and had loose soils with Dr of 21%, 14%, and 35% for models in Fig. AII-10a, AII-10b, and AII-10c, respectively. For each of these tests, companion tests with the same geometry but without any silt seams were conducted to compare the behavior. The models were subjected to a very short duration motion applied in the transverse slope direction. This motion caused liquefaction and limited soil deformations during shaking. Deformations continued after shaking and caused flow failures for models with silt seams. Fig. AII-11 shows displacement time history for case a shown in Fig. AII-10 for certain representative points (Fig. AII-10c) along with its corresponding case without silt arc. As may be seen the deformation at the end of shaking for the case with silt arc is less than that of without silt arc case. This deformation was mainly concentrated at the bottom of silt seam-sand interface. A hair-like water film was observed at the toe parts of this interface. In the case of sloping ground with horizontal seams of silt, breakage of the silt seams occurred followed by boiling of the overlying sand leading to a mudflow avalanche. This series of tests illustrates the important role of void redistribution in the failure mode and timing of lateral spreads and flow failures.

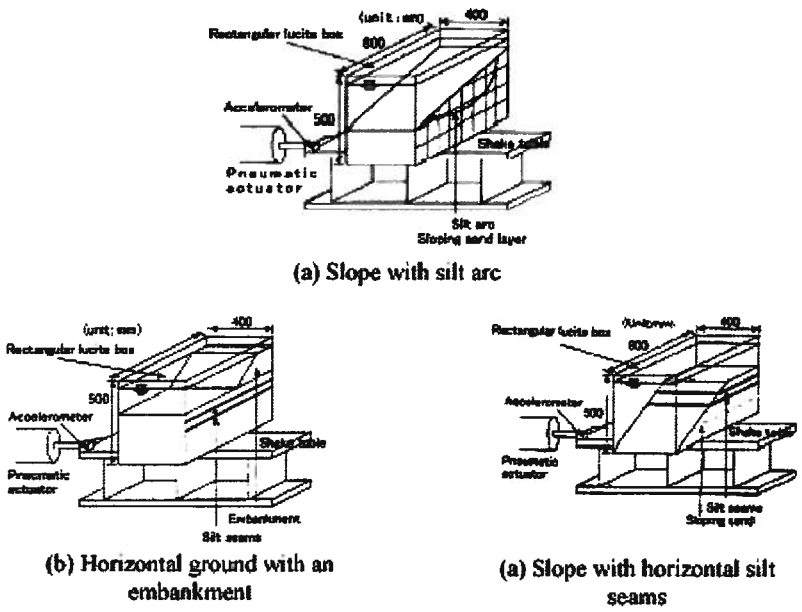

Fig. AII-9: 2-D model tests with silt layer (Kokusho, 1999, 2000).

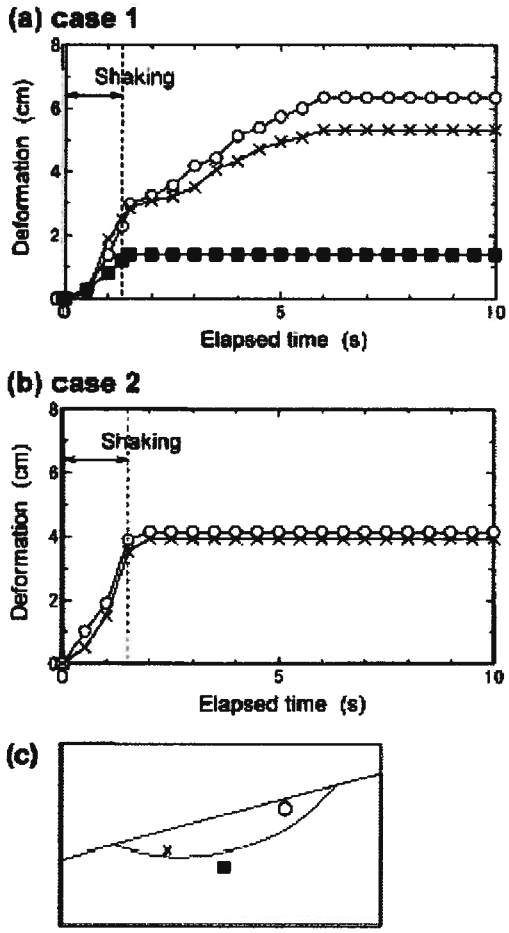

Fig. AII-10: Soil deformation vs. elapsed time for representative points in sloping ground (a) case 1, with silt arc; (b) case 2, without silt arc; (c) location of representative points (Kokusho, 1999).

Kokusho (2003) reported results of a similar set of model test results with and without silt arc that their deformation patterns after failure are shown in Fig. AII-11 which indicates most of deformation occurs at the silt-sand interface when the silt arc is present. These results are for an input acceleration of 0.31g. In Fig. AII-12c, the time histories of flow deformation of the same model subjected to weaker input acceleration of 0.18g are shown. Much larger post-shaking flow occurs in this case than when the acceleration was 0.34g; but minimal deformation takes place during shaking. This is because in the weaker motion, the slope remains steep during shaking and so the driving forces are larger during post-shaking flow along the interface.

Concurrently to the studies in Japan, several research model programs were conducted at Davis University, U.S. to investigate on low permeability sub-layer effects on seismic behavior of liquefiable soils namely, pile foundation, bridge abutments and sloping grounds using a small 1m and large 9m centrifuge facilities (Balakrishnan & Kutter (1999); Gajan & Kutter (2002) and Kutter et al., 2004). Fig. AII-12 shows a test model of river flood plain used to study the effect of relative density and thickness of sand layers on the amount of settlement and lateral spreading near bridge abutments. The models had a river channel with clay flood banks underlain by layers of sand with varying relative densities and thickness. The layers had a gentle slope with one of the banks having a bridge abutment surcharge. The models were constructed by air pluviating the sand and placing the clay in a slurry form and consolidating in a press. Water was used as the pore fluid. The models were subjected to three big shaking events. Discontinuous lateral deformations at the clay-sand interface (interface slip $\approx$1.2 m), with the clay layer moving more than the top of the sand layer, were observed for two of the models where the relative densities of the sand layer were high and/or the thickness of the looser layer was small (see Fig. AII-14). However, in cases where the sand layer was looser or thicker the deformation patterns appeared to be continuous or the clay appeared to move less than the sand. The clay layer seems to have moved by the same amount (1.5 – 1.8 m) for all the tests regardless of varying densities or thickness of the underlying sand layer (see details in Fig. AII-13 and Table AII-2). This may have been caused because of the deformations of the clay layer being limited by the river channel boundary. The observations of discontinuous deformations at the interface in some tests and the fact that the clay layer had negligible strains (almost moved as a rigid block) suggest that void redistribution played an important role in the deformation mechanism.

Kutter et al. (2004) also examined the empirical correlation proposed by Youd et al. (1999) for lateral spreading that only considers the thickness of soil layers that have $N_{1(60)}$ <15;

against their test results. They showed that thick soil layers with $N_{1(60)}$ >15 (approximately Dr = 50%) can also produce significant lateral movement.

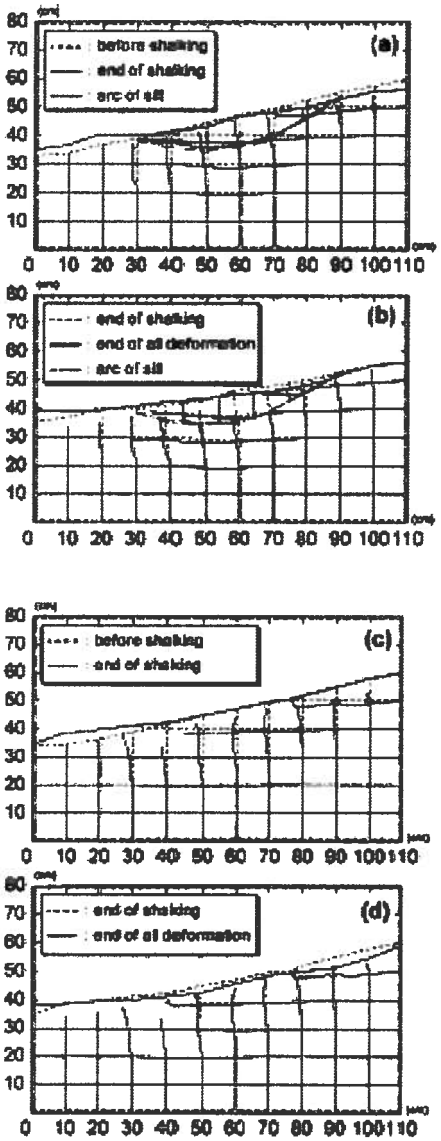

Fig. AII-11: Cross-sectional deformation for slopes (a) and (b): with buried silt arc. (c) and (d) Without silt arc. (a) and (c) during shaking. (b)and (b) after the end of shaking (Kokusho, 2003).

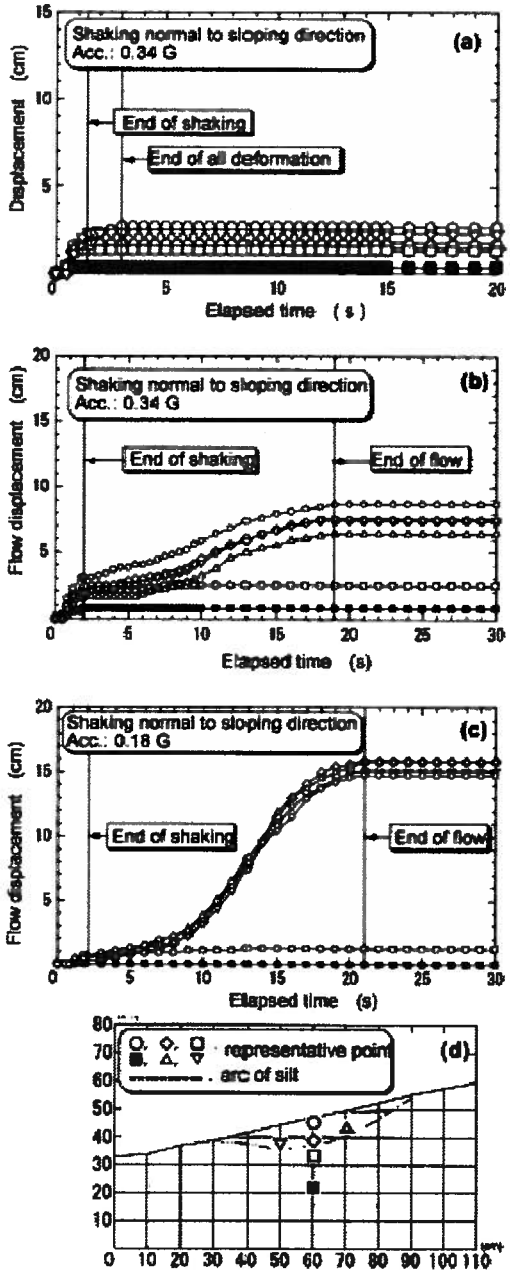

Fig. AII-12: Time-dependent flow displacement at target points shown in (d); a) without silt arc by PGA 0.34g. (b) with silt arc by PGA 0.34g. (c) with silt arc by PGA 0.18g. (Kokusho, 2003).

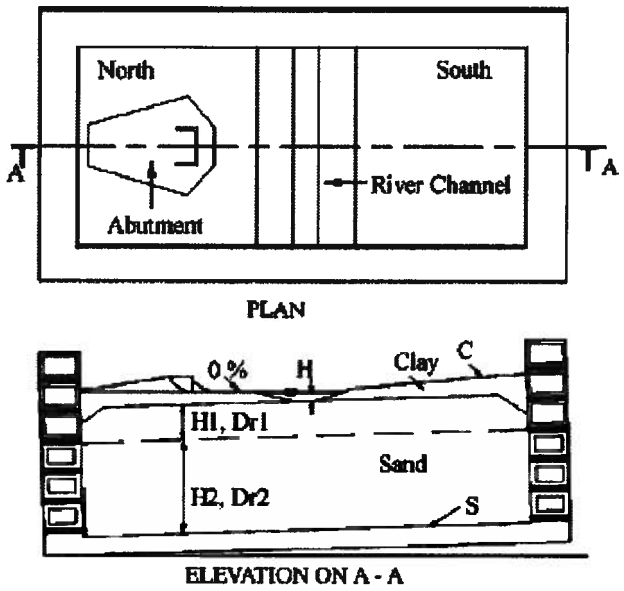

Fig. AII-13: General model configuration for lateral spreading study of bridge abutment (Kutter et al., 2004).

Table AII-2: Model tests details for lateral spreads of bridge abutments (Kutter et al., 2004).

Model code	Model details	Slope of clay (*C*)	Slope of sand (*S*)	Height of water table (*H*) (m)
C80	$H1 = 0$ m $Dr_2 = 80\%$, $H2 = 15$	9.3%	3.3%	1.2
U50	$Dr_1 = 50\%$, $H1 = 9$ m $Dr_2 = 80\%$, $H2 = 6$ m	9.0%	3.0%	1.2
U50_4.5	$Dr_1 = 50\%$, $H1 = 4.5$ m $Dr_2 = 80\%$, $H2 = 10.5$ m	9.3%	3.3%	1.2
U50_4.5S	$Dr_1 = 50\%$, $H1 = 4.5$ m $Dr_2 = 80\%$, $H2 = 7.5$ m	3.0%	3.0%	1.2
U30_4.5	$Dr_1 = 30\%$, $H1 = 4.5$ m $Dr_2 = 80\%$, $H2 = 7.5$ m	9.3%	3.3%	1.2
U30_4.5M	$Dr_1 = 30\%$, $H1 = 4.5$ m $Dr_2 = 80\%$, $H2 = 7.5$ m	9.3%	3.3%	−0.3–1.3 (variable)

Note: U30_4.5M stands for Unimproved Dr=30% sand of 4.5 m thickness with input motion (*M*) varied. *C*, *S* and *H* are marked in Fig. 3-40.

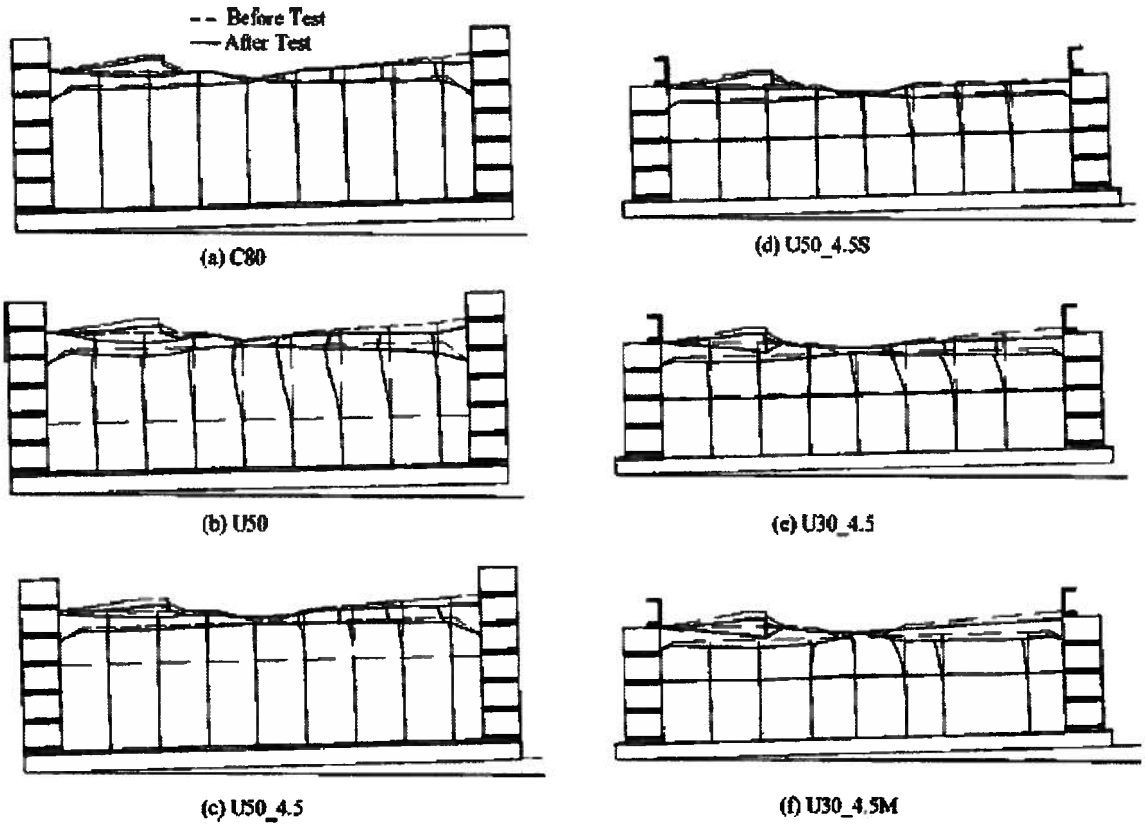

Fig. AII-14: Deformation pattern of tested models, see Fig. AII-14 and Table AII-2 for details (Kutter et al., 2004).

Davis U. research group reported results of another set of model tests to study the behavior of piles in laterally spreading ground (Singh et al. 2000, and 2001; Brandenberg et al. 2001). The models had a top, moderately over consolidated clay, layer underlain by a middle loose sand layer (Dr ≈20-30%) and a bottom dense sand layer (Dr ≈70-90%). Some models had a thin coarse sand layer on top of the clay layer. All layers had a 3° - 4.5° general slope. The clay had a 25° sloping river channel at one end. All models had single and group piles embedded in them. The models were constructed by air pluviating the sand and placing the clay in a slurry form and consolidating in a press. Water was used as the pore fluid. The models were subjected to several (more than 3) big shaking events. Lateral deformation patterns after the shaking events show a clear discontinuity at the clay-loose sand interface as shown typically on Fig. AII-15. This was attributed to loosening due to void redistribution driven by the upward hydraulic gradients produced by the excess pore pressures in the underlying sands.

Fig. AII-15: Discontinuous lateral deformations in the clay sand interface (from Kulasingam, 2003 photo by S.J. Brandenberg).

Malvick et al. (2005) presented results of a U.S.-Japan cooperative research project conducted jointly at Chuo University in Tokyo, by Prof. Kokusho and his coworkers and University of California in Davis to collaborate on a project studying the effects of void redistribution and water film formation on shear deformations due to liquefaction in layered soils. They employed 1g-shake table, small 1m-radius centrifuge and large 9-radius centrifuge facility in a 2-D study of slopes with various relative density of liquefiable sand layer comprising silt sub-layer subjected to 1 to 3 subsequent events.

The typical shake table model had a 4:1 slope that was 0.3 m high and consisted of Tokyo Bay sand (shown in Fig. AII-9). Models were typically shaken transverse to the slope by a harmonic motion (Kokusho 2003). The typical centrifuge model had a prototype 2:1 slope that was 6 m high and consisted of Nevada sand (see Fig. AII-16 and AII-17 for small and large centrifuge models respectively). Models were typically shaken along the slope by a modified earthquake ground motion (Kulasingam et al 2004). A few tests were performed at both institutions to control operation and procedures effects. Fig. AII-18 shows the shake table model configuration before and after shaking. This model consisted of a loose slope of Tokyo Bay sand with embedded silt arc. The model failed after being shaken transverse to the slope (normal to the view shown) by a 3 Hz harmonic motion for 1 s with a peak base acceleration of 0.3 g. Approximately 50% of the deformations and localization occurred for 9 seconds after shaking stopped. This shake table test is similar to other tests completed at Chuo University and described in Kokusho (1999 and 2000), Kokusho & Kojima (2002), and Kokusho (2003). For comparison, some of the tests described in these references showed 50% to 85% of the

movements occurring up to 20 s after shaking stops. The base acceleration during shaking for these models ranged from approximately 0.15 g to 0.35 g.

Fig. AII-19 shows typical centrifuge model configuration before and after shaking along with a close up of silt-sand interface showing localization. Kulasingam et al., (2004) demonstrated that a slope model of D_r = *20%* without a silt sub-layer can withstand the applied shaking event whereas a similar model with greater elative density e.g. 50% failed when a silt layer is present in the slope. Fig. AII-20 shows the initial states for the sand they used compared to the sand's steady state line. The steady state line is based on isotropically consolidated undrained and drained triaxial compression tests by Castro (2001). Initial states for the sand are shown for the confining stresses just below the silt arc near the middle of the slopes. This

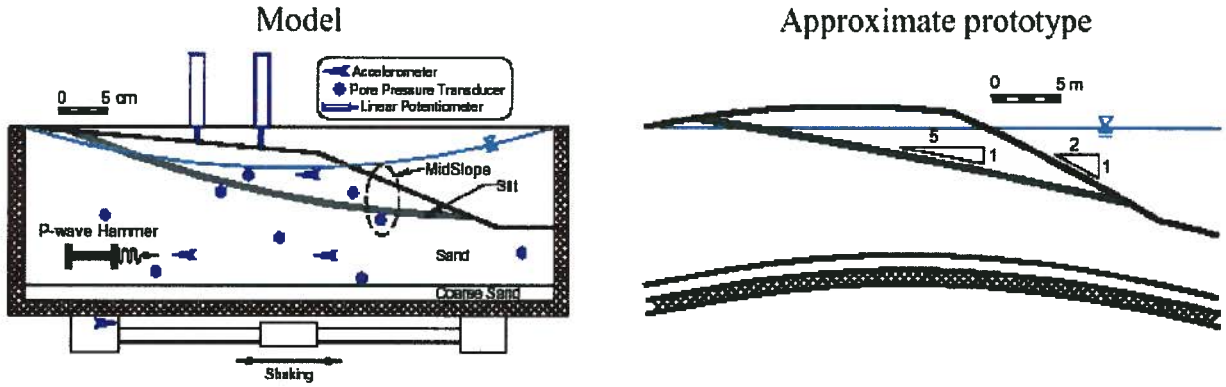

Fig. AII-16: Typical model configuration and prototype equivalent using 1m-radius centrifuge with rigid container of 560 x 280 x 180 mm (Kulasingam et al. 2001).

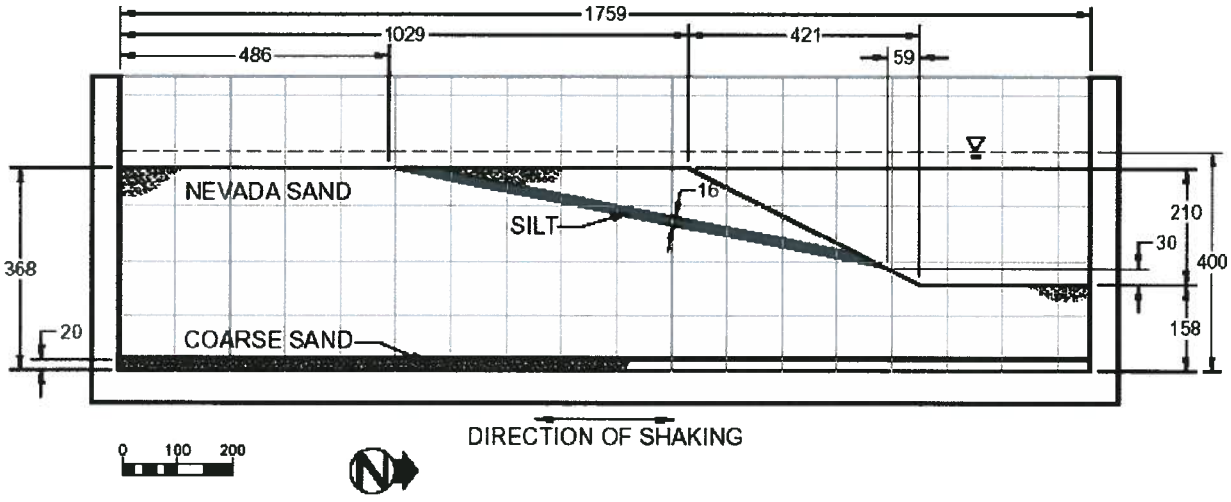

Fig. AII-17: Typical model configuration using 9-radius centrifuge with rigid container of 1759 x 700 x 600 mm (Malvick et al., 2002).

suggests that even the initial D_r = 20% models would be dense of critical and have sufficient undrained shear strength for stability. They inferred that water film formation is the extreme condition of localization that may not manifest during failure of a slope with barrier layer. Kulasingam (2003) back calculated shear strengths using limit equilibrium and Newmark sliding block methods from the models experienced localization and showed that they are much lower than that inferred from the steady state approach. He also argued that the extent to which void redistribution affected the apparent residual strength, S_r in the few case histories that control current empirical procedures is unknown. Thus it is not clear whether these empirical relations are conservative or unconservative in their implicit accounting of void redistribution effects.

Fig. AII-21 shows a typical displacement time history obtained in 1g-shaking table test and centrifuge test. Timing of localization occurrence and the potion of post shaking displacement depend on model configuration and motion characteristics i.e. level of excitation and its duration.

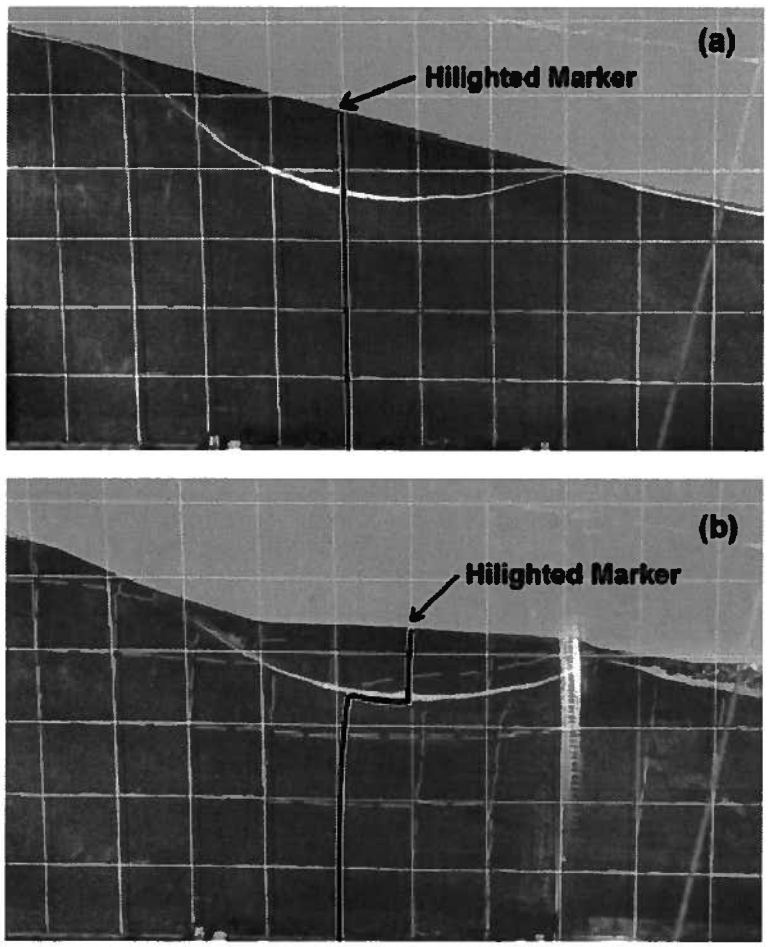

Fig. AII-18: Shake table model (a) before testing and (b) after testing (Malvick et al., 2005).

(a)

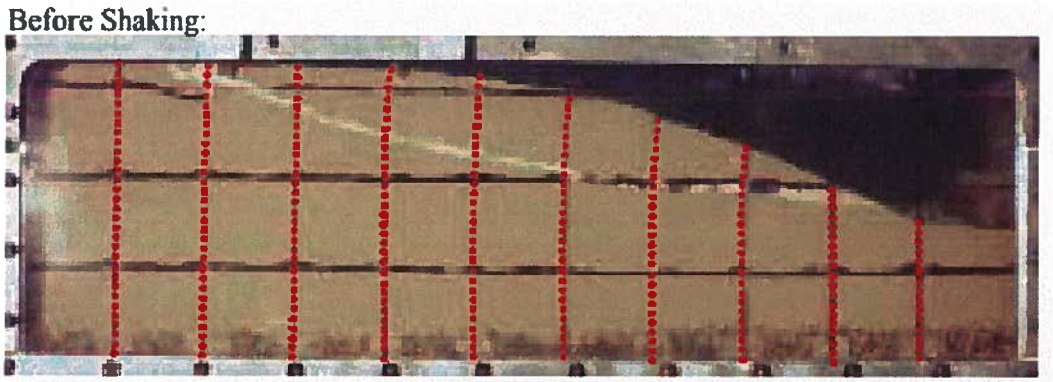

(b)

Photos from test RKS11 ($D_r \approx 50\%$, Sand with Silt Arc).

(c)

Fig. 3 AII-19: Centrifuge model configuration (a) before shaking, (b) after shaking, (c) close up of silt-sand interface after shaking (Malvick et al. 2002).

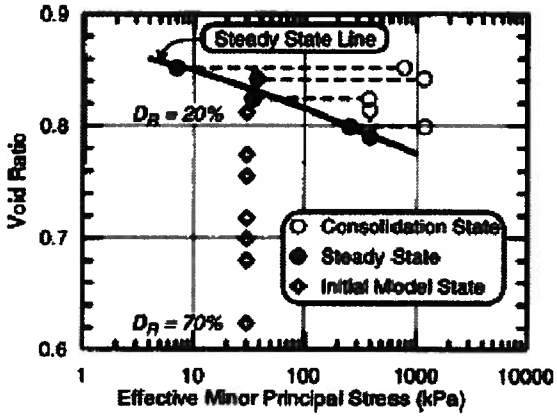

Fig. AII-20: Initial state of sand beneath silt arc at mid-slope relative to steady state line for Nevada sand (Kulasingam et al. 2004).

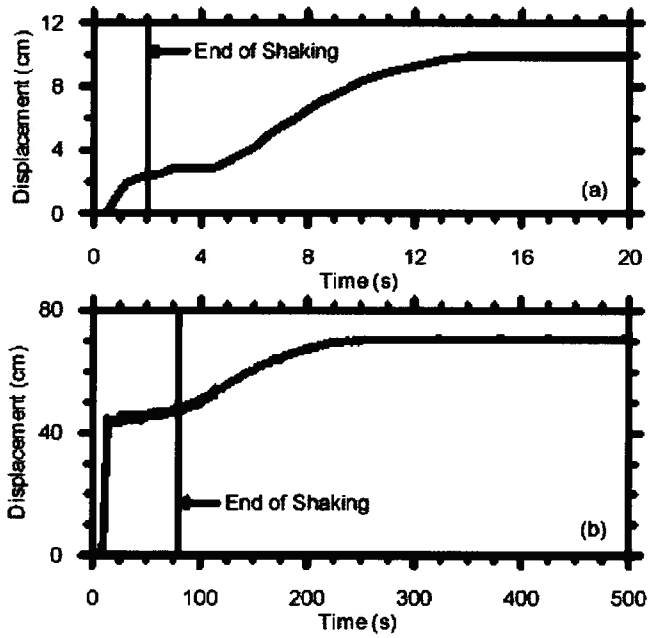

Fig. AII-21: Displacement time history above silt arc in models: (a) a 1-g shake table test and, (b) an 80-g centrifuge test (Malvick et al., 2005).

Malvick et al. (2005) concluded that several key factors including barrier shape, sand relative density, thickness/volume and permeability of liquefied layer, and earthquake characteristics control void redistribution and ground deformations. A summary of their findings are listed in Table AII-3 with a footnote for main references to specific factors. It indicates that looser materials experience larger displacements and more susceptible to localization. It also shows that thicker liquefiable layers aggravate the effect of low permeability sub-layer. The lower permeability of the liquefied layer can increase the potential for localization or water films

to form after shaking. The delays of ground displacement until after shaking were most dramatic when the ground motion was small enough to minimize earthquake-induced deformations but strong enough to trigger high excess pore pressures throughout the slope. They also concluded that the residual shear strength of liquefied soil that would be appropriate for use in a stability analysis does not depend solely on the soil's pre-earthquake state (i.e. density and confining stress), because instability may form along a zone of soil that has become loosened during void redistribution or along interfaces that have trapped water films.

Table AII-3: Findings of Davis U. and Chou U. joint research program on void redistribution

Factor	Influence
Shape of low-permeability barrier[1,2,7,8,11]	• When the shape of the low-permeability layer coincides with a kinematically admissible failure surface, it is more likely to contribute to localization and large deformations.
Relative density of the liquefied layer[1,2,7,11,12]	• Looser soils trigger liquefaction sooner during shaking. • Looser soils experience larger consolidation strains, thereby expelling more water that can drive localization or water film formation elsewhere in the slope. • Looser soils require less water inflow (dilation) at the contact with a low permeability layer before they will localize and/or form a water film. • Looser soils develop larger shear strains during shaking and larger total displacements (includes displacements along localizations or water films). • The magnitude of ground displacement depends on whether or not localization forms with the transition between these cases occurring over a small range of relative density.
Thickness (volume) of the liquefied layer[1,5,7,9,11,12]	• Thicker layers expel more water to drive localization or water film formation beneath an overlying low-permeability barrier layer. • Thicker layers take longer to reconsolidate, which increases the potential for localization or water films to form after shaking.
Hydraulic impedance of barrier layer[1,2,3,6,9] • Permeability contrast between liquefied and barrier soils • Thickness of barrier layer	• The hydraulic impedance of the barrier layer increases with increasing thickness and decreasing permeability. • Greater hydraulic impedance restricts pore water flow across the interface between the liquefied soil and the overlying barrier soil. This allows more water to accumulate, thereby making localization or water film formation more likely.
Permeability of liquefying layer[1,6,7]	• A lower permeability for the liquefied layer reduces the rate of pore pressure dissipation and consolidation, which can increase the potential for localization or water films to form after shaking. • A lower permeability for the liquefied layer reduces the permeability contrast with the overlying barrier layer, and could reduce the potential for water to accumulate at the interface if the contrast is small enough.
Earthquake[1,2,4,5,6,7,9] • Frequency content • Amplitude and duration of motion • Direction of shaking • Shaking sequence and history	• The proportion of the total ground displacement that occurs after shaking depends on how much displacement is induced during shaking versus how much occurs due to pore water flow after shaking. • Delays of ground displacement until after shaking were most dramatic when the ground motion was small enough to minimize earthquake-induced deformations but strong enough to trigger high excess pore pressures throughout the slope. • Larger amplitude and/or duration motions increase shear strains, which increases volumetric strains in the liquefying layer, thereby making localization more likely. • Shaking transverse to the slope direction may reduce inertial stresses down slope which could reduce deformations during shaking. • Prior shaking can increase the cyclic resistance of the liquefying sand, thereby reducing the potential for localization. At the same time, prior shaking can cause loosening below the barrier layer, which increases the potential for localization in subsequent shaking events.

*Specific reference to the factor:

1. Kokusho (1999), 2. Kokusho (2000), 3. Kokusho & Kojima (2002), 4. Kokusho (2003), 5. Kulasingam et al. (2001), 6. Kulasingam (2003), 7. Kulasingam et al. (2004), 8. Kutter et al. (2002), 9. Malvick et al. (2002a), 10. Malvick et al. (2002b), 11. Malvick et al. (2003), 12. Malvick et al. (2004)

APPENDIX III

CASE HISTORIES OF DELAYED GROUND FAILURES

A.III.1 Introduction

A complete list of case histories that failed during past earthquakes with some delay with pore pressure redistribution involvement is presented in this appendix. These cases were referred to in *Chapter 3*. Also additional information for cases that the ground failure was not sever is provided in Table *AIII-1*.

Table AIII-1: Ground failure case histories with void redistribution involvement.

No.	Earth structure	Earthquake [effect]	Geometry and soil conditions	Sequence of events			References
				Time	Event	Observer	
1	Barahona tailings dam, Chile	Talca earthquake, 1928 M_L = 8.2, a_{max} ≈0.12– 0.19g) [Failure of part of the dam resulting in the release of 4 million tons of tailings]	H = 65 m Dam: Fine sands (0.6mm maximum diameter) with about 20% silt content. This is the coarse fraction of the available tailings soils. Tailings: Highly inter-layered silts (very young deposits)	0	Start of main shock	G.W. Soady, engineer in charge of construction, who witnessed the behavior of the dam from his house, located 300m from the dam.	Elorza & Machado 1929; Troncoso et al. 1993
				1 minute and 40 seconds	End of ground motion. Dam did not fail. Illumination system remained working.		
				≈4 or 5 minutes	Sudden failure of the dam. Illumination system went off. Telephone line located about 200 to 300m downstream from the dam was cut almost immediately, indicating a violent failure.		
				4 days	Presence of loose saturated pockets of fine sands and silts, which liquefied when people walked on the beach.		
2	Several embankment dams (< 9), Honshu, Japan	Ojika earthquake, 1939 (M = 6.6, amax = 0.3– 0.4g) [Complete failure]	H = 1.5 – 18 m Sands FC ≈5 - 20%	0	Main shock	Not clear	Akiba & Semba 1941; Seed et al. 1978; Seed 1979
				Few hours – 24 hours	Complete failure		
3	Old slide area in Kirkwood Creek, Montana, U.S.A.	Hebgen Lake, Montana earthquake, 1959 (M = 7.3) [Slide]	Bulk of the slide mass was clay deposits. No detail information on stratigraphy. Area was stable for many years.	0	Main shock No significant movement	Not clear	Hadley 1964; Seed 1968
				After 5 days several weeks	Slide began and moved for about 30 m during this period		
4	Sub-marine slopes Alaska, U.S.A.	Anchorage earthquake, 1964 (M_s = 8.6) Valdez and Seward ports [Slide]	Large scale submarine slide with < 5° slope involving coastal area.	----	-----	-----	Coulter & Migliaccio, 1966; Lemke, 1967; Kokusho, 2003

Table AIII-1: Ground failure case histories with void redistribution involvement (Cont.).

No.	Earth structure	Earthquake [effect]	Geometry and soil conditions	Sequence of events			References
				Time	Event	Source	
5	Lateral spreading in Kawagishi-cho and Hakusan along Shinano river), Niigata, Japan.	Niigata earthquake, 1964 (M = 7.5, a_{max} = 0.16g) [Overturning of buildings due to foundation soil failure and Slide of an area of 250m by 150m, to a maximum distance of 7- 11m]	Mild slope Generally, a sandy clay layer sandwiched between sand layers. Bore hole at Hakusan: A 2 m thick sandy clay sandwiched between a 4 m thick sand layer on top and a sand layer (with sub layers of silty to gravelly sands) extending for more than 25 m at the bottom.	0	Main shock	Eye witnesses account Photos of sand boils and cracks from a high school student.	Kawakami and Asada 1966; Hamada and Shizuoka 1992; Kokusho 1999, 2000; Kokusho and Kojima, 2002; Kokusho 2003
				During shaking (< min)	Slide started		
				After shaking	Slide mass continued to move after the shaking ended Muddy water started to come out of the ground and fissures gradually expanded after the end of shaking.		
				After several minutes	Overturning of a building due to local foundation soil failure		
6	Showa bridge (over Shinano river), Niigata, Japan	Niigata earthquake, 1964 (M = 7.5) [Collapse of bridge due to foundation movements]	Near left abutment: About 1 m of surface soil (fill) overlying 4 m of liquefiable alluvial sandy soil followed by non liquefiable sands extending to 20 m.	During shaking	Bridge did not collapse.	Eye witnesses account	Hamada 1992
				0 – 1 minute after shaking	Five of its simply supported steel girders, each of about 28 m span, fall into the water.		
7	Old slide area in Baker River, Seattle, U.S.A	Seattle earthquake, 1965 (M = 6.5) [Major slide]	H ≈100m θ = 18° Laminated clays and silty clays with inter-bedded members of fine silty sand or clean fine sand; sand members occurred in irregular lenticular deposits.	March, 1964	Signs of sliding, drainage installation work for 14 months, substantial sliding during heavy rainfall periods.	Rainfall data and engineering reports	Peck 1967; Seed 1968;
				April 10, 1965	No movements for all practical purposes.		
				April 20 - 30	10 day total rainfall of 2.5 in. No significant effect.		
				April 29	Strong earthquake. No significant effect.		
				May 4 - 12	10 day total rainfall of 2.0 in. No significant effect.		
				May 15 - 16	10 day total rainfall of 2.6 in. No significant effect.		
				May 17	Movement observed in slide area.		
				May 18	Catastrophic failure.		

Table AIII-1: Ground failure case histories with void redistribution involvement (Cont.).

No.	Earth structure	Earthquake [effect]	Geometry and soil conditions	Sequence of events			References
				Time	Event	Source	
8	Lower San Fernando dam, California U.S.A.	San Fernando earthquake, 1971 (M = 6.6, a_{max} = 0.5 – 0.55g) [Failure of part of the upstream shell]	H = 43 m θ = 21.8° Hydraulic fill silty sand, which was intensely stratified by micro layers from about 0.125 to 0.5 cm thick. FC = 25%	0	Start of main shock of earthquake	Seismoscope recordings at crest (involved in sliding) and rock abutment of this dam, and at Pacoimia dam site	Seed 1979; Seed et al.1989; Castro et al. 1989; Castro et al. 1992; Baziar and Dobry 1995
				14 s	Strong motion completed – slight tilting of dam crest		
				32 - 36 s	After shock 1		
				40 s	Start of slide movements at crest of dam		
				56 - 57 s	After shock 2		
				62 - 63 s	After shock 3		
				72 - 73 s	After shock 4		
				75 - 76 s	After shock 5		
				90 s	End of main slide movement – instrument tilted about 26°		
				> 90 s	Further tilting to about 37° after 10 days		
9	Mochikoshi tailings dams, Japan	Izu – Ohshima –Kinkai earthquake, 1978 (M = 7.0, a_{max} = 0.23g) [Failure of the No.1 and No. 2 dike]	H = 20 m θ = 20.1° Starter dam: lightly compacted soils of volcanic origin; Tailings: Highly inter-layered (3 – 7cm) sandy silt and silt. FC = 80%, with high water content.	Noon	Main shock (M =7.0, failure of dike No. 1)	Surveillants and a caretaker (eye witness)	Ishihara 1984; Ishihara et al. 1990; Wride et al. 1999; Okusa et al. 1984; Marcuson et al. 1979
				Next day 7.31 a.m.	Aftershock 1 (M =5.8)		
				7.36 a.m.	Aftershock 2 (M =5.4)		
				8.30 a.m.	5 – 6 cracks of about 1 – 3 m long and 5 mm wide developed on the down slope face in parallel with the axis of the No. 2 dike		
				9.30 a.m.	A longitudinal crack, opening 5 m long and 5 cm wide in the middle of the down stream slope discovered.		
				10.30 a.m.	Small after shock (M = 4.0)		
				1.00 p.m.	Gradual sinking of the central part of the No. 2 dike followed by the failure.		
10	Sub-marine slopes, Klamath River delta California, U.S.A.	1980 earthquake [2km x 20 km of sea floor became almost flat]	Average slope = 0.25° Sand and mud, Sand boils on sea bottom at 30-70m depth.	-----	----	----	Field et al. 1982; Kokusho, 2003

Table AIII-1: Ground failure case histories with void redistribution involvement (Cont.).

No.	Earth structure	Earthquake [effect]	Geometry and soil conditions	Sequence of events			References
				Time	Event	Source	
11	Landing road bridge foundation and approach road embankment, Whakatane, New Zealand	Edgecumbe earthquake, 1987 (M = 6.3) [lateral spreading of the road embankment]	Alluvial deposits of about 4 m thick loose clean sand overlain by a 1.5m thick clayey silt crust.	0	Main shock Road was passable by car immediately after.	Eye witness account	Berrill et al. 1997, and 2001
				≈ 1 hr.	Road is not passable by car. Cracking and subsidence observed.		
12	One-story building foundation, Guam, US Territory	Guam earthquake, 1993 (Mw = 7.7, Ms = 8.1, a_{max} = 0.2 – 0.3g) [flow failure involving deformations over 5m completely destroyed a small one-story waterfront building]	Loose coral fill consisting of silty sands and gravels, and lagoonal and estuarine deposits of soft clays and loose coralline silts, sands, and gravels.	During shaking	Major part of shaking about 100 people occupying the building exit the structure without any Injury.	Eye witness account	EERI 1995; Mejia and Yeung 1995
				Towards the end of shaking	Building began sliding slowly into the harbor and then collapsed.		
13	Tapo canyon tailings dam, California, U.S.A	Northridge earthquake, 1994 (Mw = 6.7, a_{max} = 0.3 – 0.4g) [flow failure of 60m wide section of the dam]	H_{max} = 24 m Tailings: Stratified layers of soils ranging from fat clays with plasticity indices as high as 30 – 50 to non plastic sandy silts and silty sands.	0	Main shock	A neighbor	Harder & Stewart, 1996
				≈ Few minutes (< 10 minutes) after the main shock.	Rumbling / rushing noises heard (Believed to be the beginning of the flow slide).		
14	Nikawa natural slope, Japan	Hyogoken – Nanbu earthquake, 1995 (M = 7.0) [landslide]	H = 14 m θ = 20 deg. coarse sandy fill FC = 20%	≈ 0 - 20s	Main shock	Eye witness account	Wang et al. 2000; Sassa et al. 1995
				1 to 2 mins.	Second shock and land slide		
15	Sub-marine slopes, Eratini & Eliki, Greece	Aegion earthquake, 1995 (Ms = 6.2, a_{max} = 0.54g) [landslides at 3 sites]	Average slopes = 12%, 17%, 18% & 1%, Continuous interchange between silty sand and clay layers.	0 (duration ≈ 10s)	Main shock	Not clear	Bouckovalas et al. 1999; Hasiotis et al. 2002; Papatheodorou, & Ferentinos, 1997
				Post-earthquake	Land slides		
16	Sub-marine slopes, Southern coast of Izmit bay, Turkey	Kocaeli, earthqyake, 1999 (M_w = 7.4) [slide]	Average slope: 5%	-----	-----	-----	JGS, 1996; Kokusho, 2003

Barahona Tailings Dam, Chile (1928)

One of the earliest recorded occurrences of a slope failure took place after the end of earthquake shaking is the Barahona Tailings Dam failure in Chile. The 1928 Talca earthquake of Richter magnitude 8.2 caused the failure of part of the dam 2 to 3 minutes after the end of shaking, releasing 4 million tons of tailings to flow violently down the Barahona creek. The flowing tailings destroyed railways, highway bridges, and buildings and killed 54 people (Elorza and Machado 1929; Troncoso et al. 1993). Fig. AIII-1 shows the cross section and the failure surface of the Barahona Tailings Dam, which is now referred to as dam No. 1 after reconstruction. This dam was constructed by the upstream method with the foundation work starting in 1917. The upstream dikes of the dam were constructed using the coarser portion (mainly fine sands with a 20% silt content) of the tailings materials. Deposition of the fine tailings (mainly silt) in the pond started in 1921. The deposition method resulted in a highly inter-layered, under consolidated, young slime deposits at the time of the earthquake.

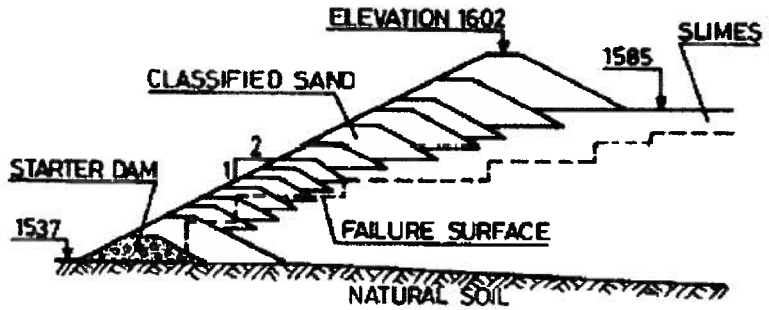

Fig. AIII-1: Cross section of the Barahona tailings dam showing the failure surface (Troncoso et al. 1993). Elevations are marked in m.

A construction engineer witnessed the delayed failure of the 400 m long longitudinal section (located near the left abutment) of the 65 m high dam, from a distance of 300 m from the dam. Fig. AIII-2 shows the shape of the failure surface. The terrace shape of the failure surface may have been the result of the presence or formation of loose horizontal layers in the inter-layered slime deposits. Void redistribution may have played a role in the failure because of the significant delay in the failure, highly inter-layered nature of the tailings soil deposits, and the shape of the failure surface. However, post-shaking creep of finer silt layers of the highly inter-

layered deposits can also result in a terraced shaped failure surface with a delay in the failure initiation. Stress redistribution may have caused the delay also.

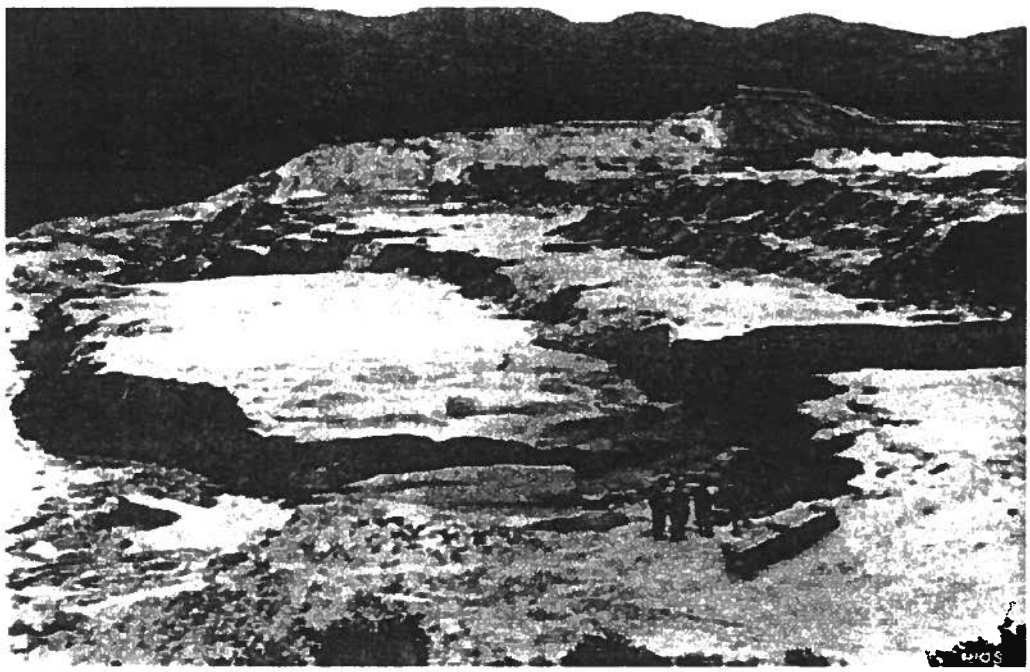

Fig. AIII-2: Photo of the failure zone showing terraces of tailings soils left in place (Troncoso et al. 1993).

Honshu Embankment Dams, Japan (1939)

The Ojika Earthquake of 1939 (magnitude = 6.6) caused severe damage to 74 low embankment dams (heights 1.5 to 18 m) forming reservoirs for irrigation purposes in the northwestern portion of Honshu, Japan (Akiba and Semba 1941; Seed et al. 1978; Seed 1979). Twelve of these embankments failed completely. Three dams which were constructed of clayey sands failed due to the washout of poorly compacted soils and piping related causes. The other nine dams, which failed completely, were constructed primarily of sands (fine contents 5% to 20%). Seed et al. (1978), quoting from the dams' investigation report by Akiba and Semba (1941), pointed out that one of the main conclusion was "there were very few cases of dam failures during the earthquake shaking, most of the failures occurring either a few hours or up to 24 hours after the earthquake". The observed delay in the failures was thought to be possibly

caused by piping through cracks induced by the earthquake or pore pressure redistribution (Seed et al. 1978; Seed 1979).

Old Slide Area, Kirkwood Creek, Montana, USA (1959)

The Hebgen Lake, Montana earthquake (M = 7.3) of 1959 is thought to have caused a slide 5 days after the earthquake in an old slide area in Kirkwood Creek (see Fig. AIII-3), which had remained stable for many years (Hadley 1959; Seed 1968). Seed (1968) described the case history as follows, "This slide area, about 400 ft to 800 ft wide and half a mile long had been stable for many years and showed no significant movement for at least five days following the earthquake. Some after this time, however, it began to slide again and moved about 100 ft in a period of several weeks. The bulk of the soil mass involved was a clayey deposit but little is known of its detailed stratigraphy. No apparent cause of the sliding, other than the earthquake, can be conceived". Seed (1968) also pointed out that liquefaction of sand lenses in clay embankments may initiate creep movements which will cause failure, day to weeks after an earthquake.

Fig. AIII-3: Kirkwood Creek landslide (Photo from the Earth Science Photographs from the U.S. Geological Survey Library, by Joseph K. McGregor and Carl Abston, U.S. Geological Survey Digital Data Series DDS-21, 1995).

Lateral Spreading in Kawagishi-cho and Hakusan, Niigata, Japan (1964)

Yoshida et al. (2005) noted that using aerial photos taken after earthquake and comparing with that of before earthquake revealed earthen flow slides or large lateral spreads at various nearly level-ground sites in Japan and in various earthquakes that had taken place. It was found that liquefaction-induced flow is not an extraordinary phenomenon. They also showed that applying steady state concept to evaluate residual strength of liquefied sand cannot explain the flow failure mechanism.

There were several lateral spreads along the banks of the Shinano River (Hamada, 1992) due to Niigata earthquake. Fig. AIII-4 shows lateral displacement vectors at an area few hundreds meters from the river bank (insignificant free face effect). As may be noted in some locations (designated as 2b and 2c) large displacements (e.g. 4 m) occurred in the directions opposite to the river whereas the slope is less than 1% or less. An area, located between the Echigo railway embankment and the left bank of the Shinano River in Kawagishi-cho, Hakusan district, suffered lateral displacements in the order of 7-11 m towards the river during that earthquake (Hamada 1992; Kawakami & Asada 1966; Kokusho 1999, 2000, 2003; Kokusho & Kojima, 2002, Yoshida et al., 2005). This area had a very gentle slope of less than 1%. The general soil profile in this area consisted of deep deposits of sands with a sandy clay layer sandwiched near the surface. The soil profile at the Hakusan transformer substation consisted of a 2m thick sandy clay sandwiched between a 4 m thick sand layer on top, and a sand layer (with sub-layers of silty to gravelly sands) extending for more than 25 m at the bottom (see Fig. AIII-5). Trenching work reported by Kokusho & Kojima (2002) and Kokosho (2003) showed the continuous nature of the sandy clay layer and additional micro layering within the top sand layer.

Liquefaction and lateral spreading caused the failure of several building foundations in Kawagishi-cho area. Kawakami & Asada (1966) described the case history as follows, "In the area where liquefaction of the ground had been occurred, many reinforced concrete buildings of multiple stories, which were settled or tilted with small breakage, were observed. The subsidence and the tilting of these buildings were not caused by the shear failure of soft ground, and slip plane in the ground or heaving of the ground around the structures could not be found. It took several minutes to overturn an apartment house in Kawagishi-cho, Niigata city, and the directions of the tilting of apartment houses in the area were the same, because this damage had no direct connection with vibration". A photo of Kawagishi-cho apartment buildings after the earthquake is shown in Fig. AIII-6. Lateral spreading occurred in the nearby area, which

included the Meikun High school and the Hakusan transformer substation, too (Kawakami & Asada 1966; Kokusho & Kojima 2002). The area of slide was measured to be 250 m by 150 m, and the maximum displacement was about 7 m. The slide mass continued to move even after the shaking ended (Kokusho 1999). Kokusho & Kojima (2002) reported pictures taken by a high school student suggested that muddy water started to come out of the ground and fissures gradually expanded after the end of shaking. Kawakami & Asada (1966) also described the failure as quite different phenomena from the usual slides of sloping ground in which the movement of upper part of the ground was due to the liquefaction of the inner part of the ground.

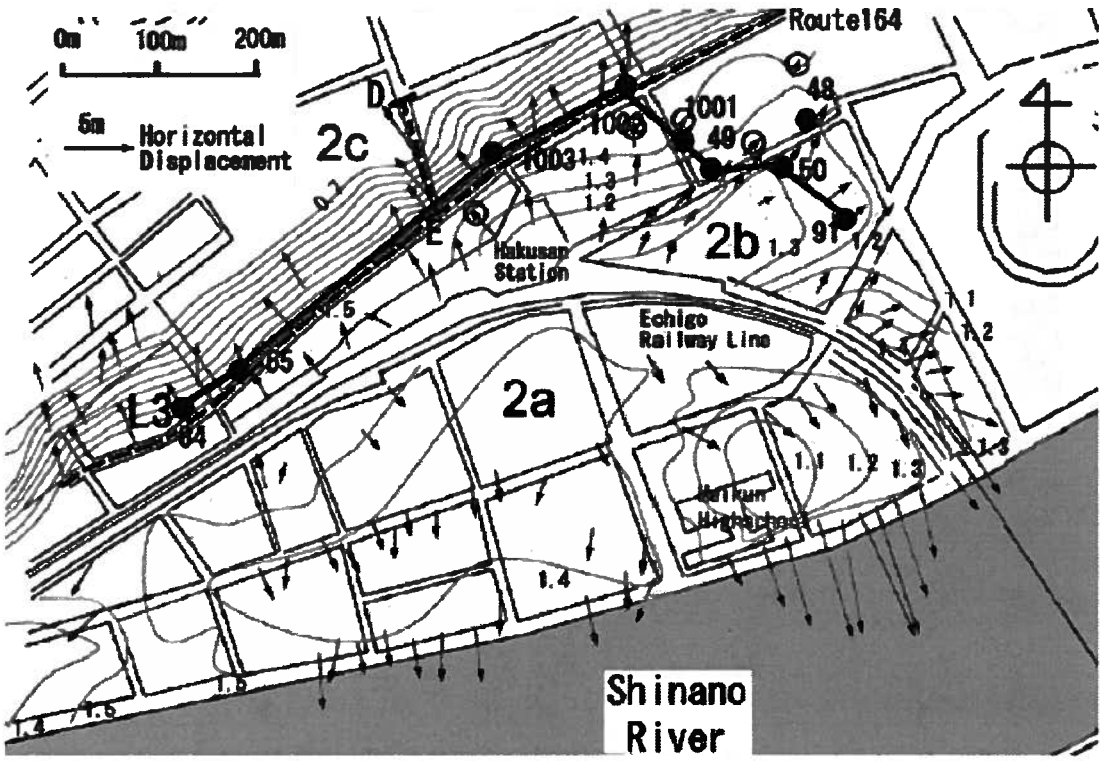

Fig. AIII-4: Lateral displacement vectors at area few hundred meters from the Shinano River in Niigata (Hamada, 1992 and Kokusho, 2003).

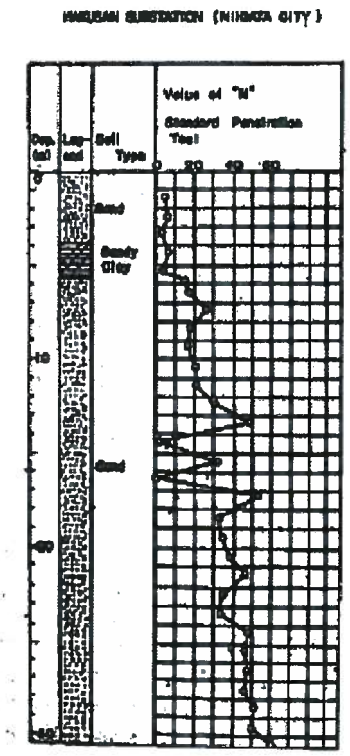

Fig. AIII-5: Soil profile and SPT results from a borehole at Hakusan Transformer Substation, Niigata (Kawakami & Asada 1966).

Fig. AIII-6: Liquefaction-induced bearing capacity failures of the Kawagishi-Cho apartment buildings (USGS, from Kramer, 1996).

Showa Bridge, Niigata, Japan (1964)

The Showa bridge, opened about five months before the 1964 Niigata earthquake (magnitude 7.5), had five of its simply supported steel girders, each of about 28 m span, fall into the water due to the earthquake (Hamada 1992). The Showa Bridge spanned across the Shinano River (Fig. 3-40). The left bank of the river moved about 4 m towards the river, whereas the movements of the right bank were very small in the area of the bridge due to the earthquake. Structural engineers had attempted to explain the failure on the basis of dynamic structural response. Hamada (1992) examined the geotechnical issues involved in the failure and expressed the case as: "Reliable eyewitnesses reported that the girders began to fall somewhat later, perhaps about 0 to 1 minute after the earthquake motion had ceased. When the earthquake motion started, many people and vehicles were on the bridge, but no lives were lost in spite of the catastrophic collapse. This suggests that there was enough time for people on the bridges to seek refuge on the banks. A taxi driver remarked that he was driving near the center of the bridge when the earthquake motion started. He immediately stopped his car on the bridge and waited for the motion to cease. After the earthquake motion abated, he ran to the left bank. Another eye witness on one bank said that damage to the revetment on the left bank of Showa Bridge began after the earthquake".

According to Hamada (1992) the failure was caused because, "The ground on the left bank and in the riverbed liquefied as a result of the earthquake motion and moved toward the river center. The ground displacements continued even after the earthquake motion ceased, probably until the excess pore water pressure dissipated. The permanent ground displacement on the left bank reached several meters, substantially deforming the foundation piles and causing the girders to fall". The deformed shape of a steel pipe pile that was extracted after the earthquake (diameter 60.9cm) suggests lateral spreading occurred in the upper 7–8m. The delayed nature of the failure suggests that the failure did not take place under locally undrained conditions. However, it is difficult to speculate on the possibility of void redistribution because data about the possible inter-layering in the alluvial sand are not available. Fig. 3-41 shows geotechnical cross section along the bridge. Kokosho & Fujita (2002) using field data from Niigata city examined different possible mechanisms responsible for large displacements in such very gentle slopes (less than 1%) and concluded that water migration to low permeability sub-layer base was the controlling mechanism in these failures. Kokosho (2003) in his proposed

correlation for flow lateral displacement for gently sloping ground (less than ≈1.5%) predicted up to 5m displacement based on data obtained from Niigata city case.

Fig. AIII-7: Collapse of the Showa Bridge (Steinbrugge Collection, Earthquake Engineering Research Center, University of California, Berkeley).

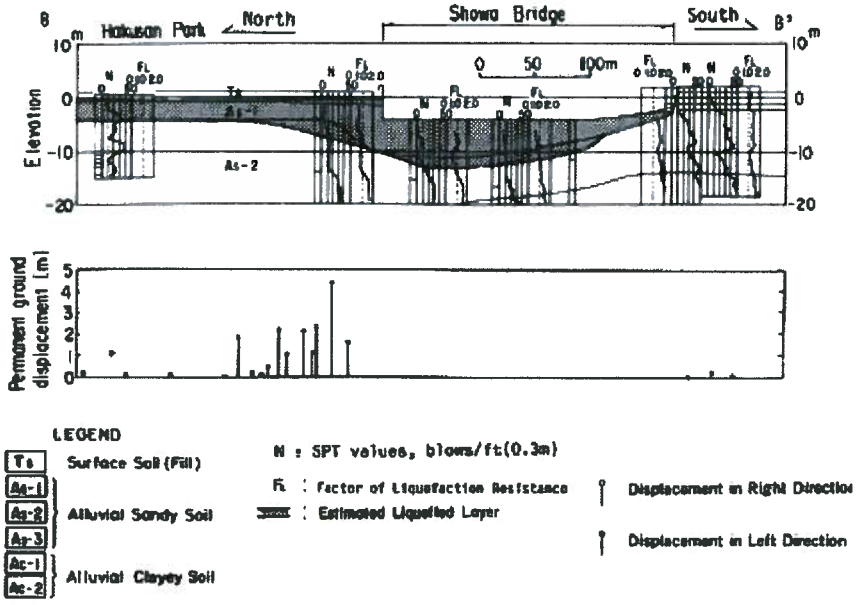

Fig. AIII-8: Soil profile in the Showa Bridge site (Hamada, 1992).

Old Slide Area in Baker River, Seattle, U.S.A (1965)

Peck (1967) described an interesting slope failure case history that he referred to as "the death of a power plant" to symbolize the destruction of the power plant caused by the failure of an old slide area in Baker River, Seattle (Fig. AIII-8). The slide area, which had a history of soil movements, was stabilized by drainage installation and remained stable for more than a year during which there were some heavy rainfall events. The soil profile consisted of laminated clays and silty clays with interbedded members of fine silty sand or clean fine sand, as shown in Fig.AIII-9. The sand members occurred in irregular lenticular deposits. The Seattle earthquake (M = 6.5, April 29, 1965) was perceptible to people on the slide area. However, no movements were observed at that time. After the earthquake there were two significant rainfall events from May 4 – 12 and May 15 – 16. There were no movements observed immediately after these events. However, some movements were observed on May 17, and the catastrophic failure occurred on May 18. Peck (1967), who worked as a consultant in the project described the failure a "On the morning of May 18, the entire hillside appeared to join in one major mass movement that spilled debris over the rock face behind the powerhouse so rapidly that it could not be removed. The emergency measures were invoked and within the day the powerhouse was completely destroyed. The activation of the slide on a scale far beyond that previously experienced, following a period of very mild precipitation compared to that in January and December, was unexpected by all parties concerned". Peck (1967) and Seed (1968), who summarized this case history, wonder whether the earthquake could have been a factor in the failure. Seed (1968) wrote about this case and the Kirkwood Creek slide, Montana, that "Clearly, it is impossible to say that liquefaction of sand lenses due to earthquake activity led to either of the slope failures discussed above. Numerous other possible causes of movements may be postulated but the fact that several instances of post-earthquake slope movements, occurring within several weeks of a significant earthquake, have been reported raises the possibility that liquefaction of sand lenses may have contributed to the development of these events".

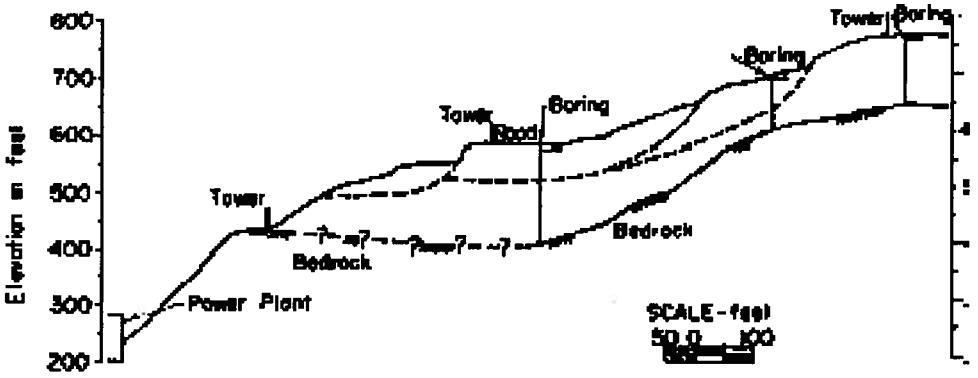

Fig. AIII-8: Section through Lower Baker River slide on February 9, 1965, before final catastrophic movements (Peck, 1967).

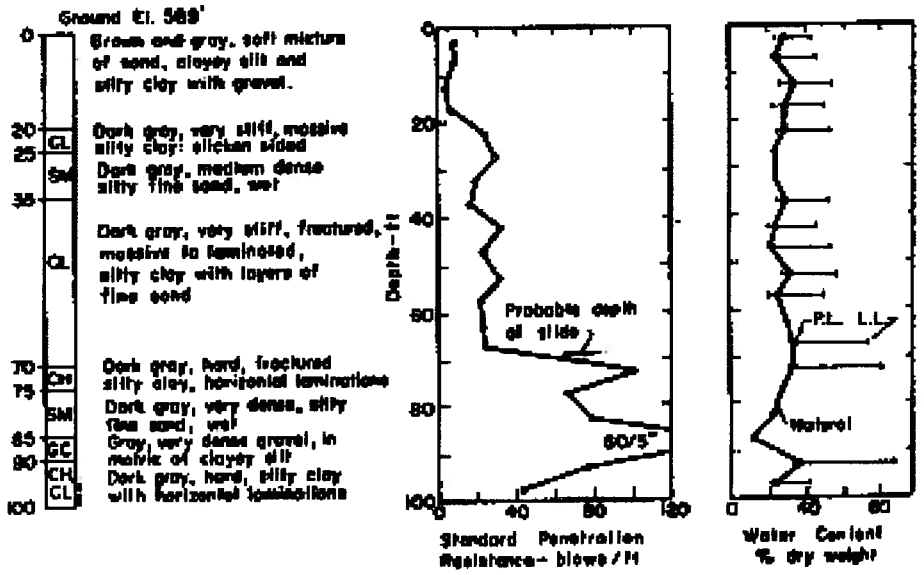

Fig. AIII-9: Borehole data near the central part of Lower Baker slide area (Peck, 1967).

Lower San Fernando Dam, San Fernando, U.S.A (1971)

The 1971 San Fernando earthquake (M = 6.6) caused the failure of part of the upstream slope of the Lower San Fernando Dam (e.g. Seed 1979). The crest moved about 1m-1.5m towards reservoir as reported by Harder et al. (1989) and settled vertically up to 1m (see Fig. AIII-10). Eighty thousand people living downstream were immediately ordered to evacuate and the water level of the reservoir was brought down without any further sliding. This failure became one of the most studied and well-documented geotechnical case histories ever (e.g. Seed et al. 1975; Seed 1979; Seed et al.1989; Castro et al. 1989; Castro et al. 1992; Baziar & Dobry 1995).

Seed (1979) reported that the slide movements started approximately 25 seconds after the end of strong shaking based on seismoscope recordings at the crest (involved in sliding) and rock abutment of this dam, and at the Pacoimia dam site. Fig. AIII-11 shows the liquefied zone in the lower section of the upstream shell of the embankment involved in the slide. The soils involved in the slide consisted of hydraulic fill silty sand, which was intensely stratified by micro-layers from about 0.125 to 0.5 cm thickness (see Fig. AIII-12).

Fig. AIII-10: Flow failure of the upstream slope of the Lower San Fernando dam (Steinbrugge collection; EERC, Univ. of California, photo from Kramer, 1996).

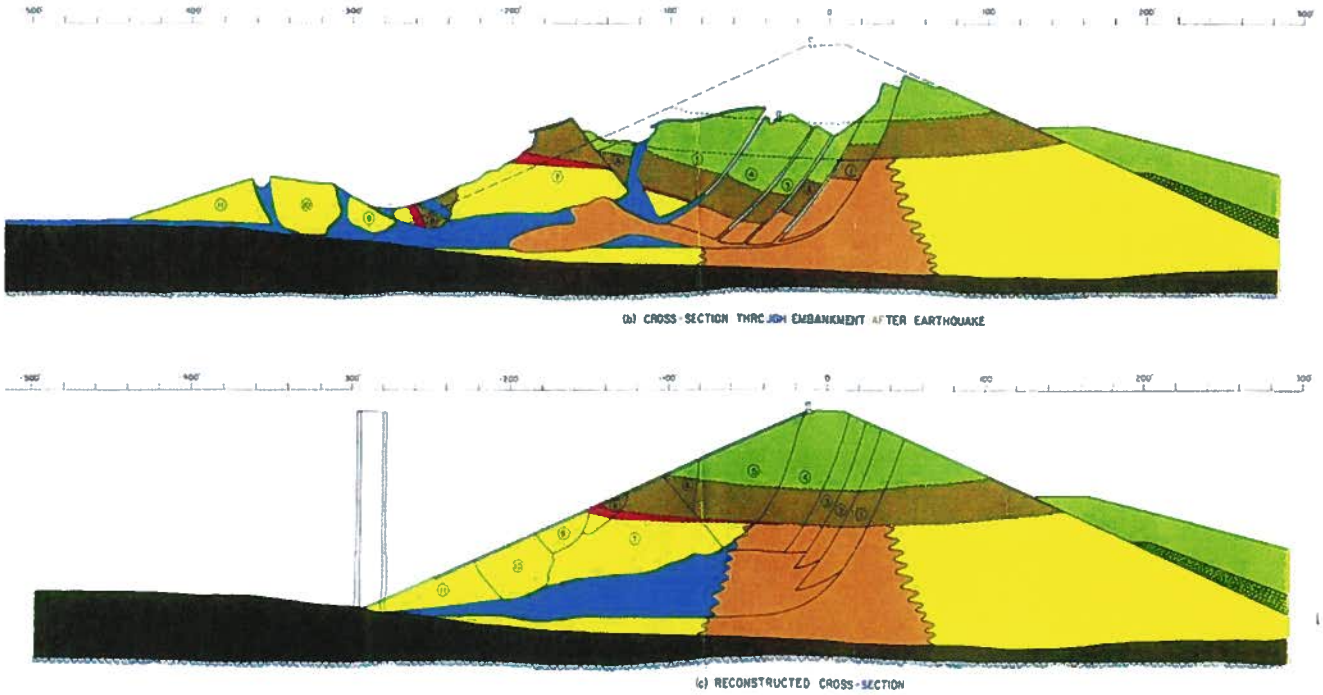

Fig. III-11: Cross section of the Lower San Fernando Dam (a) after failure; and (b) schematic reconstruction of the pre-failure section (Seed et al., 1989).

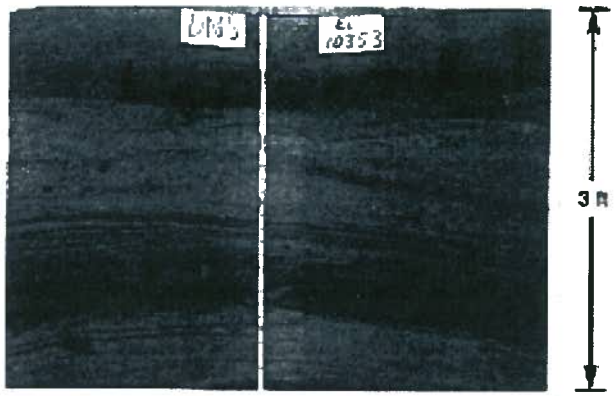

Fig. AIII-12: Micro layering in hydraulic fill, downstream shell of the Lower San Fernando Dam (Castro et al., 1989). Note that soil conditions in the upstream and downstream shells were very similar.

Several theories have been put forward to explain the delayed failure. Seed (1979) explained the delayed failure based on pore water redistribution leading to progressive failure. A later detail studies reported by Harder et al. (1989) showed that the SPT-N value, of the liquefied soil represent essentially a medium dense material with $(N_1)_{60}$ = 13 this value increases when fines content correction is applied (Beaty, 2001). This may imply that enough residual strength was available to prevent such flow failure. This increases the likelihoods of void redistribution mechanism involvement in this failed case. This mechanism of the delay in the slide was proposed by Seed (1979) also as "formation of looser lenses due to void redistribution within the liquefied, highly stratified hydraulic fill silty sand could have also led to a delayed initiation of the failure".

Mochikoshi Tailings Dams, Japan (1978)

Izu-Ohshima-Kinkai earthquake (M = 7.0) of 1978 in Japan caused the failure of two tailings dams in Mochikoshi gold mine, resulting in the release of large volumes of tailings (Ishihara 1984; Ishihara et al. 1990). The tailings, containing sodium cyanide, contaminated a stream to a distance of 30 km (Marcuson, 1979 and Marcuson et al. 1979). One of the dams, dike No.1, failed during the earthquake, whereas the other dam, dike No. 2, failed almost 24 hours after the earthquake. This case has also become a classic example to examine the validity of numerical procedures (e.g. Jitno & Byrne 1995; Olson, 2001; Byrne & Seid-Karbasi, 2003 and Seid-Karbasi & Byrne, 2004).

Fig. AIII-13 shows cross section of the dike No. 2, it also shows tailings surface before and after failure. As Ishihara (1984) reported, the starter dam was constructed in 1964 by placing soils of volcanic origin. The weight of the transporting bulldozers was thought to have compacted these soils. As the mining operations started the tailings were deposited in the ponds, and the dike was raised by placing local volcanic soils by upstream filling method. Fig. AIII-14 shows typical log of a borehole drilled at the middle of the dike No. 2 three weeks after the earthquake. The resulting tailings deposits were highly stratified (3 – 7 cm thick) sandy silt and silt (see Fig. AIII-15) with about 80% fines content with water content greater than liquid limit. The main shock of the earthquake occurred around noon. This was followed by smaller after shocks. Two after shocks of magnitudes 5.8 and 5.4 occurred the next morning around 7.30 a.m. Surveillants noticed cracks in the down stream slope around 8.30 a.m. and the dike failed around 1.00 p.m. Ishihara (1984) argued that the delayed failure occurred because of the rise in phreatic

surface due to pore water pressure migration and made an attempt to analyze it. The delay in the failure and the heterogeneous layered nature of the tailings indicate barrier effects of relatively low permeability sub-layers. Seid-Karbasi & Byrne (2004) with reference to tailings stratification and their high water content (greater than liquid limit) brought up other possible mechanisms i.e. mixing and sensitivity that can aggravate this failure initiated due to void redistribution.

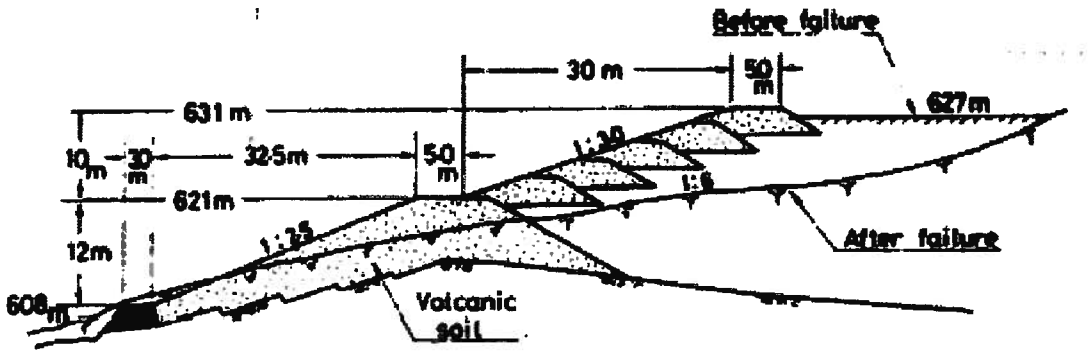

Fig. AIII-13: Cross-section of the Mochikoshi dam No. 2 showing ground profile pre and post failure (Ishihara, 1984).

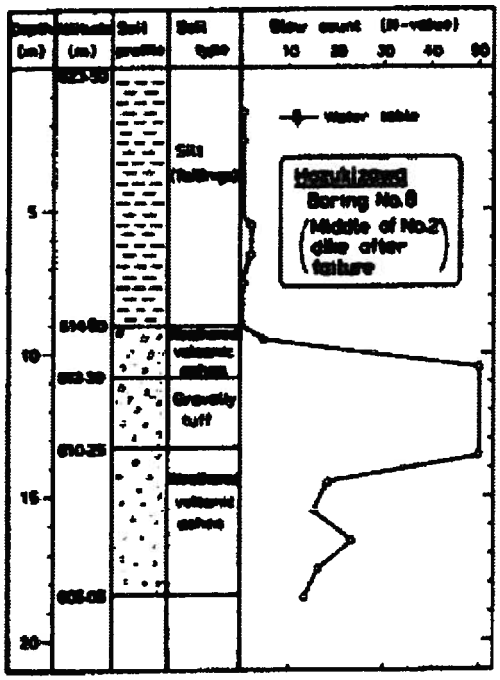

Fig. AIII-14: Soil profile and SPT blow counts at middle of the dike No. 2 after failure (Ishihara, 1984).

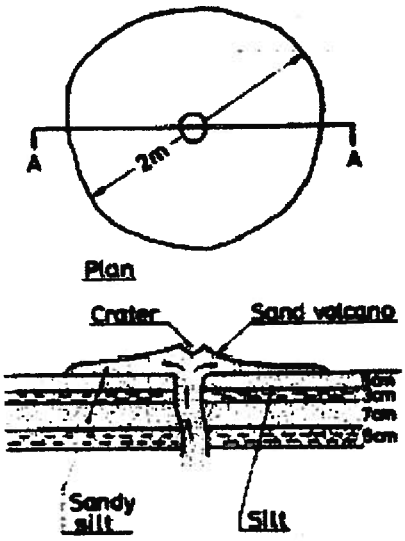

Fig. AIII-15: Cross section of a sand volcano formed on the surface of the disposal pond (Ishihara, 1984).

Lateral Spreading at Landing Road Bridge Site, Whakatane, New Zealand (1987)

Lateral spreading along the Whakatane River caused damage to the approach road embankment to the Landing Road Bridge and to the pile foundations of the bridge due to the Edgecumbe earthquake (ML = 6.3) in New Zealand (Berrill et al. 1997, and 2001). Cracking and subsidence of the ground were observed near the north abutment after the earthquake. Berrill et al. (2001) observed, "The cracks were oriented parallel to the river channel except immediately beside the bridge, where they swung around to meet the bridge axis at approximately 45°". Using crack widths measured from photos, the lateral displacement at the riverbank was estimated to be 1.5 – 2.0 m (Berrill et al. 1997, and 2001). The soil profile shown on Fig. AIII-16 consisted of alluvial deposits of about 4 m thick loose clean sand overlain by a 1.5 m thick clayey silt crust. The loose sands were underlain by non-liquefiable dense sand and gravel. The water table was located about 1.5 – 2.0 m below the ground surface. Berrill et al. (2001) reported, "An eyewitness stated that the road was passable by car immediately after the main earthquake, but one hour later he could no longer drive over it. This observation suggests that failure of the road embankment took place under static conditions, as a front of pore pressure migrated upwards from the static water table into the silty crustal stratum, weakening it to the point where it could no longer support the 4 m high road way embankment". The possibility of loosening due

to void redistribution at the interface between these two layers and resulting interface slip is a possible mechanism for the delayed lateral spreading (see Fig. AIII-17).

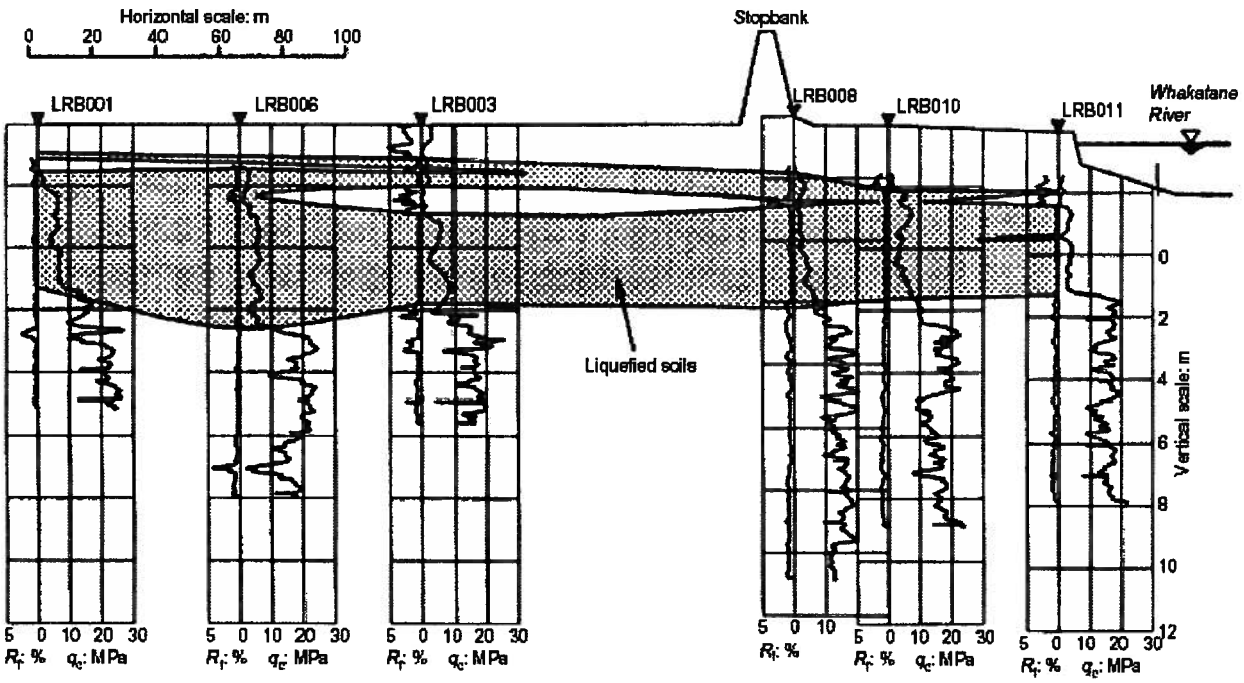

Fig. AIII-16: Cross section showing soil conditions near the bridge site. The shaded region is the estimated zone of liquefied soils (Berrill et al., 2001).

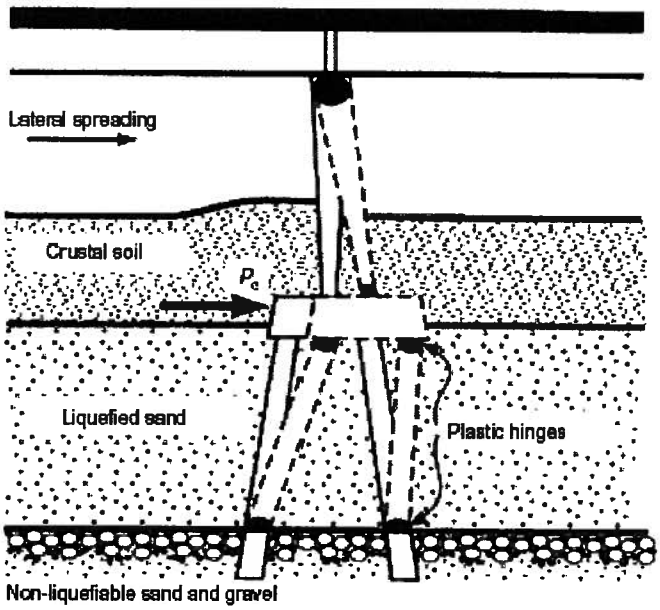

Fig. AIII-17: Substructure collapse mechanism (Berrill et al., 2001).

One-story Building Foundation, Guam, US Territory (1993)

The Guam earthquake (1993) of moment magnitude 7.7 (M_w = 7.7, M_s = 8.1) caused liquefaction and lateral spreading damages along the coast of the island of Guam (EERI 1995; Mejia & Yeung 1995). No ground motion recordings were made in Guam during the earthquake. Estimates of maximum accelerations ranged from 0.20 – 0.30 g for the areas near this site. The rupture propagation lasted about 32 seconds (EERI 1995). The estimated duration of ground motion was 30 to 60 s (EERI 1995). The soil profile consisted of loose coral fill consisting of silty sands and gravels, and lagoonal and estuarine deposits of soft clays and loose coralline silts, sands, and gravels (Mejia & Yeung 1995).

Fig. AIII-18: Damage to Andy's Hut due to liquefaction and lateral spreading (EERI, 1995).

Reconnaissance reports by EERI (1995), and Mejia & Yeung (1995) describe a lateral spreading failure involving deformations over 5 m, which completely destroyed a small one-story waterfront building called Andy's hut at Polaris point. EERI (1995) reported, "Approximately 100 patrons were inside Andy's Hut, a one-story structure that severed as an enlisted men's canteen, at the time of the earthquake (Fig. AIII-18). The building is located

directly adjacent to the harbor on two sides, with the ground retained along the shoreline by a deteriorating cantilevered steel sheet-pile seawall. Liquefaction occurred in the area beneath the building, causing lateral ground spreading that carried the structure and the seawall into the harbor, partially collapsing the building. The structure was constructed with a steel joist roof supported on concrete-block and rubble bearing walls that were badly damaged. Miraculously, no one was killed or severely injured, although the original ground surface and the structure it supported dropped roughly 1 to 1.5m and was below water in the worst affected areas". Mejia & Yeung (1995) commented on the timing of the failure that, "Reportedly, the building began sliding slowly into the harbor towards the end of the shaking, which allowed patrons to exit the structure before it collapsed". Void redistribution, after shocks, momentum and progressive failure are all possible reasons for the observed delay in initiation of the slide.

Tapo Canyon Tailings Dam, California, U.S.A

The 1994 Northridge earthquake of magnitude (Mw) 6.7 caused the flow failure of the Tapo Canyon Tailings Dam (Harder & Stewart 1996). The dam, with a maximum height of 24m, failed completely along a 60m wide section. The resulting displacements of two sections of the dam were up to 60 m and 90 m respectively. Harder & Stewart (1996), described the timing of the failure as follows, "During an interview nine days after the earthquake, a neighbor indicated that rumbling/rushing noises were heard a few minutes after the main shock, and the neighbor believed that this was beginning of the flow slide (see Fig. AIII-19 and Fig. AIII-20). The neighbor estimated that the elapsed time between the main shock and the rumbling noises was less than 10 minutes".

Harder & Stewart (1996) reported, "Rock ridges and cut slopes appear to have formed the early pond enclosure on the northern side, southeastern side, and southern corner of the pit. On the southwestern side, mine waste was apparently spoiled or piled in the dry to make wide embankments to form the early portion of the enclosure on this side of the pit". Additional stages of embankment were apparently added by upstream method of filling. The failure was thought to have resulted from the liquefaction of the tailings and possibly the embankment also. Harder & Stewart (1996) described the soil conditions in Pond No. 6, which was involved in the failure as follows, "Pond No. 6 was used to settle out fines washed out of the sand and gravel aggregate obtained during the mining process. The fines were conveyed in suspension by water flowing in trenches to the pond site. Within the pond, the fines would settle out and the water would be

reclaimed for further use by means of pumps floating on rafts. Most of the fines and resulting tailings exposed near the surface of Pond No. 6 showed the presence of sandy soils as well. The tailings apparently consisted of stratified layers of soils ranging from fat clays with plasticity indices as high as 30 – 50 to non plastic sandy silts and silty sands". Void redistribution could have played a role in the failure of the Tapo Canyon Tailings Dam as indicated by the stratified nature of the tailing deposits and the delay in the failure.

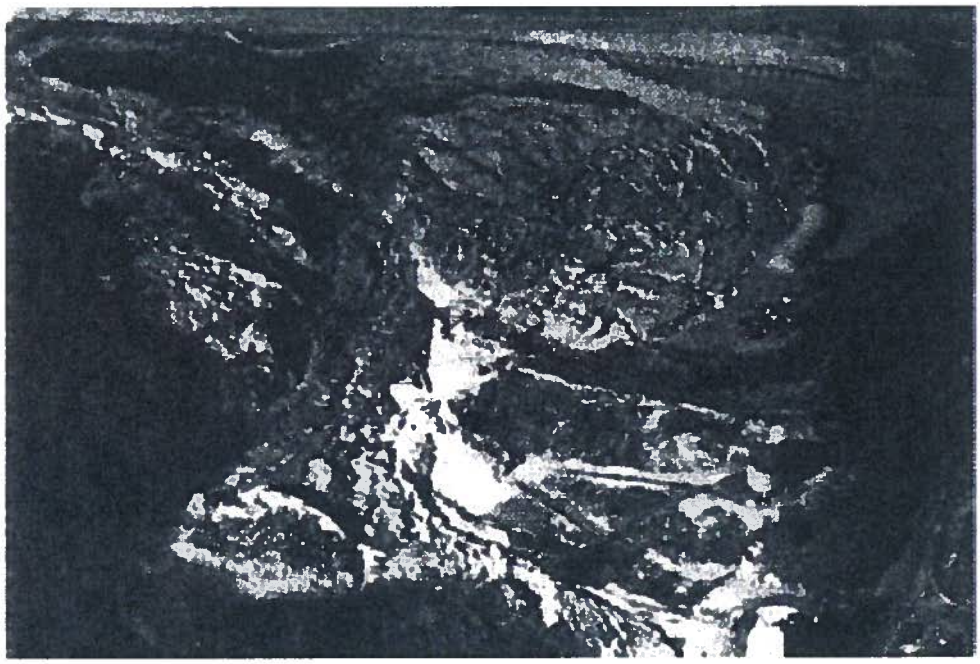

Fig. AIII-19: Aerial view of the failure (taken from Harder & Stewart, 1996; Photo originally by Yoshi Moriwaki, Woodward-Clyde Consultants).

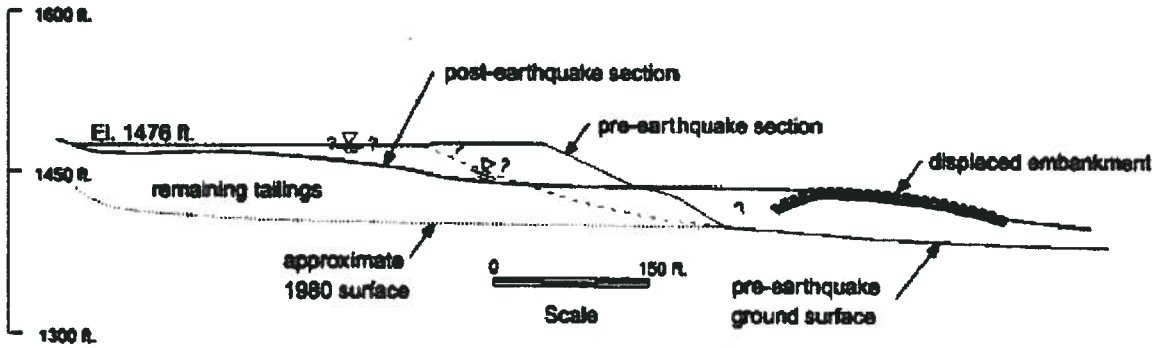

Fig. AIII-20: A section of the failed tailings dam (Harder & Stewart, 1996).

Nikawa Natural Slope, Japan (1995)

The Nikawa landslide shown on Fig. AIII-21 destroyed 11 houses and killed 34 people during the Hyogoken-Nambu (1995) earthquake (M = 7.0) in Japan (Wang et al., 2000). The landslide volume was 110,000 – 120,000 m3, and the moving distance was 175 m (Sassa et al., 1995). Wang et al. (2000) reports, "Concerning the time of the landslide, Mr. Tsunehito Tanaka, a witness who lived near the Nikawa landslide said: "the announced occurrence time of the Hyogoken-Nambu earthquake is from 5:46:51.6 on the morning of January 17, 1995. The occurrence time of the landslide was one or two minutes later. I can also remember there were two strong shocks of the earthquake. It is difficult to tell the exact time of the landslide; I can just say that the landslide occurred as soon as the second shock of the earthquake came".

The investigations revealed that the landslide occurred in the sandy fill. The sandy fill consisted of distributed Osaka group layer (Fig. AIII-22). The lower part of this layer was saturated by ground water. Wang et al. (2000), after performing laboratory tests to investigate the landslide, concluded, "after the slope failed due to the peak stress in the main shock, shear displacement was generated along the shear zone. Because the Osaka group coarse sandy soil is easily crushed, under the undrained condition, the grain crushing resulted in the built-up of excess pore water pressure. With the high excess pore pressure and the resulting low shear resistance, the long run-out landslide occurred". It is difficult to speculate on the role of void

Fig. AIII-21: Photograph of the Nikawa landslide (adapted from Kulasingam, 2003).

redistribution in this failure.

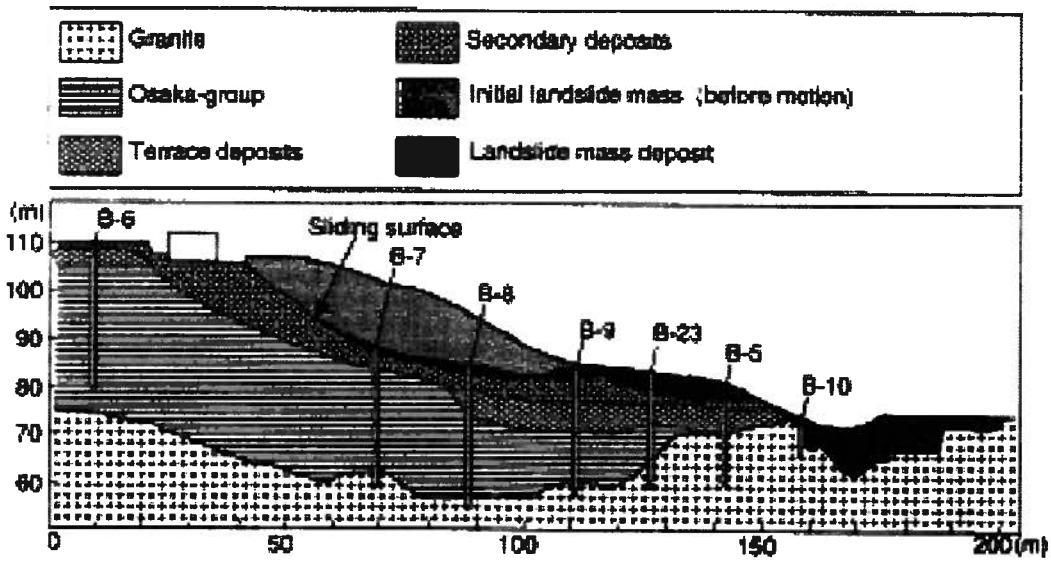

Fig. AIII-22: Geological section of the slide area (Sassa et al., 1995).

Sub-marine Landslides, Eratini, Greece (1995)

The 1995 Aegion earthquake of magnitude (Ms) 6.2 caused intense ground failures in Eratini, Greece (Bouckovalas et al. 1999). Of particular interest are damage at four sites, one within the fishing harbor of Eratini and three along the nearby 2 km beach. The coastline advanced 5 to 15 m inland in these sites. Bouckovalas et al. (1999) described the failures as follows, "Submarine geophysical surveys have showed that, in three of the above sites, the earthquake caused extensive landslides accompanied by debris flows and block rotations (see Fig. AIII-23). Reconstruction of the pre-earthquake topographic profiles along the main axis of the landslides indicates that the failure zones extended to a maximum depth of 6 to 10 m within the loose alluvial deposition, which covered the seabed. Geotechnical exploration, based on static cone penetration with skin friction measurement, revealed that the soil profile at the failure sites is characterized by a continuous interchange between silty-sand and clay layers. This profile favors the development of excess pore pressures, which may remain trapped within the clay-sealed silty sand layers for a long time after the end of shaking. Thus, zones of reduced shear

resistance are created into the soil leading to static massive failure, even for relatively small surface gradients".

Some key points they summarized about this failures are the occurrence of post-earthquake failures in gentle slopes with static factor of safety as high as 2.0, and triggering of these failures by the excess pore pressure build in very thin silty sand layers, with average thickness between 0.24 and 0.36 m. The details of this case history suggest that void and pore pressure redistribution played a role in the failure mechanism.

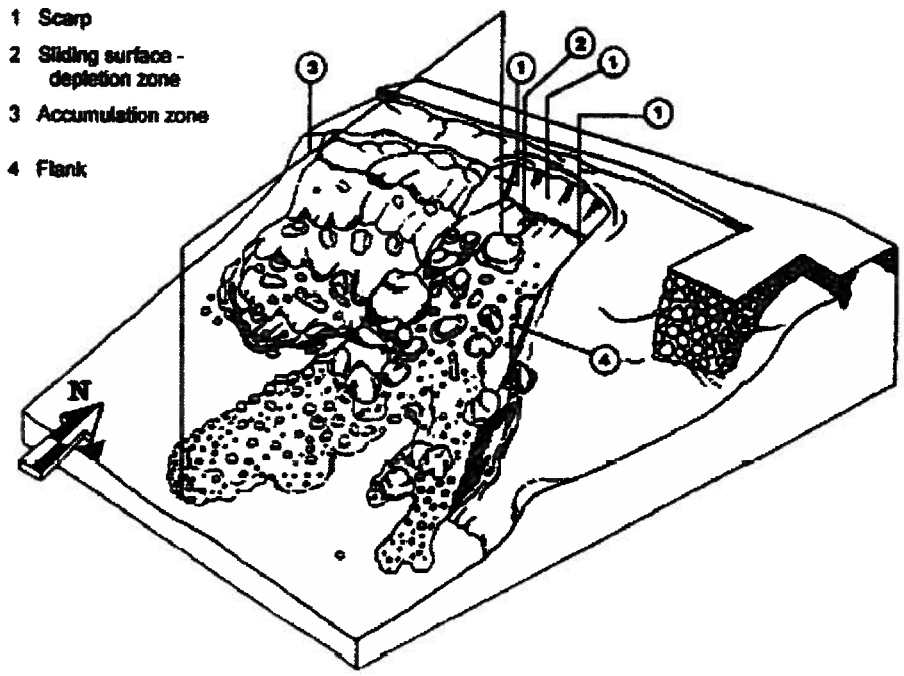

Fig. AIII-23: A "3-D perspective of a typical earthquake-induced landslide at Eratini Gulf" (Bouckovalas et al., 1999).

Table A-2: Additional ground failure cases with void redistribution involvement.

No.	Earth structure	Earthquake [effect]	Geometry and soil conditions	References
1	Flood plain at River Park, Brawley, Imperial Valley, California, U.S.A	Imperial Valley earthquake, 1979 (Mw = 6.5) Westmorland earthquake, 1981 (Mw = 5.6) [Liquefaction, Sand boils, and possible formation of a loose sand layer beneath a low permeability layer]	Mild slope Approximately 1 m thick clay and clayey silt deposit sandwiched between a 2 m thick silt and sandy silt top layer and a pint bar bottom sand layer, which is more than 8 m thick.	Youd & Wieczorek, 1982; Youd 1984
2	Mildly sloping ground at Pence Ranch, Borah Peak, Idaho, U.S.A	Borah Peak, Idaho earthquake, 1983 (Ms = 7.2) [Lateral spreading, Differential settlements, Cracking, Boiling]	Mild slope The soil profile consisted of a 1.5 – 2.5 m thick liquefiable loose clean sandy gravel (GP) overlain by a 0.5 - 0.75m thick fine silty sand (loess, SM, non plastic) top layer. The low permeability top cap was as thick as 1.4 m at some local locations. Dense gravels were found below the liquefiable gravel layer to significant depths.	Youd et al. 1985; Andrus et al. 1991; Dobry & Liu, 1992
3	Mildly sloping ground at Wildlife site, Imperial Valley, California, U.S.A	Superstition Hills earthquake, 1987 (Mw = 6.5) [Liquefaction, Sand boils, and lateral spreading with displacements up to 230 mm towards the Alamo River]	Mild slope The soil profile consisted of 2.8m of silt underlain by a 4.0m thick liquefiable sandy silt (looser upper sub-unit and medium dense lower sub-unit). This is underlain by 6.8 m of medium to stiff clayey silt. A layer of dense silt is found below this.	Youd & Bartlett, 1988; Holzer et al., 1989; Dobry et al., 1989; Dobry et al., 1992

Liquefaction at River Park near Brawley, Imperial Valley, California, U.S.A (1979)

Youd (1984) described case histories of possible re-liquefaction due to recurrence of earthquakes in the same area. He described the re-liquefaction case history at River Park, Brawley as follows, "In southern California, several sand boils with deposits about 2 m in diameter erupted on the floodplain of the New River north of Brawley during the 1979 Imperial Valley earthquake (Ms = 6.6) (Youd & Wieczorek 1982). These same sand boils reactivated slightly during the 1981 Westmorland earthquake (Ms = 6.0), producing 15-cm diameter spots on the tops of the previous deposits. These rejuvenated sand boils were at the fringe of the zone within which liquefaction effects occurred during the 1981 event". Youd (1984) described the possibility for the development of a looser sand layer below a low permeability clay and clayey

silt layer, due to liquefaction as follows, "Where drainage from the top of a layer is restricted, compaction from the bottom up can cause a loose, readily liquefiable zone to form at the top of the layer which may persist through many earthquakes until compaction is complete. A site where field evidence indicates that such a loosened layer has developed is River Park in Brawley, California. Cone penetration data from the site reveal a loose zone at the top of the buried layer of sand several meters thick (see Fig. AIII-24). The sand layer is overlain by 0.9 to 1.5 m of clay which in turn is overlain by 1.8 to 2.5 m of silt and sandy silt. Cone penetration resistance in the loose zone is as low as 10 kg/cm^2 but within a meter below it exceeded 100 kg/cm^2 indicating dense sand at that depth. The upper part of the sand layer liquefied during the 1979 Imperial Valley earthquake, producing hundreds of sand boils and a slump near a river at the west margin of the site. The loose zone most likely developed as a consequence of liquefaction and reconsolidation of the sand layer during past earthquakes with compaction beginning at the bottom of the layer and the expelled water collecting at the top of the layer beneath the impermeable clay. The loosened condition was maintained during the 1979 earthquake, and the penetration data indicate that the zone remains highly susceptible to re-liquefaction. The compaction behavior of this layer is probably typical of many granular layers in seismic zones".

This site did not show any evidence of liquefaction due to the 1987 Superstition Hills earthquake as noted as follows by Dobry et al. (1992), "After the 1987 earthquake, Holzer (1990) examined the same sites for which Youd & Wieczorek (1984) had reported liquefaction in the 1981 event, and found no evidence of liquefaction at any of them except for Wildlife". It cannot be conclusively proved whether the looser zone in the upper part of the sand layer below the clay layer is due to loosening by void redistribution during earlier earthquakes or only due to natural deposition in a looser state

Lateral spreading at Pence Ranch, Borah Peak, Idaho, U.S.A. (1983)

The 1983 Borah Peak, Idaho earthquake (Ms = 7.2) caused lateral spreading in the Pence Ranch area in Borah Peak, Idaho (Youd et al. 1985; Andrus et al. 1991; Dobry and Liu 1992). Youd et al. (1985) reported details of the post earthquake survey of the area (Fig. AIII-25). He described the main features of the spread as follows, "A curved zone of fissures and sand boils marked the head of the spread and passed beneath a house, barn, and adjacent ranch yards. The fissures were as wide as 1 ft (0.3 m) with scarps as high as 1 ft (0.3 m). Sand boil deposits as

wide as 8 ft (2.5 m) were composed of gravelly sand with pebbles as much as 1 in (25 mm) across".

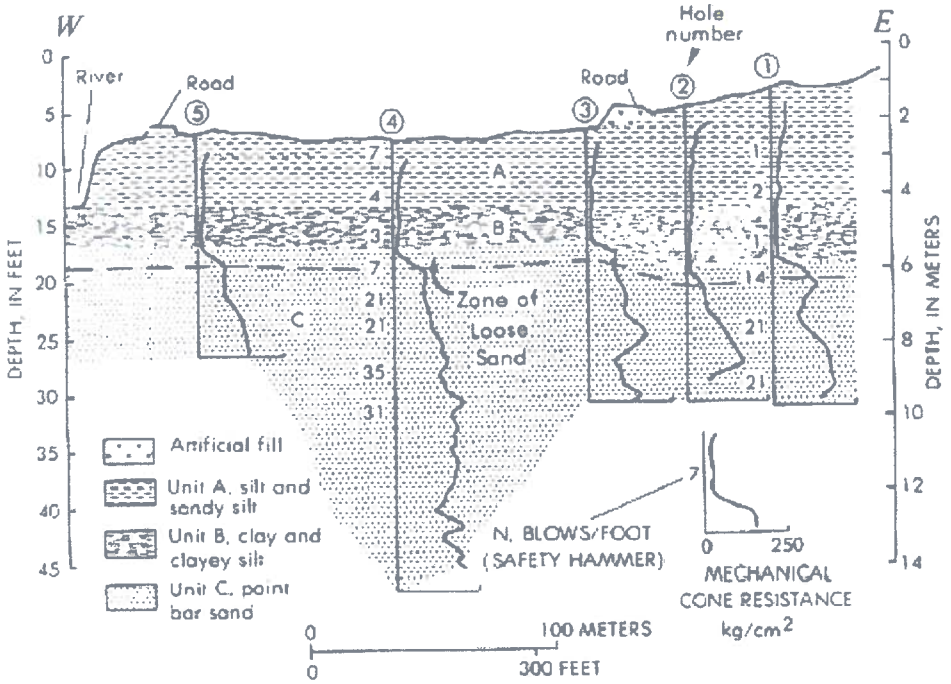

Fig. AIII-24: CPT data from River Park, Brawley, showing a looser zone immediately below the lower permeability layer (Youd, 1984).

(a) (b)

Fig. AIII-25: Lateral spreading at Pence Ranch (a) Gravel ejecta around a boil near the ranch house, and (b) Fence pulled apart by 30 inches due to lateral movements near the hay yard (Youd et al., 1985).

APPENDIX IV

BULK MODULUS OF WATER-AIR MIXTURE

A IV.1 Bulk Modulus of Pore Fluid of Water-Air Mixture

The amount of pore gas in a soil sample is related to *Skempton's B* value and the stiffness of the fluid is related to the amount of gas present and hence *B* value. Fig. *AIV-1* shows the 3-phase system of partially saturated soils. Pore gas pressure and volume change respond in accordance with *Boyle's law*, and *Henry's law* governs dissolving of free gas into the water. The effect of *Henry's law* is very small and has not considered in this study.

Assuming negligible volume change for the soil solid component ($\Delta V_s = 0$) and no escape of gas (air) from the water-gas mixture the following equations for fluid mix stiffness can be derived.

$$V_v = n \,.\, V \qquad \text{[IV-1]}$$

$$V_{water} = n \,.\, S_r \,.\, V \qquad \text{[IV-2]}$$

$$V_{gas} = n \,.\, (1 - S_r) \,.\, V \qquad \text{[IV-3]}$$

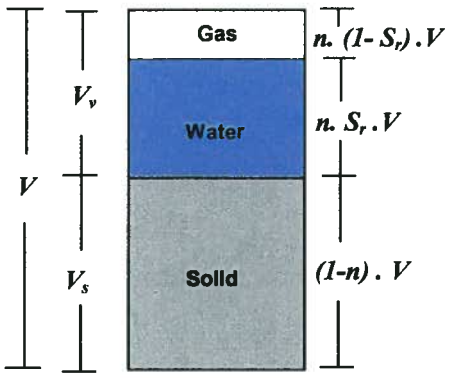

Fig. AIV-1: 3-phase system of partially saturated soil.

$$\Delta V_{water} = (\varepsilon_v)_{water} \,.\, n \,.\, S_r \,.\, V \qquad \text{[IV-4]}$$

$$\Delta V_{air} = (\varepsilon_v)_{air} \,.(1 - S_r).n. \; V \qquad \text{[IV-5]}$$

$$(\varepsilon_v)_{water} = \frac{\Delta u}{Kw} \qquad \text{[IV-6]}$$

where

n: porosity

S_r: saturation

$(\varepsilon_v)_{water}$: volumetric strain of water

K_w: bulk modulus of water

V_{gas}, V_{water}, V_v and V: volume of gas, water, voids and total volume respectively.

Based on *Boyle's gas* law volume of free gas varies with absolute gas pressure as:

$$\Delta(V \,.\, U)_{gas} = 0 \qquad \text{[IV-7]}$$

$$\Delta V_{gas} \,.\, U_{gas} + V_{gas} \,.\, \Delta U_{gas} = 0 \qquad \text{[IV-8]}$$

$$\left(\frac{\Delta V}{V}\right)_{gas} = \frac{\Delta U_{gas}}{U_{gas}} \qquad \text{[IV-9]}$$

$$(\varepsilon_v)_{gas} = \frac{\Delta U_{gas}}{U_{gas}} \qquad \text{[IV-10]}$$

As pore water pressure, u (or U) and free gas (air) pressure, u_{gas} (or U_{gas}) are the same:

$$(\varepsilon_v)_{gas} = \frac{\Delta U_{gas}}{P_{abs}} \qquad \text{[IV-11]}$$

$$P_{abs} = u + P_a \qquad \text{[IV-12]}$$

$$K_{gas} = P_{abs} \qquad \text{[IV-13]}$$

$$(\varepsilon_v)_{gas} = \frac{\Delta U}{P_{abs}} \qquad \text{[IV-14]}$$

$$\Delta V_{gas} = \frac{\Delta u}{P_{abs}} n(1 - S_r)V \qquad \text{[IV-15]}$$

$$V_{water} = \frac{\Delta u}{K_w} n.S_r.V \qquad \text{[IV-16]}$$

$$\Delta V = \Delta V_{water} + \Delta V_{gas} \qquad \text{[IV-17]}$$

$$\Delta V = \Delta u\left(\frac{1}{P_{abs}}n(1-S_r)+\frac{1}{K_w}n.S_r\right)V \qquad \text{[IV-18]}$$

$$\varepsilon_v = \left(\frac{\Delta V}{n.V}\right) = \Delta u\left(\frac{1}{P_{abs}}(1-S_r)+\frac{1}{K_w}S_r\right) \qquad \text{[IV-19]}$$

$$K_{mix} = \frac{1}{\frac{1}{P_{abs}}(1-S_r)+\frac{1}{K_w}S_r} \qquad \text{[IV-20]}$$

$$\frac{K_{mix}}{K_w} = \frac{1}{\frac{K_w}{P_{abs}}(1-S_r)+S_r} \qquad \text{[IV-21]}$$

Where

U_{gas}, u and P_{abs}: absolute gas pore pressure, (relative/gauge) pore water pressure and atmospheric pressure respectively.

K_w, K_{gas} and K_{mix}: bulk modulus of water, gas and mixture respectively.

Value of K_{mix} based on Eq. IV-20 for two extreme cases of S_r = 100% and S_r = 0 equals K_w and P_{abs} respectively. Eq. IV-21 expresses K_{mix} ratio to that of water, Kw that equals 2 GPa. In deed, K_{mix} represents an equivalent fluid to that of water-gas mixture. Fig. IV-6 shows change of ratio of mix bulk modulus to that of pure water with saturation degree for different (absolute) pore air pressures. As may be seen mix bulk modulus falls dramatically due a small reduction in saturation.

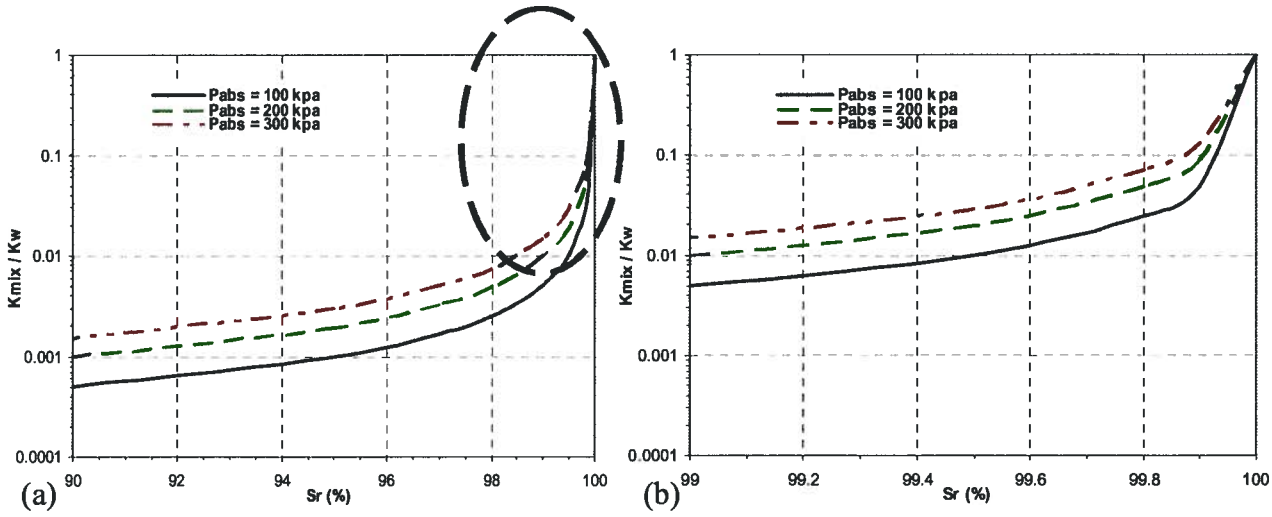

Fig. IV-2: Variation of air-water mix bulk modulus for different pore air pressures vs. saturation degree, (a) for saturation degree higher than 90%, (b) near fully saturation (> 99%).

It can be inferred from Eq. IV-20 that effect of water bulk modulus in K_{mix} magnitude is negligible ($1/K_w \approx 0$) and its value can be determined according to (absolute) pore pressure approximately, hence:

$$K_{mix} \cong \frac{P_{abs}}{1-S_r} \leq K_w \qquad \text{[IV-22]}$$

Eq. IV-20 and IV-22 assume that no gas dissolution into water occurs as the gas pressure changes. If there is enough time for dissolution to occur, the effect can be considered through *Henry's law*. Considering *Henry's law* will change S_r to (S_r + hS_r) in Eq. IV-22, in which h = ±0.02 for an air–water mixture, where h is *Henry's* volumetric coefficient of solubility (Atigh & Byrne, 2004). The effect of *Henry's law* is very small and is not considered in this study.

The mix stiffness expressed in Eq. IV-22 will change as the pore pressure changes and this can be accounted for as:

$$\frac{(K_{mix})_1}{(K_{mix})_0} = \frac{(P_{abs})_1}{(P_{abs})_0} \cdot \frac{(1-S_r)_0}{(1-S_r)_1} \qquad \text{[IV-23]}$$

For a unit volume of soil and neglecting porosity change one can derive volume of gas, V_a at different absolute pore gas pressures based on Boyle's law as:

$$P_1 \cdot V_1 = P_2 \cdot V_2 \qquad \text{[IV-24]}$$

$$V_a = n\,.\,(1\text{-}S_r) \qquad \text{[IV-25]}$$

$$P_0 \cdot n \cdot (1-S_r)_0 = P_1 \cdot n \cdot (1-S_r)_1 \qquad \text{[IV-26]}$$

$$\frac{(1-S_r)_0}{(1-S_r)_1} = \frac{(P_{abs})_1}{(P_{abs})_0} \qquad \text{[IV-27]}$$

$$\frac{(K_{mix})_1}{(K_{mix})_0} = \frac{(P_{abs})_1^2}{(P_{abs})_0^2} \qquad \text{[IV-28]}$$

Eq. IV-28 indicates that initial (absolute) pore air pressure strongly affects the bulk modulus of air-water mixture.

APPENDIX V

SKEMPTON'S B VALUE FOR PARTIALLY SATURATED SOILS

A.V.1 *Skempton's B* Value

The *Skempton's B* value which is a measure indicating soil pore pressure response (Δu) to mean total stress change ($\Delta\sigma_m$) is defined by Eq. V-1 (Skempton, 1954). In the followings it is derived for partially saturated soils:

$$B = \frac{\Delta u}{\Delta \sigma_m} \qquad [V\text{-}1]$$

Consider a dry soil skeleton that deforms due to change of effective mean stress, $\Delta\sigma'$ as:

$$(\varepsilon_v)_{ske} = \left(\frac{\Delta V}{V}\right) = \frac{\Delta \sigma'}{K_{ske}} \qquad [V\text{-}2]$$

where:

$(\varepsilon_v)_{ske}$: skeleton volumetric strain

V: skeleton (total) volume

ΔV: skeleton (total) volume change

K_{ske}: skeleton bulk modulus

Then if the voids with volume of V_v (n . V) are filled with a fluid with free gas (gas-water mixture) and compressed due to pore fluid pressure, Δu, one obtains:

$$(\varepsilon_v)_{mix} = \frac{\Delta V_{mix}}{n.V} = \frac{\Delta u}{K_{mix}} \qquad [V\text{-}3]$$

where:

$(\varepsilon_v)_{mix}$: pore fluid volumetric strain

ΔV_{mix} : pore fluid volume change

n : porosity

$n\,.\,V$: pores volume

Δu : pore fluid pressure change

K_{mix} : fluid (air-water mixture) bulk modulus

Assuming incompressible solids thus for undrained condition:

$$\Delta V = \Delta mix \qquad [V\text{-}4]$$

Introducing Eqs. III-2 and III-3 into the undrained condition of Eq. V-4 and employing Terzaghi's definition for effective stress ($\sigma = \sigma' + u$) yields:

$$\Delta V = \frac{\Delta \sigma'}{K_{ske}} V = \frac{(\Delta \sigma - \Delta u)}{K_{ske}} V \qquad [V\text{-}5]$$

$$\Delta V_{mix} = \frac{\Delta u}{K_{mix}} n.V \qquad [V\text{-}6]$$

$$\frac{(\Delta \sigma - \Delta u)}{K_{ske}} V = \frac{\Delta u}{K_{mix}} n.V \qquad [V\text{-}7]$$

$$\frac{\Delta u}{\Delta \sigma} = \frac{1}{1 + n\dfrac{K_{ske}}{K_{mix}}} \qquad [V\text{-}8]$$

Hence with referring to the definition of B coefficient (Eq. V-1):

$$B = \frac{1}{1 + n\frac{K_{ske}}{K_{mix}}} \qquad \text{[V-9]}$$

If the pore fluid contains pure water then

$$B = \frac{1}{1 + n\frac{K_{ske}}{K_{w}}} \qquad \text{[V-10]}$$

Eq. V-10 is the conventional presentation of *Skempton's B* value for fully saturated soil.

When the pore fluid contains free gas (air) one can obtain B value for partially saturated soil by substituting K_{fluid} with the equivalent fluid bulk modulus, K_{mix} as *Eq.* V-11:

$$K_{mix} = \frac{1}{\frac{1}{P_{abs}}(1 - S_r) + \frac{1}{K_w}S_r} \qquad \text{[V-11]}$$

$$B = \frac{1}{1 + n\frac{K_{ske}}{\frac{1}{P_{abs}}(1 - S_r) + \frac{1}{K_w}S_r}} \qquad \text{[V-12]}$$

$$B = \frac{1}{1 + n\frac{K_{ske}}{K_w}S_r + n\frac{K_{ske}}{P_{abs}}(1 - S_r)} \qquad \text{[V-13]}$$

For special case S_r = 100% It coincides with Eq. V-10 and for dry condition is:

$$B = \frac{1}{1 + n\frac{K_{ske}}{P_{abs}}} \qquad \text{[V-14]}$$

APPENDIX VI

GROUND CHARACTERIZATION OF WILDLIFE LIQUEFACTION ARRAY SITE

A VI.1 Introduction

In this appendix the available geotechnical data used to characterize the Wildlife Liquefaction Array WLA site is presented. These data are based on information provided in Youd et al. (1994, and 2004b); Arulanandan & Sivathasan, (2000) and Ladd et al., (1984). In addition, the new tests results carried out in the new site development campaign some 70 m away from the old site (see Fig. *AVI-2* for location) reported by Youd et al. (2004) have been used in this estimation.

A VI.2 Evaluation of *CSR* for Sandy Layer

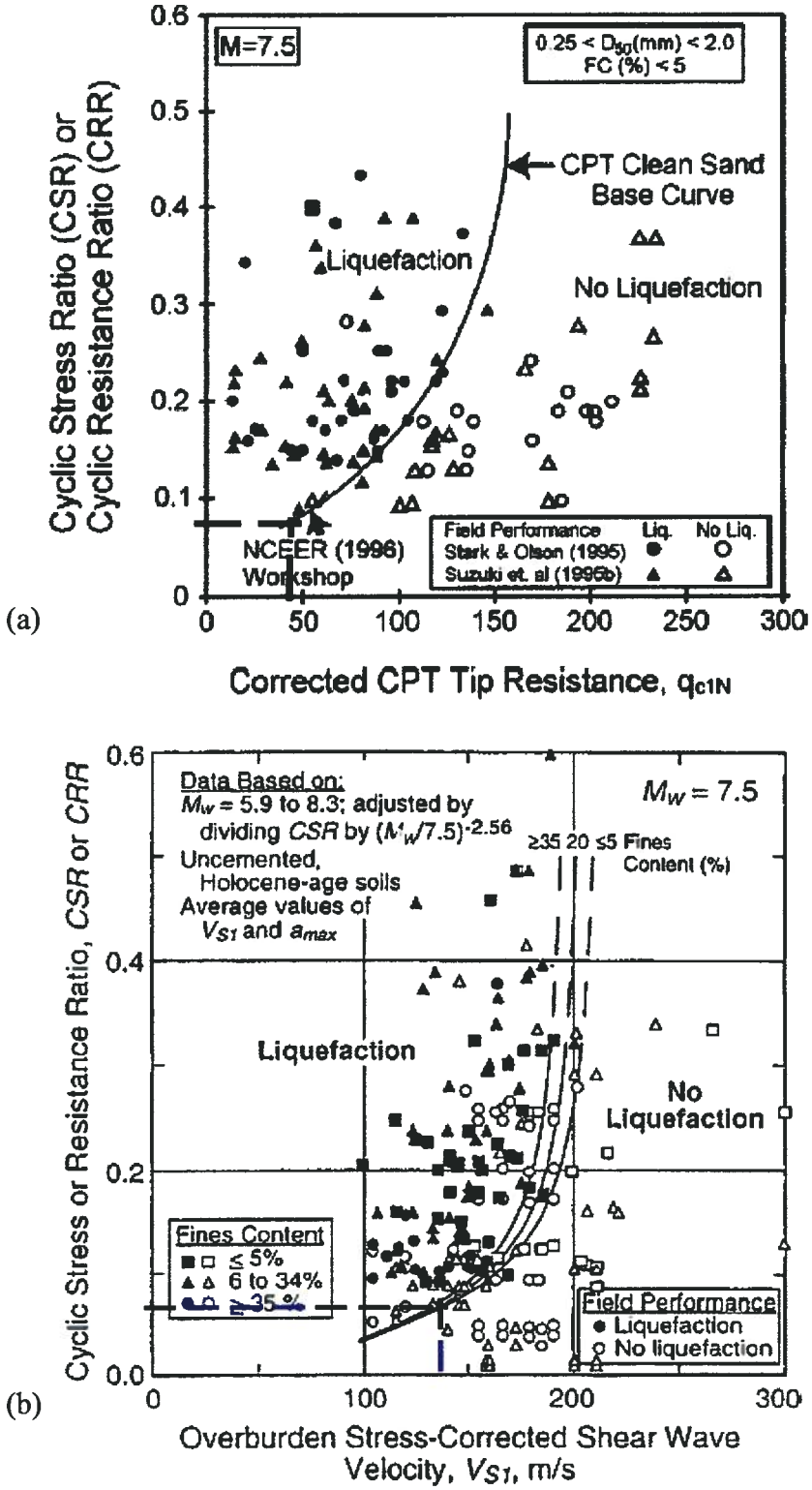

Fig. A VI-1: Evaluation of cyclic resistance ratio, *CSR* based on (a) *CPT* results (Robertson & Wride, 1998 and Youd et al., 2001) and (b) V_s measurement (Andrus & Stokoe 2000 and Youd et al., 2001).

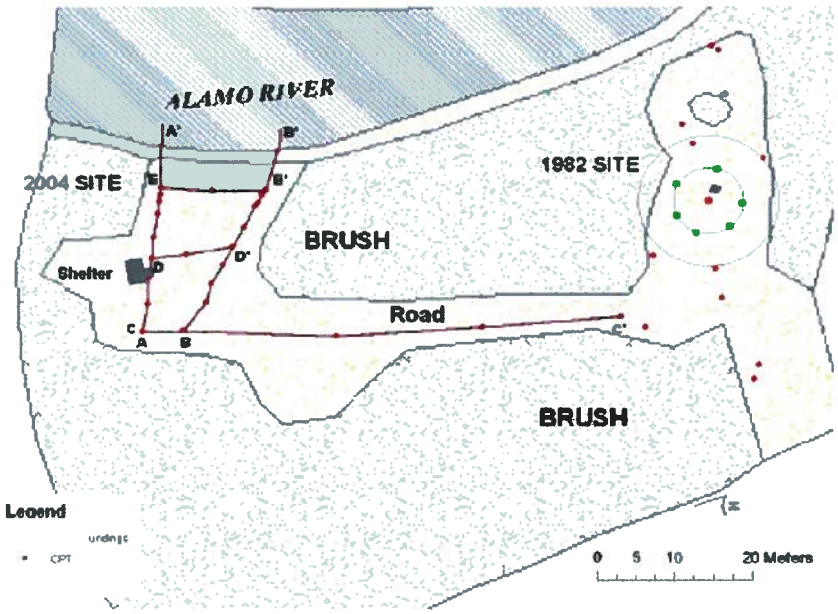

Fig. A VI-2: Map of 1982 and 2004 WLA sites showing general configurations and localities of *CPT* soundings (Youd et al., 2004).

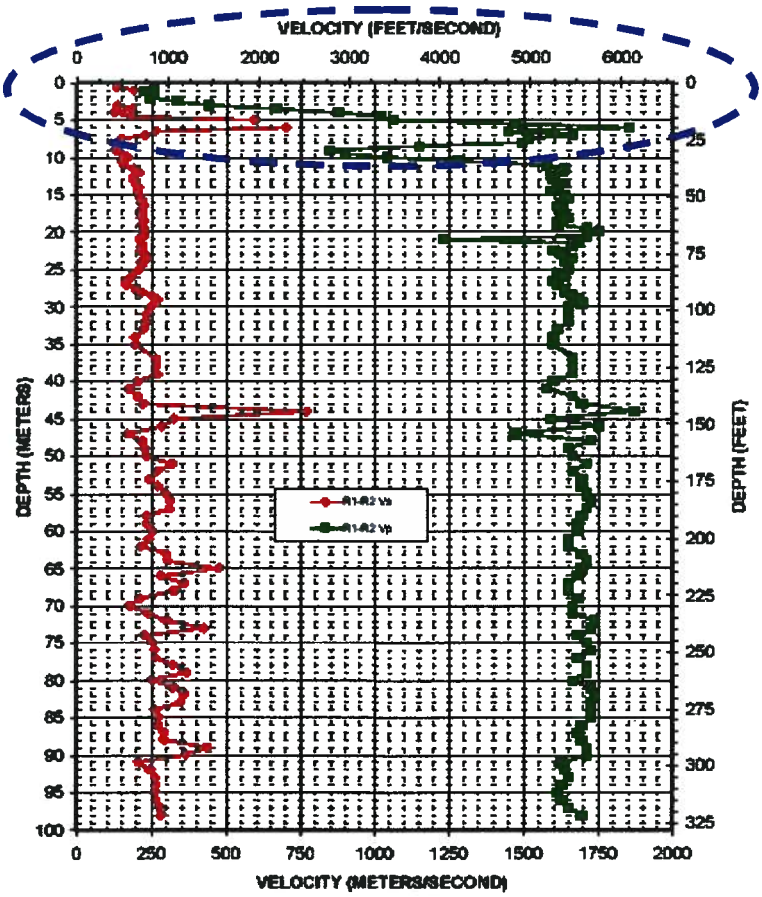

Fig. A VI-3: Measured P- and S-wave velocities with suspension logger in the 100-m deep borehole drilled at new WLA (Youd et al., 2004).

A VI.2: Estimation of Sand Layer Permeability

Table A VI-1: Range of permeability for different soils, k (m/s) suggested in Soil Mechanics textbooks by different authors

Soil	Lee, White Ingles, 1983[a]	Cuduto, 1999	Analysis Values
Silty sand	2.0×10^{-5} to 10^{-6}	10^{-4} to 10^{-5}	1.0×10^{-5}
Silt	5×10^{-6} to 10^{-7}	10^{-5} to 10^{-10}	3.0×10^{-8}
Clay	$<10^{-8}$	10^{-5} to 10^{-12}	3.1×10^{-9}

a) Based on Harr, 1977, Terzaghi & Peck, 1967 and Lambe & Whitman, 1969

Table A VI-2. Permeability, k (m/s) values considered by different investigators for Wildlife site

Layer	Arulanandan & Sivathasan, 2000	Soroush & Koohi, 2004	Gu, Morgenstern & Robertson, 1994	Analysis Values
Silty sand	2.1×10^{-5}	2.1×10^{-6}	10^{-3}	1.0×10^{-5}
Silt	3.0×10^{-6}	5.0×10^{-7}	10^{-5}	3.0×10^{-8}
Clay	3.1×10^{-9}	1.0×10^{-8}	----	3.1×10^{-9}

Note: Permeability of 2.1e-3 (cm/s) for sand layer from a field test carried out by Ladd (1984) was reported by Kulasingam (2003).

The considered permeability for the sandy layer in the analyses is compared with the recent field falling head tests results (Youd et al., 2004) conducted in new site in Fig. AIV-4.

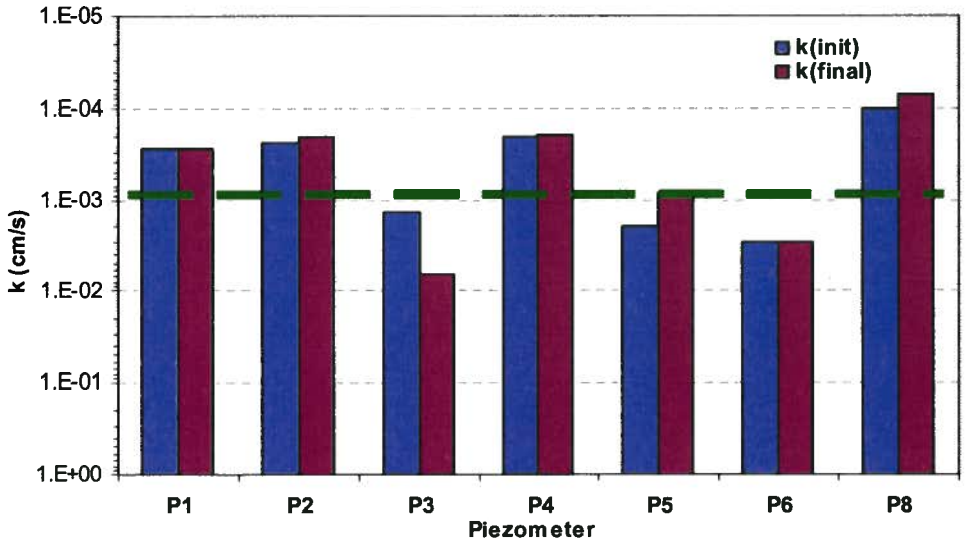

AVI-4: Field falling head tests data in sand liquefiable layer in new WLA site.

k_{init}: permeability at initial stage of testing.
k_{final}: permeability at final stage of testing.